The Structure of Molecular Liquids: Neutron Diffraction and Molecular Dynamics Simulations

Laurent Bianchi

May 2000

A thesis submitted to the university of Abertay-Dundee (U.K.) and université de Provence (France) in accordance to the requirements for the degree of Doctor of Philosophy and of Docteur de l'université de Provence.

The Structure of Molecular Liquids: Neutron Diffraction and Molecular Dynamics Simulations

Laurent Bianchi

A thesis submitted in partial fulfilment of the requirements of the University of Abertay Dundee (U.K.) for the award of the degree of Doctor of Philosophy

in collaboration with the Université de Provence (Aix-Marseille I, France) for the award of the degree of Docteur de l'université de Provence (Aix-Marseille I) Mention : Sciences Physiques

Université de Provence
(Aix-Marseille I)
Institut Universitaire des Systèmes Thermiques Industriels U.M.R.-CNRS 65 95

School of Science and Engineering,
University of Abertay-Dundee.

May 2000

I certify that this thesis is the true and accurate version that has been approved by the examiners.

Signed..... Date..22 JUNE 2000

(Director of studies)

University of Abertay-Dundee Library

Reproduction of Project Report

Author: Laurent BIANCHI

Title: The Structure of Molecular Liquids: Neutron Diffraction and Molecular Dynamics simulations

Qualification : Ph.D.

Year : 2000

Signature..

A Nacera, pour tous ces mois sans toi,
pour tous ces toi sans moi.

En hommage à Yvonne, ma grand-mere

A la mémoire de Jean Pierre

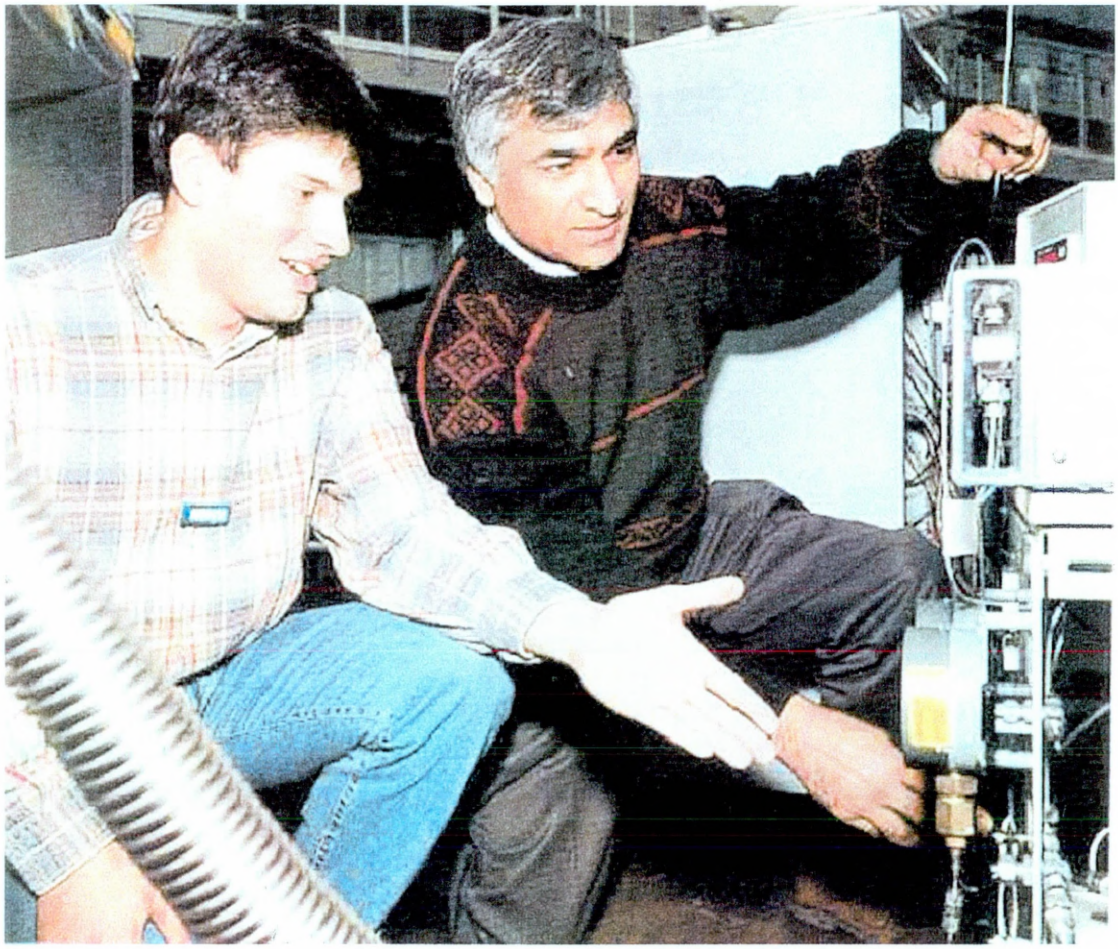

Ashok K. Adya (on the right) and myself (on the left) playing with neutrons at ISIS.

Abstract

Neutron diffraction (ND) measurements on liquid methanol (CD_3OD, $CD_3O(H/D)$, CD_3OH) under ambient conditions were performed to obtain the distinct (intra- + inter-molecular), $G^{dist}(r)$ and inter-molecular, $G^{inter}(r)$ radial distribution functions (rdfs) for the three samples. The H/D substitution on hydroxyl-hydrogen (Ho) has been used to extract the partial distribution functions, $G_{XHo}(r)$ (X=C, O, and H – a methyl hydrogen) and $G_{XX}(r)$ at both the distinct and inter-molecular levels from the difference techniques of ND. The O-Ho bond length, which has been the subject of controversy in the past, is found purely from the distinct partial distribution function, $G_{XHo}(r)$ to be 0.98 ± 0.01 Å. The C-H distance obtained from the distinct $G_{XX}(r)$ partial is 1.08 ± 0.01 Å. These distances determined by fitting an intra-molecular model to the total distinct structure functions are 0.961 ± 0.001 Å and 1.096 ± 0.001 Å, respectively. The inter-molecular $G_{XX}(r)$ function, dominated by contributions from the methyl groups, apart from showing broad oscillations extending up to ~14 Å is featureless, mainly because of cancellation effects from six contributing pairs. The Ho···Ho partial pair distribution function (pdf), $g_{HoHo}(r)$, determined from the second order difference, shows that only one other Ho atom can be found within a mean Ho···Ho separation of 2.36 Å. The average position of the O···Ho hydrogen bond determined for the first time purely from experimental inter-molecular $G_{XHo}(r)$ partial distribution function is found to be at 1.75 ± 0.03 Å.

The experimental structural results at the partial distribution level are compared with those obtained from molecular dynamics (MD) simulations performed in NVE ensemble by using both 3- and 6-site force field models for the first time in this study. The MD simulations with both the models reproduce the ND rdfs rather well. However, discrepancies begin to appear between the simulated and the experimental partial distribution functions, showing that the agreement at the rdf level does not provide a critical evaluation of appropriateness of a chosen potential model to reproduce the observed liquid structure. Both the simulations reproduce equally well the X-X partial comprising of six correlations. The ability of the 3-site model simulations to satisfactorily reproduce this function dominated by contributions from the methyl group, demonstrates that the methyl group does not participate in any bonding in the liquid. However, the main peaks of the simulated Ho-Ho pdf are found to be slightly higher and shifted to larger distances as compared to the ND results. A comparison of the simulated and ND X-Ho inter-molecular functions dominated by H-Ho correlations shows that although the 3-site model reproduces at least qualitatively the experimental features, the six-site model fails badly.

The structure of liquid benzene at 298 K is investigated by performing molecular dynamics (MD) simulations in NVE ensemble using three different force field models differing both in their functional form and in the way they were devised. Surprisingly however, they lead to similar results for the pdfs. The structural results from MD simulations are compared with the neutron diffraction (ND) results where the newly C-C, C-H and H-H inter-molecular pdfs are obtained in this study by the H/D substitution on hydrogen atoms of benzene. A good agreement is found between the simulated and experimental total inter-molecular rdfs for C_6D_6 and $C_6(H/D)_6$ experimental, but not for C_6H_6. Most of the structural properties of benzene discussed in the past have been based on the models, which showed a reasonable agreement

between the simulated and neutron inter-molecular rdf or X-ray C-C pdf. The C-C pdf extracted from the present ND studies however differs from the one obtained earlier from the X-ray measurements. Apart from that, the simulated C-C pdf reproduces the corresponding ND function better than that obtained from the X-rays. Nevertheless, comparisons between the MD and ND results for the C-H and H-H pdfs show significant discrepancies, which highlight the need to further refine the existing force field models.

Neutron diffraction (ND) measurements were also performed on benzene-methanol liquid mixture (molar ratio 1:2) under ambient conditions. The H/D isotopic substitution technique on the hydrogens of both the hydroxyl group of methanol (Ho) and benzene (HB) was used to extract the solvent-solvent, solute-solute and solute-solvent correlations. The ND structural results of the mixture are interpreted with the help of the experimental results of its pure components. The results reveal that the self-association of methanol due to hydrogen bonding is hardly disrupted by the addition of benzene. Investigations of the solute-solvent and solute-solute correlations show that although a weak association exists between benzene and methanol molecules, there is no evidence to suggest the formation of a π-hydrogen bond between them in the liquid state. The benzene molecules thus, play the role of an inert solute in the mixture.

The experimental structural results for the benzene-methanol liquid mixture are compared with those obtained from molecular dynamics (MD) simulations performed with an inter-molecular potential model built from the two force field models used in simulating the behaviour of the two pure components. The simulated structural results of the mixture are interpreted with the help of the simulated results of the pure components. Although an overall agreement is obtained between the simulated and experimental inter-molecular rdfs, a comparison of the partial distribution functions reveals that model potentials for the mixture need to be refined.

Résumé

Des mesures par diffraction de neutrons (DN) ont été conduites sur le méthanol liquide (CD_3OD, $CD_3O(H/D)$, CD_3OH), sous conditions ambiantes, afin d'obtenir les fonctions de distributions radiales (fdrs), distinctes (intra- + inter-moléculaire), $G^{dist}(r)$, et inter-moléculaires, $G^{inter}(r)$, pour les trois échantillons. La méthode de substitution isotopique H/D appliquée sur l'hydrogène du groupe hydroxyle a été utilisée pour extraire les fonctions de distributions partielles, $G_{XHo}(r)$ (X=C, O, et H – un hydrogène du groupe méthyle) et $G_{XX}(r)$ au niveau intra- + inter-moléculaire et inter-moléculaire en exploitant la méthode des différences. La longueur de la liaison intra-moléculaire O-Ho, qui a été le sujet d'une controverse par le passé, a été trouvée à 0,98 ± 0,01 Å, purement à partir de la fonction de distributions partielle $G_{XHo}(r)$, indépendamment de tout modèle intra-moléculaire raffiné contre les sections efficaces différentielles de diffraction. La longueur de liaison C-H a, elle, été déterminée directement de la fonction de distributions partielle distincte, $G_{XX}(r)$, à 1,08 ± 0,01 Å. Ces même distances déterminées avec un modèle moléculaire raffiné à partir des section efficaces différentielles distinctes donnent, respectivement, 0,961 ± 0,001 Å et 1,096 ± 0,001 Å. Bien que la fonction de distributions partielle inter-moléculaire, $G_{XX}(r)$, révèle de larges oscillations s'étendant jusqu'à des distances de l'ordre de ~14 Å, elle est dominée par les contributions du groupe méthyle et apparaît assez lisse puisque six paires de corrélations y participent. La fonction de distributions de la paire (fdp) Ho-Ho, $g_{HoHo}(r)$, déterminée par la méthode des différences au second ordre, révèle que seul un atome Ho se trouve à l'intérieur d'une sphère de diamètre 2,36 Å centrée sur un autre atome Ho. La liaison hydrogène O···Ho, mise en évidence pour la première fois expérimentalement dans cette étude, par la fonction de distributions partielle intermoléculaire, $G_{XHo}(r)$, révèle que la distance de séparation la plus probable O···Ho est de 1,75± 0.03 Å.

Ces fonctions de distributions expérimentales ont été comparées avec celles obtenues par des simulations de dynamique moléculaire (DM) dans l'ensemble micro canonique en utilisant des modèles de potentiels intermoléculaires à 3- et 6-sites. Bien que ces simulations reproduisent correctement les fdrs intermoléculaires, des désaccords apparaissent entre les fonctions de distributions expérimentales et simulées au niveau des fonctions de distributions partielles. Ainsi, un bon accord entre les modèles et les fdrs ne représente pas une condition suffisante pour évaluer l'applicabilité d'un champs de force, généralement utilisé pour obtenir des informations structurales inaccessibles par l'expérience. Par contre les deux simulations reproduisent relativement bien la fonction de distributions partielle intermoléculaire X-X comprenant six fonctions de distributions de paires. La capacité du modèle à 3 sites à reproduire de manière satisfaisante cette fonction dominée par les contributions du groupe méthyle démontre que le groupe méthyle ne participe à aucune liaison intermoléculaire dans le liquide. Cependant dans le cas de la fdp Ho-Ho, les pics principaux des fonctions simulées sont tous deux légèrement plus grands, et surtout leurs positions sont décalées vers des distances plus grandes par rapport à la même fonction obtenue par DN. Lorsque les fonctions de distributions partielles X-Ho expérimentale et simulée sont comparées, l'accord de la fonction issue du modèle à 3 sites avec sa jumelle expérimentale est meilleur qu'avec celle du modèle à 6 sites.

La structure du benzène liquide a été étudiée par des simulations de dynamique moléculaire dans l'ensemble micro canonique en utilisant trois modèles de potentiel intermoléculaire qui diffèrent non seulement dans leur forme fonctionnelle mais aussi dans la manière dont ils ont été obtenus. Malgré ces différences, les fdps obtenues sont toutes identiques. Les résultats de ces simulations sont comparés avec ceux obtenus par DN où les fdps inter-moléculaires C-C, C-H et H-H nouvellement extraites dans cette étude l'ont été en employant la substitution isotopique H/D sur les noyaux d'hydrogène des molécules de benzène. L'accord entre les simulations et l'expérience est bon pour les fdrs intermoléculaires C_6D_6 et $C_6(H/D)_6$, mais est relativement pauvre pour C_6H_6. Jusqu'ici la plupart des propriétés structurale du benzène liquide ont été discutées en s'appuyant sur la capacité qu'un modèle de potentiel intermoléculaire a, de reproduire raisonnablement la fdrs du benzène deutéré obtenue par DN ou/et la fdp C-C issue de mesures par rayons X. La fdp C-C obtenue dans le cadre de cette étude par DN est cependant différente de celle extraite par rayons X. En particulier, les fdps C-C simulées reproduisent mieux la fonction dérivée des mesures de DN que celle obtenue par rayons X. Néanmoins, lorsque les fdps C-H et H-H expérimentales et simulées sont comparées, d'importants désaccords sont observés, mettant ainsi en évidence le besoin d'affiner les champs de force existants pour ce liquide.

Des mesures par diffraction de neutrons (DN) ont été aussi conduites sur un mélange liquide de benzène et de méthanol (dans le rapport molaire 1:2) sous conditions ambiantes. La méthode de substitution isotopique sur les noyaux d'hydrogène du groupe hydroxyle des molécules de méthanol et sur ceux du benzène a été utilisée afin d'extraire les corrélations solvant-solvant, soluté-soluté et solvant-soluté. Les résultats expérimentaux du mélange sont interprétés à l'aide des résultats obtenus pour les composés purs. Ceux ci montrent clairement que la liaison hydrogène responsable de l'auto-association des molécules de méthanol est n'est absolument pas rompue par l'addition de benzène. L'étude des corrélations soluté-solvant et soluté-soluté révèle que bien qu'une faible association entre benzène et méthanol existe, il n'y a cependant aucune évidence pour suggérer la formation d'une liaison hydrogène-π entre eux à l'état liquide. Ainsi, dans le mélange, le benzène a le rôle d'un soluté inerte.

Les résultats expérimentaux du mélange ont été comparés avec ceux obtenus par dynamique moléculaire en employant un modèle de potentiel inter-moléculaire construit à partir de deux champs de forces utilisés dans les simulations numériques des composés purs. Bien qu'un accord général ait été obtenu entre les fdrs expérimentales et simulées, le champs de force construit pour simuler les propriétés structurales du mélange requiert quelques raffinements dans le but de reproduire les fonctions de distributions partielles.

Acknowledgements

I would like to say a big thank-you and heartfelt gratitude to my supervisor, Dr. A. K. Adya for his unending support. Without him this research project would never have reached the depth it did. I am also greatly indebted to him for his patience, encouragement and help at the time I could hardly understand and speak English.

Special thanks go to Prof. M. Gaune-Escard (IUSTI, France), without whom I would never have experienced such an adventure.

Sincere thanks are due to Dr. C. J. Wormald (Bristol University, U. K.) for a great deal of time and help he provided on innumerable occasions throughout the experimental part of this project.

A debt of gratitude is owed to Prof. A. K. Soper (ISIS, Rutherford Appleton laboratory, U. K.), who kindly taught me how to use his EPSR program and provided his precious neutron data on benzene.

Thanks are due to Mr. M. Black and Mr. K. Sturrock at the School of Science and Engineering of the University of Abertay Dundee (UAD), for the technical help in running the IRIS computer used for computer simulation studies.

I would also like to thank visitors and other colleagues in Dr. Adya's "Condensed Matter & Molecular Structures Research Group" during the past three years: Dr. O. N. Kalugin (Kharkov University, Ukraine) for his invaluable help in the simulation work, Dr. H. Matsuura (Tokyo institute of technology, Japan) and Mr. M. Shcherbakov for their useful contributions along the way.

Last but not the least, I would like to thank my parents. Without their constant love, support and belief in me, I would not have been able to achieve this.

Table of contents

Chapter 3: Molecular dynamics simulation methods

Chapter 4: Theoretical background to neutron diffraction

Chapter 5: Experimental methods and data reduction

Chapter 6: The structure of liquid methanol

Chapter 7: The structure of liquid benzene

Chapter 8: Structure of benzene-methanol liquid mixture

Chapter 9: Conclusions

Appendix A: The stucture of Benzene-water mixture

Glossary of symbols and short-hand terms used

Roman uppercase

A thermodynamic potential in the canonical ensemble (chapter 2)

$A(t)$ generic dynamic quantity (chapter 3)

Å angstrom

$\langle A \rangle$ time average of the quantity A (chapter3)

$\langle B \rangle$ ensemble average of the quantity B (chapter 2)

$B^{dist}(r)$ distinct background function (chapter 5)

$C(t)$ generic time correlation function (chapter 3)

$C_{vv}(t)$ velocity auto-correlation function (chapter 3)

D self-diffusion constant (chapter 3)

E, E' initial and final energies of neutron (chapter 4, 5)

$E_\lambda, E_{\lambda'}$ initial and final energies of scattering system (chapter 4)

E total (kinetic + configurational) energy (chapter 3)

E_{rec} recoil energy given to a nucleus by a incident neutron (chapter 5)

E_{kin} kinetic energy (chapter 3)

F^i flux of neutrons in the incident beam (chapter 4)

G(r) generic distribution function

$H_N(\boldsymbol{r}^N \boldsymbol{p}^N)$ Hamiltonian of the system containing N constituent units (chapter 2)

I(θ,Q_e) scattering intensity (chapter 5)

I_{xx}, I_{yy}, I_{zz} principal components of inertia tensor (chapter 3)

$\boldsymbol{I}$ molecular moment of inertia (chapter 3)

$\underline{\boldsymbol{I}}$ rotational inertia tensor (chapter 3)

$\boldsymbol{J}$ angular momentum (chapter 3)

K Kelvin

L length of one edge of the simulation cubic box (chapter 3)

L_0 moderator to sample flight path (chapter 5)

L_1 sample to detector flight path (chapter 5)

M the total number of time steps used in a production run (chapter 3)

M^* number of excluded atoms in a given molecule (chapter 3)

$M(t)$ total number of available time origin according to the time delay t (chapter 3)

N number of constituent units

N^* number of point charges in the system discounting any excluded atoms in a given molecule (chapter 3)

$N(r, \Delta r)$ number of atoms found in $V(r, \Delta r)$ (chapter 3)

N_m number of molecules in the system (chapter 4)

N_t all the different type of nuclei α appearing c_α times in the molecule (chapter 4)

N_c number of constraints on the system (chapter 3)

P_{MD} computed pressure from MD simulations (chapter 3)

P pressure

P^{LR} long-range correction to P_{MD} (chapter 3)

$Q_N(V,T)$ canonical partition function (chapter 2)

$\boldsymbol{Q}$ transferred momentum ($\boldsymbol{Q} = \boldsymbol{k} - \boldsymbol{k}'$) (chapter 4)

Qe modulus of the transferred wave vector within the static approximation (chapter 5)

$\boldsymbol{Q}$ quaternion (chapter3)

$\boldsymbol{R_i}$ position vector associated to a nucleus i of the scattering system (chapter 4)

R agreement factor (equation 5.49)

$S(\boldsymbol{Q},\omega)$ dynamic scattering function (chapter 5)

$S(\boldsymbol{Q})$ structure factor (chapter 4)

$S^{tot}(\boldsymbol{Q},\omega)$ van Hove dynamic structure factor (weighted sum of the self and distinct dynamic structure factor) (chapter 5)

$\underline{\boldsymbol{R}}$ rotational matrix (chapter 3)

$S_{\alpha\beta}^{self}(\boldsymbol{Q},\omega)$ self dynamic structure factor for the nucleus α (chapter 5)

$S_{\alpha\beta}^{dist}(\boldsymbol{Q},\omega)$ distinct dynamic structure factor for the α-βpair (chapter 5)

$\boldsymbol{T}$ torque (chapter 3)

T absolute temperature

U_c configurational energy computed from the MD simulations (chapter 3)

U generic configurational energy

U^{lr} long-range correction to U_c (chapter 3)

$\hat{V}$ neutron-matter interaction potential (chapter 4)

V volume

$V(r, \Delta r)$ volume of a spherical shell of radius r and thickness Δr (chapter 3)

$V_N(\boldsymbol{r}^N)$ potential energy function (chapter 2)

$W_{\alpha\beta}$ generic neutron weighting for the α-β pair (chapter 6, 7)

$Z = \Sigma_\lambda \exp(-E_\lambda/k_BT)$ canonical partition function (chapter 4)

$Z_N(V,T)$ potential part of the canonical partition function (chapter 2)

Roman lower case

b barn ($=10^{-24}\text{cm}^2$)

b scattering length (chapter 4)

$\bar{b}$ coherent scattering length (chapter 4)

$d\Omega$ element of solid angle (chapter 4)

$d^2\sigma/d\Omega dE'$ partial differential cross-section (chapter 4)

$d\sigma/d\Omega$ differential cross-section (chapter 4)

d_{12} bond length between atom 1 and 2 (chapter 3)

eV electron volt (chapter 5)

$e(k)$ efficiency of a detector (chapter 5)

$\boldsymbol{fi}$ force acting on atom/site i (chapter 3)

$\boldsymbol{fij}$ force on atom/site i due to j (chapter 3)

$\boldsymbol{f}^N(r^N,p^N,t)$ probability density in a $6N$ phase space dimension (chapter 9)

fs fento second ($=10^{-15}$s)

$g^{(n)}_N(r^n)$ n-particle distribution function in the canonical ensemble (chapter 2)

$g^{(n)}(r^n)$ n-particle distribution function in the grand canonical ensemble (chapter 2)

$g^{(2)}(\boldsymbol{r}^n)$ pair distribution function (chapter 2)

$\boldsymbol{g}$ constraint force (chapter 3)

$\hbar$ Planck constant/2π

k_B Boltzmann constant

$\boldsymbol{k}, \boldsymbol{k}'$ initial and final wave-vectors of neutron (chapter 4)

k_e modulus of the wave vector within the static approximation (chapter 5)

k_{max} largest reciprocal space vector used in reciprocal Ewald sum (chapter 3)

m neutron mass (chapter 4)

m_n neutron mass (chapter 5)

m_i mass of the site i

n number of particles in subsystem of liquid (chapter 2)

$n(r)$ generic running co-ordination number

ps pico second ($=10^{-12}$s)

p_λ probability of the target system being in state λ (chapter 4)

$\boldsymbol{p}$ generic term for the momentum

q_i Coulombic charge on site i

$\boldsymbol{r}$ position vector associated to the neutron (chapter 4)

r radial distance

r_{ij} distance between atom/site i and atom/site j

r_c distance at which the potential is truncated

str steradian

$\boldsymbol{s}_i$ position unit vector (chapter 2 equation 2.72)

t_{relax} relaxation time

t_{sample} sampling time

t_{equil} equilibration time

t_k discrete time (chapter 3)

t_{obs} TOF taken for a neutron to travel the total flight path ($L_0 + L_1$) (chapter 5)

t_0 an initial time or time origin (chapter 3)

t time variable

u_{ij} displacement of nucleus i relatively to nucleus j (chapter 4)

$u(r)$ effective pair potential

$\boldsymbol{v}$ generic term for the velocity

z fugacity ($=\lambda^{-3}\exp\beta\mu$) (chapter 2)

2θ scattering angle (chapter 5)

Greek uppercase

Δt time step (chapter 3)

Δ laplacian operator ($= \nabla^2$)

Φ incident neutron flux (chapter 4, 5)

$\phi_\lambda(\boldsymbol{R})$, $\phi_{\lambda'}(\boldsymbol{R})$ the initial and final wave functions of a target particle (chapter4)

Ω thermodynamic potential in the grand canonical ensemble (chapter 2 equation 2.17)

$\Sigma_S(\theta,Q_e)$ TOF differential cross-section (chapter 5)

$\Theta(\mu,V,T)$ grand canonical partition function (chapter 2)

ψ generic wave function (equation 1.1)

∇_{ri} gradient operator with respect to the position r_i (chapter 2)

Greek lowercase

$\beta = 1/k_BT$ (chapter 2)

χ^2 quality factor (chapter 5)

χ_T isothermal compressibility (chapter 2)

$\delta(x)$ Dirac delta distribution

δ_{ij} Kronecker symbol

ε energy at minimum of Lennard-Jones pair potential (chapter 3)

ε_0 permittivity of a vacuum (chapter 3)

γ_{ij} Debye-Waller factor associated to nuclei i and j(chapter 4)

λ neutron wave-length (chapter 5)

λ_e neutron wavelength within the static approximation (chapter 5)

λ, λ' initial and final states of the scattering system (chapter 4)

λ de Broglie wave-length (chapter 2, equation 2.5)

$\vec{\mu}$ dipole moment (chapter 6)

μ chemical potential (chapter 2)

θ,ϕ,ψ Euler angles (chapter 3)

ρ average number density

$\rho^{(n)}{}_N(r^n)$ n-equilibrium particle density in the canonical ensemble (chapter 2)

$\rho^{(n)}(r^n)$ n-equilibrium particle density in the grand canonical ensemble (chapter 2)

σ_i uncertainty associated to the data point i (chapter 5, section 6)

σ the distance to the zero in a Lennard-Jones pair potential (chapter 3)

σ_{coh} coherent scattering cross-section ($= 4\pi \bar{b}^{\,2}$) (chapter 4)

σ_{incoh} incoherent scattering cross-section ($= 4\pi \overline{b^2}$) (chapter 4)

σ_a absorption scattering cross-section (chapter 4)

τ dummy variable in integration over time (chapter 3)

ω angular velocity (chapter3)

ω defined by $\hbar\omega = E - E'$ (chapters 4 and 5)

Abbreviations

BM benzene-methanol

BW benzene-water

CM cyclohexane-methanol

DCS differential cross-section

EPSR empirical potential structure refinement

ESS european spallation source

EW ewald summation

FIQA Fincham's implicit quaternion algorithm

LJ Lennard-Jones

MC Monte-Carlo

MD molecular dynamics

MIN minimum noise reconstruction

MSD mean square displacement

NDIS neutron diffraction with isotopic substitution

PSF partial structure factor

QCC quantum chemical calculations

QM quantum mechanical

RF reaction field

SF shifted force

SLF self

S substituted site

SANDALS small angle neutron diffractometer for amorphous and liquid samples

TOF time of flight

VACF velocity auto-correlation function

Vlf Verlet leap-frog algorithm

X-X non-substituted site-non-substituted site

const constant

incoh incoherent

coh coherent

dist distinct

distinct intra- + inter- molecular

inter inter-molecular

pdf pair distribution function

rdf radial distribution function

rcn running co-ordination number

tot total

total coherent + incoherent

Subscripts and superscripts

* complex conjuguate

^{T} transpose

$\bar{}$ average over nuclear spin orientations and distributions

∂_t derivative with respect to t

Chapter 1

Introduction

1.1 The liquid state

The existence of matter in three different phases (solid, liquid and gas) is a fact of every day experience. Solids are rigid and give sharp Bragg peaks in a diffraction experiment (see figure 1.1), demonstrating an ordered arrangement of atoms or molecules. Instead, liquid and gases give diffuse peaks (see figure 1.1), showing that there is no long-range ordered arrangement of the constituent atoms or molecules. van der Waals was the first to point out the continuity of the liquid and gaseous states. At temperatures below the critical temperature the two fluid phases can coexist in equilibrium: the denser phase is called the liquid, and the less dense phase is called the gas. Above the critical temperature, coexistence of fluid phases is not observed. One can pass continuously from low-temperature gas to low-temperature liquid by heating above the critical temperature, compressing, and cooling. The essential difference between liquid and gas is in density; as a result, liquid and gas differ by the importance of collisional processes and short-range correlations.

The two main states of condensed matter, solids and liquids, have in common the large number of atoms or molecules subject to attractive forces sticking them together at the limit of their inter-penetrability, while the repulsive forces have a tendency to impose some structure in accordance with the geometrical form of their constituent units (atoms or molecules). Moreover, in the liquid state, the mobility, the number of interacting atoms or molecules and their proximity to each other make this state of matter more difficult to understand than the solid or the gaseous state. In the two

condensed states (solid and liquid) the molecular interactions determine both the structure and the dynamics. For the solids both properties can be directly obtained, because the order prevalent in the molecular positions and orientations of the solid state makes its structure and dynamics stable with time. In comparison, the position of atoms or molecules in the liquid state cannot be grasped due to permanent agitation of the molecules, and the structure and dynamics are obtained on average. Accordingly, one must build various statistical functions such as those describing the energy of the system (partition functions, see section 2.1-3), the average structure (radial distribution functions, see section 2.4-5) or the molecular motions (time correlation functions, see section 3.8.2). Thus, statistical methods are naturally suitable for the description of liquids, and their implementation has become systematic with the improvement of computer hardware on which numerical calculations are made. Figure 1.2 illustrates the above described features of the three states of matter.

Since a large part of the chemistry as well as the biology take place in the liquid media, understanding the liquid state is of paramount importance. Broadly speaking, the purpose of the physics of liquids is to understand why particular phases are stable in specific ranges of temperature and density. The aim is to relate the stability, structure, and dynamical properties of liquids to the size and shape of the constituent units (molecules, atoms, or ions) and the nature of the forces between them, which in turn are determined by the electronic properties. Thus, a complete theory of the liquid state would be one that explains the macroscopic properties of the liquid, ideally by solving the many-body Schrödinger equation,

$$\left(-\sum_i \frac{\hbar^2}{2m_i}\nabla_i^2 + \sum_{i<j}\frac{q_i q_j}{r_{ij}}\right)\psi = \frac{\hbar}{i}\frac{\partial\psi}{\partial t} \quad , \tag{1.1}$$

describing the motion of the nuclei and electrons, in which the sums are taken over all nuclei and electrons with appropriate masses m_i and charges q_i. Needless to say that this would be an exceedingly difficult task! Actually, the major obstacle in the development of an accurate theory of liquids is the fact that there is no idealised model compared to that for a perfect gas or harmonic solid, both of which can be

treated exactly. Therefore, the liquid state was treated as an intermediate state between a gas and a solid. This approach was widely adopted in the past, but from a theoretical point of view it is not very satisfactory, mainly because it does not take proper account of the steric factors. Lattice theories for example tend to overemphasise the solid-like character of liquids. Methods that rely on expansions in powers of the density are in some respect more useful because they allow a systematic calculation of corrections to the ideal gas behaviour. Nonetheless, they remain essentially theories of the imperfect gas, and cannot be expected to work well under triple point conditions. Thus, at present there is no comprehensive theory of the liquid state that works well for all types of liquids over a wide range of thermodynamic conditions because the mathematical solution of the statistical problem is very difficult (Wood, 1979). However, various approximate theories were developed according to the class of liquid investigated. From assumed form of the inter-atomic or inter-molecular potential energy function, by using suitable closure approximations integral equations (*e.g.* Percus-Yevick (Percus and Yevick, 1958) or hypernetted chain equations (Meeron, 1960)), it is possible to solve the statistical problem for a particular type of liquid (ionic, metallic, molecular,...). As a result, many properties such as structure can be investigated by calculating the pair correlation functions of a model system.

There are four ways of testing the accuracy of an approximate theory of liquid structure: (*i*) comparison of calculated pair correlation functions from theory with those obtained from Monte Carlo or molecular dynamics simulations using the same inter-molecular potential, (*ii*) internal consistency checks, (*iii*) comparison of calculated pair correlation functions with experimental X-ray and neutron scattering results, and (*iv*) comparison of calculated thermodynamic data with experimental results.

The first of these tests is clearly most ideal since there is no ambiguity about the potential to be used in the calculations. The second can be very useful because it can be performed even when computer simulations are not available, and there are a variety of internal consistency checks, which can be performed. One is to use a calculated pair correlation function to determine a thermodynamic quantity such as pressure in two different ways: from the virial equation directly or from the

compressibility equation indirectly. A second check could be, for instance, to compare a virial pressure with a pressure using a related thermodynamic theory. A major drawback of such tests is that they are sometimes too stringent. A calculated virial pressure, for example, is very sensitive to errors in the pair correlation functions. In the third test, comparison with experimental scattering results is complicated by the fact that for most liquids the actual inter-molecular potential is unknown. Thus, this test is actually a test of the combined errors of the theoretical method and the inter-molecular potential. The fourth test, comparing experimental and calculated thermodynamic results is relatively inappropriate. Calculated pressures are exceedingly sensitive to errors in both the potential and the calculated correlation function if the virial equation is used. However, if the energy equation is used it is sensitive only to errors in the potential. Accordingly, the best way to test the accuracy of a theory of liquid structure is to make comparison with computer simulations studies, which play the role of an experiment in providing essentially exacts results. In the absence of such studies, consistency checks are useful only for the most accurate theories.

However, whenever computer simulations and theoretical results are compared, the extent to which the potential model used is relevant of the real structure of the liquid under investigation has to be validated. Experimental structural results obtained by neutron diffraction for which the isotopic substitution technique is used can provide a crucial test for validating the model potentials used in simulations. If the model is realistic enough, the simulations in turn, may assist in the interpretation of experimental results and provide a better insight of the investigated systems. This dual role of simulation, as a bridge between models and theoretical predictions on the one hand, and between models and experimental results on the other, is illustrated in figure 1.3.

1.2 Framework of this study

In the general framework of the liquid state already mentioned in the previous section, shaded areas in figure 1.3 illustrate the setting of the work presented in this study. In this thesis the liquids pertaining to the class of molecular liquids have been studied

both experimentally and by computer simulations. Although, the theory of liquids is not considered in this work, it is worth noting that the most commonly employed theoretical model for molecular liquids is the reference interaction site model (RISM) developed by Chandler and Andersen (1972). In the original model, a molecule is regarded as a collection of hard spheres fused together, interacting with another molecule only via hard core potential, and the statistical problem is solved using an extension of the Percus-Yevick closure approximation. Several extensions / modifications were made to the RISM equations allowing its implementation with interaction site model potentials used in computer simulations to model complex molecular liquids such as benzene (Narten, 1977; Lowden and Chandler, 1974; Johnson and Hazoume, 1979; Bartsch and Bertagnolli, 1987), and methanol (Pettit and Rossky, 1983) realistically. In this work, the structural investigations of both these liquids were made under ambient conditions experimentally by using the technique of neutron diffraction with hydrogen/deuterium (H/D) isotopic substitution, and by molecular dynamics (MD) simulations. These studies on the pure components played a dual role in (i) the interpretation of the experimental structural results of the benzene + methanol mixture also obtained from neutron diffraction with hydrogen/deuterium (H/D) isotopic substitution, and (ii) selecting/testing model potentials for carrying out simulations of the mixture.

1.3 Overview of thesis contents

Chapter 2: Statistical mechanics and distribution functions

Since distribution functions are the central concern of this thesis, this chapter provides an account of what is meant by "the structure of a liquid". This is introduced by defining the concept of distribution functions for which a link between statistical mechanics and thermodynamics is made, and the role of inter-molecular potential model is highlighted.

Chapter 3: Molecular dynamics simulation methods

The methodology and techniques employed in the computer simulation work, yielding the partial pair distribution functions of the liquids under investigations, are outlined in this chapter.

Chapter 4: Theoretical background to neutron diffraction

The theoretical background for obtaining the distribution functions from the neutron diffraction data is given. The basic quantities are first defined for a monatomic liquid. These are then, generalised for the case of a molecular liquid. Finally, the technique of neutron diffraction with H/D isotopic substitution is detailed for the study of molecular liquids.

Chapter 5: Experimental methods and data reduction

The description of the instrument on which diffraction data were collected, and the procedures used for the data analyses, are outlined in this chapter.

Chapter 6: The structure of liquid methanol

The results of neutron diffraction (ND) experiments on liquid methanol under ambient conditions, performed on SANDALS instrument at the ISIS spallation neutron source are presented. The H/D substitution technique was employed on hydroxyl hydrogen in order to reveal structural features relevant to the hydrogen bonding in the liquid. The experimental results are compared and discussed with those obtained by performing MD simulations using three different model potentials.

Chapter 7: The structure of liquid benzene

This chapter describes the structure of liquid benzene under ambient conditions investigated by using H/D substitution technique of neutron diffraction and MD simulations. Experimentally, the H/D substitution on hydrogen atoms of benzene allowed us to extract the C-C, C-H, and H-H partial pair distribution functions (pdfs). The experimental structure is discussed and compared with that obtained by performing MD simulations carried out using three recent potential models.

Chapter 8: The structure of benzene-methanol mixture

The results of neutron diffraction investigation on benzene-methanol liquid mixture (1:2 molar ratio) under ambient conditions are presented in this chapter. The H/D substitution on hydrogens of both the hydroxyl group of methanol (Ho) and benzene (HB) was used to extract the solvent-solvent, solute-solute, and solute-solvent correlations. The interpretation of the structural results is made with the help of the results obtained for the pure components (presented in chapters 6 and 7). In particular, disruption of self-association of methanol molecules on addition of benzene is discussed. Based on the results of computer simulations on pure methanol and benzene two force field models were chosen for modelling the structural properties of the mixture. The simulated results on the mixture are discussed and compared with the experimental ones.

Chapter 9: General conclusions

The final chapter contains a summary of the key points emerging from the research presented in this thesis. In addition, suggestions for future work are made. Finally, some open questions are discussed.

Appendix A: The structure of Benzene-water mixture

The ND experimental structural results of supercritical benzene and water at 310° C and 165 bar where the two liquids are completely miscible over the entire composition range are presented. The structure of supercritical benzene is compared with the corresponding results obtained under ambient conditions. These experiments conducted at the partial pair distribution level formed a part of a failure experiment on benzene-water mixture, which is described briefly. Recommendations are made for a future successful attempt on this.

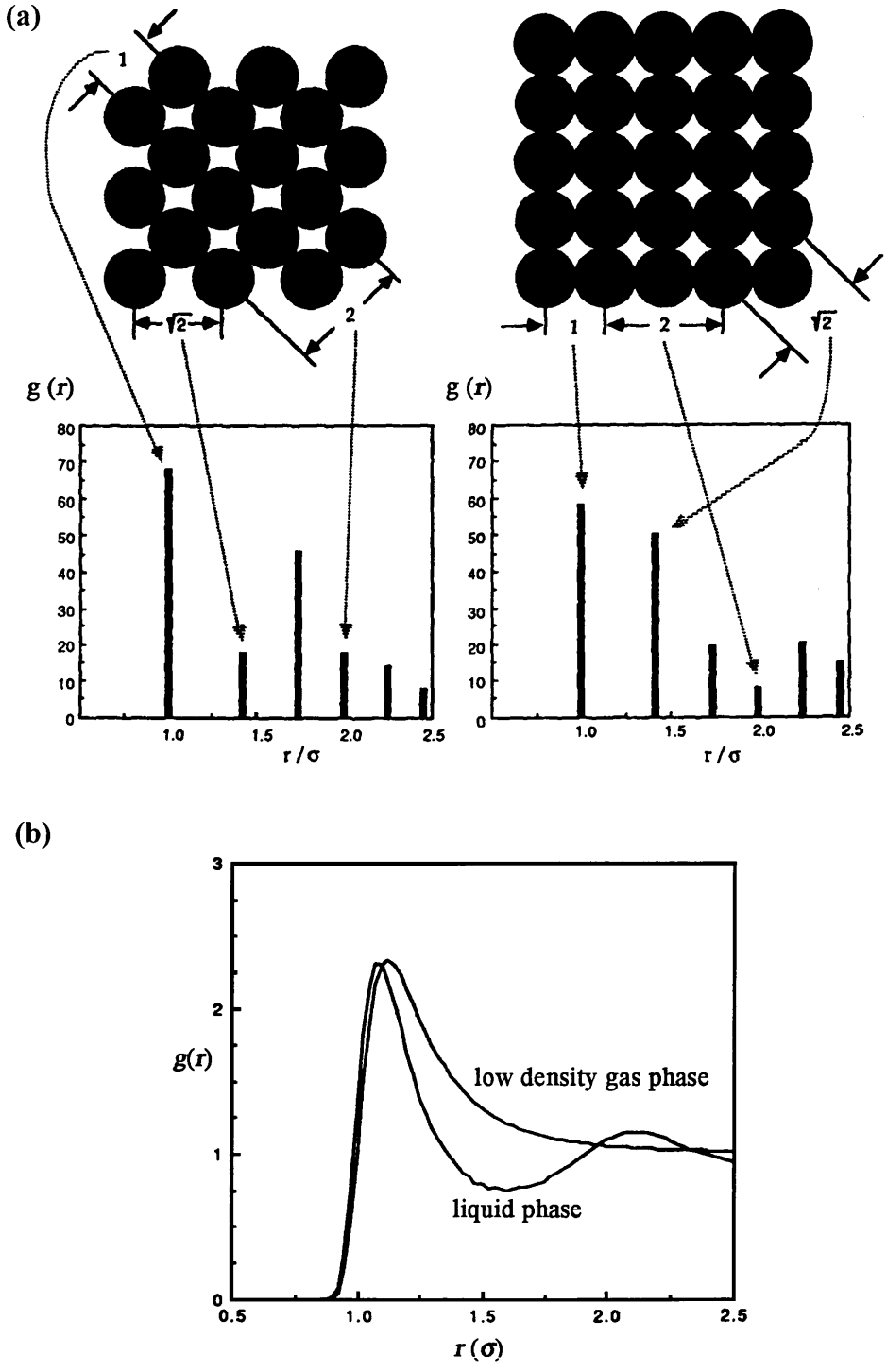

Figure 1.1 (a) The radial distribution function (rdf), $g(r)$, may be used to identify crystal lattices of different types. (b) A comparison of rdf for gas and liquid phase of a Lennard-Jones monatomic fluid (reproduced from Haile, 1992).

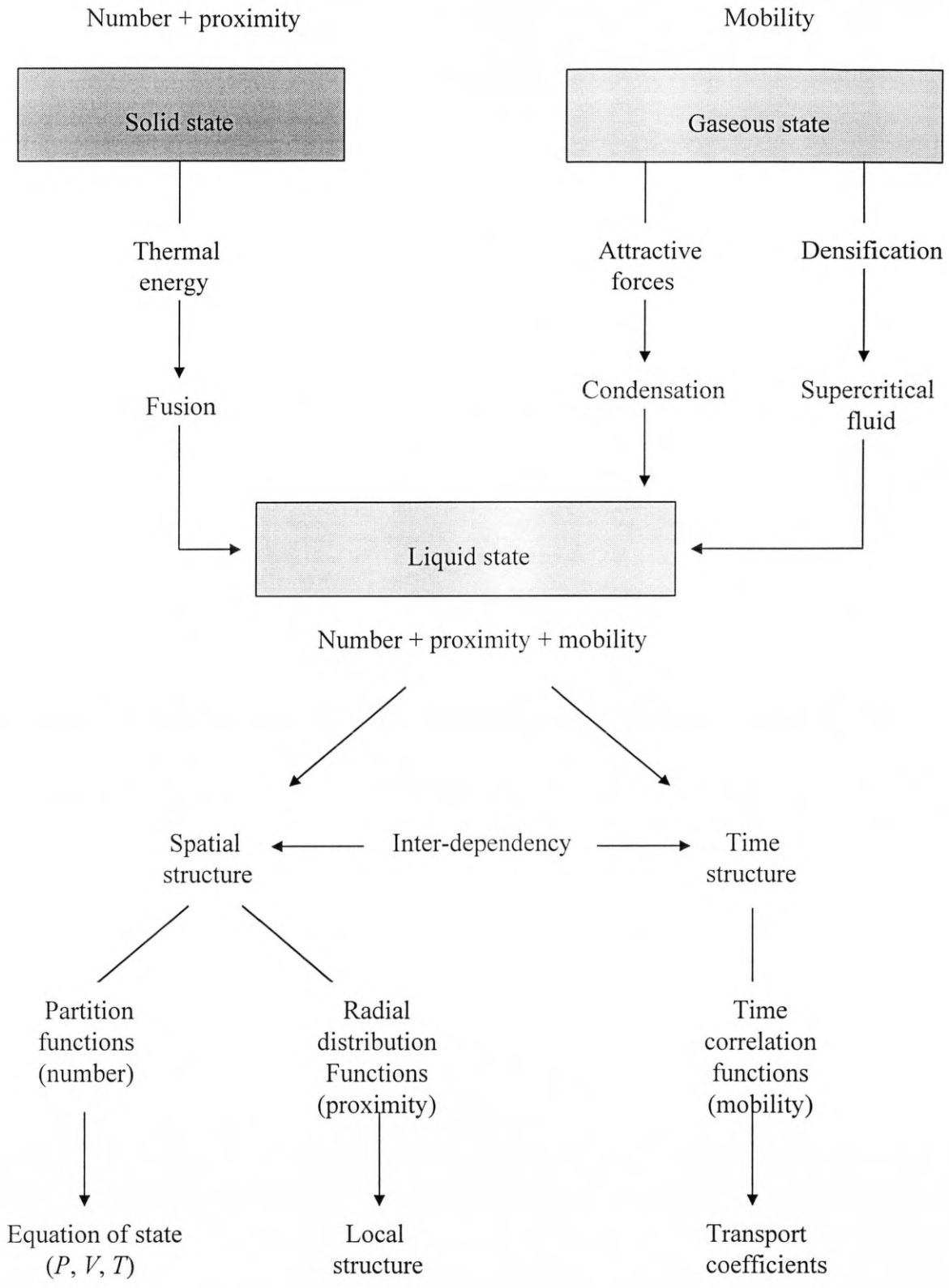

Figure 1.2 A schematic description of the three states of matter.

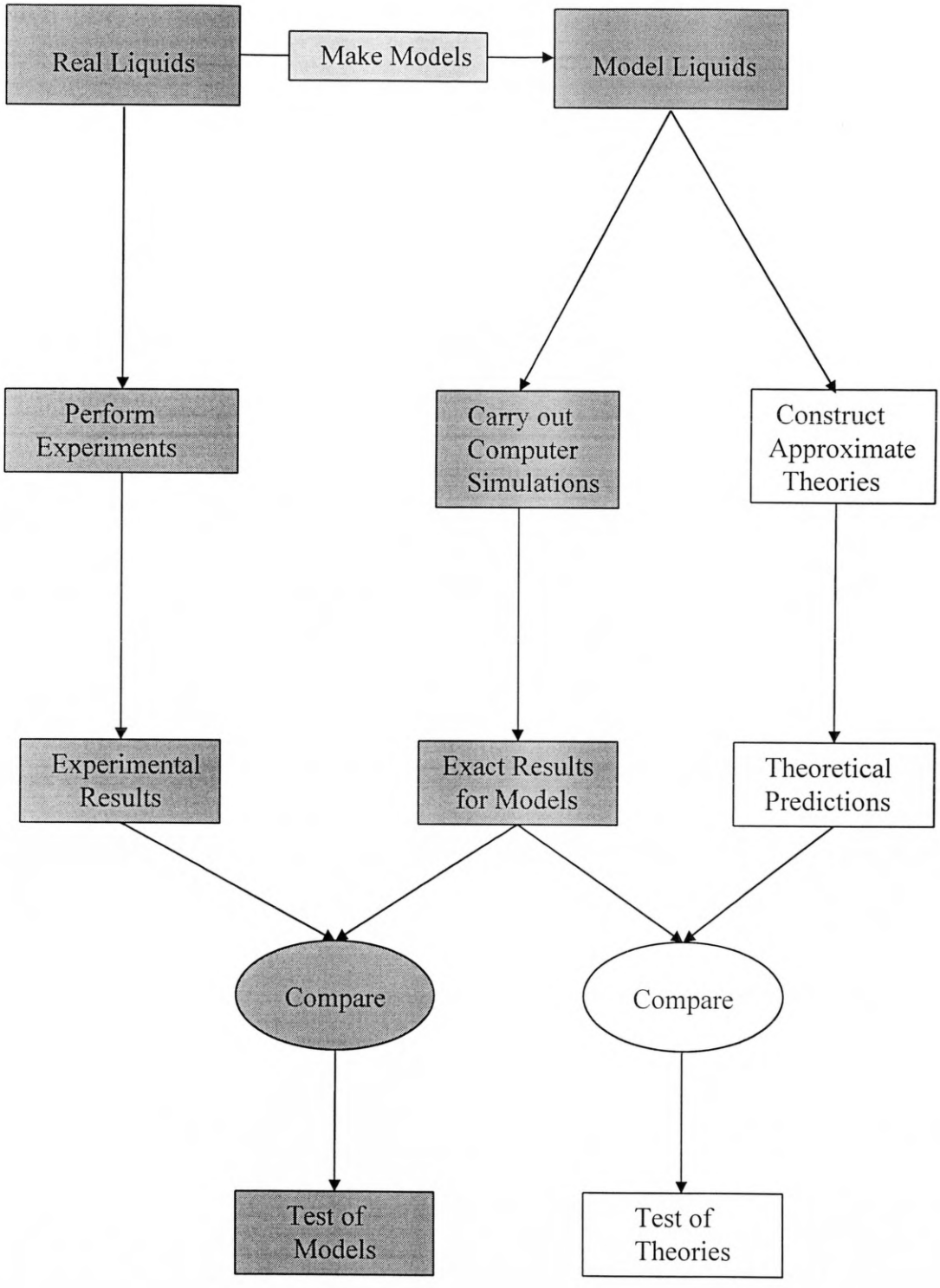

Figure 1.3 Link between experiments, simulations and theories.

Chapter 2

Statistical mechanics and distribution functions

By defining the concept of distribution functions, which are the central concern of the experimental and simulation work presented in the thesis, this section makes a link between statistical mechanics and thermodynamics, which in turn is used to validate the MD simulations presented in chapters 6-8.

2.1 Generality

Let's define the probability density $f^N(\boldsymbol{r}^N,\boldsymbol{p}^N,t)$ in a $6N$ phase space dimension. $f^N(\boldsymbol{r}^N,\boldsymbol{p}^N,t)\, d\boldsymbol{r}^N d\boldsymbol{p}^N$ is the probability to find, at a certain time t, the system of N particles in the microscopic state represented by a phase point in the $6N$ dimensional phase space, $d\boldsymbol{r}^N d\boldsymbol{p}^N$. At thermodynamic equilibrium, if we are interested in only a subset of particles of size n, we can define $f^n(\boldsymbol{r}^n,\boldsymbol{p}^n)$ for $n < N$ by

$$f^n(\boldsymbol{r}^n,\boldsymbol{p}^n)= \frac{N!}{(N-n)!} \int f^N(\boldsymbol{r}^N,\boldsymbol{p}^N) d\boldsymbol{r}^{N-n} d\boldsymbol{p}^{N-n}, \tag{2.1}$$

where $\boldsymbol{r}^N = (\boldsymbol{r}_1,...,\boldsymbol{r}_N)$ and $\boldsymbol{r}^{N-n} = (\boldsymbol{r}_{n+1},...,\boldsymbol{r}_N)$; the factor $N!/(N-n)!$ is the number of ways of choosing n particles from N others.

2.2 Canonical ensemble

The canonical equilibrium probability density for a system of N identical spherical particles is

$$f^N(\boldsymbol{r}^N,\boldsymbol{p}^N) = \frac{1}{N! Q_N(V,T) h^{3N}} exp(-\beta H_N(\boldsymbol{r}^N,\boldsymbol{p}^N)), \tag{2.2}$$

where

$$Q_N(V,T) = (h^{-3N}/N!)\int exp(-\beta H_N(\boldsymbol{r}^N,\boldsymbol{p}^N))d\boldsymbol{r}^N d\boldsymbol{p}^N \tag{2.3}$$

is the canonical partition function in which V is the volume, $H_N(\boldsymbol{r}^N,\boldsymbol{p}^N)$ the Hamiltonian of the system of N particles of mass m, T the temperature and $\beta = 1/k_BT$. h^{-3N} ensures that both $f^N(\boldsymbol{r}^N,\boldsymbol{p}^N)$ and $Q_N(V,T)$ are dimensionless. If the Hamiltonian is separated into kinetic and potential terms, $Q_N(V,T)$ may be rewritten as

$$Q_N(V,T) = Z_N(V,T)\lambda^{-3N}/N!, \tag{2.4}$$

where

$$Z_N(V,T) = \int exp(-\beta V_N(\boldsymbol{r}^N))\, d\boldsymbol{r}^N \text{ and } \lambda = (2\pi\beta\hbar^2/m)^{1/2}, \tag{2.5}$$

so that the thermodynamic potential is

$$A = -k_BT \ln Q_N(V,T). \tag{2.6}$$

2.3 Grand canonical ensemble

In this ensemble the probability density for a system of N identical spherical particles with a chemical potential μ is

$$f^N(\boldsymbol{r}^N,\boldsymbol{p}^N) = \frac{h^{-3N}}{N!\Theta(\mu,V,T)} exp(N\beta\mu)\, exp\,(-\beta H_N(\boldsymbol{r}^N,\boldsymbol{p}^N)), \tag{2.7}$$

where

$$\Theta(\mu,V,T) = \sum_N \frac{h^{-3N}}{N!}\, exp(N\beta\mu) \int exp(-\beta H_N(\boldsymbol{r}^N,\boldsymbol{p}^N))\, d\boldsymbol{r}^N d\boldsymbol{p}^N. \tag{2.8}$$

It follows that,

$$\Theta(\mu,V,T) = \sum_N exp(N\beta\mu) Q_N(V,T) \tag{2.9}$$

or,

$$\Theta\ (\mu,V,T) = \sum_N \frac{z^N}{N!} Z_N(V,T) \tag{2.10}$$

with $z = \lambda^{-3} exp(\beta\mu)$. (2.11)

The probability that the system contains precisely N particles is obtained by integrating $f^N(\boldsymbol{r}^N,\boldsymbol{p}^N)$ over $\boldsymbol{r}^N$ and $\boldsymbol{p}^N$:

$$P(N) = \int f^N(\boldsymbol{r}^N,\boldsymbol{p}^N) d\boldsymbol{r}^N d\boldsymbol{p}^N \tag{2.12}$$

or,

$$P(N) = \frac{1}{\Theta(\mu,V,T)} \frac{z^N}{N!} Z_N(V,T), \tag{2.13}$$

and the average number of particles is given by

$$< N > = \sum_N NP(N) = \partial_{lnz}(ln\,\Theta\ (\mu,V,T)). \tag{2.14}$$

Moreover,

$$\partial_{\beta\mu} < N > = \partial^2{}_{\beta\mu}(ln\,\Theta\ (\mu,V,T)) = < N^2 > - < N >^2, \tag{2.15}$$

thus,

$$\frac{\langle N^2\rangle - \langle N\rangle^2}{\langle N\rangle} = \frac{1}{\langle N\rangle} \partial_{\beta\mu} < N >. \tag{2.16}$$

In this ensemble the thermodynamic potential is defined by

$$-PV = -k_B T\ ln\,\Theta\ (\mu,V,T) = \Omega \tag{2.17}$$

$$\Omega = A - N\mu \tag{2.18}$$

$$d\Omega = dA - \mu dN - N d\mu\ . \tag{2.19}$$

It follows that

$$d\Omega = -SdT + \mu dN - PdV - \mu dN - N d\mu \tag{2.20}$$

$$d\Omega = -PdV - SdT - Nd\mu \tag{2.21}$$

$$d\Omega = -PdV - VdP\,. \tag{2.22}$$

Thus, for an isothermal change we have:

$$VdP = Nd\mu. \tag{2.23}$$

If the change also takes place at constant volume, then

$$(dP)_{V,T=\text{const}} = \frac{\partial P}{\partial N} dN, \tag{2.24}$$

and

$$(d\mu)_{V,T=\text{const}} = \frac{\partial \mu}{\partial N} dN\,, \tag{2.25}$$

so that (2.23) becomes

$$N\frac{\partial \mu}{\partial N} = \frac{\partial P}{\partial \rho}\,. \tag{2.26}$$

Since the isothermal compressibility χ_T is defined as

$$-\frac{1}{V}\frac{\partial \rho}{\partial P} = \chi_T, \tag{2.27}$$

we have $$\frac{\partial P}{\partial \rho} = \frac{1}{\rho \chi_T}\,, \tag{2.28}$$

so that $$N\frac{\partial \mu}{\partial N} = \frac{1}{\rho \chi_T}\,. \tag{2.29}$$

Substituting (2.29) in (2.16) (using the fact that at the thermodynamic limit $N = \langle N \rangle$)

we have finally $$\frac{\langle N^2 \rangle - \langle N \rangle^2}{\langle N \rangle} = \rho k_B T \chi_T. \tag{2.30}$$

2.4 Equilibrium particle densities and distribution functions

For a system at equilibrium, integration of a reduced distribution function over the remaining momenta yields an equilibrium particle density $\rho^{(n)}_N(\boldsymbol{r}^n)$, where $\rho^{(n)}_N(\boldsymbol{r}^n)d(\boldsymbol{r}^n)$ is $N!/(N-n)!$ times the probability of finding n particles of the system with the coordinates $\boldsymbol{r}^n$ around $d(\boldsymbol{r}^n)$ irrespective of the remaining particles and irrespective of all the momenta.

In the canonical ensemble, the n-particle density is defined as

$$\rho^{(n)}_N(\boldsymbol{r}^n) = \int f^n(\boldsymbol{r}^n,\boldsymbol{p}^n)d\boldsymbol{p}^n . \tag{2.31}$$

According to (2.1)

$$\rho^{(n)}_N(\boldsymbol{r}^n) = \frac{N!}{(N-n)!}\int f^N(\boldsymbol{r}^N,\boldsymbol{p}^N)d\boldsymbol{r}^{N-n}d\boldsymbol{p}^N , \tag{2.32}$$

$$\rho^{(n)}_N(\boldsymbol{r}^n) = \frac{N!}{(N-n)!}\,\frac{N!}{\lambda^{-3N}Z_N(V,T)}\int \frac{h^{-3N}}{N!}\,exp(-\beta H_N(\boldsymbol{r}^N,\boldsymbol{p}^N))d\boldsymbol{r}^{N-n}d\boldsymbol{p}^N . \tag{2.33}$$

$$\text{Since } \int exp(-\beta p^2/2m)d\boldsymbol{p}^N = \left(\frac{\lambda}{\hbar}\right)^{-3N}, \tag{2.34}$$

$$\text{we obtain } \rho^{(n)}_N(\boldsymbol{r}^n) = \frac{N!}{(N-n)!}\,\frac{1}{Z_N(V,T)}\int exp(-\beta V_N(\boldsymbol{r}^N))d\boldsymbol{r}^{N-n} . \tag{2.35}$$

In the grand canonical ensemble the n-particle density is defined as the sum:

$$\rho^{(n)}(\boldsymbol{r}^n) = \sum_{N=n} P(N)\rho^{(n)}_N(\boldsymbol{r}^n). \tag{2.36}$$

Using (2.31) and (2.13)

$$\rho^{(n)}(\boldsymbol{r}^n) = \sum_{N=n} \frac{1}{\Theta(\mu,V,T)}\,\frac{z^N}{N!}\,Z_N(V,T)\int f^n(\boldsymbol{r}^n,\boldsymbol{p}^n)d\boldsymbol{p}^n. \tag{2.37}$$

From (2.1), it follows that

$$\rho^{(n)}(\boldsymbol{r}^n) = \sum_{N=n} \frac{1}{\Theta(\mu,V,T)} \frac{z^N}{N!} Z_N(V,T) \frac{N!}{(N-n)!} \int f^N(\boldsymbol{r}^N,\boldsymbol{p}^N) d\boldsymbol{r}^{N-n} d\boldsymbol{p}^N , \tag{2.38}$$

and with the help of (2.7-10)

$$\rho^{(n)}(\boldsymbol{r}^n) = \sum_{N=n} \frac{1}{\Theta(\mu,V,T)} \frac{z^N}{N!} Z_N(V,T) \times$$

$$\frac{N!}{(N-n)!} \int \frac{h^{-3N}}{N!\Theta(\mu,V,T)} e^{(N\beta\mu)} exp(-\beta H_N(\boldsymbol{r}^N,\boldsymbol{p}^N)) d\boldsymbol{r}^{N-n} d\boldsymbol{p}^N \tag{2.39}$$

$$\rho^{(n)}(\boldsymbol{r}^n) = \frac{1}{\Theta(\mu,V,T)} \sum_{N=n} (z/\lambda^{-3})^N \left(\frac{\lambda}{\hbar}\right)^{-3N} \frac{h^{-3N}}{(N-n)!} \int exp(-\beta V_N(\boldsymbol{r}^N)) d\boldsymbol{r}^{N-n} \tag{2.40}$$

$$= \frac{1}{\Theta_N(\mu,V,T)} \sum_{N=n} \frac{z^N N!}{(N-n)!} \frac{1}{N!} \int exp(-\beta V_N(\boldsymbol{r}^N)) d\boldsymbol{r}^{N-n} . \tag{2.41}$$

If we integrate over $\boldsymbol{r}_1 \ldots . \boldsymbol{r}_n$ according to (2.12), we find that $\rho^{(n)}(\boldsymbol{r}^n)$ is normalised such that

$$\int \rho^{(n)}(\boldsymbol{r}^n) d\boldsymbol{r}^n = \langle \frac{N!}{(N-n)!} \rangle . \tag{2.42}$$

In particular,

$$\int \rho^{(1)}(\boldsymbol{r}) d\boldsymbol{r}^1 = \langle N \rangle , \tag{2.43}$$

whence for a homogeneous system,

$$\rho^{(1)}(\boldsymbol{r}) = <N>/V = \rho. \tag{2.44a}$$

In the special case of an ideal gas, $V_N(\boldsymbol{r}) = 0$ and $Z_N(V,T) = V^N$. Thus,

$$\rho^{(n)}(\boldsymbol{r}^n) = \rho^n \frac{N!}{(N-n)!} = \rho^n (1 + \vartheta(n/N)), \tag{2.44b}$$

and the pair density of an ideal gas is

$$\rho^{(2)}(\boldsymbol{r}_1, \boldsymbol{r}_2) = \rho^2 (1 - 1/N). \tag{2.44c}$$

Now, if we define the n-particle distribution function $g^{(n)}(\boldsymbol{r}^n)$ in terms of the corresponding particle density as:

$$g^{(n)}(\boldsymbol{r}^n) = \frac{\rho^{(n)}(r^n)}{\prod_{i=1}^{n} \rho^{(1)}(r^i)}, \tag{2.45}$$

for a homogeneous system we have

$$\rho^n g^{(n)}(\boldsymbol{r}^n) = \rho^{(n)}(\boldsymbol{r}^n). \tag{2.46a}$$

Whenever the system is also isotropic, the pair distribution function, $g^{(2)}(\boldsymbol{r}_1,\boldsymbol{r}_2)$ is a function only of the separation $r_{12} = |\boldsymbol{r}_2 - \boldsymbol{r}_1|$, then it is called the radial pair distribution function and written simply as $g(r)$. When the separation r_{12} is much larger than the range of the inter-particle potential $g^{(2)}(\boldsymbol{r}_1,\boldsymbol{r}_2)$ approaches its ideal-gas-limit. From equation (2.44c) and (2.46a) this limit is

$$\lim_{r_{12}\to\infty} g^{(2)}(\boldsymbol{r}_1,\boldsymbol{r}_2) \sim 1 - 1/N. \tag{2.46b}$$

In addition, from (2.42) we get

$$\int \rho^{(2)}(\boldsymbol{r}_1,\boldsymbol{r}_2) d\boldsymbol{r}_2 d\boldsymbol{r}_1 = \langle N^2 \rangle - \langle N \rangle, \tag{2.47}$$

whence

$$\int [\rho^{(2)}(\boldsymbol{r}_1,\boldsymbol{r}_2) - \rho^{(1)}(\boldsymbol{r}_1)\rho^{(1)}(\boldsymbol{r}_2)] d\boldsymbol{r}_2 d\boldsymbol{r}_1 = \langle N^2 \rangle - \langle N \rangle - \langle N \rangle^2 . \tag{2.48}$$

From (2.30) and the definition (2.46a), if the system is homogeneous, the compressibility equation is obtained:

$$\frac{\langle N^2 \rangle - \langle N \rangle^2}{\langle N \rangle} = 1 + \rho \int (g^{(2)}(\boldsymbol{r}_{12}) - 1) d\boldsymbol{r}_{12} = \rho k_B T \chi_T . \tag{2.49}$$

2.5 δ Functions and distribution functions

By working in the canonical ensemble, it is possible to obtain some useful expressions in terms of delta functions. We note first that

$$<\delta(\boldsymbol{r}-\boldsymbol{r}_1)> = \frac{1}{Z_N(V,T)}\int \delta(\boldsymbol{r}-\boldsymbol{r}_1)exp(-\beta V_N(\boldsymbol{r}^N))d\boldsymbol{r}^N \tag{2.50}$$

$$<\delta(\boldsymbol{r}-\boldsymbol{r}_1)> = \frac{1}{Z_N(V,T)}\int exp(-\beta V_N(\boldsymbol{r},\boldsymbol{r}_2....\boldsymbol{r}_N))d\boldsymbol{r}_2.....d\boldsymbol{r}_N\,. \tag{2.51}$$

The statistical average in (2.51) is a function of the co-ordinate r, but is independent of the particle label (here taken to be 1). A sum over all particle labels can therefore be written as N times the contribution from any one particle. It follows from the definition (2.35) that,

$$< \sum_{i=1}^{N} \delta(\boldsymbol{r}-\boldsymbol{r}_1) > = \rho^{(1)}_N(\boldsymbol{r}). \tag{2.52}$$

Similarly, the statistical average of $< \delta(\boldsymbol{r}-\boldsymbol{r}_1)\delta(\boldsymbol{r}'-\boldsymbol{r}_2) >$ gives

$$< \delta(\boldsymbol{r}-\boldsymbol{r}_1)\delta(\boldsymbol{r}'-\boldsymbol{r}_2) > = \frac{1}{Z_N(V,T)}\int \delta(\boldsymbol{r}-\boldsymbol{r}_1)\,\delta(\boldsymbol{r}'-\boldsymbol{r}_2)\,exp(-\beta V_N(\boldsymbol{r}^N))d\boldsymbol{r}^N \tag{2.53}$$

$$< \delta(\boldsymbol{r}-\boldsymbol{r}_1)\delta(\boldsymbol{r}'-\boldsymbol{r}_2) > = \frac{1}{Z_N(V,T)}\int exp(-\beta V_N(\boldsymbol{r},\boldsymbol{r}',\boldsymbol{r}_3....\boldsymbol{r}_N))d\boldsymbol{r}_3.....d\boldsymbol{r}_N, \tag{2.54}$$

and hence

$$< \sum_{i\neq}^{N}\sum_{j} \delta(\boldsymbol{r}-\boldsymbol{r}_1)\delta(\boldsymbol{r}'-\boldsymbol{r}_2) > = \rho^{(2)}_N(\boldsymbol{r},\boldsymbol{r}'). \tag{2.55}$$

By averaging $\frac{1}{N}\sum_{i\neq}^{N}\sum_{j} \delta(\boldsymbol{r}+\boldsymbol{r}_j-\boldsymbol{r}_i)$ it follows

$$<\frac{1}{N}\sum_{i\neq}^{N}\sum_{j} \delta(\boldsymbol{r}+\boldsymbol{r}_j-\boldsymbol{r}_i)> = <\frac{1}{N}\int \sum_{i\neq}^{N}\sum_{j} \delta(\boldsymbol{r}'+\boldsymbol{r}-\boldsymbol{r}_i)\delta(\boldsymbol{r}'-\boldsymbol{r}_j)d\boldsymbol{r}'>, \tag{2.56}$$

$$= \frac{1}{N}\int \rho^{(2)}_N(\boldsymbol{r}+\boldsymbol{r}',\boldsymbol{r}')d\boldsymbol{r}'. \tag{2.57}$$

For a homogeneous system we have seen that

$$\rho^{(2)}_N(\boldsymbol{r}+\boldsymbol{r}',\boldsymbol{r}') = \rho^2 g_N(\boldsymbol{r}), \tag{2.58}$$

so that

$$<\frac{1}{N}\sum_{i\neq j}^{N}\sum \delta(\boldsymbol{r}+\boldsymbol{r}_j-\boldsymbol{r}_i)>=\frac{1}{N}\int\rho^2 g_N(\boldsymbol{r})\,d\boldsymbol{r}'. \tag{2.59}$$

Thus $$<\frac{1}{N}\sum_{i\neq j}^{N}\sum \delta(\boldsymbol{r}+\boldsymbol{r}_j-\boldsymbol{r}_i)>=\rho g_N(\boldsymbol{r}). \tag{2.60}$$

2.6 Thermodynamics and distribution Functions

2.6.1 The energy equation

The compressibility equation (2.49) derived in the last section relates thermodynamics to $g^{(2)}_N(\boldsymbol{r}_1,\boldsymbol{r}_2)$ and is independent of any special assumptions such as pairwise additivity about the potential function. At this point, a basic assumption is to consider that the inter-molecular potential energies are in first approximation additive. Thus, the potential energy function $V_N(\boldsymbol{r}^N)$ may be written as

$$V_N(\boldsymbol{r}^N)=\sum_{i<j}^{N}V_2(\boldsymbol{r}_i,\boldsymbol{r}_j)+\sum_{i<j<k}^{N}V_3(\boldsymbol{r}_i,\boldsymbol{r}_j,\boldsymbol{r}_k)+\ldots, \tag{2.61}$$

in which the first term is a sum of pair interactions, and the second a sum of triplet interactions. In the canonical ensemble the total energy of a system of interacting particles is given by

$$E=-\partial_\beta \ln Q_N(V,T)=k_BT^2\partial_T \ln Q_N(V,T). \tag{2.62}$$

By using (2.4) and (2.5)

$$E=3/2Nk_BT+k_BT^2\partial_T \ln Z_N(V,T)=3/2Nk_BT+<U>, \tag{2.63}$$

where,

$$<U> = \frac{1}{Z_N(V,T)} \int exp(-\beta V_N(\mathbf{r}^N)) V_N(\mathbf{r}^N) d\mathbf{r}^N. \quad (2.64)$$

Because $V_2(\mathbf{r}_i,\mathbf{r}_j)$ and $V_3(\mathbf{r}_i,\mathbf{r}_j,\mathbf{r}_k)$ are independent of the choice of i, j (and k for $V_3(\mathbf{r}_i,\mathbf{r}_j,\mathbf{r}_k)$), there are respectively $N(N-1)/2$ and $N(N-1)(N-2)/6$ equal terms in the integration. By introducing (2.61) in (2.64), we obtain

$$<U> = \frac{N(N-1)}{2Z_N(V,T)} \int exp(-\beta V_N(\mathbf{r}^N)) V_2(\mathbf{r}_1,\mathbf{r}_2) d\mathbf{r}^N +$$

$$\frac{N(N-1)(N-2)}{6Z_N(V,T)} \int exp(-\beta V_N(\mathbf{r}^N)) V_3(\mathbf{r}_1,\mathbf{r}_2,\mathbf{r}_3) d\mathbf{r}^N + \ldots \quad (2.65)$$

The generalised energy equation is obtained by using equation (2.32)

$$<U> = \frac{1}{2} \int \rho^{(2)}_N(\mathbf{r}_1,\mathbf{r}_2) V_2(\mathbf{r}_1,\mathbf{r}_2) d\mathbf{r}_1 d\mathbf{r}_2 +$$

$$\frac{1}{6} \int \rho^{(3)}_N(\mathbf{r}_1,\mathbf{r}_2,\mathbf{r}_3) V_3(\mathbf{r}_1,\mathbf{r}_2,\mathbf{r}_3) d\mathbf{r}_1 d\mathbf{r}_2 d\mathbf{r}_3 + \ldots \quad (2.66)$$

Practically, apart from the simplest cases, the triplet interactions are not explicitly taken into account in $V_N(\mathbf{r}^N)$ due to their complexity. One of the most common approximation is to include their effects into an *effective pair potential*, $u(\mathbf{r}_{ij})$ so that

$$V_N(\mathbf{r}^N) \approx \sum_{i<j}^{N} u(\mathbf{r}_i - \mathbf{r}_j) = \sum_{i<j}^{N} u(\mathbf{r}_{ij}). \quad (2.67)$$

Using (2.46a), and assuming that the fluid is homogeneous and isotropic, the latter expression becomes

$$<U> = \frac{N^2}{2V^2} \int g^{(2)}_N(\mathbf{r}_1, \mathbf{r}_2) u(\mathbf{r}_{12}) d\mathbf{r}_1 d\mathbf{r}_2 \quad (2.68)$$

$$= \frac{N^2}{2V^2} \int g(\mathbf{r}_{12}) u(\mathbf{r}_{12}) d\mathbf{r}_1 d\mathbf{r}_{12} \quad (2.69)$$

$$= \frac{N^2}{2V} \int g(r)u(r)d\boldsymbol{r}. \tag{2.70}$$

Thus, the internal energy per particle is given by

$$<U>/\mathrm{N} = 2\pi\rho \int_0^\infty r^2 g(r)u(r)dr\,. \tag{2.71}$$

2.6.2 The pressure equation

Working in the grand canonical ensemble, after introducing a change of variable $\boldsymbol{r}_i = V^{1/3}\boldsymbol{s}_i$ (method of Born and Green, see Barker and Henderson, 1976), (2.10) becomes

$$\Theta\ (\mu,V,T) = \sum_N \frac{h^{-3N}}{N!} V^N exp(N\beta\mu) \int exp(-\beta V_N(V^{1/3}\boldsymbol{s}^N)d\boldsymbol{s}^N. \tag{2.72}$$

The domain of integration is now independent of the volume. We can now differentiate the logarithm of (2.72) with respect to the volume.

$$V\partial_V ln\,\Theta\ (\mu,V,T) = \sum_N \frac{h^{-3N}}{\Theta(\mu,V,T)N!} V^N exp(N\beta\mu) \int exp(-\beta V_N(V^{1/3}\boldsymbol{s}^N)$$

$$[N - \frac{1}{3k_BT}\sum_i V^{1/3}\boldsymbol{s}_i . \nabla_i V_N(V^{1/3}\boldsymbol{s}^N)]d\boldsymbol{s}^N\,, \tag{2.73}$$

$$= < N - \frac{1}{3k_BT}\sum_i \boldsymbol{r}_i . \nabla_i V_N(\boldsymbol{r}^N) >. \tag{2.74}$$

Here $\nabla_i V_N(\boldsymbol{r}^N)$ is the gradient of the function $V_N(\boldsymbol{r}^N)$ with respect to $\boldsymbol{r}_i$. But $\partial_V ln\,\Theta\ (\mu,V,T)$ is just P/k_BT, so that (2.74) becomes

$$PV/k_BT = < N - \frac{1}{3k_BT}\sum_i \boldsymbol{r}_i . \nabla_i V_N(\boldsymbol{r}^N) >, \tag{2.75}$$

which is known as the virial expression of the pressure (also called the pressure equation). For additive pair potentials we must have

$$\nabla_i u(\boldsymbol{r}_{ij}) = -\nabla_j u(\boldsymbol{r}_{ij}), \tag{2.76}$$

so that (2.75) becomes

$$PV/k_BT = \langle N - \frac{1}{6k_BT}\sum_{i\neq j} (\boldsymbol{r}_i - \boldsymbol{r}_j).\nabla_i u(\boldsymbol{r}_{ij}) \rangle \tag{2.77}$$

$$= \langle N \rangle - \frac{1}{6k_BT}\int \rho^{(2)}(\boldsymbol{r}_1, \boldsymbol{r}_2)(\boldsymbol{r}_i - \boldsymbol{r}_j).\nabla u(\boldsymbol{r}_{12}) d\boldsymbol{r}_1 d\boldsymbol{r}_2. \tag{2.78}$$

For an isotropic fluid in which the pair potential is spherically symmetric, it follows immediately that

$$P/k_BT = \rho - \frac{2\pi}{3k_BT}\rho^2 \int_0^\infty r^3 g(r)\frac{du(r)}{dr} dr. \tag{2.79}$$

Chapter 3

Molecular dynamics simulation methods

3.1 Introduction

A molecular simulation (see Allen and Tildesley, 1987; Frenkel and Smit, 1996; Haile, 1992) consists of three principal steps: (i) construction of a model, (ii) calculation of molecular trajectories, and (iii) analysis of the trajectories to obtain property values. The second step constitutes the simulation proper. In Monte-Carlo (MC) method (detailed in Allen and Tildesley, 1987; Kalos and Whitlock, 1986; Binder, 1984; Frenkel and Smit, 1996) the positions are generated stochastically such that a molecular configuration, $\boldsymbol{r}^N$ depends only on the previous configuration. The outcome of a random event in a sequence depends only on the outcome of the immediately previous event (Markov chain) and the results of the simulations are ensemble averages. In molecular dynamics (MD) simulations, given a set of initial conditions plus forces or potentials of interactions, the positions are obtained numerically by solving the differential equations of motion. Hence, the positions are connected in time so as to reveal dynamic properties also that cannot be obtained by MC simulations. The molecular dynamics method devised by Alder and Wainwright (1959) in the late 1950s for systems at equilibrium, is typically applied to an isolated system containing a fixed number of molecules N in a fixed volume V. Because the system is isolated, the total (kinetic + potential) energy E is also constant. In the *NVE* ensemble the molecular positions $\boldsymbol{r}^N$ are obtained by solving Newton's equations of motions

$$\boldsymbol{f}_i(t) = m_i \frac{d^2 \boldsymbol{r}_i(\mathrm{t})}{dt^2} = -\nabla_{\boldsymbol{r}_i} V^N(\boldsymbol{r}^N), \tag{3.1}$$

where $\boldsymbol{f}_i(t)$ are the forces on i caused by the N-1 other particles. Integrating (3.1) once yields the atomic momenta; integrating a second time produces the atomic positions. Thus, repeatedly integrating twice for several thousand time-steps produces individual atomic trajectories. Any time average of the macroscopic property $\langle A \rangle$, which is formally given by

$$\langle A \rangle = \lim_{t\to\infty} \frac{1}{t} \int_{t_0}^{t_0+t} A(\boldsymbol{r}^N, \boldsymbol{p}^N) d\tau, \tag{3.2a}$$

where t_0 is the initial time, can be approximated by the sum,

$$\langle A \rangle = \frac{1}{M} \sum_{k=1}^{M} A(\boldsymbol{r}^N(t_k), \boldsymbol{p}^N(t_k)), \tag{3.2b}$$

in which the trajectory is obtained from a simulation of a system containing N constituent units over M discrete times, t_k. According to the ergodic hypothesis, the time averages (3.2) provided by molecular dynamics should be the same as the ensemble averages, discussed in section 2.1, obtained by Monte-Carlo simulations.

3.2 Inter-molecular potential models

As mentioned in chapter 1.1, the accuracy of an approximate theory of the liquid structure is best tested by comparing the results obtained from it with those from computer simulations. This is so, because there is no ambiguity about the potential to be used in the calculations and the simulations. However, the extent to which the potential model used is representative of the real structure of the liquid under investigation is a central question. Throughout its development in the past four decades, simulations became increasingly dependent on the availability of realistic model potentials, especially because experimental techniques probing the liquid state are becoming ever more accurate. Since potential interactions between atoms are quantum in nature, the natural way to perform a computer simulation is to solve the many-body Schrödinger equation (1.1) at each time step. Approximate methods in MD simulations (Car and Parrinello, 1985) have been developed using density

functional theory (Kohn, and Sham, 1965) to perform these first-principle MD simulations. However, in spite of a fast improvement of computer hardware, such a method is still restricted to simple systems (in which the number of electrons and nuclei to be treated is not too large). Consequently, in the field of molecular liquids these methods are still in their infancy, and have only been applied to very small molecules for studying the bulk structural properties. Promising results of *ab-initio* MD simulations have been reported in the case of water (Laasonen et al., 1993; Fois et al., 1994; Sprik et al., 1996). In contrast to the *ab-initio* MD simulation method, usually, in conventional MD simulations of molecular liquids there is no attempt to solve the complex many-body problem. Here, the interactions between atoms are modelled by empirical or semi-empirical effective pair potentials whose functional forms are purely arbitrary. With the success of modelling liquid argon in the early days (Maitland et al., 1981; Hansen and McDonald, 1986; Allen and Tildesley, 1987; Ciccotti et al., 1987) by using a phase-transferable potential, the use of effective Lennard-Jones (LJ) model potential types such as:

$$V(r) = 4\varepsilon\left\{(\sigma/r)^{12} - (\sigma/r)^{6}\right\}, \tag{3.3}$$

became very common. ε and σ are the Lennard-Jones (LJ-12-6) parameters between different interacting sites, and r is the site-site separation. It is not surprising that in computer simulations of molecular liquids that followed, various authors devised their models by using this simple functional form. In the seventies, these and various other functional forms of the force fields were devised completely empirically, *i.e.*, by using theoretical and/or computer simulation methods in which the potential parameters were refined so as to reproduce various physical properties ideally taken from the three phases of matter. These refinements, however, were often made only in the phase of interest under specific thermodynamic conditions. The birth in the seventies and the development in the eighties of quantum mechanical (QM) calculations helped theoreticians considerably in their task. The increasing sophistication of these methods in conjunction with growing computing power led to the structural investigations of small clusters containing few molecules. It also enabled development of model potentials for simple and complex system purely from *ab-initio* calculations. From this respect, all the force fields used in the present work originated

to a different degree from QM calculations. When these are fully parameterised from QM calculations, they are obtained by investigating the potential energy surface of the dimer for which different functional form of polynomial are fitted. Specific examples are the methanol force field of Anwander *et al.* (1992) and the benzene model of Smith and Jaffe (1996) both which have been used in computer simulations reported in this thesis (see sections 6.2 and 7.3). Nevertheless, it is clear from the above discussion that the condition that such potentials "work", is at best locally satisfied. An effective pair potential empirically devised, and accounting for many-body effects in an average way is likely to fail when applied outside the range of thermodynamic states for which it has been designed. *Ab-initio* potential models are parameterised using gas-phase energy surfaces from accurate electronic structure calculations. They may be superior under just those conditions, but when extrapolated to condensed phases, they suffer from exactly the same weakness as effective potentials. Being a gas-phase model does not guarantee that it can be transferred to the liquid phase. An alternative to this is to combine both empirical and *ab-initio* approach to build, what is called, a semi-empirical potential model. This is the case for the two LJ-12-6 model potentials used in the simulation of liquid methanol (Haughney et al., 1986), and the one for liquid benzene (Jorgensen and Severance, 1990) (see sections 6.2 and 7.3). Moreover, for liquid benzene, an additional LJ-9-6 potential model derived from a new general all-atom force field for alkane and benzene compounds (Sun, 1998), obtained using state-of-art *ab-initio* and empirical parameterisation techniques, is also used in the simulations reported in this thesis (see section 7.3). Thus, the simulation work reported here was carried out by using only effective pair potentials described in more detail in relevant chapters.

3.3 Periodic boundary conditions

Because the size of the system is limited by the speed of execution of the host computer, molecular dynamics is typically applied to systems containing several hundred or few thousand atoms generally placed in a cubic box (see figure 3.1). To overcome the problem of surface effects the periodic boundary conditions are implemented (Born and Von Karman, 1912). The cubic box, of edge length L, is replicated throughout space to form an infinite lattice. In the course of the simulation,

as a molecule moves in the original box, its periodic image in each of the neighbouring boxes moves exactly in the same way (see atom 6 of figure 3.2). Thus, as a molecule leaves the central box, one of its images will enter through the opposite face so that there is no wall and no surface at the boundary of the central box. The key question is whether the properties of a small, periodic sample are truly representative of the macroscopic system that the model is designed to simulate. There is no easy answer to this, it depends very much on the form of the potential and the properties under investigations. Broadly speaking, provided the long-range interactions of the intermolecular potential used are handled by a suitable treatment (see section 3.7), the properties of a small (N >100) but infinitely periodic system should be similar to those of the real macroscopic system which it represents. Actually, the effects of periodicity are more pronounced on dynamic properties (Haile, 1992) than equilibrium properties such as thermodynamics and local structure.

3.4 Potential truncation

For a system of N molecules interacting with a pairwise additive potential such as (2.67), the double sum accumulates $N(N-1)/2$ terms to calculate. However, in principle for each molecule considered we should also include all interactions between molecules and images of other molecules lying in the surrounding boxes, which is impossible to calculate in practice. For a short-range potential energy function, we can restrict this summation by making an approximation. Consider molecule 1 to rest at the centre of a region, which has the same size and shape as the basic simulation box (see figure 3.2). Molecule 1 interacts with all the molecules whose centres lie within this region, which is called the "minimum image convention": for instance molecule 1 interacts with molecules 2, 3, 4, 6, 7D, 5B and 8A. Since a short-range potential model extends over a modest range of pair separation, a considerable saving in computer time is achieved by neglecting pair interactions beyond a spherical cut-off distance r_C. In this case only molecules 2, 3, 4, 7D and 5B contribute to the force on 1. For the potential models employed in this study, that are mostly Lennard-Jones (LJ) types, $r_C = L/2$. It has to be noted that a greater value cannot be taken in order to keep the consistency with the "minimum image convention". Moreover this is a reasonable approximation in the sense that

usually for the LJ potential used (see equation 3.3), the value of the energy at a boundary of a cutoff sphere with a radius $r_C = L/2 > 2.5\sigma$ (2Å < σ < 3.9Å) is just 1.6% of the well depth. However, because of the potential truncation at r_C, a simulation can provide only a portion of properties, such as the internal energy and pressure, that are directly related to the potential. Simulation results for such properties must, however, be corrected for long-range interactions ($r > r_C$) that are neglected during a run (see section 3.8.1).

3.5 Integration of the equation of motions

A standard method for solution of ordinary differential equations such as (3.1) is the finite difference approach. Many different algorithms such as predictor-corrector, Verlet's, Gear's predictor-corrector, velocity-Verlet, Verlet leap-frog fall into the general finite difference pattern and several reviews exist on the subject (Gear, 1966, 1971; Van Gunsteren and Berendsen, 1977; Berendsen and Van Gunsteren, 1986). In the MD simulations reported in this work the algorithm used is a derived form of the Verlet scheme (Verlet, 1967), called the Verlet leap-frog algorithm (Hockney and Eastwood, 1981). The algorithm requires values of positions $\boldsymbol{r}$ and forces $\boldsymbol{f}$ at time t while the velocities $\boldsymbol{v}$ are at half-integer time steps behind. The first step is to advance the velocities to $t+\Delta t/2$ as follow

$$\boldsymbol{v}\,(t+\Delta t/2) \leftarrow \boldsymbol{v}\,(t-\Delta t/2) + \Delta t\,\boldsymbol{f}(t)/m, \tag{3.4a}$$

where m is the mass of a site (or atom) and Δt is the time-step. The positions are then advanced using the new velocities:

$$\boldsymbol{r}\,(t+\Delta t) \leftarrow \boldsymbol{r}\,(t) + \Delta t\,\boldsymbol{v}\,(t+\Delta t/2). \tag{3.4b}$$

Molecular dynamics simulations normally require properties that depend on position and velocity *at the same time* (such as the sum of potential and kinetic energy). The velocity at time t is obtained from the average of the velocities half a time-step either side of time t:

$$v\,(t+\Delta t/2) = (v\,(t+\Delta t/2) + v\,(t-\Delta t/2))/2. \qquad (3.5)$$

The advantage of such an algorithm apart from its simple form is that it is time reversible and generates trajectories in the micro-canonical ensemble in which the total energy (kinetic + potential) is conserved. Thus, if this property drifts or fluctuates significantly during the course of simulation it indicates that either the time step is too large or the potential cut-off too small.

3.6 Molecular dynamics of molecules

In the molecular dynamics simulation of polyatomic systems, it may be necessary to consider the flexibility of molecules. The natural approach would be to consider the atoms of one molecule independently and interacting with others pertaining to the same entity *via* intra-molecular potential keeping the geometry of the molecule invariant throughout the simulation. It proves to be quite useful to divide intra-molecular motion into so-called "hard" mode and "soft" mode (Clarke, 1997). Typical of the latter are tortional motions for which the forces involved may be small enough to be coupled with inter-molecular movements. In contrast, "hard" modes such as bond vibrations have much larger force intensity. It results that the intra-molecular vibration modes are at higher frequencies than those of rotational and translational motions. In other words, if we are interested in the molecular bond vibrations an extremely small time step is required ($\Delta t < 10^{-16}$s). This practically makes the calculations of the structural properties, which are of interest in this work, too long. In any case the purely quantum nature of these intra-molecular forces makes the classical approach used to treat them highly questionable, especially for bond vibrations (Allen and Tildesley, 1987). The alternative to the use of flexible molecules for simulating molecular liquids is to employ the constraint method and rigid bodies models to ensure the conservation of the geometry.

3.6.1 Constraint method

This technique has been devised to handle the simulation of these systems where certain (uninteresting) degrees of freedom are constrained, while others are free to

evolve under the influence of inter- (and intra-) molecular forces (Ryckaert et al., 1977). Moreover, it can also be used for totally rigid molecules and is in competition with the quaternion algorithms discussed in the next section. Both techniques have been used in this work for the simulation of liquid methanol (see section 6.2). The basic ideas are best described in terms of a simple molecular model for which we choose a non-linear methanol molecule (see section 6.2). Let us constrain the O-Ho and O-CH_3 bonds, denoted respectively as d_{12} and d_{23}, to a fixed length (see figure 3.3). The bond angle is fixed by constraining the Ho-CH_3 distance. The equations of motions (3.1) take the form

$$m_1 \frac{d^2}{dt^2} \boldsymbol{r}_1 = \boldsymbol{f}_1 + \boldsymbol{g}_1,$$

$$m_2 \frac{d^2}{dt^2} \boldsymbol{r}_2 = \boldsymbol{f}_2 + \boldsymbol{g}_2, \text{ and} \qquad (3.6)$$

$$m_3 \frac{d^2}{dt^2} \boldsymbol{r}_3 = \boldsymbol{f}_3 + \boldsymbol{g}_3.$$

Here the $\boldsymbol{f}$'s are the usual forces (of equation (3.1)) and $\boldsymbol{g}$'s are the constraint forces which are not known but their role will be to keep the desired bond lengths constant, *i.e.*

$$(\boldsymbol{r}_{12})^2-(d_{12})^2 = 0,$$

$$(\boldsymbol{r}_{23})^2-(d_{23})^2 = 0, \text{ and} \qquad (3.7)$$

$$(\boldsymbol{r}_{13})^2-(d_{13})^2 = 0.$$

Since the constraints must be directed along the bonds and conform to Newton's third law, the $\boldsymbol{g}$'s are given by:

$$\boldsymbol{g}_1 = \lambda_{12} \boldsymbol{r}_{12} - \lambda_{13} \boldsymbol{r}_{13},$$

$$g_2 = \lambda_{23}\, r_{23} - \lambda_{12}\, r_{12}, \tag{3.8}$$

$$g_3 = \lambda_{13}\, r_{13} - \lambda_{23}\, r_{23},$$

where λ are undetermined multipliers. For updating the positions the application of the constraint in the Verlet algorithm introduces a new term,

$$r_1(t+\Delta t) = r'_1(t+\Delta t) + (\Delta t^2/m_1)\,\lambda_{12}\, r_{12}(t) - (\Delta t^2/m_1)\,\lambda_{13}\, r_{13}(t) \tag{3.9}$$

$$r_2(t+\Delta t) = r'_2(t+\Delta t) + (\Delta t^2/m_2)\,\lambda_{23}\, r_{23}(t) - (\Delta t^2/m_2)\,\lambda_{12}\, r_{12}(t) \tag{3.10}$$

$$r_3(t+\Delta t) = r'_3(t+\Delta t) + (\Delta t^2/m_3)\,\lambda_{13}\, r_{13}(t) - (\Delta t^2/m_3)\,\lambda_{23}\, r_{23}(t). \tag{3.11}$$

Here the primes indicate positions that would have been obtained in the absence of any constraints. By subtracting the above three expressions each other give:

$$r_{12}(t+\Delta t) = r'_{12}(t+\Delta t) + \Delta t^2(m_1^{-1} + m_2^{-1})\lambda_{12}\, r_{12}(t) - \Delta t^2 m_1^{-1}\lambda_{13}\, r_{13}(t) - \Delta t^2 m_2^{-1}\,\lambda_{23}\, r_{23}(t) \tag{3.12}$$

$$r_{23}(t+\Delta t) = r'_{23}(t+\Delta t) - \Delta t^2/m_3^{-1}\,\lambda_{13}\, r_{13}(t) + \Delta t^2(m_2^{-1} + m_3^{-1})\lambda_{23}\, r_{23}(t) - \Delta t^2 m_2^{-1}\,\lambda_{12}\, r_{12}(t) \tag{3.13}$$

$$r_{13}(t+\Delta t) = r'_{13}(t+\Delta t) - \Delta t^2/m_3^{-1}\,\lambda_{23}\, r_{13}(t) + \Delta t^2(m_1^{-1} + m_3^{-1})\lambda_{13}\, r_{13}(t) - \Delta t^2 m_1^{-1}\,\lambda_{12}\, r_{12}(t). \tag{3.14}$$

If we now take the square modulus of both sides and apply the constraint conditions (3.7) we obtain a triplet of quadratic equations in the λ's. These equations are solved in an iterative fashion within a given tolerance and this approach has been called the SHAKE algorithm (Ryckaert et al., 1977). The programme package, DL_POLY_2.0 (Smith and Forester, 1996), used for the simulations employs a leapfrog variant of SHAKE.

1. In a first stage the leapfrog algorithm calculates the motion of the atoms in the system by assuming a complete absence of rigid bond forces.

2. In the second stage, only atoms 1 and 2 are considered first and the rest (atom 3) are ignored. Equations (3.9-11) are used to update the positions of only these two atoms as follows:

a. Putting $\lambda_{23} = \lambda_{31} = 0$, we subtract equations (3.9) and (3.10) and square the results.

b. Recalling the requirement (3.7), and ignoring the second order term gives

$$(d_{12})^2 = \boldsymbol{r'}_{12}^2\,(t+\Delta t) + 2\,\lambda_{12}\,\boldsymbol{r'}_{12}\,(t+\Delta t)\,\boldsymbol{r}_{12}\,(t)\,\Delta t^2(m_1^{-1} + m_2^{-1}). \qquad (3.15)$$

This can be solved for λ_{12} and new values obtained for the positions $\boldsymbol{r}_1\,(t+\Delta t)$ and $\boldsymbol{r}_2\,(t+\Delta t)$ of atom 1 and 2, using equations (3.9) and (3.10)

3. The same steps, as above, are then applied to atoms 2 and 3, after putting $\boldsymbol{r'}_1(t+\Delta t) = \boldsymbol{r}_1\,(t+\Delta t)$ and $\boldsymbol{r'}_2(t+\Delta t) = \boldsymbol{r}_2\,(t+\Delta t)$.

4. The procedure is iterated until all constraints with respect to equation (3.7) are satisfied.

However, for geometries more complicated than the three-site methanol molecule considered above, although the structure could be defined in terms of bond constraints the network of rigid bonds so produced caused problems. In particular with simulations involving six-site methanol molecules problems arose due to the presence of too many linked triangular constraints for which the SHAKE algorithm became unstable. Similar difficulties were encountered for twelve-site benzene. In this case, because all the constraints act in the plane of the ring, none of them act to preserve the planarity of the molecule. Moreover, massless sites cannot be included in the simple constraint approach. For those molecular geometries where SHAKE algorithm failed,

we used the rigid bodies and the quaternion rotational integration algorithms, which are described in the next section.

3.6.2 Rigid molecular models

A rigid body is a collection of point atoms whose local geometry is time invariant. The motion of the body can be separated into translational and rotational motion. A rigid body has associated with it a rotational inertia tensor $\underline{I}$, whose components are given by $I_{\alpha\beta} = 1/2\sum_{sites} mr_\alpha r_\beta$ where r is the site to an arbitrary origin distance and m the site masses. In DL_POLY the local body frame is defined to be that in which the rotational inertia tensor $\underline{I}$ is diagonal (denoted $\underline{I}'$) and the components satisfy $I_{xx} \geq I_{yy} \geq I_{zz}$. Usually in classical mechanics, the properties characterising rotational motion are the change of orientation rate (conventionally described by the Euler angles, φ, θ, Ψ), the angular velocity ω (or angular momentum J), the moment of inertia $\underline{I}$, and the torque T. However, when equations of the rotational motion analogous to the translational case are derived, they show a singularity due to the presence of terms in $1/\sin\theta$, so that whenever $\theta \rightarrow 0$ the solution diverges (Allen and Tildesley, 1987). A much more satisfactory approach, suggested by Evans (1977), is to use four quaternion parameters as generalised co-ordinates for the description of the molecular orientations. They produce well-behaved equations of motion without troublesome singularities. The way in which such a quaternion may represent the orientation of a rigid body is discussed in detail by Goldstein (1980). A quaternion q is a set of 4 scalar quantities:

$q = (q_0, q_1, q_2, q_3)$ satisfying the condition $q^2 = q_0^2 + q_1^2 + q_2^2 + q_3^2 = 1$

The orientation of a local body frame with respect to the space fixed frame is described *via* the four dimentional unit vector q for which,

$$q_0 = \cos\theta/2 \cos[(\varphi+\Psi)/2]$$

$$q_1 = \sin\theta/2 \cos[(\varphi-\Psi)/2]$$

$q_2 = \sin\theta/2 \sin[(\varphi - \Psi)/2]$

$q_3 = \cos\theta/2 \sin[(\varphi + \Psi)/2]$ (3.16)

The rotational matrix required to transform from the local body frame to the space fixed frame is given by the unitary matrix

$$\underline{\boldsymbol{R}} = \begin{bmatrix} q_0^2 + q_1^2 - q_2^2 - q_3^2 & 2(q_1 q_2 - q_0 q_3) & 2(q_1 q_3 + q_0 q_2) \\ 2(q_1 q_2 + q_0 q_3) & q_0^2 - q_1^2 + q_2^2 - q_3^2 & 2(q_2 q_3 - q_0 q_1) \\ 2(q_1 q_3 - q_0 q_2) & 2(q_2 q_3 + q_0 q_1) & q_0^2 - q_1^2 - q_2^2 + q_3^2 \end{bmatrix}, \quad (3.17)$$

So that if $\boldsymbol{d'}_\alpha$ is the position of a site in the local body frame with respect to its center of mass (c.o.m), its position in the space fixed frame is given by

$$\boldsymbol{d}_\alpha = \underline{\boldsymbol{R}} \cdot \boldsymbol{d'}_\alpha . \quad (3.18)$$

The translational force acting upon the rigid unit is

$$\boldsymbol{F} = \sum_\alpha \boldsymbol{f}_\alpha , \quad (3.19)$$

where $\boldsymbol{f}_\alpha$ is the force on a rigid unit site α, and the sum includes all sites in the body. The translational motion can be integrated by the standard leapfrog algorithm:

$$\boldsymbol{v}_{\text{c.o.m}}(t+\Delta t/2) \leftarrow \boldsymbol{v}_{\text{c.o.m}}(t-\Delta t/2) + \Delta t\, \boldsymbol{F}(t)/M \quad (3.20)$$

$$\boldsymbol{r}_{\text{c.o.m}}(t+\Delta t) \leftarrow \boldsymbol{r}_{\text{c.o.m}}(t) + \Delta t\, \boldsymbol{v}_{\text{c.o.m}}(t+\Delta t/2), \quad (3.21)$$

where M is the mass of the rigid body, $\boldsymbol{v}_{\text{c.o.m}}$, the rigid body centre of mass (c.o.m.) velocity and $\boldsymbol{r}_{\text{c.o.m}}$, is the c.o.m. position. The torque $\boldsymbol{T}$ acting upon the body in the space fixed frame is

$$\boldsymbol{T} = \sum_{\alpha} \boldsymbol{d}_{\alpha} \times \boldsymbol{f}_{\alpha} \,. \tag{3.22}$$

Transformed to the local body frame this is

$$\boldsymbol{T}' = \underline{\boldsymbol{R}}^{\mathrm{T}} . \boldsymbol{T} \,, \tag{3.23}$$

where $\underline{\boldsymbol{R}}^{\mathrm{T}}$ is the transpose of the unitary matrix $\underline{\boldsymbol{R}}$ (see equation 3.17). The angular velocity transformed to the local body frame $\omega' = \underline{\boldsymbol{R}}^{\mathrm{T}} . \omega$ can then be integrated using the leapfrog algorithm and the diagonal rotational inertia tensor, $\underline{\boldsymbol{I}}'$.

$$\omega'(t+\Delta t/2) \leftarrow \omega'(t-\Delta t/2) + \Delta t \, \underline{\boldsymbol{I}}'^{-1} . \boldsymbol{T}'(t) \,. \tag{3.24}$$

The new quaternions corresponding to a time step Δt further cannot be found so simply. DL_POLY uses Fincham's implicit algorithm (FIQA) to do this (Fincham, 1992). In this algorithm the new quaternions are found by solving the implicit equation

$$\boldsymbol{q}(t+\Delta t) = \boldsymbol{q}(t) + \frac{\Delta t}{2} \left(\underline{\boldsymbol{Q}}[\boldsymbol{q}(t)] \boldsymbol{w}'(t) + \underline{\boldsymbol{Q}}[\boldsymbol{q}(t+\Delta t)] \, \boldsymbol{w}'(t+\Delta t) \right), \tag{3.25}$$

where $\boldsymbol{w}' = [0, \omega']^{\mathrm{T}}$ and $\underline{\boldsymbol{Q}}[\boldsymbol{q}]$ is

$$\underline{\boldsymbol{Q}} = \frac{1}{2} \begin{bmatrix} q_0 & -q_1 & -q_2 & -q_3 \\ q_1 & q_0 & -q_3 & -q_2 \\ q_2 & q_3 & q_0 & -q_1 \\ q_3 & -q_2 & q_1 & q_0 \end{bmatrix} . \tag{3.26}$$

The above equation is solved iteratively with

$$\boldsymbol{q}(t+\Delta t) = \boldsymbol{q}(t) + \frac{\Delta t}{2} \left(\underline{\boldsymbol{Q}}[\boldsymbol{q}(t)] \boldsymbol{w}'(t) \right) \tag{3.27}$$

as the first guess with the constraint $\boldsymbol{q}^2$ $(t+\Delta t)$ =1 imposed at each step. Using this elegant method suitable for rigid molecules that are not too complex, the geometry of the molecule is kept invariant throughout the simulation. By uncoupling the translational motion of the c.o.m from the rotational motion, and using a four dimensional vector (quaternion), the troublesome singularities are removed.

3.7 Long range forces

Those interactions that decay no faster than r^{-3}, can be a problem as their range may be greater than half the box length. The charge-charge coulombic interaction, which decays as r^{-1} is a serious concern in molecular dynamics simulations. One way to tackle these Coulombic interactions would be to use a larger simulation box, but this is usually impractical. Three methods have been used to handle these coulombic interactions in our simulations (reported in sections 6.2, 7.3 and 8.3): the truncated and shifted coulomb sum, the reaction field model, and the Ewald summation.

3.7.1 Truncated and shifted coulomb sum

This form of Coulomb sum has the advantage that it drastically reduces the range of electrostatic interactions, without giving rise to a violent step in the potential energy at the cutoff. The form of the potential function is

$$U_{ij}(r_{ij}) = \frac{q_i q_j}{4\pi\varepsilon_0}\left\{\frac{1}{r_{ij}} - \frac{1}{r_{cut}}\right\}, \tag{3.28}$$

with q_i the charge on atom labelled i, r_{cut} the cutoff radius and r_{ij} the magnituge of the separation vector, $\boldsymbol{r_{ij}} = \boldsymbol{r_j} - \boldsymbol{r_i}$. The force on atom j derived from this potential, within the radius, r_{cut} is

$$\boldsymbol{f}_j = \frac{q_i q_j}{4\pi\varepsilon_0 r_{ij}^{\ 3}}\boldsymbol{r}_{ij}, \tag{3.29}$$

with the force on atom i the negative of this. In order to make both the energy and force zero at r_{cut}, a further refinement consists in truncating the r^{-1} potential at r_{cut} and adding a linear term to the potential. The potential then takes the form:

$$U_{ij}(r_{ij}) = \frac{q_i q_j}{4\pi\varepsilon_0}\left\{\frac{1}{r_{ij}} + \frac{r_{ij}}{r^2{}_{cut}} - \frac{2}{r_{cut}}\right\}, \tag{3.30}$$

so that the force on atom j is given by

$$\boldsymbol{f}_j(r_{ij}) = \frac{q_i q_j}{4\pi\varepsilon_0}\left\{\frac{1}{r^2{}_{ij}} - \frac{1}{r^2{}_{cut}}\right\}\boldsymbol{r}_{ij}/|r_{ij}|. \tag{3.31}$$

This removes the heating effects that arise from the discontinuity in the forces at the cutoff in the simple truncated and shifted potential.

3.7.2 Reaction field method

In this method, a sphere is constructed around the molecule with a radius equal to r_{cut}. The interaction with molecules that are within this sphere is calculated explicitly. To this is added the energy of interaction with the medium beyond the sphere, which is modelled as a continuum of dielectric constant ε_1. The reaction field model coded into the DL_POLY is the implementation of Neumann's formalism (Neumann, 1985). In this model, the total Coulombic potential is given by:

$$U_c = \frac{1}{4\pi\varepsilon_0}\sum_{i<j} q_i q_j \left\{\frac{1}{r_{ij}} + \frac{B_0 r^2{}_{ij}}{2r^3{}_{cut}}\right\}, \tag{3.32}$$

where the second term on the right is the reaction field correction to the explicit sum. The constant B_0 is defined as

$$B_0 = \frac{2(\varepsilon_1 - 1)}{2\varepsilon_1 + 1}. \tag{3.33}$$

The effective pair force on an atom j arising from another atom i within the cavity is then given by

$$f_j = \frac{q_i q_j}{4\pi\varepsilon_0}\left\{\frac{1}{r^3_{ij}} + \frac{B_0}{r^3_{cut}}\right\}\boldsymbol{r}_{ij}. \tag{3.34}$$

3.7.3 The Ewald summation method

The Ewald sum is the best technique for calculating electrostatic interactions in a periodic system (Allen and Tildesley, 1987; De Leeuw et al., 1980). The basic model for a neutral periodic system is an assembly of charged points mutually interacting *via* the Coulomb potential. In the Ewald method each point charge is neutralised by the superposition of a spherical Gaussian cloud of width α and opposite charge centred on the point charge. These extra distributions screen the interaction between neighbouring charges. The screened interactions become short-ranged, and the screened potential is calculated by summing in the *real space*. The real space sum ranges over all periodic images of the simulation box, but in the DL_POLY implementation, the parameters are chosen to restrict the sum to the simulation box and its nearest neighbours (the minimum images of the box contents). A second set of gaussian charges are added, this time with the same charges as the original point charges and again centred on the point charges (so nullifying the effect of the first set of Gaussian) are also superposed. The potential due to these Gaussians is obtained from the Poisson's equation and is solved as a Fourier series in the *reciprocal space*. The complete Ewald sum requires a correction, known as the self-energy correction, which arises from a Gaussian acting on its own site, and is constant, and needs to be subtracted. For molecular systems, as opposed to systems comprising simply of point charges (such as ionic liquids), additional modifications are necessary to correct for the excluded intra-molecular Coulombic interactions. In the real space sum these are just omitted. However, the effects of individual gaussian charges cannot easily extracted, and the correction is made in the real space. It amounts to removing terms corresponding to the potential energy of a point charge l due to the gaussian charge on neighbouring charge m (or vice versa). This correction appears as the final term in the full Ewald formula below. The total electrostatic energy is given by

$$U_c = \frac{1}{2V\varepsilon_0}\sum_{k\neq 0} k^{-2}\exp(-k^2/4\alpha^2)\left|\sum_j^N q_j \exp(-i\boldsymbol{k}.\boldsymbol{r}_j)\right|^2 + \frac{1}{4\pi\varepsilon_0}\sum_{i<j}^{N^*}\frac{q_i q_j}{r_{ij}} erfc(\alpha\, r_{ij})$$

$$-\frac{1}{4\pi\varepsilon_0}\sum_{molecules}\sum_{l\leq m}^{M^*} q_l q_m \left\{\delta_{lm}\frac{\alpha}{\sqrt{\pi}} + \frac{erf(\alpha\, r_{lm})}{r_{lm}^{1-\delta_{lm}}}\right\}, \qquad (3.35)$$

where

$$erfc(x) = 2/\pi^{1/2}\int_x^\infty exp(-t^2)dt$$

(3.36)

$$erf(x) = 2/\pi^{1/2}\int_0^x exp(-t^2)dt\,.$$

N is the number of point charges in the system and N^* the same number after discounting any excluded intra-molecular interactions. M^* represents the number of excluded atoms in a given molecule. V is the simulation box volume and $\boldsymbol{k}$ is a reciprocal lattice vector defined by

$$\boldsymbol{k} = l\boldsymbol{u} + m\boldsymbol{v} + n\boldsymbol{w}, \qquad (3.37)$$

where l, m, n, are integer and $\boldsymbol{u}$, $\boldsymbol{v}$, $\boldsymbol{w}$ are devised from the vectors ($\boldsymbol{a}$, $\boldsymbol{b}$, $\boldsymbol{c}$) defining the simulation cell. The convergence of the Ewald sum reported in this work was controlled by three variables: the real space cutoff r_{cut}, the width of the gaussians α, and the largest reciprocal space vector $\boldsymbol{k}_{max}$ used in the reciprocal sum. The adherence to the relation Uc=-Wc (Wc is the Coulombic virial) shows the extent to which the Ewald sum has correctly converged with the three chosen variables, thus providing a quick check on the accuracy of the Ewald sum by using the simulation software.

3.8 Calculated properties

In the previous sections we focused attention on the simulation itself, that is, on computing the phase space trajectory for a system of model molecules. In this section we turn our attention to the analysis of computed trajectories. The analysis involves evaluating macroscopic properties that pertain to an entire system of molecules. The properties considered here are simple thermodynamic and dynamic quantities that are used merely to validate the simulation results before attempting to investigate the static structure of the systems under consideration.

3.8.1 Simple thermodynamic properties

Although a variety of thermodynamic functions can be calculated from averages of either the Hamiltonian or its spatial and momentum derivatives, in this section we discuss only those functions or properties that were actually evaluated from the simulation runs reported in this thesis, and these are temperature, pressure and internal energy.

a. Temperature

In the microcanonical ensemble the temperature fluctuates. The temperature is directly related to the kinetic energy of the system as follows:

$$E_{kin} = \sum_{i=1}^{N} \frac{|\boldsymbol{p}_i|^2}{2m_i} = \frac{k_B T}{2}(3N - N_c) \approx \sum_{k=1}^{M}\sum_{i=1}^{N} \frac{1}{2m_i M}|\boldsymbol{p}_i(t_k)|^2 . \qquad (3.38)$$

According to the theorem of the equipartition of energy each degree of freedom contributes *kT/2* of the total kinetic energy of the system. If there are *N* particles (atoms or sites) each with three degrees of freedom then the kinetic energy should equal *3NkT/2*. *Nc* represents the number of constraints on the system. In a molecular dynamics simulation the total linear momentum of the system is often constrained to a value of zero. This has the effect of removing three degrees of freedom from the system. Moreover, other types of constraints also need to be considered. For

instance, in the simulation of 216 three-site methanol molecules for which the SHAKE algorithm was used (see section 3.6.1), three bond lengths per molecule were kept fixed, and these constraints have to be subtracted, thus $Nc = 3N_{molecules} - 3 = 645$.

b. Internal energy (configurational energy)

In section 2.6.1 we saw that the internal energy can be calculated from a knowledge of the pair distribution functions in the case of a pair-wise additive potential model. Practically, for a system subjected to the periodic boundary conditions the configurational energy is calculated as the average of the pair potential function $u(r)$,

$$\langle U_c \rangle = \frac{1}{M} \sum_{k=1}^{M} \sum_{\text{all sites a,b}} u_{ab}(r(t_k)) . \tag{3.39}$$

However, while the simulations usually employ truncated model potential, it is desirable that the properties are evaluated for a fully un-truncated potential. From this viewpoint, expression such as (3.39) is incomplete because the simulation ignores interactions between atoms separated by distances greater than the cut-off distance, r_C. Therefore, simulation results for $<U_c>$ must be corrected for the long range contribution U^{lr}. The estimation of this residual contribution for each site-site pair potential is given by the following expression, calculated by using equation (2.71)

$$<U^{lr}_{ab}> = 2\pi \frac{NaNb}{V} \int_0^{r_c} r^2 \, g_{ab}(r) \, u_{ab}(r) \, dr + 2\pi \frac{NaNb}{V} \int_{r_c}^{\infty} r^2 \, g_{ab}(r) \, u_{ab}(r) \, dr. \tag{3.40}$$

The first term on the right hand side of (3.40) is calculated explicitly via (3.39). The second term is the required long-range correction. The complete expression for the configurational energy is then

$$<U> = <U_c> + U^{lr}. \tag{3.41}$$

In the absence of data at $r > r_c$, the usual approximation consists in taking the ideal gas limit,1, for $g_{ab}(r)$ (see equation 2.46b). Thus, the correction for each site-site pair potential is typically estimated by

$$<U^{lr}_{ab}> = 2\pi \frac{NaNb}{V} \int_{r_c}^{\infty} r^2 \; u_{ab}(r)\, dr. \tag{3.42}$$

For very common model potentials such as the Lennard-Jones (LJ-12-6) model or a exponential potential (see section 7.3.1), DL_POLY calculates these corrections routinely. However, for the other model potentials used in the work presented here, these contributions were evaluated separately. It can be clearly seen that for a potential $u_{ab}(r)$ in the form r^{-3}, the integral in equation (3.42) does not converge. In the case of the coulombic interactions, these corrections are handled by the special treatment the coulombic potential requires (see previous section).

c. Pressure

As for the configurational energy, the pressure can also be calculated from a knowledge of the pair distribution functions in the case of a pairwise additive potential model (see equation 2.79). Practically, however, for a system subjected to the periodic boundary conditions the pressure is calculated by using the virial equation of state (see equation 2.75),

$$PV/k_BT = < N - \frac{1}{3k_BT} \sum_i \; \boldsymbol{r}_i \, \nabla_i u\,(\boldsymbol{r}_{ij}) > \tag{3.43}$$

$$= < N - \frac{1}{3k_BT} \sum_i \; \boldsymbol{r}_i \boldsymbol{f}_i >. \tag{3.44}$$

The latter expression is more conveniently expressed in a form which is explicitly independent of the coordinates. This is done by writing $\boldsymbol{f}_i$ as the sum of forces $\boldsymbol{f}_{ij}$ on atom i and j

$$\sum_i \boldsymbol{r}_i \boldsymbol{f}_i = \sum_i \sum_{j \neq i} \boldsymbol{r}_i \boldsymbol{f}_{ij} = 1/2 \sum_i \sum_{j<i} \boldsymbol{r}_i \boldsymbol{f}_{ij} + \boldsymbol{r}_j \boldsymbol{f}_{ji} \; . \tag{3.45}$$

The second equality follows because the indices i and j are equivalent. Newton's third law, $\boldsymbol{f}_{ji}=-\boldsymbol{f}_{ij}$, is then used to switch the force indices

$$\sum_i \boldsymbol{r}_i \boldsymbol{f}_i = 1/2 \sum_i \sum_{j<i} \boldsymbol{r}_{ji} \boldsymbol{f}_{ij} = \sum_i \sum_{j<i} \boldsymbol{r}_{ij} \boldsymbol{f}_{ij}\,, \tag{3.46}$$

and the pressure in a MD simulation run is calculated from a phase trajectory by,

$$\frac{P_{MD}}{k_B T} = \frac{N}{V} - \frac{1}{3MVk_B T} \sum_{k=1}^{M} \sum_i \sum_{i<j} r_{ij}(t_k) \frac{d}{dr_{ij}} u(r_{ij}(t_k))\,. \tag{3.47}$$

Just as for the configurational energy, when a truncated potential is used, a long-range correction must be added to the molecular dynamics result for the virial. Thus, the full expression for the pressure is

$$P = P_{MD} + P^{LR}. \tag{3.48}$$

The long-range correction is estimated by proceeding in the same way as for the internal energy. The second term of equation (2.79) yields for each potential pair, *a-b*,

$$P^{LR}{}_{ab}/k_B T = -\frac{2\pi NaNb}{3k_B TV^2} \int_{r_c}^{\infty} r^3 \frac{d}{dr} u_{ab}(r)\, dr, \tag{3.49}$$

where it was assumed that $g_{ab}(r)$ =1 beyond the cutoff. As for the internal energy DL_POLY calculates these corrections routinely for the most commonly used model potentials. However, for the other model potentials used in the present study, these contributions were evaluated separately. Again for potentials, $u_{ab}(r)$ varying as r^{-3}, the integral (3.49) does not converge. For the coulombic interactions, these correction are handled by the special treatment they require, and this has already been discussed in the previous section.

3.8.2 Single particle dynamics

From the static properties, we turn now to the calculation of dynamics properties used for the validation of the MD simulations. For a microscopic time dependent property, A, the time correlation function $C(t)$ which is a measure of how the value of A at $t_0+\tau$ related to the same property at time t_0, is defined by,

$$C(t)=\lim_{\tau\to\infty}\frac{1}{\tau}\int_0^{\tau}A(t_0)A(t_0+t)dt_0 = <A(t_0)\,A(t_0+t)>. \tag{3.50}$$

This integral represents an average accumulated over many time origins t_0, for whith each origin is taken from an already equilibrated system. The quantity A is sampled at the time origin and sampled again after a delay time t. Thus, the correlation function C depends on the length of the delay, and because it is an equilibrium property, it is independent of the time origin chosen. In the limit of no delay time,

$$C(0)= <A(t_0)^2>. \tag{3.51}$$

In the other extreme case, the long-time limit, the time correlation functions usually become uncorrelated after long delay times,

$$\lim_{\tau\to\text{large}} C(t) = <A>^2. \tag{3.52}$$

It is customary to normalise the time correlation functions as

$$\hat{C}(t) = <A(t_0)\,A(t_0+t)>/<A(t_0)^2>, \tag{3.53}$$

so that $\hat{C}(0)=1$.

a. Velocity auto-correlation function

In the MD simulation work presented in this thesis the only time correlation function investigated are the velocity auto correlation functions (VACF) for which the property A is the velocity of atoms. Because atomic motions are chaotic and not periodic, the long time limit of the velocity auto-correlation function is the square of the average velocity of the N atoms. For systems at equilibrium (non flowing systems) $\langle v \rangle^2 = 0$, and so

$$\lim_{\tau \to \text{large}} C_{vv}(t) = \langle \boldsymbol{v}(t_0)\, \boldsymbol{v}(t_0+t) \rangle = 0. \tag{3.54}$$

Thus, the normalised VACF, $\hat{C}_{vv}(t)$ starts from 1 and decays to 0. If the velocities of N atoms are stored in the memory of a computer at n discrete times, theVACF $C_{vv}(t)$ is given from the approximate time average

$$C_{vv}(t) = \frac{1}{M(t)N} \sum_{k}^{M(t)} \sum_{i}^{N} \boldsymbol{v}_i(t_k)\, \boldsymbol{v}_i(t_k+t). \tag{3.55}$$

Here, $M(t)$ is the total number of available time origins, and its value changes with the delay time t,

$$M(t) = n - \frac{t}{\Delta t}, \tag{3.56}$$

where Δt is the time step at which velocities of N atoms were stored. Quantities with small relaxation time can thus be determined with greater statistical precision than longer time processes, since it is possible to include a greater number of data sets from a given simulation.

b. Self diffusion coefficient

To a first approximation, the change of a relevant quantity (such as mass, energy or momentum), called the flux, is proportional to the gradient of the property with the

constant of proportionality being the relevant transport property coefficient. For example, the flux of matter in the z direction, J_z equals the diffusion coeficient (D) multiplied by the concentration gradient (Fick's first law):

$$J_z = -D\frac{dN(z,t)}{dz}, \tag{3.57}$$

where $N(z,t)$ is the number of atoms per unit volume (i.e. length) located at position z at time t. The time dependence of the diffusive behaviour is governed by Fick's second law, which gives the rate of change of concentration with time:

$$\frac{\partial N(z,t)}{\partial t} = -D\frac{\partial^2 N(z,t)}{\partial^2 z}. \tag{3.58}$$

It is necessary to impose two boundary conditions for the spatial dependence and one boundary condition for the temporal dependence (the equation is second order in space and first order in time). For a set of initial conditions, the solution of the latter expression is:

$$N(z,t) = \frac{N_0}{2\sqrt{\pi Dt}}\exp\left(\frac{-z^2}{4Dt}\right). \tag{3.59}$$

At any time $t > 0$, the second moment of the distribution gives the mean-square displacement of atoms:

$$< [z(t)- z(0)]^2> = 1/N_0 \int z^2 N(z,t)dz\,. \tag{3.60}$$

Putting (3.59) into (3.60) and performing the integration, the mean-square displacement (MSD) is simply related to diffusion coefficient, D

$$< [z(t)- z(0)]^2> = 2Dt. \tag{3.61}$$

This result applies when the time t is large compared to the average time between collisions of atoms. The three-dimensional analogue of (3.61) is

$$\lim_{t\to\infty}\frac{\left\langle[\boldsymbol{r}(t)-\boldsymbol{r}(0)]^2\right\rangle}{6t}=D. \tag{3.62}$$

This is the well-known relation due to Einstein. Equation (3.62) implies that the MSD grows linearly at large delay times. In a MD simulation, the MSD are calculated using a similar procedure as that used for the VACF (see equation 3.55),

$$\mathrm{MSD}(t)=\frac{1}{M(t)N}\sum_{k}^{M(t)}\sum_{i}^{N}\boldsymbol{r}_i(t_k+t)-\boldsymbol{r}_i(t_k). \tag{3.63}$$

Note that in computing the right hand side of the above equation, it is important not to switch attention from one periodic image to another. In other words, the MSD should not be limited by the edges of the periodic box. This was achieved by storing a set of "uncorrected" positions.

One alternative approach to the calculation of the self-diffusion coefficient is via the VACF. For example, the diffusion coefficient depends upon the way in which the atomic position $\boldsymbol{r}(t)$ changes with time. At a time t, the difference between $\boldsymbol{r}(t)$ and $\boldsymbol{r}(0)$ is given by:

$$\boldsymbol{r}(t)-\boldsymbol{r}(0)=\int_0^t\boldsymbol{v}(t')dt'. \tag{3.64}$$

When squared and averaged over times origins, equation (2.2.64) becomes

$$\left\langle[\boldsymbol{r}(t)-\boldsymbol{r}(0)]^2\right\rangle=\int_0^t dt'\int_0^{t'}dt''\left\langle\boldsymbol{v}(t'')\boldsymbol{v}(t')\right\rangle. \tag{3.65}$$

The properties of symmetry with respect to time inversion and invariance under time translation dictate that equation (3.65) can be combined with the definition of the time correlation function (3.50) to give

$$\left\langle [\boldsymbol{r}(t)-\boldsymbol{r}(0)]^2 \right\rangle = 2\int_0^t dt' \int_0^{t'} dt'' \left\langle \boldsymbol{v}(t'-t'')\boldsymbol{v}(0) \right\rangle . \tag{3.66}$$

By changing from variables t' and t'' to t' and $s = t' - t''$ and integrating by parts, one finds that

$$\left\langle [\boldsymbol{r}(t)-\boldsymbol{r}(0)]^2 \right\rangle = 2\int_0^t dt' \int_0^{t'} ds \left\langle \boldsymbol{v}(s)\boldsymbol{v}(0) \right\rangle$$

$$= 2t\int_0^t ds \left\langle \boldsymbol{v}(s)\boldsymbol{v}(0) \right\rangle (1-s/t) . \tag{3.67}$$

Taking the long time limit and using equation (3.62),

$$\lim_{t\to\infty} \frac{\left\langle [\boldsymbol{r}(t)-\boldsymbol{r}(0)]^2 \right\rangle}{2t} = \int_0^\infty ds \left\langle \boldsymbol{v}(s)\boldsymbol{v}(0) \right\rangle = 3D . \tag{3.68}$$

This establishes the general relation between the MSD (via the Einstein relation) and the VACF (via the Green-Kubo relations). Practically speaking, the slow decay of the VACF can present problems when deriving the self-diffusion coefficient because it requires the VACF to be integrated over time varying from zero to infinity. This, so called "long time tail" of the VACF makes a significant contribution to the integral (3.68). Unfortunately, the statistical uncertainties (for a fuller account see Allen and Tildesley, 1987) associated with this part of the VACF has to be calculated are sometimes huge since only fewer segments of appropriate length can be extracted from the simulation. Using the MSD approach, the value of the diffusion coefficient given by the Einstein relation 3.6.2 is correct only at longer time. However, during the computation less data are also collected at longer than shorter delay times so that the statistical uncertainties associated with this collection of data still remain

problematic. As a result, for a consistency check, the self-diffusion coefficients reported in this thesis were computed using both (MSD and VACF) the approaches.

3.8.3 Static structure

For homogeneous and isotropic substances, the distribution function defined by equation (2.60) may be written as

$$\rho g(r) = <\frac{2}{N} \sum_{i<j}^{N} \delta(r - r_{ij})>. \tag{3.69}$$

The radial distribution function $g(r)$ describes how atoms organise themselves around one another "local structure" and, it is proportional to the probability of finding two atoms separated by a distance r. As stated in the introduction (chapter 1), this function plays a central role in statistical mechanical theories of the liquid state, and it can also be extracted from X-rays or ND experiments. Since MD simulations provide positions of individual atoms as function of time, $g(r)$ can be readily computed. To obtain an expression for evaluating $g(r)$ from simulation data, we start by rewriting (3.69) using a small but finite shell thickness Δr,

$$\rho \sum_{\Delta r} g(r) V(r, \Delta r) = \frac{2}{N} \sum_{\Delta r} \left\langle \sum_{i<j}^{N} \delta(r - r_{ij}) V(r, \Delta r) \right\rangle. \tag{3.70}$$

Here $V(r, \Delta r)$ is the volume of the spherical shell of radius r and thickness Δr. The double sum in the right hand side of equation (3.70) gives the number, $N(r,\Delta r)$ of atoms found in the spherical shell of radius r and thickness Δr, with the shell centred on another atom. It then follows that,

$$\rho \sum_{\Delta r} g(r) V(r, \Delta r) = \frac{2}{N} \sum_{\Delta r} \langle N(r, \Delta r) \rangle. \tag{3.71}$$

The latter expression must be satisfied term by term, for each spherical shell. Thus

$$g(r) = \frac{\langle N(r,\Delta r)\rangle}{\frac{1}{2}N\rho V(r,\Delta r)}. \tag{3.72}$$

Writing the time average explicitly over a total of M time-steps gives

$$g(r) = \frac{\sum_{k=1}^{M} N_k(r,\Delta r)}{M\frac{1}{2}N\rho V(r,\Delta r)}, \tag{3.73}$$

where N_k is the result of the counting operation at time t_k in the run. Physically, (3.73) can be interpreted as the ratio of a local density $\rho(r)$ to the system density ρ. For the simulations reported here, the shell thickness, Δr was ~ 0.05Å with M ~ 20000. These values were chosen as a compromise between providing a sufficiently large sampling population for statistically reliable results and small enough to resolve important features of $g(r)$.

3.9 Path to equilibrium

3.9.1 Initialisation

In all the work presented in the forthcoming chapters, the MD simulations were performed on isolated systems. The independent thermodynamic properties are the number of particles N, system volume V, and the total (kinetic + configurational) energy E. The initial positions of all the atoms within a molecule were assigned by generating an original cubic box whose edge length is related to the experimental density. The atom co-ordinates were determined from the known molecular geometry. This original box was replicated n times in three dimensions so as to build a cubic lattice containing n^3 molecules with values of n = 5 or 6. The size of the simulated system was large enough to enable properties of interest to be determined with reasonable accuracy without making the simulations prohibitively expensive. The initial velocities of all the atoms were assigned by randomly selecting them from

a Maxwell-Boltzmann distribution at the required temperature. However, for benzene and benzene-methanol systems, the above procedure of assigning positions and velocities produced large repulsive force causing numerical failure of the finite-difference algorithm. For such problematic simulations, the time step was decreased to 1fs during the first few thousand time-steps and the potential used was switched on gradually. Once the full potential was implemented, the time step Δt chosen was set back to 0.002 ps. Relatively long runs were performed which insured that the trajectory covered the whole phase space, thereby avoiding the occurrence of instabilities in the integration algorithm due to energy overlaps between atoms. Such instabilities would otherwise lead to a violation of total energy and momentum conservation.

3.9.2 Equilibration

The first stage in a simulation is the equilibration phase, which is required to bring the system to equilibrium from the starting configuration. Various parameters during the simulation were monitored, and when they achieved stable values, the accumulation run was started. It was during this accumulation phase that thermodynamic properties and other data were calculated. The parameters monitored during the equilibration included the kinetic, potential and total energies, the temperature and pressure. The total energy E, in the micro-canonical ensemble, after "a successful first move" was set by scaling the atomic velocities every few time- steps (typically 5 to 10). Let superscript D and A designate the "desired" and "actual" values of the properties. For example, based on the atomic positions and velocities obtained after few time-steps, the actual total energy is

$$E^A = {E_{kin}}^A + U. \tag{3.74}$$

Using the desired value for the kinetic energy ${E_k}^D$, each assigned component of a velocity vector is scaled according to

$$v_{ix}^{\text{new}} = v_{ix}^A \sqrt{\frac{E_{kin}^D}{E_{kin}^A}}\,. \tag{3.75}$$

The same scaling is also applied to the y- and z-components of the velocity. During this process, it is obvious that the total energy is not conserved. During the first several thousand time-steps, a certain amount of kinetic energy is removed from the system every 5 steps. Physically, this speeds up the time taken for a molecule to loose any "memory" of its original configuration at t=0. During the initial phase of a run, as the system relaxes from its initial condition, energy is exchanged between the potential and kinetic modes and the temperature drifts from its set point. Once the scaling leads to stable thermodynamic quantities it is then switched off, and, the conservation of the total energy is obtained (see figure 3.4), as it should (in the *NVE* ensemble). After this preliminary equilibration stage, the system was allowed to evolve for several thousand time-steps freely (without scaling). To ensure that the system was equilibrated, the system is sampled for the thermodynamic quantities described in the previous section, every few time-steps during the whole period of the equilibration run. On equilibration, the properties considered, should fluctuate about stable average values (see figure 3.4). The magnitude of these fluctuations depends on the system size; in particular the fluctuations decrease as $N^{1/2}$. It is worth noting that the pressure exhibits larger fluctuations than does the configurational energy. These large fluctuations occur because *rdu/dr* usually changes more quickly with r than does the potential $u(r)$.

3.10 Validation of MD simulations

The approach followed was that of Van Gusteren and Mark (1998). When attempting to validate the results of molecular simulation, the following issues should be considered: (i) checking the simulation package, (ii) the quality of the model, (iii) accuracy of the force field, (iv) degree of sampling, statistics and convergence.

The results presented in this work were achieved by performing MD simulations on a Silicon Graphics 4000 serial computer using the UNIX operating system, for which DL_POLY_2.0 package (Smith and Forester, 1996) was installed. Because a same code used in different computational environments, that is, changing the compiler and computer, may induces some differences in the results, an initial task was to ensure

that the results obtain after a first compilation of the code are valid. This was done by performing preliminary MD simulations on the well-known liquid argon at 84°C and then on a widely used potential model for liquid methanol. The structural, thermodynamics and dynamics properties were compared with values of literature. Then only, the simulations of the systems relevant of this work were carried out.

The choice of molecular atomic model that are explicitly simulated, the type of equations of motion used, the treatment of boundary of the system, the quality of the assumptions and approximations inherent in the molecular model used determine the accuracy of the results that can be obtained from a simulation. For instance, electrostatic interactions are extremely long range and approximations in their treatment (see section 3.7) are necessary. For non-polar or non-ionic liquid it may be reasonable to neglect these interactions beyond a long cutoff distance but for polar liquids such as methanol, this may be inadequate.

The test of a force field should involve calculation of as many different properties as possible. Three general types of properties can be distinguished the dynamic, thermodynamic and structural, and these are the focus in the present MD studies reported here. In this work, at least one of each was considered: the self-diffusion coefficient for the dynamics, the heat of vaporisation, temperature and pressure for the thermodynamics, and the radial distribution functions for the structure.

The degree of sampling, statistics and convergence are important issues. The central question in this respect is whether the length of a MD simulation is sufficiently long to yield reliable trajectory averages of the properties of interest. Trajectory averages will only be representative when the equilibration time of the simulation, t_{equil} is longer than the relaxation time, t_{relax} of the property investigated and when the sampling time, t_{sample} is much longer than t_{relax}. For instance, the convergence to a constant slope in the calculation of the MSD gives an indication of t_{relax} for computing the radial distribution functions.

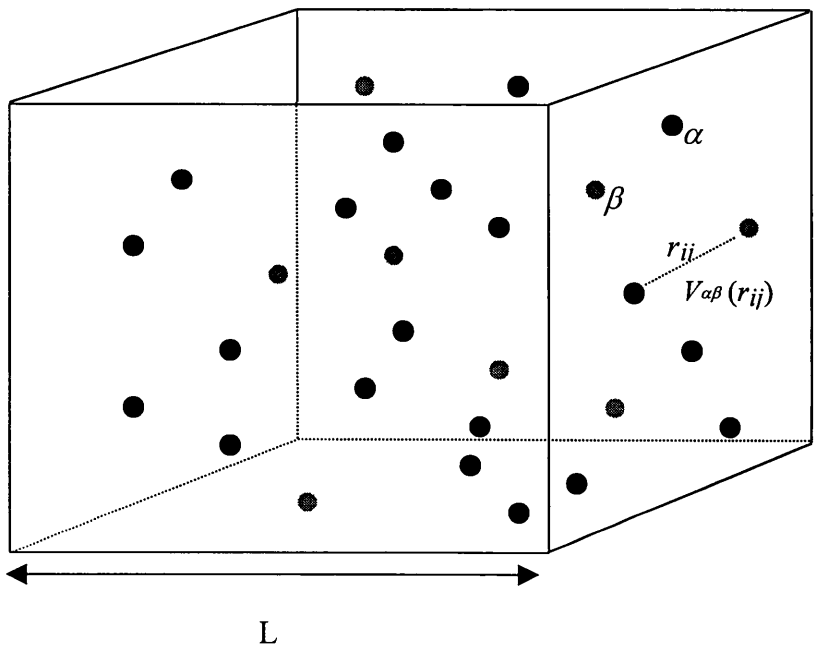

Figure 3.1 A simple example of a cubic simulation box of edge-length L, in which there are two atomic species, α and β, interacting via the pair potential $V_{\alpha\beta}$. $V_{\alpha\beta}$ is a function of the relative distance of the α atom number *i* and the β atom number *j*.

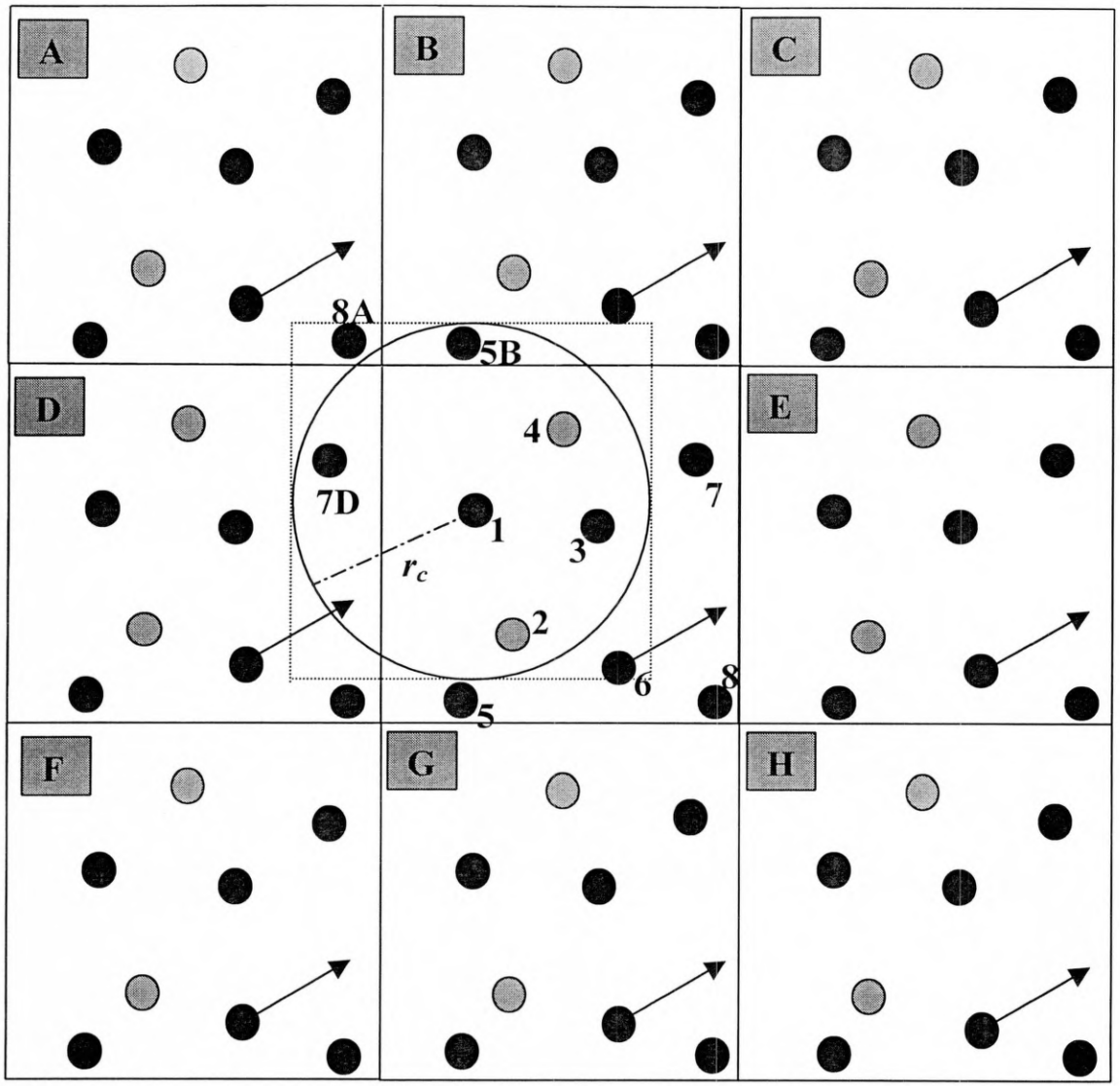

Figure 3.2 The periodic boundaries and the minimum image convention in a two dimensional system. The central box is replicated 8 times and when molecule/atom number 6 is moved all its images proceed exactly in the same way in all the image boxes. The central box contains 8 molecules/atoms, and the box constructed (dashed lines) with molecule 1 at its centre also contains 8 molecules. Applying a potential cutoff at $r_C = L/2$ molecule 1 interacts only with 3 molecules of the central box and 2 from its image (box D and B) (adopted from Allen and Tildesley, 1987).

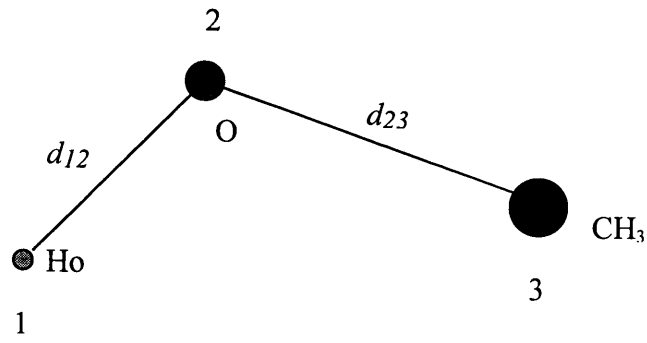

Figure 3.3 Simple 3-site molecular model of a non linear molecule, methanol.

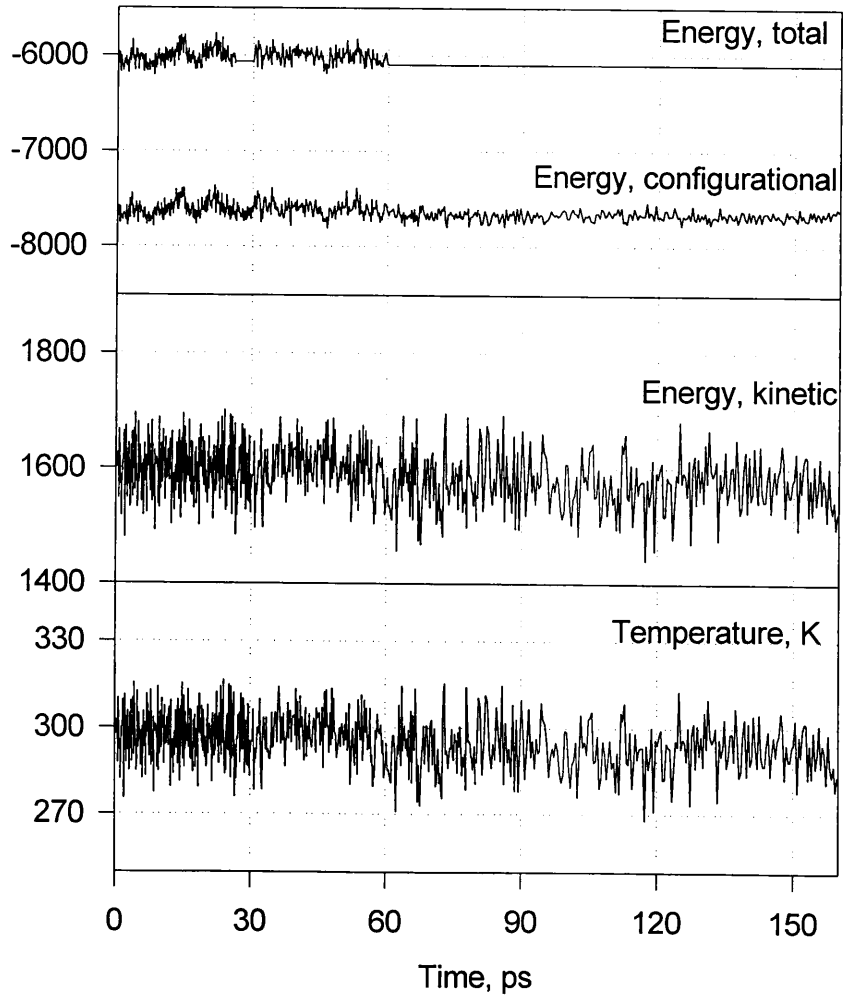

Figure 3.4 Time evolution of the configurational, kinetic, total energies and the temperature (for run 6, see section 6.2) of the MD simulations of 216 methanol molecules.

Chapter 4

Theoretical background to neutron diffraction

4.1 Introduction

Since the first neutron diffractometer was built in 1945 at the Argonne National Laboratory (U.S.A.) (Zinn, 1947), and the early measurements made by Chamberlain (1950) who studied liquid sulphur, lead and bismuth our knowledge of the liquid matter has greatly increased using intense neutron source and technically advanced experimental technique in neutron scattering. Thermal neutron beams are particularly valuable probe because their wavelengths are of the same magnitude as the atomic spacing in liquids and solids. Such neutron beams are provided at the central facilities such as the Rutherford Appleton laboratory (RAL, Didcot, U.K.), which is currently the most powerful spallation neutron source in the world. Design of specific instruments such as SANDALS diffractometer at the RAL has largely improved our understanding of hydrogenated liquids. SANDALS instrument, on which all the data were collected, is described in the next chapter. In this chapter, theoretical background to neutron diffraction is described. Basic expressions relevant of a monatomic liquid are first derived. These are then generalised for the particular case of molecular liquids, and finally an account on the hydrogen/deuterium (H/D) isotopic substitution technique of neutron diffraction as applied to such molecular liquids is provided. A detailed account of the neutron diffraction theory can be found in the text books by Squires (1978) and Lovesey (1986).

4.2 Partial neutron scattering cross section

The geometry of a scattering experiment is shown in figure 4.1. Consider a neutron beam with an initial wave vector $\boldsymbol{k}$ scattered into a state with a wave vector $\boldsymbol{k'}$. The basic quantity that is measured is the partial differential cross section, which gives the fraction of neutrons of incident energy E scattered into an element of solid angle $d\Omega$ in the direction θ, φ, with final energy between E' and $E'+dE'$. It is denoted by

$$\frac{d^2\sigma}{d\Omega dE'}, \tag{4.1}$$

and has the dimension of area/energy. The general expression for the partial differential cross section (Squires 1978; Lovesey, 1986) within the Born approximation (i.e. neglecting the multiple scattering events) (Cohen-Tannoudji et al., 1977; Sears, 1989), is given by

$$\frac{d^2\sigma}{d\Omega dE'} = \frac{k'}{k}\left(\frac{m}{2\pi\hbar^2}\right)^2 \overline{\sum_{\lambda,\lambda'} p_\lambda \left|\left\langle \boldsymbol{k'},\lambda'\middle|\hat{V}\middle|\boldsymbol{k},\lambda\right\rangle\right|^2 \delta(\hbar\omega + E_\lambda - E_{\lambda'})}, \tag{4.2a}$$

where, for a system consisting of a neutron associated with the position vector $\boldsymbol{r}$, and a target of N particles associated with the position vectors $\boldsymbol{R_i}$

$$\left\langle \boldsymbol{k'},\lambda'\middle|\hat{V}\middle|\boldsymbol{k},\lambda\right\rangle = \int d\boldsymbol{r}\int d\boldsymbol{R}^N \phi^*_{\lambda'}(\boldsymbol{R}^N) e^{-i\boldsymbol{k'}.\boldsymbol{r}} \hat{V}(\boldsymbol{r},\boldsymbol{R}^N) e^{i\boldsymbol{k}.\boldsymbol{r}} \phi_\lambda(\boldsymbol{R}^N). \tag{4.2b}$$

The latter equations (4.2a and 4.2b) take into account that a target system of N particles which are in a range of accessible initial state λ changed into a range of accessible final state λ' after their interaction (through the potential $\hat{V}$) with the incident neutron of mass m. The condition of conservation of energy of the system target + neutron is built by using the delta function for which $\hbar\omega = E-E'$. The weight for the eigenstate $|\lambda>$ associated to its eigenfunction, $\phi_\lambda(\boldsymbol{R})$, of a particular target particle is denoted by p_λ. In the canonical ensemble for a classical fluid, for example, it is given by (see chapter 2 equation 2.2-5)

$$p_\lambda = \frac{e^{-E_\lambda / k_B T}}{Z_N(V,T)}. \tag{4.3}$$

Finally, the horizontal bar stands for any relevant averages over and above those included in the weights p_λ such as, for example, the distribution of isotopes, and the nuclear and neutron spin states.

4.3 Fermi pseudo-potential

The nucleon-nucleon interactions, which cause the scattering, have a range of about 10^{-14} to 10^{-15}m. In contrast, the wavelengths of thermal neutrons (10^{-10}m) are much larger than the neutron-nucleus interactions. In these circumstances the neutron-nucleus scattering analysed in term of partial waves (Cohen-Tannoudji et al., 1977; Sears 1989) can only contain s-waves so as to be isotropic, and is characterised by a single complex parameter b called the scattering length. We may distinguish two types of nuclei. In the first type, b varies rapidly with the energy of the neutron. The scattering for such nuclei is a resonance phenomenon and is associated with the formation of a compound nucleus with energy close to an excited state. The imaginary part of the scattering length corresponds to the strong absorption of the neutron by the nucleus. The nuclei of molecules studied in this work belong to the second type, in which the compound nucleus (original + neutron) is not formed near an excited state. The imaginary part of the scattering is very small so that absorption is small and the scattering length is independent of the energy of the neutron. In general, we can have different scattering lengths not only for each atomic type, but also for each isotope, and these depend on the relative neutron and nuclear spins (if the latter exists). The form of the potential, $\hat{V}$ that, using the Born approximation, gives isotropic scattering is a delta function in the form

$$\hat{V}(\boldsymbol{r}) = \sum_{j=1}^{N} \frac{2\pi\hbar^2}{m} b_j \delta(\boldsymbol{r} - \boldsymbol{R}_j), \tag{4.4}$$

where b_j is the scattering length of the nucleus j occurring as a phenomenological constant, which is obtained directly from neutron-optical experimental measurements (Fermi and Zinn, 1946).

4.4 Static approximation

If we substitute (4.4) in (4.2) it follows that

$$\frac{d^2\sigma}{d\Omega dE'} = \frac{k'}{k} \overline{\sum_{\lambda,\lambda'} p_\lambda \left| \sum_j b_j \langle \lambda' | \exp(i\boldsymbol{Q}.\boldsymbol{R}_j) | \lambda \rangle \right|^2 \delta(\hbar\omega + E_\lambda - E_{\lambda'})} . \tag{4.5}$$

However, if the energy of the scattered neutron is such that $E' >> \hbar\omega$, the term E_λ-$E_{\lambda'}$ in the argument of the δ function of (4.5) can be ignored in absence of fine resolution energy. Thus, the energy conservation can be reasonably neglected and k can be considered to be equal to k' to a good approximation. Since

$$E - E' = \hbar\omega \text{ and } dE' = d\hbar\omega , \tag{4.6}$$

the partial scattering cross-section (4.5) becomes

$$\frac{d^2\sigma}{d\Omega dE'} = \overline{\sum_{\lambda,\lambda'} p_\lambda \left| \sum_j b_j \langle \lambda' | \exp(i\boldsymbol{Q}.\boldsymbol{R}_j) | \lambda \rangle \right|^2 \delta(\hbar\omega)} . \tag{4.7}$$

Having removed the energy discrimination on the final states, equation (4.7) can be simplified by taking the sum over the final state. This can be performed using the closure relation

$$\sum_{\lambda'} |\lambda'\rangle\langle\lambda'| = 1, \tag{4.8}$$

to simplify

$$\sum_{\lambda'}\left|\sum_j b_j\langle\lambda'|\exp(i\boldsymbol{Q}.\boldsymbol{R}_j)|\lambda\rangle\right|^2 = \sum_{\lambda'}\sum_{j,j'} b_{j'}^* b_j \langle\lambda'|\exp(i\boldsymbol{Q}.\boldsymbol{R}_{j'})|\lambda\rangle^* \langle\lambda'|\exp(i\boldsymbol{Q}.\boldsymbol{R}_j)|\lambda\rangle$$
$$= \sum_{\lambda'}\sum_{j,j'} b_{j'}^* b_j \langle\lambda|\exp(-i\boldsymbol{Q}.\boldsymbol{R}_{j'})|\lambda'\rangle\langle\lambda'|\exp(i\boldsymbol{Q}.\boldsymbol{R}_j)|\lambda\rangle, \tag{4.9}$$

so that

$$\frac{d\sigma}{d\Omega} = \int_0^\infty \frac{d^2\sigma}{d\Omega dE'} dE' = \overline{\sum_\lambda p_\lambda \sum_{j,j'} b_{j'}^* b_j \langle\lambda|\exp i\boldsymbol{Q}(\boldsymbol{R}_j - \boldsymbol{R}_{j'})|\lambda\rangle}, \tag{4.10}$$

and is known as the static approximation. For the case when the averaging over nuclear spin orientations and distributions (denoted by the horizontal bar), is independent of the thermal averaging:

$$<(\quad)> = \sum_\lambda p_\lambda \langle\lambda|(\quad)|\lambda\rangle, \tag{4.11}$$

it follows that,

$$\frac{d\sigma}{d\Omega} = \sum_{j,j'} \overline{b_{j'}^* b_j} \left\langle \exp i\boldsymbol{Q}(\boldsymbol{R}_j - \boldsymbol{R}_{j'}) \right\rangle \tag{4.12}$$

4.5 Scattering from a monatomic system

The quantity $\overline{b_{j'}^* b_j}$ in equation (4.12) is the value $b_{j'}{}^* b_j$ averaged over random nuclear + neutron spin orientations and random isotope distribution. Since b_j and $b_{j'}$ are not correlated for $j \neq j'$,

$$\overline{b_j^* b_j} = \overline{b_{j'}^*}\,\overline{b_j} = (\bar{b})^2 \tag{4.13}$$

otherwise, if $j=j'$

$$\overline{b_j^* b_j} = \overline{b_j}^2 = \overline{b^2}, \tag{4.14}$$

so that, in general, for a monatomic system

$$\overline{b_{j'}^* b_j} = (\bar{b})^2 + \delta_{jj'}(\overline{b^2} - (\bar{b})^2) = \frac{\sigma_{\text{coh}}}{4\pi} + \delta_{jj'}\frac{\sigma_{\text{incoh}}}{4\pi}, \tag{4.15}$$

where σ_{coh} and σ_{incoh} are the atomic coherent and incoherent scattering cross sections. By using (4.13) and (4.14), (4.12) can be written as

$$\frac{d\sigma}{d\Omega} = \sum_j \overline{b^2} + \sum_{j \neq j'} (\bar{b})^2 \left\langle \exp i\boldsymbol{Q}(\boldsymbol{R}_j - \boldsymbol{R}_{j'}) \right\rangle. \tag{4.16}$$

The second term of the right hand side can be written as a Fourier integral of a delta function,

$$\sum_{j \neq j'} \left\langle \exp i\boldsymbol{Q}(\boldsymbol{R}_j - \boldsymbol{R}_{j'}) \right\rangle = \int e^{i\boldsymbol{Q}\boldsymbol{r}} d\boldsymbol{r} \sum_{j=j'} \left\langle \delta(\boldsymbol{r} - \boldsymbol{R}_{j'} + \boldsymbol{R}_j) \right\rangle. \tag{4.17}$$

Identifying the latter expression with (2.60), that is

$$\rho g(\boldsymbol{r}) = \sum_{j=j'} \left\langle \frac{1}{N} \delta(\boldsymbol{r} - \boldsymbol{R}_{j'} + \boldsymbol{R}_j) \right\rangle, \tag{4.18}$$

it follows that

$$\sum_{j \neq j'} \left\langle \exp i\boldsymbol{Q}(\boldsymbol{R}_j - \boldsymbol{R}_{j'}) \right\rangle = N\rho \int d\boldsymbol{r}\, e^{i\boldsymbol{Q}\boldsymbol{r}} g(r) \tag{4.19a}$$

$$= (2\pi)^3 N\rho\delta(\boldsymbol{Q}) + N\rho \int (g(\boldsymbol{r}) - 1) e^{i\boldsymbol{Q}\boldsymbol{r}} d\boldsymbol{r}. \tag{4.19b}$$

In the second term of the right hand side of (4.19b) the high r value, 1, of g(r) (see 2.46b) was extracted, so that the Fourier integral is well behaved. Because the delta

function contributes only in the forward direction corresponding to no scattering, it is then dropped. Inserting (4.19) in (4.16) gives

$$\begin{aligned}\frac{d\sigma}{d\Omega} &= N\overline{b_j^2} + N\rho\left(\bar{b}\right)^2 \int \left(g(\boldsymbol{r})-1\right)e^{i\boldsymbol{Q}\boldsymbol{r}}\,d\boldsymbol{r} \\ &= N\left(\overline{b_j^2} - \left(\bar{b}\right)^2\right) + N\left(\bar{b}\right)^2\left(1+\rho\int \left(g(\boldsymbol{r})-1\right)e^{i\boldsymbol{Q}\boldsymbol{r}}\,d\boldsymbol{r}\right). \\ &= N\frac{\sigma_{\text{incoh}}}{4\pi} + N\frac{\sigma_{\text{coh}}}{4\pi}\left(1+\rho\int \left(g(\boldsymbol{r})-1\right)e^{i\boldsymbol{Q}\boldsymbol{r}}\,d\boldsymbol{r}\right).\end{aligned} \tag{4.20}$$

By defining the static structure factor $S(Q)$ as

$$S(Q)-1 = \rho\int \left(g(\boldsymbol{r})-1\right)e^{i\boldsymbol{Q}\boldsymbol{r}}\,d\boldsymbol{r}, \tag{4.21}$$

(4.20) becomes

$$\frac{d\sigma}{d\Omega} = N\left(\overline{b_j^2} - \left(\bar{b}\right)^2\right) + N\left(\bar{b}\right)^2\left(1+(S(Q-1))\right). \tag{4.22}$$

Note that $S(Q)$ as well as as g($\boldsymbol{r}$) are dimensionless. It is worth noting that the limit $Q\rightarrow 0$ of (4.21) is related to the isothermal compressibility χ_T through the compressibility equation (see equation 2.49) so that

$$\lim_{Q\rightarrow 0} S(Q)\text{-}1 = \rho\int(\,g(\boldsymbol{r})\text{-}1)\,d\boldsymbol{r} \;=\; \rho k_B T\chi_T - 1\,. \tag{4.23}$$

For liquids it is assumed that the scattering system is isotropic so that $g(\boldsymbol{r})$ can be replaced by $g(r)$, and (4.21) becomes

$$
\begin{aligned}
S(Q) &= 1+\rho\int_0^{\infty} r^2 dr\,(g(r)-1)\int_0^{\pi} e^{iQr\cos\theta}\sin\theta\, d\theta\int_0^{2\pi} d\phi \\
&= 1+2\pi\rho\int_0^{\infty} r^2 dr\,(g(r)-1)\int_{-1}^{1} e^{iQr\cos\theta} d\cos\theta \\
&= 1+4\pi\rho\int_0^{\infty} r^2 dr\,(g(r)-1)\frac{\sin Qr}{Qr}
\end{aligned}
\tag{4.24}
$$

for which the momentum transfer $Q=\frac{4\pi}{\lambda}\sin\theta$. Alternatively, $g(r)$ can be extracted by back Fourier transformation of (4.21)

$$
\begin{aligned}
g(r)-1 &= \frac{1}{(2\pi)^3\rho}\int_0^{\infty} Q^2 dQ\,(S(Q)-1)\int_{-1}^{1} e^{-iQr\cos\theta} d\cos\theta\int_0^{2\pi} d\varphi \\
&= \frac{1}{(2\pi)^2\rho}\int_0^{\infty} Q^2 dQ\,(S(Q)-1)\int_{-1}^{1} e^{-iQr\cos\theta} d\cos\theta \\
g(r) &= 1+\frac{1}{2\pi^2\rho}\int_0^{\infty} Q^2 dQ\,(S(Q)-1)\frac{\sin Qr}{Qr}.
\end{aligned}
\tag{4.25}
$$

4.6 Scattering from molecular liquids

The above discussion was restricted to systems with a single component. However, the molecular liquids considered in this thesis are constituted of different atomic species and the above treatment has to be generalised. Consider a multi-component system of N atoms pertaining to N_m molecules. If the atomic types are labelled as α and β, and if $j(\alpha)$ atoms of type α appear c_α times in the molecule, we can rewrite:

$$
\sum_j \Rightarrow \sum_\alpha \sum_{j(\alpha)} = \sum_\alpha N_m c_\alpha = N .
$$

On introducing the above notation in the sums involved in the scattering cross section, (4.12) can be written as,

$$
\frac{d\sigma}{d\Omega} = N\sum_\alpha c_\alpha \overline{b_\alpha^2} + \sum_{\alpha\beta} \overline{b_\alpha}\,\overline{b_\beta} \sum_{\substack{j(\alpha)\, j'(\beta) \\ j\neq j' \text{ if } \alpha=\beta}} \sum \left\langle \exp i\boldsymbol{Q}(\boldsymbol{R}_j - \boldsymbol{R}_{j'}) \right\rangle .
\tag{4.26}
$$

Defining the pair distribution function $g_{\alpha\beta}(\boldsymbol{r})$ as

$$N\rho c_\alpha c_\beta g_{\alpha\beta}(\boldsymbol{r}) = \sum_{\substack{j(\alpha)\, j'(\beta) \\ j\neq j' \text{ if } \alpha=\beta}} \sum \left\langle \delta(\boldsymbol{r} - \boldsymbol{R}_j + \boldsymbol{R}_{j'}) \right\rangle, \tag{4.27a}$$

the second term of (4.26) can be written as

$$\sum_{\alpha\beta} \overline{b_\alpha b_\beta} \sum_{\substack{j(\alpha)\, j'(\beta) \\ j\neq j' \text{ if } \alpha=\beta}} \sum \left\langle \exp i\boldsymbol{Q}(\boldsymbol{R}_j - \boldsymbol{R}_{j'}) \right\rangle = N\rho \sum_{\alpha\beta} \overline{b_\alpha}\,\overline{b_\beta} c_\alpha c_\beta \int g_{\alpha\beta}(\boldsymbol{r}) e^{i\boldsymbol{Q}\boldsymbol{r}} d\boldsymbol{r}$$

$$= N\rho \sum_{\alpha\beta} \overline{b_\alpha}\,\overline{b_\beta} c_\alpha c_\beta \left((2\pi)^3 \delta(Q) + \int (g_{\alpha\beta}(\boldsymbol{r}) - 1) e^{i\boldsymbol{Q}\boldsymbol{r}} d\boldsymbol{r} \right). \tag{4.27b}$$

Defining

$$S_{\alpha\beta}(Q) = 1 + \rho \int \left(g_{\alpha\beta}(\boldsymbol{r}) - 1 \right) e^{i\boldsymbol{Q}\boldsymbol{r}} d\boldsymbol{r} \tag{4.28}$$

and dropping the delta function in (4.27b) which contributes only in the forward direction corresponding to no scattering, (4.26) becomes either

$$\frac{d\sigma}{d\Omega} = N \sum_\alpha c_\alpha \overline{b_\alpha^2} + N \sum_{\alpha\beta} \overline{b_\alpha}\,\overline{b_\beta} c_\alpha c_\beta (S_{\alpha\beta}(Q) - 1). \tag{4.29}$$

or

$$\frac{d\sigma}{d\Omega} = N \sum_\alpha c_\alpha \left(\overline{b_\alpha^2} - \left(\overline{b_\alpha} \right)^2 \right) + N \sum_\alpha c_\alpha \left(\overline{b_\alpha} \right)^2 + N \sum_{\alpha\beta} \overline{b_\alpha}\,\overline{b_\beta} c_\alpha c_\beta (S_{\alpha\beta}(Q) - 1). \tag{4.30}$$

While treating the diffraction data on molecular liquids, it is a customary to normalise the total differential cross section (DCS) (4.29,30) to the molecular unit and write (4.30) as a sum of distinct, self and incoherent DCS,

$$\left.\frac{d\sigma}{d\Omega}\right|_{\text{tot}} = \left.\frac{d\sigma}{d\Omega}\right|_{\text{coh}}^{\text{dist}} + \left.\frac{d\sigma}{d\Omega}\right|_{\text{coh}}^{\text{self}} + \left.\frac{d\sigma}{d\Omega}\right|_{\text{incoh}} \tag{4.31}$$

in which

$$\begin{aligned}
\left.\frac{d\sigma}{d\Omega}\right|_{\text{coh}}^{\text{dist}} &= \sum_{\alpha,\beta} c_\alpha c_\beta \overline{b_\alpha}\,\overline{b_\beta}(S_{\alpha\beta}(Q)-1) \\
\left.\frac{d\sigma}{d\Omega}\right|_{\text{coh}}^{\text{self}} &= \sum_{\alpha} c_\alpha (\overline{b_\alpha})^2 = \sum_{\alpha} c_\alpha \frac{\sigma_{\alpha,\text{coh}}}{4\pi} \\
\left.\frac{d\sigma}{d\Omega}\right|_{\text{incoh}} &= \sum_{\alpha} c_\alpha (\overline{b_\alpha^{\,2}} - (\overline{b_\alpha})^2) = \sum_{\alpha} c_\alpha \frac{\sigma_{\alpha,\text{incoh}}}{4\pi}.
\end{aligned} \tag{4.32}$$

In the latter expressions the summations run over all different types of α nuclei appearing c_α times in the molecule. As for the monatomic liquid case, (4.28) yields the partial structure factor for an isotropic molecular liquid, $S_{\alpha\beta}(Q)$ as

$$S_{\alpha\beta}(Q) - 1 = 4\pi\rho \int_0^\infty r^2 dr \left(g_{\alpha\beta}(r) - 1\right) \frac{\sin Qr}{Qr}, \tag{4.33}$$

and its Fourier transform $g_{\alpha\beta}(r)$ as,

$$g_{\alpha\beta}(r) = 1 + \frac{1}{2\pi^2 \rho} \int_0^\infty Q^2 dQ \left(S_{\alpha\beta}(Q) - 1\right) \frac{\sin Qr}{Qr}. \tag{4.34}$$

The peak positions in $g_{\alpha\beta}(r)$ (see figure 1.1b for an illustration) correspond to preferred inter-atomic correlations between α and β atoms. The area under such features is related to the co-ordination number, $\bar{n}_\alpha^\beta$, which may be defined as the average number of atoms of type β at a distance between 0 and r from atoms of type α,

$$\bar{n}_\alpha^\beta(r) = 4\pi\rho c_\beta \int_0^r r'^2 \, g_{\alpha\beta}(r') dr', \tag{4.35}$$

Since $\lim_{Q\to\infty} S_{\alpha\beta}(Q) = 1$, the total DCS should oscillate about the sum of self plus incoherent terms,

$$\left.\frac{d\sigma}{d\Omega}\right|_{\text{coh}}^{\text{self}} + \left.\frac{d\sigma}{d\Omega}\right|_{\text{incoh}} = \sum_{\alpha} c_{\alpha}\bar{b}_{\alpha}^{\,2} + \sum_{\alpha} c_{\alpha}\frac{\sigma_{\alpha,\text{incoh}}}{4\pi}. \tag{4.36}$$

The distinct DCS involves coherent scattering from distinct nuclei of either different molecules (inter-molecular DCS) or the same molecule (intra-molecular DCS). (4.31) can thus be written as:

$$\begin{aligned}\left.\frac{d\sigma}{d\Omega}\right|_{\text{tot}} &= \left.\frac{d\sigma}{d\Omega}\right|_{\text{coh}}^{\text{inter}} + \left.\frac{d\sigma}{d\Omega}\right|_{\text{coh}}^{\text{intra}} + \left.\frac{d\sigma}{d\Omega}\right|_{\text{coh}}^{\text{self}} + \left.\frac{d\sigma}{d\Omega}\right|_{\text{incoh}} \\ &= \left.\frac{d\sigma}{d\Omega}\right|_{\text{coh}}^{\text{dist}} + \left.\frac{d\sigma}{d\Omega}\right|_{\text{coh}}^{\text{self}} + \left.\frac{d\sigma}{d\Omega}\right|_{\text{incoh}}.\end{aligned} \tag{4.37}$$

The distinct radial distribution function (rdf), $G^{\text{dist}}(r)$ can be obtained by Fourier transformation of the distinct DCS:

$$\begin{aligned}G^{dist}(r) - 1 &= \frac{1}{2\pi^2 r\rho\left(\sum_{\alpha} c_{\alpha}\bar{b}_{\alpha}\right)^2}\int_0^{\infty}\sum_{\alpha,\beta} c_{\alpha}c_{\beta}\overline{b_{\alpha}}\,\overline{b_{\beta}}(S_{\alpha\beta}(Q)-1)Q\sin(Qr)dQ \\ &= \frac{1}{2\pi^2 r\rho\left(\sum_{\alpha} c_{\alpha}\bar{b}_{\alpha}\right)^2}\int_0^{\infty}\left.\frac{d\sigma}{d\Omega}\right|_{\text{coh}}^{\text{dist}} Q\sin(Qr)dQ \\ &= \frac{1}{\left(\sum_{\alpha} c_{\alpha}\bar{b}_{\alpha}\right)^2}\sum_{\alpha,\beta} c_{\alpha}c_{\beta}\overline{b_{\alpha}}\,\overline{b_{\beta}}(g_{\alpha\beta}(r)-1),\end{aligned} \tag{4.38}$$

where $\left(\sum_{\alpha} c_{\alpha}\bar{b}_{\alpha}\right)^2$ is an arbitrary factor used to normalise the rdf to the scattering of the molecular unit, to ensure firstly that $G^{\text{dist}}(r)$ is dimentionless, and secondly, the summation of all the weights associated to each of the partial pair distribution (pdf),

$g_{\alpha\beta}(r)$ is 1. From this respect the $G^{\text{dist}}(r)$, that can be rewritten as a weighted sum of pdfs, $g_{\alpha\beta}(r)$:

$$G^{\text{dist}}(r)==\frac{1}{\left(\sum_{\alpha} c_\alpha \bar{b}_\alpha\right)^2}\sum_{\alpha,\beta} c_\alpha c_\beta \overline{b_\alpha}\,\overline{b_\beta} g_{\alpha\beta}(r) = \sum_{\alpha,\beta} W_{\alpha\beta} g_{\alpha\beta}(r), \tag{4.39}$$

includes contributions from both intra- and inter-molecular correlations and can in principle, provide information on structural arrangement in a simple liquid. However, for molecular liquids considered this information cannot be obtained straightforwardly from $G^{\text{dist}}(r)$, because this function is dominated by the intra-molecular contributions that mask the low-r range of the inter-molecular structure. Provided the intra-molecular structure is known, its contribution to the distinct DCS can be calculated from:

$$\left.\frac{d\sigma}{d\Omega}\right|_{\text{coh}}^{\text{intra}} = \sum_{\substack{l=1 \\ l\neq l'}}^{N/N_m}\sum_{l'=1}^{N/N_m} \bar{b}_l \bar{b}_{l'} \frac{\sin Q r_{ll'}}{Q r_{ll'}} e^{-\frac{1}{2}\gamma_{ll'}^2 Q^2}, \tag{4.40}$$

where $r_{ll'}$ is the distance between nuclei number l and l', and, the Debye-Waller factor, $\gamma_{ll'}$ ($\gamma_{ll'}^2=\left\langle \boldsymbol{u}_{ll'}^2 \right\rangle/2$) is proportional to the mean square amplitude of vibration $\boldsymbol{u}_{ll'}$ of nucleus number l relative to l'. At high Q, the inter-molecular DCS approaches zero. Thus, by fitting (4.40) to the distinct DCS in the high Q-range, the intra-molecular DCS can be obtained which on subtraction from the distinct DCS yields the inter-molecular DCS. At $Q\rightarrow 0$, the inter-molecular structure factor normalised to a molecular unit, $i_{\text{m}}(Q)$ defined as,

$$i_{\text{m}}(Q)=\left(\sum_{\alpha=1} c_\alpha \bar{b}_\alpha\right)^{-2} \left.\frac{d\sigma}{d\Omega}\right|_{\text{coh}}^{\text{inter}} = \left(\sum_{\alpha=1} c_\alpha \bar{b}_\alpha\right)^{-2}\left[\left(\frac{\partial\sigma}{\partial\Omega}\right)_{\text{coh}}^{\text{dist}} - \left(\frac{\partial\sigma}{\partial\Omega}\right)_{\text{coh}}^{\text{intra}}\right], \tag{4.41}$$

is related to the isothermal compressibility, χ_{T} as in the case of monatomic liquid (see equation 4.23) via

$$i_m(0)=\lim_{Q\to 0} i_m(Q) = \rho k_B T \chi_T - 1. \quad (4.42)$$

4.7 Method of isotopic substitution

The Fourier transformation of the inter-molecular DCS can, in principle, provide information on structural arrangement in a simple liquid. However, for molecular liquids this information cannot be obtained straightforwardly since it comprises of several pdfs, $g_{\alpha\beta}(r)$, and this often leads to a featureless inter-molecular distribution function. However, it is possible to obtain some (or all) of the partial distribution functions by separating some of the partial structure factors, $S_{\alpha\beta}(Q)$ of an inter-molecular DCS by employing the isotopic substitution technique. The isotopic substitution technique of ND (NDIS) was originally pioneered and applied to molten metals by Enderby and co-workers (Enderby and Barnes 1990; Edwards et al., 1975). This technique has later been applied to a variety of liquids such as molten salts (Adya et al. 1998), aqueous and non-aqueous electrolyte solutions (Enderby and Neilson, 1981; Neilson and Adya, 1997).

It is worth noting that the technique can also provide very useful insight on the intra-molecular structure of a molecule in its liquid phase when it is applied on distinct DCS since some of the intra-molecular bond distances that may be mixed up in $G^{dist}(r)$ can be revealed (see section 6.1.3 and 8.2.3a). This method relies on the fact that the scattering length of an element varies from one isotope to another, so that if an atom is substituted with one of its isotope it changes the DCS. The differences in the scattering lengths between isotopes of oxygen and those of carbon are so small (Sears, 92) that these substitutions cannot be exploited with the currently available neutron sources and diffractometers. Thus for the investigated liquids (benzene, methanol and the mixture) containing C, H and O, the only isotopic substitutions possible are those on the various hydrogen sites. The scattering lengths of the two isotopes: hydrogen (H) and deuterium (D) vary considerably (b_D = 6.671 fm, b_H = -3.739 fm), thus presenting a good contrast.

To illustrate the method, we consider a general system in which only one hydrogen site (hereafter referred to as *S*) is substituted (the particular case of a binary mixture

where, also, more than one site is substituted, will be treated in chapter 8.2.1b). A ND measurement on a single sample yields to

$$\left.\frac{d\sigma}{d\Omega}\right|_{\text{coh}}^{\text{dist/inter}} = \sum_{\alpha,\beta} c_\alpha c_\beta \overline{b_\alpha}\,\overline{b_\beta}(S_{\alpha\beta}(Q)-1) \tag{4.43}$$

If measurements are performed on three chemically identical samples with D, H and H/D (50:50 mixture), on the substituted site, the above equation can be written as a weighted sum of the three partial structure factors:

$$\begin{aligned}\left.\frac{d\sigma}{d\Omega}\right|_{\text{coh}}^{\text{inter/dist}} &= c_X^2\,\overline{b_X}^2(S_{XX}(Q)-1) + 2c_X c_S\,\overline{b_X}\,\overline{b_S}(S_{XS}(Q)-1) \\ &\quad + c_{SS}^2\,\overline{b_S}^2(S_{SS}(Q)-1).\end{aligned} \tag{4.44}$$

Here X refers to any non-substituted site. The composite coherent scattering length, $\bar{b}_X$ and concentration, c_X are defined as:

$$\bar{b}_X = \sum_{\alpha\neq S}\frac{c_\alpha \bar{b}_\alpha}{c_X} \text{ and, } c_X = \sum_{\alpha\neq S} c_\alpha\,. \tag{4.45}$$

The structure factors, $S_{XS}(Q)$ and $S_{XX}(Q)$ can then be written as:

$$S_{XS}(Q)-1 = \sum_{\alpha\neq S}\frac{c_\alpha \bar{b}_\alpha (S_{\alpha S}(Q)-1)}{c_X \bar{b}_X}, \tag{4.46}$$

$$S_{XX}(Q)-1 = \sum_{\alpha\neq S,\beta\neq S}\frac{c_\alpha c_\beta \bar{b}_\beta \bar{b}_\alpha (S_{\alpha\beta}(Q)-1)}{{c_X}^2 {\bar{b}_X}^2}. \tag{4.47}$$

The *S*-*S* partial structure factor can be extracted from the second order difference:

$$S_{SS}(Q)-1 = B^{-1}\left[0.5^{\,1}\left.\frac{d\sigma}{d\Omega}\right|_{\text{coh}}^{\text{inter/dist}} + 0.5^{\,2}\left.\frac{d\sigma}{d\Omega}\right|_{\text{coh}}^{\text{inter/dist}} - {}^{3}\left.\frac{d\sigma}{d\Omega}\right|_{\text{coh}}^{\text{inter/dist}}\right], \tag{4.48}$$

where

$$B = \frac{c_S^2}{4}(\bar{b}_D - \bar{b}_H)^2, \tag{4.49}$$

and, superscripts 1, 2 and 3 refer to the heavy (D), light (H) and the mixture (H/D) sample, respectively. The X-S scattering function, $S_{XS}^{\text{inter/dist}}(Q)$ can be obtained from the first-order difference:

$${}^{12}\Delta_S^{\text{inter/dist}}(Q) = \left[{}^{1}\left.\frac{d\sigma}{d\Omega}\right|_{\text{coh}}^{\text{inter/dist}} - {}^{2}\left.\frac{d\sigma}{d\Omega}\right|_{\text{coh}}^{\text{inter/dist}} \right], \tag{4.50}$$

by removing the $S_{SS}(Q)$ contribution as:

$$S_{XS}^{\text{inter/dist}}(Q) - 1 = \frac{1}{L}\left[{}^{12}\Delta_{\text{S}}^{\text{inter/dist}}(Q) - M(S_{SS}(Q) - 1)\right], \tag{4.51}$$

in which,

$$L = 2c_S c_X(\bar{b}_X\bar{b}_D - \bar{b}_X\bar{b}_H), \tag{4.52}$$

$$M = c_S^2\left(\bar{b}_D{}^2 - \bar{b}_H{}^2\right). \tag{4.53}$$

Finally the non-substituted sites - non-substituted sites (X-X) scattering function can be extracted by removing the $S_{XS}^{\text{dis/inter}}(Q)$ and $S_{SS}(Q)$ from the "heavy" sample 1:

$$\begin{aligned} S_{XX}^{\text{inter/dist}}(Q) - 1 = (c_X^2\bar{b}_X{}^2)^{-1} \times \; & \left[{}^{1}\left(\frac{d\sigma}{d\Omega}\right)_{\text{coh}}^{\text{inter/dist}}(Q) - \right. \\ & \left. 2c_X c_S\bar{b}_D\bar{b}_S(S_{XS}^{\text{inter/dist}}(Q) - 1) - c_S{}^2\bar{b}_D{}^2(S_{SS}(Q) - 1) \right]. \end{aligned} \tag{4.54}$$

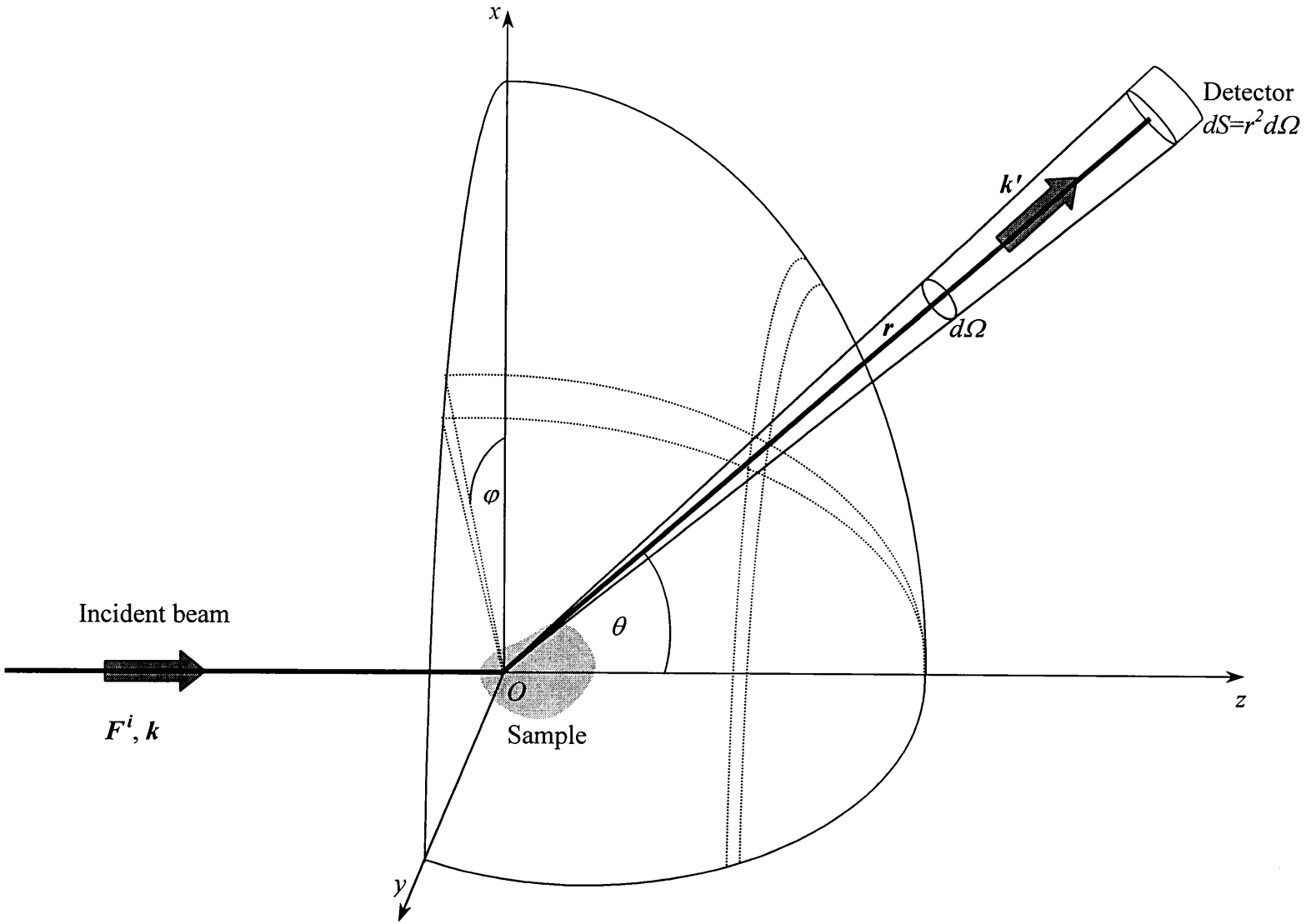

Figure 4.1 The incident beam with a flux of particles F^i is scattered by a sample placed at the origin O. The detector placed far from the zone of influence of the neutron-target potential interaction measures the number dn of particles scattered per unit of time into the solid angle $d\Omega$, centred around the direction defined by the polar angles θ and φ (adopted from Hannon, 1999).

Chapter 5

Experimental methods and data reduction

5.1 The time-of-flight technique

All the experiments were performed on the Small Angle Neutron Diffractometer for Amorphous and Liquid Samples (SANDALS) at the ISIS spallation neutron source of the Rutherford Appleton Laboratory (Didcot, Oxfordshire, UK). SANDALS is positioned on the N1 beam line (see figure 5.1a). Briefly, bunches of protons emerging from a linac at ~70 Mev are accumulated (till about 2.510^{13} protons) and accelerated in a synchrotron (up to ~800 MeV). These are then pulsed (typically the pulse frequency is ~50 Hz and its width is about ~0.4 μs) and projected towards a tantalum target which is non-fissioning, and neutrons are produced by spallation process. A pulse of fast neutrons less than ~1μs wide is produced from the collision with the target (in the ratio 1 proton for ~ 15 neutrons) and pass into a methane moderator maintained at 100 K which slows ~ 80% of the neutrons down to wavelengths in the range 0.05-4.5Å. The neutrons spectrum produced comprises of an epithermal region where the intensity varies as $1/E$ and a thermal region where a Maxwellian "hump" occurs whose maximum corresponds to the average temperature of the moderator. Neutrons emerge from the moderator in all directions; they are collimated to define the pulsed beam (see figure 5.2). On SANDALS, the full sized beam is a circle of diameter 3.2cm. The neutron beam obtained is used to illuminate the various samples for which the time-of-flight (TOF) neutron diffraction technique is employed to collect the diffraction patterns. This technique involves measuring the TOF, t_{obs}, taken for a neutron to travel the total flight path (from the moderator to the sample, L_0, and sample to a detector, L_1) via the sample, assuming the static

approximation to be valid (i.e. initial and final neutron energies are the same E=E' which leads to $|\boldsymbol{k}| = |\boldsymbol{k}'| = k_e$),

$$t_{obs} = \frac{m_n}{\hbar}\left(\frac{L_0}{k} + \frac{L_1}{k'}\right), \tag{5.1a}$$

$$t_{obs} = \frac{m_n}{\hbar}\frac{(L_0 + L_1)}{k_e}. \tag{5.1b}$$

where m_n is the neutron mass. It is then straightforward to determine the neutron wavelength for a detector forming an angle 2θ between a transmitted and a scattered neutron wave vector (see figure 5.3). The modulus of the transferred wave vector $\boldsymbol{Q} = \boldsymbol{k}$-$\boldsymbol{k}'$ becomes within the static approximation, Q_e which is given by

$$Q_e = \frac{4\pi}{\lambda_e}\sin\theta. \tag{5.2}$$

The TOF technique obviates the need to monochromatise the neutron beam. Even though the raw neutron flux produced initially is less than that produced on a reactor source, the final flux available for neutron diffraction is of comparable order of magnitude.

5.2 Neutron detectors

The detectors on the instrument (see figure 5.1b-E) are situated on a constant resolution surface, and give the angular coverage from 3.8° to 37° (in 2θ). Their concentration at low scattering angles optimises the use of epithermal neutrons and minimises the requirement to make inelasticity corrections to the data (see section 5.5.6). At the time of the experiments, there were currently 1180 zinc sulphide ZnS(Ag)/^{6}Li scintillator detectors combined into 18 detector groups, each associated to a constant angle 2θ. Although the incident flight path (distance between the

moderator and the sample) is 11 m, the final flight paths (distance from the sample to the different detectors) are in the range 0.75-4.0 m. The available Q_e-range is 0.1 to 50 $Å^{-1}$. The advantages of using scintillation detectors are that they use much denser neutron absorber, ^{6}Li than gas counters. Thus, they can be made, within a few millimetres thickness, at least twice as efficient as a ^{3}He gas-tube detector. This allows the installation of a large number of detectors on the instrument, thus improving the statistics during the data acquisition. The reaction

$$^6\mathrm{Li} + {}^1\mathrm{n} \rightarrow {}^4\mathrm{He} + {}^3\mathrm{He} + 4.79\mathrm{Mev} \tag{5.3}$$

leads to a large amount of energy to be deposited in the scintillator material (ZnS(Ag)), which, in turn, emits a flash of light detected by a photomultiplier tube (see figure 5.4). Consider a region of thickness of D containing a number density n_v of absorbing atoms with neutron absorbing cross section $\sigma_{abs}(k)$. If we look at a thin slice of the volume distance x from the surface and of thickness δx, the neutron flux $n(x)$ of wavelength λ across the slice will be reduced by

$$\delta n = -n_v \sigma_{abs}(\lambda) n(x) \delta x . \tag{5.4}$$

Integrating the above equation, it follows that

$$n(D) = n(0) \exp(-n_v \sigma_{abs}(\lambda) D) , \tag{5.5}$$

and the efficiency of the detector is defined as

$$e(\lambda) = \frac{n(0) - n(D)}{n(0)} = 1 - \exp(-n_v \sigma_{abs}(\lambda) D) . \tag{5.6}$$

Usually the absorption cross-section used proportional to the neutron wavelength

$$\sigma_{abs}(\lambda) = \lambda \sigma^0_{abs} , \tag{5.7}$$

where σ^0_{abs} is a constant. For good performance the ideal neutron detector should

have high neutron detection efficiency, a low intrinsic detector background, a low sensitivity to non-neutron events (in particular γ rays), and a good stability. Because no matter how good a detector is, it is always "dead" for a short while (typically 2-10μs for ZnS detector) after a neutron event has occurred. A dead-time correction has to be made (Soper et al., 1989).

5.3 Data collection

Basically, the data acquisition using a TOF ND experiment consists in recording each neutron event and giving it a label corresponding to the number of the detector in which it occurred and to the time of arrival at the detector. The clock measuring this time of arrival is set to 0 every time a pulse of protons hits the tantalum target. The counting of this event is incremented for each detector pulses after pulses so as to build a histogram of events. The counts are sorted into discrete time channels. In addition to the detection and collection of the scattered neutrons, the brightness of successive pulses may vary, for instance due to a small change in the moderator temperature. Also, from time to time protons beam steering can modify the energy dependence of the spectrum. In order to counteract this effect an incident monitor is placed just before the sample, and it records the incident spectrum. A transmission monitor is also mounted on SANDALS. Together with the incident monitor it may be used for measuring the total (coherent + incoherent + absorption) cross section of the sample as a function of λ.

5.4 Conducting the experiment

In order to obtain the total DCS of a sample, the standard method is to normalise the scattering from the sample to the scattering from a vanadium sample of known incoherent scattering (see section 5.5.4). However, before that, the background when no sample is in the beam, originating from neutrons and other forms of radiation, must be subtracted from the vanadium, the container, and the sample + container measurements. The spectra must also be normalised by the appropriate monitor counts so that four measurements are needed,

(i) The various samples + can spectrum (S)

(ii) The can alone spectrum (C)

(iii) The vanadium spectrum (V)

(iv) The background spectrum (B).

The total DCS of the sample is then determined from

$$\text{normalised sample spectrum} = \frac{S-C}{V-B}. \tag{5.8}$$

However, before this expression can be used, several corrections are to be made to the data, and these corrections are discussed in the next section. The choice of the container material is dictated by the requirement that it must not react with the sample, and it should mostly scatter incoherently so that no additional structure is added to the scattering pattern. Moreover, it should have a low absorption cross-section to avoid excessive attenuation of the beam, and be sufficiently thin to minimize multiple scattering effects. At the same time, it is desirable to keep the sample in a sealed environment and attain a good statistics in the data acquisition. Flat plate geometry cans (see figure 5.5) made of titanium/zirconium "null" alloy having a nominal scattering length of 0 were used for all the measurements reported here. Accordingly, the vanadium bar used to calibrate the data was also a flat plate slab.

5.5 Correction to the data

The procedure of obtaining accurate structure factor entails making corrections to the data for counter dead time, detector efficiencies, background scattering, multiple scattering, attenuation and inelasticity. The data were analysed using ISIS ATLAS package. The steps in the general sequence of analyses, as shown in the flow diagram of figure 5.6, are now described in turn.

5.5.1 Selection of the "good" detectors

Typically, neutrons illuminate each sample for several hours (6-11 hours) at stretch,

during which the counts are accumulated and stored in several files (runs) of 2-3 hours each. It is likely that during the long runs some detectors will become noisy, unstable or even dead. It becomes necessary to remove such bad detectors from the raw data files and this is done by running a program PURGED in the ATLAS suite of programs. The values chosen for the detector stabilities allowed 10% variation in the counts for an individual detector, and 2% variation in the total counts from all the detectors over the series of runs for a given sample.

5.5.2 Summing the data

Dead time corrections, which are normally of the order of only a few percents, are made to the detector spectrum files, and the incident and transmission monitor counts. While the incident and transmission monitor counts are just converted to wavelength, the corrected detector counts over the various runs of a same sample are summed and converted to a Q_e scale for the various groups of detectors, each detector spectra corresponding to a constant scattering angle (2θ). This is done by running the NORM program of the ATLAS package. At this stage, the scattering intensity $I(\theta,Q_e)$ for each of the 18 detector groups is given by neutron counts per Q_e-bin (see figure 5.7). This quantity is proportional to the incident neutron flux, $\Phi(k_e)$, the solid angle defined by the detector opening surface, $d\Omega$, the detector efficiency, $e(k_e)$, and the total TOF DCS of the sample + can (uncorrected for absorption and multiple scattering), $\Sigma^{\text{uncorr}}(Q_e)$:

$$I_{S+C+B}(\theta,Q_e)= \Phi(k_e)\, e(k_e) d\Omega N \Sigma_{S+C}^{\text{uncorr.}}(\theta,Q_e) + I_B, \qquad (5.9)$$

where N is the number of scattering units in the neutron beam and I_B, the background intensity. The incident flux and detector efficiency are represented as a function of k_e to emphasise that they are not a function of the scattering angle. The incident intensity measured by the incident monitor has the form

$$I_m(k_e)= \Phi(k_e)\, e_m(k_e) \qquad (5.10)$$

where $e_m(k_e)$ is the monitor detectors efficiency.

5.5.3 Absorption and multiple scattering corrections

As mentioned in section 4.3, the scattering length is complex and its imaginary part is associated to the absorption phenomenon. Clearly, even if this effect is not a major correction to be applied to the data obtained in these studies, attenuation of the beam occurs and such an effect must be corrected. Additionally, since we wish to extract a total DCS corresponding to single diffraction events, the data have to be corrected for the multiple scattering events. In all the DCS expressions obtained in chapter 4, the multiple scattering was neglected by virtue of the Born approximation (Cohen-Tannoudji et al., 1977; Sears, 1989). Practically, the absorption corrections are treated independently from the multiple scattering corrections. But, the multiple scattering are subtracted before the attenuation corrections can be applied since the latter are calculated only for the case of single scattering. In so doing, two approximations are made: (i) that multiply scattered neutrons are attenuated by the same amount as singly scattered neutrons, and (ii) that no neutrons are scattered in both the sample and the container. The second approximation is good only for a thin-walled container as is the case in the present studies. For a cell with thick walls, alternative routes exist, for example to use a Monte-Carlo simulation (Mildner and Carpenter, 1977) to solve the neutron transport equation (Sears, 1975) where both effects are included and correlated. For the simple case of a sample held in a thin-walled container, the general formalism of Soper and Egelstaff (1980), which employes numerical integrations to estimate these corrections, was used, $N\Sigma_{S+C}^{\text{uncorr.}}(Q_e)$ in (5.9) is modified to

$$I_{S+C+B}(\theta,Q_e)= \Phi(k_e)\, e(k_e) d\Omega\, [N_S \Sigma_S(\theta,Q_e)\, A_{S,S+C} + Nc\, \Sigma_C(\theta,Q_e)\, A_{C,S+C} + M_{SC}(k_e)] + I_B\,. \qquad (5.11)$$

Similarly, for the empty cell it follows that

$$I_{C+B}(\theta,Q_e)= \Phi(k_e)\, e(k_e) d\Omega Nc(\, \Sigma_C(\theta,Q_e)\, A_{C,C} + Mc(k_e)) + I_B, \qquad (5.12)$$

where in the last two expressions, $\Sigma_C(\theta,Q_e)$ and $\Sigma_S(\theta,Q_e)$ are the unattenuated single

scattering total TOF DCS of the can and the sample, respectively. N_c and N_s are, respectively, the number of scattering units of the cell and of the sample. The coefficients $A_{I,J}$ are the Paalman and Pings (1962) attenuation factors for scattering in I and attenuation in J, and M_{SC} and M_C, the total multiple scattering DCS for the sample + can and can alone, respectively. Attenuation coefficients depend on the sample geometry, scattering angle and through their dependence on the scattering and absorption cross-sections, on wavelength. These coefficients can be calculated within the static approximation to whatever numerical precision is required. Instead, the multiple scattering contributions cannot be evaluated exactly because they require a knowledge of the structure and dynamics of the sample. The method of calculation assumes this coefficient to be independent of the scattering angle, although dependent on the wavelength since it uses the total cross section. Both the corrections were evaluated by using a program CORAL in the ATLAS suite of programs.

5.5.4 Standard sample calibration

A characteristic of neutron scattering is the ability to perform an independent estimate of the instrumental calibration. This calibration consists in removing the unknown quantity, $e(k_e)d\Omega/e_m(k_e)$ appearing when a detector spectrum after subtraction of the background (of equation 5.11 and 5.12) is normalised to the incident monitor (equation 5.10). The estimation of this calibration quantity is achieved by measuring the TOF spectrum for vanadium standard because it gives a signal which is almost elastic and scatters largely incoherently thus giving extremely small Bragg peaks in the observed spectrum

$$I_{V+B}(\theta,Q_e)= \Phi(k_e)\, e(k_e)d\Omega N_V[\,\Sigma_V(\theta,Q_e)A_{V,V} + M_V(k_e)] + I_B\,. \qquad (5.13)$$

However, firstly because the scattering usually exhibits statistical noise, and secondly even the extremely small Bragg peaks must be removed from the data, some kind of smoothing is routinely done. After removing the background, Chebyshev polynomials are fitted to the vanadium data, $I_V(\theta,Q_e)$ in order to remove the noise and Bragg peaks, thus leaving the underlying structure. This is done by running a program VANSLAB in the ATLAS suite of programs. Once the attenuation and multiple scattering coefficients have been evaluated, the vanadium calibration,

$C_V(\theta,Q_e)$ is obtained from (5.13) and (5.10) using the smoothed spectrum

$$C_V(\theta,Q_e)= I_V(\theta,Q_e)\text{-}I_B / I_m(k_e)N_V[\Sigma_V(\theta,Q_e)A_{V,V} + M_V(k_e)]= e(k_e)d\Omega/ e_m(k_e)\,. \qquad (5.14)$$

5.5.5 Determination of the total DCS

The total TOF DCS for a given sample and for each detector group (illustrated in figure 5.8a) is then calculated using the program ANALYSE in the ATLAS package. The sequence of steps in this analysis are outlined below.

1 Subtract background.

$$I_{S+C}(\theta,Q_e)= I_{S+C+B}(\theta,Q_e)\text{-}I_B$$

$$I_C(\theta,Q_e)= I_{C+B}(\theta,Q_e)\text{-}I_B$$

2 Normalise to the vanadium and the monitor spectrum.

$$N\Sigma_{S+C}^{\text{uncorr.}}(\theta,Q_e) = I_{S+C}(\theta,Q_e)/ [I_m(k_e)\, C_V(\theta,Q_e)]$$

$$N\Sigma_{C}^{\text{uncorr.}}(\theta,Q_e) = I_C(\theta,Q_e)/ [I_m(k_e)\, C_V(\theta,Q_e)]$$

3 Subtract multiple scattering.

(Sing stands for single scattering)

$$I^{\text{Sing}}_{S+C}(\theta,Q_e)=N_S\Sigma_S(\theta,Q_e)\,A_{S,S+C}+Nc\,\Sigma_C(\theta,Q_e)\,A_{C,S+C}=N\Sigma_{S+C}^{\text{uncorr.}}(\theta,Q_e)\text{-}M_{SC}(k_e)$$

$$I^{\text{Sing}}_{C}(\theta,Q_e)=Nc\,\Sigma_C(\theta,Q_e)\;A_{C,C}=N\Sigma_{C}^{\text{uncorr.}}(\theta,Q_e)\text{-}M_C(k_e)$$

4 Attenuation corrections

$$N_S \Sigma_S(\theta, Q_e) = \frac{I_{S+C}^{Sin}(\theta, Q_e) - I_C^{Sin}(\theta, Q_e)(A_{c,sc} / A_{c,c})}{A_{S,SC}}$$

5 Normalise to the amount of sample in the beam

$$\Sigma_S(\theta, Q_e) = \left.\frac{d\sigma}{d\Omega}\right|_{tot} (\theta, Q_e) \tag{5.15}$$

Thus, the total TOF DCS (b sr^{-1}molecule^{-1}) within the static approximation, for a molecular liquid (see section 4.6) can be written as:

$$\left.\frac{d\sigma}{d\Omega}\right|_{tot} = \sum_{\alpha} c_\alpha \overline{b_\alpha^2} + \sum_{\alpha\beta'} \overline{b_\alpha}\,\overline{b_\beta} c_\alpha c_\beta (S_{\alpha\beta}(Q) - 1). \tag{5.16}$$

5.5.6 Inelasticity effects

a. A simple picture of the recoil effects

The TOF ND data analyses procedures described so far implicitly assume that the static approximation is valid for any scattering event. However, in neutron scattering the static approximation fails if the scattering centres can be easily knocked out of their positions by the momentum of the scattering collision. These recoil effects are straightforward in a monatomic system. Consider, the impact of a neutron of mass m_n with an incident energy E on a nucleus of mass m_nA where A is the mass number of the nucleus. The recoil energy, E_{rec}, resulting from the transfer of momentum $\hbar\boldsymbol{Q}$ to a single nucleus is given from the momentum conservation,

$$\hbar\boldsymbol{Q} = \boldsymbol{p}' - \boldsymbol{p} \tag{5.17}$$

where $\boldsymbol{p}$ and $\boldsymbol{p}'$ are the momenta of the nucleus before and after the collision. The gain in the kinetic energy of the nucleus is given by:

$$\frac{1}{2m_n A}(\boldsymbol{p}'^2 - \boldsymbol{p}^2) = \frac{1}{2m_n A}(\hbar^2 Q^2 - 2\hbar \boldsymbol{p}.\boldsymbol{Q}). \tag{5.18}$$

For a fixed $\boldsymbol{Q}$, the average $\boldsymbol{p}.\boldsymbol{Q}$ is zero. Therefore, the average gain in energy of a nucleus is

$$E_{rec}=\hbar^2Q^2/2m_nA. \tag{5.19}$$

It appears from equation 5.19 for a fixed Q, that while such an effect will be small for a heavy nucleus, for lighter nuclei such as H and D for which the mass number A=1 and 2, the recoil is large. However, from a simple "billiard ball" analysis (following classical mechanics) in which an incident ball hits another ball initially at rest, one can show that, in the laboratory frame, the kinetic energy change, E-E', involved in the collision where the incident ball deflected by an angle 2θ from its initial direction, is proportional to $\sin^2\theta$. Intuitively, however, whatever the mass of the nucleus the smaller detector angles, the smaller the change E-E'. Although the scattering is elastic in the frame of the centre of mass of the neutron + scattering unit, it appears inelastic in the laboratory frame in which the neutron is detected. This causes a particular effect in that neutrons can arrive either later or earlier than they would have done if the scattering were elastic. Thus, since the neutron can exchange energy with the scattering system the dynamic effects, almost invariably, have to be considered.

b. Total TOF DCS versus total DCS

These dynamic effects are described via the Van Hove (1954) dynamic structure factor, $S^{tot}(Q,\omega)$ ($\omega = E$-$E'/\hbar$). In order to extract the structural information from the Van Hove dynamic structure factor (Powles, 1973a), one has to perform the integral:

$$\left.\frac{d\sigma}{d\Omega}\right|_{tot} = \int_{\substack{-\infty \\ \text{const } Q}}^{+\infty} \left.\frac{d\sigma}{d\Omega d\omega}\right|_{tot} d\omega = \int_{\substack{-\infty \\ \text{const } Q}}^{+\infty} \frac{k'}{k} S^{tot}(Q,\omega)d\omega\,, \tag{5.20}$$

or more generally, for a molecular system in which $S^{tot}(Q,\omega)$ is separated into a self and a distinct term, the total DCS may be written as:

$$\left.\frac{d\sigma}{d\Omega}\right|_{tot} = \frac{k'}{k} \int_{\substack{-\infty \\ \text{const } Q}}^{+\infty} \left(\sum_{\alpha} c_\alpha \overline{b_\alpha^2} S_\alpha^{self}(Q,\omega) + \sum_{\alpha,\beta} c_\alpha c_\beta \overline{b_\alpha}\,\overline{b_\beta} S_{\alpha,\beta}^{dist}(Q,\omega) \right) d\omega . \tag{5.21}$$

In a TOF experiment, neutrons arrive at the detector at time t_{obs} after the generation of the neutron burst at time $t_0 = 0$, and k_e is determined through equation 5.1b. However, for a system for which the static approximation is not well satisfied, k and k' will differ from k_e in such a way that equation 5.1a is satisfied. In other words, a neutron with an incident energy greater than E_e may loose energy in the sample, and arrive at the detector within the same time channel as those neutrons scattered elastically. This situation can be expressed as

$$t_{obs} = t - t_0 = L_0 / v + L_1 / v' = (m/h)\left[L_0\lambda + L_1\lambda'\right] \tag{5.22}$$

where

$$\lambda' = \lambda\left[1 - (m\omega\lambda^2 / \pi h)\right]^{-1/2}, \tag{5.23}$$

and hence, t is a function of λ and ω:

$$t_{obs} = t - t_0 = (m\lambda / h)\left(L_0 + L_1\left[1 - (m\omega\lambda^2 / \pi h)\right]^{-1/2}\right). \tag{5.24}$$

Following Powles' formalism (Powles, 1973b), the number of neutrons detected in a frequency range $\Delta\omega$ at ω is proportional to $S^{tot}(Q,\omega)\ \Delta\omega$, and consequently the number detected in the time channel of width Δt at t is proportional to $S^{tot}(Q,\omega)\ \partial\omega/\partial t\,|_\lambda\ \Delta t$. As a result, for a system containing Ns scattering units the count rate normalised to the incident monitor count per unit of solid angle at time t and at fixed angle 2θ is

$$I_S(\theta,t) = N_S \int_{\text{const } t} d\lambda \frac{\Phi(\lambda)}{\Phi(\lambda_e)} \frac{e(k')}{e_m(k_e)} \frac{k'}{k} S^{tot}(Q,\omega) \left.\frac{\partial\omega}{\partial t}\right|_\lambda , \tag{5.25}$$

where the integration is made over the incident flux $\Phi(\lambda)$ and, for given λ, it is implied that the values of k', Q and ω correspond to neutrons arriving at the detector at time t_{obs}. Considering Q_e, which can be written using 5.1b and 5.2 as

$$(t-t_0)Q_e = (2m/h)(L_0 + L_1)\lambda \sin\theta\,, \tag{5.26}$$

the count rate can be expressed as a function of Q_e:

$$\mathrm{I}_S(\theta, Q_e) = N_S \int_{\text{const } t} d\lambda \frac{\Phi(\lambda)}{\Phi(\lambda_e)} \frac{e(k')}{e_m(k_e)} \frac{k'}{k} S^{\text{tot}}(Q,\omega) \left.\frac{\partial\omega}{\partial t}\right|_{\lambda} \frac{dt}{dQ_e}\,. \tag{5.27}$$

Finally, since in (5.27) t is fixed and in view of (5.24), the integrand may be regarded either as a function of λ or ω. Transforming the integration to one over ω, it follows that

$$\begin{aligned} \mathrm{I}_S(\theta, Q_e) &= N_S \int_{\text{const } t} d\omega \frac{\Phi(\lambda)}{\Phi(\lambda_e)} \frac{e(k')}{e_m(k_e)} \frac{k'}{k} S^{\text{tot}}(Q,\omega) \left.\frac{\partial\lambda}{\partial\omega}\right|_{t} \left.\frac{\partial\omega}{\partial t}\right|_{\lambda} \frac{dt}{dQ_e} \\ &= N_S \int_{\text{const } t} d\omega \frac{\Phi(\lambda)}{\Phi(\lambda_e)} \frac{e(k')}{e_m(k_e)} \frac{k'}{k} S^{\text{tot}}(Q,\omega) \left(-\left.\frac{\partial\lambda}{\partial t}\right|_{\omega} \frac{dt}{dQ_e} \right) \end{aligned} \tag{5.28}$$

Deriving (5.26)

$$\frac{dt}{dQ_e} = -(t-t_0)/Q_e \tag{5.29}$$

and deriving (5.24)

$$\left.\frac{\partial\lambda}{\partial t}\right|_{\omega} = (t-t_0)^{-1}\lambda(1+A)^{-1} \tag{5.30}$$

where,

$$A = \frac{(m/h\pi)\lambda^2 L_1 \omega\left(1 - m\omega\lambda^2/\pi h\right)^{-3/2}}{L + L_1(1 - m\omega\lambda^2/\pi h)^{-1/2}}\,, \tag{5.31}$$

(5.28) becomes

$$I_S(\theta,Q_e) = Q_e^{-1} N_S \int_{\text{const } t} d\omega (1+A)^{-1} \lambda \frac{\Phi(\lambda)}{\Phi(\lambda_e)} \frac{e(k')}{e_m(k_e)} \frac{k'}{k} S^{\text{tot}}(Q,\omega). \tag{5.32}$$

The count rate for the vanadium is found in the same fashion just by inserting $\delta\omega$ (since the scattering is almost elastic) in 5.32

$$I_V(\theta,Q_e) = Q_e^{-1} \lambda_e \frac{e(k_e)}{e_m(k_e)} N_V \Sigma_V(\theta,Q_e). \tag{5.33}$$

Thus, (5.14) becomes

$$C_V(\theta,Q_e) = Q_e^{-1} \lambda_e \frac{e(k_e)}{e_m(k_e)} \tag{5.34}$$

Finally for all time t, dividing (5.32) with (5.34) and normalizing to the molecule, the total TOF DCS is given by

$$\Sigma_S(\theta,Q_e) = \int_{\text{const } \theta} d\omega (1+A)^{-1} \frac{\lambda}{\lambda_e} \frac{\Phi(\lambda)}{\Phi(\lambda_e)} \frac{e(k')}{e(k_e)} \frac{k'}{k} S^{\text{tot}}(Q,\omega) \tag{5.35}$$

From the latter expression, it can be seen that the experimental arrangement corresponds to the integration of the dynamic structure factor weighted by a complicated function depending on various experimental parameters. Moreover, the integration path of (5.35) is over ω at constant θ, while the required path is over ω at constant Q in (5.20). From (5.35) it is clear that $\Sigma_S(\theta,Q_e)$ is equal to (5.15) only in the limit of no inelastic scattering. In the general case, since there is a difference between $\Sigma_s(\theta,Q)$ of (5.35) and total DCS given by (5.15), we must make a correction to this difference in order to determine the total DCS. These are called inelasticity effects on the measured total DCS, and are illustrated in figure 5.8b. It is worth noting that the reactor experiment case appears as a particular case of (5.35), recovered by setting L_1=0 which forces k=k_e (with still $k \neq k'$).

c. Inelasticity corrections

The most common approach used to correct the inelasticity effects is due to Placzek (1952) who expanded the total DCS (equation 5.35 set for L_1=0) as a power series in $m_n A^{-1}$. The method assumes that the nuclear masses are bigger than that of the neutron whose energy is much larger than the excitation energy of the system. Based on these assumptions the corrections can be calculated without knowing $S^{tot}(Q,\omega)$ explicitly (De Gennes, 1959; Placzek, 1952; Rahman et al., 1962), and these are related to E_{rec}, the sample temperature, T, the incident neutron energy, E, and the detector efficiency. Interestingly, Placzek showed that the inelasticity correction to the distinct DCS is zero to a first order. The consequence of this result is that, in the first order approximation, the correction has to be applied only to the self-dynamic structure factor, $S^{self}(Q,\omega)$ while that for the distinct DCS can be neglected. The situation becomes more problematic for molecular liquids. For such systems, the dynamics is complicated by the fact that translational, rotational and vibrational motions occur together. Depending on the incident neutron energy and the sample temperature, the molecule considered may be either rigid or vibrating due to the thermal and/or neutron excitation. As a result, rather than a generalisation, the Placzek method was modified within different energy regimes (Powles and Rickayzen, 1976; Rickayzen and Powles, 1976; Egelstaff and Soper, 1980a, 1980b). Moreover, the treatment of the inelasticity effects increases in complexity with that of the molecule considered (Powles, 1979). For instance, treating an asymmetric vibrating polyatomic molecule such as methanol, where in addition, the hydrogen bonding makes a perturbation of some quantum vibrational states of the molecule, becomes impossible. In the TOF experiments, neutrons are produced over a wide range of energy so that they are likely to cover various energy regimes. Some authors (Powles, 1978a, 1978b; Blum and Narten, 1976a) combined the results obtained from different methods developed for particular regimes. However, this approach was shown to lead to inconsistent results (Egelstaff and Soper, 1980a), so that currently there is no general method valid for all regimes. Additionally, in the case of molecules containing light nuclei such as hydrogen for which the scattering is seen from moderate angle and is induced by a thermal neutron, the Plazcek method is impractical because a large number of higher order terms in the expansion need to be

taken into account. As a result, the pertinence of correcting the self-term only, and to neglect distinct dynamic structure factor corrections may not be a sensible approximation. (Powles, 1978a) showed that if the correction to $S^{dist}(Q,\omega)$ is ignored it may lead to an error of few percents in the determination of an intra-molecular bond distance. Clearly it appears that if one wants to compete with the accuracy of determination of the intra-molecular structure of a molecule claimed by other methods such as electron diffraction, say 0.001Å, the need of a reliable inelasticity correction is of paramount importance. For a reactor experiment, an easy way to check the procedures and assumptions used to tackle inelasticity corrections is to run the experiment with a slightly different neutron incident energy, and verify that they lead to the same results (distinct DCS). This was done for both deuterated benzene (Bartcsh et al., 1985) and methanol (Montague et al., 1981). Unfortunately, for methanol the uncertainties associated with the extracted inter-molecular radial distribution functions were of little use in discriminating potential models used in computer simulations of the liquid (Haughney et al., 1987) (see figure 5.9). It is not surprising then to find that H/D substitution on the hydroxyl group of methanol led to unresolved Ho-Ho pdf (Montague et al., 1984). An alternative treatment to the Placzek method for system containing light elements, which has been hardly exploited experimentally, was given by Wick (1954) who used similar kind of series expansion. Interestingly the leading terms in Wick's series are equivalent to the corresponding terms in the Placzek's method, whose series is simpler. Consequently, in the particular case where the wavelength of the incident neutron is short and the scattering is seen from small angles, the Placzek approach is still applicable (Powles, 1978a), and it gives comparable results to the Wick's series (Egelstaff and Soper, 1980a, 1980b). This situation is realised experimentally in the design of SANDALS instrument, which is optimised to use the epithermal flux of neutrons at small scattering angles (3.8° to 37° in 2θ). Thus, the assumption of correcting only $S^{self}(Q,\omega)$, which may not be taken as granted in reactor based experiments, is probably reasonable for this particular experimental arrangement.

d. The procedure used for the inelasticity correction

Under the assumption that the dynamic corrections to the distinct DCS are small, equation (5.35) for each detector group is conveniently written as,

$$\Sigma_S(\theta,Q) = \sum_\alpha c_\alpha \overline{b_\alpha^2}\Sigma_\alpha^{self}(Q,\theta) + \sum_{\alpha\beta} \overline{b_\alpha}\,\overline{b_\beta} c_\alpha c_\beta (S_{\alpha\beta}(Q) - 1) \tag{5.36}$$

where

$$\Sigma_\alpha^{self}(\theta,Q_e) = \int_{\text{const }\theta} d\omega (1+A)^{-1} \frac{\lambda}{\lambda_e}\frac{\Phi(\lambda)}{\Phi(\lambda_e)}\frac{e(k')}{e(k_e)}\frac{k'}{k} S_\alpha^{self}(Q,\omega). \tag{5.37}$$

The distinct DCS (second term on the right hand side of (5.36)) can be extracted provided the self-term is corrected for the inelasticity. However, because the inelasticity effects are different for each angle, these have to be corrected for each group of detectors separately. The conventional method consists in fitting each spectra of a given total TOF DCS by a polynomial expression usually in the form $A_0 + A_2Q^2 + A_3Q^4$. However, we applied these corrections with a method (Postorino et al., 1994) initially developed by Soper *et al.* (1992) by using a program HDSUB_B available in the ATLAS suite of programs. This method makes use of three total TOF DCS obtained for three H/D substituted samples, and attempts to correct them consistently for each detector group separately at a time. The approach assumes that the self-scattering term can be described by a product of two smoothly varying functions, $M(Q,\theta)$ and $\Delta(Q,\theta,x)$

$$\sum_\alpha c_\alpha \overline{b_\alpha^2}\Sigma_\alpha^{self}(Q,\theta) = M(Q,\theta)\Delta(Q,\theta,x). \tag{5.38}$$

$M(Q,\theta)$ is an overall form factor, which corresponds to the self-scattering for the so-called "null" sample, i.e., that sample for which the average scattering length of the substituted hydrogen is zero. $\Delta(Q, \theta, x)$ is the correction function which takes account of the true composition of a particular sample compared to the "null" sample. Here, x is the fraction of all substituted hydrogens, which are protons in each sample. For instance, x = 1 and x = 0 correspond to all substituted hydrogens being protons and deuterons, respectively. Because of the negative scattering length of the proton, the composition x = 0.64 will have zero scattering length for the substituted hydrogens ("null" sample). For this particular case $\Delta(Q, \theta, 0.64)$=1. To estimate $M(Q,\theta)$, the three following functions are formed

$$A(Q,\theta) = \frac{x_0 \Sigma_H(Q,\theta) + (1-x_0)\Sigma_D(Q,\theta) - \Sigma_{HD}(Q,\theta)}{x_0(1-x_0)(\bar{b}_H - \bar{b}_D)^2}, \tag{5.39}$$

where Σ_H, Σ_D and Σ_{HD}, respectively referred to as the light, heavy and light + heavy (mixture) total TOF DCS, are defined by (5.36). x_0 is the atomic fraction of the protonated sample used to make up the mixture sample, which does not necessarily have to be the null sample.

$$B(Q,\theta) = \frac{\left(\Sigma_H(Q,\theta) - \bar{b}_H{}^2 A(Q,\theta)\right) - \left(\Sigma_D(Q,\theta) - \bar{b}_D{}^2 A(Q,\theta)\right)}{(\bar{b}_H - \bar{b}_D)}, \tag{5.40}$$

and, finally

$$C(Q,\theta) = \Sigma_H(Q,\theta) - \bar{b}_H B(Q,\theta) - \bar{b}_H{}^2 A(Q,\theta). \tag{5.41}$$

The function (5.39) is just the site-site partial structure factor (PSF) derived directly from the total TOF DCS. It is the same as the one obtained from the distinct DCS defined by equation (4.48). Remembering equation (4.54) one can see that (5.41) is equal to the X-X PSF plus a residual single atom scattering term, which is $M(Q,\theta)$. Thus,

$$C(Q,\theta) = M(Q,\theta) + c_X^2 \bar{b}_X{}^2 (S_{XX}(Q,\theta) - 1), \tag{5.42}$$

where

$$M(Q,\theta) = \frac{\bar{b}_D \Sigma_H^{self} - \bar{b}_H \Sigma_D^{self}}{\bar{b}_D - \bar{b}_H}. \tag{5.43}$$

For all the samples reported in this thesis it was sufficient to estimated $M(Q,\theta)$ by least square fitting a Chebychev polynomial of order 2 or 3 to expression (5.42) on a log E scale where E is the incident neutron energy. This is due to the fact that all the hydrogen containing samples investigated so far show a linear decline in the value of

$M(Q,\theta)$ with log E for each group of detectors. The choice of the order of polynomial is governed by the requirement that $M(Q,\theta)$ is not expected to have oscillations characteristic of the distinct term. This polynomial fit to the single atom scattering is further refined by forcing the Fourier transform (equation 4.34) of the interference term obtained from $C(Q,\theta)$ to its zero limit below $r = r_{min}$, which is lower than any known intra-molecular bond distance in the X-X distribution function. In order to estimate the quantity $\Delta(Q, \theta, x)$ in (5.38), the ratio of the measured total TOF DCS to $M(Q,\theta)$ is taken for each sample in turn,

$$R(Q,\theta,x) = \frac{\Sigma_{H,D,HD}(Q,\theta)}{M(Q,\theta)} \tag{5.44}$$

followed by a similar polynomial fit to $R(Q,\theta, x)$, using the same logarithmic scale as before, and once again the guiding criterion is that the order of the polynomial must not be so large that $\Delta(Q, \theta, x)$ reproduces the obvious interference scattering. Polynomials of the order 1 or 2 were used in the present work. Although, the empirical method described here lacks formal rigor, but since the data recorded at different scattering angles require different recoil corrections to the self-scattering, the correctness of the distinct DCS obtained can be established if at the end of the analysis there is a high degree of overlap between the data at different angles (see figure 5.8c). It is worth noting that any residual inelastic contributions should come at fixed neutron energies rather than Q values, and are likely to be averaged out by merging the data over the scattering angles.

e. Validation of the method

It was mentioned earlier that for the reactor experiments the procedures used to tackle inelasticity corrections may be checked by running the experiment with a slightly different neutron incident energy, and verifying that they lead to the same results. Unlike the reactor case, for the TOF experiments this cannot be done routinely on SANDALS, since it requires changing the neutron moderator. However, recently Soper et al.(1997) performed two ND H/D substitution experiments on liquid water under the same thermodynamic conditions (573 K, 100 bar), one using a water moderator at 300 K, while the other used the usual methane moderator at 100 K.

Although liquid water is not explicitly relevant to this work (see Appendix A), it nevertheless presents some similarities with methanol in that, it is a light molecule forming strong hydrogen bonds and has similar or even worse problems for applying the inelasticity corrections. Because the two moderators produce markedly different incident neutron spectra due to the different neutron thermalization temperatures, the corresponding inelasticity effects are substantially different in the two cases, especially at low Q. By using the procedure outlined previously, they extracted the inter-molecular $g_{OO}(r)$, $g_{OH}(r)$ and $g_{HH}(r)$ partial pair distribution functions for both cases. Soper *et al.* (1997) found that although there are small differences at a quantitative level, these are far smaller (see figure 5.10) than those obtained at the total inter-molecular level, for example, for methanol by using a reactor source (Montague et al., 1981) (see figure 5.9).

5.5.7 Merging the data

Once the inelasticity corrections have been applied to the spectrum of each detector group separately, we get the distinct DCS for each scattering angle:

$$\left.\frac{d\sigma}{d\Omega}\right|_{\text{dist}} = \sum_{\alpha\beta} \overline{b_\alpha}\,\overline{b_\beta} c_\alpha c_\beta (S_{\alpha\beta}(Q) - 1). \tag{5.45}$$

These are, then, merged (using the MERGE routine of the ATLAS package) to form a single composite distinct DCS with improved statistics over an optimum Q-range. In practice, the choice of the Q-ranges for each detector group, defined by giving two limiting wavelength values of the incident neutron flux, depends to some extent on the individual judgment of the experimentalist. Typically, the limiting values chosen in this work were 0.07 Å and 3.5 Å. This leads to Q values in the range ~ 0.1Å^{-1} for the lowest angle detector group to ~50 Å^{-1} for the highest. This allowed a large Q-range within a spectrum from a particular detector group, and a good overlapping Q-region with other spectra. In practice, the range beyond 40 Å^{-1} is never used because it originates only from the highest detector groups with poor counting statistics as compared to lower Q values for which the data are obtained from several detector groups. Thus, in this work the single composite distinct DCS was truncated at 40 Å^{-1} after confirming that there is no residual structure at higher Q values.

5.6 Determination of the various distribution functions

Various scattering functions were (e.g. distinct DCSs, inter-molecular DCSs or partial DCSs) obtained in previous sections can be converted to r-space directly according to equations 4.34 or 4.38. However, the real space distribution functions obtained by direct Fourier determination normally contain spurious features. One of the main causes of these errors is the statistical noise in the Q-space data, which, when three or more signals are combined together, becomes especially significant. It is worth noting that the statistical noise at high Q contributes significantly to the spurious low-r ripples because of the Q dependence of the Fourier transform. Conversely, this also means that the usually extrapolated low-Q portion of the data has little effect on the real space functions. Thus, by varying Q_{max} it is possible to distinguish between spurious features and the real data in the resulting transforms. In addition, even if the inelasticity corrections are carried out with care some residual inelasticity may still be present in the data. Since these effects are expected to be slowly varying with Q (a low order polynomial), they cause a systematic offset to the data points manifesting themselves in the real space as a high frequency ripple at low r. It is interesting to note that for an experiment performed at a pulsed source, the available Q-range is normally large enough to ensure that any scattering function has gone to zero before the maximum Q value available is reached. Thus, the oscillations resulting from the termination step of the experimental data have very little influence on the real space function as compared to the data obtained from a reactor source. In the latter case these effects are usually overcome by fitting some sort of window function to the high-Q portion of the experimental data in such a way that the data are smoothly forced to zero by the last experimental point. In the present study, the method used for inverting the experimental scattering functions was the minimum noise reconstruction (MIN) technique (Soper et al., 1993; Soper, 1986, 1990) (MCGOFR program). This method is particularly well suited for transforming noisy signals such as the higher order difference functions obtained in the present study. The MIN technique is similar to maximum entropy methods (Allen and Tildesley, 1987) except that the function maximized is not the entropy. A smoothness criterion is used instead. By applying tight restrictions to the form a distribution function can take, it is designed to find a solution, which is as smooth as possible, but nonetheless, consistent

with the original data within the experimental uncertainties. In the case where the original data suffers from a residual inelasticity effect, a slowly varying background function, $B^{dist}(r)$, may be subtracted from the data if necessary. The basic idea of how the method works can be described as follows:

1. Set $g_{\alpha\beta}(r)=0$ for $r < r_{min} = r_0 - \delta$ where r_0 is the smallest distance expected
   $g_{\alpha\beta}(r)=1$ for $r_{min} < r$ from the distribution function, e.g., the smallest intra-molecular bond distance and δ=0.2 Å.

2. Using (4.33) calculate $S_{\alpha\beta}^{fit}(Q)$ from the modelled $g_{\alpha\beta}(r)$.

3. Determine the quality factor, $\chi^2 = \sum_i \frac{\left(S_{\alpha\beta}^{orig}(Q_i) - S_{\alpha\beta}^{fit}(Q_i)\right)^2}{2\sigma_i^2} + \lambda N_i$

between the fitted and the original data for which a data point i has the uncertainty σ_i, augmented by the noise constraint N_i monitored by the user via λ. A small value of λ will correspond to good fits but noisy model distributions, while too large a value of λ will lead to a very smooth model distribution, but a poor fit to the original data.

4. Move at random a single point in the $g_{\alpha\beta}(r)$ and recalculate the new $S'^{fit}_{\alpha\beta}(Q)$.

5. If $\chi'^2 < \chi^2$ accept the move, otherwise accept it with a probability $\exp\left(\frac{\chi^2 - \chi'^2}{T_i}\right)$,

where T_i is a global temperature factor applicable to all the data point. This Monte Carlo sampling method is actually used to speed up the process of convergence quite significantly.

6. Repeat from step 2 several thousands steps of the Monte Carlo procedure till the program has converged to a stable $g_{\alpha\beta}(r)$ for which the fitted data must be as close as possible to the original data according to the smoothness requirement, and the following tight restrictions applied to build the distribution function.

Consider, for example, that a distinct DCS needs Fourier inversion. The tight restrictions to be input by the user are of three types:

(i) $G^{dist}(r)=0$ for $r<r_{min}=r_0-\delta$ (r_0 is the smallest intra-molecular bond distance)

$G^{dist}(r)\geq 0$ for $r_{min}<r$ (5.46)

$$\text{(ii)}\ 4\pi\rho\int_0^\infty r^2 dr(G^{dist}(r)-1)=\rho\chi_T k_B T-1+\lim_{Q\to 0}\frac{1}{\left(\sum_\alpha^{N_t} c_\alpha \bar{b}_\alpha\right)^2}\frac{\partial\sigma}{\partial\Omega}\bigg|_{coh}^{intra}, \quad (5.47)$$

which force the distinct DCS to have the right low-Q limit for its inter-molecular (see 4.42), and intra-molecular part (second term in the right hand side of (5.47)).

(iii) For the background function $B^{dist}(r)$, the constraints are roughly the inverse of (i), namely

$B^{dist}(r)$ = any value insuring that $G^{dist}(r)=0$ if $r<r_0+\delta$

$B^{dist}(r)<0$ if $G^{dist}(r)<0$ and $r_0+\delta<r$ † (5.48)

$B^{dist}(r)=0$ if $G^{dist}(r)>0$ and $r_0+\delta<r$

Recently, it has been argued (Pusztai and McGreevy, 1998) that the method may lead to over-smoothing the data thereby removing some real structure from the data. In order to avoid this happening, the Fourier transformation was done step-by-step by adopting the following approach:

- First, the program was run with a small λ value, thus producing noisy distribution functions and noisy MIN fits. At the same time r_0 was set to zero so as to switch off the background generation.

† Constraint not switched on in this study, because the condition $G(r)>0$ was never imposed. This, in fact, provides an additional check of the correctness of the data reduction, when a distribution function expected to be positive over the whole r range is considered.

- By varying the Q_{max} value it was possible to distinguish between spurious and real features in the resulting transforms. A sufficiently high-Q value is then chosen to cover all the structural features exhibited by the data (typically 35-40 $Å^{-1}$ for transformation of the distinct DCS and 15-20$Å^{-1}$ for the inter-molecular DCS).

- The value of λ was increased gradually to remove the spurious ripples in the r-space functions (referred as to RFS1), checking back that the MIN fits are neither too noisy nor too smooth while staying consistent with the original data within the experimental uncertainties.

- Then, r_0 was increased slowly so as to switch on the background generation (if necessary). The distribution functions obtained by this process became smoother than RFS1 in the r-region where the residual inelasticity effects are not expected to occur. The value of λ was then reduced until the new function agreed with RFS1. The procedure of refining r_0 and next λ was continued up to the point where r_0 corresponded to the smallest distance expected from the distribution function.

- A final check run was made with a bigger λ value in order to verify that the r-space function was really a compromise between being not too noisy and too smooth. Ideally, if there was no residual inelasticity left in the data, the MIN fit obtained at the very end should match pretty well the original data, otherwise an offset to the data points is seen when MIN fit and original data are compared[††].

5.7 Separation of the intra-molecular DCS from the distinct DCS

The Fourier transformation of the distinct DCS does not usually provide much information on the inter-molecular structure of the liquid due to overlapping of the intra- and inter-molecular distances. For instance, the intra-molecular structure of methanol and benzene extends respectively up to ~3Å and ~5Å, where the largest

[††] In the following chapters (6, 7 and 8), the fitted data will be referred to as MIN fit or back Fourier transform.

intra-molecular distances are larger than the shortest inter-molecular distance. There are two ways of separating the intra- and inter- molecular contributions to the distinct DCS. In the first method, the separation is achieved by means of Fourier transformation of the distinct DCS but its application is limited to only those cases where the largest intra-molecular distances are shorter than the shortest inter-molecular distances. Since this condition was never met for the systems investigated in the present study, another method was used. This is based on the fact that the distinct DCS of a molecular liquid can be separated at least into two regions (Powles, 1973a): one at high Q that is more sensitive to the molecular structure, and the other at low Q containing information about structural order and the interaction between the different molecules (see for instance figure 5.11). The method involved fitting the intra-molecular scattering described by equation (4.40) to the distinct DCS in the Q range (≥6 Å^{-1}) where the weighted sum of all inter-molecular contributions is negligible (assertion checked by back Fourier transform of the combined pdfs obtained from MD simulations of the system). In order to achieve the fit of the distinct DCS, an agreement factor R was minimised:

$$R = \left(\frac{\sum_{Q_{min}}^{Q_{max}} \left[\left. \frac{\partial \sigma}{\partial \Omega} \right|_{coh}^{dist} - \left. \frac{\partial \sigma}{\partial \Omega} \right|_{fit}^{intra} \right]^2}{Q_{max} - Q_{min}} \right)^{1/2}, \qquad (5.49)$$

where $\left. \frac{d\sigma}{d\Omega} \right|_{coh}^{intra}$ is the fitted model function obtained from equation (4.40) and, Q_{min} and Q_{max} (typical values 6 Å^{-1} and 35 Å $^{-1}$) define the range of the fit. Two algorithms were used for this purpose. In the first method a quasi-Newton routine (Numerical Algorithm Group, 1995a) was employed for finding a minimum value of R subject to fixed upper and lower bounds of the independent variables, intra-molecular distances r_{ij} and the corresponding Debye-Waller factor, γ_{ij}, for each pair ij of nuclei pertaining to the molecule. The analytical expressions for all r_{ij} are provided by the user (see for example Adya and Wormald (1992) where explicit cases of ethylene, ethane, and carbon dioxide are treated) and the numerical solution is calculated by varying the r_{ij} and the corresponding γ_{ij} so as to refine equation 4.40

against the data *via* (5.49). The second algorithm differs only in the way it finds an approximation to the minimum of R. The user provides an initial guess at the position of the minimum and the algorithm proceeds by using a simplex method (Numerical Algorithm Group, 1995b). Practically, in contrast to the quasi-Newton algorithm, it was noticed that for a molecule such as methanol, described by a large number of variables the first method was more robust than the simplex method for which the search of the minimum is not constrained in a particular area of the parameter space. In all cases, the stability of the numerical solution (uncertainties associated with the structural parameters) was checked by varying the range of the fit: 6 to 8 $Å^{-1}$ (for low Q) and 30 to 35 $Å^{-1}$ (for high Q).

5.8 The data analyses

5.8.1 General checks

Given the likelihood of errors in parameters such as the actual amount of sample and sample container in the beam, uncertainties in the mixture composition, which may induce various kinds of errors during the data analyses, it is necessary to employ few simple rules to check the results at different stages of the analysis.

The first of these checks is made when the experiment is in progress. Usually, the neutron counts for a sample are stored in various short-duration runs (2-3 hours each). It is necessary to perform checks to ensure that different short scans for a given sample are consistent with each other. For instance, some amount of the sample may disappear due to a poor sealing or leak in the cell; the pressure inside the cell may reach above its tolerance value causing a leak in the cell. Note that the cell + sample are placed in a high vacuum environment. In addition, drift in the data may also occur due to several instrumental problems, such as a shift in the moderator temperature, etc; that may arise during the experiment. Any of these problems can cause an inconsistency between the different scans.

After merging the data from different group of detectors, the experimental high-Q limit of the single total TOF DCS for the cell is compared to the theoretical value obtained from equation (4.36). This is done to check the correctness of the

dimensions of the cell. Note that the total TOF DCS (equation 5.15) for each detector groups are always consistent together because the cell scattering is hardly affected by inelasticity effects. As for the cell, the total TOF DCS of each sample during analysis is compared with its expected theoretical limit. However, only a qualitative comparison is of use here because due to the inelasticity effects, the more protonated hydrogens are present in the sample the worse is the agreement. Typical agreement obtained for the liquids studied in this work are within ~3-5% (a fully deuterated sample), 6-12% (a protonated sample), and 4-9% (a H/D mixture sample) of the theoretical value calculated from equation 4.36. Nevertheless, no matter how fair is this agreement, the high Q limit of a light sample must be at a higher value than a heavy sample, and the high Q limit of the light + heavy mixture sample must lie in-between these two values (see figure 5.12). This is because the incoherent scattering cross-section of light hydrogens is about 40 times larger than that of deuterium (Sears, 1992). If significant discrepancies are noticed at this point, it may be either that bad attenuation and multiple scattering corrections were applied, in which case the data are re-analysed from scratch, or that what was effectively measured is not what was expected (see appendix A).

At this stage, the data have not been corrected for the inelasticity effects, and for the systems investigated here, much effort was spent in applying these corrections.

5.8.2 The particular case of the systems studied

a. The pure components

The general strategy followed to correct the data from these effects is summarized in figure 5.13 for pure liquids.

- Consider three total DCS, obtained the H/D substitution on specific nucleus of the molecule (for instance Ho, the hydroxyl hydrogen of methanol or H, the hydrogens of benzene). HDSUB_B program is run at least twice (referred to as procedure 1 and 2 in figure 5.13) with different Chebychev polynomial order (typically 2 or 3 for $M(Q,\theta)$ and 1 or 2 for $\Delta(Q, \theta, x)$).

- The output of the program consists of nine files corresponding to, (i) the three files (heavy, light, and mixture, samples) containing each the various detector groups spectra corrected from the inelasticity (.INT files), (ii) the three single distinct DCSs (merged over a number of detector group chosen by the user, .MINT files), and (iii) the three S-S, X-S, and X-X PSFs extracted from the three single distinct DCS according to equations 4.48, 4.51 and 4.54, respectively, but only the .INT files are considered. First, only the various spectra of the heavy sample are considered, because the inelasticity effects are less pronounced for this sample than for the light and mixture samples.

- A good agreement between the spectra from neighbouring groups in the .INT file is usually observed for the heavy sample, and after checking that the low Q limit for each spectrum is in reasonable agreement with equation (5.47), these are merged together for both procedures, and generally, the two single distinct DCS obtained (from procedure 1 and 2) are very close to each other. An intra-molecular fitting is then done on both the single DCSs. The comparison of the structural parameters obtained from such a fitting provides a useful check that no residual elasticity effects is present in the distinct DCS (Powles, 1978b), or that the data were not over fitted by using a too high Chebychev polynomial order during the inelasticity corrections.

- The scattering length(s) of the substituted site(s) was(were) changed in order to build an expected intra-molecular DCS for the light and the mixture samples. For each sample, three criterion: (i) a good agreement between the spectra from neighbouring groups, (ii) a general agreement of each spectrum with its intra-molecular DCS beyond ~6 $Å^{-1}$, and (iii) the low Q limit of each spectrum to be in reasonable agreement with equation (5.47), were used to select different detector groups that can be merged together.

- Once the three single distinct DCS are obtained, the S-S, X-S and X-X PSFs are extracted. Although all the S-S PSFs obtained in this study are inter-molecular partials, X-X and X-S partials contain both intra- and inter-molecular contributions. Interestingly, on Fourier transformation (constrained by equations 5.46-48) of the X-X and X-S PSFs some of the overlapping intra-

molecular peaks (such as carbon – a methyl hydrogen and oxygen-hydroxyl hydrogen for methanol) in the distinct DCS get separated (see chapter 6.1). These intra-molecular peaks provided further checks of the correctness of the data reduction. For instance, the calculation of the co-ordination number of these intra-molecular peaks gave a good indication that the data were correctly normalised. In addition, a good MIN fit as compared to the original data, gave confidence that the data were free from residual inelasticity. If these effects are still present in the data, they usually manifest themselves as significant ripples in the low r region (see section 5.6) and produce an offset in the Q-space data when MIN fit and original data are compared.

b. The mixture

For the mixture, the procedure used is slightly modified to include information known determined experimentally for the pure liquids as a consistency check. The approach is summarised in figure 5.14 and can be described as follows.

- As for the case of the pure components, the three total DCS for benzene-methanol system, with substitutions on specific nuclei, were used to run HDSUB_B program with different order of Chebychev polynomial. Those corrected spectrum (.INT file) of the heavy sample showing good agreement with the spectra from neighbouring groups were merged to form a single distinct DCS. The general approach adopted in order to combine the various distinct DCS was to merge those regions of each spectrum that overlapped with at least one other neighbouring group at lower or higher scattering angle. A good agreement between the spectra from neighbouring groups provided confidence in the accuracy of the corrections employed, especially those which vary greatly with the scattering angle e.g. attenuation and inelasticity.

- At this stage, an assumption is made that the intra-molecular structure of the mixture can be described by a linear combination of those of the pure components. The intra-molecular DCS for the mixture is built from those of the pure components and compared with the distinct DCS in the relevant high-Q range (beyond ~6 $Å^{-1}$), as a first simple check of the assumption made.

- The scattering length(s) of the substituted site(s) is(are) changed in order to build an expected intra-molecular DCS for the light and the mixture distinct DCSs. For each sample, two criterion: (i) a good agreement between the spectra from neighbouring groups, (ii) a general agreement of each spectrum with its intra-molecular DCS beyond 6 $Å^{-1}$, were used to select different detector groups to be merged. The third criterion (used for the pure components case) could not be used because the compressibility of the mixture at this composition, temperature and pressure as far as we are aware, is not available in the literature.

- Once the three single distinct DCSs are obtained, the X-X, X-S and S-S PSFs are extracted. The X-X and X-S partials containing both intra- and inter-molecular contributions were Fourier transformed so that to separate some overlapping intra-molecular peaks mixed up in the distinct DCS (see section 8.2.3.a.II). This also helped to verify whether the intra-molecular structure of the mixture is correctly described by the assumption that the intra-molecular structure is additive. Moreover, even if some of the intra-molecular peaks are still mixed up in the X-X and X-S PSFs, it is still possible to combine some of the partials obtained for methanol and benzene and compare in the intra-molecular region the built function with the mixture PSF (see section 8.2.3.a.II). As for the case of the pure liquids, apart to provide direct information about the intra-molecular structure, these intra-molecular peaks provided further check of the correctness of the data reduction, and that the composition of the mixture was effectively what is expected. For instance, the calculation of the co-ordination number of these intra-molecular peaks was a good indication that the data are correctly normalised, and this associated to a good MIN fit in comparison with the original data, gave confidence that the data are free from residual inelasticity.

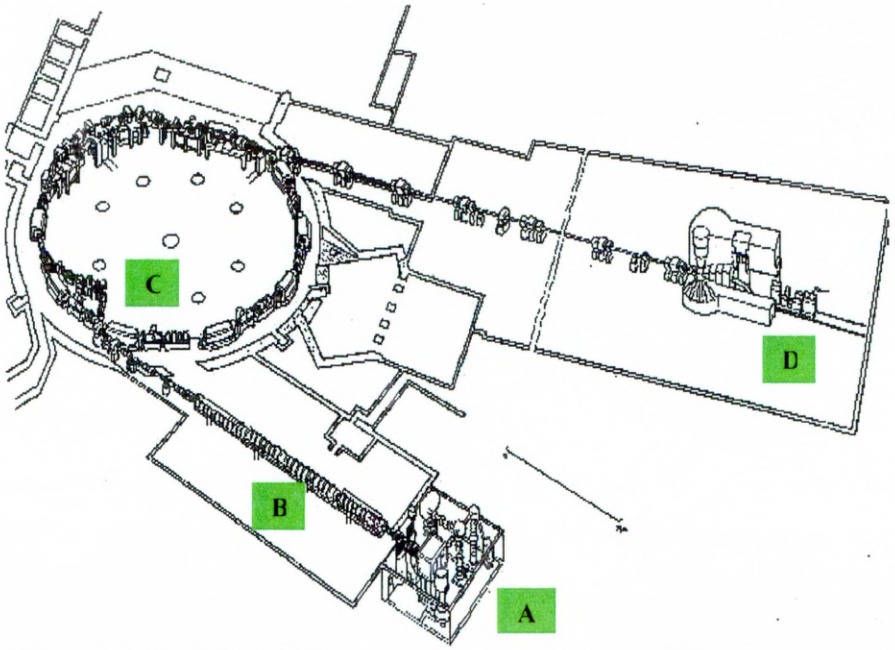

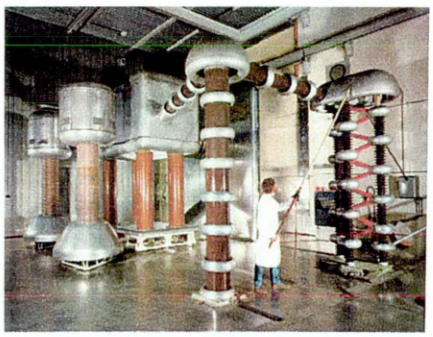

C

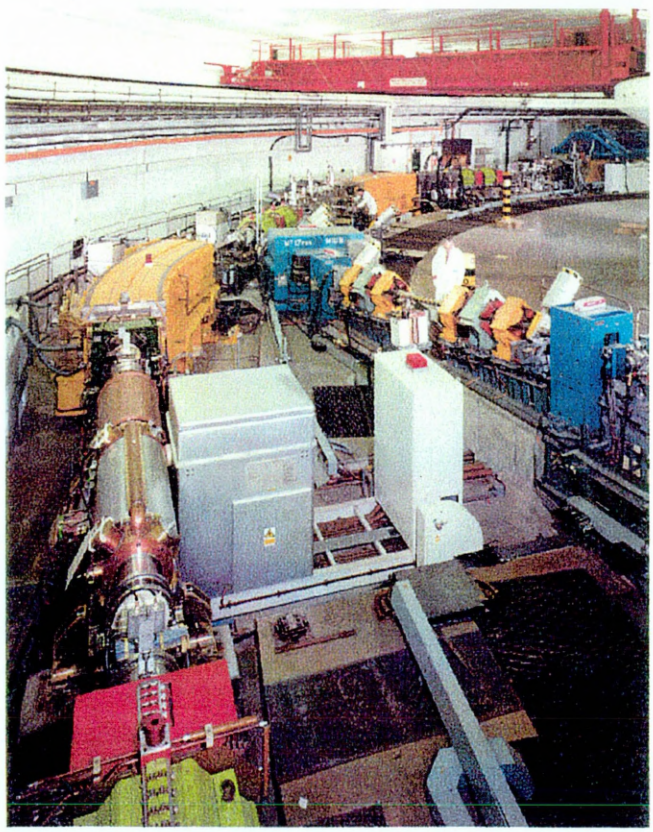

Figure 5.1a An overview of the ISIS facility. (A) The ion-source high voltage area, (B) the LINAC, (C) one of the two accelerating cavities of the synchrotron

D

E

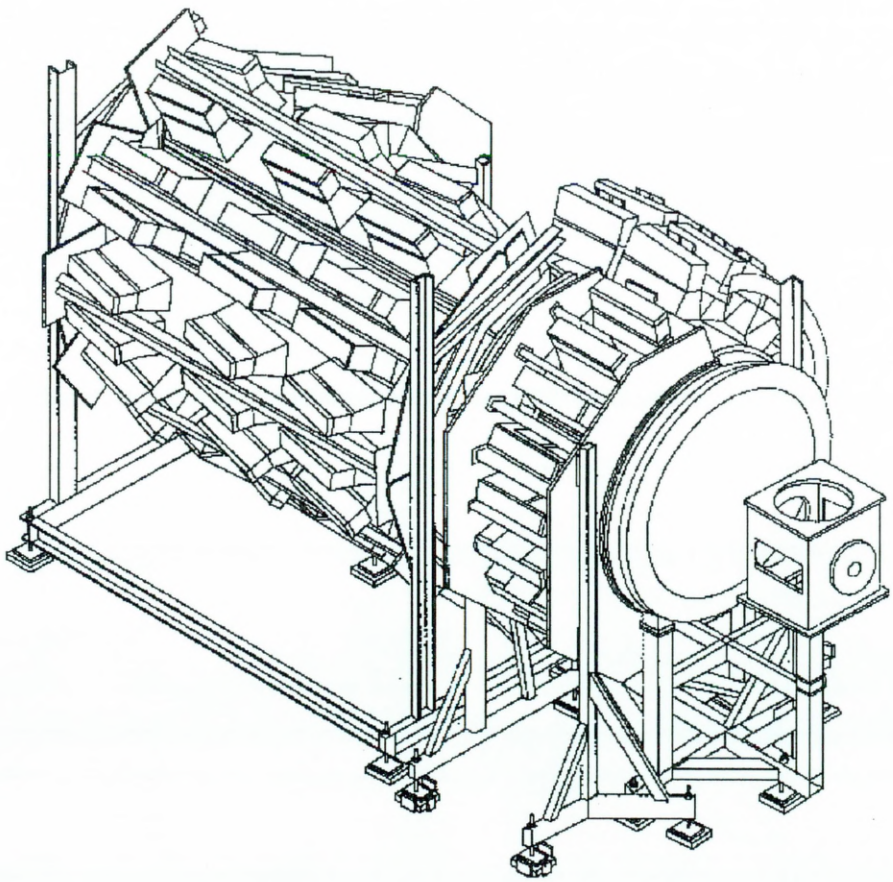

Figure 5.1b (D) The experimental hall (all around the target station), in which different instruments used for specific studies are installed. The SANDALS cabin where the experiments were conducted is shown in (D'). The detectors (E) are hidden on the ground floor, underneath the cabin.

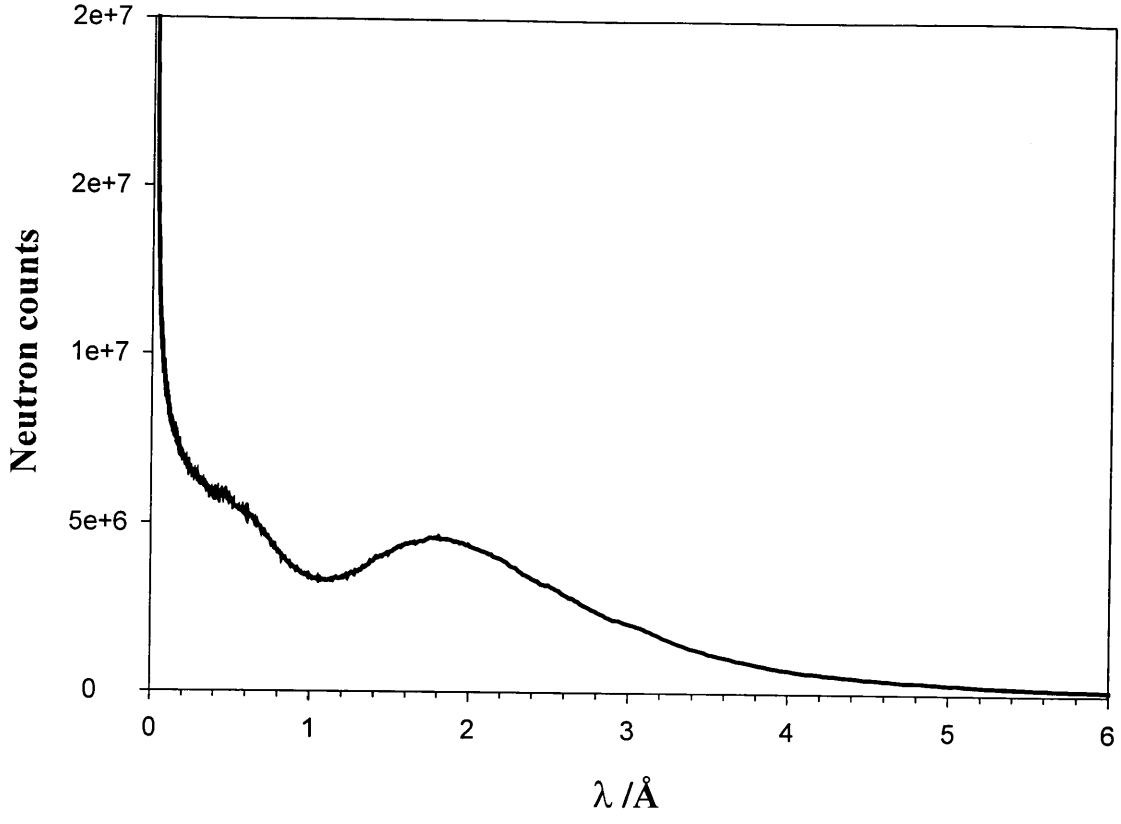

Figure 5.2 The moderated neutron beam spectrum seen from the incident monitor.

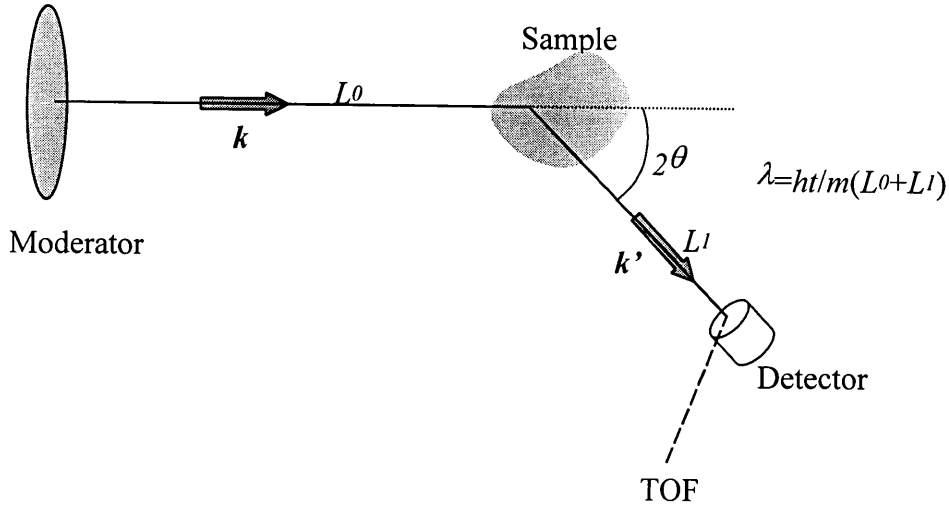

Figure 5.3 Schematic of a neutron diffractometer for an accelerator-based source.

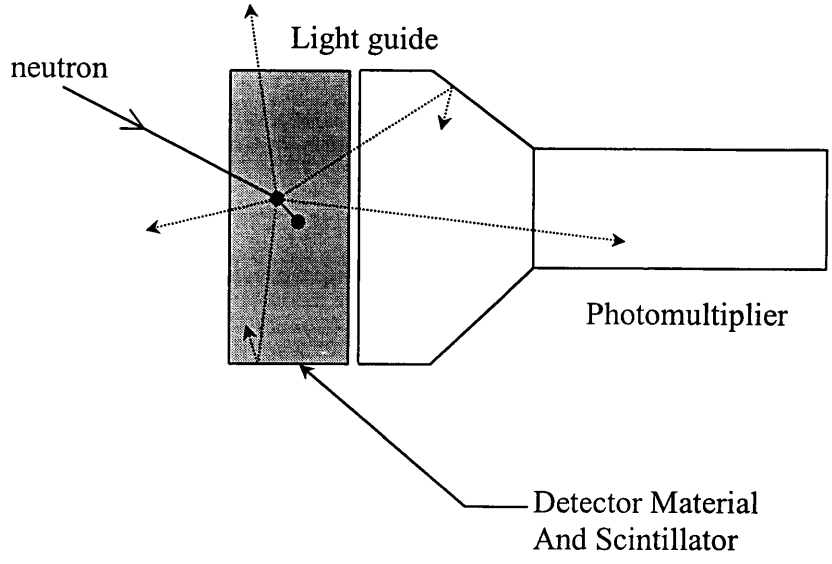

Figure 5.4 Schematic of a scintillator detector (adopted from Windsor (1981))

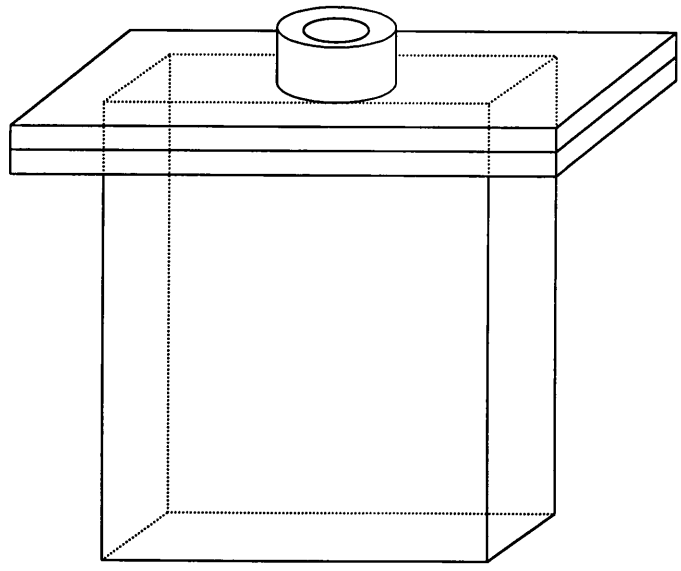

Figure 5.5 Schematic of the sample container used for this work on SANDALS: a flat plate Ti/Zr sample can.

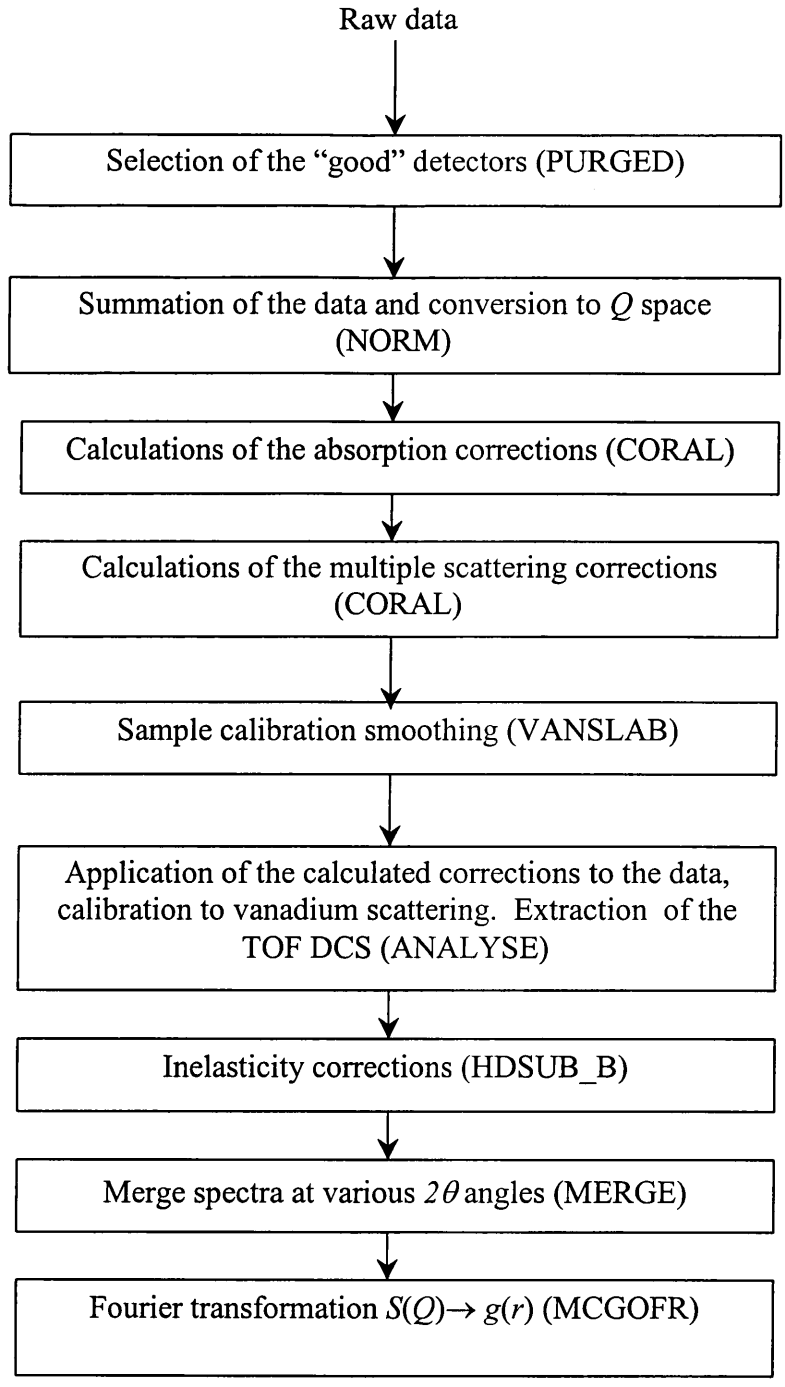

Figure 5.6 The main steps followed in the data analyses of TOF neutron data collected on SANDALS instrument.

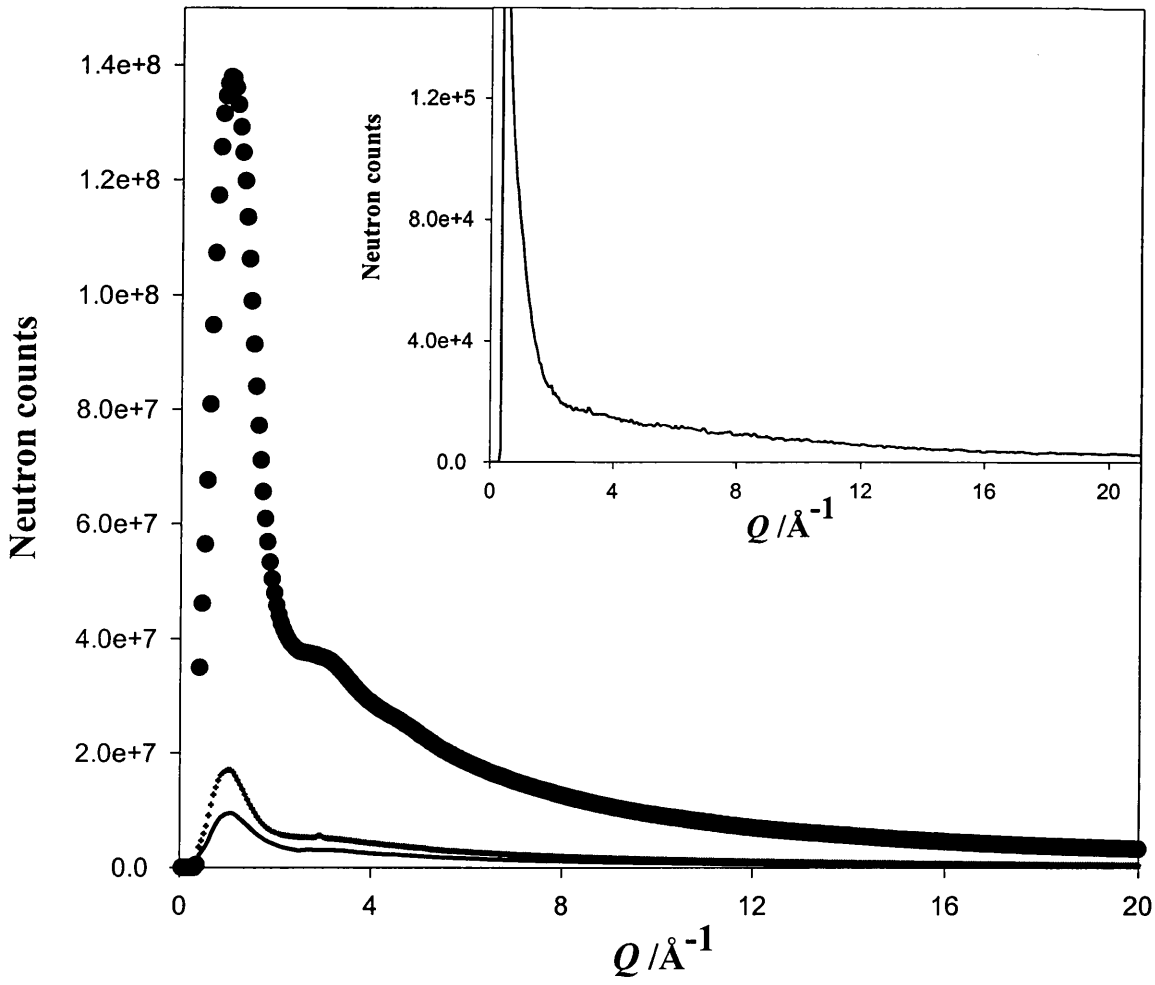

Figure 5.7 The scattering intensity collected by the first group of detectors for C_6H_6+CD_3OD mixture (o), the empty cell (+), the vanadium standard (line), and the background presented in the inset.

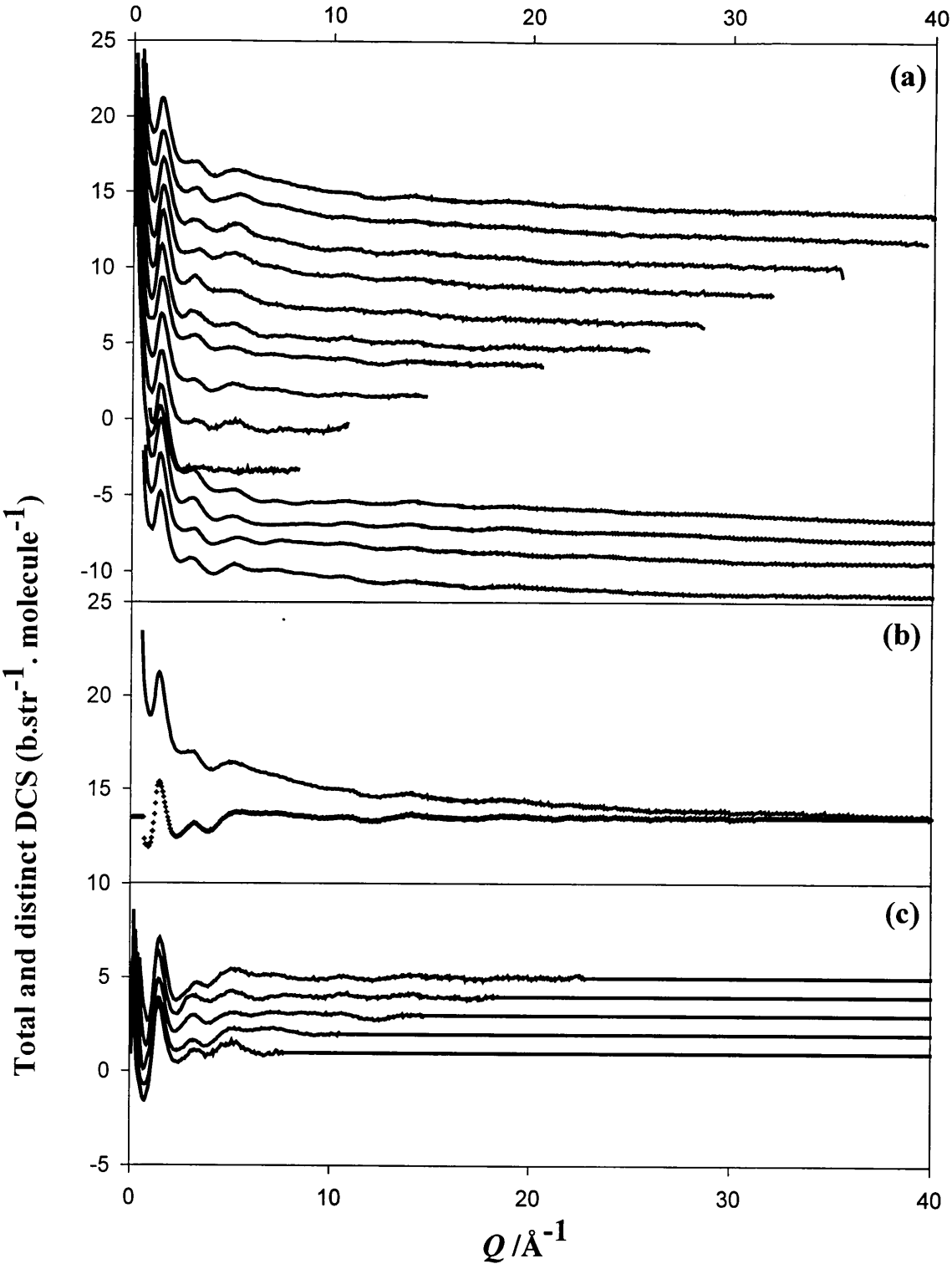

Figure 5.8 (a) The total DCS for some of the different groups of detectors, obtained for liquid mixture C_6H_6+CD_3OD (from top to bottom displaced by –2 each time, group 1 to 14). (b) the total DCS of C_6H_6+CD_3OD (line) for the first group of detector along with its distinct counterpart after applying the inelasticity corrections (+). (c) some of the distinct DCS corresponding to different groups of detectors, obtained for C_6H_6+ CD_3OD (from top to bottom displaced by –1 each time, groups 4, 6, 7, 8 and 9).

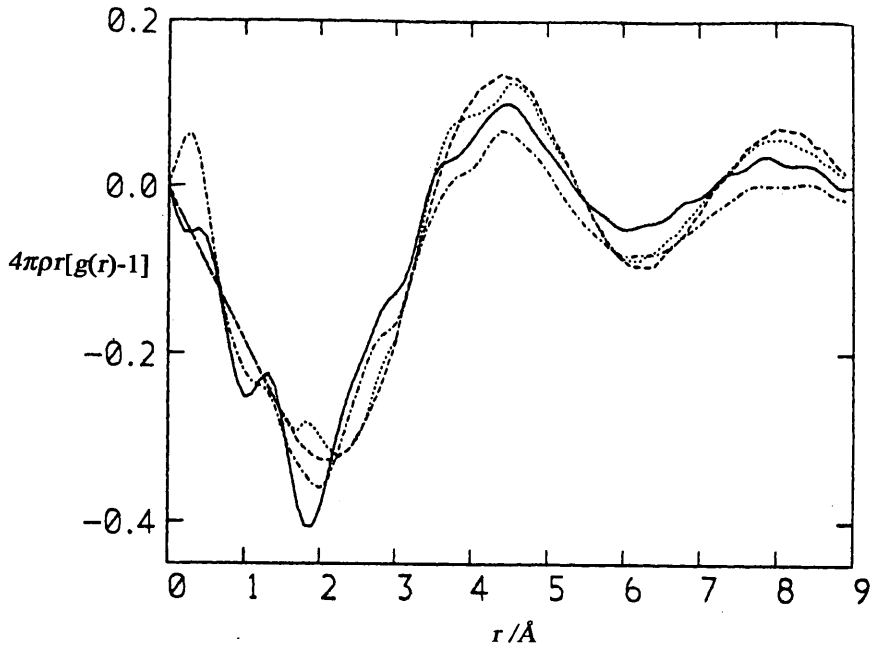

Figure 5.9 The intermolecular rdf of liquid methanol under ambient conditions. Full and dash-dot curves are, respectively, ND data from a reactor neutron source for which the neutron wavelength was 0.7Å and 0.5Å (Montague et al., 1981). All other curves result from MD simulations performed with various potential models (reproduced from Haughney et al., (1987)).

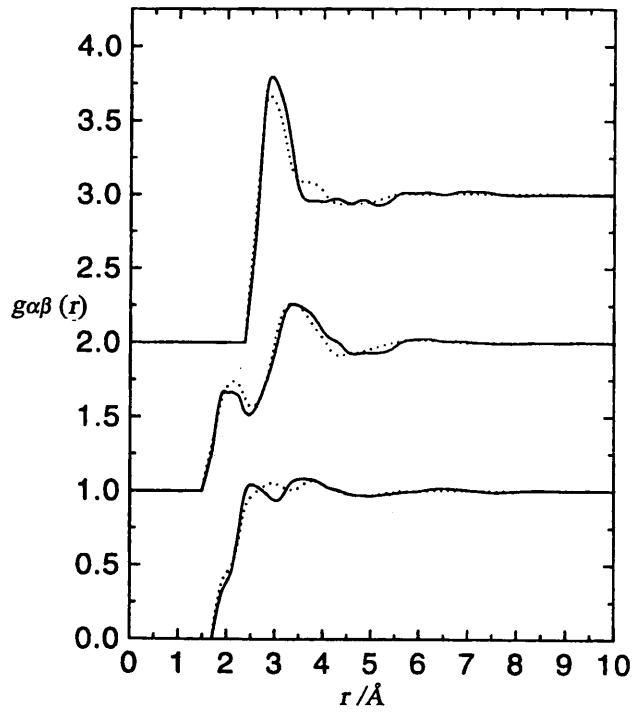

Figure 5.10 Comparison of the HH, OH and OO water intermolecular pdfs (from bottom to top) extracted using SANDALS, from two separate experiments performed at the same thermodynamic state (573K and ~100 bar), but with different conditions of the moderator. Full line and dotted curves correspond respectively to pdfs obtained using methane moderator at 109 K and a water moderator at 300 K (reproduced from Soper et al. (1997)).

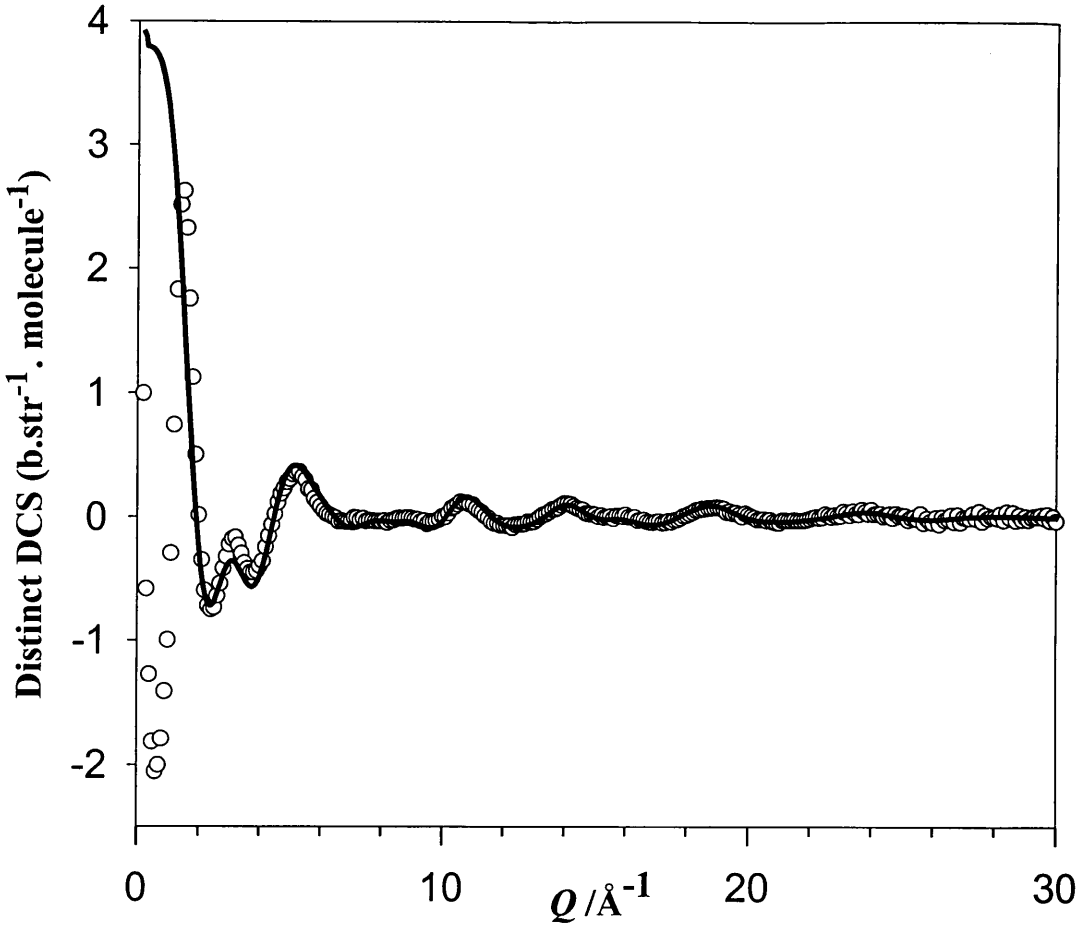

Figure 5.11 The distinct DCS for C_6H_6+CD_3OD (symbols) along with its intra-molecular contribution (line).

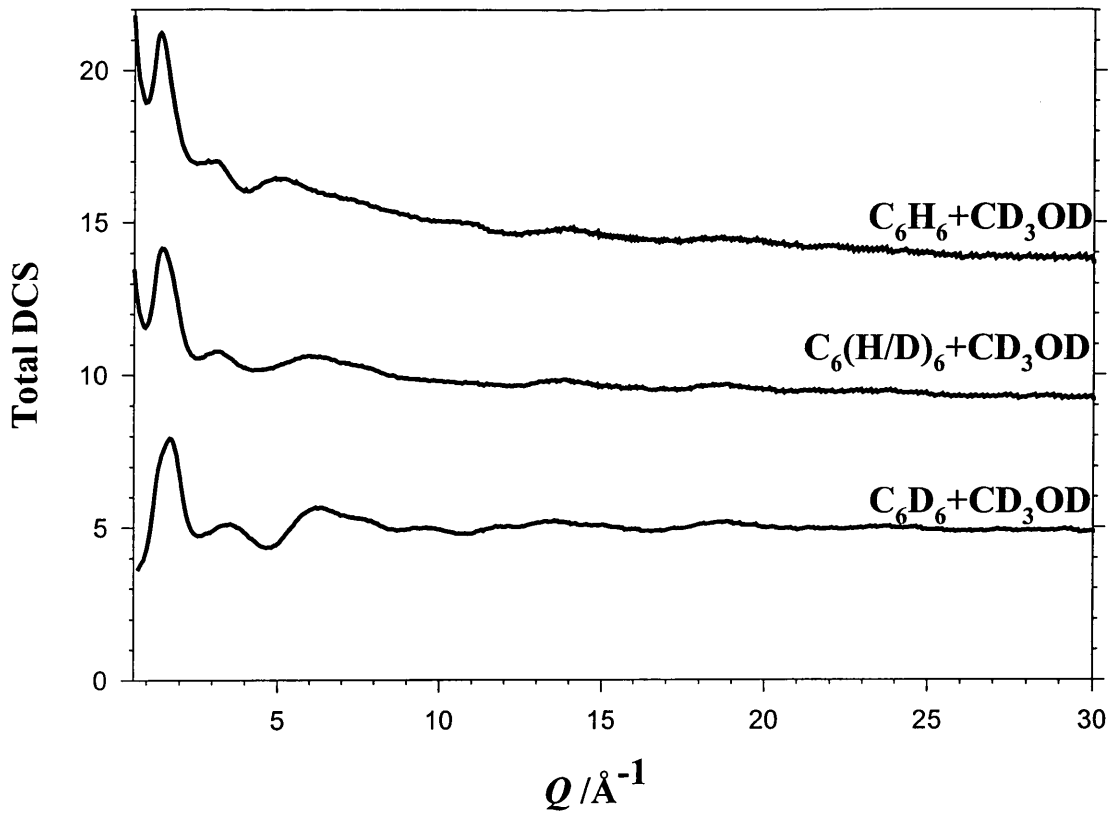

Figure 5.12 The distinct DCS corresponding to the first detector group (2θ =11.4°) for H/D substituted benzene in methanol. One can see the extent to what the inelasticity "droop" increase with the amount of protonated hydrogen used.

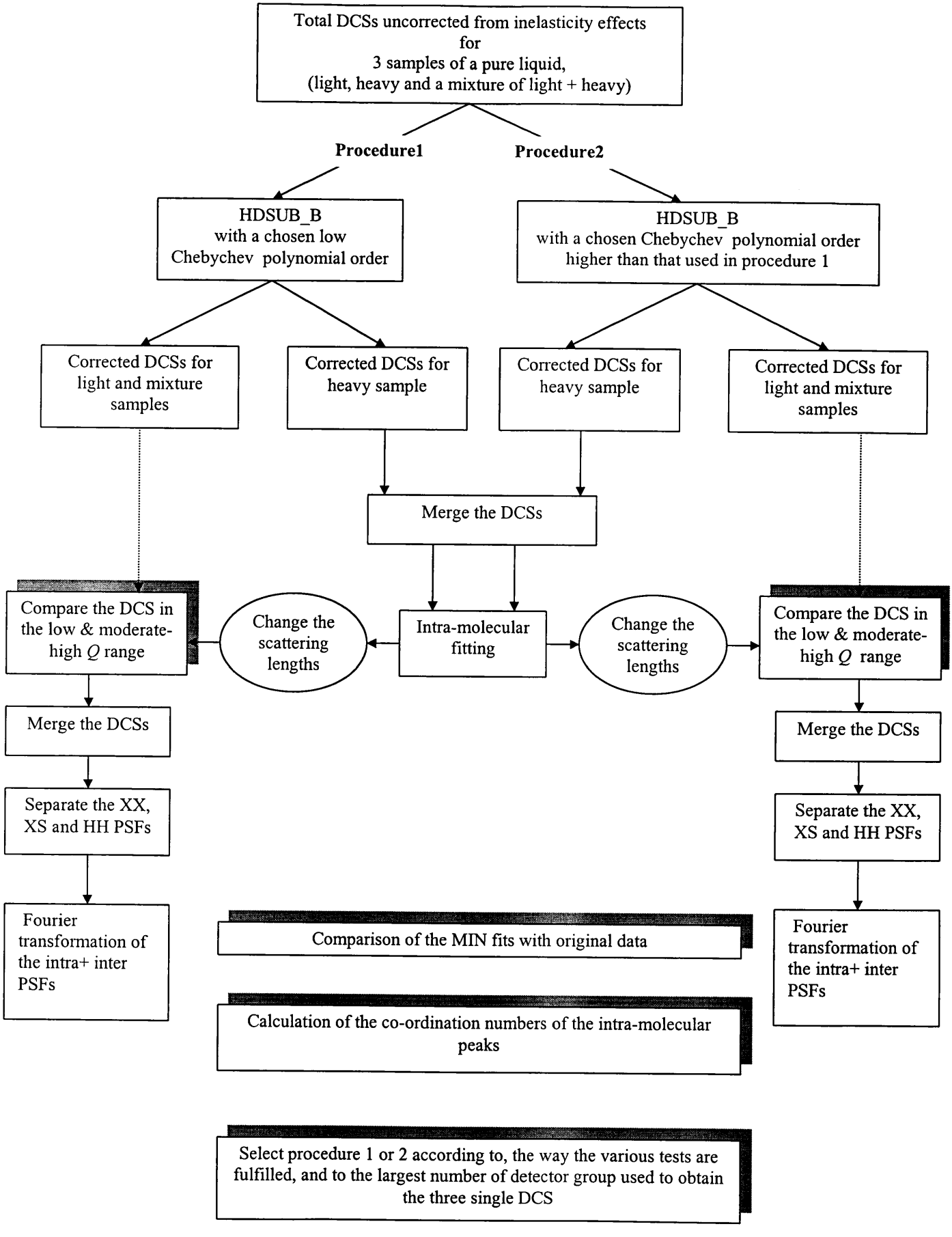

Figure 5.13 Flow diagram showing the main aspects in processing the data analysis after the ANALYSE stage (see figure 5.6), for the three H/D substituted pure samples.

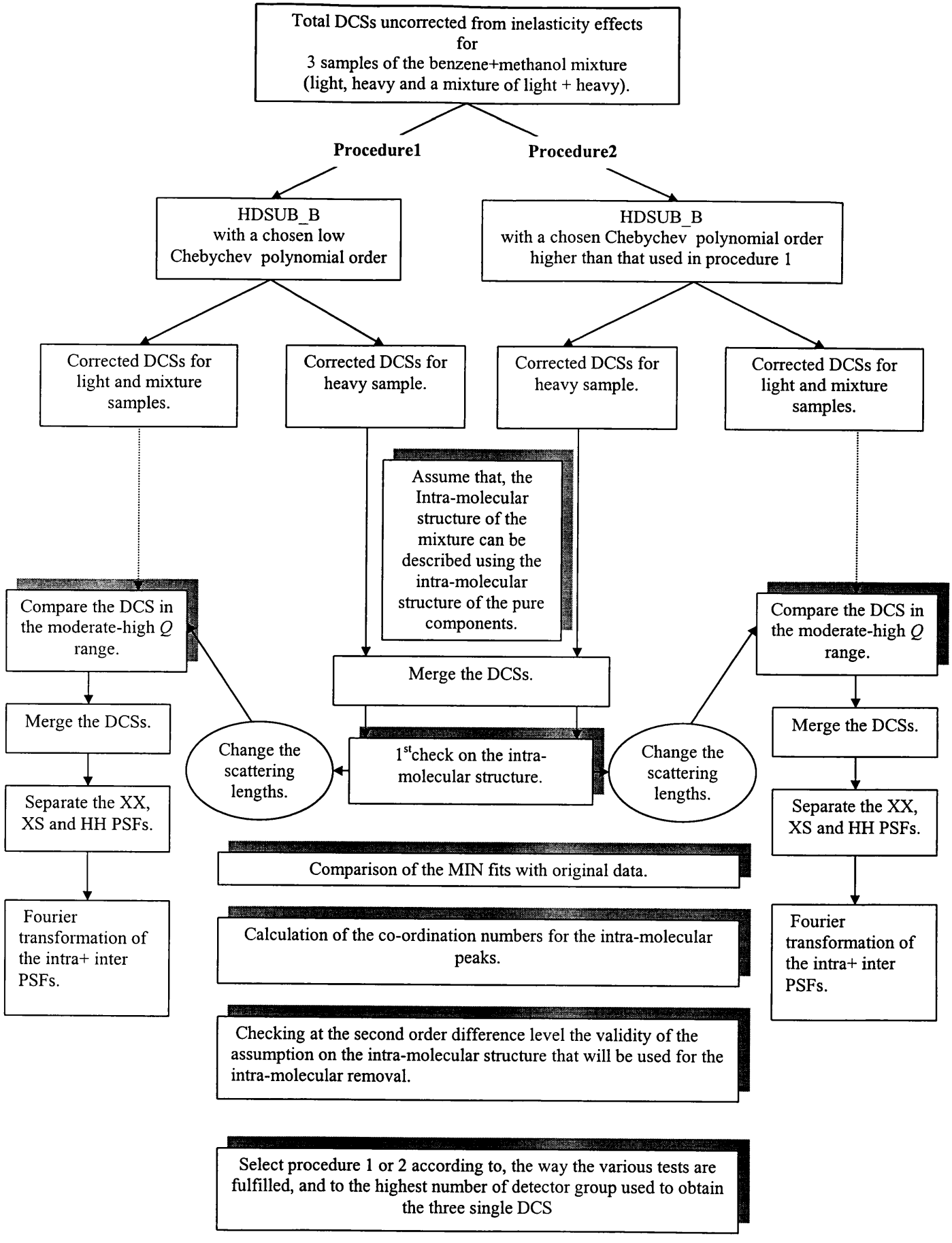

Figure 5.14 Flow diagram showing the main steps in the data analyses after the ANALYSE stage (see figure 5.6) for the three sets of benzene-methanol TOF DCSs, in which the H/D substitution is used.

Chapter 6

The structure of liquid methanol[1]

6.1 The neutron diffraction structural study

6.1.1 Introduction

Methanol is the simplest alcohol that can be studied by diffraction methods in order to characterise the hydrogen bonding in alcohols. It is not surprising, therefore, that this system has been extensively studied by both X-rays (Zachariasen, 1935; Harvey, 1938; Wertz and Kruh, 1967; Magini et al., 1982; Narten and Habenschuss, 1984) and neutron diffraction (ND) (Tanaka et al., 1985; Montague et al. 1981, 1984; Montague and Dore, 1986) for several decades. Since X-rays are scattered by electrons, they are relatively insensitive to light elements such as hydrogen. Some authors treated the X-ray data of methanol by considering it to consist of only two scattering centres (methyl and hydroxyl groups) (Zachariasen, 1935; Narten and Habenschuss, 1984). This two scattering centre approach has been used in earlier studies to show that the hydroxyl groups are linked by inter-molecular hydrogen bonds. Each hydroxyl group was found (Zachariasen, 1935) to be linked to two hydroxyl groups of the neighbouring molecules at a distance of ~2.5 Å. In a later investigation, Narten and Habenschuss (1984) report the OH···OH inter-molecular distance to be 2.8 Å, and very recently Weitkamp *et al.* (2000) report the O···O distance as 2.72 Å. In contrast to X-ray diffraction, ND measurements can reveal structural details of further

[1] Results recently published in *J. Chem. Phys.* (2000). **112**, 4231. *Molec. Simul.* (2000) **25**, (due to appear in august), and *J.Phys.: Condens. Matter* (1999). **11**, 9151.

significance because hydrogen nuclei can also be detected with neutrons.

The earlier ND studies by Montague *et al.* (1981) and Tanaka *et al.* (1985) were mainly focussed on investigating the intra-molecular structure of liquid methanol purely from an intra-molecular form factor fitting to the diffraction data. From these studies it was found that the O-Ho (Ho = hydroxyl hydrogen) bond length becomes significantly longer (0.99Å for Tanaka *et al.* (1985) and 1.03 Å for Montague *et al.* (1981)) as compared to that in its solid (0.97 Å, α-phase and 0.92 Å, β-phase (Robyr et al. (1994)) or gas phase (0.9451 Å (Lees and Baker, 1968)). Since the inter-molecular radial distribution function (rdf) comprises of many pair contributions, this function provided very limited information on the inter-molecular structure such as hydrogen bonding. One way to separate some of these contributions from a neutron diffraction experiment, is to use the isotopic substitution technique (see section 4.7). Montague *et al.* (1984) in a later investigation used the H/D substitution on the hydroxyl hydrogen to extract additional structural information. They found the Ho-Ho peak to be at 2.4 Å. However, they were unable to obtain a well-resolved Ho-Ho partial pair distribution function (pdf), possibly due to the limitations of the diffractometer used at that time and/or the difficulty encountered in correcting the data for the inelasticity effects. Very recently, two further structural investigations (Weitkamp et al., 2000; Yamaguchi et al., 1999) on liquid methanol have been made. Weitkamp *et al.* (2000) used the H/D substitution technique on both methyl and the hydroxyl hydrogens to obtain the inter-molecular partial distribution function, Y-Ho (Y= C and O). Surprisingly, their data show no sign of a sharp feature, which could be identified with the O···Ho hydrogen bond. Yamaguchi *et al.* (1999) used the H/D substitution on the hydroxyl hydrogen to extract X-X (X=C, O and H a methyl hydrogen), X-Ho and Ho-Ho partials at the distinct (intra- + inter-molecular) level. The neutron data were then used by them to constrain empirical potential structure refinement (EPSR) (Soper, 1996) computer simulation of the liquid. In the following sections (6.1.2-4), the results of H/D substitution neutron experiments on liquid methanol, where the data have been used to extract the X-X, X-Ho and Ho-Ho partials at both the intra-+inter- and inter-molecular levels are reported. These results provide new insights into the inter-molecular structure, especially the hydrogen bonding in methanol.

6.1.2 Experimental and data reduction

At the time of the experiment, 18 groups of detectors installed on SANDALS instrument covered scattering angles (2θ) from 3.8 to 36.5°, thus making it possible to measure the DCS over a wide range of momentum transfers, $\hbar Q$ (typically $Q \sim 0.1$-50 $Å^{-1}$). The container used was a parallelepiped (Benmore and Soper, 1998) made out of Ti/Zr alloy having an overall nominal coherent scattering length of zero. The samples (purchased from Cambridge Isotope Laboratories, Inc) used in the experiment were CD_3OD (99.8% deuterated), CD_3OH (99.5% deuterated) and $CD_3O(H/D)$ (a 1:1 mixture of CD_3OD and CD_3OH). Scattering intensities were measured for each sample at 298 ±1 K. The raw data were corrected for background, container scattering, absorption and multiple scattering and, normalised to scattering from a vanadium slab using the standard ATLAS suite of programs outlined in sections 5.5.1-5. After merging the total DCS obtained from the various groups of detectors for each sample, the observed values (in barns $molecule^{-1}$, see table 6.1) at the high-Q limit of these functions for CD_3OD, CD_3OH and $CD_3O(H/D)$ are respectively, 3.56, 8.58 and 6.18 as compared to the theoretical values of 3.26, 9.22 and 6.24 calculated from equation (4.36). Despite the fact that the inelasticity corrections are different for the three samples ($CD_3OD < CD_3O(H/D) < CD_3OH$) and, up to this stage such corrections have not been applied to any of the above data, the comparison is satisfactory, highlighting the correctness of data normalisation procedures employed. After applying the inelasticity corrections using the method described in section 5.5.6.d and following the approach presented in section 5.8.2.a, data from different detector groups were combined (see section 5.5.7) and normalised to the molecular unit to give a single normalised distinct DCS for each sample (see figure 6.1).

6.1.3 Results and discussion

a. Distinct radial distribution functions (rdfs)

The normalised distinct DCSs were Fourier transformed using the minimum noise reconstruction (MIN) technique described in section 5.6 to obtain the corresponding distinct rdfs. The low r cut-off (0.75 Å) was chosen to be lower than any known intra-molecular distance in methanol. The Q_{max} (35Å^{-1}) used for Fourier transformation was a compromise between minimising the statistical noise effects at high-Q and, accounting for all the structural features at low-r. The $G^{dist}(r)$ for the three samples are plotted in figure 6.2. The back Fourier transforms of the $G^{dist}(r)$, also shown in figure 6.1 are found to be in excellent agreement with the distinct differential cross-sections from which they are obtained. The $G^{dist}(r)$ can be split into three regions. The region beyond ~3 Å contains purely inter-molecular correlations and these oscillations extend up to ~14 Å (figure 6.2 inset), suggesting that methanol is a highly ordered liquid. In the region between 0.75 Å and 1.5 Å where only intra-molecular correlations contribute, the first peak at 1.06 Å arises from an overlap of O-Ho (Ho = hydroxyl hydrogen) and C-H (H = a methyl hydrogen) distances, although C-H correlations dominate this peak. The second peak at ~1.42 Å can clearly be assigned to the intra-molecular C-O distance in methanol. In the third region from 1.5 Å to 2.9 Å, since inter- and intra-molecular correlations overlap, no distances can be assigned from the distinct rdfs. In order to interpret the results further it becomes imperative to separate the intra-molecular contributions from the distinct differential cross-sections.

b. Separation of intra- and inter-molecular correlations

The average molecular geometry of methanol in its gaseous state (see figure 6.3) was elucidated earlier by microwave studies and electron diffraction measurements (Lees and Baker, 1968; Ivash and Dennison, 1953; Venkateswarlu and Gordy, 1955; Swallen, 1955; Kimura and Kubo, 1959). However, in liquid methanol, which is usually considered as a strongly H-bonded associated liquid, it is still not clear how the hydrogen bonding affects the intra-molecular structure. Most of the information

concerned with the effect of H-bonding on the change of intra-molecular structure in going from the gaseous to the liquid phase has been provided directly from experiments such as infrared (IR) and Raman spectroscopic measurements (Falk and Whalley, 1961; Serrallach et al., 1974; Furic et al., 1993). For instance, the IR measurements reveal that the most prominent spectral changes occur in the O-Ho stretching mode, ν_s in the region near 3500 cm^{-1} (3681 cm^{-1} for the gas phase as compared to 3328 cm^{-1} for the liquid (Shimanouchi, 1972)). This has been interpreted as a consequence of lengthening of the O-Ho covalent bond in the liquid phase. Also, the vibrational mode, ν_t, in which the hydrogen atom moves out of the C-O-Ho plane, originates from a hindered rotation of the O-Ho group in the gaseous molecule. This vibration has a mean frequency (Stuart and Sutherland, 1956) of about 225 cm^{-1} for the gaseous CH_3OH, which gets shifted and becomes a very broad band in the range 450-850 cm^{-1} in the liquid. This change has been attributed to the hindered rotation perturbed by the formation of the hydrogen bond (Stuart and Sutherland, 1956) in the liquid. But, because spectroscopists define hydrogen bonds with regard to their effect on the vibrational motions of the bonds involved, the information gained is of little use to a diffractionist who seeks specific bond lengths and bond angles to characterise intra-molecular structure in the liquid. Table 6.2 summarises the intra-molecular structure of methanol in its solid, liquid and gas phases obtained from different experimental techniques. While the intra-molecular structural parameters obtained from various studies are found to be in good agreement with each other in the gas phase, relatively large differences are seen in the liquid. This is particularly true for those parameters involving O and Ho, *i.e.*, those atoms involved in the hydrogen bonding. Since these parameters are obtained by fitting the model function described by equation (4.40) to the distinct DCS, the uniqueness of the molecular structure obtained by fitting several parameters cannot be ascertained. In order to check the uniqueness of the molecular model and, to see the effect it will have on the inter-molecular structure, we followed two approaches.

In the first approach, seven structural parameters *i.e.*, $r_{C\text{-}O}$, $r_{O\text{-}Ho}$, $r_{C\text{-}Hi}$, $\angle$ COHo, $\angle$ H_iCH_j, torsional angle, $\angle$ H_3COHo, the tilt angle τ, and, the Debye Waller factors γ_{ij} (equation 4.40) were varied to fit the DCS data of CD_3OD. Similar to the observation made earlier by Montague *et al.* (1981), it was noticed that the rotational

angle ($\angle$ H_3COHo) had no effect on the quality of the fit. It was thus kept fixed at a value of 180° corresponding to a staggered conformation. The structural parameters obtained from our best fit (fit1 in table 6.2) although fall within the range of the values reported in literature, large differences can still be seen in $\angle$ COHo, $r_{O\text{-}Ho}$ and the tilt angle between the various values. In the second approach, we kept the bond lengths and bond angles fixed to their gas phase values and fitted only the Debye-Waller factors, γ_{ij}. The parameters of this fit (fit2) are also listed in table 6.2. In both cases, the best fit was obtained by using the same quasi Newton algorithm as described previously (see section 5.7) where the agreement factor, R (equation 5.49) is minimised.

The difference in the agreement factor, R obtained from the two approaches does not permit us to say that one model is better than the other. Moreover, the intra-molecular structure factors calculated from both the models are found to be identical, within the experimental uncertainty of the distinct DCS, in the Q-range (6-35Å^{-1}) of the fit (see figure 6.4). Nevertheless, small differences between the two models can clearly be seen (figure 6.4 inset) at low Q (~2-5Å^{-1}). In this respect, it will be instructive to see how and to what extent these differences in molecular structure manifest themselves in the inter-molecular structure.

c. Inter-molecular structure

The inter-molecular differential cross-sections normalised to a molecular unit, $i_m(Q)$ for CD_3OD, CD_3OH and $CD_3O(H/D)$ defined by equation (4.41), were obtained after subtracting the intra-molecular part and, these are shown in figure 6.5 for the two models described in the previous section. The inter-molecular rdfs for the three samples obtained by Fourier transformation of the $i_m(Q)$ functions using the MIN technique are shown in figure 6.6. The back Fourier transforms of the inter-molecular rdfs shown (figure 6.5) superimposed on the functions from which they are obtained, agree well with each other, suggesting that no residual artefacts are present in the data. Moreover the low Q limits of the normalised inter-molecular DCSs of the three samples agree (see table 6.1) reasonably with the theoretically calculated value from adiabatic compressibility, χ_T (see equation 4.42).

It is worth noting that the two molecular models do not produce any perceivable difference in the total inter-molecular functions. The negative peak centred at ~1.73 Å (see figure 6.6) in the $G^{inter}(r)$ of CD_3OH is a real feature arising due to the negative scattering length of hydrogen. Since the total inter-molecular rdf consists of several different pair contributions, it cannot reveal structural details of much significance.

d. H/D substitution analysis

The general relations were summarised in section 4.7. Their extension to methanol, in which the substituted site is the hydroxyl hydrogen, Ho, is made simply by setting in the expressions (4.44-54) S = Ho, X=C, H, O and i = 1, 2, 3, respectively, for CD_3OD, CD_3OH, $CD_3O(H/D)$. The distinct or inter-molecular rdf of methanol consists of 10 partial pair distribution functions if all the methyl hydrogens, H_1, H_2 and H_3 are considered identical (see equation 4.43). The H/D substitution technique on hydroxyl hydrogen (Ho) allowed us to extract three partial distribution functions, $g_{HoHo}(r)$, $G_{XHo}(r)$ and $G_{XX}(r)$ at the second- or higher- order difference level. Two procedures were used to perform the H/D second-order differences on (*i*) distinct and (*ii*) inter-molecular DCS functions of the three samples.

I. *Ho-Ho pair distribution function*

The Ho-Ho partial structure factor was extracted from the DCS of the three samples by using equation (4.48). The $S_{HoHo}(Q)$ is shown in figure 6.7a. A slightly different extent of deuteration on the methyl hydrogens of the two samples (99.8% for CD_3OD, 99.5% for CD_3OH) gives rise to a small contribution from the H-Ho (see table 6.3), but this is negligible. Since the intra-molecular terms in the $S_{HoHo}(Q)$ will cancel (see equation 4.48), the two procedures by using the three distinct DCS or the three inter-molecular DCS yield identical results. The pdf, $g_{HoHo}(r)$ plotted in figure 6.7b was obtained by Fourier transformation of $S_{HoHo}(Q)$, and the back Fourier transform of the $g_{HoHo}(r)$, also plotted in figure 6.7a is in good agreement with the original data. The main peak position in $g_{HoHo}(r)$ at 2.36 Å is in close agreement with the value (2.4 Å)

found by other workers (Montague et al., 1984; Weitkamp et al., 2000; Yamaguchi et al., 1999). The running co-ordination number, n_{Ho}^{Ho} calculated from equation 4.35, also shown in figure 6.7b reveals that in spheres of radii 2.36 and 2.78 Å respectively, there are an average of about one (0.99 ± 0.06) and two (2.02 ± 0.06) other Ho atoms from a central Ho atom.

II. *X-Ho partial distribution function*

The X-Ho scattering function, $S_{XHo}^{\text{inter/dist}}(Q)$ consists of a weighted sum of O-Ho, C-Ho and H-Ho pair contributions. The residual contributions to $S_{XHo}^{\text{inter/ dist}}(Q)$ from other pairs such as C-H, H-H and H-O, arising due to small difference in the extent of deuteration of different samples, as described before for the $S_{HoHo}(Q)$, are negligible (see table 6.3). This scattering function was extracted at both, the intra- + inter-molecular, $S_{XHo}^{\text{dist}}(Q)$ (figure 6.8a), and inter-molecular, $S_{XHo}^{\text{inter}}(Q)$ (figure 6.8b) levels. For the inter-molecular case, two geometric models (see Section 6.1.3.b) were used for removal of the intra-molecular structure. The Fourier transforms, $G_{XHo}^{\text{dist}}(r)$ and $G_{XHo}^{\text{inter}}(r)$ are shown in figures 6.9a and 6.9b, respectively. The back Fourier transforms of these functions shown in figures 6.8a and 6.8b are in good agreement with the original scattering functions from which they are obtained. It is interesting to see that the partial distribution function, $G_{XHo}^{\text{dist}}(r)$ (figure. 6.9a) has clearly isolated the O-Ho intra-molecular peak which could not be resolved from any of the distinct $G(r)$ (see figure 6.2), since the first peak here consists of C-H and O-Ho overlapping distances. The O-Ho peak, in very close agreement with the value reported recently by Weitkamp *et al.* (2000), is found to be at 0.98(1) Å. This value is slightly different from the one we found (0.961(1) Å, see table 6.2) from the intra-molecular form factor fitting (see section 6.1.3.b).

It may be recalled that although the two molecular models did not produce any perceivable difference in either the distinct DCS (section 6.1.3.b) or the total inter-molecular radial distribution functions (section 6.1.3.c), clear differences can now be seen in the partial $G_{XHo}^{\text{inter}}(r)$ (see figure 6.9b) below ~3 Å. It is in this region that

residual features arising from inappropriate intra-molecular model are expected and, the real structure could possibly be anywhere in-between the two $G_{XHo}^{inter}(r)$ shown in figure 6.9b. The first sharp feature present in both the partials occurs at ~1.78 Å (fit 1) and ~1.73 Å (fit 2) with an average distance of 1.75 ± 0.03 Å. We assign it to the O···Ho hydrogen bond for the first time from experimental measurements alone. Several simulations (Jorgensen et al., 1996; Gao et al., 1995; Marchi and Klein, 1989; Palinkas et al., 1987; Jorgensen, 1986; Haughney et al. 1987; Bianchi et al., 1999, 2000) have also reported the existence of the hydrogen bond in liquid methanol at nearly the same distance (1.75-1.95 Å). From this point of view it is rather puzzling to note that in one of the latest experimental work on liquid methanol, Weitkamp *et al.* (2000) failed to detect this peak. It can also be noticed from figure 6.9b that the intra-molecular structure appreciably alters the height of the first O···Ho peak which is not fully isolated because of small contributions from two other pdfs (H-Ho and C-Ho) to the $G_{XHo}^{inter}(r)$ below ~ 2 Å. However, since the two (H-Ho and C-Ho) pairs contribute equally to the two (fit1 and fit2) $G_{XHo}^{inter}(r)$, the differences in their heights and running co-ordination numbers (figure 6.9b inset) show clearly that small difference in the molecular model used alters the inter-molecular structure significantly. For instance, figure 6.9b (inset) reveals that at 2 Å the O···Ho co-ordination number is 0.82(3) for fit 1 and only 0.51(3) for fit 2. The two $G_{XHo}^{inter}(r)$ functions however, show a perfect match in the inter-molecular range above ~ 3 Å where no residual intra-molecular contributions are expected.

At this point it is instructive to compare our structural results with those of Yamaguchi *et al* (1999) who recently performed exactly the same experiments on the same instrumental set up (SANDALS). Although the experimental total X-Ho, X-X and Ho-Ho partial structure functions obtained by using direct difference methods of neutron diffraction in both the studies are in excellent agreement, different approaches are used in interpretation of the structural results. Yamaguchi *et al* used an Empirical Potential Structure Refinement (EPSR) where intra- and inter-molecular potentials used in computer simulations were modified to obtain best agreement between the experimental and calculated structure functions. Although the EPSR resulted in a detailed model for the inter-molecular partials allowing analyses of the size

distribution of hydrogen bonded clusters, application of EPSR with flexible molecular model to the total structure functions may lead to strange molecular parameters during subsequent refinements of molecular configurations. It needs to be stressed that firstly, because Yamaguchi *et al* did not report the intra-molecular parameters obtained or used during EPSR, it is not possible to compare the two sets of results. Secondly, as shown above for the $G_{XHo}^{inter}(r)$, small changes in the molecular model used strongly influence the nearest-neighbour hydrogen-bond structure (see figure 6.9b).

III. *X-X partial distribution function*

The non-substituted atom - non-substituted atom (X-X) scattering function was also extracted at both the intra- + inter-, $S_{XX}^{dist}(Q)$ (figure 6.10a inset), and inter-, $S_{XX}^{inter}(Q)$ (figure 6.10a) molecular levels. Their Fourier transforms, $G_{XX}^{dist}(r)$ and $G_{XX}^{inter}(r)$ are shown in figures 6.10b (inset) and 6.10b, respectively. The back Fourier transforms of the $G_{XX}^{dist/inter}(r)$ functions shown superimposed on the $S_{XX}^{dist/inter}(Q)$ (figure 6.10a) are in good agreement with each other. Again, it is interesting to see that the partial distribution function, $G_{XX}^{dist}(r)$ (figure 6.10b inset) has clearly isolated the C-H intra-molecular peak which could not be resolved from the first peak (see figure 6.2) of any of the distinct $G(r)$ consisting of C-H and O-Ho overlapping distances. The C-H peak centred at 1.08 ± 0.01 Å is in very close agreement with the value obtained from the intra-molecular fitting (see section 6.1.3.b and table 6.2). The two $G_{XX}^{inter}(r)$ (see figure 6.10b) functions obtained by using two different molecular models are in very good agreement, suggesting that this function consisting of six pair contributions (see table 6.3) is hardly affected by a small difference in the molecular structure. This could possibly be due to the cancellation effects from various contributing pairs to the $G_{XX}^{inter}(r)$. It is not surprising then to see that this function shows broad oscillations centred at ~ 4, 8 and 12 Å, similar to the ones seen in the total $G(r)$ (figure 6.2 inset). Table 6.3 also shows that out of the six contributions, three of them: H-H, C-C and C-H taken together account for ~67% of the total. The $G_{XX}^{inter}(r)$ is thus dominated by

the methyl-methyl contributions and, the broad oscillations observed in figure 6.10b can be assigned to the packing of the methyl groups.

6.1.4 Summary of the ND study

Neutron diffraction (ND) data on three methanol (CD_3OD, $CD_3O(H/D)$ and CD_3OH) samples have been used to determine intra- + inter- (distinct) and inter-molecular DCS functions. These functions were then used to extract the X-Ho (X=C, O, and H) and X-X partial distribution functions by employing the difference techniques of ND. The O-Ho and C-H overlapping distances in the distinct $G(r)$ have been isolated in the X-Ho and X-X partials. These distances are 0.98 ± 0.01 Å and 1.08 ± 0.01 Å, respectively, in comparison to 0.961 ± 0.001 Å and 1.096 ± 0.001 Å, obtained from an intra-molecular fitting (fit 1) to the DCS data. The extent to which inter-molecular structure is affected by a difference in the model chosen for molecular structure has been investigated. Although the total inter-molecular and partial X-X distribution functions are found to be identical with the two molecular models chosen, quantitative differences in the peak height and shape can be seen in the X-Ho partial distribution function, especially at low r. The average position of the O···Ho (1.75 ± 0.03 Å) hydrogen bond observed in the X-Ho partial lies in the range (1.75-1.95 Å) of values predicted by various computer simulations. The Ho-Ho partial pair distribution function (pdf), independent of the molecular model chosen, shows a pronounced peak at a mean Ho···Ho separation of 2.36 Å. The results also reveal that in spheres of radii 2.36 and 2.78 Å respectively, there are an average of about one (0.99 ± 0.06) and two (2.02 ± 0.06) other Ho atoms from a central Ho atom.

6.2 The molecular dynamics study

6.2.1 Introduction

Since the pioneering computer simulations on liquid methanol performed by Jorgensen (1979), many potential models have been parameterised to reproduce various structural and dynamical properties of liquid methanol (Jorgensen, 1980,

1981, 1986; Palinkas et al., 1987; Hawlicka et al., 1989; Haughney et al., 1986; Caldwell and Kollman, 1995; Gao et al., 1995; Jorgensen et al. 1996, Wang et al., 1996; Buck et al., 1998). Two classes of models can be distinguished: the three-site models (Jorgensen, 1981, 1986; Palinkas et al., 1987; Haughney et al., 1986; Buck et al., 1998) in which usually the carbon atom along with the three methyl hydrogens is treated as a unified interaction site and, the six-site models where all the atoms are explicitly considered (Hawlicka et al., 1989; Caldwell and Kollman, 1995; Jorgensen et al. 1996; Wang et al., 1996). By using these different potential models conflicting conclusions (Jorgensen, 1986; Buck et al., 1998; Svishchev and Kusalik, 1994; Wright and El-Shall, 1996) have been made about the favoured structure of liquid methanol, which is governed mainly by its hydrogen-bonding interactions. Moreover, it has been reported (Haughney et al., 1987) (see also section 5.5.6e and figure 5.9) that changes made to the potential induce only small changes in those features that are correlated with the hydrogen bond formation. Since such features are hardly detected by X-rays and, contribute too little to be observed in the total neutron radial distribution functions (rdfs), a critical evaluation of different models cannot be done. Thus, reproducing the total inter-molecular rdf consisting of 21[†] partial pair distribution functions (pdfs) in methanol is not a proof that a fine tuning of the model potential has been achieved, as was also inferred by Hawlicka *et al.* (1989). A critical test of potential models should be done at the partial distribution function level. A comparison of the simulated structural results with those derived experimentally at the pdf level can help in discriminating against spurious models. In the present section, we present results of MD simulations carried out on 216 methanol molecules by using the DL_POLY_2.0 MD simulation package (see chapter 3). Three different potential models were used in these simulations. Two of them were introduced by Haughney *et al.* (1987), and these are the 3-site potential models, while the third is a 6-site potential (hereafter referred to as APR6 model) tested for the first time in this work. The results are discussed by comparing the simulated results with the neutron diffraction results.

[†] Considering the three methyl hydrogen separately

6.2.2 Computational details

a. Molecular geometry

Each methanol molecule was treated as a rigid, non-polarisable object. Seven different MD runs were performed. The first six runs were performed using two potential models (denoted as J2 and H1) parameterised by Haughney *et al.* (1987). For runs 1-5, the methanol molecule and the Lennard-Jones (LJ) potential consisted of 3 sites, corresponding to the oxygen (O), the methyl group (C) treated as a united atom and the hydrogen of the hydroxyl group (Ho). For the sixth run (H1+CH_3), hydrogens (H) of the methyl group were explicitly taken into account in the geometry of the molecule (see figure 6.3) and were treated as dead load without any potential interaction. For runs 1-6, the bond lengths and bond angles, d_{OHo}, d_{CO}, d_{CH}, and $\angle$COHo and $\angle$HCH (listed in table 6.4) were taken from the millimeter wave studies of Lees and Baker (1968). For the seventh run the structural parameters were taken from Anwander *et al.* (1992) (ref. 42 therein). The calculated moments of inertia along the principal axes, I_A, I_B, I_C, of the methanol molecule, along with their experimental values (Lees and Baker, 1968; Ivash and Dennison, 1953) are also listed in table 6.4. One can see that the 3-site geometrical model underestimates the moments of inertia (m.o.i.) because it considers the methyl group as a united carbon atom. However, the m.o.i. from the two 6-site geometrical models are in good agreement with each other and also with those obtained by *ab-initio* quantum chemical calculations (QCC) at the second order Møller-Plesset level (MP2) with TZV(2p,2d)++ basis set. The QCC were performed by using GAMESS programme package (Schmidt et al., 1993). All the values are also reported in table 6.4. These 6-site geometric models are found not to produce any perceivable difference for the calculated m.o.i. Any differences in the structure of liquid methanol produced by using these two different geometrical models can thus be assigned to the different forces fields employed in the simulations (H1+CH_3 and APR6), and do not result from the use of different geometric models.

b. Inter-molecular potentials

H1 and J2 (Haughney et al., 1986, 1987) are the potential models semi-empirically parameterised to reproduce basic macroscopic properties of liquid methanol. Three interacting sites corresponding to oxygen (O), the methyl group (C) treated as united atom, and hydrogen of the hydroxyl group (Ho) are considered in these models. For each pair the inter-molecular potential is the sum of Lennard-Jones (LJ) and Coulomb parts,

$$V_{ij}(r_{ij}) = \frac{q_i q_j}{4\pi\varepsilon_0 r_{ij}} + 4\varepsilon_{ij}\left[\left(\sigma_{ij}/r_{ij}\right)^{12} - \left(\sigma_{ij}/r_{ij}\right)^{6}\right], \tag{6.1}$$

where ε_{ij} and σ_{ij} are the Lennard-Jones (LJ) parameters between sites i and j of distinct molecules, q_i is the partial charge on site i and, r_{ij} is the site-site separation. Table 6.5 summarises the force field parameters used in the MD simulations for these two potential models. Cross interactions were obtained from the Lorentz-Berthelot (Allen and Tildesley, 1987) rules:

$$\varepsilon_{ij} = \sqrt{\varepsilon_{ii}\varepsilon_{jj}} \text{ and } \sigma_{ij} = (\sigma_{ii} + \sigma_{jj})/2. \tag{6.2}$$

Runs 1 and 2 were performed with J2 whereas runs 3-6 were performed with H1. For all the runs, the used partial Coulombic charges coincided with the interacting sites. In the sixth run three hydrogens of the methyl group were explicitly taken into account as dead load and this extended model is denoted as H1+CH_3. The 6-site potential model, APR6 used in the simulations (run 7) was parameterised from an *ab-initio* study of the interaction energy hypersurface for the methanol dimer by Anwander *et al.* (1992). The pair potential was derived from the fit of 332 calculated CEP-31G**/HF dimer energies using a polynomial expression,

$$V_{ij}(r_{ij}) = A_{ij}/r_{ij}^{l} + B_{ij}/r_{ij}^{m} + C_{ij}/r_{ij}^{n} + q_i q_j/4\pi\varepsilon_0 r_{ij} \quad \text{with } l > m > n. \tag{6.3}$$

O, C, Ho, and methyl hydrogens (H) are the interaction sites, A_{ij}, B_{ij} and C_{ij} are the

fitted parameters between sites i and j of distinct molecules, the l, m, n are the exponents, q_i is the partial charge on site i and, r_{ij} is the site-site separation. All these parameters are given by Anwander *et al.* (1992).

It is interesting to note (see table 6.4) that the H1+CH_3 model gives values for the angle between the dipole moment vector and the OHo bond direction, $\angle\vec{\mu},\vec{OHo}$ of the methanol molecule that are closer to the experimental values than those given by APR6 or MP2/TZV(2p,2d)++ QCC. However, since experimental data of dipole moments for liquids have large uncertainties, which depend on the theory used in the data treatment (McClellan, 1989; Le Fevre, 1953), only qualitative comparison can be made. Table 6.4 shows that APR6 and MP2/TZV(2p,2d)++ QCC give a better representation of electrostatic interactions since both produce a dipole moment (2.08 D and 1.88 D, respectively) in better agreement with the experimental gas phase value of 1.69 D than the H1+CH_3 model (2.33 D). In addition, the electrostatic interactions in the J2 and H1 models being similar, they give similar values for the dipole moments of 2.2 D and 2.3 D, respectively. These values are larger than the gas phase experimental value of 1.69 D (see table 6.4). This enhancement in the dipole moment was intentionally made (Haughney, 1987) to take approximate account of the induction forces in methanol. In the APR6 model however, the dipole-dipole and charge-induced-dipole interactions are taken into account by a large number of terms with exponents, n=3.

c. Treatment of the long-range interactions and algorithms

Shifted force (SF) potential was employed for run 1 to avoid truncation errors (see section 3.7.1). A reaction field (RF) model was applied to runs 2-4 (see section 3.7.2), and, Ewald summation (EW) was used for runs 5 and 6 (see section 3.7.3). The parameters for EW were chosen as a compromise between keeping absolute values of Coulombic energy and Coulombic virial the same and, the time required for an MD run.

The MD simulations were performed at 298.15 K in the NVE ensemble with 216 methanol molecules placed in a cubic box of edge length 24.45 Å in order to match

with the experimental density, 0.78637 g/cm^3 (Riddick et al., 1986). A cut-off radius equal to half the box length was applied to all the interactions (see section 3.4) and, periodic boundary conditions were applied (see section 3.3). In all the MD runs, the time step used was 0.002 ps. During the various MD simulation runs two different algorithms were used. For runs 1, 2, 3 and 5, the equations of motion were integrated by using Verlet leap-frog (Vlf) algorithm (see section 3.5) coupled with SHAKE algorithm (see section 3.6.1) for preserving the geometry of the methanol molecule. For runs 4, 6 and 7, the molecule was considered as a rigid body. Therefore, in addition to the Verlet leap-frog algorithm used for translational motion, the Fincham's implicit quaternion algorithm (FIQA) was used for rotational motion of rigid bodies (see section 3.6.2). Table 6.6 summarises the details of the seven MD simulation runs.

6.2.3 Validation of the simulated results

For runs 1-6, the computed configurational energy, U (see section 3.8.1b) shows good agreement (see table 6.6) with its experimental counterpart (Riddick et al., 1986) evaluated from the enthalpy of vaporisation, $\Delta_{vap}H^{\exp}$ by

$$U_{\exp} = \Delta_{vap}H^{\exp} - PV = \Delta_{vap}H^{\exp} - RT\,. \tag{6.4}$$

This relation is based on the assumption that intra-molecular energy is the same in both the liquid and the gas phase, and that the gas obeys the ideal gas law. For run 7, the presence of inverse cubic terms in the APR6 model does not allow to calculate the potential truncations to the configurational energy and pressure by using standard treatments (see section 3.8.1b and c). As a result, exact comparison of thermodynamic properties obtained from the simulation by using the APR6 model with the corresponding experimental values cannot be made (table 6.6) because equation 3.42 and 3.49 do not converge.

The translational diffusion coefficient of the centre-of-mass of the hydrogenated methanol molecules was calculated from the mean square displacement (MSD) via the

Einstein relation, and also according to the Green-Kubo relation (see section 3.8.2) by integrating the velocity autocorrelation function (VACF), $C_{vv}(t)$. The normalised VACF, $\hat{C}_{vv}(t)$ defined as,

$$\hat{C}_{vv}(t) = \langle \mathbf{v}(t)\mathbf{v}(0) \rangle / \langle \mathbf{v}(0)\mathbf{v}(0) \rangle = C_{vv}(t) / \langle \mathbf{v}(0)^2 \rangle \tag{6.5}$$

and the MSD curves are shown in figures 6.11-13. The calculated diffusion coefficients are listed in table 6.6 together with experimental data. One can see that runs 1-5 fail to reproduce the experimental diffusion coefficient. This effect is clearly seen in the smaller slopes in the MSD curves of runs 1-5 as compared to that of run 6 (see figure 6.13). This can be attributed to the fact that the calculated moments of inertia in runs 1-5 are not in agreement with their experimental values (Lees and Baker, 1968; Ivash and Dennison, 1953). In addition, the main difference in the VACFs (see figure 6.11) lies in a feature at 0.24 ps, which is a clearly defined peak in runs 1-5, but becomes a shoulder in run 6. All the runs however, in agreement with previous dynamical studies (Haughney, 1987; Palinkas et al., 1991; Alonso et al., 1992), show the typical cage effect (observed after 0.2 ps) coming from a close packing of the molecules. In general, the diffusion coefficients estimated from the MSDs have uncertainties of different origins (Allen and Tildesley, 1987) than those determined from the VACFs. In this respect, agreement between the calculated diffusion coefficients for run 6 using both methods of calculation and experiment (Hurle and Woolf, 1980) is satisfactory (see table 6.6). When the two six sites models, H1+CH_3 and APR6 are compared, it can be seen that while the MSDs are similar (see figure 6.12 inset), the two VACFs are clearly different (see figure 6.12). The appearance of a negative correlation region with its minimum at about 0.4 ps for MD simulations performed with both the models can be interpreted as being due to the "rebound" of the tagged molecule against the cage formed by its nearest neighbours. The first minimum at ~0.2 ps is much emphasised in the APR6 relative to that in the H1+CH_3 model. To what extent this feature may be associated with relaxation processes occurring with different life times can not be ascertained from present studies, since the analysis is only based on translational motion of the center of mass.

6.2.4 Results and discussion

a. The simulated partial pair distribution functions

The pdfs, $g_{\alpha\beta}(r)$ were computed for all the runs from the equilibrated configurations. It may be recalled that only run 6 for which the 3 methyl hydrogens are treated as dead load, and run 7 where all the atoms are considered, yield 21 pdfs while all other runs yield only 6 pdfs. Thus for comparing the simulation results with those obtained experimentally, most of the discussion in the next section will be focused on the pdfs obtained from runs 6 and 7. However, it will be instructive to compare results from other runs, where possible.

The results of the simulations corresponding to run 6 are compared with earlier X-ray diffraction (Zachariasen, 1935; Wertz and Kruh, 1967; Magini et al., 1982; Narten and Habenschuss, 1984) and MD simulation (Svishchev and Kusalik, 1994; Jorgensen, 1980, 1981, 1986; Palinkas et al., 1987; Gao et al., 1995; Jorgensen et al. 1996; Shilov et al., 1999; Marchi and Klein, 1989), studies in tables 6.7 and 6.8. Although the results differ at a quantitative level, the agreement seems to be satisfactory. For instance, while the run 6 simulation shows the main peak position of O-C pdf at 3.6 Å (see figure 6.14), the X-ray studies (Wertz and Kruh, 1967) report it at 3.8 Å (see table 6.7). The height, co-ordination number and position of the simulated O-C pdf are in reasonable agreement with other computer simulations (table 6.7). The simulated O-O pdf (see figure 6.15) shows a main peak at 2.79 Å with a co-ordination number of 1.87, which again agrees with the X-ray work of Narten *et al.* (1984) (see table 6.8). The simulated C-C pair exhibits a broad peak at 4.18 Å (see figure 6.14). It has been suggested (Wertz and Kruh, 1967) that two distinct C-C contributions occur at ~3.8 Å and ~ 4.4 Å, which may lead to such broadening. The simulated results for the C-C pair (see table 6.7) are again consistent with experimental and other computer simulation studies. It is not surprising that the earlier simulations reproduced the X-ray structure rather well since firstly, no other structural measurements capable of discriminating between different models were available at that time and secondly, the models were parameterised to obtain a better

agreement with the liquid structure obtained from X-ray studies.

The partial pair distributions functions (pdfs) (except Ho-Ho, which will be discussed in detail in section 6.2.4.bII) obtained from the APR6 simulation are plotted together with those obtained using the H1+CH_3 model in figures 6.14-16. It is worth noting that while the APR6 potential was parameterised using gas phase energy hypersurface obtained from *ab-initio* QCC of methanol dimers, the H1+CH_3 model was devised especially for the liquid state (Haughney et al., 1987). Figures 6.14-16 show that there is reasonable agreement between the APR6 and H1+CH_3 generated pdfs. This suggests that the APR6 model potential obtained from first principles may be transferable to the liquid phase of methanol, as was also suggested earlier from the good agreement between the two diffusion coefficient values. Co-ordination numbers as well as positions of extrema of the pdfs are compared with the experimental results in table 6.9. It can be seen from figure 6.15 and table 6.9 that the main peaks of the O-Ho and O-O simulated partials obtained with the APR6 model are smaller and are shifted towards higher distances compared to those obtained with the H1+CH_3 model. This may suggest that there are fewer H-bonded molecules for the liquid simulated with the APR6 model. The most pronounced differences, as expected, are seen (figure 6.16) in the case of H-H, C-H, Ho-H and O-H pdfs. Indeed, since in APR6 the methyl hydrogens are treated as interaction sites, the simulated partials obtained from this model show more structure than those from the H1+CH_3 model in which the methyl hydrogens were used merely as a dead load. As a result, the H1+CH_3 model has a tendency to average out (see *e.g.*, H-H and C-H pdfs in figure 6.16) the structural features exhibited by the APR6. Thus, the two peaks in the C-H pdf at 3.65 Å and 4.8 Å in the APR6 model have become a broad single peak in the H1+CH_3 model.

b. Comparison with the neutron diffraction results

Only two MD studies (Haughney, 1987; Hawlicka et al., 1989) compared the simulated structures with the ND measurements (Montague et al., 1981, 1984) only at the total rdf level. It needs to be stressed that such a comparison at the total rdf level cannot provide useful information. In the following, by comparing the simulated

structure with the ND results, both, at the total and the partial distribution function level it is shown that no critical validation of any potential model can be done at the total rdf level.

I. *Total radial distribution functions (rdfs)*

The 9 partial pdfs (figures 6.14-16) plus the Ho-Ho pdfs (discussed later) obtained by the APR6 and H1+CH_3 MD-simulations were combined in the ratio of their relative neutron weights, $W_{\alpha\beta}$ (listed in table 6.3) to reconstruct the total inter-molecular rdf for deuterated methanol. Figure 6.17 shows that the total rdfs from both the APR6 and H1+CH_3 models reproduce satisfactorily the experimental rdf. Although the rdfs from both the simulations are somewhat shifted towards higher distances at low r, it is worth noticing that even the shoulder observed experimentally at 2.8 Å is well reproduced by the simulations. At higher distances, although the periodicity of the oscillations is in agreement with the ND results, ND data smears out more rapidly. It can be seen that although the two model potentials are fundamentally different, both reproduce equally well the experimental structure of liquid methanol at the total rdf level. This underlines the fact that no critical validation of any potential model can be done at the total rdf level. The simulated pdfs, $g_{\alpha\beta}(r)$ from run 6 were combined in the ratio of their neutron weights, in order to reconstruct the total inter-molecular rdfs for the two remaining samples (CD_3O(H/D) and CD_3OH). The two MD distribution functions plotted in figure 6.17 (inset) show a good agreement with their neutron counterparts. It can be seen that even the negative peak for CD_3OH at ~1.7 Å seen in the ND results is predicted by the MD simulation. The oscillations occurring at larger distances are also mimicked in phase with the ND results, although these are somewhat damped as for CD_3OD. However, since the total rdfs consist of several different contributions, a comparison at the total rdf level can reveal nothing further.

II. *Partial distribution functions*

Ho-Ho partial

The simulated Ho-Ho pdfs obtained from the first 6 runs are compared with the

neutron results in figure 6.18. All the six MD runs show impressive agreement with each other although it is worth noting that runs 1-5 failed to reproduce the experimental translational diffusion coefficient. No structural differences can be seen between the results obtained by using J2 and H1 models. Moreover, various algorithms and techniques applied within the same force field (runs 1-2 for J2 or 3-6 for H1, in table 6.6) do not produce any change in the Ho-Ho pdf. Since methanol is considered to be a strongly associated liquid due to its polarity, we expected that the Ho-Ho pdf obtained by using different techniques to handle long-range interactions would at least differ. However, we do not see any significant difference in the size, shape or peak position in the Ho-Ho pdfs. Moreover, it is interesting to point out that not only the Ho-Ho pdfs, but also the O-Ho and O-O pdfs (not shown) of runs 1-6 are all identical although in the first 5 runs the molecule consists of three sites, and for these runs the computed moments of inertia do not agree with the experimental values.

Although the MD and ND results are in fair agreement (Figure 6.18a) with each other, discrepancies still exist at a quantitative level. For instance, (*i*) the main peak maxima are shifted ~ 0.13 Å towards high *r*, (*ii*) the peaks are bigger and more symmetric, (*iii*) the height at the first minimum is lower and, (*iv*) there are fewer correlations at shorter distances in the MD simulations as compared to the neutron results. This comparison reveals that the MD simulations do not allow closer approach of the two hydroxyl hydrogens and, suggests less mobility between the first and next-nearest neighbours. The running co-ordination numbers, $n_{Ho}^{Ho}(r)$ for the ND and MD Ho-Ho pdfs, displayed in figure 6.18b, confirm these findings. Table 6.10 compares the peak position and co-ordination number obtained from the current simulations of run 6 with other simulations and experimental studies. It can be seen that the co-ordination number obtained from our MD simulation compares well with those obtained from others. Nevertheless, all the simulations underestimate this value in comparison to the ND result. Also, there are discrepancies between the peak positions of the Ho-Ho pdf obtained not only from various simulations but also with the experiment.

When the Ho-Ho pdf obtained from run 7 (APR6) is compared with the one experimentally obtained and the simulated H1+CH_3 partials, it shows an overall

agreement (see figure 6.19). However, it can be seen that relative to the experimental and the H1+CH_3 functions the APR6 is even more shifted towards higher distances. For instance, while the main peak maximum of the H1+CH_3 MD simulations is shifted by ~ 0.13 Å (see table 6.10), for APR6 it is shifted by ~ 0.22 Å as compared to the ND results (see table 6.9). In addition, as for the other runs, the minimum distance of closest approach and the rdf at low-r values from the APR6 simulations are found to be significantly different from the experimental results. It may be that the model potentials used in all the simulations underestimate the closest approach of the two Ho atoms. Nevertheless, the height of the first minimum (see figure 6.19), linked with the mobility between the first and next-nearest neighbours, in the simulated APR6 pdf is quite close to the experimental one.

X-Ho partial

The $G_{XHo}^{\text{inter}}(r)$ distribution function obtained from the simulated partials for runs 6 and 7, added in the ratio of their neutron weights, are presented in figure 6.20 along with the two neutron equivalent functions (corresponding to the intra-molecular removal of fit 1 and 2). The relative weights of the C-Ho, O-Ho and H-Ho partials are about 0.20, 0.18 and 0.61, respectively and reference to figures 6.14-16 reveals that the main correlation contributing to the first peak in the $G_{XHo}^{\text{inter}}(r)$ is the O-Ho. Although the two models agree with each other within experimental errors, they fail to reproduce the ND peak at a quantitative level. Since the inter-molecular structure in this partial is affected by a difference in the molecular model chosen for methanol, it is instructive to see whether the observed differences between the simulated and ND partials arise from an inappropriate molecular model. However, since these differences can also be seen in figure 6.21 where the intra- + inter-molecular distribution functions from the two models are compared with the ND data, it is reasonable to conclude that the potential models chosen in the simulations are still inappropriate to give a quantitative account of the observed structure. At r-values greater than ~2.8Å, figures 6.20 and 6.21 show that there are obvious discrepancies between the two simulations and the experiment. While the H1+CH_3 model seems to be better in reproducing (see inset in figure 6.20) (*i*) the peak at ~ 5 Å, (*ii*) the shape of the experimental curve between ~3-5 Å (although the peak along with its right shoulder at ~3-5 Å is significantly

overemphasised) and also, (*iii*) the dropping tail at the low *r*-end, the APR6 model fails badly in reproducing the experimental function. Nevertheless, even H1+CH_3 model does not give a quantitative description of the experimental features. Again, reference to figures 6.14-16 and the relative weights of the three contributions (see table 6.3) reveal that the differences in the two models arise mainly from the Ho-H and, to a lesser extent, from the C-Ho partials.

X-X partial

The experimental X-X partial, $G_{XX}^{\text{inter}}(r)$ is a weighted sum of the 6 non-substituted atom - non-substituted atom contributions. Out of the six contributions contained within this function, three of them: H-H (38%), C-H (25%), and H-O (22%), taken together represent 85% of the total. This rdf is thus dominated by contributions from the methyl groups. The MD equivalents of this function were constructed from the simulated pdfs as before, and the results from both the ND and MD are displayed in figure 6.22. The overall agreement between the two simulations and the experiment is satisfactory. The closest distance of approach in the H1+CH_3 model is seen to be lower than both the experimental distance and the value from the APR6 model because of the absence of any hard core potential on the methyl hydrogens. It would appear that the methyl hydrogens, which are specific interaction sites in the APR6 model, cannot come closer together as they can in the case of H1+CH_3 model potential. Although the oscillations smear out more quickly in the ND than in the simulations, the two models reproduce the experimental results equally well at higher distances. This is contrary to the fact that clear differences can be seen in figure 6.16 between the two models in the contributing H-H, C-H and O-H pdfs. A plausible explanation is that cancellation effects play a role when $G_{XX}^{\text{inter}}(r)$ is computed from a neutron-weighted sum of the three contributing terms. It is worth noting that, the simulated and experimental X-X partials have the same period of oscillation as that observed already in the inter-molecular rdfs shown in figure 6.17. This proves firstly, that the inter-molecular rdfs is dominated predominantly by the methyl group contributions. Secondly, since no potential is imposed on the methyl hydrogens in the H1+CH_3 model, the agreement between the simulated and experimental X-X partials demonstrates, as suggested before (Zachariasen, 1935; Steytler et al., 1985), that the

methyl groups do not participate in any inter-molecular bonding. Thus, for run 7, addition of 3 methyl hydrogens as specific interaction sites has not improved the results any further. In this respect, our results do not support the suggestion made by Anwander *et al* (1992) that methyl group participates in hydrogen bonds of the form Me-HO::HCH_2-OH and bifurcated H-bonds of the form Me-HO::H_2CH-OH.

6.2.5. Summary of the MD study

Three different potential models were used to perform seven different molecular dynamics simulation runs that differed in the techniques employed for integrating the equations of motion and for treatment of the long-range interactions. The first five of them considered the methyl group to be a united carbon atom. The sixth and the seventh runs, treated the methyl hydrogens explicitly as dead load and as specific interacting sites, respectively. The last two reproduced the experimentally observed diffusion coefficient. The 6-site potential (APR6) derived from *ab-intio* quantum chemical calculations (Anwander et al., 1992) was tested for the first time here against the experimental results. However, the presence of inverse cubic terms within the APR6 potential makes it impossible to estimate the potential truncation corrections required for accurate calculation of thermodynamic properties such as enthalpy of vaporisation, pressure, *etc.* using standard techniques. Comparison of the ND and MD results at the total inter-molecular radial distribution function level does not permit us to say that one model (H1+CH_3 or APR6) is better than the other. However, a comparison of the simulated functions with the corresponding three experimental partial distribution functions, $g_{HoHo}(r)$, $G^{inter}_{HoX}(r)$ and $G^{inter}_{XX}(r)$ reveals that the carbon atom treated as a united interaction site is found to be a good approximation for predicting the correlations involving all atoms other than the hydroxyl hydrogen. Although in APR6 the methyl hydrogens are treated as specific interaction sites, the H1+CH_3 model with the three methyl hydrogens treated as dead load does a better job, though only qualitatively, in reproducing the experimental structural features. This shows that the methyl hydrogens do not participate in any inter-molecular bonding. It is evident that although the models considered in this work give a qualitative picture of the structure of liquid methanol, these models warranty further refinement to achieve quantitative agreement with the experimental results.

Table 6.1 The sample parameters.

Parameter	CD_3OD	CD_3OH	$CD_3O(H/D)$
Temperature / (K)	298±1 K	298±1 K	298±1 K
Pressure / (bar)	1	1	1
Number density / (molecule $Å^{-3}$)	0.01487	0.01487	0.01487
σ_a at 1.8 Å / (b molecule^{-1})	8.422×10^{-3}	0.3428	0.1756
[a] b_c C / (fm)	6.646	6.646	6.646
[b] b_c H / Ho (methyl / hydroxyl) / (fm)	6.650/ 6.650	6.619 / -3.739	6.635 / 1.456
[a] b_c O / (fm)	5.803	5.803	5.803
$\left(\sum_{\alpha}^{Nm} c_\alpha b_\alpha\right)^2$ / (b molecule^{-1})	15.249	8.161	11.430
[d] $lim_{Q\to\infty}\left(\frac{\partial\sigma}{\partial\Omega}\right)_{dist}$ / (b molecule^{-1})	3.26 (~3.56)	9.22 (~8.58)	6.24 (~6.18)
[c] $10^9\chi_T$ / (Pa^{-1})	1.211	--	--
[d] $i_m(0)^*$	-0.921 (-0.867)	-0.921 (-0.80)	-0.921 (-0.85)

[a] from Sears (1992). [b] calculated according to the isotopic composition of the sample. [c] from Lide (1995). [d] theoretical values are compared with the experimental values given in parenthesis, * $i_m(0)$ is the low Q-limit of the normalised intermolecular structure factor (see section 6.1.3c).

Table 6.2 Average structure of methanol in terms of intra-molecular distances ($r_{\alpha\beta}$/Å) and associated Debye-Waller factors ($\gamma_{\alpha\beta}$/Å) obtained by least squares refinement, as compared to other available experimental data·

	Methanol(l)				
Parameters	***Fit1***[x]	***Fit 2***[w]	***Other studies***	***Methanol (g)***	***Methanol (s)***
r C-H_i	1.096(1)	1.0936	1.085±0.005[n]	1.098[a], 1.093[b]	1.01(2)[c] for i=3
			1.070±0.005[o], 1.086[s]	1.0936[f],1.096[g]	1.04(2)[c] for i=1,2
			1.062±0.002[p], 1.09[r]	1.096[h], 1.095[i]	
r C-O	.415(3)	1.4246	1.437(2)[d], 1.437(3)[e]	1.428[a], 1.434[b]	1.419[c]
			~1.5[m], 1.43(5)[n], 1.427[s]	1.4246[f], 1.427[g]	1.42[k]
			1.41(1)[o], 1.42(4)[p], 1.495[r]	1.427[h], 1.428[i]	1.44[l]
r O-Ho	0.961(1)	0.9451	0.99±0.01[n], 0.983[s]	0.967[a], 0.937[b]	0.918(8)[c]
			1.03 ±0.011[o], 1.027±0.008[p],	0.9451[f], 0.956[g]	0.97[u]
			1.031[r]	0.953[h], 0.960[i]	
∠ H_iCH_j [v]	110.4(3)	108.63	109.5±0.5[n], 108.63[o,p,q]	109.1 [a], 109.5 [b]	119.5(9)[c]
				108.63 [f], 109.03 [g]	
				109.07 [h], 109.47 [i]	
∠ COHo [v]	111.0	108.54	112.0±3[n], 99.7±2.2[o]	107.26 [a], 105.93 [b]	120.2(5)[c]
	(±3)		103.4±1.2[p], 89.2[r], 101.7[s]	108.54 [f], 108.87 [g]	104.7[u]
				108.4 [h], 109 [i]	
∠H_3COHo [v]	0[t]	0			
tilt angle τ [v]	6.2(±3)	3.27	0±3[n], 3.16[o,p,q]	3.27 [f], 3.34 [g], 3.3 [h]	
γ O-Ho	0.069(4)	0.072	0.06±0.04[o], 0.049±0.03[p]	0.073±0.015[i], 0.069[j]	
			0.100[s]		
γ C-H_i	0.069(2)	0.0698	0.09±0.03[o], 0.07±0.02[p],	0.080±0.01[i], 0.079[j]	
			0.103[s]		
γ C-O	0.060(1)	0.060	0.064(2)[d], 0.094(0)[e], 0.094[s]	0.049±0.005[i], 0.050[j]	
			0.099±0.07[o], 0.037±0.04[p]		
γ C-Ho	0.08(2)	0.099	0.09±0.06[o], 0.047±0.035[p]		
γ H_1-Ho	0.23(2)	0.22	0.13±0.07[o], 0.125±0.047[p]		
γ H_2-Ho	0.23(2)	0.22	0.13±0.07[o], 0.125±0.047[p]		
γ H_3-Ho	0.11(1)	0.11	0.13±0.07[o], 0.125±0.047[p]		
γ O-H_1	0.091(1)	0.093	0.063±0.03[o], 0.08±0.035[p]	0.099±0.01[i], 0.104[j]	
γ O-H_2	0.091(1)	0.093	0.063±0.03[o], 0.08±0.035[p]	0.099±0.01[i], 0.104[j]	
γ O-H_3	0.2(1)	0.084	0.063±0.03[o], 0.08±0.035[p]	0.099±0.01[i], 0.104[j]	
γ H_i-H_j	0.105(5)	0.108	0.102±0.037[o], 0.11±0.03[p]	0.133[j]	
$10^{+3}R_{factor}$	6.251	6.757			

[a] CH_3OH, Swallen (1955). [b] Ivash and Dennison (1953). [c] β-phase of CD_3OD, at 168 K obtained by combining X-ray and Neutron Diffraction (ND) data, Robyr et al. (1994). [d] X-ray diffraction data of CH_3OH, Narten and Habenschuss (1984). [e] X-ray diffraction data of CH_3OH, Magini et al. (1982). [f] microwave studies of CD_3OH, CH_3OD and CH_3OH, Lees and Baker (1968). [g] microwave studies, Venkateswarlu and Gordy (1955). [h] Nishikawa (1956). [i] electron diffraction data of CH_3OH, Kimura and Kubo (1959). [j] theoretical values, Kimura and Kubo (1959). [k] solid CH_3OH at -110°C, Tauer and Lipscomb (1952). [l] solid CH_3OH at -160°C, Tauer and Lipscomb (1952). [m] X-ray diffraction data of CH_3OH, Zachariasen (1935). [n] ND data of CD_3OD, Tanaka et al. (1985). [o] ND data of CD_3OD at a reactor source using λ=0.5 Å, Montague et al. (1981). [p] ND data of CD_3OD at a reactor source using λ=0.7 Å, Montague et al. (1981). [q] fixed to the value obtained from the microwave gas phase studies of Lees and Baker (1968). [r] ND data with H/D substitution, Montague and Dore (1986). [s] ND data with H/D substitution, Weitkamp et al. (2000). [t] fixed. [u] α-phase of CD_3OD, Robyr et al. (1994). [v]angles given in degrees. [w] structural parameters fixed to the values given in reference Lees and Baker (1968). [x] the uncertainties (given in parenthesis) associated with the structural parameters were calculated by varying the range of the fit: 6 to 8 $Å^{-1}$ (for low Q) and 30 to 35 $Å^{-1}$ (for high Q).

Table 6.3 The intermolecular neutron weights of the various inter-molecular rdfs, and partial distribution functions in liquid methanol.

pair αβ	$^1G(r)$	$^2G(r)$	$^3G(r)$	$G_{XHo}(r)$ [a]	$G_{XX}(r)$	$g_{HoHo}(r)$ [a]
C C	0.0290	0.0541	0.0386	0.0000	0.0422	0.0000
C H	0.1739	0.3234	0.2315	0.0019	0.2526	0.0000
C O	0.0506	0.0945	0.0675	0.0000	0.0737	0.0000
C Ho	0.0580	-0.0609	0.0170	0.2054	0.0000	0.0000
H H	0.2610	0.4832	0.3466	0.0055	0.3780	0.0000
H O	0.1518	0.2824	0.2021	0.0016	0.2206	0.0000
H Ho	0.1740	-0.1820	0.0507	0.6148	0.0000	0.0049
O O	0.0221	0.0413	0.0295	0.0000	0.0322	0.0000
O Ho	0.0506	-0.0532	0.0148	0.1794	0.0000	0.0000
Ho Ho	0.0290	0.0171	0.0019	0.0000	0.0000	0.9951

[a] : The residual contributions C-H, and H-O in $G_{XHo}(r)$ and, H-Ho in $g_{HoHo}(r)$ appear because the extent of deuteration on methyl hydrogen of different samples is slightly different (99.8% for CD_3OD, 99.5% for CD_3OH); 1, 2 and 3 stand for CD_3OD, CD_3OH and $CD_3O(H/D)$, respectively

Table 6.4 Molecular geometry, moments of inertia and dipole moment of the methanol molecule.

Model	*Experimental*[c]	*Experimental*[d]	*J2*[e]	*H1*[e]	*H1+CH$_3$*[e]	*APR6*[f]	*Ab initio MP2/TZV (2p,2d)++ QCC*
Parameter			*(3sites)*	*(3sites)*	*(6sites)*	*(6sites)*	
d_{OHo}, Å	0.937	0.9451±0.0034	0.9451	0.9451	0.9451	0.956	0.95825
d_{CO}, Å	1.434	1.4246±0.0024	1.4246	1.4246	1.4246	1.427	1.4286
d_{CHi}, Å	--	1.0936±0.0032	1.0936	1.0936	1.0936	1.096	1.0838 (i=3)
							1.0893 (i=1, 2)
∠COHo,°	105.93	108.53 ±0.48	108.53	108.53	108.53	108.9	107.60
∠OCH$_i$,°	--	--	--	--	--	106.6 (i=3)	106.5 (i=3)
						111.6 (i=1, 2)	111.8 (i=1,2)
∠H$_i$CH$_j$,°	109.5	108.63 ± 0.70	--	--	108.63	109.0	108.68 (i=1, 2; j=3)
							109.21 (i=1; j=2)
∠τ,°	--	3.27 ± 0.18			3.27	--	--
τ(HoOCH$_3$)	--	--			180.0	180.0	180.0
I_A, amu· Å^2	3.961	3.96277	0.7368	0.7368	3.9178	3.9596	3.92
I_B, amu· Å^2	20.533	20.4834	16.7356	16.7356	20.4780	20.5332	20.5130
I_C, amu· Å^2	21.283	21.2679	17.4725	17.4725	21.2147	21.2828	21.2548
q_{Ho} (e)	--	--			0.431	0.338	0.313[a]
q_o (e)	--	--			-0.728	-0.549	-0.492[a]
q_c (e)	--	--			0.297	-0.104	-0.171[a]
q_{Hi} (e)	--	--			0.0	0.105	0.11 (i=1,2)
							0.130 (i=3)
$\mu_{\|\|}$, D	-0.885	--			--	--	-1.029[b]
$\mu\perp$, D	1.44	--			--	--	1.487[b]
μ, D	1.69	--	2.22	2.33	2.33	2.08	1.88[a] (1.81)[b]
$\angle\,\vec{\mu}\overrightarrow{OHo}$	50.6	--	50.9	55.8	55.8	65.3	66.4

[a] From the Mulliken population analyses; [b] Dipole moments calculated directly from molecular orbital MP2/TZV (2p,2d)++ wave functions; [c] From Ivash and Dennison (1953), [d] From Lees and Baker (1968), [e] From Haughney et al. (1987), [f] From Anwander et al. (1992).

Table 6.5 H1 and J2 Force field parameters for the methanol molecule.

Parameter	*J2*	*H1*	*H1 + CH_3*
σ_{HoHo}, Å	0.0	0.0	0.0
σ_{OO}, Å	3.071	3.083	3.083
σ_{CC}, Å	3.775	3.861	3.861
σ_{HH}, Å	- -	--	0.0
ε_{HoHo}, kJ/mol	0.0	0.0	0.0
ε_{OO}, kJ/mol	0.71130	0.73117	0.73117
ε_{CC}, kJ/mol	0.86611	0.75786	0.75786
ε_{HH}, kJ/mol	- -	- -	0.0
q_{Ho} (e)	+0.435	+0.431	+0.431
q_O (e)	-0.700	-0.728	-0.728
q_C (e)	+0.265	+0.297	+0.297
q_H (e)	--	- -	0.0

Table 6.6 Details of the MD runs for liquid methanol at 298.15 K. Values of simulated configurational (potential) energy, pressure and diffusion coefficient are compared with the experimental data.

	Run 1	***Run 2***	***Run 3***	***Run 4***	***Run 5***	***Run 6***	***APR6***	***Experiment***
Force-field model	J2	J2	H1	H1	H1	H1 + CH_3 (6 sites)	EW	- -
Long-range (Coulomb) Interactions treatment	SF	RF	RF	RF	EW	EW	NVE	- -
Algorithm	Vlf + SHAKE	Vlf + SHAKE	Vlf + SHAKE	FIQA rigid body	Vlf + SHAKE	FIQA, rigid body	FIQA, rigid body	- -
Equilibration time, ps	94	110	100	150	60	70	80	- -
Sampling time, ps	40	50	100	50	100	40	100	- -
$< T >$, K	287.5 ± 8.7	289.5 ± 8.8	295.8 ± 8.7	298.8 ± 9.6	292.7 ± 9.0	301.1 ± 9.2	293.6 ± 8.9	Ambient temperature
$-< U >_{corr}$, kJ/mol [d]	35.9 ± 0.2	36.4 ± 0.2	35.3 ± 0.3	35.1 ± 0.2	35.5 ± 0.2	35.3 ± 0.2	[e]	34.95 [a]
$- < U >_{uncorr}$, kJ/mol [d]							18.5±0.2	
$< P >_{corr}$, kbar [d]	0.14 ± 0.37	0.19 ± 0.38	0.74 ± 0.39	0.77 ± 0.39	0.77 ± 0.36	0.85 ± 0.39	[e]	Ambient pressure
$< P >_{uncorr}$, kbar [d]						1.04±0.39	6.6±0.28	
D $\times 10^9$, m^2/s [b]	1.31 (1.04)	1.38 (1.29)	1.13 (0.91)	1.15 (1.08)	1.24 (1.30)	2.01 (1.92)	1.94 (2.05)	2.42_5 [c]

[a] Experimental potential energy was calculated from the experimental enthalpy of vaporization (ΔH_{vap}) according to equation 6.4, ΔH_{vap} was taken from Riddick et al. (1986); [b] First values were obtained from the center of mass (c.o.m) velocity auto-correlation function (VACF), values in brackets were obtained using the c.o.m mean square displacement (MSD); [c] from Hurle and Woolf (1980); [d] corr/uncorr stand for values corrected/uncorrected for the potential truncation; [e] a proper estimation of these values cannot be made (see text); Vlf stands for Verlet leap-frog algorithm (Hockney, 1970), SHAKE for the algorithm used to constrain the methanol geometry (Ryckaert et al., 1977), EW for Ewald summation, SF for shifted force potential and RF for reaction field model, FIQA stands for Fincham's Implicit Quaternion algorithm (Fincham, 1992).

Table 6.7 Characteristics of the C-C and C-O partial pdfs, in liquid methanol obtained with H1+CH_3 model for the MD run 6 as compared to available experimental data and computer simulation studies.

Pdf	r_{M1} *(exp.) /Å*	r_{M1} */Å*	$g(r_{M1})$	*n(r)*	*n(r)* [h]
C-O	3.8[a]	3.6 [h]	2.01 [h]		
		3.62[b]	1.94[b]	6.1(4.5)[b]	5.22(4.53)
		3.62[g]	-	5.1(4.5)[g]	5.22(4.53)
		3.64[c]	-	4.0 (4.2)[c]	4.1(4.23)
		3.6[d]	-	-	-
C-C	3.8 , 4.4[a,f]	4.18 [h]	2.07 [h]		
		4.10[g]	-	12.0(5.88)	12.3(5.88)
		4.15[b]	-	12.8(6.0)[b]	12.7(5.99)
		4.1[d]	-	-	-
		4.1[e]	-	-	-

[a] From Wertz and Kruh (1967); [b] from Palinkas et al. (1987); [c] from Jorgensen (1980); [d] from Jorgensen (1981); [e] From Gao et al. (1995). [f] broad peak consisting of one peak at 3.8 Å and another at 4.4 Å; [g] from Shilov et al. (199); [h] this work (run 6). r_{M1} is the position of 1st maximum; $g(r_{M1})$, the height of first maximum and $n(r)$, the co-ordination number calculated up to a distance r.

Table 6.8 Characteristics of the O-O partial pdf in liquid methanol obtained with H1+CH_3 model for the MD run 6 as compared to available experimental data and other computer simulation studies.

r_{M1}(exp.) / Å	n (r) (exp.)	r_{M1} / Å	r_{M2} / Å	$g(r_{M1})$	n(r)	n(r) [l]
2.76-2.80[a]	-	2.79 [l]	4.87 [l]	3.38 [l]		
		2.7[d]	4.9[d]	-	2.0 (3.4-3.5)	2.0 (3.43)
2.66 [b](cryst)	-	2.8[e]	-	-	-	-
		2.88[m]	4.78	-	1.9(3.46)	2.0(3.43)
		2.75[f]	4.7[f]	-	2.0[f]	2.05
		2.85[g]	4.9[g]	3.25[g]	2.0(3.41)[g]	2.0(3.43)
		2.75[h]	4.7[h]	-	2.0(3.4)[h]	2.0(3.43)
		2.81[i]	-	-	-	-
2.798[c]	1.8(3.25[k])					1.87(3.23)

[a] from Magini et al. (1982); [b] from Tauer and Lipscomb (1952); [c] from Narten and Habenschuss (1984); [d] from Gao et al. (1995); [e] from Svishchev and Kusalik (1994); [f] from Marchi and Klein (1989); [g] from Palinkas et al. (1987); [h] from Jorgensen (1986); [i] from Jorgensen (1981); [j] at the minimum of the first peak; [k] distance assumed; [l] this work (run 6); [m] from Shilov et al. (1999). r_{Mi} is the position of ith maximum; $g(r_{M1})$ = height of first maximum and $n(r)$, the co-ordination number calculated up to r.

Table 6.9 Characteristics of the pdfs, $g_{ij}(r)$ in liquid methanol obtained with the H1+CH_3 and APR6 (values in parenthesis) models compared with the available experimental data.

Pdf	r_{M1} *(experimental)*/ Å	r_{M1} / Å	r_{m1} / Å	$g(r_{M1})$	r_{M2} / Å	$n(r_{m1})$	*n(r) (experimental)*
O-O	2.76-2.80[a],2.66[b], 2.798[c]	2.79 (2.88)	3.53 (3.58)	3.38 (2.68)	4.93 (4.88)	2.07 (2.09)	
						1.87 (1.71)	1.8 [c]
O-C	3.8[d]	3.60 (3.68)	4.48 (4.53)	2.01 (1.8)	5.10 (5.03)	5.00 (5.04)	
O-Ho	1.75±0.03[e]	1.88 (1.93)	2.63 (2.68)	3.47 (2.7)	3.38 (3.48)	0.98 (0.96)	
O-H	--	3.65 (3.85)	4.10 (4.10)	1.30 (1.16)	4.50 (4.60)	1.94 (1.81)	
Ho-Ho	2.4[h], 2.36[e]	2.49 (2.58)	3.38 (3.53)	2.79 (2.64)	-- (--)	2.32 (2.70)	2.8 [f]
Ho-C	--	2.83 (2.83)	3.28 (3.23)	1.01 (0.81)	4.08 (4.23)	1.13 (0.90)	
Ho-H	--	3.70 (3.85)	5.85 (4.15)	1.21 (1.08)	-- (4.75)	6.80 (1.93)	
C-C	3.8 and 4.4[d,g]	4.18 (4.13)	5.90 (5.99)	2.07 (1.96)	8.00 (8.04)	12.3 (12.9)	
C-H	--	4.65 (3.65)	6.05 (4.25)	1.30 (1.24)	7.90 (4.80)	7.60 (2.10)	
H-H	--	4.85 (4.40)	6.20 (6.30)	1.13 (1.15)	7.95 (8.10)	5.77 (6.00)	

a: from Magini et al. (1982); b: from crystalline data, Tauer and Lipscomb (1952); c: from Narten and Habenschuss (1984); d: from Wertz and Kruh (1967); e: the ND work presented in section 6.1; f: calculated up to r = 3.37 Å which is the minimum after the first peak; g: 3.8 and 4.4 Å correspond to two distinct C-C contributions; r_{Mi} is the position of ith maximum; r_{m1}, position of first minimum; $g(r_{M1})$ = height of first maximum and n, the co-ordination number; h: from Montague et al. (1984).

Table 6.10 Characteristics of Ho-Ho pdf, in liquid methanol obtained with the H1+CH_3 model for the MD run 6 as compared to available experimental data and computer simulation studies.

r_{MI} (exp.) /Å	$g(r_{MI})$(exp.)	r_{MI} / Å	$g(r_{MI})$	$n(r)$	$n(r)$ [h]	$n^{ND}(r)$[c]
		2.49[h]	2.79[h]			
2.4[a]	-	2.45[d]		-	-	-
		2.45[e]		2.3(3.31)[e]	2.26(3.28)	2.74(3.31)
2.36[c]	2.46	2.35-2.40[f]		2.1-2.2(3.25)[f]	2.26(3.28)	2.69(3.28)
		2.50[b]		2.3(3.38)[b]	2.32(3.38)	2.8(3.38)
		2.26[g]		2.4(2.89)[g]	1.94(2.88)	2.2(2.88)

[a] From Montague et al. (1984); [b] from Shilov et al. (1999); [c] the ND work presented in section 6.1; [d] from Marchi and Klein (1989); [e] from Palinkas et al. (1987); [f] from Jorgensen (1986); [g] from Jorgensen (1981); [h] this work (run 6); r_{MI} is the position of 1st maximum, $g(r_{MI})$ = height of first maximum and $n(r)$, the coordination number calculated up to r.

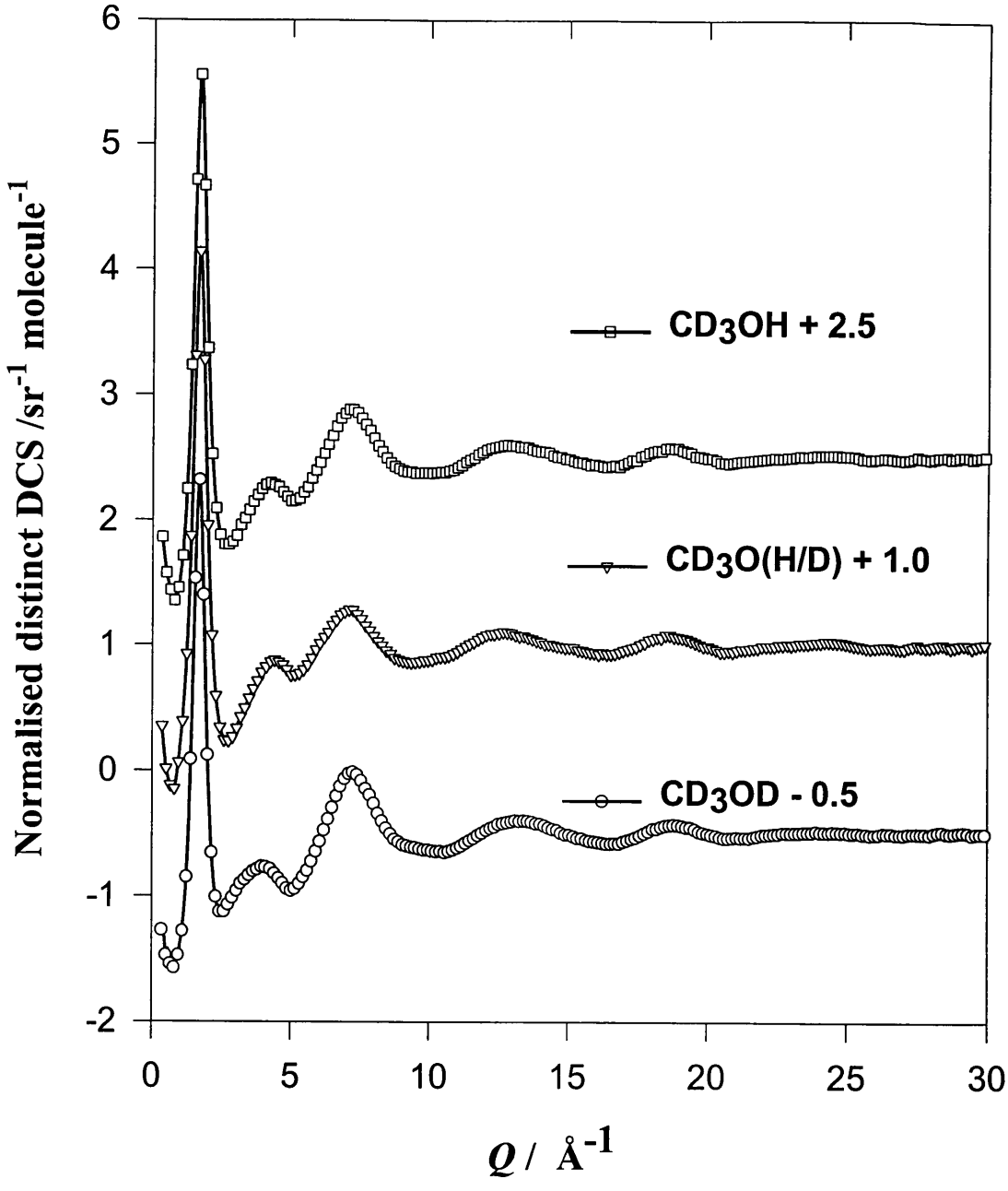

Figure 6.1 The normalised distinct differential scattering cross-sections per molecule (symbols) for CD_3OH, $CD_3O(H/D)$ and CD_3OD along with the back Fourier transforms (lines) of their respective radial distribution functions of figure 6.2.

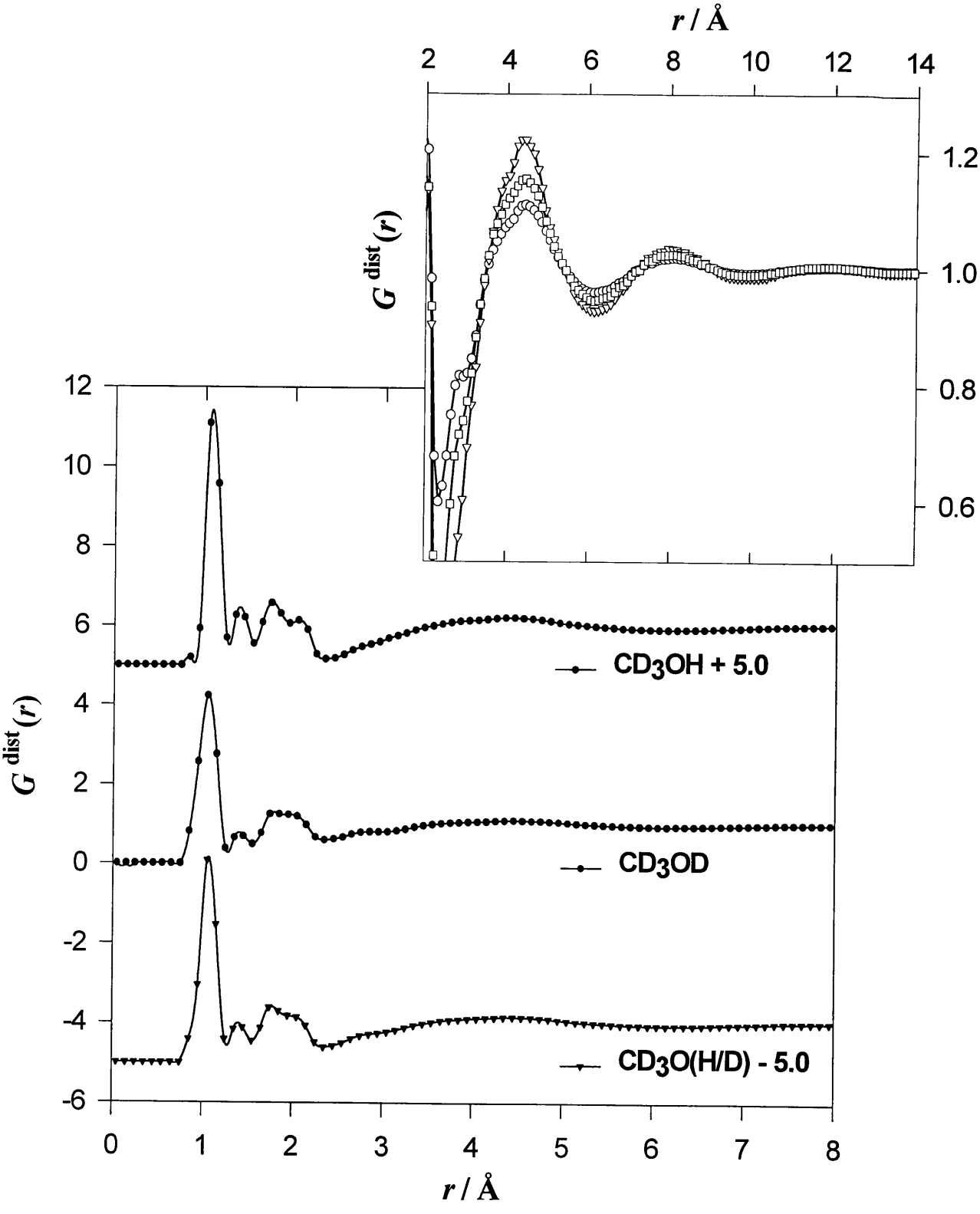

Figure 6.2 The distinct radial distribution functions, $G^{dist}(r)$, for CD_3OH, $CD_3O(H/D)$ and CD_3OD. The inset shows the same functions on a magnified scale, CD_3OH (triangles), $CD_3O(H/D)$ (squares) and CD_3OD (circles).

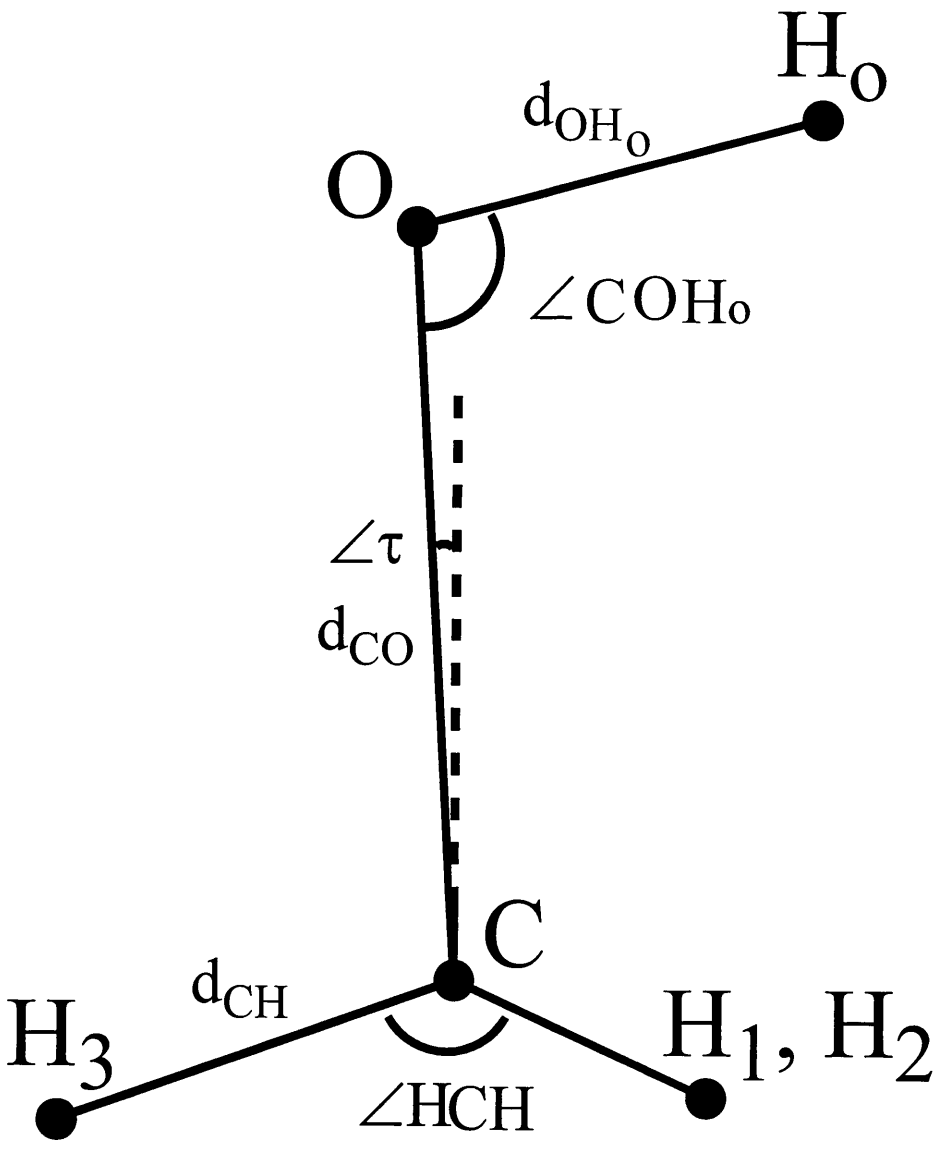

Figure 6.3 The molecular model of methanol used in defining the molecular parameters for least squares refinement. While H_3, C, O and Ho lie in the symmetry plane of the molecule, H_1 and H_2 point in and out of the symmetry plane.

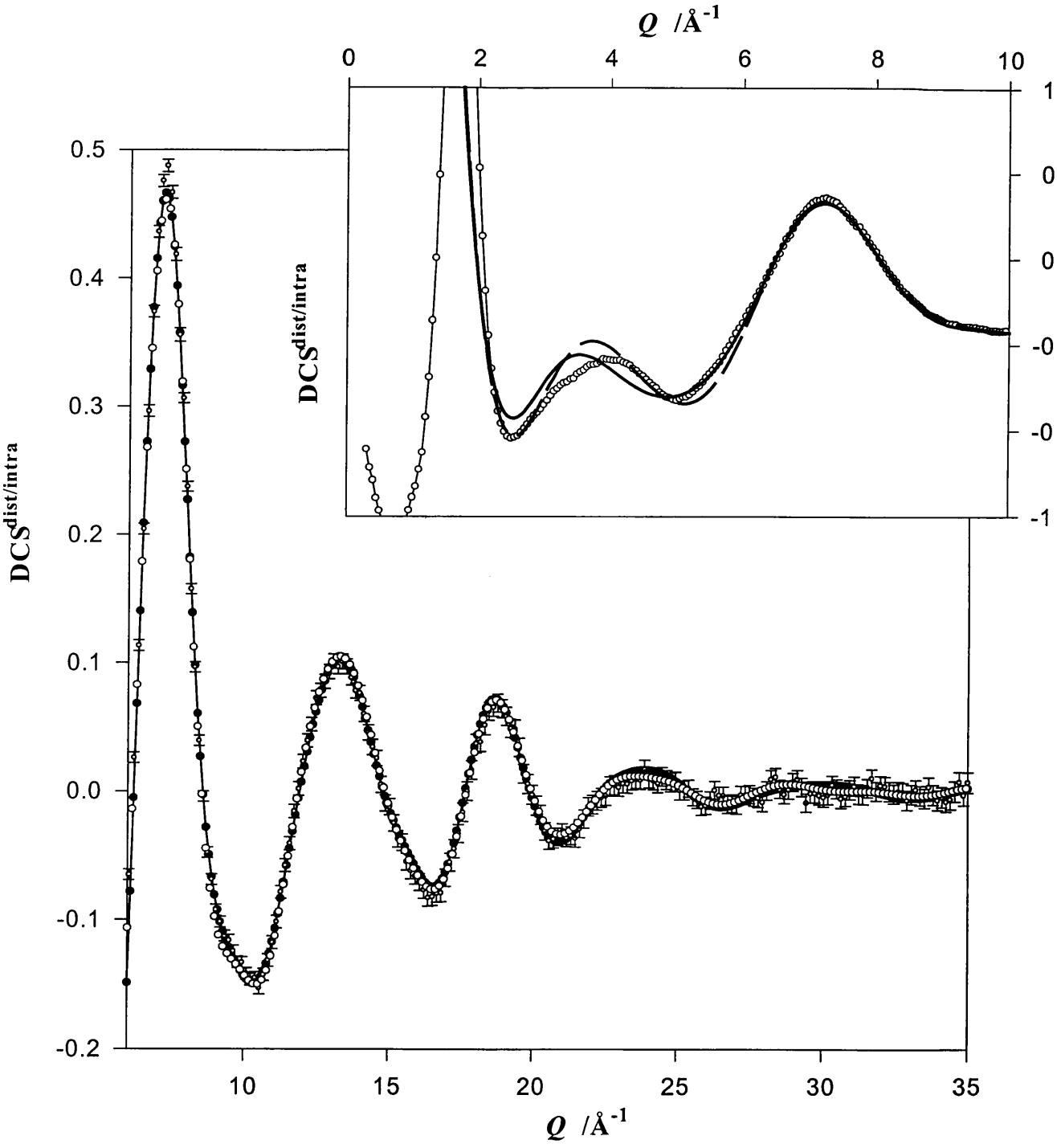

Figure 6.4 The distinct differential scattering cross-section for CD_3OD (circles with error bars) along with the two intra-molecular structure factors, black circles: fit 1, open circles: fit 2. The inset shows the two intra-molecular structure factors (fit 1: solid line, fit 2: broken line) and the distinct differential scattering cross-section for CD_3OD (circles) in the low Q-range.

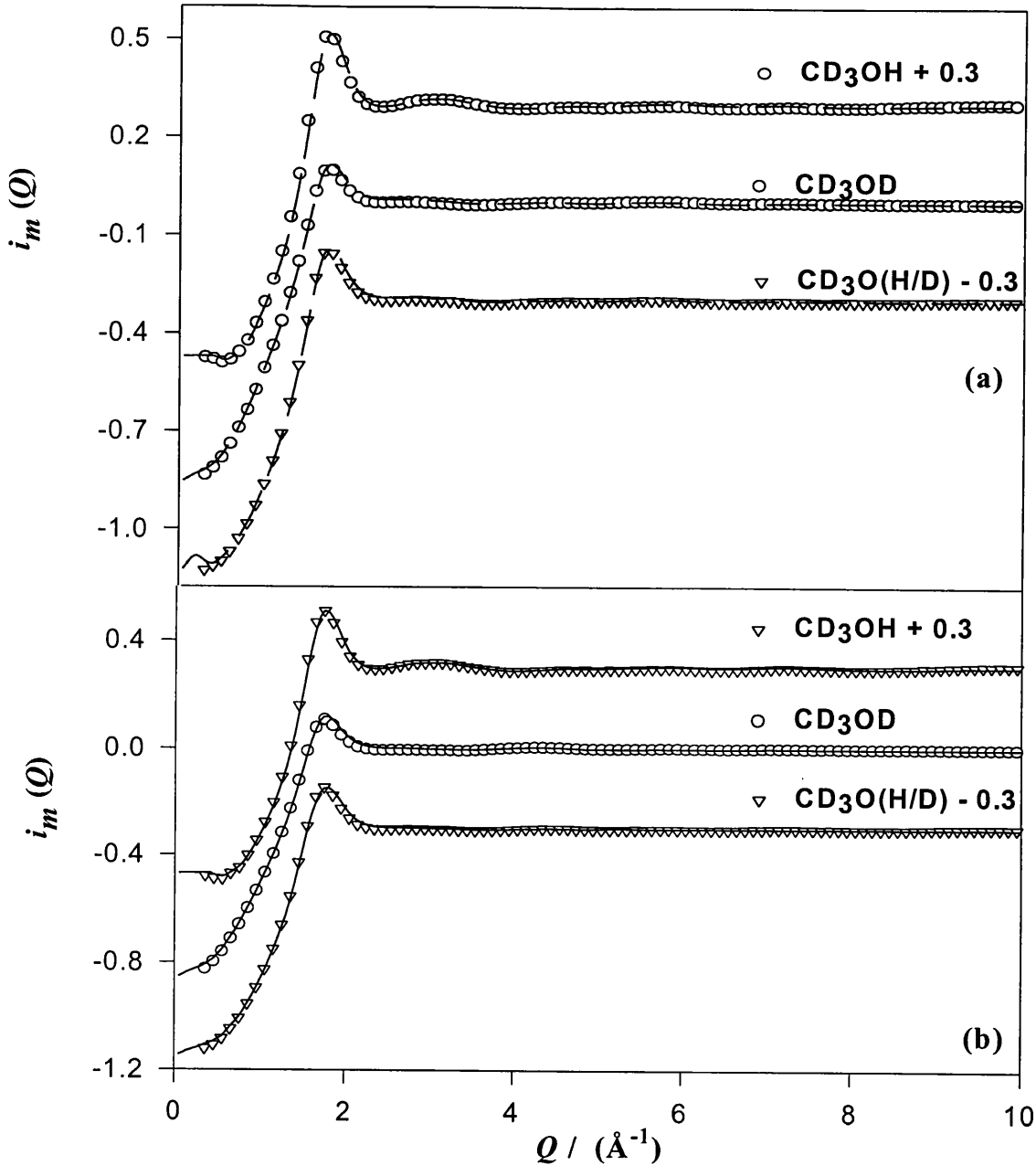

Figure 6.5 The inter-molecular differential cross-sections normalised to a molecular unit, $i_m(Q)$ (symbols) for CD_3OD, CD_3OH and $CD_3O(H/D)$ obtained after subtraction of the intra-molecular structure factor of (a): fit 2 and, (b): fit 1. The back Fourier transforms of their corresponding inter-molecular radial distribution functions (figure 6.6) are also shown as lines.

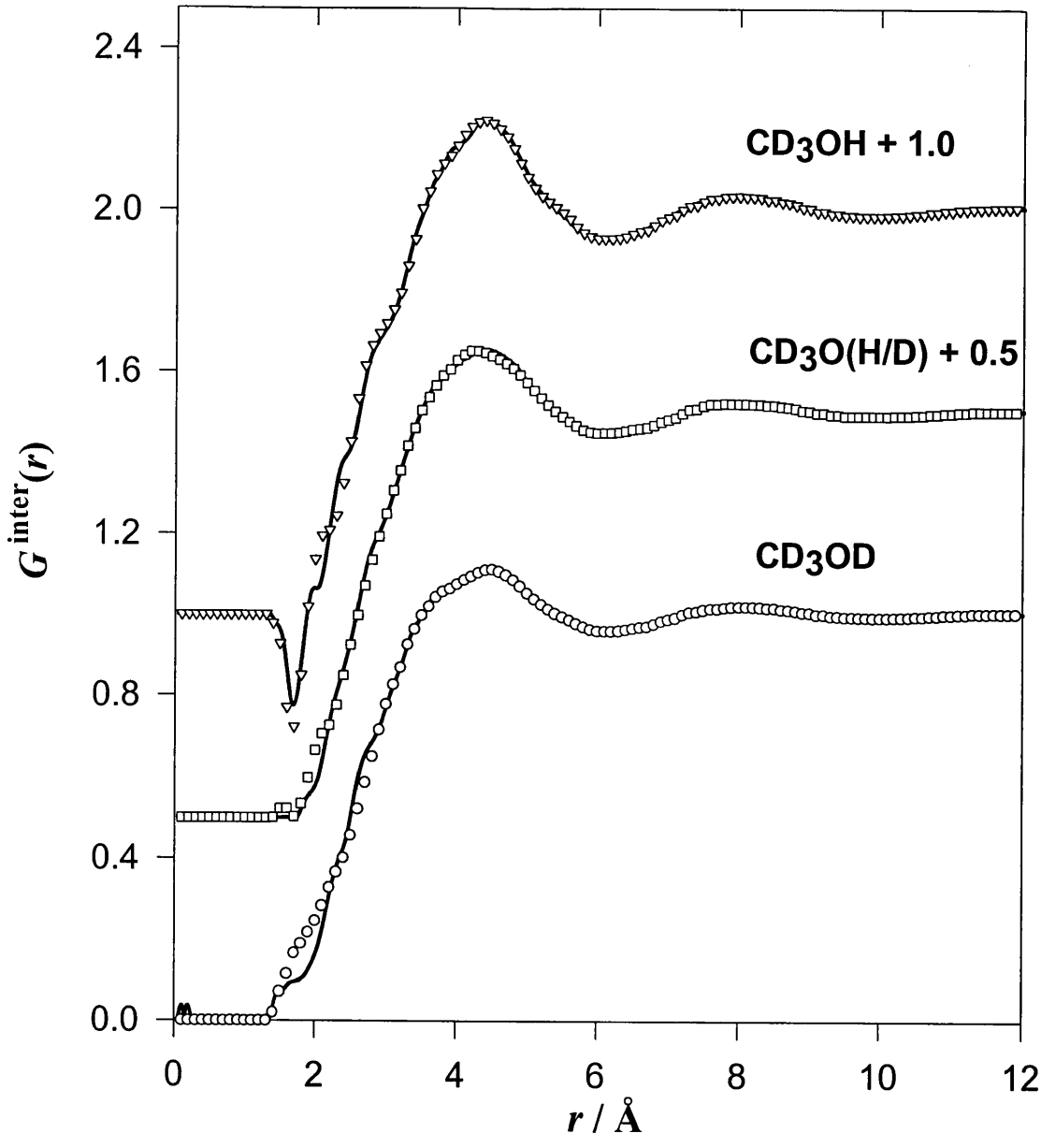

Figure 6.6 The inter-molecular radial distribution functions for CD_3OD, CD_3OH and $CD_3O(H/D)$ obtained after removal of the intra-molecular structure of: fit 1 (symbols) and fit 2 (lines).

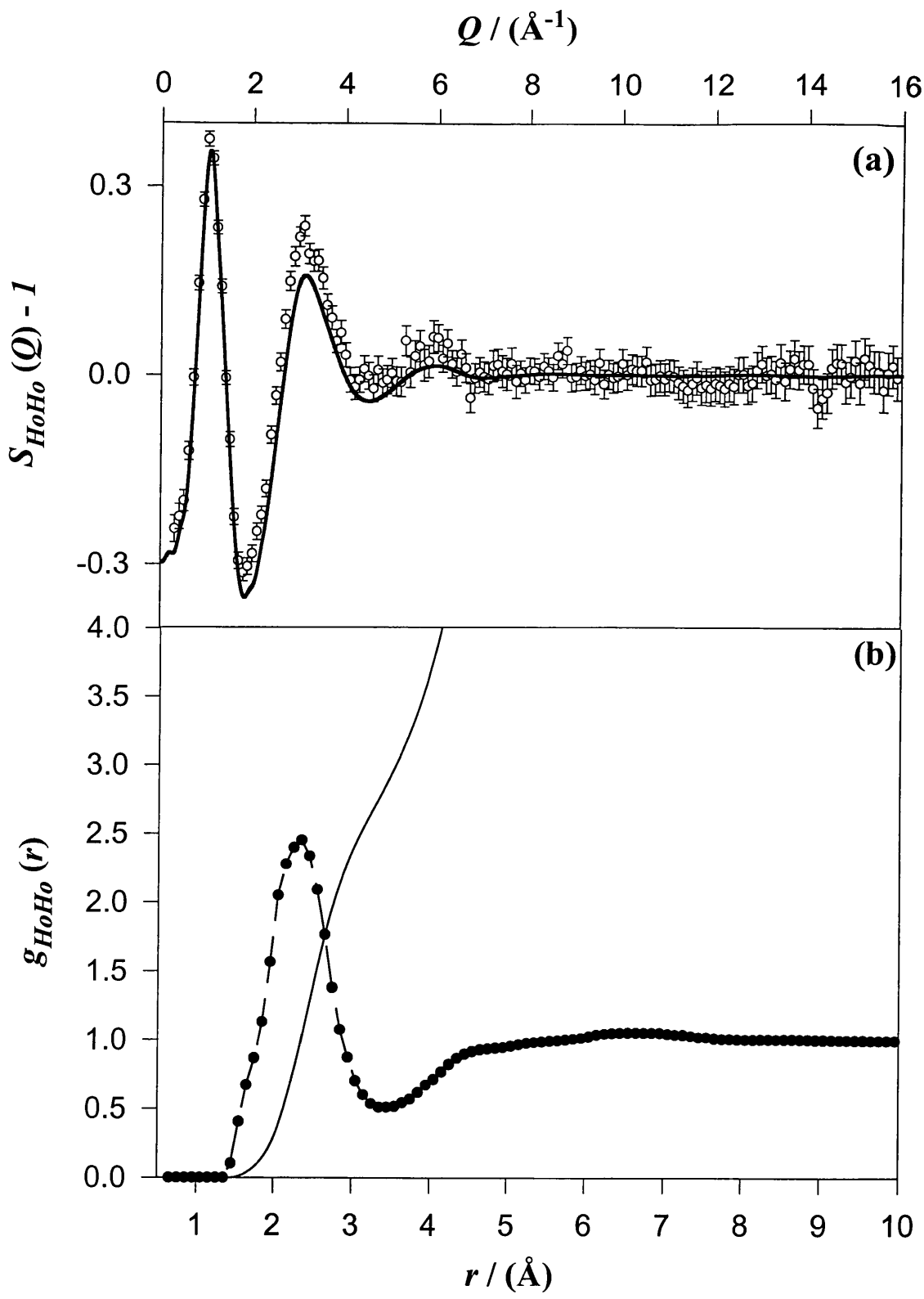

Figure 6.7 (a) The Ho-Ho partial structure factor (circles with error bars) along with the back Fourier transform (line) of the corresponding partial pair distribution function, $g_{HoHo}(r)$ shown in figure 6.7b. (b) The Ho-Ho partial pair distribution function (circles and broken line) along with its running co-ordination number (solid line).

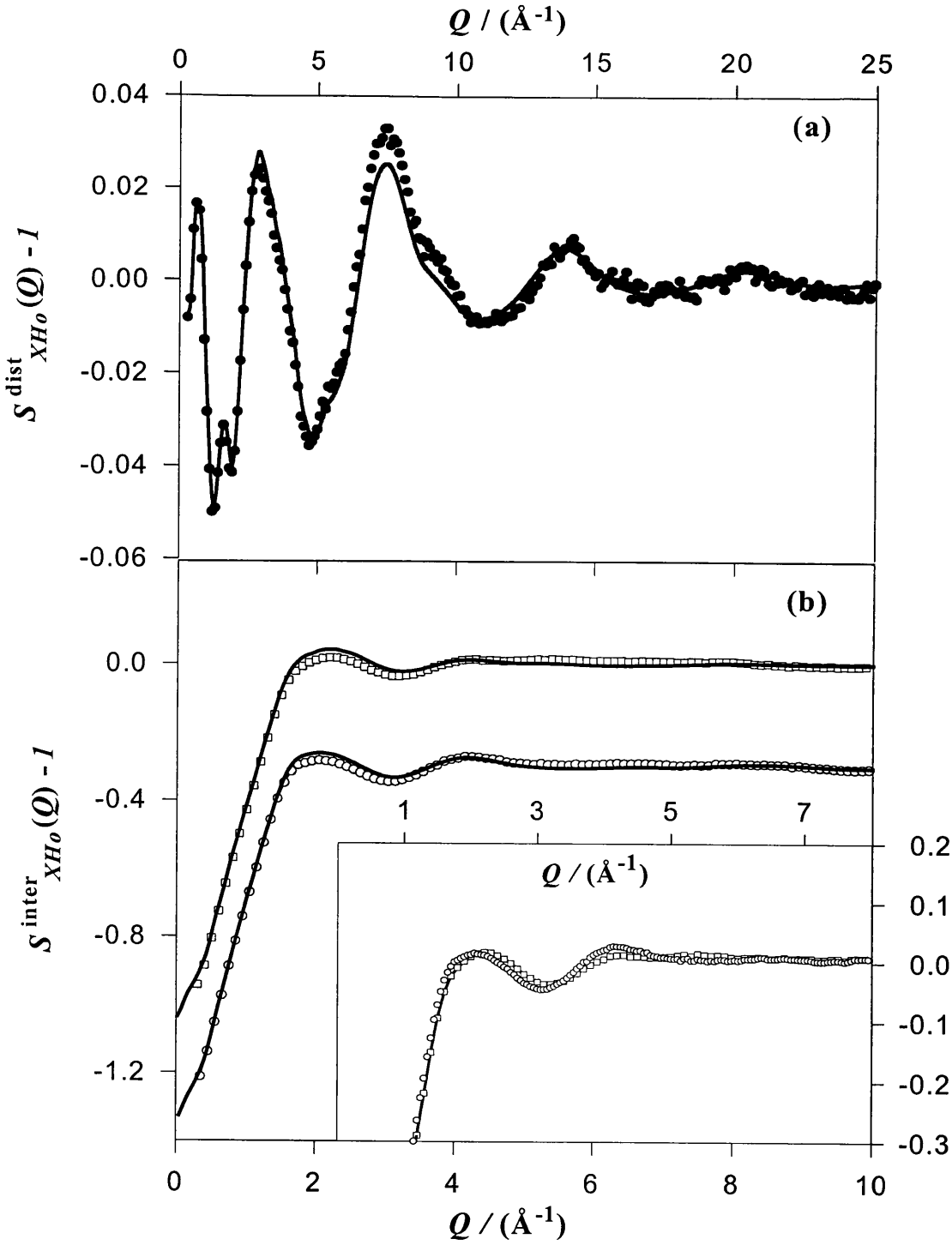

Figure 6.8 (a) The distinct X-Ho scattering function, $S^{dist}_{XHo}(Q)$ (circles) and the back Fourier transform (line) of the X-Ho partial distribution function of figure 6.9a. (b) The inter-molecular scattering function, $S^{inter}_{XHo}(Q)$, obtained after removal of intra-molecular structure of: fit 1 (bottom, shifted by – 0.3) and, fit 2 (top) along with the back Fourier transforms (lines) of their corresponding inter-molecular X-Ho pdfs (figure 6.9b). The inset shows the two $S^{inter}_{XHo}(Q)$ functions (corresponding to fit 1 and fit 2), superimposed on an enlarged scale.

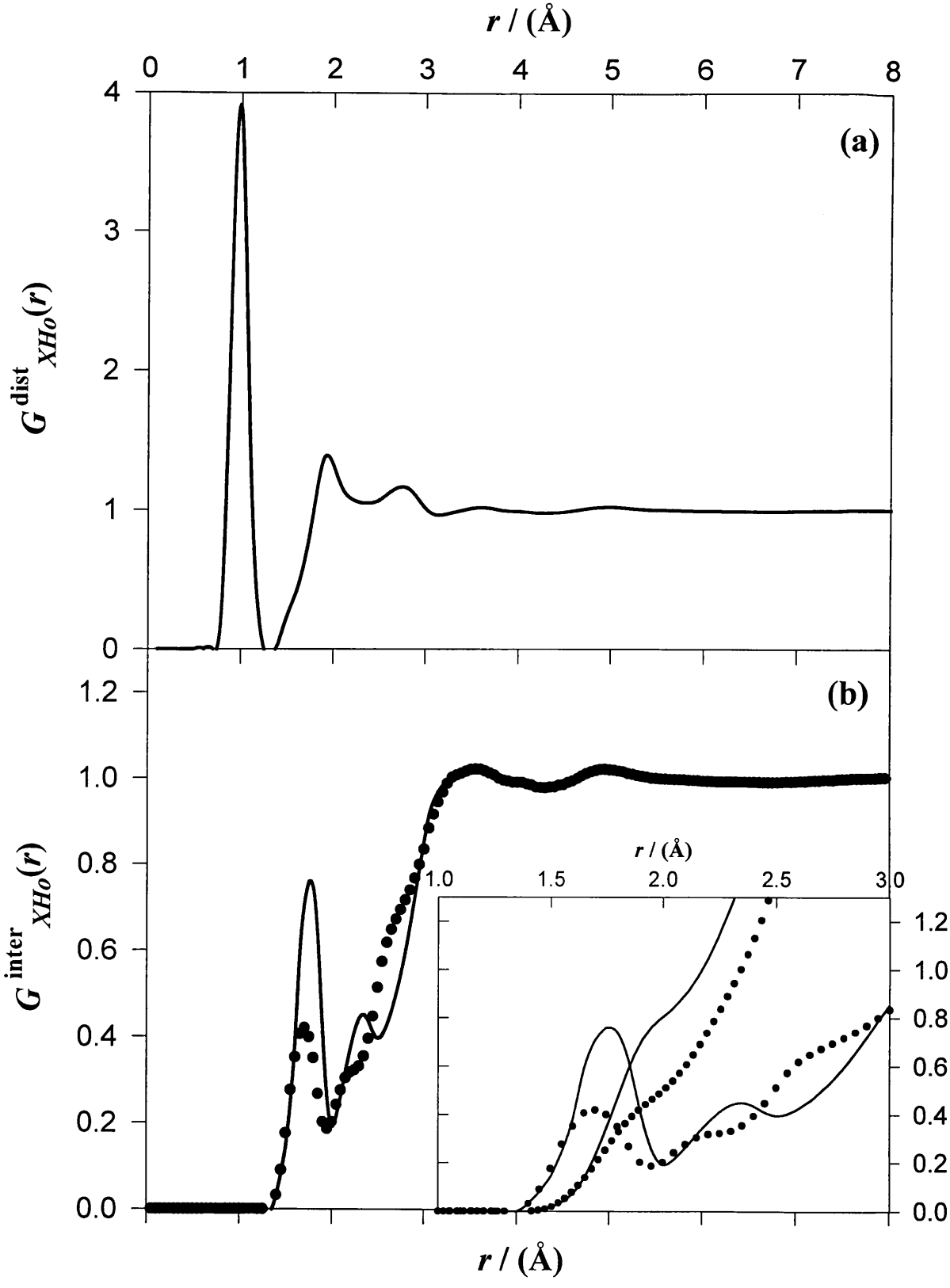

Figure 6.9 (a) The X-Ho distinct partial distribution function, $G^{dist}_{XHo}(r)$. (b) The X-Ho inter-molecular partial distribution functions obtained after removal of molecular structure of: fit 1 (line) and, fit 2 (circles). The inset shows the same functions on a different scale along with the O····Ho running co-ordination number, fit 1 (line) and, fit 2 (circles).

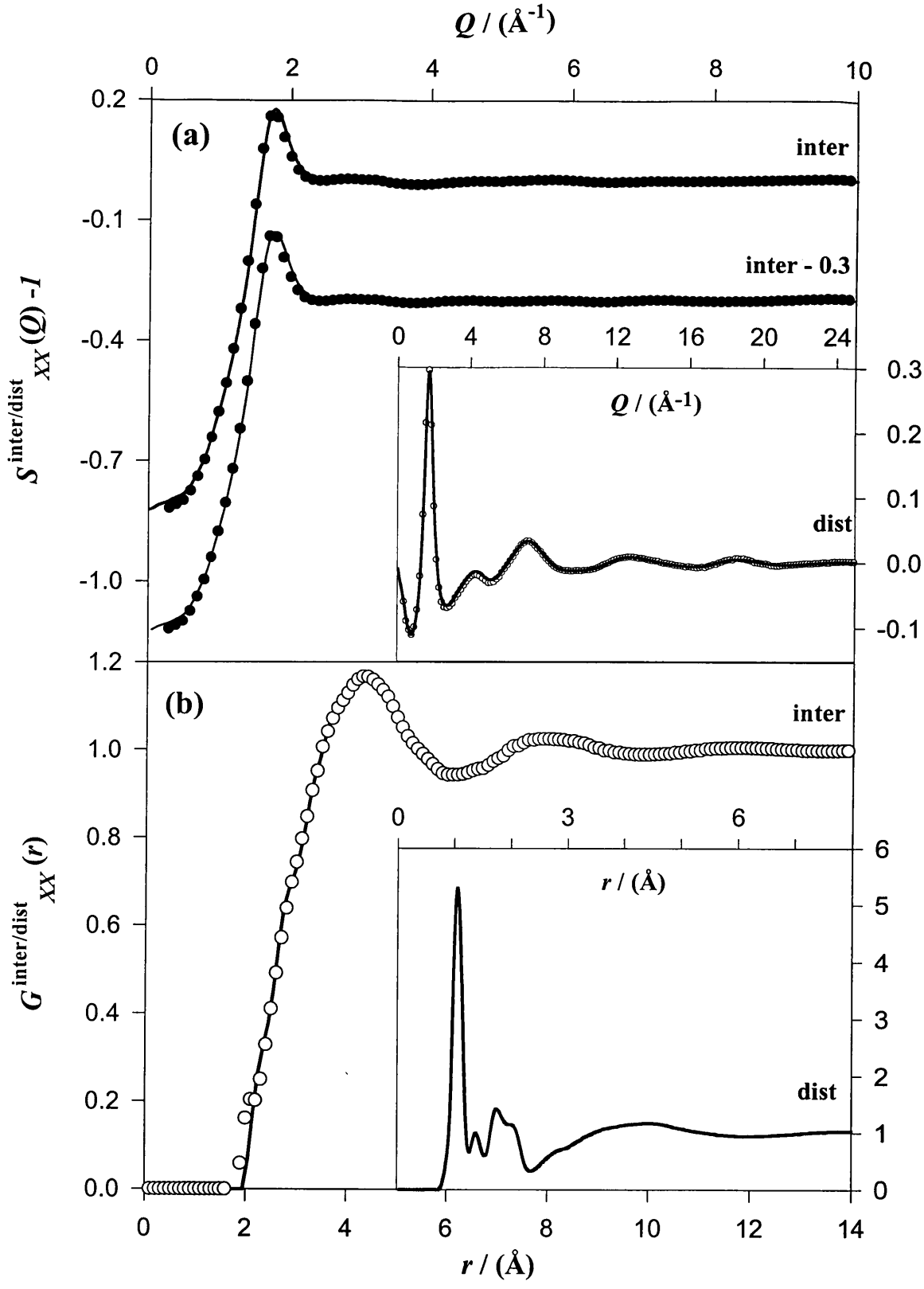

Figure 6.10 (a) The inter-molecular scattering function, $S_{XX}^{inter}(Q)$ (circles) obtained after removal of molecular structure of: fit 1 (bottom) and, fit 2 (top). The back Fourier transforms (lines) of the corresponding inter-molecular X-X partial distribution functions (figure 6.10b) are also shown superimposed. The distinct X-X scattering function, $S_{XX}^{dist}(Q)$ (circles) along with the back Fourier transform (line) of the X-X partial distribution function (inset figure 6.10b) are shown in the inset. (b) The X-X inter-molecular partial distribution functions, $G_{XX}^{dist}(r)$ corresponding to intra-molecular fit 1 (symbols) and fit 2 (line). The inset shows the X-X distinct partial distribution function.

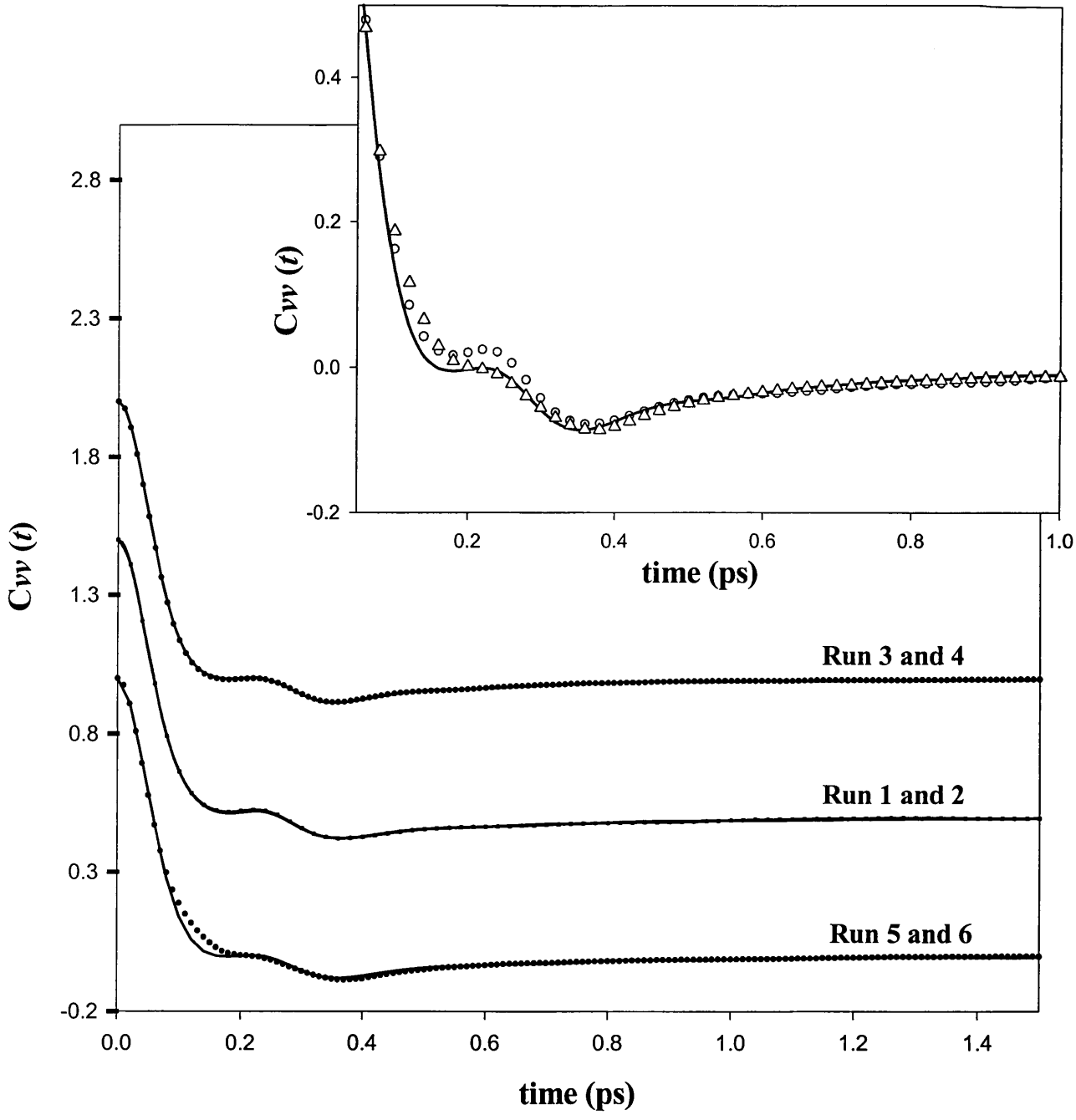

Figure 6.11 Normalised centre-of-mass (c.o.m) velocity auto correlation functions $C_{vv}(t)$, obtained for the six MD runs (bottom: runs 5 (-) and 6 (•); middle: runs 1 (■) and 2 (-) displaced by 0.5; top: runs 3 (-) and 4 (•) displaced by 1). Inset shows runs 1 (o), 4 (-) and 6 (Δ) superimposed on an enlarged scale.

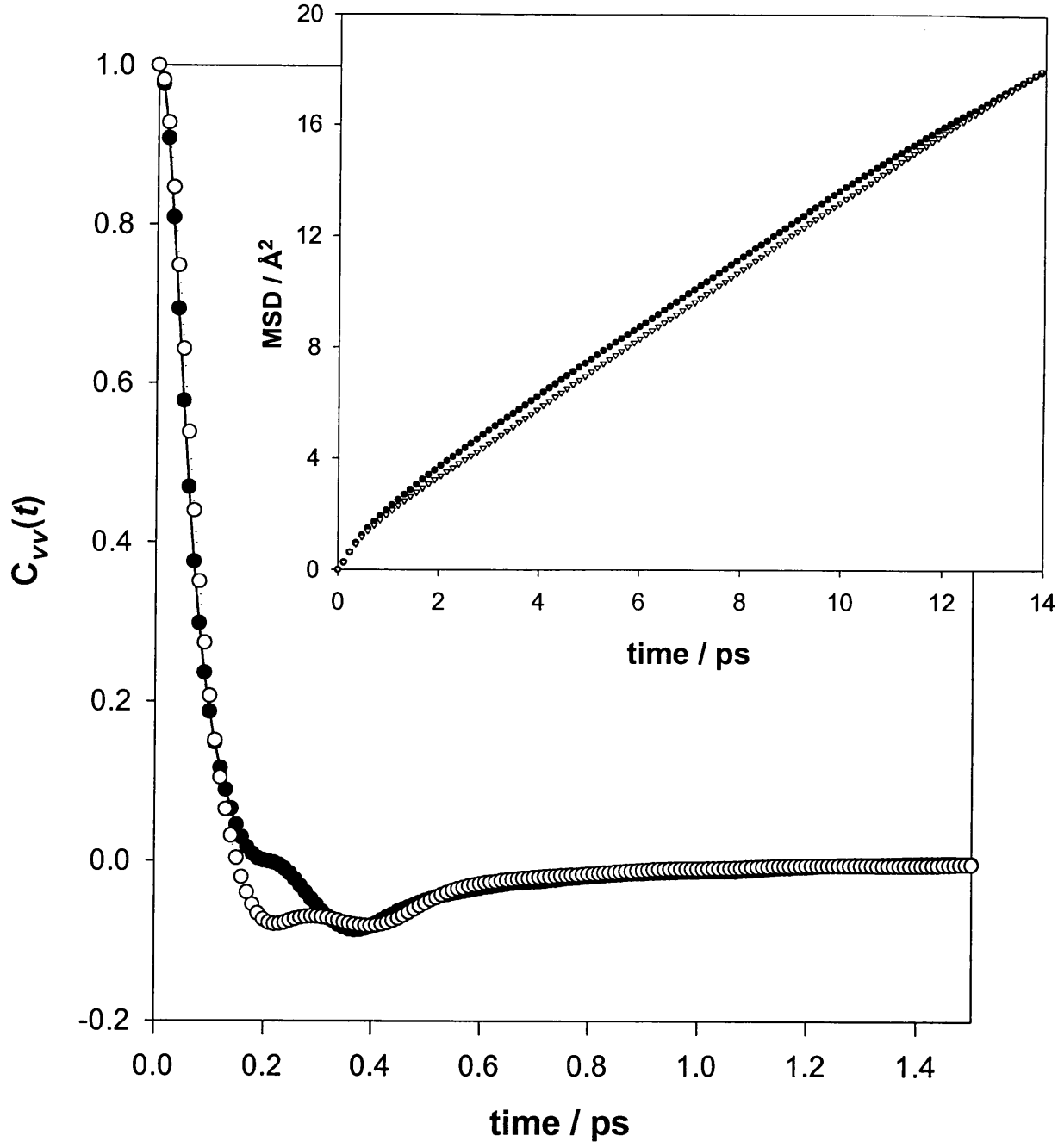

Figure 6.12 Normalised centre-of-mass (c.o.m) velocity auto correlation functions (VACFs), $C_{vv}(t)$ obtained for the H1+CH_3 model (•) and the APR6 model (O). Also shown in the inset is the c.o.m mean square displacement for the H1+CH_3 model (•) and the APR6 model (∇).

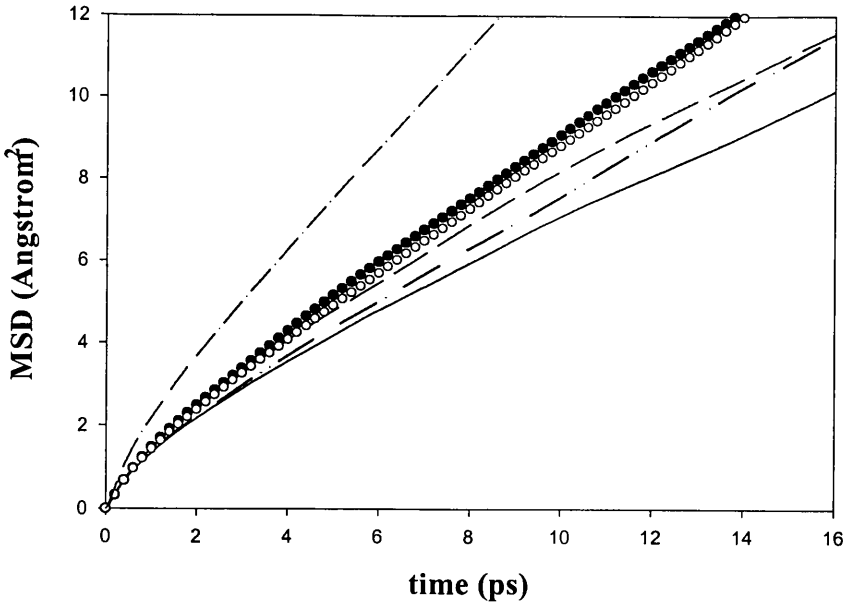

Figure 6.13 Centre-of-mass (c.o.m) mean square displacements (MSD) obtained for the six MD runs (run 1: solid line, run 2: • , run 3 :dashed line, run 4: dash-dot-dot, run 5: o and run 6: dash and dots).

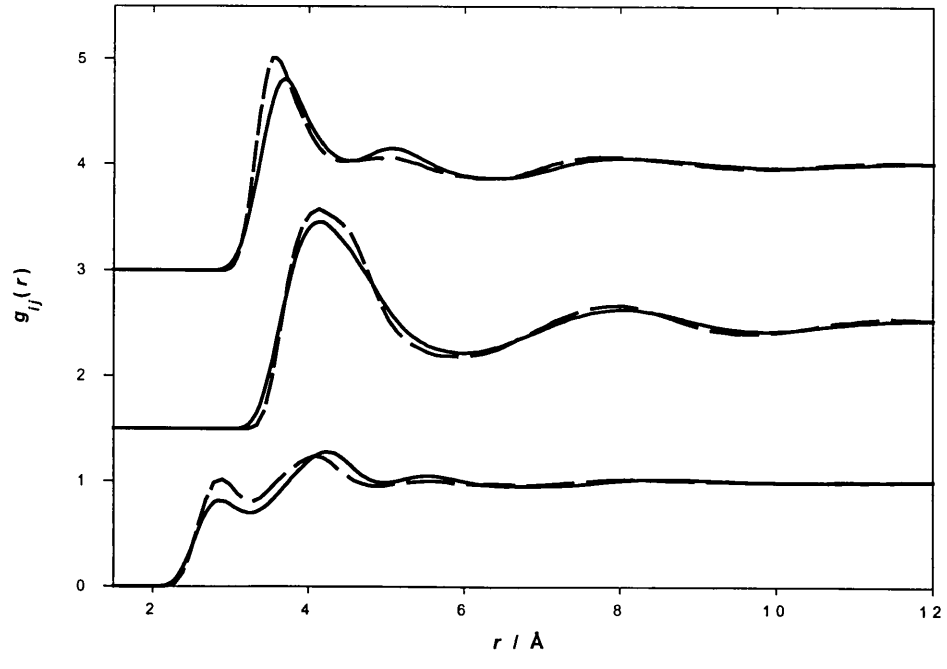

Figure 6.14 Ho-C (bottom), C-C (middle, displaced by +1.5) and O-C (top, displaced by +3) pdfs (dashed lines: the H1+CH_3 model, solid lines: the APR6 model).

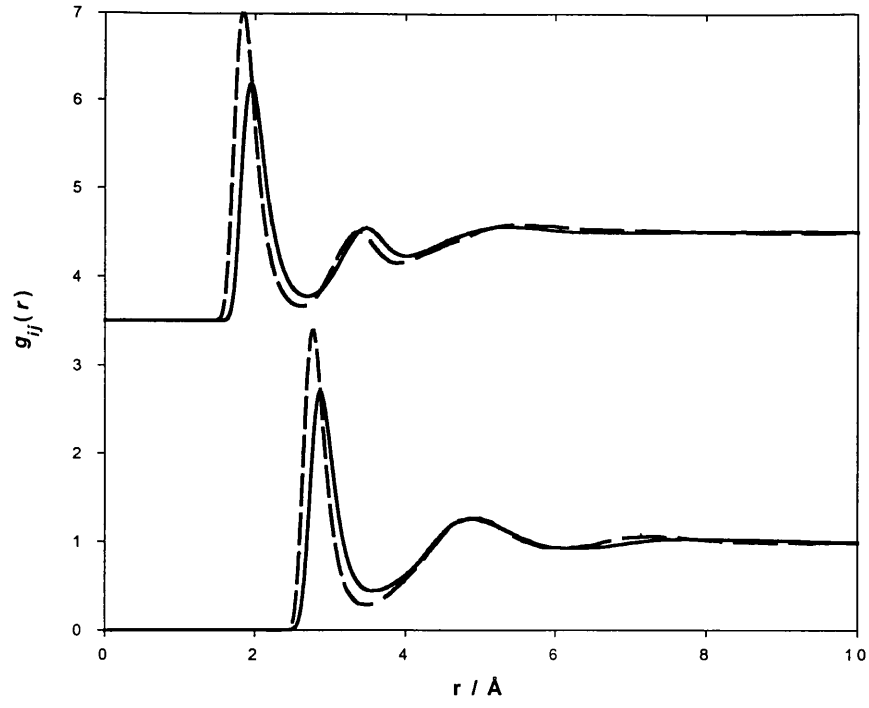

Figure 6.15 O-Ho (top, displaced by +3.5) pdf obtained from the MD simulations with the APR6 (solid line) and H1+CH_3 (dashed line) models. Comparison of O-O pdf (bottom) obtained with the APR6 (solid line) and the H1+CH_3 (dashed line) models.

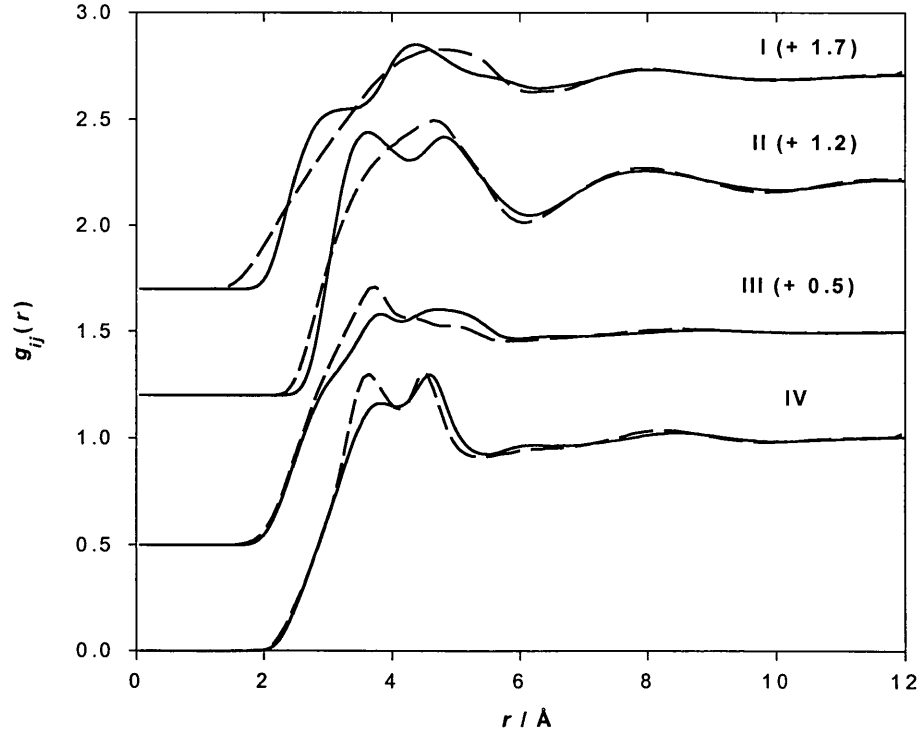

Figure 6.16 H-H (I), C-H (II), Ho-H (III) and O-H (IV) pair distribution functions (dashed lines: the H1+CH_3 model; solid lines: the APR6 model). These correlations have been obtained by averaging over the three methyl hydrogens: H_1, H_2 and H_3.

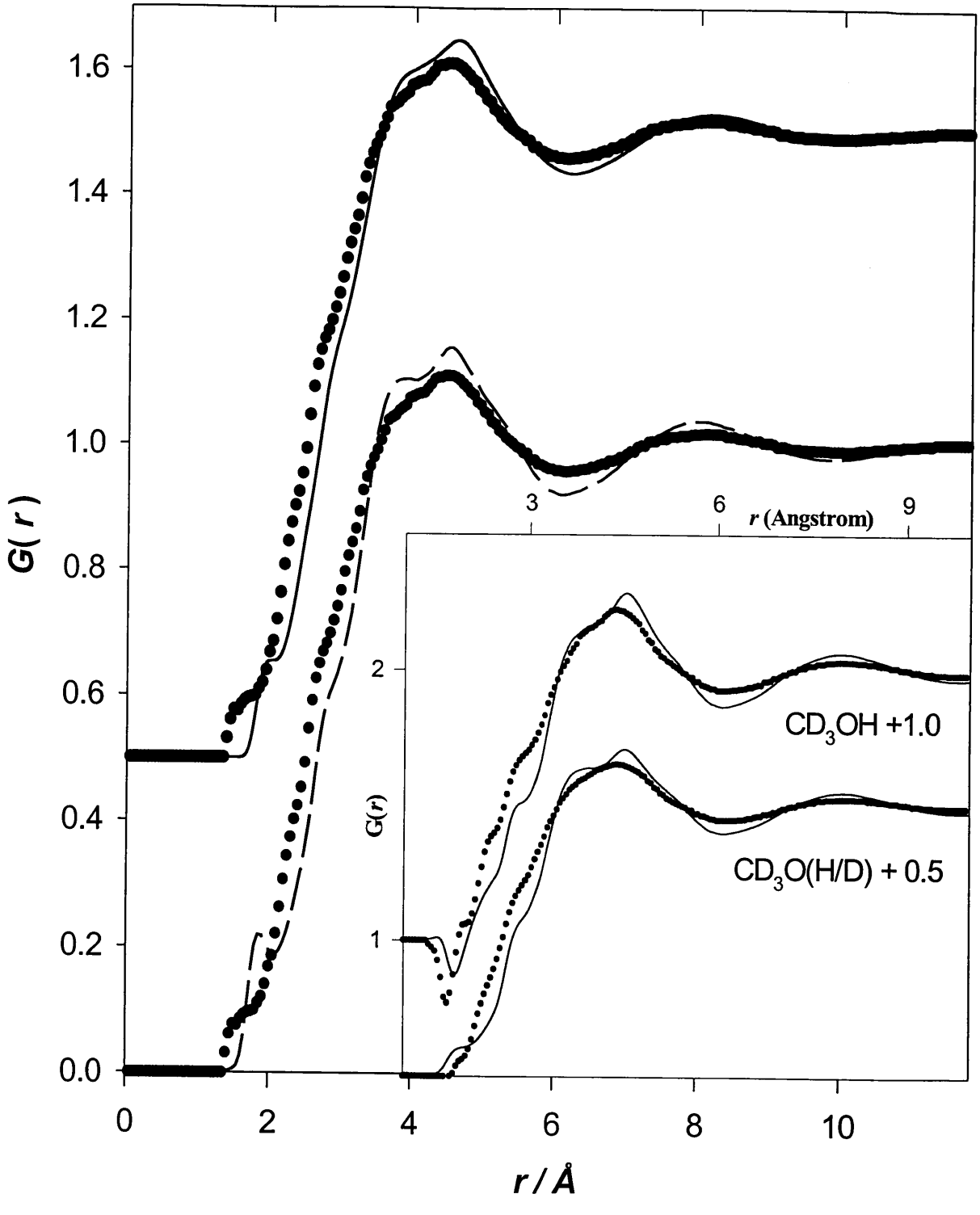

Figure 6.17 Inter-molecular radial distribution function for CD_3OD obtained from MD simulation with the H1+CH_3 model (dashed line) and the APR6 model (solid line displaced by +0.5) compared to the ND results (symbols). The inset shows the inter-molecular radial distribution functions for CD_3OH and $CD_3O(H/D)$ obtained from MD run 6 (lines) and ND experiments (circles).

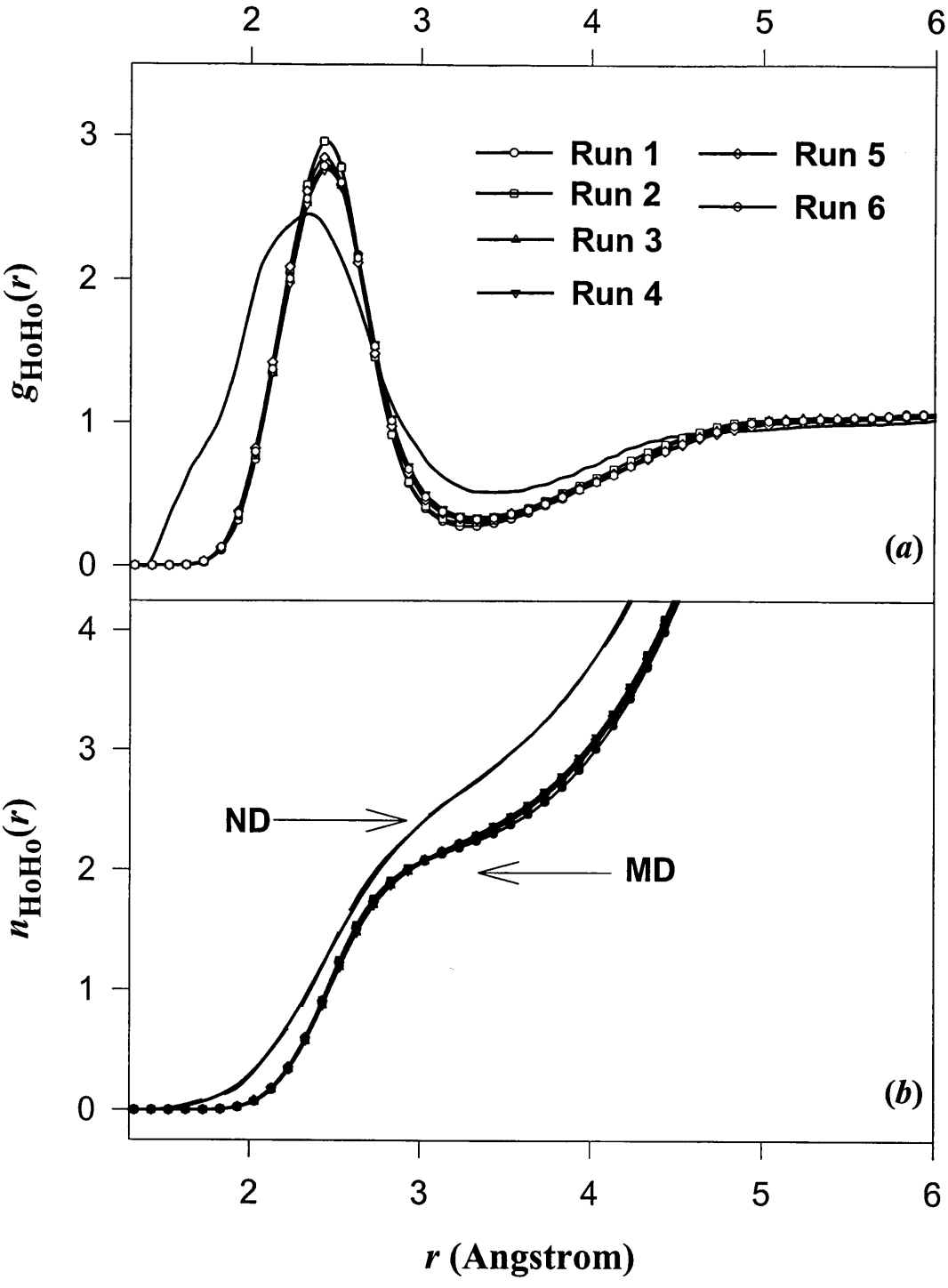

Figure 6.18 (*a*) Ho-Ho partial pair distribution function obtained from runs 1-6 (lines and points) as compared to the one obtained from ND H/D substitution experiments (line). (*b*) The running co-ordination number of Ho-Ho pair, n_{HoHo}, obtained from the ND data (solid line) and the MD runs 1-6 (line and points).

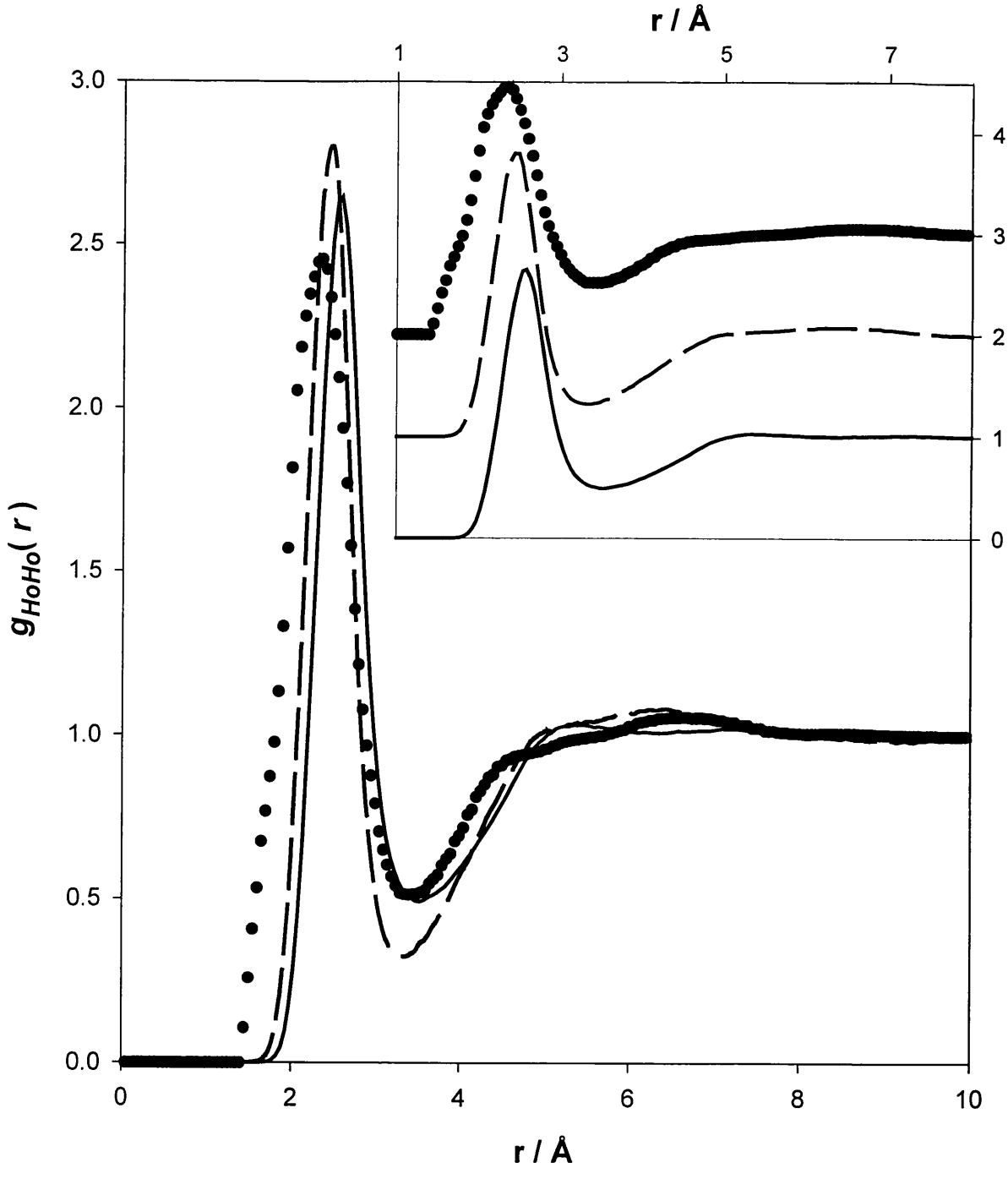

Figure 6.19 Ho-Ho partial distribution function for CD_3OD obtained from MD simulation with the H1+CH_3 model (dashed line) and the APR6 model (solid line) compared to the one obtained experimentally (symbols). Inset: APR6 model (bottom), H1+CH_3 model (middle, displaced by +1) and experimental (top, displaced by +2).

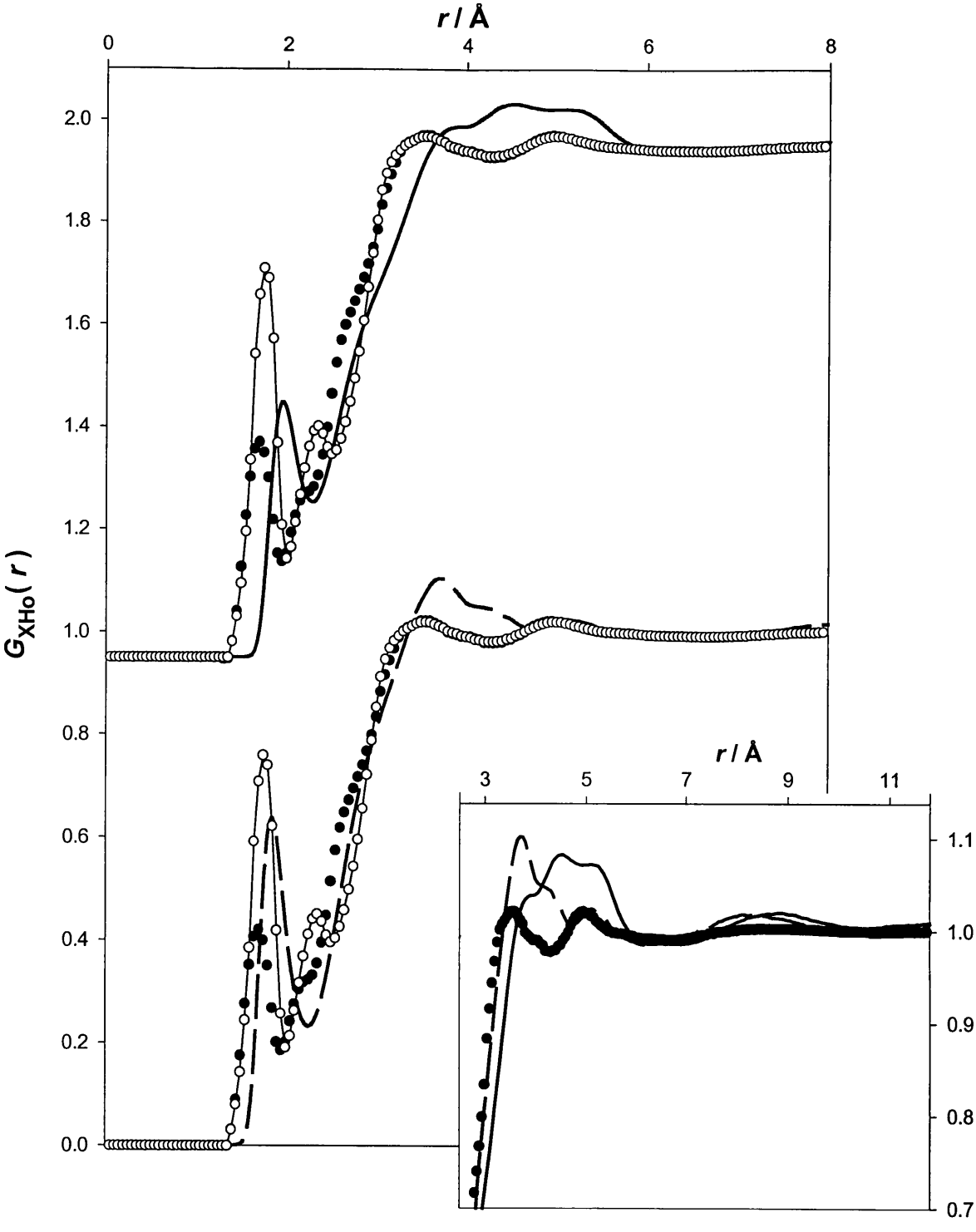

Figure 6.20 Inter-molecular X-Ho partial distribution functions obtained from MD simulations with the H1+CH_3 model (dashed line) and the APR6 model (solid line displaced by +0.95) compared to the ones obtained experimentally (white symbols fit 1, black symbols fit2). The same functions are overlaid on a different scale in the inset.

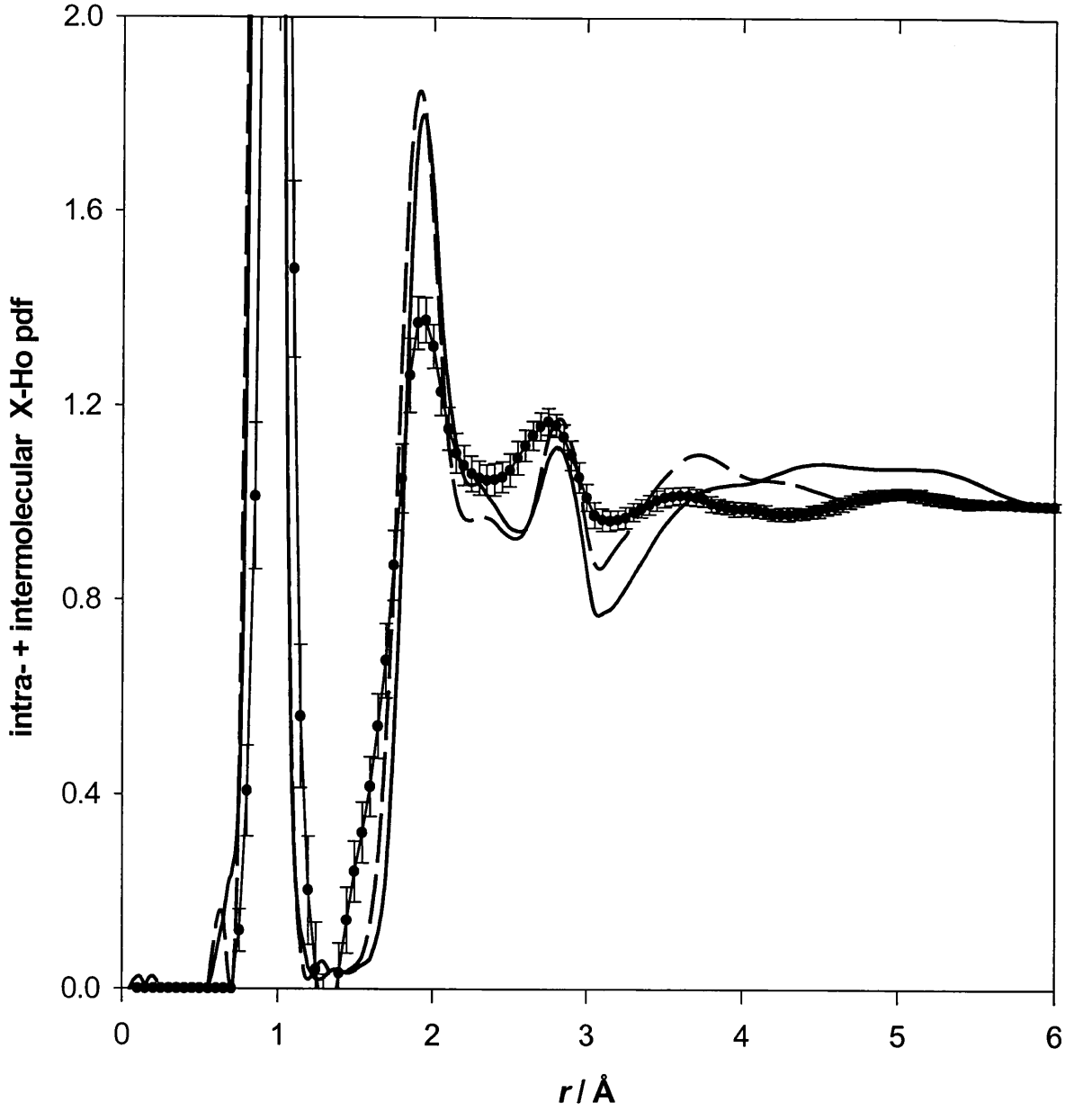

Figure 6.21 Intra- + intermolecular X-Ho partial distribution functions obtained from MD simulations with the H1+CH_3 model (dashed line) and the APR6 model (solid line), reconstructed according to the used geometrical model of methanol, as compared to the one obtained experimentally (symbols with error bars).

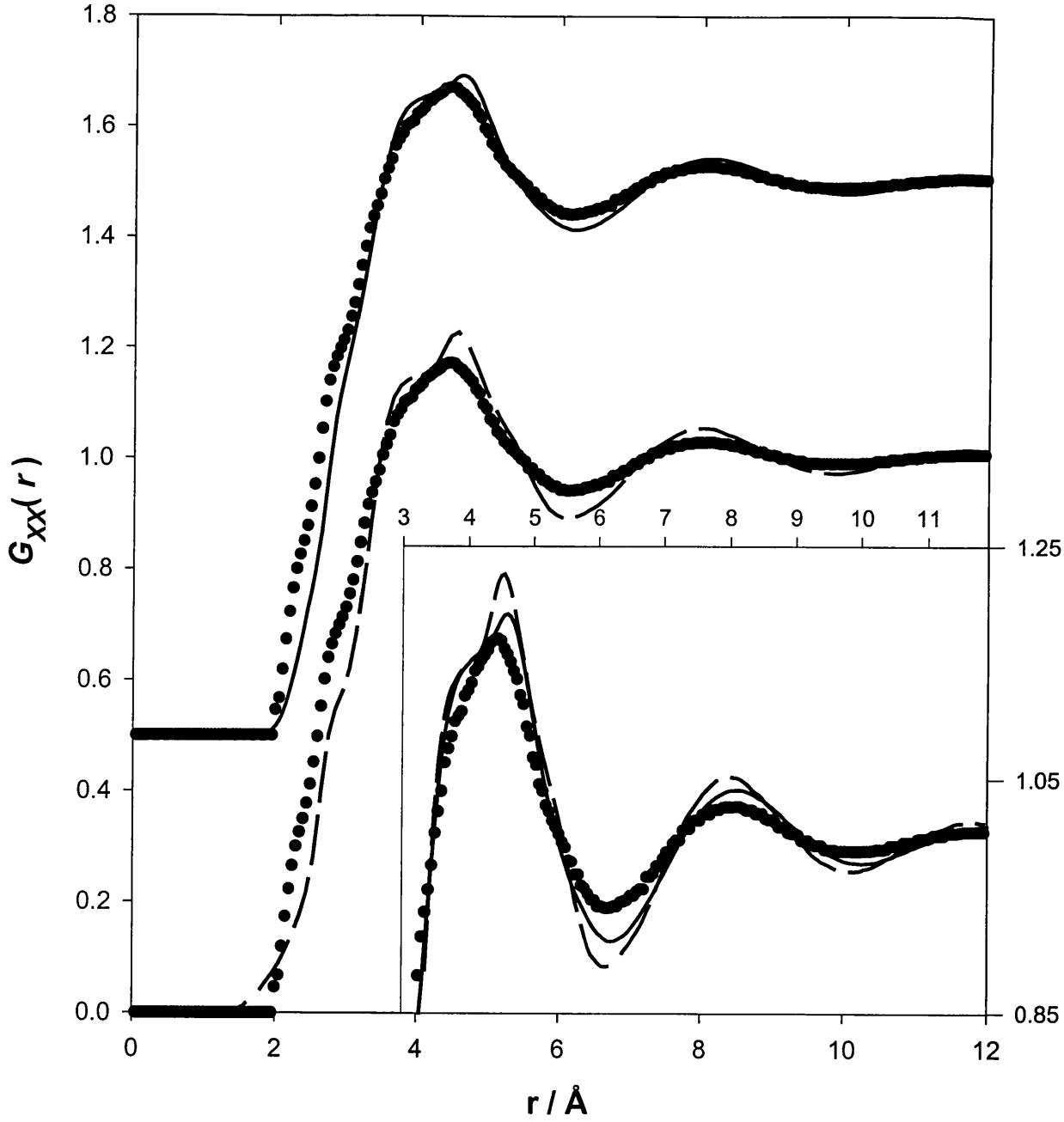

Figure 6.22 The X-X partial distribution functions obtained from MD simulations using the H1+CH_3 model (dashed line) and the APR6 model (solid line displaced by +0.5) compared to the partial distribution function obtained experimentally (symbols). The same functions are overlaid on a different scale in the inset.

Chapter 7

The structure of liquid benzene

7.1 Introduction

Structural studies on liquid benzene are not new. Actually, the pioneering work on the application of X-rays diffraction techniques to the study of liquids was carried out on liquid benzene by Debye and Scherrer in 1916, and since then, many investigations of the liquid by diffraction experiments (Katzoff, 1934; Pierce, 1937; Narten, 1967, 1977; Matsumoto, 1982; Misawa and Fukunaga, 1990; Felici et al., 1990; Bartsch et al., 1985; Cabaço et al., 1996, 1997) have been reported in the literature.

Narten (1967) fitted a geometrical model originating from the solid state structure (see figure 7.1) to the X-rays diffraction data obtained on the protonated (C_6H_6) liquid. From these studies he suggested a loose similarity of molecular arrangement between the liquid and the crystal (Cox et al., 1958). Three different configurations of benzene molecules in its solid phase have been reported (see figure 7.1): (i) T configuration, in which the planes of two molecules are inclined at 84° and with a molecular centre separation of 5.12 Å, (ii) L configuration, in which the pairs of molecules fit together like six-toothed bevel gear wheels whose axes are almost at right angles with a separation of 6.1 Å between the molecular centres, and (iii) parallel configuration, in which the axes of the two molecules are inclined at 27° with a centre-centre separation of 6 Å. In a later investigation, Narten (1977) interpreted the single X-rays diffraction data by decomposing the scattered intensity into contributions from CH groups rather than from C and H atoms separately. The

hydrogen atoms in a CH group were treated not like spikes pointing toward the corners of a tetrahedron, but rather like bulges in the electron density, showing a sizeable angular spread when viewed from the centre of the tetrahedron. The scattering of X-rays from a CH group was thus described, with good accuracy, by a single scattering factor. Since the spherical part of the scattering cross section was found to be nearly equal to the total cross-section of a CH group, Narten concluded that the spherical term is an excellent approximation to the scattering amplitude of the CH group in the liquid. Accordingly, benzene was treated as a homo-nuclear molecule consisting of CH groups with a spherical distribution of the electron density. Since the carbon nucleus was chosen as the origin of the scattering factor expansion, the structure function extracted was claimed to be descriptive of the carbon-carbon interactions in the liquid. The X-rays data were then used to find parameters of a Reference Interaction Site Model (RISM) of benzene (see section 1.2). The RISM results showed that although benzene molecules in the liquid were predominantly oriented in a L-shaped configuration, the stacked and T-shaped orientations were also observed. These results confirmed the earlier suggestion, that the arrangement of benzene molecules in the liquid is similar to that in the solid state.

Due to the large incoherent scattering cross section of hydrogen, and the problematic inelasticity corrections associated with light elements, ND studies have so far been carried out only with deuterated benzene (Matsumoto, 1982; Misawa and Fukunaga, 1990; Felici et al., 1990; Bartsch et al., 1985; Cabaço et al., 1996, 1997). The inter-molecular radial distribution function (rdf) accessible from a ND experiment comprises of a weighted sum of the C-C, D-D and C-D pair distribution functions, and it is is invariably featureless due to cancellation effects from the three contributing pairs. Thus, any attempts to reveal the microscopic structure of liquid benzene have been based on modelling the ND inter-molecular rdfs.

For instance Cabaço *et al.* (1997) employed molecular dynamics (MD) simulations using Williams (Williams and Cox, 1984; Williams and Houpt, 1986) (exp-6) potential to reproduce the inter-molecular ND rdf of deuterated benzene, C_6D_6. Their

simulation results showed that, the orientational local order in the liquid is almost isotropic. In contrast, Felici *et al.* (1990) fitted the ND inter-molecular rdf with a geometric model for which the liquid was divided into two zones around each molecule: (i) an inner one containing twelve first nearest-neighbours ordered in a solid-like structure, and (ii) an outer one composed of a completely homogeneous and disordered liquid. The results of the fitted model suggested that the local orientation of the molecule in the liquid is close to that in the crystal (Cox et al., 1958). Misawa and Fukunaga (1990) also modelled their ND structural data in a similar way, but found that the T-shaped configuration is the most probable orientation of benzene molecules in the liquid. Bartsch *et al.* (1986) combined their neutron and X-rays diffraction data to further interpret the structure of liquid benzene, and found that the preferred orientation of the molecules in the liquid is consistent with a L-shaped configuration. Such conflicting results may well be resolved by using the isotopic substitution technique of neutron diffraction (NDIS) to extract the three C-C, C-H and H-H pair distribution functions (pdfs). Since a reasonable agreement between the modelled and the experimental results at the inter-molecular rdf level is not sufficient to assess the quality of the model, comparison of the model results with the three experimental pdfs should provide a critical test of the validity of the model. However, the NDIS technique could not be applied so far to liquid benzene because, firstly isotopes of carbon are not suitable for ND measurements due to small contrast in their scattering lengths (^{12}C: 6.6511(16) fm and ^{13}C: 6.19(9) fm). Secondly, no instrument suitably optimised to deal with the light elements, and to minimise or reduce the inelasticity corrections was available.

Recently, A. K. Soper (SANDALS instrument scientist, ISIS, RAL) carried out a neutron diffraction experiment on liquid benzene by employing the H/D substitution technique on its hydrogen atoms. The ND data, kindly provided by him, are used here to extract the C-C, C-H and H-H pdfs both at the intra- + inter- and inter-molecular levels. These experimental results are then compared with those obtained from molecular dynamics (MD) simulations performed on 125 benzene molecules with three different force field models (Jorgensen and Severance, 1990; Smith and

Jaffe, 1996; Sun, 1998).

7.2 Experimental results

7.2.1 Distinct radial distribution functions (rdfs)

The raw neutron scattering intensities collected for C_6D_6, C_6H_6 and $C_6(H/D)_6$ samples under ambient conditions were analysed using the ATLAS suite of programs described in section 5.5. The distinct differential cross sections (DCSs) for the three samples extracted from the experimental data (see figure 7.2) were Fourier transformed using the minimum noise reconstruction (MIN) technique described in section 5.6. The low r cut-off (0.80 Å) was chosen to be lower than any known intra-molecular distance in benzene. The Q_{max} (35 $Å^{-1}$) used for Fourier transformation was a compromise between minimising the statistical noise effects at high-Q and, accounting for all the structural features at low-r. The $G^{dist}(r)$ for the three samples plotted in figure 7.3 can be split into three regions. The region beyond ~5 Å contains purely inter-molecular correlations, but it appear featureless. In the region between 0.8 and 1.5 Å where only intra-molecular correlations contribute, the first peak at 1.085±0.005 Å (see figure 7.3a) arises from the C-H intra-molecular distances. The size and sign of this peak varies according to the isotopic composition of the sample. For instance, for C_6H_6 the resulting peak is negative (see figure 7.3c). The second peak observed for all the rdfs at 1.40±0.005 Å corresponds to the C-C intra-molecular distances. From figure 7.3.b in which the C-H contributions do not overlap much with the C-C intra-molecular distances as compared to the rdfs of fully protonated and deuterated samples, the C-C bond length is found at 1.398 Å. In the third region from ~1.5 to 5 Å, no distances can be assigned from the distinct rdfs since inter- and intra-molecular correlations overlap.

7.2.2 Separation of intra- and inter- molecular correlations

Provided the intra-molecular structure is known, its contribution to the distinct DCS

can be calculated from equation 4.40. A survey of the intra-molecular structure of benzene investigated experimentally (see table 7.1) shows that in all the three phases, the geometry of the benzene molecule hardly changes. From this respect the C-H and C-C bond distances obtained from the distinct rdfs are in very close agreement with those obtained by Cyvin (1968) (see table 7.1) from gas phase measurements. It is worth noting that the internal motion of benzene at 300 K in the gas and liquid phases was theoretically investigated by Laaksonen *et al.* (1995). These authors performed MD simulations in which a single benzene molecule was treated as a solute, for which a set of quantum mechanical intra-molecular forces and atomic charges were calculated at each time step of the simulation. The surrounding 255 "solvent" molecules were described by using empirical intra-molecular force field, and a Lennard-Jones 12-site model for handling the intermolecular interactions between the benzene molecules. The results from these simulations showed, from a conformational analysis of the planar, boat, chair and twisted structures, that the structure of benzene in its liquid phase is effectively a planar hexagon. The geometry fluctuations are even smaller and damped than in the gas phase due to the stabilising effects of the inter-molecular interactions. Such a planar structure was thus adopted in the present studies. The bond lengths (C-C = 1.397 Å and C-H = 1.084 Å) and bond angles ($\angle$CCH = $\angle$CCC = 120°) were kept fixed, and only the Debye-Waller factor γ_{ij} (also given in table 7.1) were fitted to the distinct DCS of the deuterated benzene by using equation 4.40. This was done by minimising the agreement factor R defined by equation (5.49) between Q_{min} (6 Å^{-1}) and Q_{max} (35 Å^{-1}), which defines the range of the fit. The fitting was done by using both the simplex and the quasi-Newton algorithms (see section 5.7). Figure 7.2 shows the calculated intra-molecular structure factors along with their corresponding distinct DCSs. It can be seen that the intra-molecular contributions largely dominate the scattering. The inter-molecular DCSs, obtained after subtracting the intra-molecular structure factors from the distinct DCSs for the three samples were normalised to the molecular unit, and these are shown in figure 7.4.

$$i_m(Q) = \left(\sum_{\alpha}^{Nm} c_\alpha \bar{b}_\alpha\right)^{-2} \left(\frac{d\sigma}{d\Omega}\right)^{inter} \tag{7.1}$$

$$= \sum_{\alpha} \sum_{\beta} \frac{c_\alpha c_\beta \bar{b}_\alpha \bar{b}_\beta}{\left(\sum_{\alpha}^{Nm} c_\alpha \bar{b}_\alpha\right)^2} (S_{\alpha\beta}^{inter}(Q) - 1) \tag{7.2}$$

$$= \sum_{\alpha} \sum_{\beta} W_{\alpha\beta} (S_{\alpha\beta}^{inter}(Q) - 1), \tag{7.3}$$

The corresponding inter-molecular rdfs, obtained by Fourier transformation of the inter-molecular DCSs using the minimum noise reconstruction (MIN) technique (see section 5.6 and equation (4.38)), are plotted in figure 7.5. The back Fourier transformations also shown in figure 7.4 are in good agreement with the inter-molecular DCS functions from which the rdfs were obtained. When these inter-molecular rdfs are superimposed on their corresponding distinct rdfs (see figure 7.3) they appear to be relatively broad and featureless. These functions are thus, not very revealing since each one of them comprises of C-C, C-H and H-H inter-molecular correlations (see the neutron weight, $W_{\alpha\beta}$, listed in table 7.2 for the three samples). Moreover, it can be seen that all the experimental peaks exhibited in the C_6D_6, C_6H_6 and $C_6(H/D)_6$ distinct rdfs originate from the C-C, C-H and H-H intra-molecular distances, which dominate the whole pattern in these distribution functions..

7.2.3 H/D substitution analysis

a. Distinct pdfs

The three different isotopic contrasts on the hydrogens of benzene give rise to different weights of the three contributing pdfs to the DCS of the three different samples. Since each one of them comprises of C-C, C-H and H-H correlations,

setting X=C, S=H and i =1, 2, 3, respectively for C_6D_6, C_6H_6 and $C_6(H/D)_6$ in the expressions (4.44-54), the distinct C-H and C-C partial structure factors (PSFs) (see figure 7.6) were separated using the procedure (HDSUB_B) described in section 5.8. The distinct C-C and C-H pdfs obtained by Fourier transformation using the MIN technique are shown in figure 7.7. The back Fourier transforms of these functions shown (figure 7.6) superimposed on the functions from which they are obtained, are in good agreement with each other. The residual inelasticity effects, if still present in the PSFs, would have manifested themselves in the pdfs as high frequency ripples at low r thereby leading to incorrect co-ordination number associated with the C-H and C-C intra-molecular correlations. However, such a ripples cannot be seen in the pdfs shown in figure 7.7. The co-ordination numbers calculated for the C-H and C-C intra-molecular peaks (see figure 7.7) are within 6% of the expected value 1 and 2, suggesting that any residual inelasticity effects if still present in the data, are extremely small. The C-C pdf exhibits two well-defined peaks at 1.396 Å and ~2.42 Å which correspond respectively to the C_1-C_2 and C_1-C_3 –type of distances (see figure 7.1). A shoulder on the right side of the C_1-C_3 peak at ~2.80 Å corresponds to the C_1-C_4 –type of distances. The distinct C-H pdf shows three peaks at 1.082 Å, 2.156 Å, and 3.40 Å corresponding respectively to the C_1-H_1, C_1-H_2 and C_1-H_3 type of intra-molecular distances. A small hump centred at ~3.89 Å arises from the C_1-H_4 type of distances. These values for the intra-molecular distances observed in the experimental C-C and C-H pdfs are fully consistent with the intra-molecular distances used for the removing the intra-molecular structure from the various distinct DCSs.

b. Inter-molecular pdfs

The inter-molecular H-H, C-H and C-C PSFs (see figure 7.8) were extracted from the distinct DCSs after subtracting the intra-molecular contributions. These were Fourier transformed to obtain the corresponding inter-molecular pdfs (see figure 7.9). Although these functions will be discussed in details, and compared with their simulated counterparts in section 7.4, it is worth noting that the back Fourier

transforms of the C-C and C-H pdfs shown (figure 7.8) superimposed on the data from which they are obtained, are in good agreement. For the H-H PSF however, a slight residual inelasticity effect can still be seen in the data (see figure 7.8). This was removed by subtracting from the data a slowly varying background in Q during the Fourier transformation (see section 5.6). The origin of a small peak at ~2.4Å in the H-H pdf (see figure 7.9) can thus not be ascertained. The residual inelasticity effects might have given rise to this feature or it may also be real since such inter-molecular H···H distances have been observed in the solid phase of benzene both experimentally (Cox et al., 1958) and by computer simulations (Linse, 1984; Anderson et al., 1987).

7.3 The MD simulations results

7.3.1 Inter-molecular potential models

As mentioned in section 3.2, the investigation of the structure of small clusters, particularly dimers, by Quantum mechanical (QM) calculations present an attractive way of devising potential models. For liquid benzene, although this approach was early employed (Karlstrom et al., 1983; Linse, 1984) as a powerful alternative to the empirical method used so far (Evans and Watts, 1975, 1976a, 1976b; Steinhauser, 1982; Claessens et al., 1983; Adam et al., 1984), at high level of theory it is unfortunately not always possible to use techniques such as analytic gradient method to sample automatically the dimer interaction surface energy (Spirko et al., 1999). Despite this, Smith and Jaffe (1996) made a detailed study of the dimer structure, and proposed a new potential model for liquid benzene that qualitatively reproduced their QM results (Jaffe and Smith, 1996). For each atomic pair the force field, in which the cross interaction (C-H) term did not originate from any combination rule, consisted of a sum of an exp-6 and a Coulombic term :

$$V_{ij}(r) = \frac{q_i q_j}{4\pi\varepsilon_0 r_{ij}} + A_{ij}\exp(-r_{ij}/B_{ij}) - \frac{C_{ij}}{r_{ij}^6}, \qquad (7.4)$$

where A_{ij}, B_{ij}, C_{ij} are the potential parameters between sites i and j of distinct molecules, q_i is the partial charge on site i and, r_{ij} is the site-site separation. Table 7.3 summarises the force field parameters used in the MD simulations.

Since the modelling of the inter-molecular interactions is sometimes too complex to be purely considered by the QM methods, molecular mechanics (often combined with the use of *ab initio* calculations) has played a significant role in trying to circumvent this difficulty (Jorgensen et al., 1984). One of the key features of the force fields so devised, is that they are usually designed to be transferable within specific classes of molecules. For instance, the all-atom model of benzene by Jorgensen and Severance (1990) is an extension of the well-known all-atom OPLS force field developed by Jorgensen and co-workers (Jorgensen and Tirado-Rives, 1988; Jorgensen and Briggs, 1989; Jorgensen et al., 1990) for organic and biomolecular systems. The functional form of this model is given for each pair of atoms by the sum of a Coulombic and a Lennard-Jones (LJ-12-6) term:

$$V_{ij}(r_{ij}) = \frac{q_i q_j}{4\pi\varepsilon_o r_{ij}} + 4\varepsilon_{ij}\left[\left(\sigma_{ij}/r_{ij}\right)^{12} - \left(\sigma_{ij}/r_{ij}\right)^{6}\right], \tag{7.5}$$

where ε_{ij} and σ_{ij} are the LJ-12-6 parameters between sites i and j of distinct molecules. q_i is the partial charge on site i, and r_{ij} is the separation between the sites i and j. The cross interactions were obtained from the geometric mean combining rules: $\varepsilon_{ij} = \sqrt{\varepsilon_{ii}\varepsilon_{jj}}$ and $\sigma_{ij} = \sqrt{\sigma_{ii}\sigma_{jj}}$. The force field parameters for the LJ-12-6 model are also included in table 7.3. The third force field model used in current simulations on liquid benzene has also its origin in a general force field, called COMPASS (Sun, 1998) (condensed-phase optimised molecular potentials for atomistic simulation studies), recently developed using a hybrid approach consisting of both *ab initio* and empirical methods. The functional form of the inter-molecular interactions for this force field is given for each pair of atoms by the sum of a Lennard-Jones (LJ-9-6) and Coulombic terms:

$$V_{ij}(r_{ij}) = \frac{q_i q_j}{4\pi\varepsilon_0 r_{ij}} + 2\varepsilon_{ij}\left(\frac{r_{ij}^0}{r_{ij}}\right)^9 - 3\varepsilon_{ij}\left(\frac{r_{ij}^0}{r_{ij}}\right)^6 . \tag{7.6}$$

The parameters ε_{ii}, r_{ii}^0 and the partial charges q_i for the LJ-9-6 model are included in table 7.3. The cross interactions (also listed in table 7.3) are obtained from the Waldman and Hagler (1993) sixth power arithmetic mean combining rules:

$$\varepsilon_{ij} = 2(\varepsilon_{ii}\varepsilon_{jj})^{1/2}\frac{(r_i^0 r_j^0)^3}{(r_i^0)^6 + (r_j^0)^6} , \tag{7.7}$$

$$r_{ij}^0 = \left(\frac{(r_i^0)^6 + (r_j^0)^6}{2}\right)^{1/6} . \tag{7.8}$$

7.3.2 Methodology

Each benzene molecule was treated as a rigid, non-polarisable planar object. For the three different MD runs the benzene molecule consisted of 12 sites, corresponding to the six carbons (C) and the six hydrogens (H). The geometrical model (referred to as fit in table 7.1) for the molecule was the same as that used for removing the intra-molecular structure from the ND distinct DCSs. The MD simulations were performed at 298.15 K in the NVE ensemble with 125 benzene molecules placed in a cubic box of edge length 26.48 Å in order to match experimental density, 0.873 g/cm^3 (Deul et al., 1991) of benzene at 298 K. A cut-off radius equal to half the box length was set for all the interactions (see section 3.4) and, periodic boundary conditions (see section 3.3) were applied. In all the MD runs, time-step was equal to 2 fs. In addition to the Verlet leap-frog algorithm (see section 3.5) used for integrating the equations of the translational motion, the Fincham's implicit quaternion algorithm (see section 3.6.2) (FIQA) was used for rotational motion of rigid bodies. The long-range interactions were treated using Ewald summation (see section 3.7.3) (EW). Table 7.4 summarises the details of the various MD simulation runs.

7.3.3 Validation of the simulations

The configurational energy, U (see section 3.8.1), and translational diffusion coefficient, D (see section 3.8.2) of the centre-of-mass of fully hydrogenated benzene molecule, averaged over equilibrated runs are listed in table 7.4 together with the available experimental data. The computed average energies and pressures for all the runs (see table 7.4) compare very well with the experimental values (American Petroleum Institute, 1953; Yaws, 1977). The diffusion coefficient was calculated from both the centre of mass (c.o.m) mean square displacement (MSD) (see figure 7.10), *via* the Einstein relation and according to the Green-Kubo relation by integrating the velocity auto-correlation function (VACF) (see figure 7.10). In principle, within the same potential model both methods should give the same results, but inadequate statistical averaging leads in practice to a spread of values (seen in table 7.4). Comparison of the simulated diffusion coefficients with the LJ-9-6 and exp-6 models shows a satisfactory agreement with the experimental value though the exp-6 model gives slightly better results. However, the results obtained with the LJ-12-6 model are in poor agreement with the experimental results, probably because the lower temperature in this case induces fewer collisions in the system. The reasonably good agreement as seen above between the simulated and experimentally determined properties (see table 7.4) validates the present MD simulations.

7.3.4 The simulated inter-molecular pdfs

The pair distribution functions (pdfs), $g_{\alpha\beta}(r)$ computed for all the runs from the equilibrated configurations are displayed in figure 7.11. Although three different potential models were used, the partial pdfs obtained from them show an impressive agreement with each other. Similarly, when these functions are Fourier transformed and compared in Q-space (see insets figure 7.11), they match each other perfectly. Thus, in the following section dealing with a comparison of the experimental and simulation results, the discussion will be based on results obtained from only one model. Although the simulation using the LJ-12-6 model reproduced the

experimental diffusion coefficient only poorly, the structural results from this model are of similar quality to those obtained with the others two models. Surprisingly, the same two models: exp-6 and LJ-12-6 predicted different structures for the benzene dimer. While the lowest energy structure in the exp-6 model was found to be a parallel displaced form with no energy minimum corresponding to the T-shaped or sandwich dimmers (Jaffe and Smith, 1996), the global minimum of the interaction energies in the LJ-12-6 model corresponded to a T-Shaped structure for the dimer (Jorgensen and Severance, 1990). Since the C-C, C-H and H-H pdfs obtained from the MD simulations using the two (exp-6 and LJ-12-6) models resemble each other so closely (see figure 7.11), it is difficult to comprehend the predictions of two different (T-shaped vs. parallel displaced) dimer conformations resulting from the same two models. For the same reasons, it is also difficult to foresee that the two models would lead to different orientational correlations between nearest-neighbours. While some differences in the thermodynamic, dynamic and structural properties obtained from the exp-6 and LJ-9-6 models could have been expected since both models are of different nature, they appear to produce similar results. This shows that a "good" general model can perform equally well as a force field designed especially for a given system. Moreover, for the exp-6 model, Smith and Jaffe (1996) emphasised that its ability to reproduce the structure of liquid benzene better than the other force fields (Evans and Watts, 1976; Williams and Starr, 1977; Claessens et al., 1983) was due to the softer C-H pair potential which did not originate from any combination rule. However, it is worth noting that our results show no difference not only between the C-H pdfs obtained from exp-6 model and LJ models (see figure 7.11), but also between the other two partials obtained from different models. For both the LJ models (LJ-12-6 and LJ-9-6) the C-H interactions were, in fact, obtained from the combination rules.

7.4 Comparison of experimental with simulation results

7.4.1 Inter-molecular radial distribution function

The simulated pdfs, $g_{CC}(r)$, $g_{CH}(r)$, and $g_{HH}(r)$ obtained from each of the three simulations were combined according to the neutron weights, $W_{\alpha\beta}$, (listed in table 7.2) in order to reconstruct the inter-molecular radial distribution functions (rdfs) for each sample (C_6D_6, C_6H_6 and $C_6(H/D)_6$). The simulated intermolecular rdfs for C_6D_6 corresponding to the three different models are compared with their neutron counterpart in r- and, after Fourier transformation, in Q-space, in figure 7.12. All the models satisfactorily reproduce the experimental functions (inter-molecular rdf and DCS). The experimental $C_6(H/D)_6$ rdf (see figure 7.13) comprises mainly of C-C and C-H contributions (see table 7.2) and one can see that the agreement of all the simulated rdfs with the corresponding experimental function is quite reasonable. However, for C_6H_6 (see figure 7.14) the oscillations occurring at larger distances are slightly out of phase with the ND results, and in the region 1.7 - 6.5 Å the agreement is only qualitative. While the simulated functions reveal two peaks at ~ 5.0 Å and ~ 6.2 Å, the experimental $G(r)$ shows a single broad peak at ~ 5.7 Å. In the low-r range (up to ~ 3.6 Å), the simulated structural features are shifted towards higher distances by about 0.35 Å. In addition, the first experimental peak at 2.1 Å, originating from the positive contribution of the H-H correlations occurs at lower r, and is higher than all its MD equivalents. Similarly, the negative peak at 2.85 Å originating from the negative contribution of the C-H pair in the experimental $G(r)$, occurs at 3.2 Å in the simulated functions. Such differences manifest themselves in the Q-space data (see inset figure 7.14), and the agreement between the experimental and simulated functions is poor. The reason for a poor agreement in the $G(r)$ of C_6H_6 between ND and MD can be easily understood if one looks at table 7.2, which reveals that the neutron weights of the contributing pairs in C_6H_6 are an order of magnitude bigger than in the other two samples. This has two important consequences. Firstly, any small differences between the experimental and simulated functions observed in the case of C_6D_6 and $C_6(H/D)_6$ get magnified in the $G(r)$ of C_6H_6. This is especially

true in the low-r region where only H-H and C-H correlations contribute, and both contributions are of opposite sign. Secondly, the shortest C-H and H-H distances get nicely isolated in the rdf of C_6H_6. In this respect the rdf of hydrogenated benzene is better than C_6D_6 and $C_6(H/D)_6$ rdfs in checking the relative performance of different models in better reproducing the experimental data.

7.4.2. Inter-molecular pair distribution functions

Interpretation of preferred orientations in liquid benzene from different models has so far been based on first checking that the model reproduces the C-C pdf obtained from X-rays diffraction (Narten, 1977) or the inter-molecular rdf obtained from ND of the deuterated sample only (Bartsch et al., 1985; Cabaço et al., 1997). Often, simulators (Steinhauser, 1982; Claessens et al., 1983; Linse, 1984; Gupta et al., 1988; Smith and Jaffe, 1996; Jorgensen and Severance, 1990) also tried to reproduce the C-C partial pdf obtained by X-rays diffraction (Narten, 1977) as a criteria to judge the quality of the potential models used in the simulations. Interestingly, the C-C pdf has been obtained in the present studies purely from the H/D substitution technique of ND and these results also permit to investigate to what extent the X-rays distribution function of Narten represents the C-C pdf. In this respect, figure 7.9 compares the ND and X-rays C-C pdf obtained by Narten. The two experimental pdfs are found to be quantitatively different up to r-values of ~6 Å. The X-rays partial overestimates the distance of closest approach between carbons atoms. The shoulder at ~3.5 Å interpreted by Narten as resulting from a small number of molecules having a "stacked" configuration in the liquid is not present in the ND pdf. Also, the peak at ~ 4.0 Å observed in the X-rays data and found to be consistent to L configurations becomes a shoulder in the neutron pdf. In addition, the peaks at ~4.9 and ~6.1 Å are shifted to larger distances in the X-rays pdf. These differences manifest themselves in the PSFs (see figure 7.8 inset). For instance, the valley at ~2.6 $Å^{-1}$ is shifted towards slightly higher-Q values in the X-rays data, and the height of the two main peaks at ~1.4 and 2 $Å^{-1}$ are different. While the first peak in the neutron data is lower than its X-rays equivalent, the second at 2 $Å^{-1}$ is higher. One wonders if such

differences between both the C-C pairs originate from a difference in the intra-molecular models used for extracting the inter-molecular parts of the distinct scattering functions. Figure 7.6 inset reveals that in the Q region beyond ~6 $Å^{-1}$ where mainly the intra-molecular correlations occur, neutron and X-rays data are in excellent agreement. However, significant differences can be noticed in the low Q region. The molecular model used in the X-rays work and the neutron C-C intra-molecular structure factor are superimposed to each other they show a perfect match in the Q-range 0-16 $Å^{-1}$ (figure 7.7 inset) of the X-rays data. It can thus be concluded that the differences observed in the two experimental inter-molecular C-C pdfs do not originate from the removal of the intra-molecular structure. Since X-rays are scattered by electrons, it may be that the π-electron cloud correlations contribute to the X-rays' inter-molecular partial significantly. The X-rays function is thus not ideally suited for comparing with the pdf computed from MD simulations for which the interacting sites are located on the position of the various carbon nuclei. This is crucial since most earlier computer simulations (Steinhauser, 1982; Claessens et al., 1983; Linse, 1984; Gupta et al., 1988; Smith and Jaffe, 1996; Jorgensen and Severance, 1990) discussing microscopic structural details, such as orientational correlations between neighbouring molecules in liquid benzene, either reproduced the lower or the higher-r range of the C-C X-rays pdf of Narten. These simulations, however, failed to reproduce the experimental features over the entire r-range. Also, the simulated C-C pdfs obtained from our own simulations using three different models fail to reproduce the lower r-range of the X-rays data. In view of the above discussion, structural interpretation of liquid benzene done in the past is still open to question, and remains to be confirmed at a quantitative level. Since the interacting sites of the models used in the simulations are placed on the nuclei, it is more natural to compare the simulation results with those obtained from ND rather than X-rays. From this point of view, it is worth noting (see figures 7.9 and 7.11) that the three different models reproduce equally well the ND C-C pdf at a quantitative level.

The simulated C-H and H-H partial pdfs (see figure 7.9) do not show the same level of agreement with their neutron counterparts as the C-C partials. For the C-H partial,

although the comparison is only qualitative (see also inset of the figure for a comparison in Q-space), the simulated pdfs underestimate the closest approach correlations. Also, in the region ~ 2.7-5.0 Å, the experimental structural features seem to be averaged out by all the three simulations (only one model is shown for clarity). For the H-H partial pdf, the disagreement between ND and MD is even more pronounced. The closest approach of the hydrogen atoms is underestimated and several features are not reproduced at all by the three simulations. For instance, the experimental peak at ~3.5 Å is not reproduced by the simulations. Differences between ND and MD can also be observed in the H-H PSFs in the Q-space. It appears that the MD simulations could satisfactorily reproduce the ND inter-molecular rdfs for C_6D_6 and $C_6(H/D)_6$ due to cancellation errors between the C-H and H-H partials when weighted sums are taken over all the three partials to construct neutron-equivalent simulated inter-molecular rdfs. Since all the MD simulations systematically underestimated the closest approach of the C-H and H-H correlations, the experimental C_6H_6 inter-molecular rdf is poorly reproduced by the MD simulations.

7.5. Conclusions

The three inter-molecular C-C, C-H and H-H pair distributions functions (pdfs) in liquid benzene have been extracted for the first time, from a neutron diffraction (ND) experiment by employing the H/D isotopic substitution technique. The ND structural results have been compared with those obtained by the MD simulations using three different model potentials. One of the key features of this study is that all the simulated C-C partials are found to reproduce in a quantitative way the experimental partial extracted from the ND measurements, while their comparison with the X-rays (Narten, 1977) partial is even far from qualitative. The X-rays C-C partial has been used in the past for validating most of the potential models used so far for simulating liquid benzene. These models were then used to predict a variety of structural characteristics of the liquid. All the models tested here reproduce very well the experimental inter-molecular radial distribution functions of C_6D_6 or $C_6(H/D)_6$

obtained from ND. However, it has been clearly illustrated that the capability of a model to reproduce the inter-molecular rdf in C_6D_6 is not a proof that a fine tuning of the potential model has been achieved since significant discrepancies between the MD and ND results still exist for the C-H and H-H pdfs. Such marked differences contribute to the poor agreement observed between the MD and ND results for the C_6H_6 inter-molecular rdf, and highlight the need to further refine the potential model used in the simulations. This is particularly true if a detailed analysis of the preferred orientational correlations, which might exist in the liquid, is required.

Table 7.1. Average benzene structure in terms of intra-molecular distances ($r_{\alpha\beta}$ / Å) and associated Debye-Waller factors ($\gamma_{\alpha\beta}$ / Å) obtained by least squares refinement as compared to other available experimental data.

parameters	*fit*	*Benzene (l)*	*Benzene(g)*	*benzene(s)*
r C-C	1.397[r]	1.390[g], 1.416[j], 1.38[k],1.395[m] 1.41[n], 1.378[o], 1.389[p]	1.397[d], 1.397[e], 1.396[f]	1.392[a], 1.398[b], 1.398[c], 1.3978[h], 1.3972[i], 1.41[l]
r C-H	1.084[r]	1.082[g], 1.09[j], 1.09[k], 1.081[m] 1.072[o], 1.083[p]	1.084[d], 1.083[f],	1.077[b], 1.090[c], 1.0825[h], 1.0864[i], 1.085[l]
γ C_1-C_2	0.0605	0.064764[g], 0.0849[n], 0.038[o], 0.0104[p]	0.0459[q]	
γ C_1-C_3	0.0776	0.076902[g], 0.101[n], 0.035[o], 0.0017[p]	0.0547[q]	
γ C_1-C_4	0.0873	0.082208[g], 0.06[n], 0.037[o], 0.0034[p]	0.0597[q]	
γ C_1-H_1	0.0776	0.092246[g], 0.037[o], 0.0715[p]	0.0771[q]	
γ C_1-H_2	0.1089	0.1218[g], 0.07[o], 0.0713[p]	0.1004[q]	
γ C_1-H_3	0.1326	0.119784[g], 0.08[o], 0.0989[p]	0.0960[q]	
γ C_1-H_4	0.0873	0.116396[g], 0.08[o], 0.1370[p]	0.0942[q]	
γ H_1-H_2	0.1931	0.18914[g], 0.08[o], 0.1283[p]	0.1561[q]	
γ H_1-H_3	0.1640	0.160258[g], 0.08[o], 0.1674[p]	0.1321[q]	
γ H_1-H_4	0.1059	0.142646[g], 0.08[o], 0.095[p]	0.1191[q]	
R_{factor}	0.053			

a: crystal structure of benzene at -3°C by X-rays diffraction from Cox et al. (1958); b: ND of solid benzene at -55°C, from Bacon et al. (1964); c: ND of solid benzene at -135°C, from Bacon et al. (1964); d: raman spectroscopic measurements, from Langseth and Stoicheff (1956); e: electron diffraction measurements, from Bastiansen (1957); f: infrared measurements of C_6H_6 and C_6D_6 , from Cabana et al. (1974); g: ND measurements of C_6D_6 in the temperature range 282-348K, from Cabaço et al. (1997); h: neutron powder diffraction data collected at 4K on C_6D_6 , from David et al. (1992); i: single crystal neutron structure refinement of C_6D_6 at 15K, from Jeffrey et al. (1987); j: ND measurements of C_6D_6 at room temperature, from Misawa and Fukunaga (1990). k: ND measurements on C_6D_6 at room temperature, from Felici et al. (1990); l: NMR investigation of solid benzene, from Andrew and Eades (1953); m: ND measurements on C_6D_6 at room temperature, from Matsumoto (1982); n: X-rays diffraction of C_6H_6 at 298K, from Narten (1967); o: ND measurements of room temperature C_6D_6 at a reactor source using λ=0.5 Å, p: using λ=0.7 Å, from Bartsch et al. (1985); q: calculated from spectroscopic data, from Bastiansen and Cyvin (1957); r: fixed to the value given by Langseth and Stoicheff (1956), and Cyvin (1968).

Table 7.2. The neutron weights of the various intermolecular radial distribution functions in liquid benzene.

pair α-β	C_6D_6	$C_6(H/D)_6$	C_6H_6
C C	0.249	0.673	5.227
C H	0.500	0.295	-5.881
H H	0.251	0.032	1.654

Table 7.3. Force field parameters used for the three MD simulations of liquid benzene.

Parameter	exp-6	Parameter	LJ-12-6	Parameter	LJ-9-6
A_{CC}, kJ/mol	330748.8264	ε_{CC}, kJ/mol	0.29288	ε_{CC}, kJ/mol	0.2847024
A_{CH}, kJ/mol	16278.2784	ε_{CH}, kJ/mol	0.191735	ε_{CH}, kJ/mol	0.1136234
A_{HH}, kJ/mol	9983.84328	ε_{HH}, kJ/mol	0.12552	ε_{HH}, kJ/mol	0.0962964
B_{CC}, Å	0.27777778	σ_{CC}, Å	3.55	r^0_{CC}, Å	3.915
B_{CH}, Å	0.29282577	σ_{CH}, Å	2.93104	r^0_{CH}, Å	3.574
B_{HH}, Å	0.26737968	σ_{HH}, Å	2.42	r^0_{HH}, Å	2.878
C_{CC}, kJ. Å^6/mol	2174.20524				
C_{CH}, kJ. Å^6/mol	520.9049088				
C_{HH}, kJ. Å^6/mol	103.0957632				
q_C(e)	-0.11	q_C(e)	-0.115	q_C(e)	-0.127
q_H(e)	0.11	q_H(e)	0.115	q_H(e)	0.127

Table 7.4. Details of the MD simulation runs for liquid benzene at 298.15 K. Values of configurational (potential) energy, pressure and diffusion coefficient are compared with experimental data.

	Run 1	Run 2	Run 3	Experiment
Force-field model	exp-6	LJ-9-6	LJ-12-6	- -
Equilibration time, ps	74	60	74	- -
Sampling time for pdfs, ps	40	40	40	- -
Sampling time for dynamics, ps	100	100	100	- -
$< T >$, K	297.4±9.9	301.7±10.4	292.5±9.6	298
$- < U >$, kJ/mol	31.23± 0.25	30.72±0.26	31.41±0.24	31.37[a] 31.12[b]
$< P >$, kbar	-0.398±0.22	0.235±0.21	-0.135±0.27	- -
[c]$D \cdot 10^9$, m^2/s	2.354 (2.526)	1.777 (2.053)	1.579 (1.551)	2.27[d] 2.20[e]

a: Experimental potential energy was calculated from the experimental enthalpy of vaporization (ΔH_{vap}) at 298 K according to equation (6.4), enthalpy of vaporization was taken from (American Petroleum Institute, 1953) and b: from (Yaws, 1977); c: first values were obtained from the (c.o. m) velocity auto-correlation function (VACF), values in brackets were obtained from the (c.o.m) mean square displacement (MSD); d: from Falcone et al. (1967); e: from McCool et al. (1972).

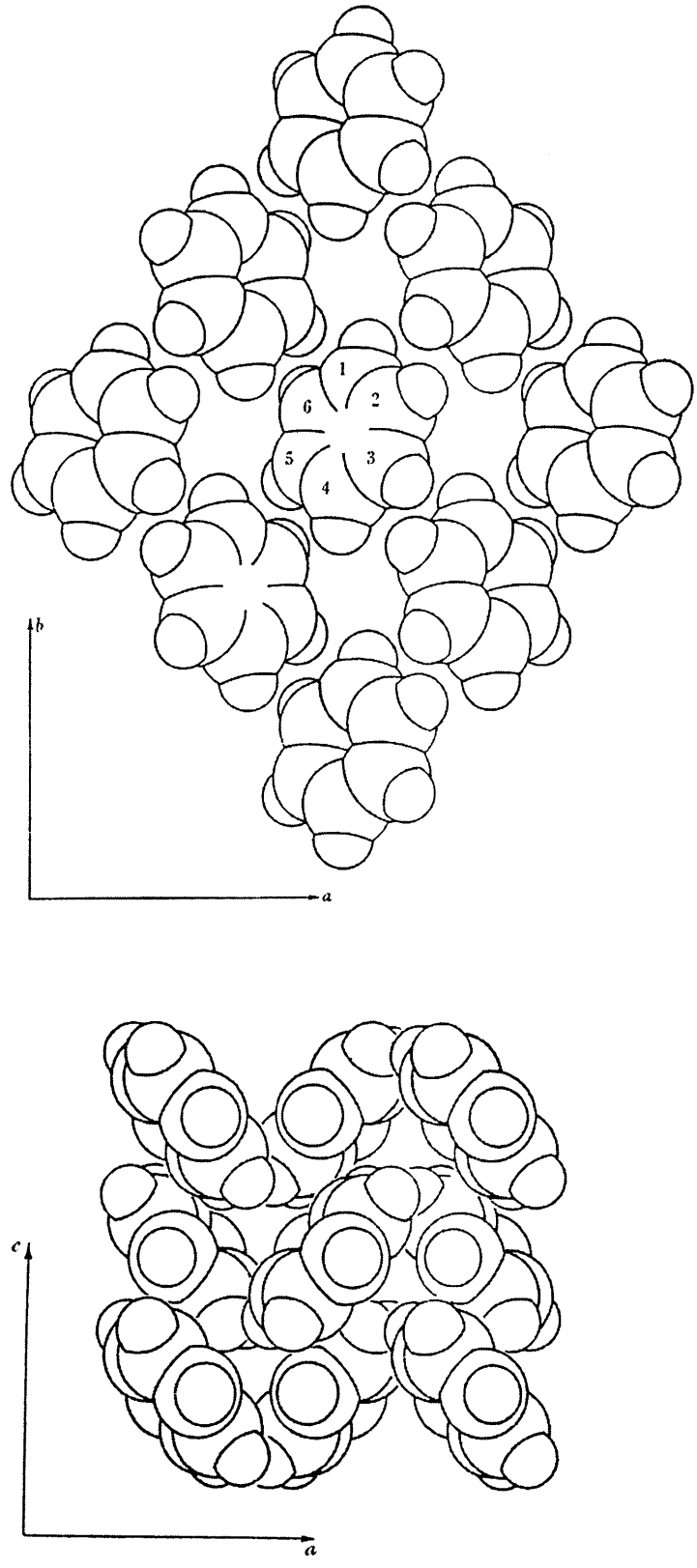

Figure 7.1 Diagram of the crystal structure of benzene, top: viewed down the *c*-axis; bottom: viewed down the *b* axis (reproduced from Cox et al. (1958)).

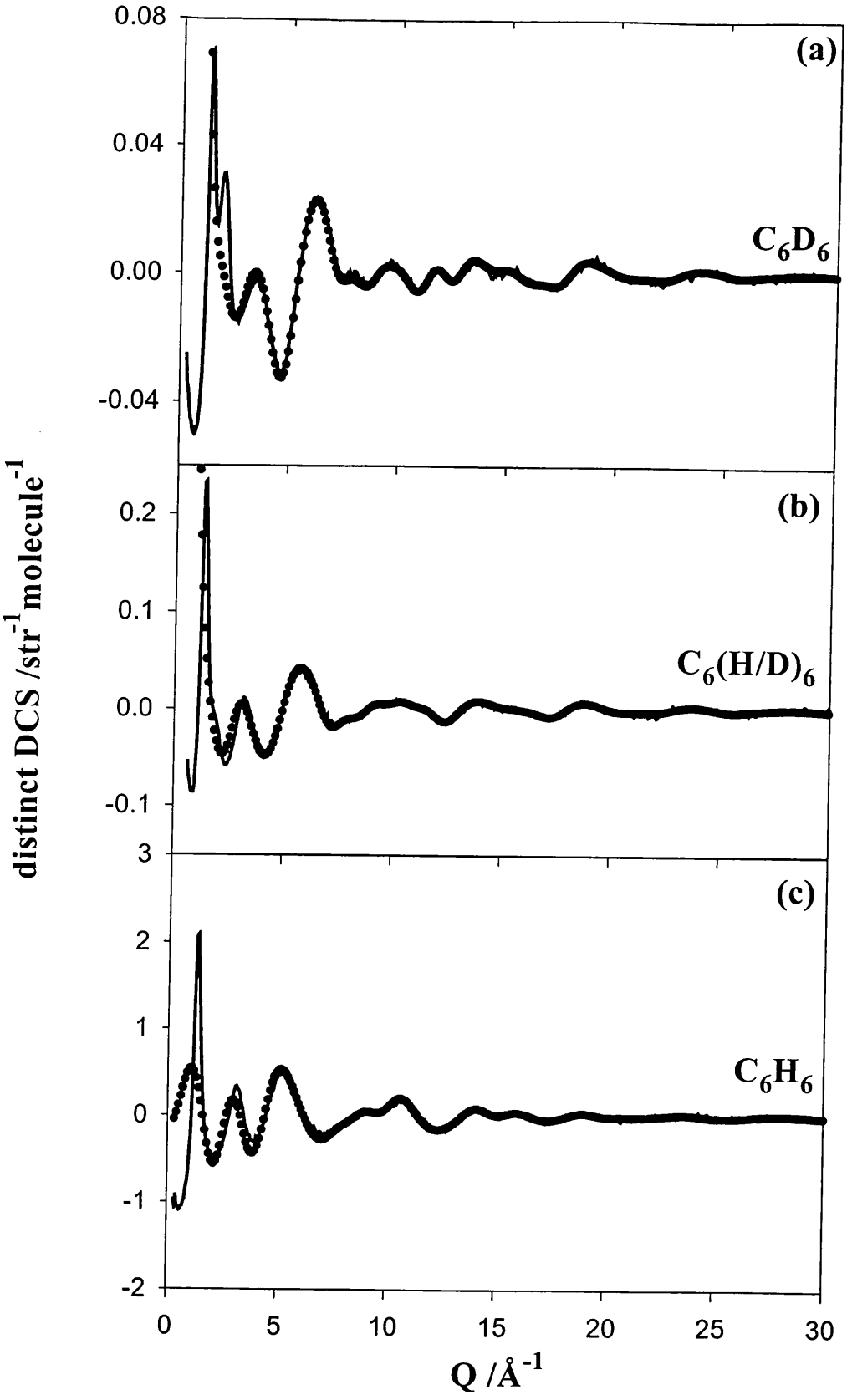

Figure 7.2. The distinct differential cross sections normalised to the scattering unit for the three benzene samples (lines) presented along with their corresponding intra-molecular DCSs (symbols).

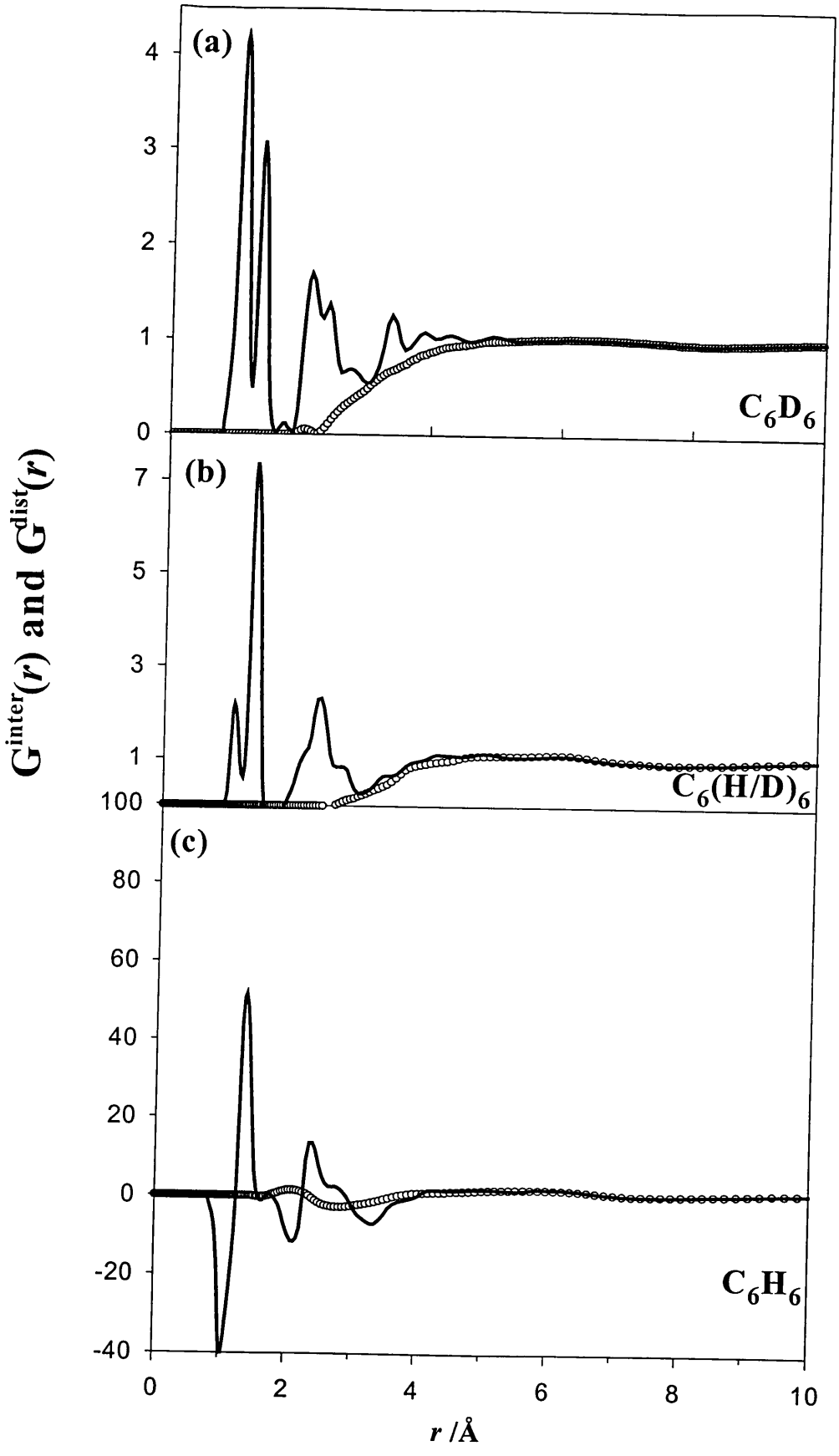

Figure 7.3. The three intra- + inter-molecular rdfs of C_6D_6, $C_6(H/D)_6$ and C_6H_6 (lines) presented for comparison with their respective inter-molecular contributions (symbols).

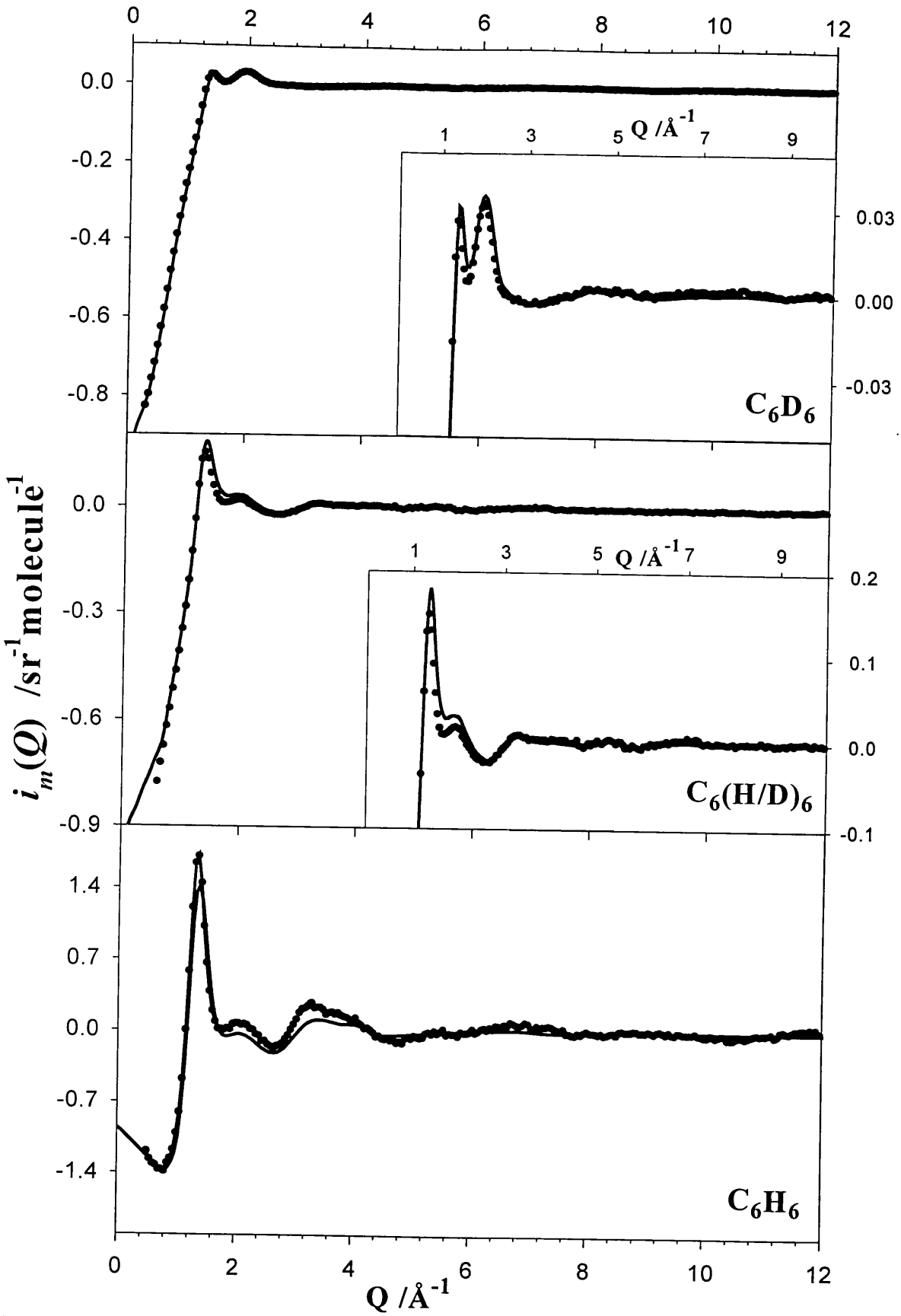

Figure 7.4. The three inter-molecular DCSs of liquid benzene (symbols) along with the back Fourier transforms (line) of the corresponding radial distribution functions shown in figure 7.5. Insets show the same functions on an enlarged scale.

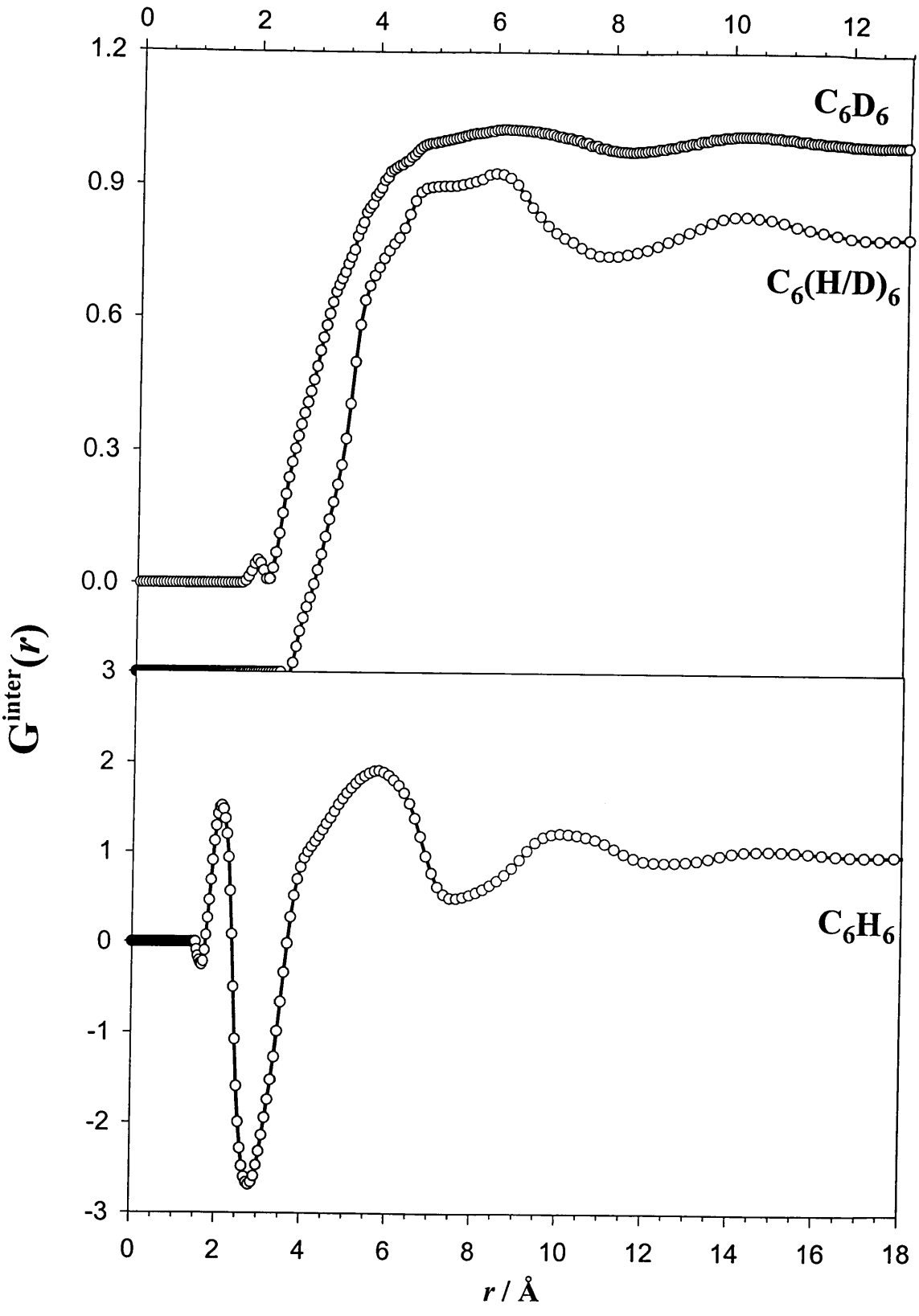

Figure 7.5. The C_6D_6, $C_6(H/D)_6$ and C_6H_6 intermolecular rdfs obtained from the Fourier transformation of the DCS functions shown in figure 7.4.

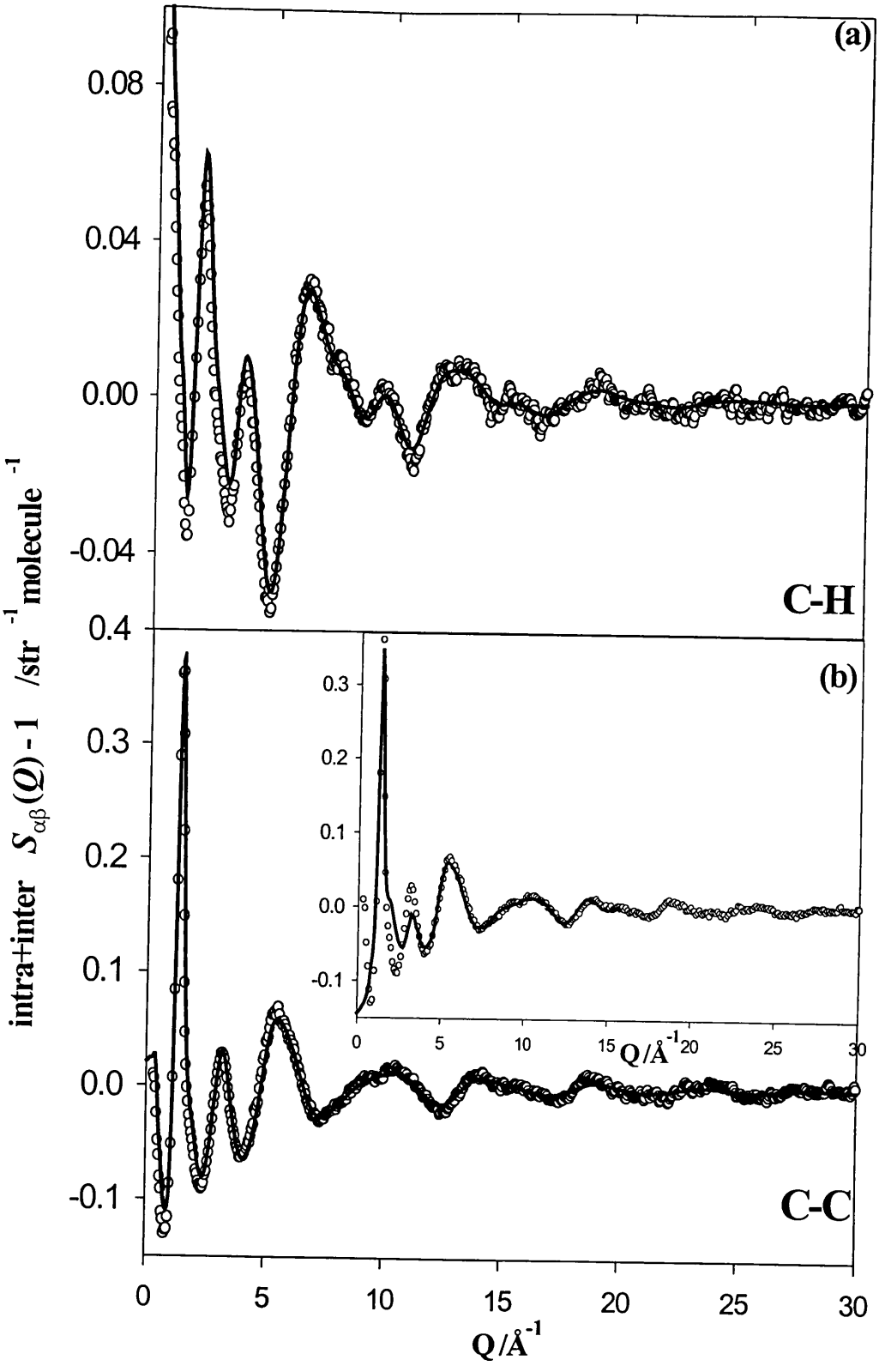

Figure 7.6. The C-C and C-H inter-+ intra-molecular partial structure factors (PSFs) (symbols) obtained from higher order differences, directly from the three distinct DCS presented in figure 7.2. The back Fourier transformed (lines) of the pdfs of figure 7.7 are superimposed on the original data from which they were obtained. The inset compares the ND distinct C-C DCS (symbols) with the X-rays structure function of Narten (1977) (solid line).

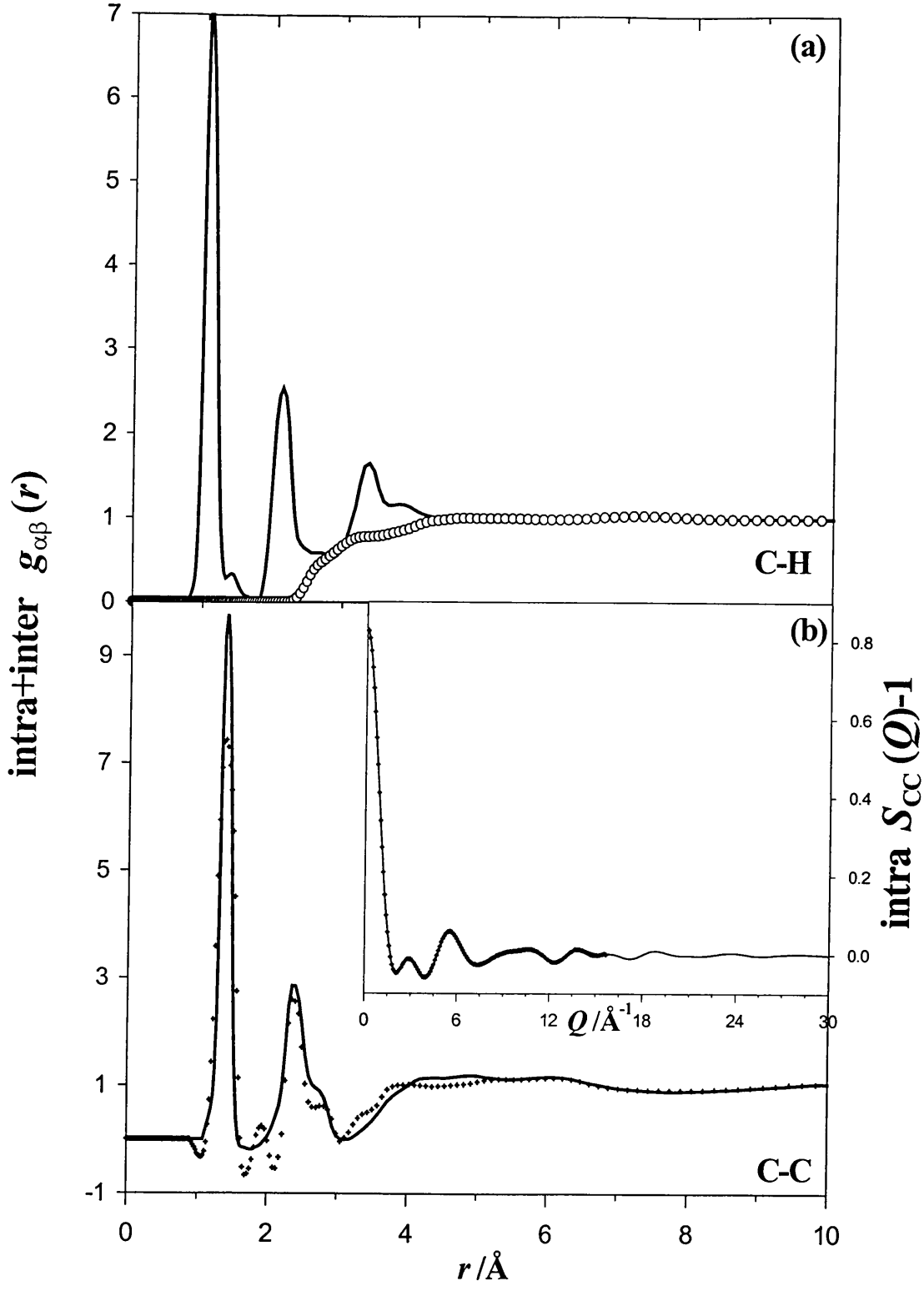

Figure 7.7. (a) The C-H inter- + intra- molecular pdfs (lines) obtained after Fourier transformation of the corresponding PSFs of in figure 7.6 compared with its inter-molecular contributions (white circles). (b) The ND C-C inter- + intra- molecular pdfs (lines) obtained after Fourier transformation of the corresponding PSFs of figure 7.6 compared with its X-rays C-C counterpart (+). The inset shows the ND (solid line) and X-rays (+) C-C intra-molecular structure factors.

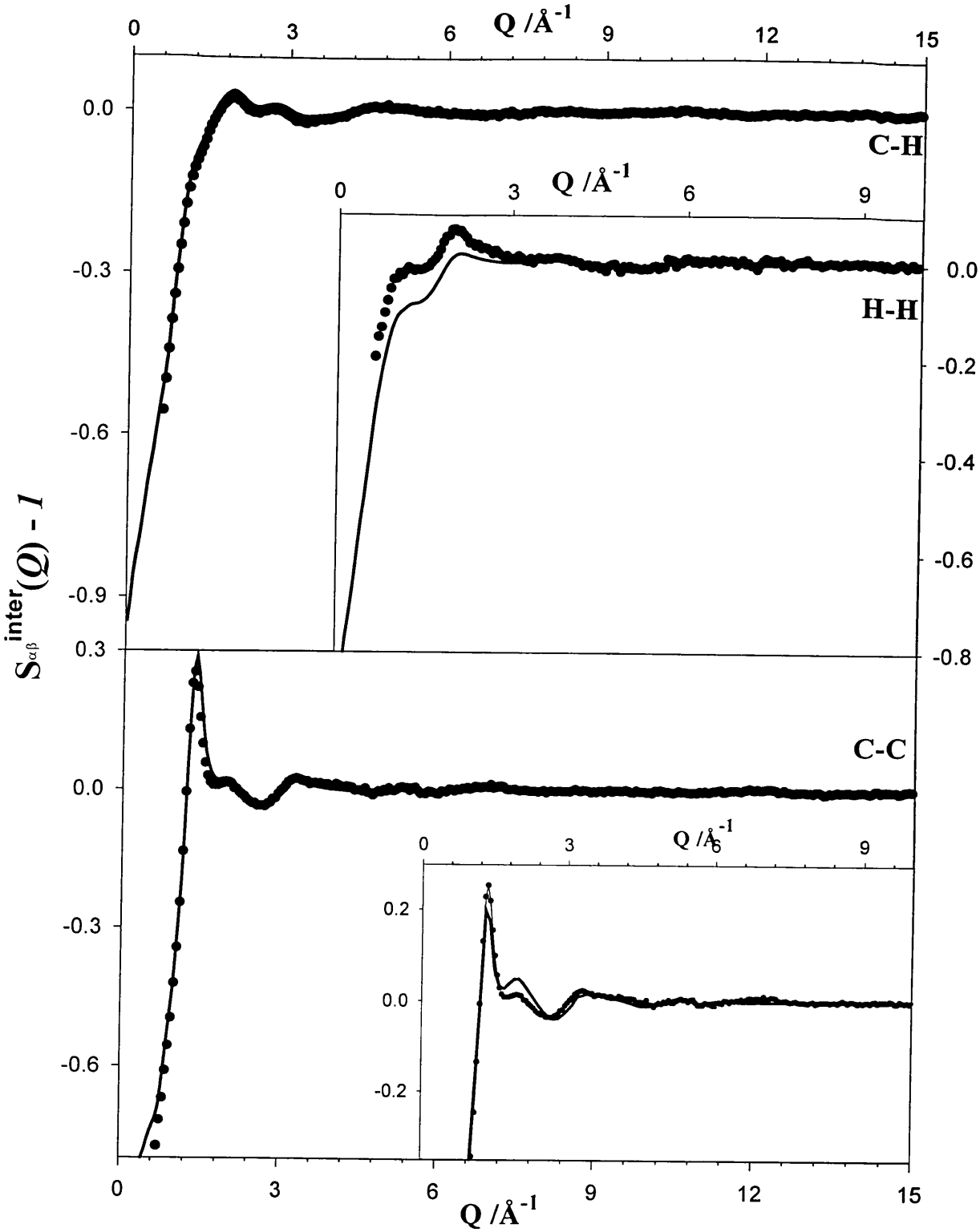

Figure 7.8. The C-C, C-H and H-H inter-molecular partial structure factors (PSFs) (symbols) obtained from the second- and higher- order differences, after removing the intra-molecular structure from the three distinct DCS presented in figure 7.2. The back Fourier transforms (lines) of the pdfs of figure 7.9 are superimposed on the original data from which they were obtained. Note that although the MIN fits of C-C and C-H PSFs are in good agreement with the data, for the H-H pair an offset is seen when MIN fit and original data are compared; probably due to a slight inelasticity residual still left in the data. The inset compare the X-rays C-C inter-molecular PSFs obtained by Narten (1977) (line) with its ND counterpart (symbols).

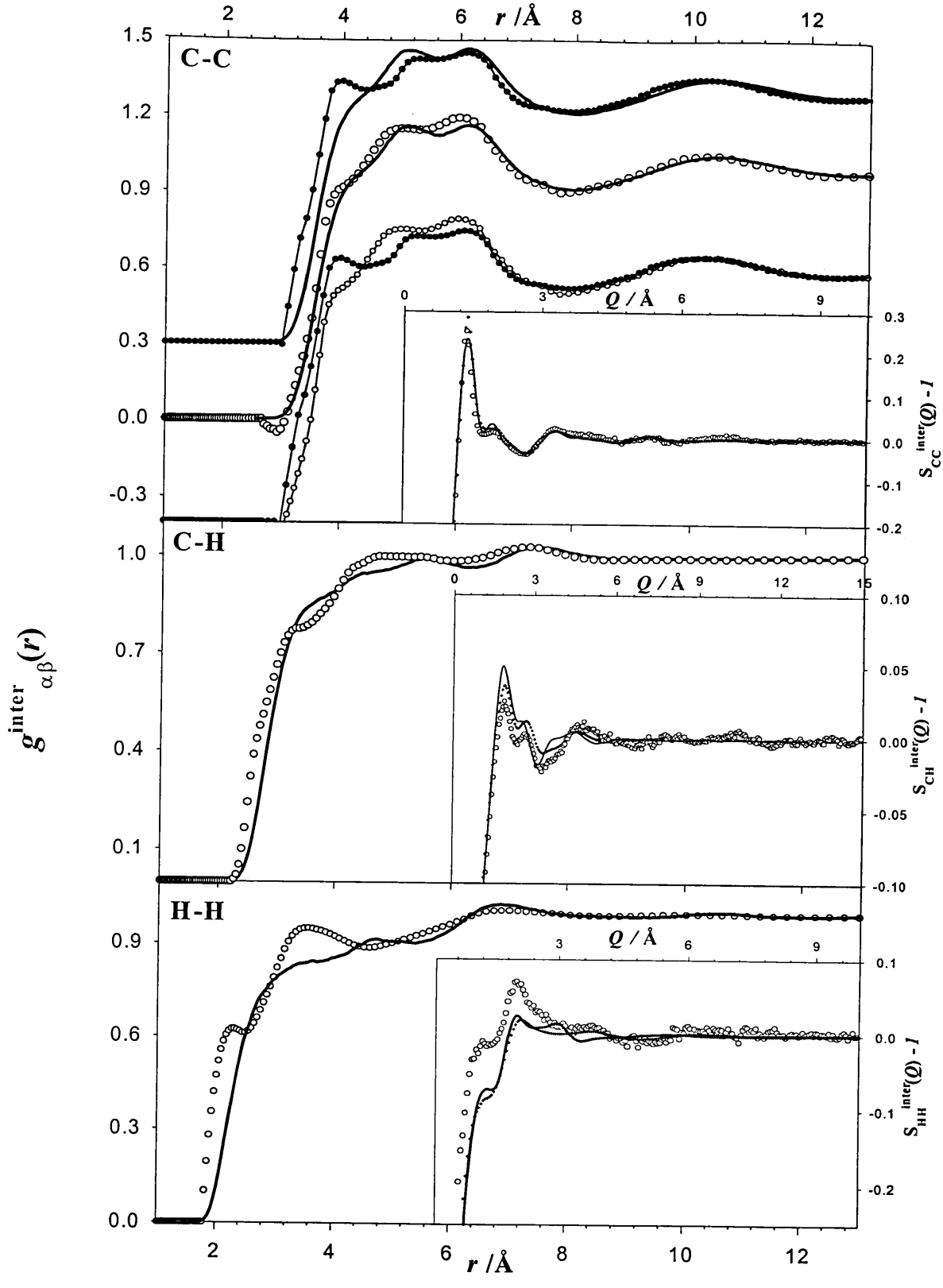

Figure 7.9. The experimental C-C, C-H and H-H inter-molecular pdfs obtained after Fourier transformation of the corresponding PSFs shown in figure 7.8 (white circles) compared to their simulated equivalent with the LJ-9-6 model (solid lines). The C-C pdf obtained from the present MD work (solid line) is compared with the one (black circles) extracted by Narten (1977) from X-rays diffraction experiment. Insets compare in Q-space the simulated (solid line), experimental (white circles) and MIN fit (+) C-C, C-H and H-H intermolecular PSFs.

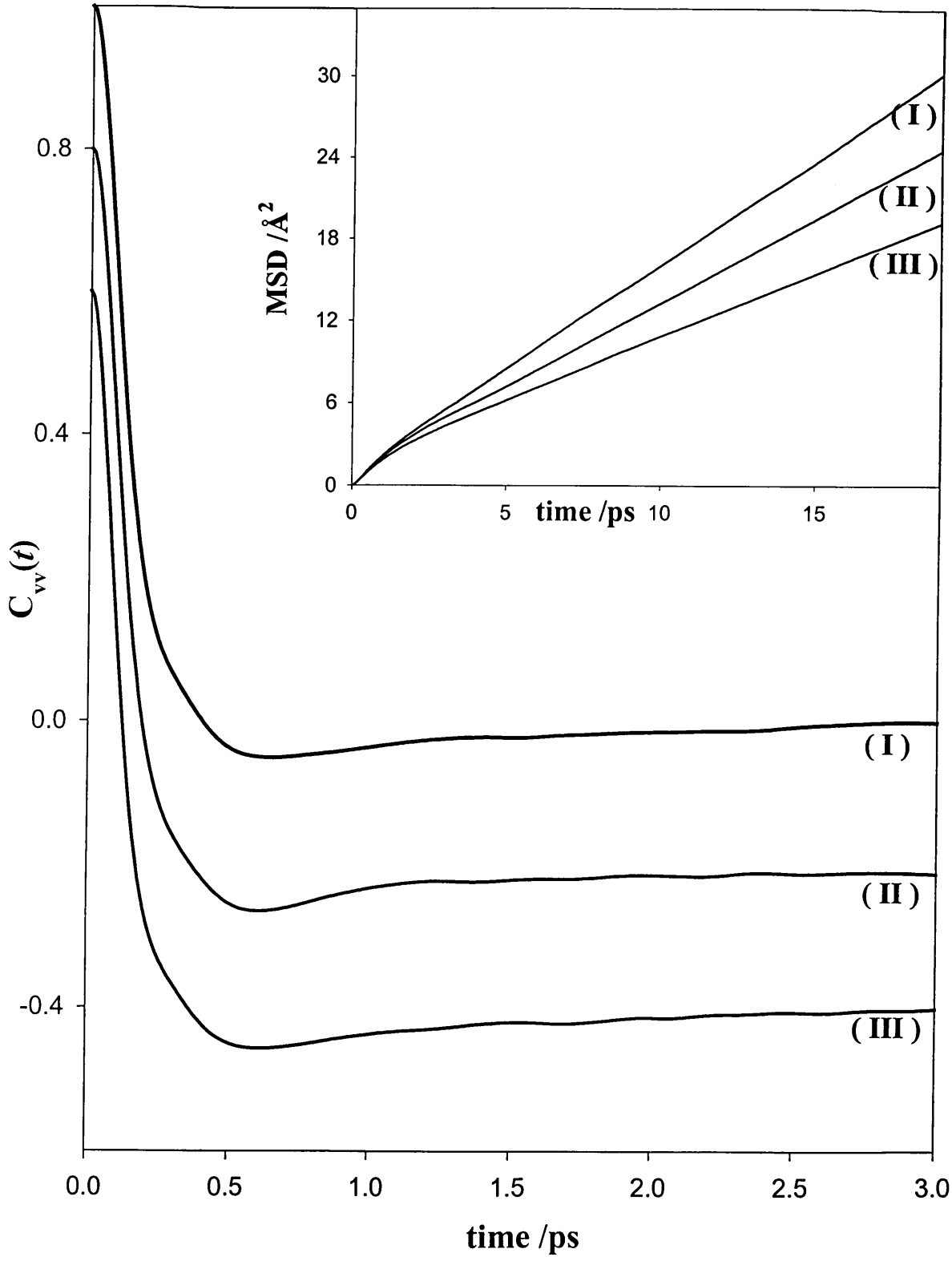

Figure 7.10. Normalised center-of-mass (c.o.m) velocity auto correlation functions (VACFs), $C_{vv}(t)$ obtained for the exp-6 (I), the LJ-9-6 (II) (displaced by –0.2), and the LJ-12-6 (III) (displaced by –0.4) models. Also shown in the inset are the c.o.m mean square displacements for the three model potentials used in the MD simulations.

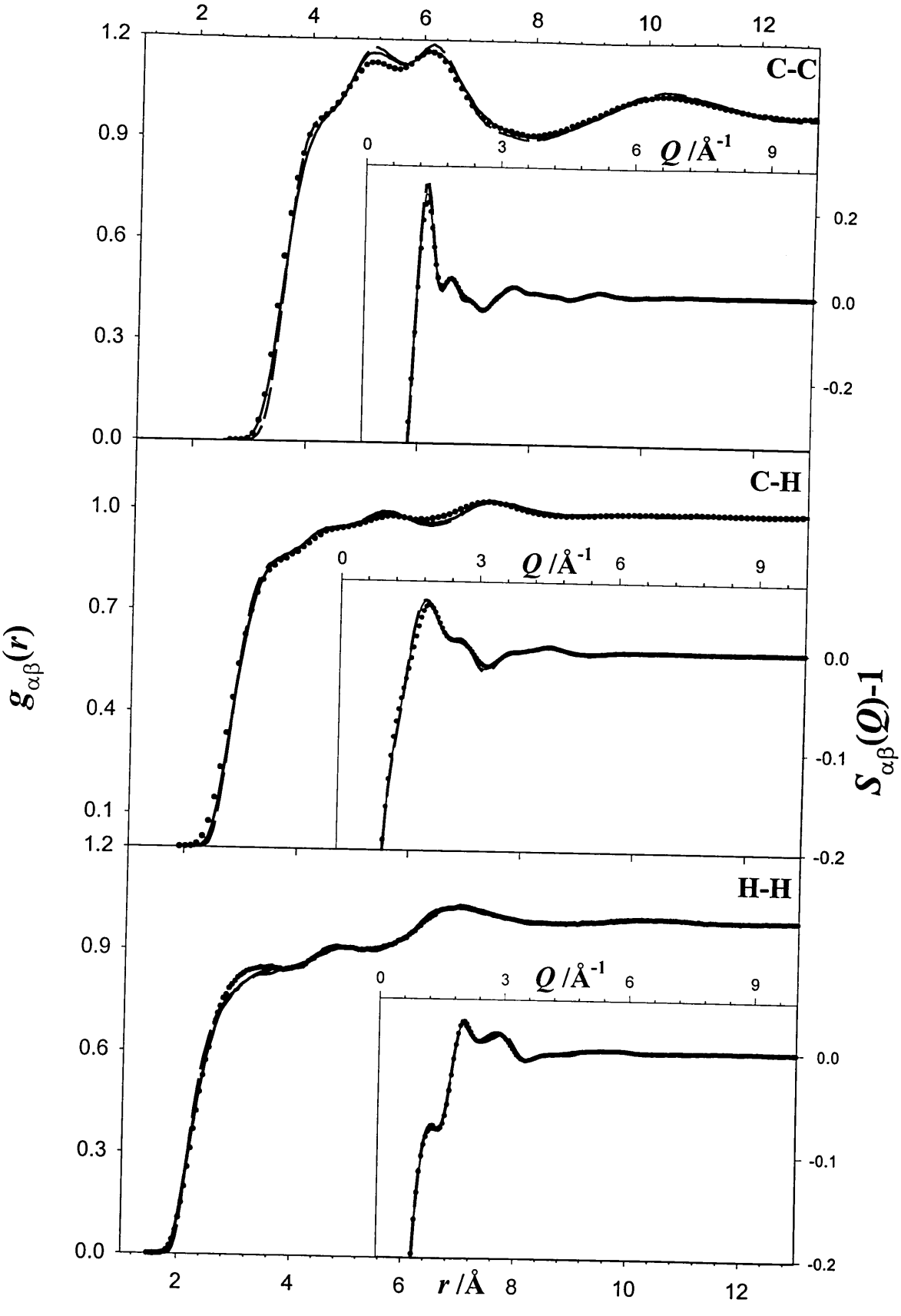

Figure 7.11. The simulated C-C, C-H and H-H inter-molecular pdfs obtained from the three MD simulations with the exp-6 (black circles), the LJ-9-6 (solid lines) and the LJ-12-6 (broken lines) models. Insets compare the C-C, C-H and H-H inter-molecular PSFs obtained from the same three MD simulations.

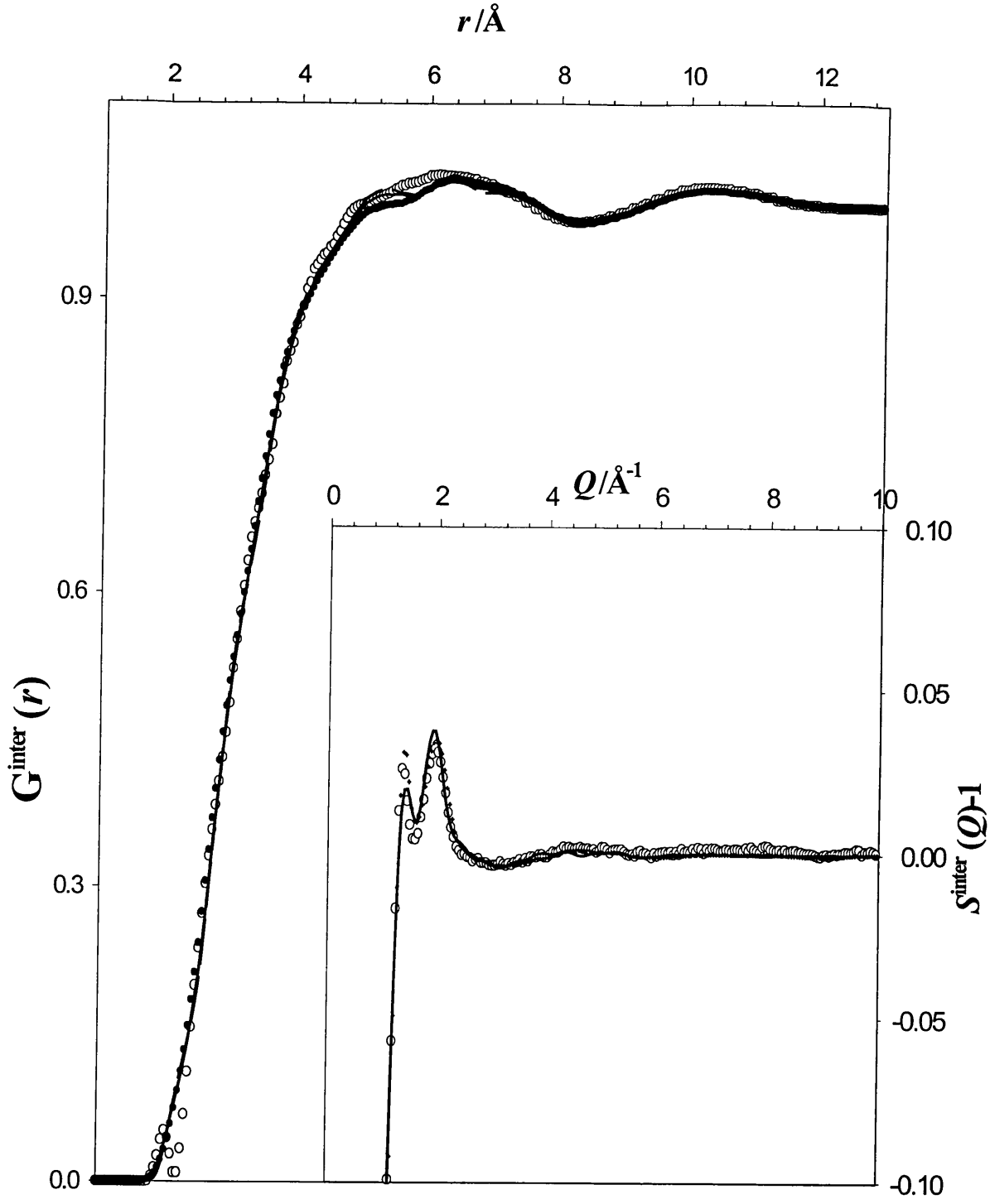

Figure 7.12. Inter-molecular radial distribution function for C_6D_6 obtained from MD simulation with the exp-6 (black circles), the LJ-9-6 (solid lines) and the LJ-12-6 (broken lines) models compared to the ND results (white circles). The inset shows the simulated (LJ-9-6) inter-molecular DCS of C_6D_6 (solid line), its ND counterpart (white circles) along with the MIN fit (+).

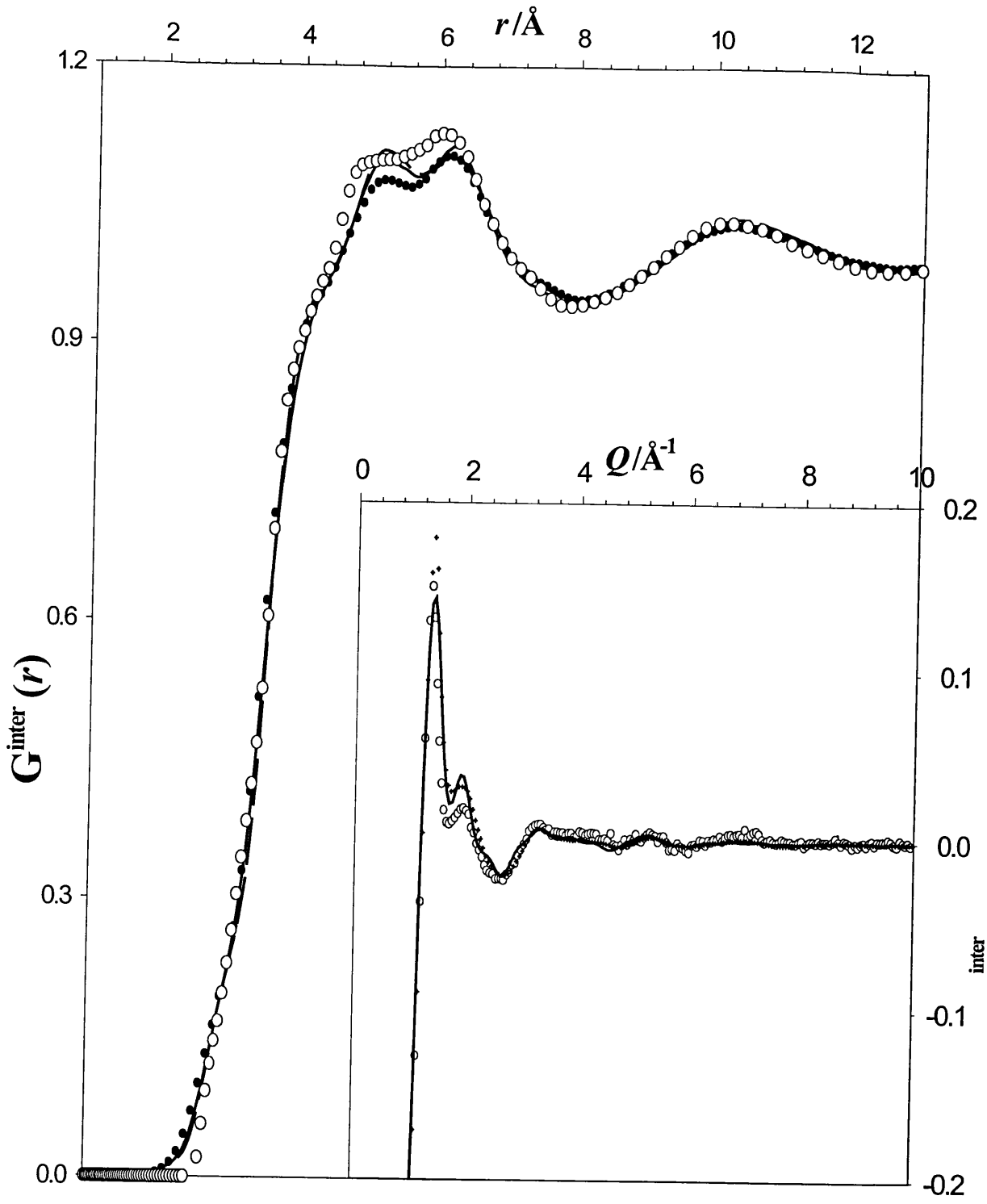

Figure 7.13. Inter-molecular radial distribution function for $C_6(H/D)_6$ obtained from MD simulation with the exp-6 (black circles), the LJ-9-6 (solid lines) and the LJ-12-6 (broken lines) models compared to the ND results (white circles). The inset shows the simulated (LJ-9-6) inter-molecular DCS of $C_6(H/D)_6$ (solid line), its ND counterpart (white circles) along with the MIN fit (+).

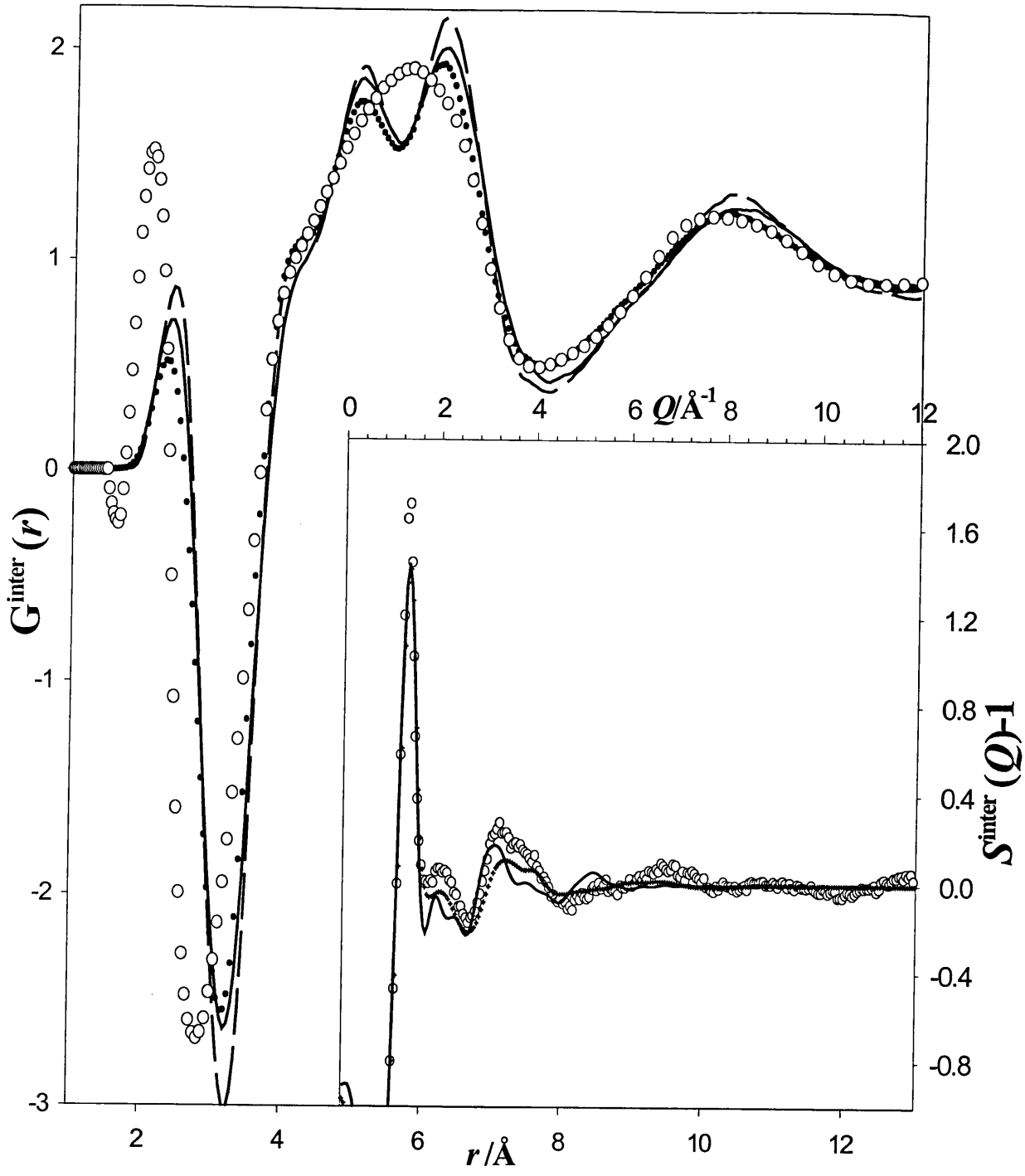

Figure 7.14. The intermolecular radial distribution function for C_6H_6 obtained from MD simulation with the exp-6 (black circles), the LJ-9-6 (solid lines) and the LJ-12-6 (broken lines) models compared to the ND results (white circles). The inset shows the simulated (LJ-9-6) inter-molecular DCS of C_6H_6 (solid line), its ND counterpart (white circles) along with the MIN fit (+).

Chapter 8

Structure of benzene-methanol liquid mixture

8.1 Introduction

Numerous experimental (Engdahl and Nelander, 1985, 1987; Wanna et al, 1986; Gotch and Zwier, 1992; Pribble et al., 1995; Pribble and Zwier, 1994; Gutowsky et al., 1993; Arunan and Gutowsky, 1993; Cheng et al., 1995; Suzuki et al., 1992) and theoretical (Augspurger et al., 1992, 1993; Fredericks et al., 1996; Linse, 1988; Bredas and Street, 1989; Cheney and Schultz, 1990; Williams, 1992; Gregory and Clary, 1996) studies have been reported on the benzene-water complex because of the peculiar interaction between hydrophobic π-electron of benzene and hydrophilic hydrogens of water. This π-H interaction has become an exciting topic (Klemperer, 1993; Rodham et al., 1993; Dougherty and Stauffer, 1990; Kim et al., 1994; Lee et al., 1995) not only due to its importance in biology (Jeffrey and Saenger, 1991) but also because in many cases it even plays a dominant role in determining crystal packing (Berkovitch-Yellin and Leiserowitz, 1984) and molecular conformations (Satanoka et al., 1988; Seiler and Dunitz, 1989; Chao and Chen, 1996; Muller et al., 1996). The substitution of methanol for water has interesting consequences. First, despite the strong hydrogen bonding between methanol molecules, benzene is very soluble in methanol under ambient conditions, in notable contrast to the immiscibility of benzene and water. Second, each methanol molecule is capable of acting only as a single hydrogen donor to its neighbours, whereas water can donate two hydrogens in order to forms hydrogen bonds. The investigations of the benzene-methanol system have so far been mainly concentrated in the gas phase (Wormald and Sowden, 1997; Wormald, 1997; Garret and Zwier, 1992; Pribble et al., 1997). One of the best thermodynamic evidence for association between unlike molecules comes from

measurements of the gas imperfection. From the results of the excess molar enthalpy measurements in the vapour phase for benzene + methanol (molar ratio 1:1) it has been suggested that interactions of the hydroxyl group with the π-electron system of the benzene make a contribution to the association between unlike molecules in benzene + methanol mixture (Wormald and Sowden, 1997; Wormald, 1997). Also, multiphoton ionisation (Garret and Zwier, 1992) and resonant ion-dip infrared spectroscopic studies (Pribble et al., 1997) of benzene-(methanol)$_n$ clusters with n =1, 2, 3 suggest that the methanol molecules are H-bonded chains which retain the π hydrogen-bonding with benzene, while clusters with n = 4 and 5 do not posses a π-H bond. These results have been corroborated by density functional theory calculations (Hagemeister et al., 1998) on small clusters. Although such studies are relevant to the structure of the mixture in the gas phase, it is of interest in the present study to investigate whether this π H-bond is present in the liquid phase.

Even though neutron diffraction (ND) is one of the most powerful technique to study the liquid state structure, such a mixture of molecular liquids as benzene + methanol presents several difficulties which need to be overcome. The intra-molecular structure of benzene and methanol largely dominates the measured intra- + inter- molecular (distinct) differential scattering cross section (DCS). In real space, intra-molecular distances contribute up to ~5 Å in the total radial distribution functions (rdfs). Even if the intra-molecular correlations are removed from the distinct DCS, the resulting inter-molecular DCS, (or the inter-molecular rdf obtained by Fourier transformation) consists of a sum of 21 partial structure factors (or pair distribution functions). Thus, interpretation of the results from total measurements is almost impossible. The neutron diffraction isotopic substitution (NDIS) technique can provide detailed structural information by resolving the total DCSs (or rdfs) into partial structure factors (or distribution functions). In the present studies, isotopic substitution on hydroxyl hydrogen (Ho) of methanol and hydrogens (HB) of benzene was used in order to extract the solute-solute (HB-HB), solvent-solvent (Ho-Ho) and solute-solvent (Ho-HB) correlations. The structural results for the mixture, discussed in section 8.2, are compared with those obtained on the pure components (benzene and methanol reported in chapter 6 and 7, respectively), to explore how addition of

benzene disrupts the hydrogen bonding in liquid methanol.

The only computer simulation results reported on this system so far, are those by Adachi and Nakanishi (1991, 1993), who performed the calculations at several compositions of the mixture (mole fraction of methanol 0.05, 0.1, 0.25, 0.5, 0.75). They found that the shape of self-associating complex of methanol molecules changes from spherical in lower methanol content to flexible chain-like in concentrated solutions. However, the benzene-methanol mole ratio 1:2, relevant to the present ND experiment was not covered. For their simulation work, they devised potential functions for the benzene-methanol and benzene-benzene interactions by fitting polynomial expressions to the dimer energies calculated from an *ab initio* study with the rather rudimentary STO-3G basis set at the MP2 level. The methanol-methanol terms were however taken from the work of Jorgensen (1979). As for the APR6 model of methanol (see section 6.2), their force field comprises of several inverse cubic terms so that the potential truncation corrections (see section 3.8.1b and c) cannot be estimated. Thus, in the present computer simulation study, we chose to perform MD simulations on this mixture by choosing two potential models from the previous MD studies of the pure components already reported in sections 6.2 and 7.3. For the potential models chosen in our simulation studies, the calculations are free from the problems of potential truncation corrections. In section 8.3, we present the results of these MD simulations, and compare them with the results obtained from the ND measurements on H/D substituted benzene-methanol.

8.2. Experimental study

8.2.1 Theoretical background for the mixture

a. Basic relations

The basic relations for the pure components were summarised in section 4.6; their extension to a mixture of molecular liquids is outlined below. Consider a mixture,

with an average number density ρ (molecule Å^{-3}), composed of two molecular species labelled 1 and 2, with molar fractions x_1 and $x_2 = 1\text{-}x_1$, respectively. A molecular unit is defined here as x_1 times the molecule 1 plus x_2 times the molecule 2. Accordingly, the factor for normalising the scattering to the molecular unit will be one-third of the weighting of molecule 1 plus two-thirds of that of the molecule 2. The total differential cross section (DCS) per molecule obtained after applying various corrections (described in section 5.5.1-5) to the neutron data consists of a coherent and incoherent part

$$\left(\frac{\partial\sigma}{\partial\Omega}\right)_{\text{tot}} = \left(\frac{\partial\sigma}{\partial\Omega}\right)_{\text{coh}} + \left(\frac{\partial\sigma}{\partial\Omega}\right)_{\text{incoh}} . \tag{8.1}$$

The coherent DCS is usually separated into a distinct and a self term. The distinct DCS involves coherent scattering due to distinct nuclei of either different molecules (inter-molecular DCS) or the same molecule (intra-molecular DCS). Therefore, (8.1) can be written as

$$\left(\frac{\partial\sigma}{\partial\Omega}\right)_{\text{tot}} = \left(\frac{\partial\sigma}{\partial\Omega}\right)_{\text{coh}}^{\text{intra}} + \left(\frac{\partial\sigma}{\partial\Omega}\right)_{\text{coh}}^{\text{inter}} + \left(\frac{\partial\sigma}{\partial\Omega}\right)_{\text{coh}}^{\text{self}} + \left(\frac{\partial\sigma}{\partial\Omega}\right)_{\text{incoh}} . \tag{8.2}$$

The last two terms in (8.2) give rise to the so-called self scattering (SLF) term whose value is the high-Q limit of the total DCS. Under the static approximation these two terms can be written as :

$$\left(\frac{\partial\sigma}{\partial\Omega}\right)_{\text{self}} = \sum_{i=1}^{2} x_i \sum_{\alpha_i}^{\text{Nm}_i} c_{\alpha_i} \bar{b}_{\alpha_i}{}^2 + c_{\alpha_i} b_{\alpha_i}^{\text{incoh}\ 2} , \tag{8.3}$$

where b_{α_i} and $b_{\alpha_i}^{\text{incoh}}$ are, respectively the coherent and the incoherent scattering length of the nucleus α in the molecule i, and the sum runs over all different (N_{mi}) types of α nuclei appearing c_α times in the molecule i. Once the SLF term is subtracted, the distinct radial distribution function (rdf) $G^{\text{dist}}(r)$ can be obtained by Fourier transformation of the distinct DCS

$$2\pi^2 r\rho(\mathrm{G^{dist}}(r)\text{-}1) = \left(\sum_{i=1}^{2} x_i \sum_{\alpha i}^{\mathrm{Nm}_i} c_{\alpha_i} \bar{b}_{\alpha_i}\right)^{-2} \int_0^{\infty} \left(\frac{\partial\sigma}{\partial\Omega}\right)_{\mathrm{coh}}^{\mathrm{dist}} Q\sin(Qr)dQ\,. \tag{8.4}$$

The distinct rdf $G^{\mathrm{dist}}(r)$, which consists of a weighted sum of pdfs, $g_{\alpha\beta}(r)$:

$$\mathrm{G^{dist}}(r) = \sum_{i,j=1}^{2} x_i x_j \sum_{\alpha_i}^{\mathrm{Nm}_i} \sum_{\beta_j}^{\mathrm{Nm}_j} \frac{c_{\alpha_i} c_{\beta_j} \bar{b}_{\alpha_i} \bar{b}_{\beta_j}}{\left(\sum_{i=1}^{2} x_i \sum_{\alpha_i}^{\mathrm{Nm}_i} c_{\alpha_i} \bar{b}_{\alpha_i}\right)^2} g_{\alpha_i\beta_j}(r) = \sum_{i,j=1}^{2} \sum_{\alpha_i}^{\mathrm{Nm}_i} \sum_{\beta_j}^{\mathrm{Nm}_j} W_{\alpha_i\beta_j} g_{\alpha_i\beta_j}(r)\,, \tag{8.5}$$

includes contributions from intra as well as inter-molecular correlations. At large Q the inter-molecular DCS approaches 0, and the contribution to the distinct DCS comes only from the intra-molecular DCS. The intra-molecular contributions can then be calculated using

$$\left(\frac{\partial\sigma}{\partial\Omega}\right)_{\mathrm{coh}}^{\mathrm{intra}} = \sum_{k=1}^{2} x_k \sum_{i=1}^{n_k} \sum_{\substack{j=1 \\ i\neq j}}^{n_k} \bar{b}_i^{\,k} \bar{b}_j^{\,k} \frac{\sin Qr_{ij}^k}{Qr_{ij}^k} e^{-\frac{1}{2}(\gamma_{ij}^k Q)^2} \quad \text{with} \quad (\gamma_{ij}^k)^2 = \frac{1}{2}\left\langle (u_{ij}^k)^2 \right\rangle, \tag{8.6}$$

where r_{ij}^k is the distance between the nuclei i and j in the molecule k, the Debye-Waller factor γ_{ij}^k is proportional to the mean square amplitude of vibration u_{ij}^k of atom i relative to atom j. After subtracting the intra-molecular part from the distinct DCS, the inter-molecular pair distribution function, which contains details of the structural arrangement of the molecules in the mixture, can be obtained by Fourier transformation.

b. Neutron diffraction with isotopic substitution (NDIS)

The distinct (dist.) DCS for a binary mixture obtained from a single neutron diffraction experiment can be written as a weighted sum of the partial structure factors, $S_{\alpha i\beta j}(Q)$:

$$\left(\frac{d\sigma}{d\Omega}\right)_{\mathrm{coh}}^{\mathrm{dist}}(\mathrm{Q}) = \sum_{i=1}^{2} x_i \sum_{\alpha_i}^{\mathrm{Nm}i} \sum_{\beta_j}^{\mathrm{Nm}j} c_{\alpha_i} c_{\beta_j} \bar{b}_{\alpha i} \bar{b}_{\beta j} (S_{\alpha_i\beta_j}(Q) - 1)\,. \tag{8.7}$$

In the benzene-methanol (BM) mixture case, the distinct DCS consists of 21 partial structure factors (PSFs). As mentioned in section 4.7, it is not possible to use isotopic substitution on carbon and oxygen since the change in scattering length of their isotopes is negligible. The only practicable substitutions are those involving hydrogen and deuterium because their isotopic contrasts are significant. In a particular situation where the substitution is done on a unique hydrogen site (*i.e.* Ho or HB) denoted by *S*, the distinct (dist.) DCS obtained from a single neutron diffraction experiment can be written as a weighted sum of the substituted site to substituted site, $S_{SS}(Q)$, the non-substituted to non-substituted sites, $S_{XX}(Q)$, and the non-substituted to substituted sites, $S_{XS}(Q)$ PSF terms:

$$\left(\frac{d\sigma}{d\Omega}\right)_{\text{coh}}^{\text{dist}}(\mathrm{Q}) = c_{\mathrm{X}}^2\,\bar{b}_X{}^2\,(S_{XX}(Q)-1) + 2c_X c_S \bar{b}_X \bar{b}_S\,(S_{XS}(Q)-1) + c_S^2\,\bar{b}_S{}^2\,(S_{SS}(Q)-1), \tag{8.8}$$

where

$$\bar{b}_X = \sum_{i=1}^{2} x_i \sum_{\alpha_i \neq S}^{N_{mi}} \frac{c_{\alpha_i}\bar{b}_{\alpha_i}}{c_X}\ , \text{ and} \tag{8.9}$$

$$c_X = \sum_{i=1}^{2} x_i \sum_{\alpha_i \neq S}^{N_{mi}} c_{\alpha_i}\ , \tag{8.10}$$

so that

$$c_S = \sum_{i=1}^{2} x_i \sum_{\alpha_i}^{N_{mi}} c_{\alpha_i} - c_X\,. \tag{8.11}$$

If the distinct DCS is measured for three different samples in which, for instance, the substituted site is alternatively fully deuterated (heavy), fully protonated (light), and

consists of a mixture of heavy + light (atomic fraction 0.5) hydrogens (mix), the $S_{SS}(Q)$ PSF can be extracted:

$$S_{SS}(Q)-1=A^{-1}\left[0.5\left(\frac{d\sigma}{d\Omega}\right)_{\text{coh}}^{\text{heavy}}(Q)+0.5\left(\frac{d\sigma}{d\Omega}\right)_{\text{coh}}^{\text{light}}(Q)-\left(\frac{d\sigma}{d\Omega}\right)_{\text{coh}}^{\text{mix}}(Q)\right], \tag{8.12}$$

$$\text{with}\quad A=\frac{c_S^2}{4}\left[\bar{b}_D-\bar{b}_H\right]^2. \tag{8.13}$$

The $S_{XS}(Q)$ PSF, which can be written as

$$S_{XS}(Q)-1=\sum_{i=1}^{2}x_i\sum_{\alpha_i\neq S}^{Nm_i}\frac{c_{\alpha_i}\bar{b}_{\alpha_i}(S_{\alpha_i S}(Q)-1)}{c_X\bar{b}_X}, \tag{8.14}$$

may be obtained from the first-order difference:

$$\Delta_S(Q)=\left[\left(\frac{d\sigma}{d\Omega}\right)_{\text{coh}}^{\text{heavy}}(Q)-\left(\frac{d\sigma}{d\Omega}\right)_{\text{coh}}^{\text{light}}(Q)\right], \tag{8.15}$$

by removing the $S_{SS}(Q)$ PSF obtained earlier from the second-order difference (equation 8.12):

$$S_{XS}(Q)-1=(B)^{-1}\left(\Delta_S(Q)-A(S_{SS}(Q)-1)\right), \tag{8.16}$$

$$\text{with}\quad B=2c_Sc_X\bar{b}_X(\bar{b}_D-\bar{b}_H). \tag{8.17}$$

In a similar way, the $S_{XX}(Q)$ PSF, which can be written as

$$S_{XX}(Q)-1=\sum_{i=1}^{2}x_i\sum_{\alpha_i\neq S,\beta_i\neq S}^{Nm_i}\frac{c_{\alpha_i}c_{\beta_i}\bar{b}_{\alpha_i}\bar{b}_{\beta_i}(S_{\alpha_i\beta_i}(Q)-1)}{c_X{}^2\bar{b}_X{}^2} \tag{8.18}$$

may be extracted by removing the $S_{XS}(Q)$ and $S_{SS}(Q)$ PSFs from the distinct or inter-molecular DCS of the heavy sample

$$S_{XX}(Q) - 1 = (C)^{-1} \times \tag{8.19}$$

$$\left[\left(\frac{d\sigma}{d\Omega} \right)_{\text{coh}}^{\text{heavy}} (Q) - 2c_X c_S \bar{b}_D \bar{b}_X (S_{\text{XS}}(Q) - 1) - c_S{}^2 \bar{b}_D{}^2 (S_{SS}(Q) - 1) \right]$$

$$\text{with } C = c_X^2 \, \bar{b}_X{}^2 . \tag{8.20}$$

In the case where both hydroxyl hydrogen (Ho) and hydrogen of benzene (HB) are involved in the isotopic substitution, the $S_{SS}(Q)$ PSF contains three contributions,

$$S_{SS}(Q) - 1 = \frac{1}{c_S^2}\left[c_{Ho}^2 (S_{HoHo}(Q) - 1) + 2c_{Ho}c_{HB}(S_{HoHB}(Q) - 1) + c_{HB}^2 (S_{HBHB}(Q) - 1)\right], \tag{8.21}$$

where

$$c_S = c_{Ho} + c_{HB}. \tag{8.22}$$

Provided the intra-molecular part (see equation 8.6) of the distinct DCS of the B:M system is known, it can be removed from each of the three distinct data sets to yield the inter-molecular $S_{XX}(Q)$ and $S_{XS}(Q)$ PSFs. However, the $S_{SS}(Q)$ PSF extracted is invariably an inter-molecular function irrespective of whether it is derived from the inter- or the distinct DCS.

8.2.2 Experimental and data reduction

At the time of the experiment, the SANDALS instrument was equipped with 18 groups of detectors covering scattering angles (2θ) from 3.8 to 36.5°. The container used was a flat plate cell (Benmore and Soper, 1998) made out of Ti/Zr alloy having

an overall nominal coherent scattering length of zero (see figure 5.5). The pure components (purchased from Cambridge Isotope Laboratories, Inc) used in the experiment were CD_3OD (99.8% deuterated), CD_3OH (99.5% deuterated), $CD_3O(H/D)$ (a 1:1 mixture of CD_3OD and CD_3OH), and for benzene: C_6D_6 (99.6% deuterated), C_6H_6 and $C_6(H/D)_6$ (a 1:1 mixture of C_6D_6 and C_6H_6). Since the magnitude of the signal in any of the substituted atom - substituted atom PSFs, obtained at the second-order difference level, is proportional to the square of the atomic fraction of the isotopically exchanged atomic species, the signal will be heavily wheighted by the benzene terms if an appropriate composition is not chosen. All the mixtures in the present studies were prepared in the B:M molar ratio of 1:2. This was chosen as a compromise to allow satisfactory extraction of the methanol terms at the second-order difference level, while at the same time being in the concentration regime where the spectroscopic gas- phase studies (Pribble et al., 1997) of benzene-$(methanol)_2$ clusters suggested the existence of π hydrogen-bonding in this mixture. Keeping these goals in view, the H/D substitution was made on the hydroxyl hydrogen (Ho) of methanol and hydrogen atoms (HB) of benzene. Measurements were performed on the following seven H/D-substituted samples (label indicated in parenthesis on the right).

$C_6D_6 + CD_3OD$ (I)

$C_6D_6 + CD_3OH$ (II)

$C_6D_6 + CD_3O(H/D)$ (III)

$C_6H_6 + CD_3OD$ (IV)

$C_6(H/D)_6 + CD_3OD$ (V)

$C_6(H/D)_6 + CD_3O(H/D)$ (VI)

$C_6H_6 + CD_3OH$ (VII)

The scattering intensities were measured for each sample at 298 ±1 K and ambient pressure. The raw data were corrected for background, container scattering, absorption, multiple scattering and, normalised to scattering from a vanadium slab using the standard ATLAS suite of programs (see sections 5.5.1-5). To check the correctness of data normalisation procedures employed, the high-Q limit of the total

DCS obtained for each sample reported in table 8.1 are compared with the theoretical values calculated from equation (8.3). Despite the fact that up to this stage the inelasticity corrections have not been applied to any of the data, and that this effect increases with the amount of protonated hydrogen present in each sample, the agreement between the observed and theoretically calculated values for each sample can be considered as satisfactory. The distinct DCS for each group of detector was extracted from the total DCS after applying the inelasticity corrections according to the methods already described in sections 5.5.6d and 5.8.2b. The combined data from different detector groups were then normalised to the molecular unit to give a single distinct DCS for each sample shown in figures 8.1 and 8.2. As for the pure components, Fourier inversions of the various sets of the mixture DCSs to the desired distribution functions were obtained using the minimum noise reconstruction (MIN) technique outlined in section 5.6.

8.2.3 Results and discussion

a. Distinct distribution functions

I. *Radial distribution functions*

Since the intra-molecular structure of benzene and methanol dominate the region ~0.9-5 Å, the inter- and intra-molecular distances overlap (see e.g. figure 8.2b for mixture I) in the total radial distributions functions (rdfs). The Fourier transformation of the measured distinct DCS, thus, does not provide any information on the inter-molecular structure. In addition, the first sharp feature at ~1.1 Å contains contributions from the CB-HB[1] bond of benzene as well as the O-Ho and C-HM bonds of methanol, and the ~1.4 Å peak comprises of the CB-CB and CM-O bond distances in benzene and methanol, respectively. Thus, even the assignment of the intra-molecular bond distances of each of the component species present in the mixture cannot be made from the distinct rdfs. Although, removal of the intra-

[1] CB and HB will hereafter be referred to as carbon and hydrogen of benzene, while CM, O, Ho and HM to carbon, oxygen, hydroxyl hydrogen and methyl hydrogen of methanol, respectively.

molecular structure is imperative to gain some insight of the structure of the mixture, it would not be reasonable to fit equation 8.6 directly to the distinct DCS due to the presence of a large number of floating parameters. For various ND investigations of binary mixtures of hydrocarbons (Bartsch et al., 1986; Adya and Wormald, 1993; Cabaço et al., 1998), weighted linear combinations of the intra-molecular cross sections deduced from the study of the pure components were found to be a satisfactory option rather than fitting equation 8.6 directly to the distinct DCS. This, however, assumes that the intra-molecular structure of each of the two components does not change in passing from the pure liquid to the mixture. While the molecular structure of benzene molecule is not expected to change much in the presence of methanol as compared to that in pure benzene, the assumption that the molecular geometry of methanol stays the same in passing from the pure liquid to the mixture cannot be ascertained in the first instance. For example, the O-Ho intra-molecular bond distance is very sensitive to the strength of the hydrogen bonding association between the methanol molecules as shown by spectroscopic measurements (Falk and Whalley, 1961; Serrallach et al., 1961; Furic et al., 1993), and a lengthening of this bond (see section 6.1.3d) results from this effect. A change in the length of the O-Ho intra-molecular bond can thus be used as an indication of the change in the structure of the methanol molecule in passing from pure liquid to the mixture. Consequently, the assumption of using a weighted linear combination of the intra-molecular structure factors of the pure components for this particular mixture has to be tested first, and is considered in the following section.

II. *Partial distribution functions*

H/D Substitution on HB

From the ND measurements on mixtures I, IV and V (see section 8.2.2) in which the H/D substitution was made on the HB sites, the X-HB and the X-X (X= CB, CM, HM, O and Ho) PSFs (see figure 8.3) were extracted and Fourier transformed (see figure 8.4). The $G_{XHB}(r)$ shown in figure 8.4a comprises of 5 pair-correlations, of which only one contains an intra-molecular contribution. In this respect, the first peak

at ~1.08 Å in the $G_{XHB}(r)$ can be assigned purely to the intra-molecular CB-HB distances. The other two features occurring at ~2.16 Å and ~3.4 Å, probably contain contributions from both intra- and inter- molecular distances. Figure 8.4a compares the X-HB partial distribution function in the mixture with the CB-HB pdf in pure benzene obtained earlier (see section 7.2). Focusing our attention on the CB-HB intra-molecular peak, comparison shows that the intra-molecular CB-HB bond does not change much in passing from pure benzene to the mixture since there is less than 0.010(5) Å difference between the two distances.

The $G_{XX}(r)$ partial shown in figure 8.4b is comprised of 15 correlations, which makes its interpretation rather difficult. Nevertheless, as shown below, this function provides useful information when it is compared with the CB-CB partial pdf for pure benzene and the total rdf for pure CD_3OD obtained earlier. For instance, while the full intra-molecular structure of CD_3OD contributes to the intra-molecular structure of the $G_{XX}(r)$ partial, only the CB-CB partial of benzene participates to this function, thereby reducing the intra-molecular range from ~5Å in any of the total rdfs (see e.g. figure 8.2.b) to ~3Å here. When one focuses on the intra-molecular region, the first peak centred at ~1.1 Å of figure 8.4b contains the CM-HM and O-Ho intra-molecular overlapping distances. A comparison of this feature with the one obtained for pure methanol shows (see figure 8.4b) that the peak maximum occurs at the same distance as in pure methanol, suggesting that the methyl group geometry and the O-Ho bond distance do not change much from that in pure methanol. In the second peak at ~1.41 Å, the CB-CB and CM-O intra-molecular distances overlap. A comparison of the $G_{XX}(r)$ with the function obtained by combining both the distinct CB-CB of pure benzene and the distinct rdf of CD_3OD (see inset figure 8.4b), suggests that the intra-molecular structure may well be represented, for this partial, by a linear combination of the intra-molecular structure of both the pure components.

H/D Substitution on Ho

Using the ND measurements on mixtures I, II and III (see section 8.2.2), in which the labelled atom is the hydroxyl hydrogen of methanol, Ho, the Y-Y and the Y-Ho (Y=

CB, HB, CM, Hm and O) PSFs (see figure 8.5) were extracted. These functions were Fourier transformed, and are shown in figures 8.6a and 8.6b, respectively. The $G_{YY}(r)$ distribution contains 15 pairs and the intra-molecular correlations dominate this function since the HM-HM, HM-CM, HM-O, and CM-O intra-molecular correlations in CD_3O- of methanol, and the full intra-molecular structure of C_6D_6 extend the range of the intra- and inter-molecular overlapping distances (~ 1.5Å - 5Å). The $G_{X'X'}(r)$ (X'=HM, CM and O) obtained from the study of pure methanol that contains the CD_3O- intra-molecular correlations and the C_6D_6 distinct rdf are plotted along with the $G_{YY}(r)$ partial in figure 8.6a, which reveals (i) that CB-HB and CM-HM distances contribute to the first peak centred at 1.09 Å, (ii) that the CB-CB and CM-O intra-molecular correlations contribute to the second peak at 1.41 Å, and (iii) that up to ~1.5 Å only the intra-molecular distances participate in the $G_{YY}(r)$ partial. By assuming additivity of the molecular structure, the two distribution functions obtained for the pure components (shown in figure 8.6a) are combined and compared with the $G_{YY}(r)$ partial in figure 8.6a inset. One can see that these two functions are in very good agreement. Since it was found from the $G_{XHB}(r)$ partial reported earlier (see figure 8.4a) that the CB-HB intra-molecular bond in the mixture did not change much as compared to that in pure benzene, it can then be concluded that the same is true for the CM-HM intra-molecular distances.

The $G_{YHo}(r)$ partial shown in figure 8.6b consists of 5 pair correlations (O-Ho, CM-Ho, HM-Ho, CB-Ho and HB-Ho), of which three contain intra-molecular contributions. Accordingly, the first peak at ~0.97 Å originates purely from the O-Ho intra-molecular bond distance. When $G_{YHo}(r)$ is compared with the $G_{X'Ho}(r)$ partial (X'=HM, C and O) obtained for pure methanol (Figure 8.6b), one can see that the O-Ho bond length in methanol has not changed on adding benzene to it. Although a shortening of the O-Ho intra-molecular bond length could have been associated to weaker hydrogen bonding between the methanol molecules, no perceivable change in this distance probably reflects that the strength of the hydrogen bonding at this composition of the mixture is the same as that in pure liquid methanol.

H/D Substitution on Ho and HB

By employing the H/D substitution technique on mixture I, VI, and VII, two atomic sites are labelled at the same time so that H can be either HB or Ho (see section 8.2.1b). In this respect, the Z-H (Z=HM, CM, O and CB) and the Z-Z PSFs (see figure 8.7) comprise of 8 and 10 pair contributions, respectively. Although these ($G_{ZH}(r)$ and $G_{ZZ}(r)$) functions do not provide any information additional to the one obtained from the partials already discussed, they simply help in further authenticating that the intra-molecular structure in the mixture can be considered as additive of those of its pure components. The Fourier transforms of these PSFs are presented in figures 8.8a and 8.8b. The two intra-molecular peaks occurring at ~1.08 Å and ~1.41 Å in $G_{ZZ}(r)$ are contributions from the CM-HM + CB-CB and CM-O interactions, respectively (see figure 8.8a). Assuming additivity of the molecular structure of the pure components, the CB-CB partial in benzene and the $G_{X'X'}(r)$ (X'=HM, CM and O) partial in methanol, both obtained from higher order differences, are combined and compared with the $G_{ZZ}(r)$ function in figure 8.8a inset. The peaks sizes and distances of the added distribution function are in good agreement with those of the $G_{ZZ}(r)$. In the region ~1.5-2.2 Å of the $G_{ZZ}(r)$, two humps observed at 1.79 Å and 2.07 Å correspond to the HM-HM and HM-O intra-molecular contributions. The good agreement of the added distribution function with $G_{ZZ}(r)$ in the region up to ~2.2 Å, provides further proof that the CH_3O geometry in methanol has not changed on adding benzene to it.

From figure 8.8b, where $G_{ZH}(r)$ is compared with a combined distribution function containing $G_{X'Ho}(r)$ and CB-HB partials of the pure components, it can be seen that, (i) the first peak comprising of O-Ho and CB-HB intra-molecular bond is well represented by assuming additivity of the intra-molecular structure (see inset fig 8.8b), and (ii) the intra-molecular structure of benzene largely dominates this partial.

The above results obtained for the various partial distributions functions at the distinct level, and their comparison with those of the pure components show that the intra-molecular structure of methanol does not change much with addition of benzene, and

vice versa. It is worth noting that, comparison made of the ND results obtained from three separate ND measurements on methanol, benzene and BM system at the partial level provides the severest check on the consistency/accuracy of all sets of data and correctness of the entire data reduction procedures employed in obtaining these functions. It must be stressed that the good agreement of the partials obtained for the mixture with those calculated from the pure components (all obtained from higher order NDIS difference methods) in the limited r-range where only the intra-molecular structure participates, and where usually the inelasticity effects are quite drastic, is highly gratifying.

b. Inter-molecular distribution functions

I. *Inter-molecular radial distribution functions*

The intra-molecular DCS of the mixture was built (using equation (8.6)) as a linear combination of the corresponding intra-molecular DCSs for pure liquid methanol (fit 1 of section 6.1.3b) and benzene (section 7.2.2) weighted by their respective mole fractions. Since the extent of deuteration in each of the seven mixture samples of the B:M system is different, the intra-molecular DCS for each one of them was calculated separately (see e.g. figures 8.1, 8.2 and inset of figure 8.9). The inter-molecular DCSs normalised to a molecular unit defined as,

$$i_m(Q) = \left(\sum_{i=1}^{2} x_i \sum_{\alpha_i}^{Nm_i} c_{\alpha_i} b_{\alpha_i}\right)^{-2} \left[\left(\frac{\partial\sigma}{\partial\Omega}\right)_{\text{coh}}^{\text{dist}} - \left(\frac{\partial\sigma}{\partial\Omega}\right)_{\text{coh}}^{\text{intra}}\right] \tag{8.23}$$

were then extracted for each of the seven samples by subtracting their corresponding intra-molecular parts. Not surprisingly, it can be seen (figures 8.2a and 8.9 insets), that the intra-molecular part of the distinct DCS dominates largely the scattering in the Q range from ~5 to 30 Å^{-1}. The inter-molecular DCS, thus, contributes only in the range ~0-6 Å^{-1}. The inter-molecular rdfs for all the the seven mixture samples obtained by Fourier transformation of the $i_m(Q)$ functions are shown in figure 8.10. Since each of these distribution functions is composed of 21 pair-correlations (see

table 8.2) superimposed on each other, they are all featureless. They can, therefore, reveal structural details of no further significance.

II. *Inter-molecular partial distribution functions*

Using the same approach as that used previously for the distinct DCSs (see section 8.2.3aII), the H/D substitution technique can also be employed at the inter-molecular DCS level in order to extract the solute-solute, solvent-solvent and solute-solvent correlations. Interestingly, by comparing these correlation functions for the mixture with those obtained for the pure components, one can explore how the hydrogen bonding in pure methanol changes when benzene is added to it.

H/D Substitution on HB

The S_{HBHB} (Q) PSF was extracted (see figure 8.11a) according to equation 8.12 by combining the DCSs of mixture I, IV and V in which the labelled sites are the hydrogens of benzene. It is worth noting that this function can be obtained either from the distinct or inter-molecular DCSs independently. This is so because the intra-molecular structure cancels in equation 8.12. The inter-molecular pdf g_{HBHB} (r) obtained by Fourier transformation of S_{HBHB} (Q) is plotted in figure 8.11b. A comparison of the HB-HB running co-ordination numbers (figure 8.11b inset) shows that for similar distances, co-ordination numbers for the mixture are lower than those in pure benzene. Also, the average distance between two closest HB atoms increases significantly in the mixture because of the presence of the methanol molecules in-between. However, the shape of the partial distribution function obtained for the mixture resembles the one obtained in pure benzene. The pdf shows three features at ~ 2.4, 4 and 7 Å, which are also present though at slightly shorter distances in pure benzene. Since larger distances between two benzene molecules occur in the mixture, addition of methanol has probably weakened the benzene-benzene interactions, which may be associated to a relative loss of orientational correlations between them.

The X-HB and X-X PSFs extracted from the higher order differences are shown in figure 8.12a. As reported in table 8.3, the X-X PSF comprises of 15 contributions. The distribution function obtained (see figure 8.12b) by Fourier transformation of the PSF is thus featureless and of little use. Although the X-HB partial shows some structural features at ~ 4 and 7Å, this function still comprises of 5 contributions which makes further interpretation of the results difficult.

H/D Substitution on Ho

The Ho-Ho correlations are of interest to investigate the change in hydrogen bonding between methanol molecules on addition of benzene to methanol. Using the mixtures I, II and III in which the Ho atom is labelled, the $S_{HoHo}(Q)$ PSF was extracted (see figure 8.13a). Since the intra-molecular contributions in the three terms on the right hand side of equation 8.12 cancel out, the $S_{HoHo}(Q)$ partial extracted either from the distinct or the inter-molecular DCS yields identical results. Slightly different extent of deuteration of the CD_3OH and CD_3OD samples gives rise to a very small contribution from the HM-Ho pair (see table 8.3), but its effect is small enough to be ignored. The ratio of the height of the first maximum to that of the first minimum of $g_{HoHo}(r)$ pdf plotted in figure 8.13b can be used as a simple criterion to assess whether addition of benzene disrupts the self-association of the methanol molecules at this particular composition. A value of ~ 6.6 for this ratio in the mixture compared to ~ 4.8 in pure methanol shows that there is far less mobility of the hydrogen atoms between the inner and the outer co-ordination shell in the mixture than that in pure methanol. It is also interesting to note that the main peak position in $g_{HoHo}(r)$ at ~2.36 Å, occurs at nearly the same distance as in pure methanol.

A comparison of the Ho-Ho running co-ordination number (rcn) in the mixture with that in pure methanol can help in quantifying the effect of addition of benzene on the methanol hydrogen bonding. For instance, a larger value of the Ho-Ho rcn in the mixture can be interpreted as a strengthening of the methanol hydrogen bonding with reduced likelihood of π-hydrogen bond formation. On the other hand, smaller co-ordination number in the mixture relative to that in pure methanol can be interpreted

as a weakening of the methanol hydrogen bonding induced by addition of benzene. The Ho-Ho running co-ordination numbers (rcn) plotted in figure 8.13b, reveal that in spheres of radii 2.4 Å and 3 Å there are an average of 1 ± 0.01 and 2 ± 0.01 other Ho atoms, respectively from a central Ho atom. These co-ordination numbers are very close to those obtained in pure methanol (see section 6.1.3dI) where 1 and 2 other Ho atoms were found to occur in spheres of radii 2.36 Å and 2.78 Å, respectively from a central Ho atom. Although the density effect rises with increasing *r*, it is much less pronounced for the Ho-Ho pdf than the HB-HB pdf (see inset figure 8.11b). This is again consistent with the fact that methanol retains its hydrogen bonding in the mixture as compared to benzene, which does not show such an association with itself. For instance, both the Ho-Ho rcns (see inset figure 8.13b) lead to similar co-ordination numbers inside the first co-ordination shell (up to ~3.5Å). In addition, a comparison of the Ho-Ho pdfs shows that the minimum distance of closest approach of the two Ho atoms in the mixture occurs at lower *r* although this effect is relatively small as seen in the Ho-Ho rcns. Interestingly, Munk *et al.* (1993), from the excess volume measurements of liquid mixtures of alkanols with aromatic hydrocarbons, pointed out that as long as the concentration of the alkanols is not too small, strong interaction among their molecules prevails, thereby causing only a small volume change upon mixing. In the region approaching lowest concentrations however, the strong interaction among pairs of alkanols is finally replaced by weak interactions between alkanols and aromatic hydrocarbons, thus resulting in a big increase of excess volume. At the composition of interest in this study, since the excess volume is very small (-0.0221 $cm^3.mol^{-1}$), the strong interaction among methanol molecules is largely retained in the mixture, as also revealed by the above discussion on the pdfs.

The H/D substitution on the Ho atom allows us to extract the Y-Ho (Y= CB, HB, CM, HM and O) PSF (see figure 8.14a) which, after Fourier transformation (see figure 8.14b) is also very instructive of the hydrogen bonding in methanol. The relative weights (see table 8.3) of the methanol-methanol X'-Ho (X'= CM, O and HM) correlations in the mixture contribute ~ 44%, while the CB-Ho and HB-Ho pdfs contribute ~55% to this partial. This partial is thus representative of both solvent-solvent and solute-solvent association, and it can be compared with the X'-Ho partial

extracted from pure methanol. The 55% benzene-methanol contributions should be significant enough to show the existence of the π hydrogen-bond formation in the mixture. If such a bond occurs, it should manifest itself in the Y-Ho partial, and should also induce differences in the methanol-methanol structure (X'-Ho partial in the mixture) compared to that in pure methanol. However, the results reveal (see figure 8.14) that (*i*) hardly any change can be seen from a comparison of the shapes of both the partials, (*ii*) the sharp feature at ~1.78 Å exhibited by the Y-Ho pdf, and assigned to the O···Ho bond between the methanol molecules in the mixture, occurs at the same position as that in pure methanol.

It may be recalled that in the study of pure liquid methanol (see section 6.1.3b), the X'-Ho pdf, and also the O···Ho co-ordination number was found to be altered by the residual features arising from inappropriate intra-molecular model. For instance, it is probable that the feature seen at 2.35 Å in figure 8.14b is an artefact introduced by removing an inappropriate intra-molecular structure. Also, the shape of the main peak at ~1.78 Å may well be affected by the molecular model used. But since the intra-molecular structure of methanol does not change in the mixture (see section 8.2.3a.II) and the same model (corresponding to fit 1 of table 6.2) was used to obtain the X'-Ho and Y-Ho pdfs, any differences between the two partials cannot result from such intra-molecular residual feature. For instance, the feature at 2.35 Å is present in both the Y-Ho and X'-Ho partials. Although the absolute values of the O···Ho rcn obtained may be affected by the same residual feature, these values should be taken with caution. However, differences in the rcn in the mixture and in pure methanol cannot be assigned to this residual effect. In the Y-Ho and X'-Ho pdfs the O···Ho peak may not be well isolated due to contributions from, respectively, four (CB, HB, HM and CM-Ho) and two (HM and CM-Ho) other pairs, which will also induce some differences in the two functions. However, the results of molecular dynamics simulations on pure methanol (see section 6.2.4b) and its mixture with benzene presented in section 8.3 suggest that at low *r* (below ~2.5 Å), the low-*r* tails of the functions resulting from the contributions of the 'other pairs' are of equal magnitudes (see figure 8.14b). Accordingly, rather than discussing the absolute values of co-ordination numbers, which have to be taken with extreme caution, only a comparison

of the Y-Ho with X'-Ho rcns is valuable. Figure 8.14b (inset) shows that the Y-Ho and X'-Ho rcns are very close to each other. Thus, the above results again confirm the already drawn conclusion (from the analyses of the Ho-Ho pdf) that at this composition of the mixture, the hydrogen bonding of methanol is hardly disrupted by the addition of benzene.

The inter-molecular Y-Y PSF was also extracted, and it is shown in figure 8.15. However, its Fourier transformation gives a partial distribution function comprising of many contributions (see table 8.3). This results in a very smooth function (see inset figure 8.15), which is not very informative of the various correlations in the mixture.

H/D substitution on Ho and HB

In the previous section, we concluded on the effect of adding the solute to the solvent indirectly, by looking how the solvent-solvent correlations changed from pure methanol to that in the mixture. The use of H/D substitution on both the Ho and HB sites in the mixture should allow a more direct investigation of the solute-solvent correlations. In particular, if there is any evidence of a π-hydrogen bond formation between the benzene and methanol molecules in the liquid phase under the experimental conditions, similar to the suggestion from the density functional theory studies of small clusters, which are relevant of the gas phase (Hagemeister et al., 1998), its signature should be found in the Ho-HB pdf.

The H-H PSF (H=HB, or Ho) may also be obtained either from the distinct or the inter-molecular DCSs of mixtures I, VI and VII by using the second-order differences (see figure 8.16a). However, because the two atomic sites are substituted at the same time, the H-H PSF comprises of a weighted sum of Ho-Ho (6%), HB-HB (56%) and HB-Ho (38%) correlations (see equation 8.21 and table 8.3). This makes the interpretation of the H-H partial distribution function obtained on Fourier transformation of the H-H PSF rather difficult (see figure 8.16b). However, when the experimental Ho-Ho and HB-HB pdfs of figures 8.13 and 8.11, respectively are combined together in the ratio of the H-H partial, the function so obtained already

shows the characteristics (e.g. the peak at 2.36 Å originating mainly from the Ho-Ho pdf and the two humps at ~ 4.3 Å and ~7 Å) of the H-H pdf. Thus, it suggests that association of benzene with methanol must be weak. In principle, by removing the contributions of the Ho-Ho and HB-HB PSFs in equation 8.21 (referred to as method 1 in the figure captions, see figure 8.17) the Ho-HB PSF may be extracted. Unfortunately, several factors such as the residual inelasticity or the statistical noise make it difficult to assess the errors introduced in the resulting Ho-HB PSF obtained by such higher order difference procedure. However, it is possible to extract the same Ho-HB PSF by using a different set of mixtures II, IV and VI in which the labelled atoms are again Ho and HB. The site-site PSF obtained by using equation 8.12 also contains the Ho-Ho, Ho-HB and HB-HB correlations in which the heavy sample this time is the mixture II,

$$S_{SS}(Q)-1=\frac{1}{c_S^2}\left[c_{Ho}^2(S_{HoHo}(Q)-1)-2c_{Ho}c_{HB}(S_{HoHB}(Q)-1)+c_{HB}^2(S_{HBHB}(Q)-1)\right]. \quad (8.24)$$

This equation differs from equation 8.21 in only the weighting of the Ho-HB partial. Accordingly, the Ho-HB PSF can be extracted by taking a difference of the two equations (8.24 and 8.21) (referred to as method 2, see figure 8.17). Because the contributions of the errors in the two methods are not the same, this should provide a check on the accuracy of the results obtained. Figure 8.17a shows the Ho-HB PSFs obtained by the two methods. The differences in the two PSFs reflecting the effect of different propagated errors in the two methods seem to be very small indeed. It is also interesting to note that the reconstructed Ho-HB PSF, from the MIN technique (lines in figure 8.17a) by the two methods resemble closely. Since both partials (see figure 8.17b) show feature in the region ~1.5 - 3.5 Å which is broad and not intense, it may only be associated to some very weak benzene-methanol correlations. In the light of the above discussion and that already made on the HB-HB pdf, it appears that at the investigated composition, benzene simply plays the role of an inert solute.

The inter-molecular Z-H (Z = HM, CM, O and CB) and Z-Z PSF were also extracted, and are shown in figure 8.18a. However, on Fourier transformation they yield partial

distribution functions (see figure 8.18b) comprising of 8 and 10 pair contributions respectively (see table 8.3). Thus, they are not very informative of the contributing pair-correlations in the mixture.

8.2.4 Summary of the ND study

The neutron diffraction (ND) data on seven different benzene-methanol mixture samples prepared in the molar ratio 1:2 have been used to determine the intra- + inter-(distinct) molecular DCS functions. The use of Hydrogen / Deuterium (H/D) substitutions made on the hydroxyl hydrogen (Ho), benzene hydrogens (HB), and both Ho and HB, showed that the intra-molecular structure of benzene and methanol did not change in passing from the pure components to the mixture. In particular, the O-Ho intra-molecular distance observed in pure methanol at 0.98 ± 0.01 Å was found to be unchanged. The intra-molecular structure factors of the pure components were then used to separate the intra-molecular structure from the distinct DCSs of the mixture samples. Fourier transformation of the inter-molecular DCSs yielded the inter-molecular radial distribution functions. Since these functions comprise of twenty-one pair distribution functions (pdfs), they cannot provide any useful information on the inter-molecular structure of the mixture. The H/D substitution on the various atomic sites was used to separate some of the partial distribution functions. As revealed by the HB-HB pdf, the larger distances occurring between the benzene molecules indicate weaker benzene-benzene interactions due to the presence of methanol molecules. This in turn, suggests a loss of their relative orientational correlations in the mixture. On the self-association of methanol in the mixture it was found that the inter-molecular O···Ho and Ho-Ho bond distances in the mixture are similar to those in pure methanol. Moreover, the Ho-Ho and O···Ho running co-ordination numbers in the mixture do not differ from those in pure methanol. Thus, at the investigated composition, the hydrogen bonding of methanol is retained in the mixture. The HB-Ho solute-solvent correlations extracted from two different sets of three H/D substituted samples were found to be consistent to each other. These show that association of benzene with methanol is very weak, suggesting that benzene simply plays the role of an inert solute in the mixture.

8.3 The MD simulation study

8.3.1 Methodology

Each methanol molecule in the mixture was treated as a rigid object consisting of six atomic sites corresponding to the oxygen (O), the carbon (CM), the hydrogen of the hydroxyl group (Ho) and three methyl hydrogens (HM), while each benzene molecule consisted of twelve atomic sites corresponding to the six carbons (CB) and the six hydrogens (HB). This treatment is similar to that employed in the MD studies of each of the pure components (see sections 6.2 and 7.3). The structural parameters of methanol were taken from the millimetre wave studies of Lees and Baker (1968) (listed in table 6.4) whereas those of benzene were taken from Cyvin (1968) (listed in table 7.1).

Since the 3-site model potential for methanol (referred here as H1 model) parameterised by Haughney *et al.* (1987) reproduced its experimental structural features better than the 6-site model (see section 6.2), the 3-site potential model was used in simulating the behaviour of benzene-methanol mixture. The model treats the methyl hydrogens as a dead load, and it consists of three sites corresponding to oxygen (O), the methyl group treated as a unified carbon (CM) and hydrogen of the hydroxyl group (Ho), interacting via Lennard-Jones (LJ) potential. The inter-molecular potential is thus written as a sum of Lennard-Jones and Coulomb parts,

$$V_{ij}(r_{ij}) = \sum_{i=1}^{3}\sum_{j=1}^{3} \frac{q_i q_j}{4\pi\varepsilon_0 r_{ij}} + 4\varepsilon_{ij}\left[(\sigma_{ij}/r_{ij})^{12} - (\sigma_{ij}/r_{ij})^{6}\right], \qquad (8.25)$$

where ε_{ij} and σ_{ij} are the LJ parameters between sites i and j of distinct molecules, q_i is the partial charge on site i and r_{ij} is the site-site separation. The potential parameters are listed in table 6.5. Although, for pure liquid benzene, the three MD simulations performed with different 12-site model potentials led to similar structural results (see section 7.4), benzene in the mixture was treated by the all-atom model of Jorgensen

and Severance (1990) (referred to as JS12). As for methanol, the functional form of this model is given for each pair of atoms by the sum of a Coulombic and a Lennard-Jones (LJ-12-6) term. The force field parameters for benzene are all summarised in table 7.3. The cross interactions between atomic pairs pertaining to different molecules (CB-CM, CB-O, HB-CM and HB-O) were obtained from Lorentz-Berthelot rules $\varepsilon_{ij} = \sqrt{\varepsilon_{ii}\varepsilon_{jj}}$ and $\sigma_{ij} = (\sigma_{ii} + \sigma_{jj})/2$. Such a simple model does not suffer from the drawback of the potential model used by Adachi and Nakanishi (1991, 1993). The presence of various inverse cubic terms in their force field makes the potential truncation corrections to the calculation of some simple thermodynamics properties impossible with a standard treatment (Allen and Tildesley, 1987).

The equations of motion were integrated using the Verlet leap-frog algorithm for translational motion (see section 3.5), and the Fincham's implicit quaternion algorithm (FIQA) for rotational motion of rigid bodies (see section 3.6.2). The MD simulations were performed in the NVE ensemble at 298.15 K with 144 methanol and 72 benzene molecules placed in a cubic box with periodic boundary conditions (see section 3.3). The box length of 27.31 Å was chosen so as to match the experimental density, 0.83456 g/cm^3 of the mixture at the benzene-methanol molar ratio 1:2 (Munk et al., 1993). A cut-off radius equal to half the box length was applied to all the interactions (see section 3.4). In all the MD simulation runs, the time step was equal to 0.002 ps. Ewald summation (EW) was used for handling the long range coulombic interactions (see section 3.7.3).

Table 8.4 summarises the details of the MD simulations, and compares some of the calculated thermodynamic properties with their experimental values. The agreement seems reasonable, suggesting that the Lorentz-Berthelot mixing rules are probably adequate.

8.3.2 Results and discussion

ND measurements performed on seven different H/D substituted benzene-methanol mixtures yielded the total inter-molecular radial distribution functions (rdfs), each of

which contains 21 pdfs. The simulated pdfs displayed in figures 8.19-23 combined in the ratio of their neutron weights (listed in table 8.2) are compared with their experimental counterparts (rdfs) in figure 8.24. Although, they are found to be in reasonable agreement with each other, these functions cannot provide useful information because of the presence of a large number of contributing pairs.

a. Methanol association

The simulated partial pair distribution functions (pdfs), $g_{\alpha\beta}(r)$ common to both pure methanol and methanol in the mixture are plotted together in figures 8.19 and 8.20. It can be seen that although the shapes of all the ten pdfs pertaining to methanol in the mixture are similar to those in pure methanol, the heights of the main peaks in the former are bigger, due to the density effect. Of these, the O-Ho, Ho-Ho and O-O pdfs are indicative of the hydrogen bonding between methanol molecules, and the positions of the main peaks in these functions remain unchanged (see table 8.5). Moreover, in the low-r range (up to ~3.5 Å), where the hydrogen bonding distances are expected to occur, the O-Ho, O-O (see figure 8.19) and Ho-Ho (see figure 8.26c inset) co-ordination numbers in the mixture are similar to those in pure methanol (see also table 8.5). The ratio of the height of first maximum to that of the first minimum, $g(r_{M1})/g(r_{m1})$ calculated for each of the three pairs (see table 8.5) can be used as a qualitative indication of the relative stability of the hydrogen bonding in the mixture vis a vis that in methanol. Similar values for these ratios (see table 8.5) suggest that mobility between the inner and outer co-ordination shell of the various methanol atoms involved in the hydrogen bonding in the mixture is similar to that in pure methanol. Figure 8.25 presents instantaneous configurations of methanol molecules both in pure methanol and in the mixture. Both plots show the existence of methanol network formed by hydrogen bonding between different molecules. Dimeric, trimeric and polymeric species in the form of linear and bent chains are all visible both in pure methanol as well as in the mixture. Relatively small number of monomers are also found to be present in the mixture, and the blank space in the mixture plot is taken up by the incoming benzene molecules. It may be safely concluded from the above

discussion that the extent and "strength" of hydrogen bonding in methanol is not diminished by addition of benzene at the investigated composition.

A comparison of the Ho-Ho pdf obtained from the simulation with the one obtained from NDIS experiments shows (see figure 8.26a) that the agreement is only qualitative. It can be seen that, similar to that in pure methanol (see figure 8.26b), the main peak is shifted by ~ 0.13Å toward higher r. Moreover, although the position and depth of the first minimum are correctly reproduced, the MD peak is higher than the experimental one. The $g(r_{M1})/g(r_{m1})$ ratios computed from the simulated and experimental results differ (see table 8.5). A comparison of these values with those in pure methanol (see table 8.5) shows that the loss of mobility of the Ho atoms in passing from pure methanol to the mixture is predicted to a lesser extent by the simulations. Also, the minimum distance of closest approach between two Ho atoms is underestimated in the simulation. In addition, the Ho-Ho rcns presented in figure 8.26c reveal that the simulation underestimates the co-ordination numbers at all r-values in comparison to the ND results. Similar trend is observed for the Ho-Ho rcn in pure methanol also (see figure 8.26d). The difference between the HoHo rcns in the mixture and pure methanol should give a quantitative indication of the extent to which benzene disrupts the self-association of the methanol molecules. The differences obtained from the MD results shown along with those from NDIS experiments in figure 8.26d inset are both close to zero. This further authenticates the already reached conclusion that hydrogen bonding in methanol is hardly affected upon addition of benzene to it.

The H/D substitution on the hydroxyl hydrogen permits us to look at the correlations of this atom with its closest neighbours both in the case of pure methanol and benzene-methanol mixture through the inter-molecular $G_{X'Ho}(r)$ and $G_{YHo}(r)$ partial distribution functions (see figure 8.27), respectively. These functions comprise of a weighted sum of three (CM-Ho, O-Ho and HM-Ho) and five (CM-Ho, O-Ho, HM-Ho, CB-Ho and HB-Ho) pdfs, respectively, and as seen earlier from the ND study of pure methanol, removal of an inappropriate methanol intra-molecular structure could produce artefacts in the experimental inter-molecular X'-Ho partial (see section

6.1.3b). Thus, for a correct assessment of the quality of the potential models used in the simulations of pure methanol, comparison between the simulated and experimental X'-Ho partial (see section 6.2.4b) was done at both the inter- and inter- + intra- molecular levels. Since these artefacts, if they exist, are likely to affect the ND Y-Ho partial, only qualitative comparison with its simulated counterpart is of use at the inter-molecular level, especially in the region 0-3 Å where these effects occur. Figure 8.27a shows that the agreement obtained in this range is reasonable. At r greater than 3 Å where no residual from the intra-molecular structure of methanol is expected to affect the partial, the agreement although satisfactory, is not quantitative. For instance, the simulated function is shifted slightly toward higher r as compared to the experimental partial.

The relative weights (see table 8.3) of the X'-Ho (X'= CM, O and HM) pdfs of about 9, 8 and 27% make ~ 44% methanol-methanol contributions to the Y-Ho partial. The CB-Ho and HB-Ho benzene-methanol (B-M) pdfs contribute equally, and give rise to a contribution of ~55% to this partial. These B-M correlations should be indicative of the π hydrogen-bond formation in the mixture, and if such a bond occurs, it should manifest itself in the Y-Ho partial. Such a bonding should also induce differences in the methanol-methanol structure in the mixture relative to that in pure methanol. Accordingly, the Y-Ho partial should differ from the inter-molecular X'-Ho partial obtained in pure methanol. Since the two experimental partials (see section 8.2.3bII) were obtained after removal of the same intra-molecular model (fit1 of table 6.2), the differences noted between the Y-Ho and X'-Ho partials originate from the effect of adding benzene to methanol. Figure 8.27b compares the Y-Ho partial with the X'-Ho partial obtained from both the simulations and the ND experiments. Although, the two functions resemble each other in both cases, the differences observed are only very slight. This can be understood if one combines the CB-Ho and HB-Ho pdfs in the ratio of their relative neutron weights of the Y-Ho partial. Such a function representative of the association between benzene and methanol is found (see bottom of figure 8.27a) to be completely featureless. The above results thus, do not support the formation of a π hydrogen-bond in the liquid mixture at the investigated composition. The $G_{YY}(r)$ partial distribution function, also obtained from the NDIS on

the Ho atom is a weighted sum of 15 different pair contributions. The methanol-methanol, methanol-benzene and benzene-benzene correlations contribute ~20%, 50%, and 30%, respectively to this partial. The MD equivalent of this function was constructed, as before, from the simulated pdfs, and the results from both ND and MD are displayed in figure 8.27c. Because this partial comprises of many pairs, it appears invariably featureless and not very revealing. Although slight differences can be seen, the overall agreement between MD and ND functions is satisfactory.

b. Benzene association

The simulated partial pair distribution functions (pdfs), $g_{\alpha\beta}(r)$ common to both pure benzene and benzene in the mixture are plotted together in figures 8.21 and 8.22. It can be seen that the CB-HB, CB-CB and HB-HB pdfs in the mixture resemble those obtained in pure benzene (see figures 8.21 and 8.22). For instance, the shoulder at ~4.2 Å and both the peaks at 5.13 Å and 6.21 Å observed in the CB-CB pdf in the mixture are located at the same positions as those in pure benzene. The only notable change in these partials is in the period of the oscillations that are larger and smear out quickly in the mixture than in pure benzene. This is attributable to the density effect, which makes the average separation between two closest atoms larger in the mixture (see the running co-ordination numbers of the various pairs in insets of figure 8.21 and 8.22). Figure 8.22b compares the HB-HB partial obtained in pure benzene and in the mixture from both the simulations and the ND experiments. Although the two functions resemble each other in both cases, when MD and ND functions are compared (see figure 8.22b) several features are not reproduced by the simulations. For instance, the experimental peak at ~3.5 Å is absent in the simulations. Moreover the small peak at ~2.4 Å in the experimental HB-HB pdf of pure benzene, which became a shoulder in the mixture (at ~2.6 Å), is also not reproduced by the simulations. It is worth reminding that such differences in the shapes and positions of the various features of the HB-HB pdfs between MD and ND were also observed in pure benzene (see section 7.4). The fact that the average separation between the closest benzene atoms is larger in the mixture than in pure benzene (see figure 8.22b), reflects that the incoming methanol molecules push the benzene molecules away from

each other. This, in turn, may be associated to a relative loss of the benzene-benzene orientational correlations in the mixture. Since the CB-CB, HB-HB and CB-HB pdfs in the mixture are very close to those in pure benzene, it suggests that the orientational correlations in pure benzene are very weak, and its structure is mainly dominated by the packing effects.

The inter-molecular $G_{XX}(r)$ (X=Ho, O, CM, HM, CB) and $G_{XHB}(r)$ partial distribution functions obtained from the ND H/D substitution on the HB atoms are compared in figure 8.28 with their simulated counterparts constructed by summing the respective pdfs in the ratio of their neutron weights. They show reasonable overall agreement with each other, but they differ at a quantitative level. For instance, although the MD results reproduce the experimental hump at ~7.4 Å in the $G_{XHB}(r)$, the shoulder at ~2.6 Å is not reproduced by the simulations. For the $G_{XX}(r)$ partial, both the main broad peak and the foot of the $G_{XX}(r)$ at ~2 Å partial are overemphasised in the MD simulations. Since the $G_{XHB}(r)$ and $G_{XX}(r)$ partials comprise respectively of a weighted sum of five and fifteen pdfs, further interpretation of these functions is difficult.

c. Benzene - methanol association

In section 8.3.2a, the effect of adding a solute (benzene) to the solvent (methanol) was investigated indirectly by observing how the solvent-solvent correlations changed in passing from pure methanol to the mixture. More directly however, the eight simulated partial pdfs, $g_{\alpha\beta}(r)$ pertaining to the benzene-methanol contributions in the mixture (see figure 8.23) should allow us to investigate the extent to which benzene and methanol are associated. Among these pairs, the Ho-CB, O-HB, O-CB, and Ho-HB pdfs are of particular interest since it is from them that a signature of a π-hydrogen bond formation can be found. From a multiphoton ionisation studies of small benzene-methanol clusters, Garrett et al. (1992) and Pribble et al. (1997) suggested that when a π-hydrogen bond between a benzene and a methanol molecule is formed, the lowest energy structure is the one in which the hydroxyl group of methanol points towards the benzene ring (see figure 8.29). If such an association

were possible in the liquid mixture under investigation, the simple criterion $d_{OHB} > d_{CBHO}$, $d_{OHB} > d_{OCB}$ and $d_{HBHo} > d_{CBHO}$ must be satisfied, where $d_{\alpha\beta}$ is the closest distance of approach between α and β atoms. However, the simulated pdfs reveal (see figure 8.23) exactly the reverse situation ($d_{OHB} \sim d_{CBHO} \sim 2.2$ Å, $d_{OCB} \sim 2.97$ Å, and $d_{HBHo} \sim 1.9$ Å), indicating that the hydroxyl group is pointing away from the benzene ring. Interestingly, from the MD study at room temperature by Laaksonen et al. (1998) for which two benzene molecules were placed in a cubic box containing 254 water molecules (benzene and water do not form a homogeneous mixture under ambient conditions) the simple criterion $d_{OHB} > d_{CBHW}$ (HW=hydrogen atom of water), $d_{OHB} > d_{OCB}$ and $d_{HBHW} > d_{CBHW}$ is satisfied (see figure 8.30). In this regard, the local structure of water around benzene molecule was found to be consistent with the hydrogen of water pointing towards the ring cavity of benzene. Thus, the highest probability to find the water oxygen around the benzene molecule is above the benzene ring. Accordingly, Laaksonen et al. (1998), by constructing of angular spatial distribution functions, interpreted the presence of a shoulder at a distance of 2.5 Å in the CB-HW pdf as an indication that the hydrogen atoms of water occasionally come close to the benzene ring region. Such a shoulder is also found (see figure 8.23) at the same distance in the Ho-CB pdf of benzene-methanol system, but similar conclusion cannot be drawn since our simple criterion is not satisfied.

The use of the H/D substitution technique on both Ho and HB sites allowed us to extract an experimental partial distribution function, $G_{HH}(r)$ comprising of Ho-Ho, Ho-HB and HB-HB pairs, contributing respectively ~6%, ~37%, and ~56% to the H-H partial. The simulated H-H partial obtained by adding the three pdfs in the ratio of their neutron weights is compared with its experimental counterpart in figure 8.31a. One can see that the experimental partial is reproduced only qualitatively. For instance, the simulated peaks at low-r are slightly shifted towards larger distances. Although the weighting of the Ho-HB solute-solvent correlations is larger than that of the Ho-Ho pair, the latter contribution has a marked influence on the overall structure. This together with the HB-HB contribution mask any features of the Ho-HB pdf (see figure 8.31a) in the H-H partial. Experimentally, the Ho-HB pdf has been the subject of residual experimental errors (see discussion in section 8.2.3b). It was thus obtained by using two independent methods as a consistency check on the accuracy of the

results. Although the two experimental pdfs differ in some detail, these differences are never larger than those exhibited when any of the experimental pdf is compared with the simulated function (see figure 8.31b). For instance the simulated Ho-HB pdf is significantly shifted towards higher *r*.

8.4 Conclusions

Two different model potentials employed previously for the computer simulation studies of the two pure components and tested against the experimental results obtained by ND H/D substitutions on liquid methanol and benzene in chapter 6 and 7, respectively, were used to perform a MD simulation of benzene-methanol mixture (molar ratio 1:2). The simulated structure of the mixture was interpreted with the help of the results obtained from the simulations of the pure components. The results show that the hydrogen bonding of methanol molecules in pure methanol is not disrupted by the addition of benzene. Similar conclusion was reached from the ND experimental structural results (see sections 8.2.3 and 8.2.4). From the investigations of the solute-solvent and solute-solute correlations, the formation of a π-hydrogen bond between benzene and methanol cannot be supported. Only a weak association between the solute and the solvent is found. The structure of benzene in the mixture is found to be very similar to that in pure benzene, suggesting that benzene plays the role of an inert solute in the mixture. This is again consistent with the findings from the ND experiments. Although the simulations of the mixture, with a 3-site model for the methanol and an all-atom 12-site model for the benzene, give a relatively good account of its structural behaviour and the extent to which addition of benzene affects the structure of methanol, the agreement between the simulated and experimental structural functions of the mixture is only qualitative.

Table 8.1. The thermodynamic conditions and the sample parameters used in the data analyses of the benzene-methanol mixtures.

Samples / Parameters	C_6D_6 + CD_3OD	C_6D_6 + CD_3OH	C_6D_6 + $CD_3O(H/D)$	C_6H_6 + CD_3OD	$C_6(H/D)_6$ + CD_3OD	$C_6(H/D)_6$ + $CD_3O(H/D)$	C_6H_6 + CD_3OH
Temperature / (K)	298±1 K	298±1 K	298±1 K	298±1 K	298±1 K	298±1 K	298±1 K
Pressure / (bar)	1	1	1	1	1	1	1
number density [d] / (molecule Å^{-3})	0.0106	0.0106	0.0106	0.0106	0.0106	0.0106	0.0106
σ_a at 1.8 Å / (b molecule^{-1})	4.893×10^{-2}	0.239	0.128	0.678	0.347	0.459	0.901
[a] b_c C / (fm)	6.646	6.646	6.646	6.646	6.646	6.646	6.646
[b] b_c Hm / Ho (methyl / hydroxyl) / (fm)	6.6502 / 6.6502	6.619 / -3.739	6.635/1.456	6.6502 / 6.6502	6.6502 / 6.6502	6.635/1.456	6.619 / -3.739
[a] b_c HB / (fm)	6.629	6.629	6.629	-3.739	1.445	1.445	-3.739
[a] b_c O / (fm)	5.803	5.803	5.803	5.803	5.803	5.803	5.803
$\left(\sum_{i=1}^{2} x_i \sum_{\alpha_i}^{Nm_i} c_{\alpha_i} \bar{b}_{\alpha_i}\right)^2$ / (b molecule^{-1})	27.650	20.789	24.098	10.142	17.821	14.993	6.179
[c] $lim_{Q\to\infty}\left(\frac{\partial\sigma}{\partial\Omega}\right)_{dist}$ /(b molecule^{-1})	4.32 (~ 4.5)	8.29 (~8.2)	6.31(~6.6)	16.11(~14.5)	10.21(~9.3)	12.20(~11.1)	20.08(~17.7)

a: from Sears (1992); b: calculated according to the isotopic composition and purity of the sample; c: theoretical values are compared with the experimental values given in parenthesis, the differences increase with the amount of protonated hydrogen present in the various samples due to the inelasticity effects; d: the density was calculated according to the experimental value of the excess volume for the (1:2) benzene-methanol mixture, from Munk et al. (1993).

Table 8.2. The inter-molecular neutron weights of the various total distribution functions in benzene-methanol (1:2) liquid mixture.

pair $\alpha\beta$	mixture I	mixture II	mixture III	mixture IV	mixture V	mixture VI	mixture VII
Ho Ho	0.0071	0.0030	0.0004	0.0194	0.0110	0.0006	0.0101
Ho O	0.0124	-0.0093	0.0031	0.0338	0.0192	0.0050	-0.0312
Ho CM	0.0142	-0.0106	0.0036	0.0387	0.0220	0.0057	-0.0357
Ho HM	0.0426	-0.0317	0.0107	0.1163	0.0662	0.0172	-0.1068
Ho CB	0.0426	-0.0318	0.0107	0.1162	0.0662	0.0172	-0.1072
Ho HB	0.0425	-0.0318	0.0107	-0.0654	0.0144	0.0037	0.0603
O O	0.0054	0.0072	0.0062	0.0148	0.0084	0.0100	0.0242
O CM	0.0124	0.0165	0.0142	0.0339	0.0192	0.0229	0.0555
O HM	0.0372	0.0493	0.0426	0.1014	0.0577	0.0685	0.1658
O CB	0.0372	0.0495	0.0427	0.1014	0.0577	0.0686	0.1664
O HB	0.0371	0.0493	0.0426	-0.0570	0.0125	0.0149	-0.0936
CM CM	0.0071	0.0094	0.0081	0.0194	0.0110	0.0131	0.0318
CM HM	0.0426	0.0564	0.0488	0.1162	0.0661	0.0784	0.1898
CM CB	0.0426	0.0567	0.0489	0.1161	0.0661	0.0786	0.1906
CM HB	0.0425	0.0565	0.0488	-0.0653	0.0144	0.0171	-0.1072
HM HM	0.0640	0.0843	0.0731	0.1744	0.0993	0.1174	0.2836
HM CB	0.1279	0.1693	0.1464	0.3486	0.1984	0.2353	0.5695
HM HB	0.1276	0.1689	0.1460	-0.1961	0.0431	0.0512	-0.3204
CB CB	0.0639	0.0850	0.0733	0.1742	0.0991	0.1178	0.2859
CB HB	0.1275	0.1695	0.1463	-0.1960	0.0431	0.0512	-0.3217
HB HB	0.0636	0.0846	0.0730	0.0551	0.0047	0.0056	0.0905

Table 8.3. The inter-molecular neutron weights of the various partial distribution functions in benzene-methanol (1:2) liquid mixture.

pair $\alpha\beta$	$g_{HBHB}(r)$	$G_{XHB}(r)$ [a]	$G_{XX}(r)$ [a]	$g_{HoHo}(r)$ [a]	$G_{YHo}(r)$ [a]	$G_{YY}(r)$ [a]	$G_{HH}(r)$ [a]	$G_{ZH}(r)$ [a]	$G_{ZZ}(r)$ [a]	$g_{HoHB}(r)$ [a] method 1	$g_{HoHB}(r)$ [a] method 2
Ho Ho	0.0000	0.0000	0.0127	0.9822	0.0004	0.0001	0.0624	0.0001	0.0000	0.0029	0.0000
Ho O	0.0000	0.0000	0.0222	0.0000	0.0797	0.0001	0.0000	0.0278	0.0001	0.0000	0.0000
Ho CM	0.0000	0.0000	0.0254	0.0000	0.0912	0.0001	0.0000	0.0318	0.0001	0.0000	0.0000
Ho HM	0.0000	0.0000	0.0762	0.0177	0.2731	0.0004	0.0011	0.0950	0.0003	0.0001	0.0000
Ho CB	0.0000	0.0000	0.0762	0.0000	0.2737	0.0004	0.0000	0.0952	0.0003	0.0000	0.0000
Ho HB	0.0000	0.1127	0.0001	0.0000	0.2730	0.0004	0.3737	0.0002	0.0002	0.9880	0.9911
O O	0.0000	0.0000	0.0097	0.0000	0.0000	0.0065	0.0000	0.0000	0.0123	0.0000	0.0000
O CM	0.0000	0.0000	0.0221	0.0000	0.0000	0.0148	0.0000	0.0000	0.0281	0.0000	0.0000
O HM	0.0000	0.0000	0.0665	0.0000	0.0007	0.0443	0.0000	0.0002	0.0842	0.0000	0.0000
O CB	0.0000	0.0000	0.0664	0.0000	0.0000	0.0444	0.0000	0.0000	0.0844	0.0000	0.0000
O HB	0.0000	0.0984	0.0001	0.0000	0.0000	0.0443	0.0000	0.0830	0.0002	0.0000	0.0000
CM CM	0.0000	0.0000	0.0127	0.0000	0.0000	0.0085	0.0000	0.0000	0.0161	0.0000	0.0000
CM HM	0.0000	0.0000	0.0761	0.0000	0.0008	0.0507	0.0000	0.0003	0.0964	0.0000	0.0000
CM CB	0.0000	0.0000	0.0761	0.0000	0.0000	0.0508	0.0000	0.0000	0.0967	0.0000	0.0000
CM HB	0.0000	0.1127	0.0001	0.0000	0.0000	0.0507	0.0000	0.0950	0.0002	0.0000	0.0000
HM HM	0.0000	0.0000	0.1143	0.0001	0.0025	0.0759	0.0000	0.0009	0.1443	0.0000	0.0000
HM CB	0.0000	0.0000	0.2284	0.0000	0.0025	0.1521	0.0000	0.0009	0.2893	0.0000	0.0000
HM HB	0.0000	0.3382	0.0003	0.0000	0.0025	0.1517	0.0034	0.2844	0.0006	0.0089	0.0089
CB CB	0.0000	0.0000	0.1141	0.0000	0.0000	0.0762	0.0000	0.0000	0.1450	0.0000	0.0000
CB HB	0.0000	0.3380	0.0003	0.0000	0.0000	0.1521	0.0000	0.2851	0.0006	0.0000	0.0000
HB HB	1.0000	0.0000	0.0000	0.0000	0.0000	0.0758	0.5594	0.0002	0.0004	0.0000	0.0000

[a] The residual contributions appear because the extent of deuteration on benzene and methanol used in the various samples are not 100%; these contributions are however very small.

Table 8.4. Details of the MD simulations and the simulated thermodynamics properties for benzene-methanol mixture at 298.15 K.

	simulations	Experiment
Force-field model	(H1 + CH_3) + JS12	- -
Long-range (Coulomb) interactions treatment	EW	- -
Algorithm	Vlf +FIQA, Rigid body	- -
Equilibration time, ps	64	- -
Sampling time, ps	64	- -
< T >, K	297.5 ± 8.8	298 ±1
- < U >, kJ/mol	33.44 ±0.22	34.95 [a]
$< \Delta H_x^M >$, kJ/mol [a]	0.563±0.22	0.463[b], 0.438[c]
< P >, kbar	0.44 ± 0.29	~ 0.001

[a] The simulated enthalpy of mixing of 1:2 benzene-methanol was calculated from the simulated configurational energy of the mixture, of pure methanol (35.3 ± 0.22 kJ/mol) and of pure benzene (31.41± 0.24 kJ/mol). [b] From Goates et al. (1961). [c] From Letcher et al. (1991). EW stands for Ewald summation, Vlf for Verlet leap-frog algorithm, FIQA for Fincham's Implicit Quaternion algorithm.

Table 8.5. Characteristics of the Ho-Ho, O-Ho, and O-O partial pdfs for the simulated liquid methanol and benzene-methanol mixture as compared to the the same functions obtained from experimental data (values in parenthesis).

Pdf	r_{MI}[d]	$g(r_{MI})$	r_{mI}[d]	$g(r_{mI})$	$g(r_{MI})/g(r_{mI})$	r^d, n=1	r^d, n=2	r^d, n=3
Ho-Ho in pure methanol	2.49 (2.36)	2.79 (2.46)	3.38 (3.45)	0.32 (0.51)	8.72 (4.82)	2.51 (2.36)	2.96 (2.78)	4.0 (3.56)
Ho-Ho in the mixture	2.49 (2.36)	5.33 (4.34)	3.42 (3.5)	0.56 (0.66)	9.52 (6.57)	2.51 (2.4)	3.19 (3.0)	4.23 (3.85)
O-Ho[a] in pure methanol	1.88 (1.78)	3.47 (3.73[b])	2.63	0.16	21.69	2.74 (2.15[b])	3.49	4.02
O-Ho[a] in the mixture	1.88 (1.78)	6.71 (9.5[b])	2.62	0.32	20.97	2.91 (2.2[b])	3.59	4.25
O-O in pure methanol	2.79 (2.76-2.8[c])	3.38	3.53	0.28	12.07	2.84	3.43	4.2
O-O in the mixture	2.79	6.6	3.54	0.50	13.2	2.86	3.68	4.43

[a] values obtained after removing the intra-molecular DCS corresponding to fit1 ; [b] values to be taken with caution since the intra-molecular structure removal might have induced some artefacts in these functions (see section 6.1.3d and 8.2.3b); [c] from Narten and Habenschuss (1984); [d] values given in Å; r_{MI} is the position of the first maximum;; r_{mI}, position of the first minimum;; $g(r_{MI})$ = height of first maximum, $g(r_{mI})$ = height of first minimum; $r, n= i$ is the distance value at which the co-ordination number value i occurs.

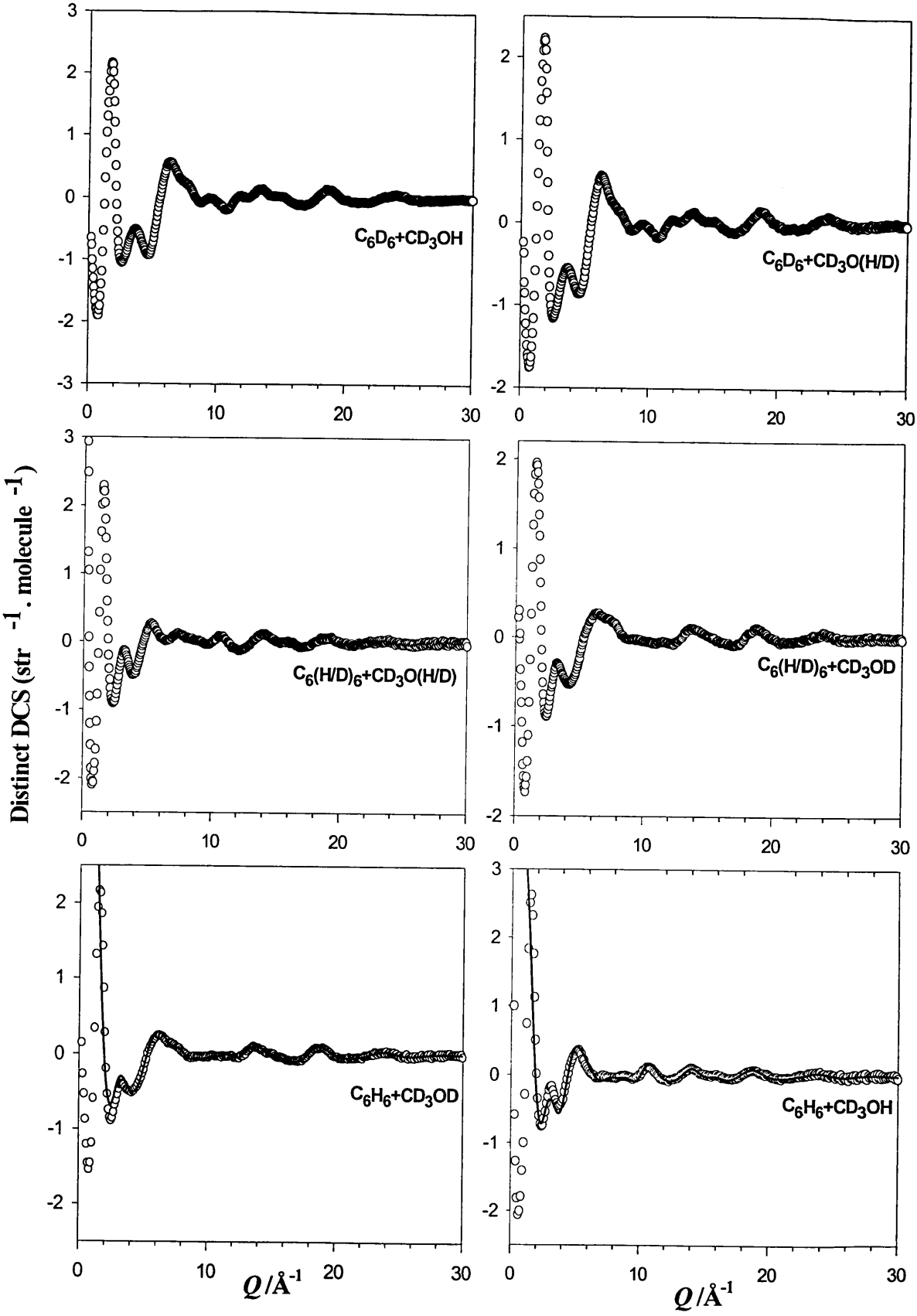

Figure 8.1. The various distinct differential cross sections per molecule for the different benzene-methanol samples.

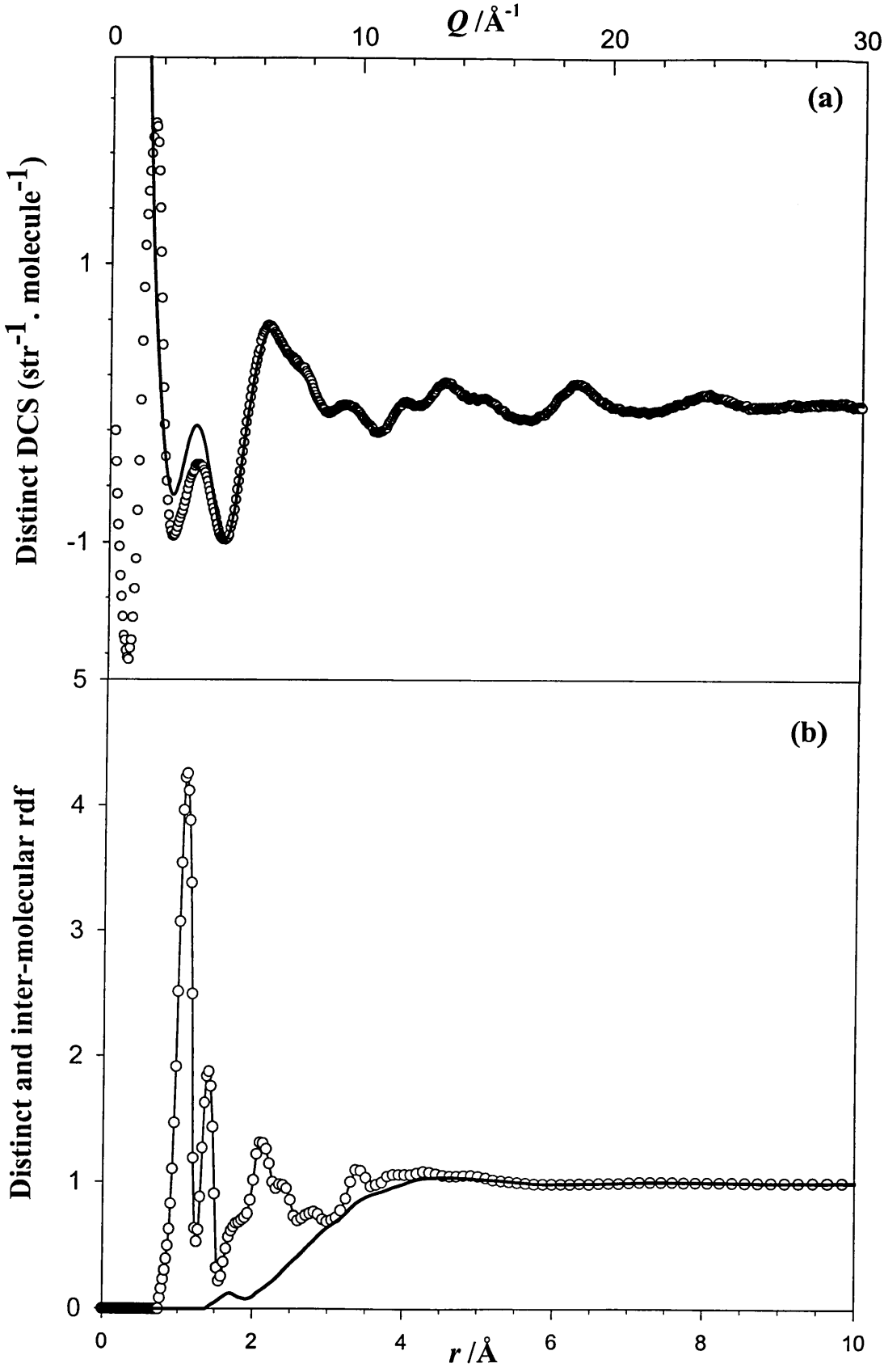

Figure 8.2. (a) The distinct DCS for C_6D_6+CD_3OD (circles) along with its intra-molecular structure factor (solid line). (b) The distinct rdf for the C_6D_6+CD_3OD mixture (symbols) compared to its corresponding inter-molecular rdf (solid line).

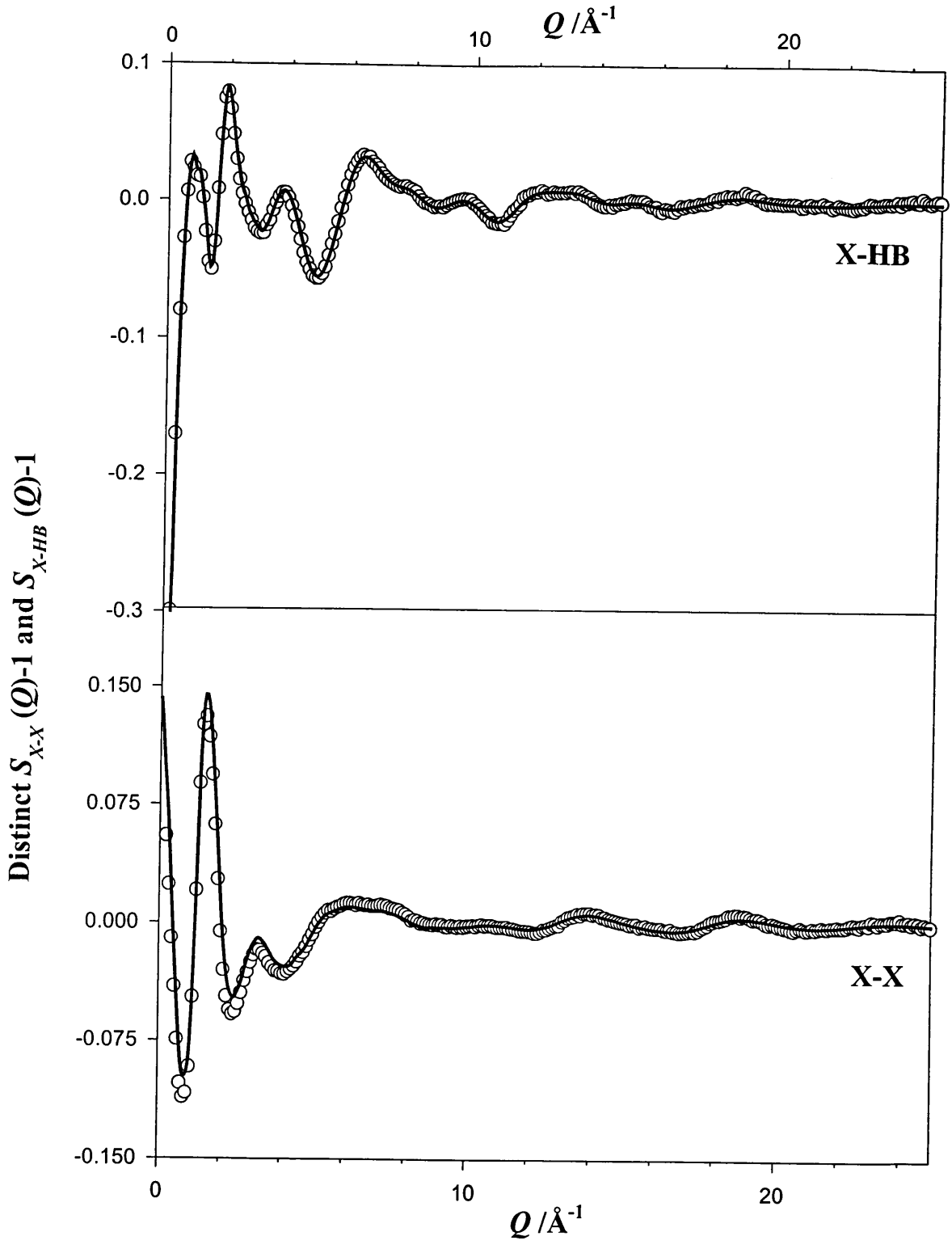

Figure 8.3. The distinct X-X (X=CB, CM, HM, O and Ho) and X-HB PSF (symbols) obtained from higher order difference method along with the back Fourier transforms (lines) of their respective partial distribution functions of figure 8.4.

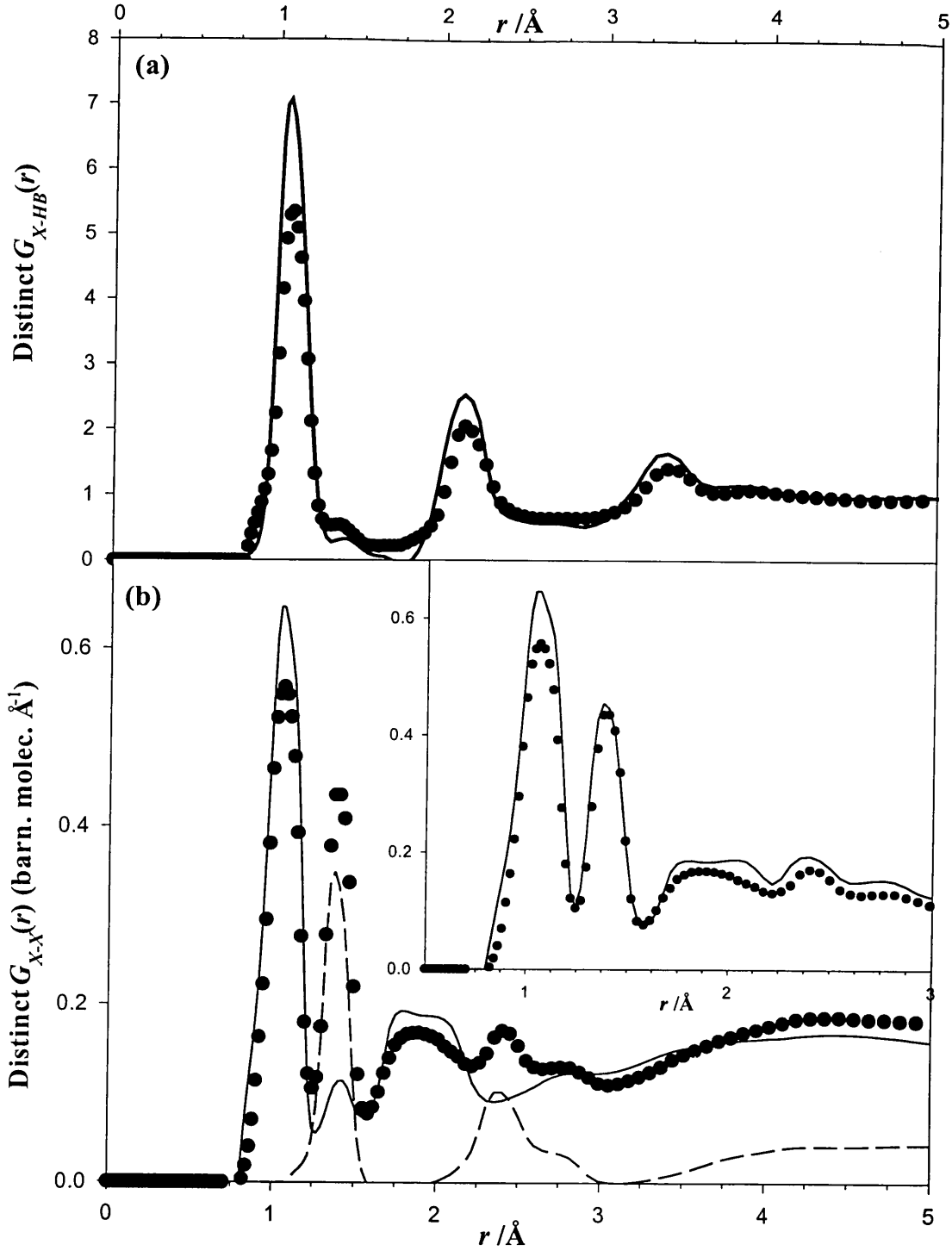

Figure 8.4. (a) The distinct X-HB partial distribution function (symbols) compared to the distinct CB-HB pdf of pure benzene (line). (b) The distinct X-X partial distribution function (symbols) along with the distinct rdf of CD_3OD (line), and the distinct CB-CB pdf of pure benzene (dashed line). These functions are all presented on an absolute scale (each partial was multiplied by its corresponding molecular number density, and its normalisation factor $(\Sigma b_i)^2$, in addition the pure components functions were weighted by their molar fraction x_i for which they are represented in the mixture). The inset shows the distinct X-HB partial distribution function (symbols) along with an added function (line) obtained from combining the distinct rdf of pure CD_3OD, and the distinct CB-CB pdf of pure benzene. The quantitative comparison of the two functions is of interest only in the range ~ 0-1.7Å only.

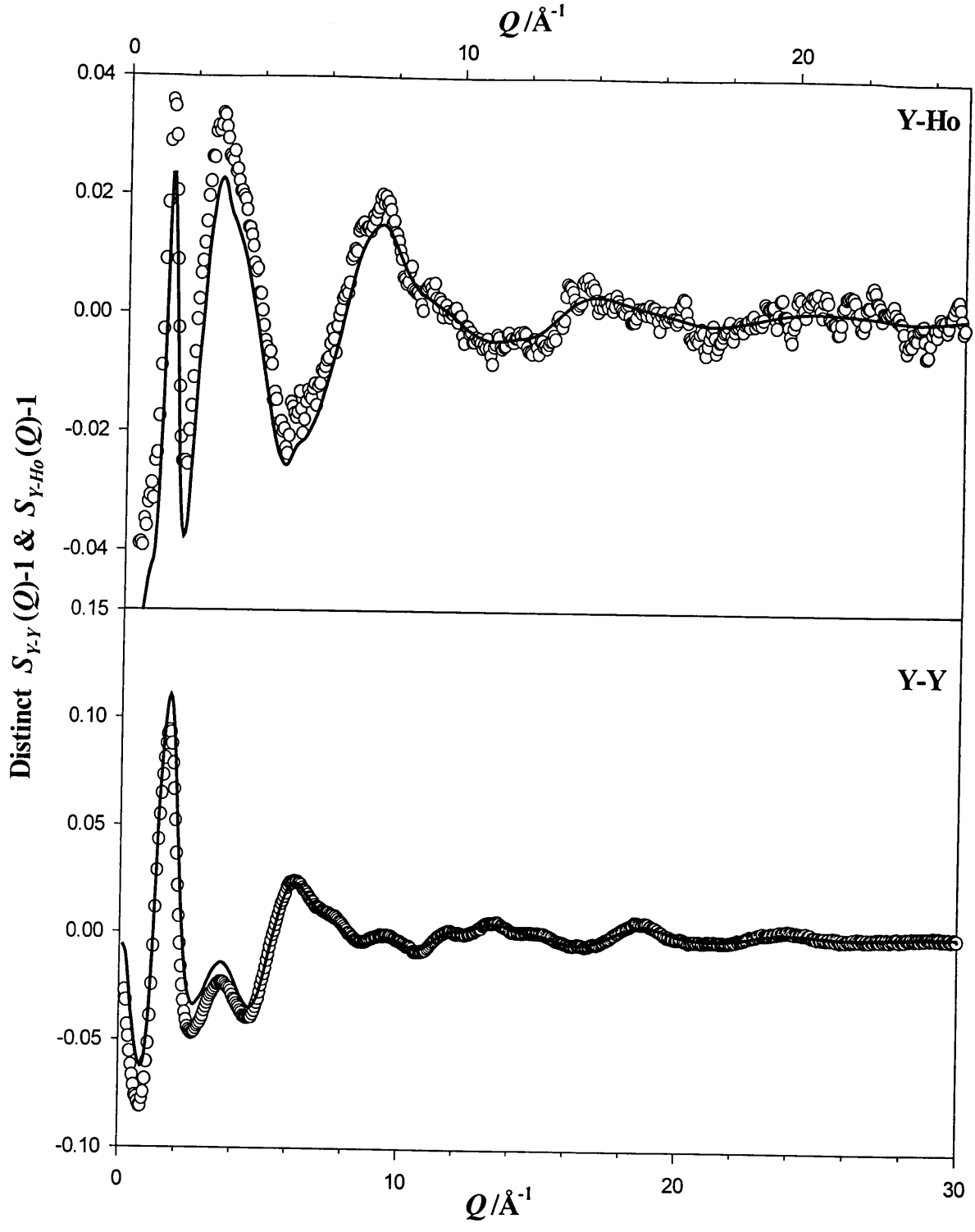

Figure 8.5. The distinct Y-Y (Y=CB, HB, CM, HM, and O) and Y-Ho PSFs (symbols) obtained from higher order difference method along with the back Fourier transforms (lines) of their respective partial distribution functions of figure 8.6.

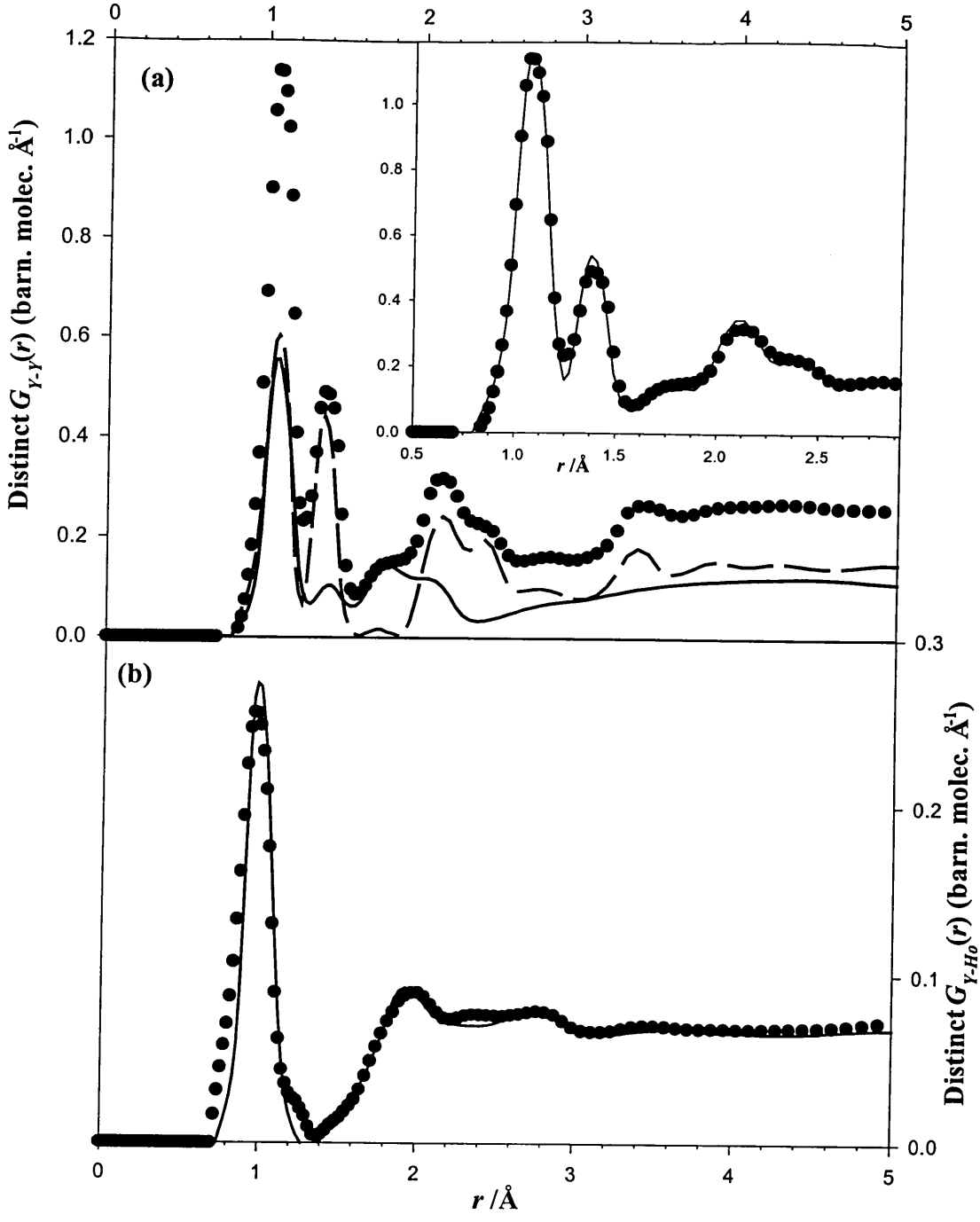

Figure 8.6. (a) The distinct Y-Y partial distribution function (symbols) along with the distinct partial distribution function X'-X' (X'=HM, CM and O) of methanol (line), and the distinct rdf of pure C_6D_6 benzene (dashed line). These functions are all presented on an absolute scale (each partial was multiplied by its corresponding molecular number density, and its normalisation factor $(\Sigma b_i)^2$, in addition the pure components functions were weighted by their molar fraction x_i for which they are represented in the mixture). The inset shows the distinct Y-Y partial distribution function (symbols) along with an added function (line) obtained from combining the distinct rdf of pure C_6D_6, and the distinct X'-X' partial of pure methanol. The quantitative comparison of the two functions is of interest only in the range ~ 0-1.7Å only. (b) The distinct Y-Ho partial distribution function (symbols) compared to the distinct X'-Ho partial of pure methanol (line).

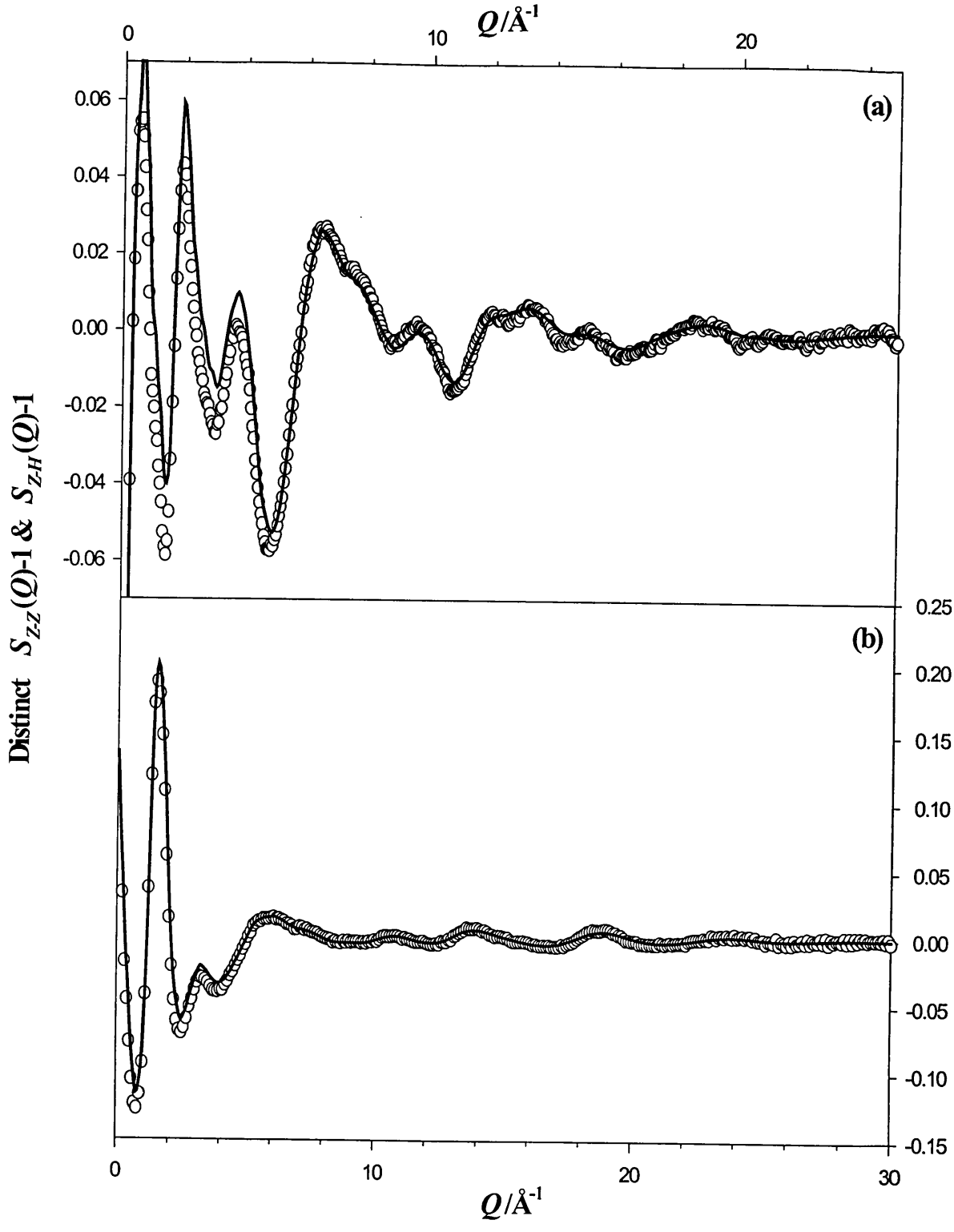

Figure 8.7. The distinct Z-Z (b) (Z = CM, HM, O, and CB) and Z-H (a) (H=Ho and HB) PSFs (symbols) obtained from higher order difference method along with the back Fourier transforms (lines) of their respective partial distribution functions of figure 8.8.

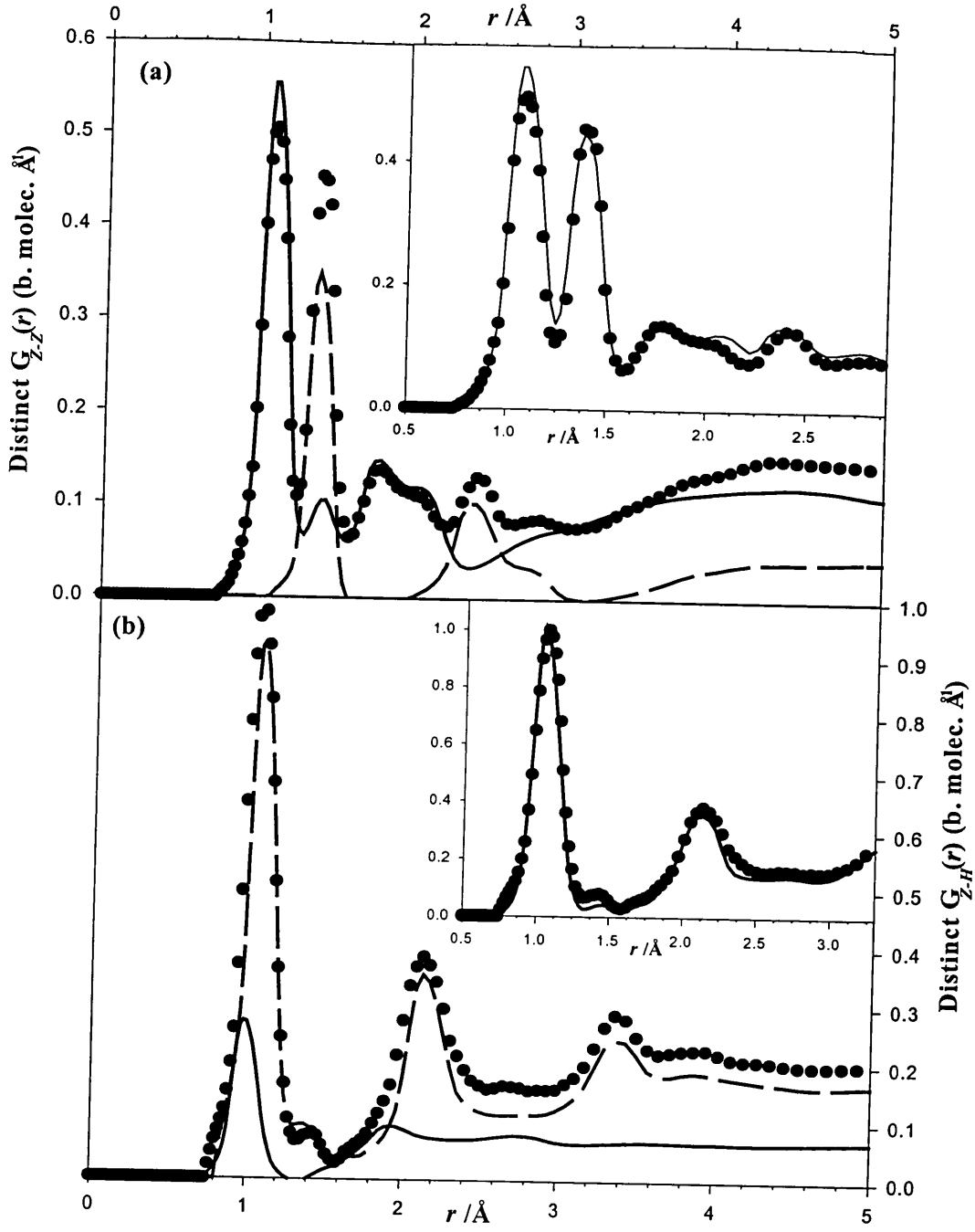

Figure 8.8. (a) The distinct Z-Z partial distribution function (symbols) along with the distinct partial distribution function X'-X' (X'=HM, CM and O) of methanol (line), and the distinct CB-CB pdf of pure benzene (dashed line). These functions are all presented on an absolute scale (each partial was multiplied by its corresponding molecular number density, and its normalisation factor $(\Sigma b_i)^2$, in addition the pure components functions were weighted by their molar fraction x_i for which they are represented in the mixture). The inset shows the distinct Z-Z partial distribution function (symbols) along with an added function (line) obtained from combining the distinct CB-CB pdf of pure benzene, and the distinct X'-X' partial of pure methanol. The quantitative comparison of the two functions is of interest only in the range ~ 0-1.7Å only. (b) The distinct Z-H partial distribution function (symbols) along with the distinct X'-Ho partial of pure methanol (line) and the CB-HB pdf of pure benzene (dashed line). The inset shows the distinct Z-H partial distribution function (symbols) along with an added function (line) obtained from combining the distinct CB-HB pdf of pure benzene, and the distinct X'-Ho partial of pure methanol. The quantitative comparison of the two functions is of interest only in the range ~ 0-1.7Å only.

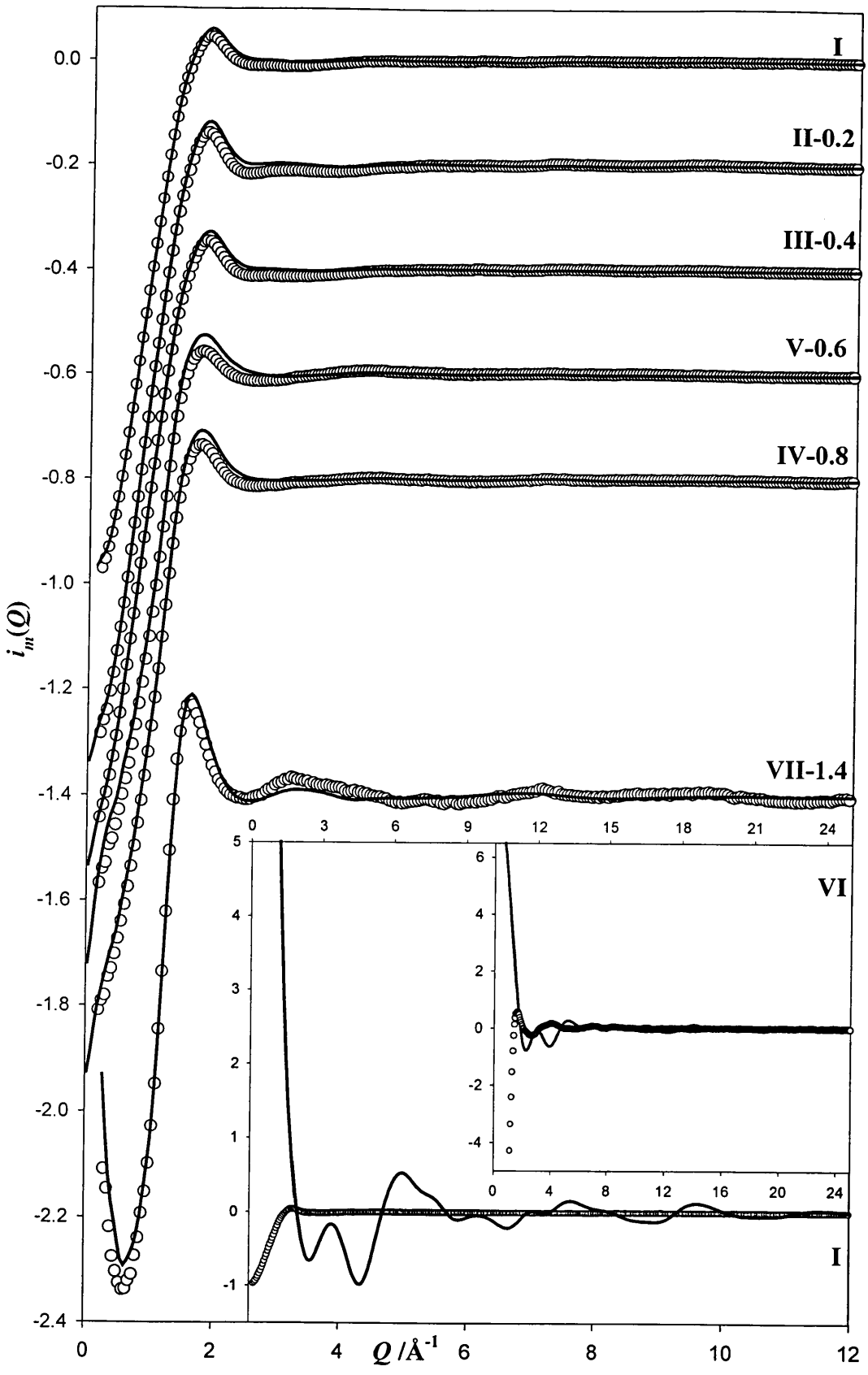

Figure 8.9. Some of the inter-molecular DCS obtained for different benzene-methanol samples presented along with the back Fourier transforms (lines) of their respective intermolecular rdf of figure 8.10. In the inset, the magnitude of the inter-molecular and intra-molecular DCS is compared for the mixtures number I and IV.

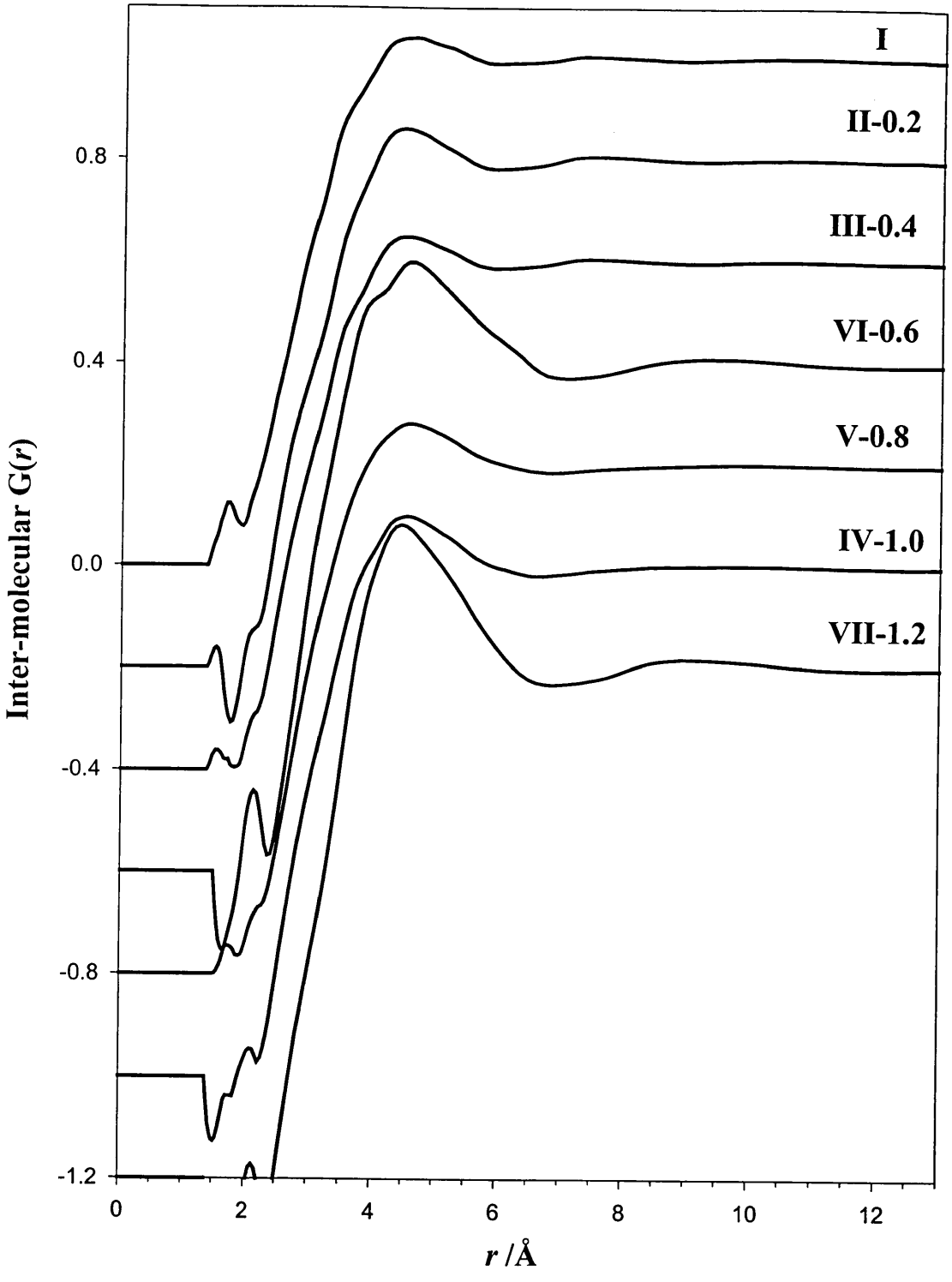

Figure 8.10. The inter-molecular rdf of some benzene-methanol samples obtained after Fourier transformation of the inter-molecular DCS presented in figure 8.9.

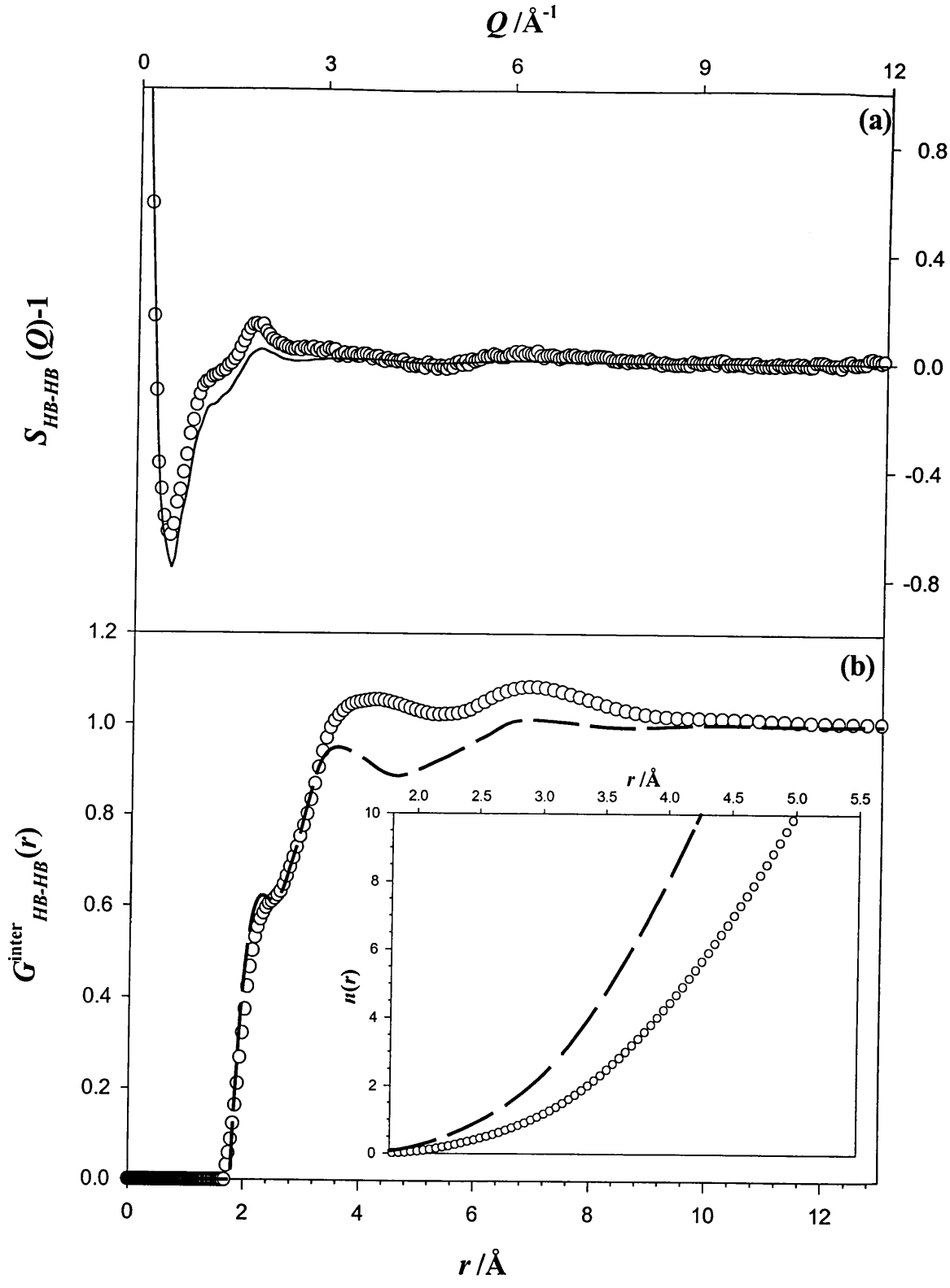

Figure 8.11. (a) The inter-molecular HB-HB PSF (symbols) obtained from second order difference along with its MIN fit (line). (b) The inter-molecular HB-HB pdf (symbols) corresponding to the MIN fit shown in (a) compared to the inter-molecular HB-HB pdf of pure benzene (dashed line). The inset compares the running co-ordination number of the HB-HB pair in pure benzene (line) and in the mixture (symbols).

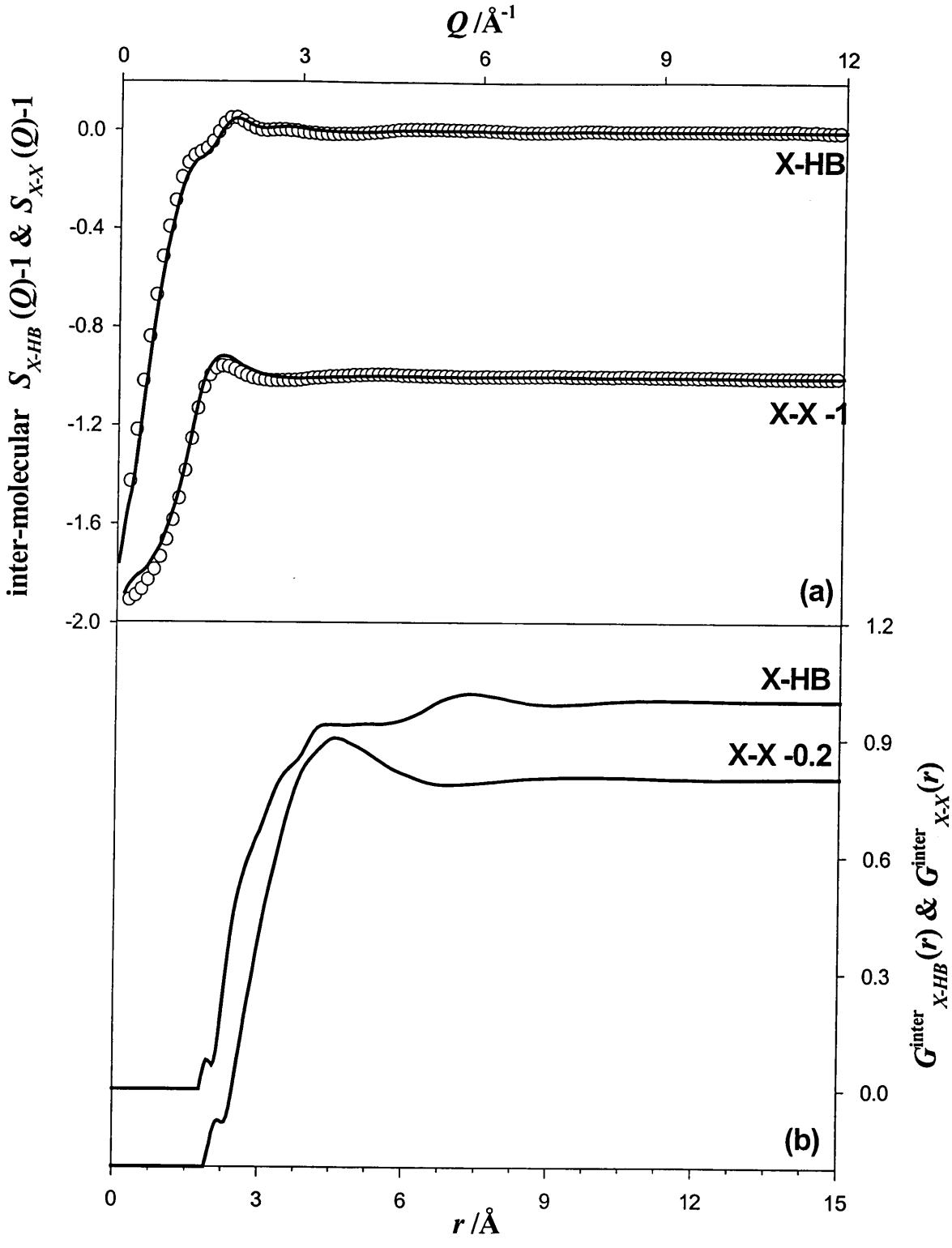

Figure 8.12. (a) The inter-molecular X-X and X-HB PSFs (symbols) along with their respective back Fourier transform (lines) of their inter-molecular partials presented in (b).

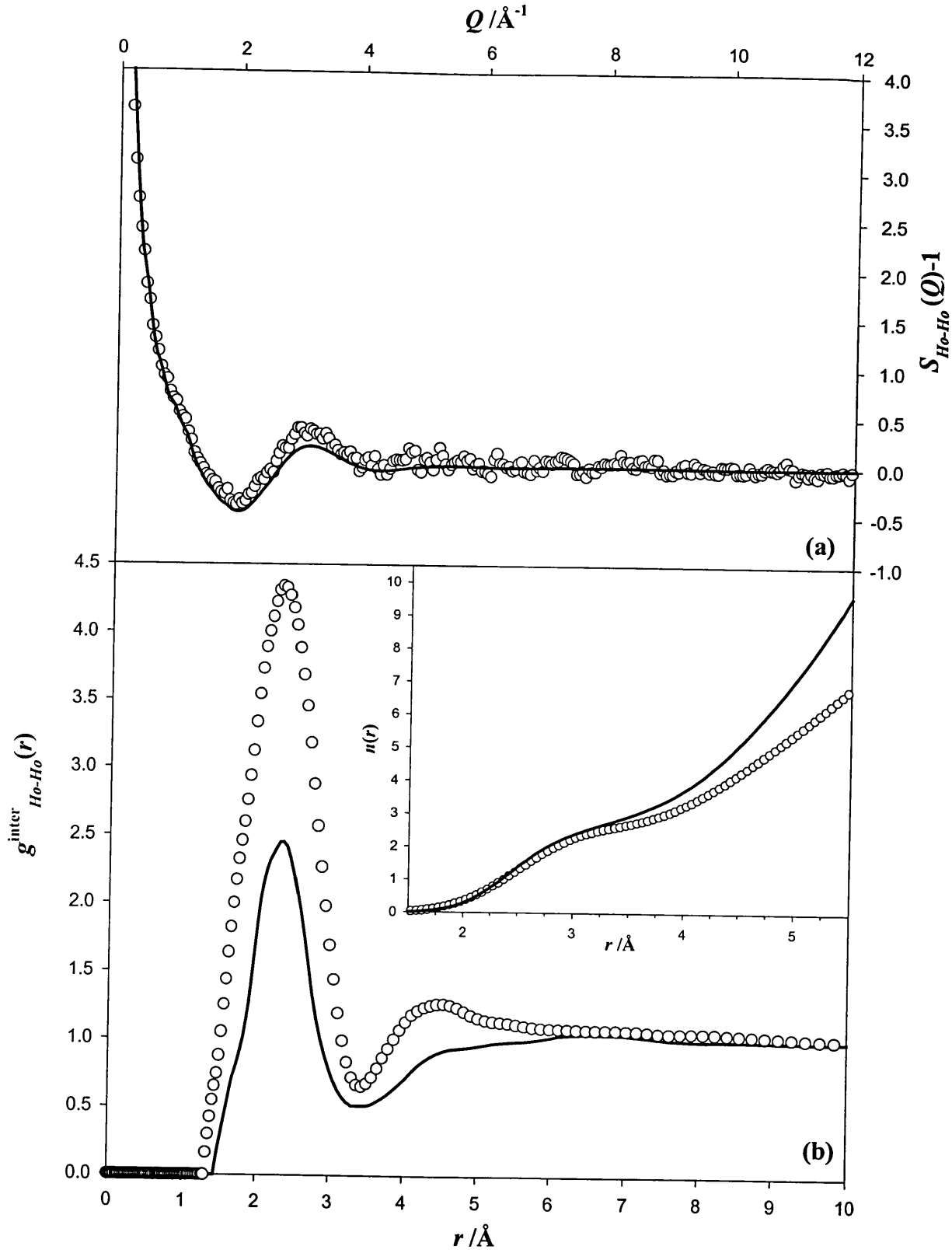

Figure 8.13. (a) The Ho-Ho PSF (symbols) along with its MIN fit (line). (b) The Ho-Ho pdf in the mixture (symbols) compared to its pure counterpart (line). In the inset, the running co-ordination number of the Ho-Ho pair in pure methanol (line) and in the mixture is compared (symbols).

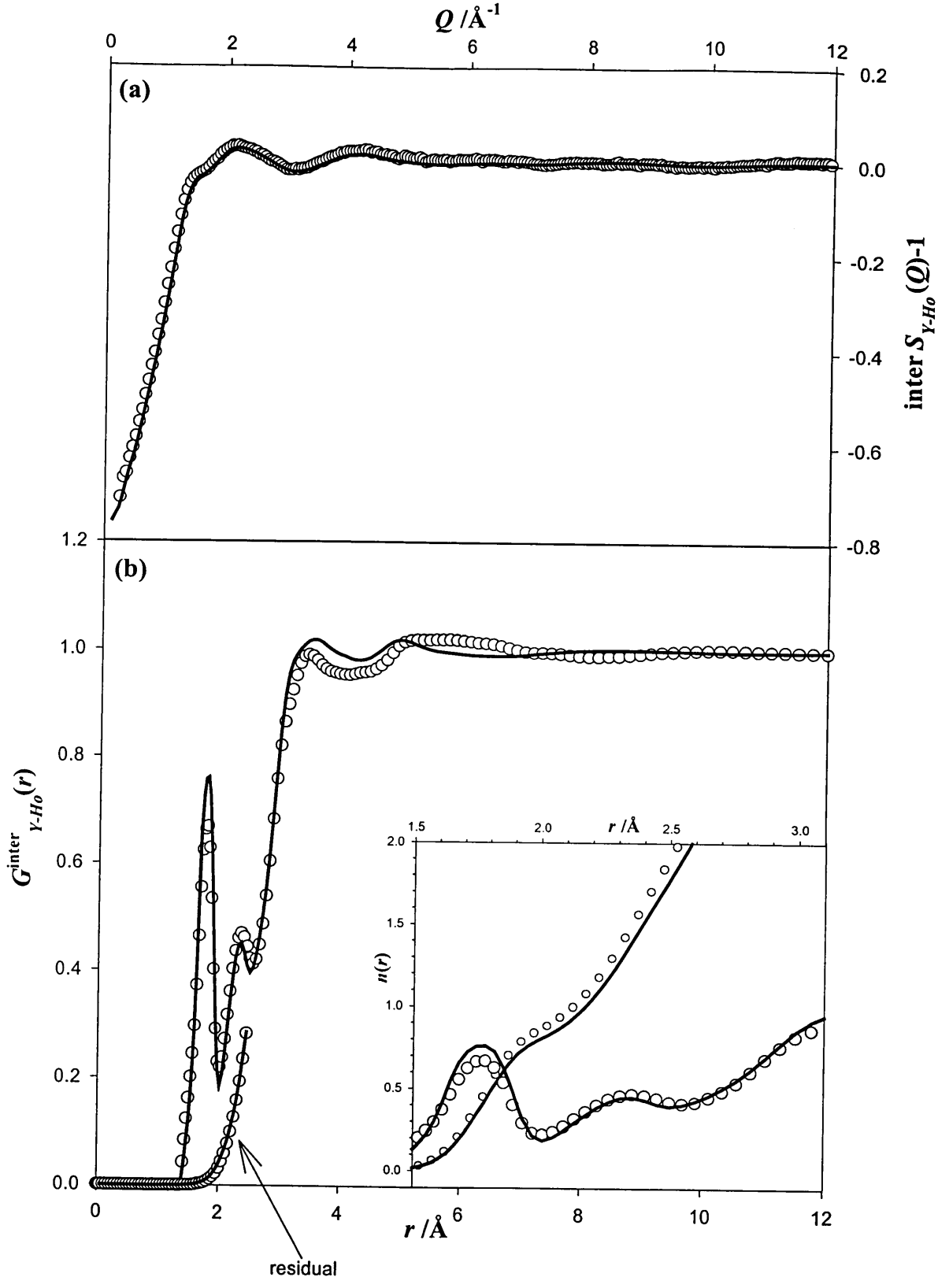

Figure 8.14. (a) The inter-molecular Y-Ho PSF (symbols) along with its MIN fit (line). (b) The Y-Ho partial in the mixture (symbols) compared to the pure methanol X'-Ho partial (line). The low-r tails arising from HM and CM-Ho contributions for the X'-Ho function (line), and CB, HB, CM, and HM-Ho contributions for the Y-Ho partial (symbols) obtained by combining the pdf computed in the MD simulations of methanol and the mixture (see section 6.2 and 8.3), and referred to as "residual" in the figure, are also shown. In the inset, the O···Ho peak position and running co-ordination number from the inter-molecular X'-Ho (line) and the Y-Ho (symbols) partials are compared.

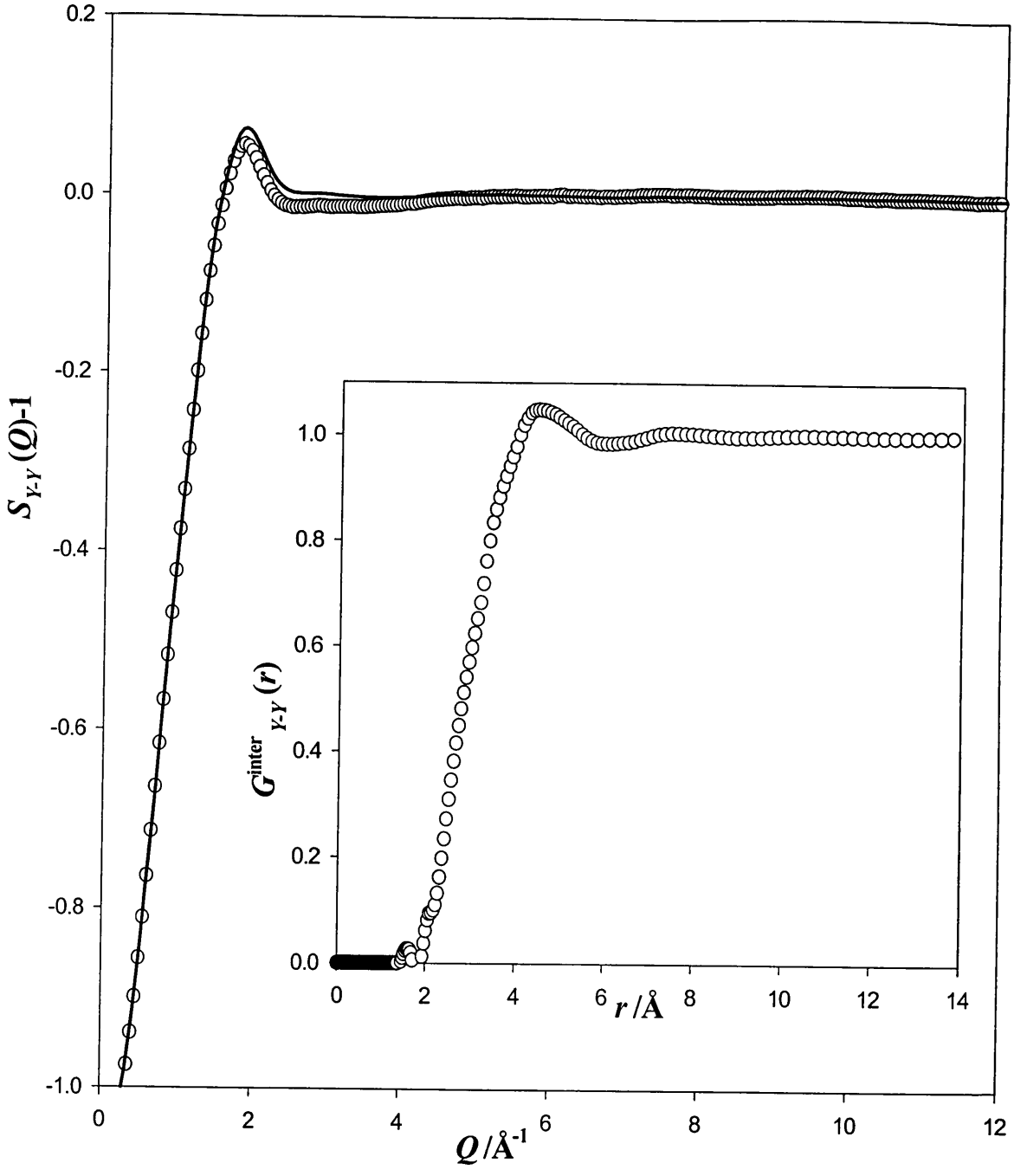

Figure 8.15. The inter-molecular Y-Y PSF (symbols) along with the back Fourier transform (line) of the inter-molecular partials presented in the inset.

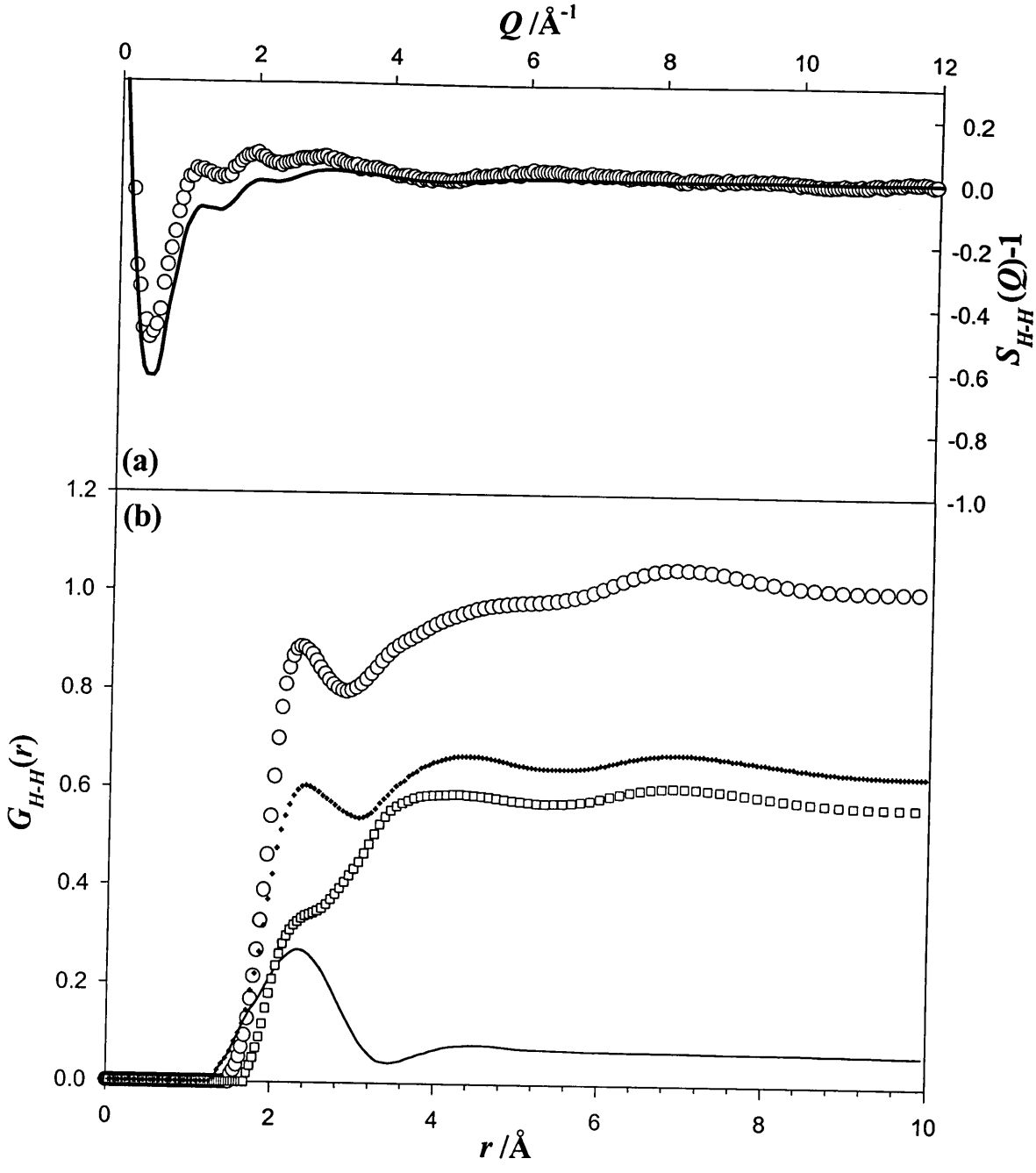

Figure 8.16. (a) The inter-molecular H-H PSF (circles) along with the back Fourier transform (line) of the inter-molecular H-H partial presented in (b) (circles). The experimental Ho-Ho (line), HB-HB (squares) pairs weighted in the ratio of the H-H partial distribution function, and their combination (+) are also presented in (b).

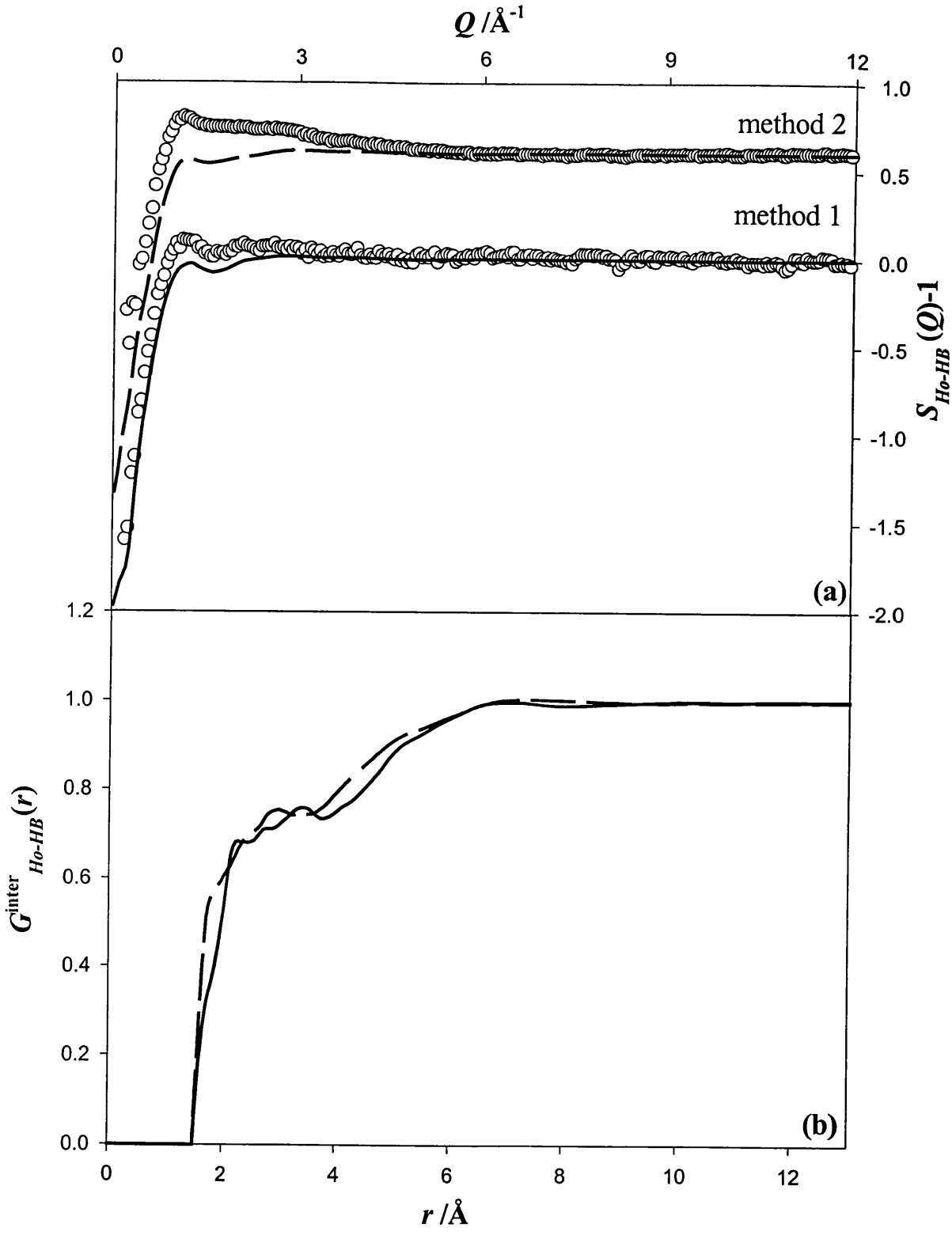

Figure 8.17. (a) The Ho-HB PSFs (symbols) obtained from two different sets of mixture samples (see text) along with the back Fourier transform (line and dotted line) of the inter-molecular partials presented in (b) (method 1: line, method 2: dashed line).

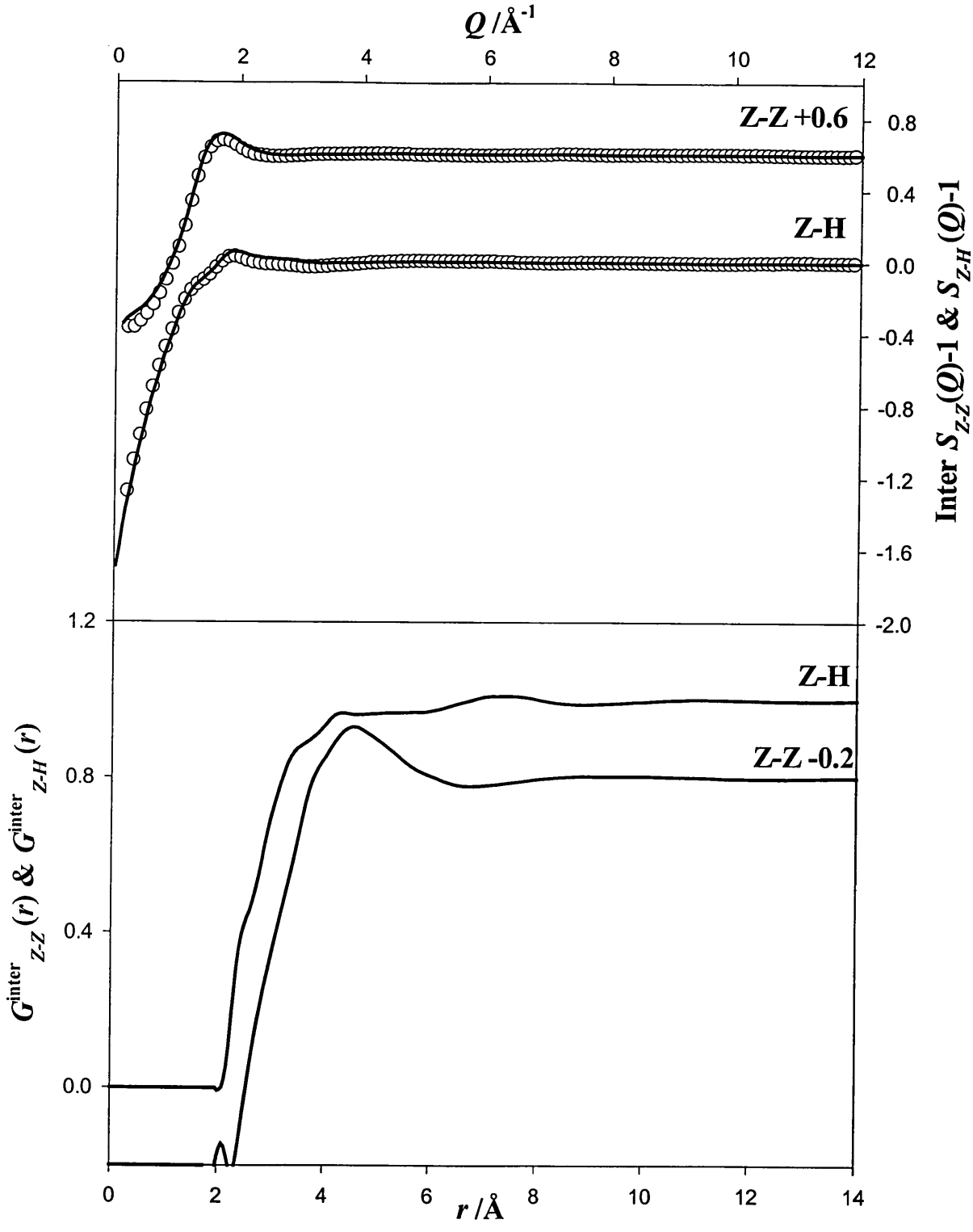

Figure 8.18. The inter-molecular Z-H and Z-Z PSFs (symbols) along with the corresponding back Fourier transform (lines) of the inter-molecular partials distribution functions presented in (b)

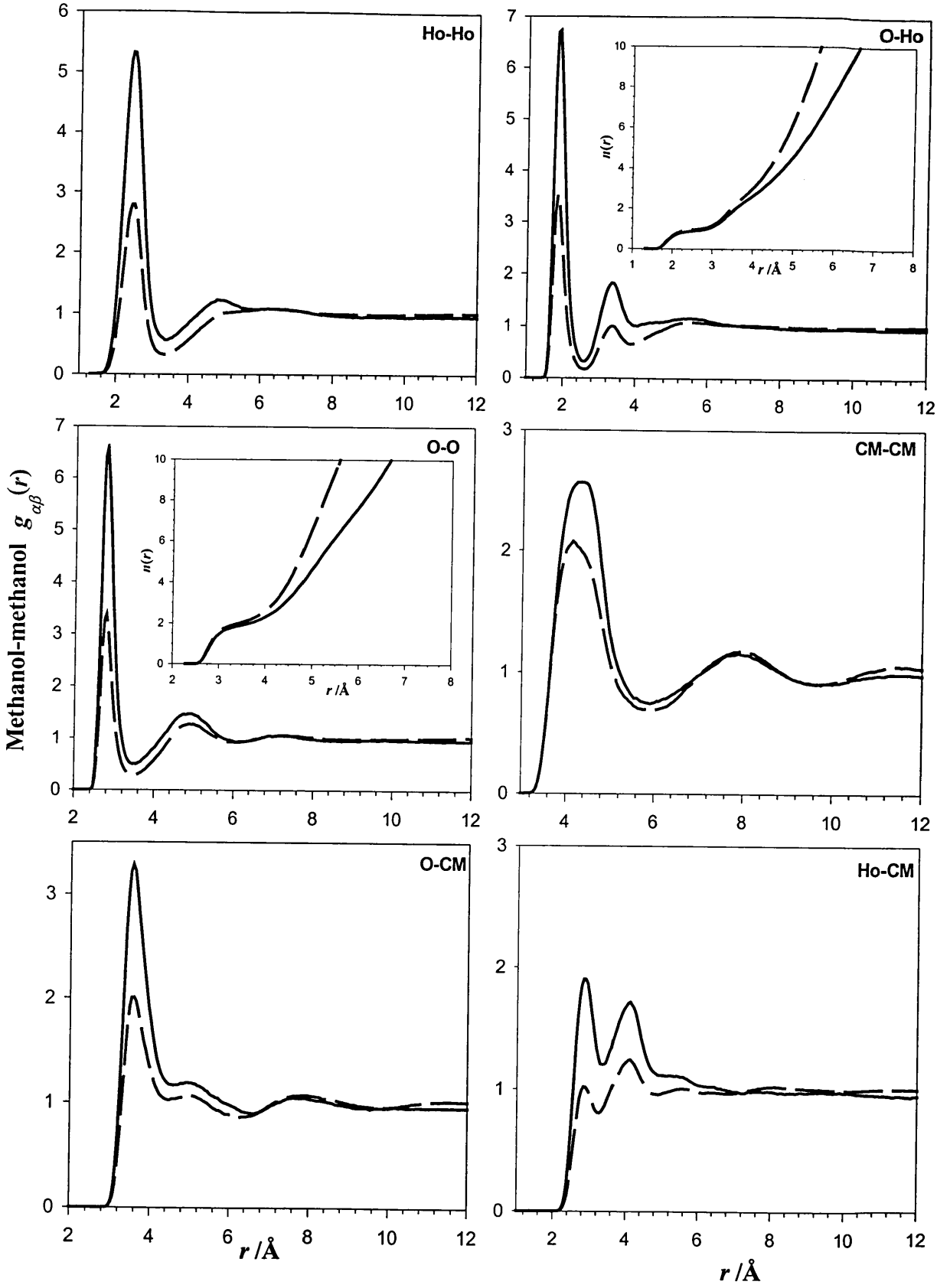

Figure 8.19. Some of the intermolecular methanol-methanol pdfs (lines) computed from the MD simulations of benzene-methanol mixture, compared to those of pure methanol obtained with the same H1+CH_3 model (dashed lines). The insets compare the various α-β running coordination numbers for methanol in the mixture (line) with those obtained in the pure component (dashed line).

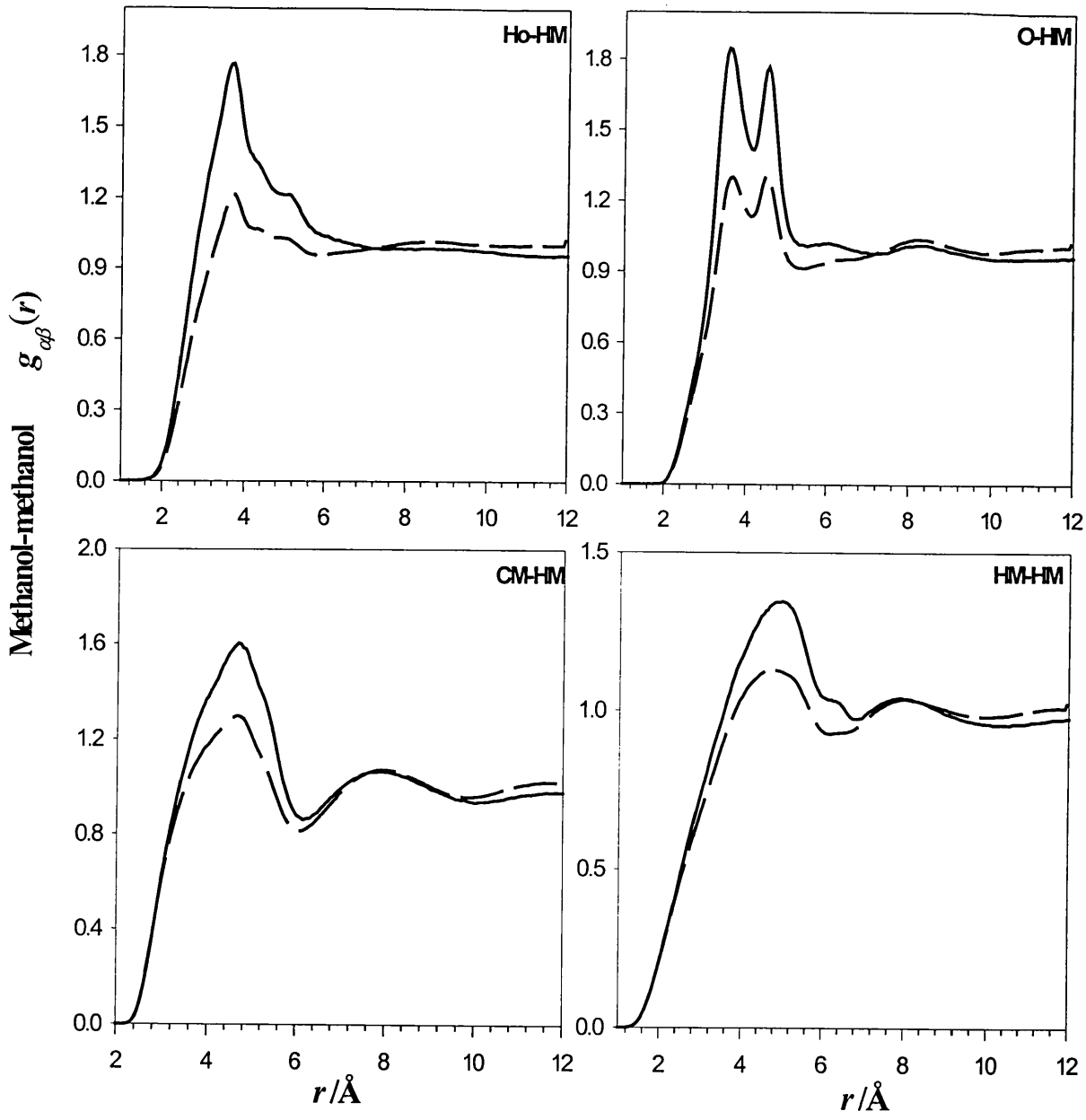

Figure 8.20. Some of the inter-molecular methanol-methanol pdfs (lines) computed from the MD simulations of benzene-methanol mixture, compared to those of pure methanol obtained with the same H1+CH_3 model (dashed lines).

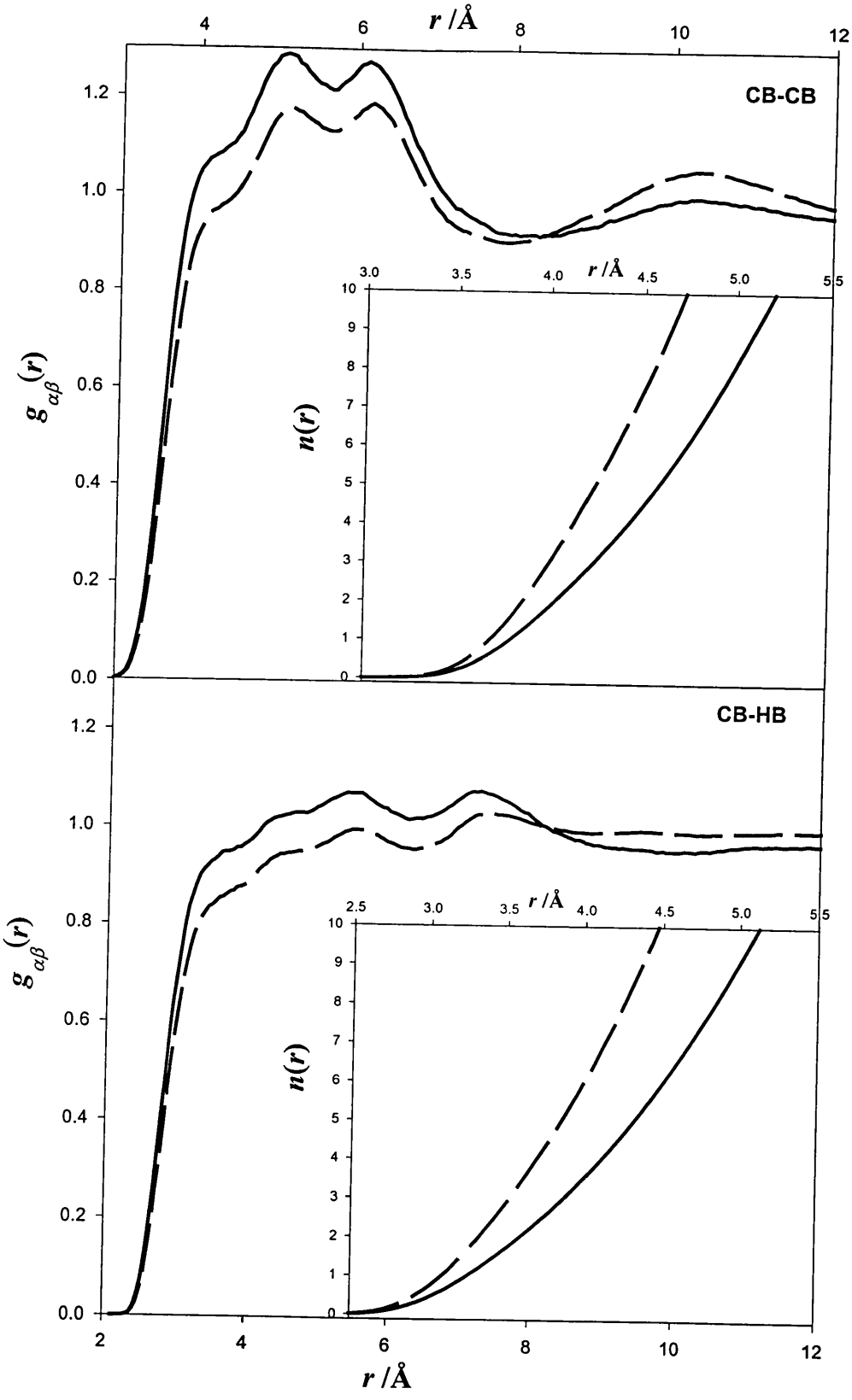

Figure 8.21. The inter-molecular CB-CB and CB-HB benzene-benzene pdfs (lines) computed from the MD simulations of benzene-methanol mixture, compared with those of pure benzene obtained with the same LJ12-6 force field model (dashed lines). The insets compare the CB-CB (top box) and CB-HB (bottom box) running co-ordination numbers for benzene in the mixture (line) with those obtained in the pure component (dashed line).

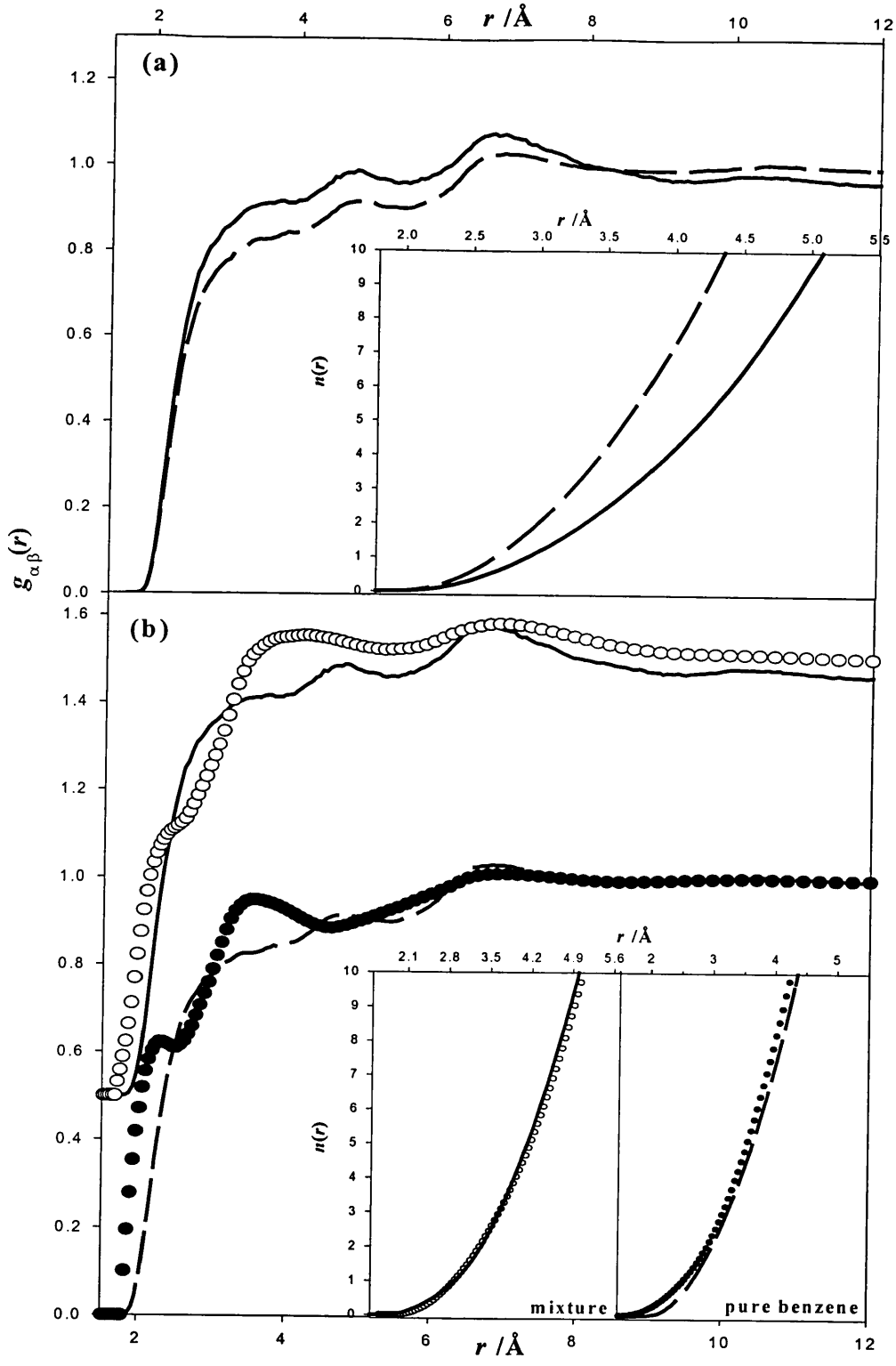

Figure 8.22. (a) The inter-molecular HB-HB benzene-benzene pdfs (lines) computed from the MD simulations of benzene-methanol mixture, compared with those of pure benzene obtained with the same LJ12-6 force field model (dashed lines). The inset shows the HB-HB running co-ordination numbers for benzene in the mixture (line) with those obtained in the pure component (dashed line). (b) The experimental inter-molecular HB-HB pdf obtained in the mixture (white circles) and in pure benzene (black circles) displayed along with their computed counterparts (mixture: lines, pure benzene: dashed lines). The inset shows experimental HB-HB running co-ordination numbers in the mixture and in pure benzene (symbols) with those obtained by MD simulation (lines).

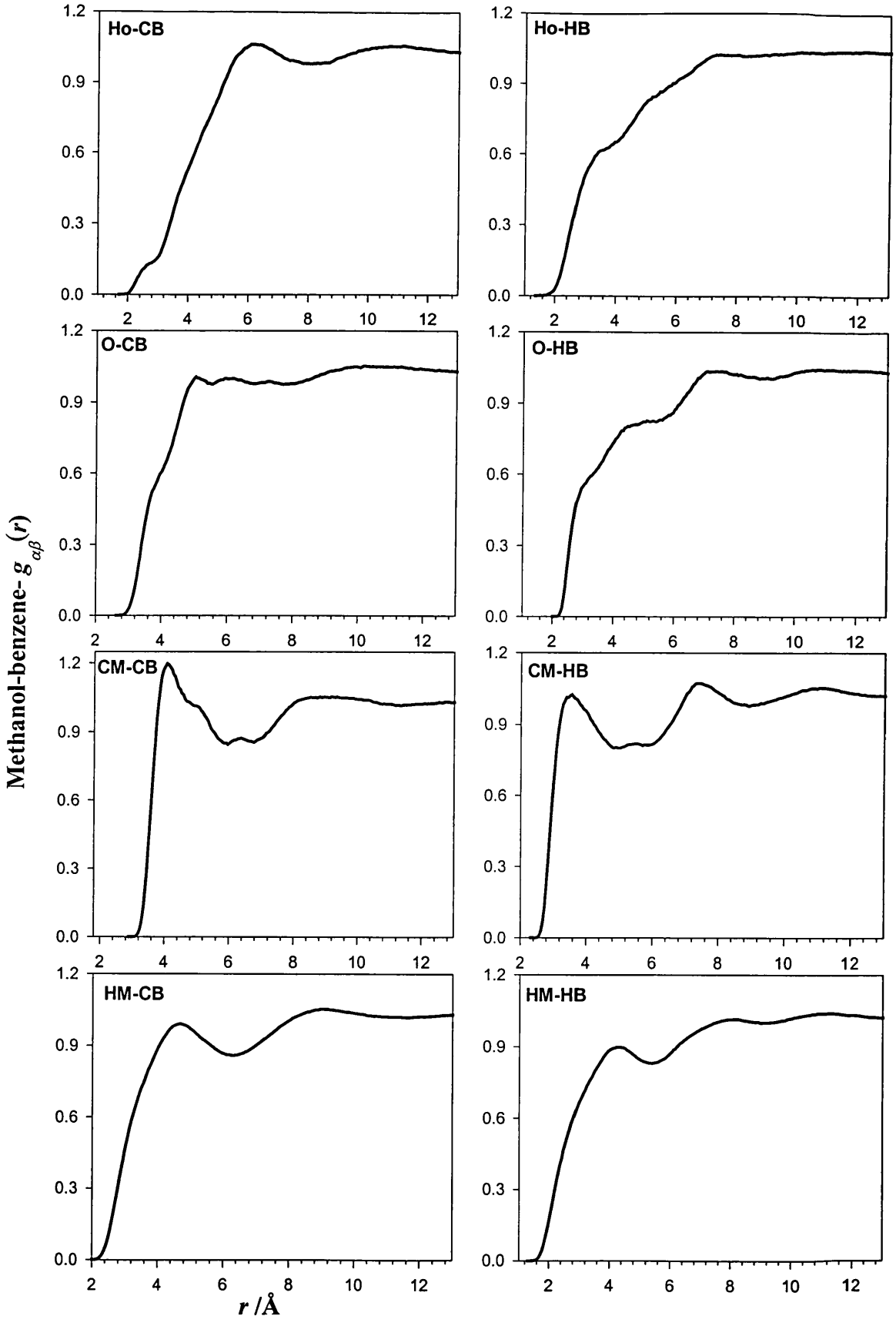

Figure 8.23. The inter-molecular methanol-benzene pdfs computed from the MD simulations.

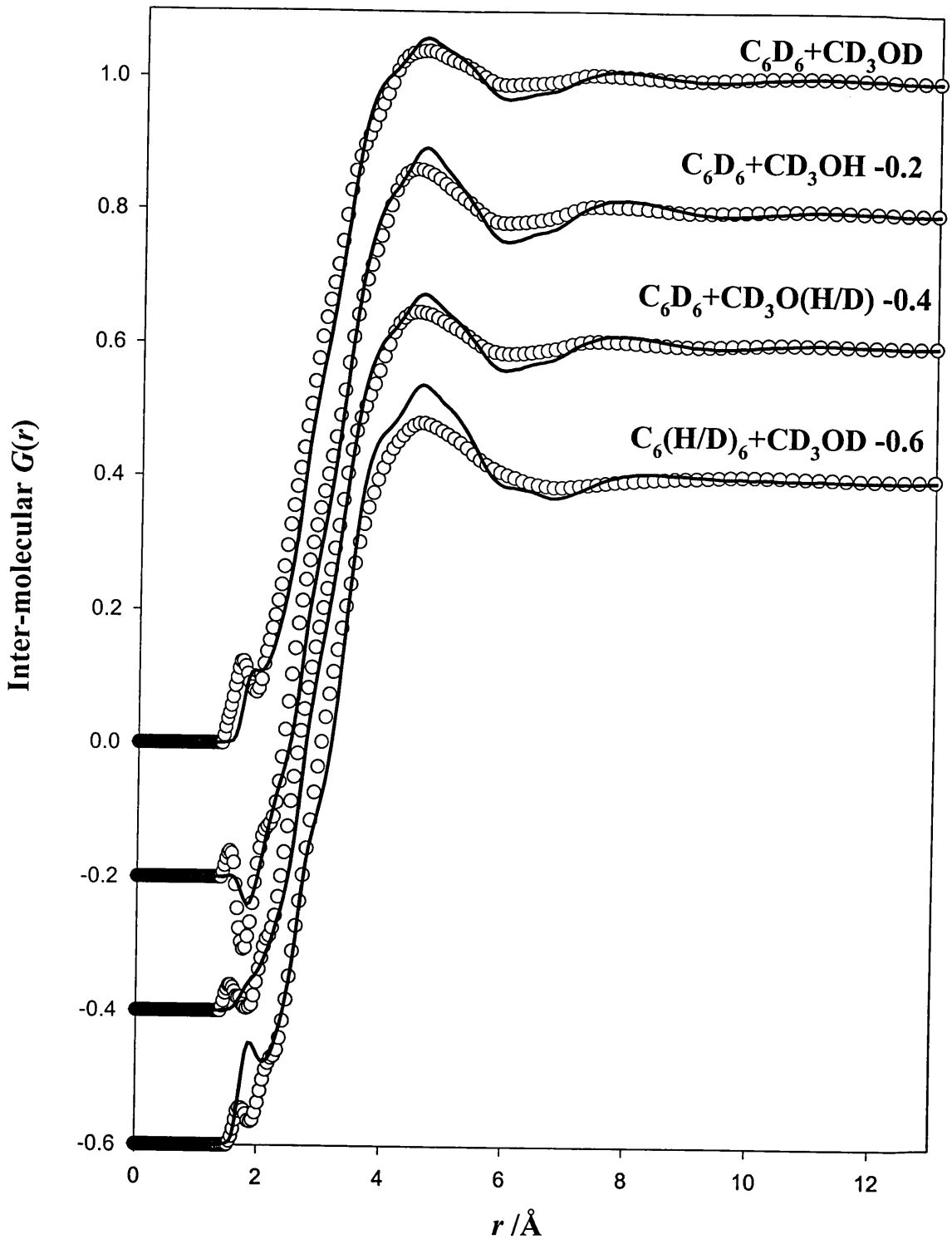

Figure 8.24. The inter-molecular rdf of some benzene-methanol samples obtained experimentally (symbols) along with their reconstructed counterparts (lines).

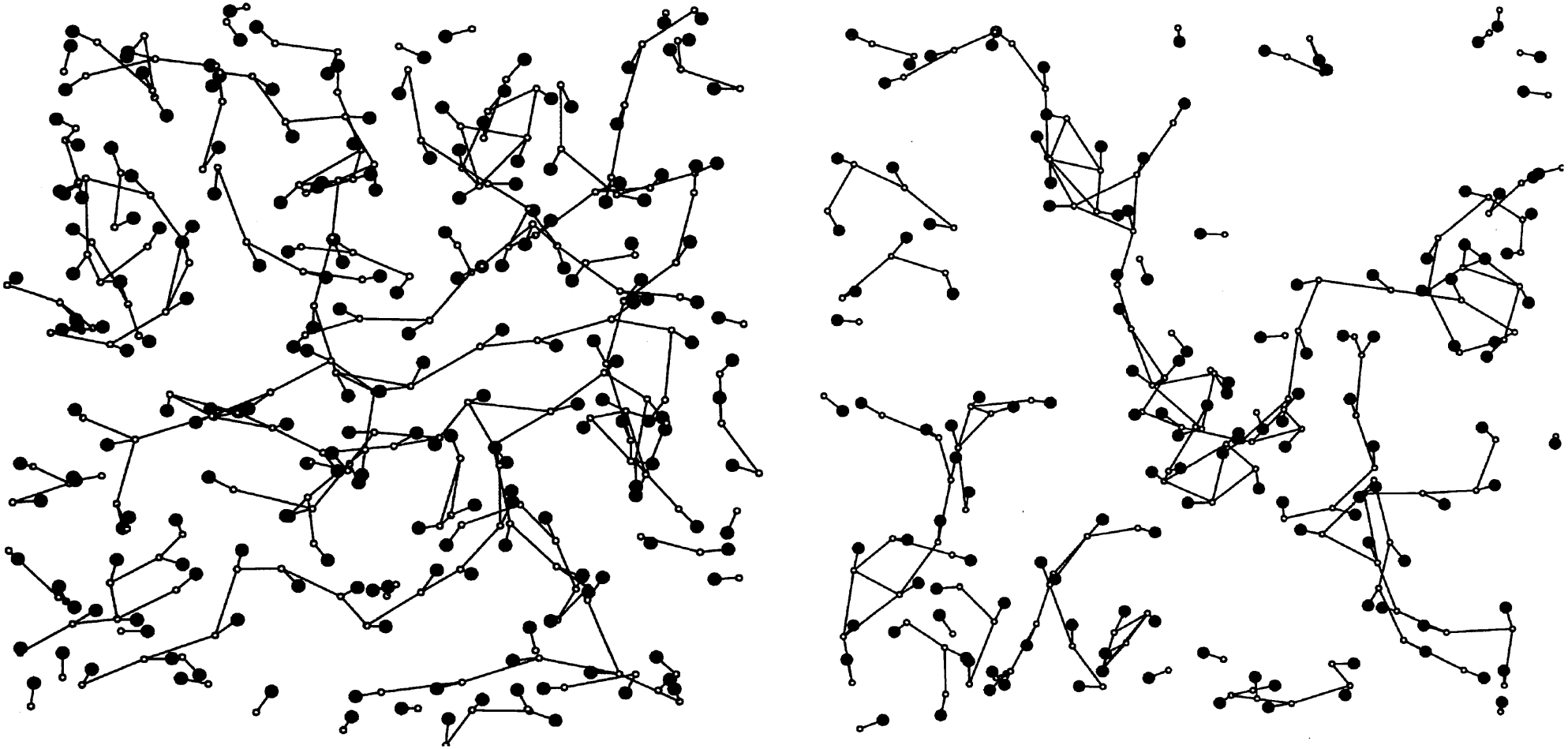

Figure 8.25 Instantaneous configuration of methanol molecules in pure methanol, from the simulation with the H1 model (left) and in the mixture (right). Small circles, Ho; large circles O, the long lines represent hydrogen bonds.

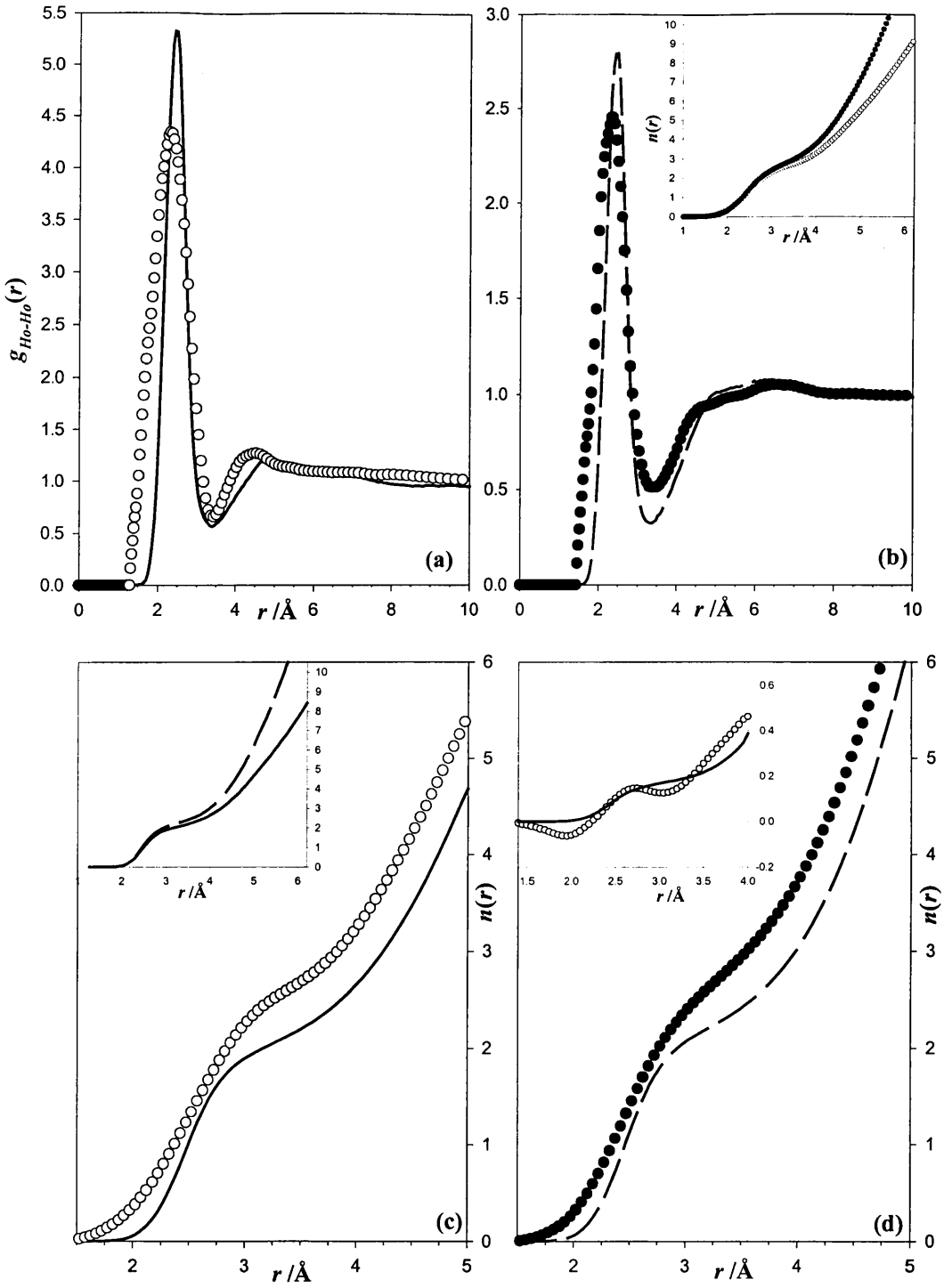

Figure 8.26. (a) The ND (white symbols) and MD (line) Ho-Ho pdf obtained in the mixture. (b) The ND (black symbols) and MD (dashed line) Ho-Ho pdf obtained in pure methanol. The inset shows both experimental Ho-Ho running co-ordination numbers obtained in the mixture (white circles) and in pure methanol (black symbols). (c) Both the experimental (white symbols) and simulated (line) Ho-Ho running co-ordination numbers (white symbols) in the mixture. The inset shows how the Ho-Ho running co-ordination numbers changes going from the pure liquid (dashed line) to the mixture (line). (d) Both the experimental (black symbols) and simulated (dashed line) Ho-Ho running co-ordination numbers (white symbols) in pure methanol. The inset shows the difference pure methanol-mixture Ho-Ho running co-ordination numbers for the experimental (symbols) and the simulations (line).

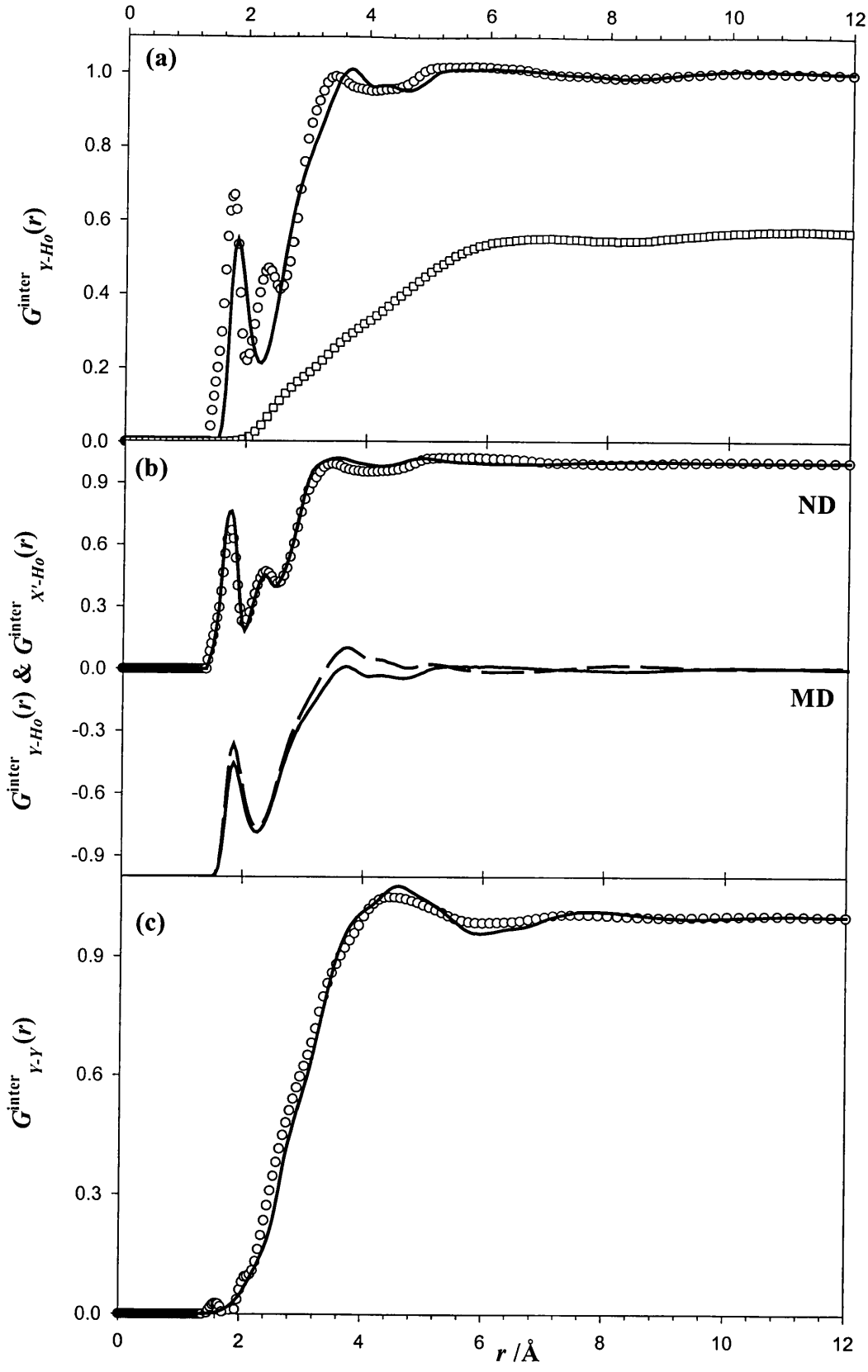

Figure 8.27. (a) The ND (circles) and MD (line) Y-Ho partial along with the weighted sum of the CB-Ho and HB-Ho pdf, in the ratio of the Y-Ho partial (squares). (b) The simulated Y-Ho (line) and X'-Ho (dashed line) partials are plotted together (bottom), and for comparison the ND experimental Y-Ho (circles) and X'-Ho (line) partials are also displayed along (top). (c) The simulated (line) and the ND (circles) Y-Y partial distribution function.

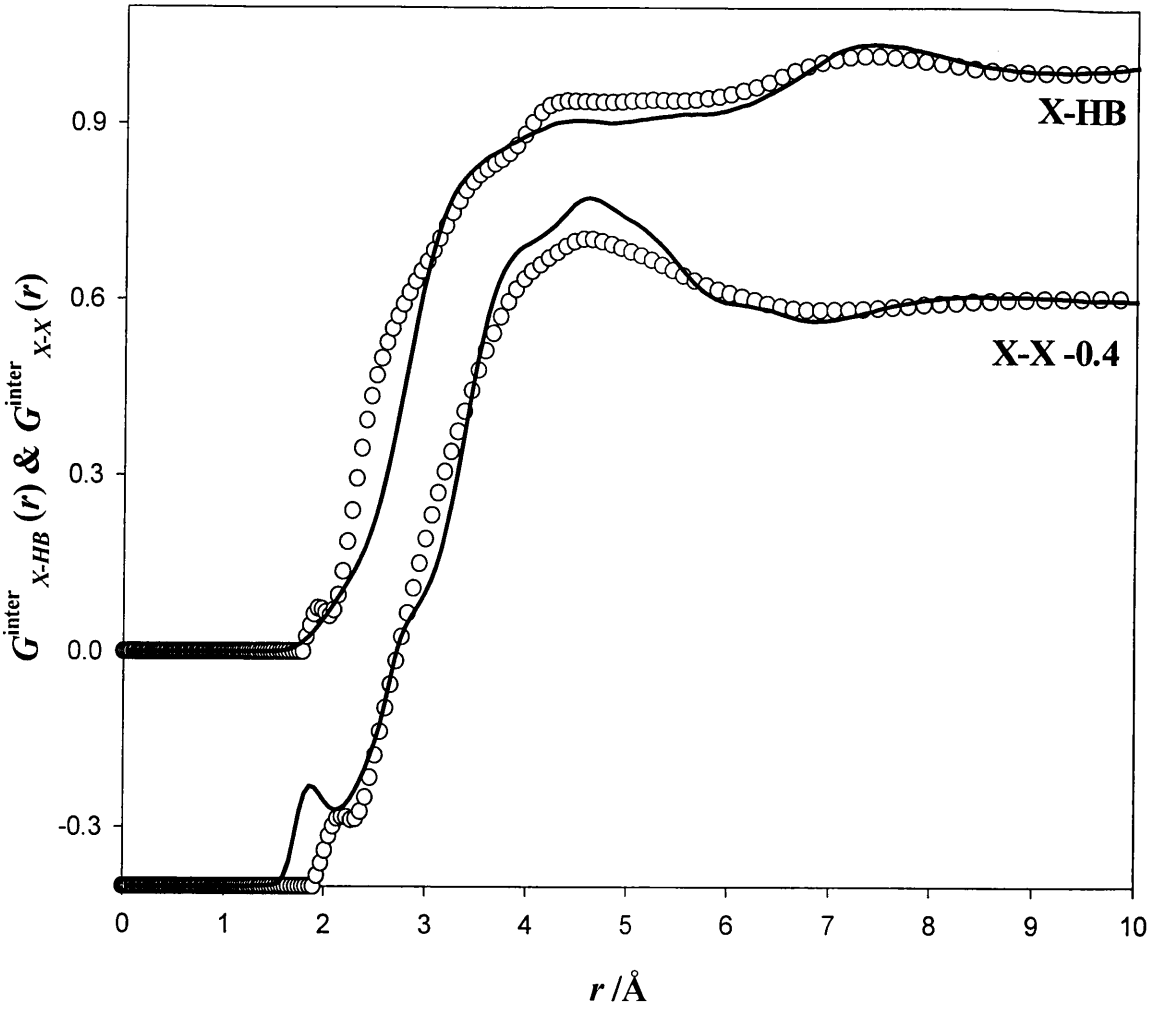

Figure 8.28. The simulated (line) and experimental (white circles) inter-molecular X-HB and X-X partial distribution functions.

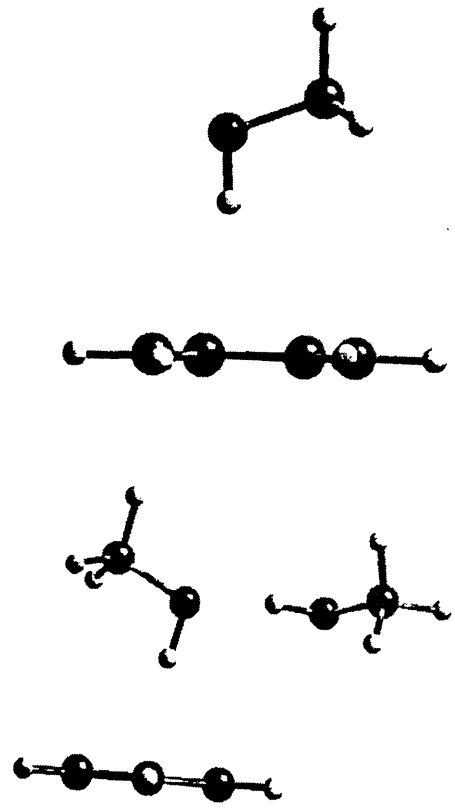

Figure 8.29. Lowest energy structures for benzene + (methanol)$_n$ clusters from the study of Garrett *et al.* (1992). Top view $n = 1$, bottom view $n = 2$.

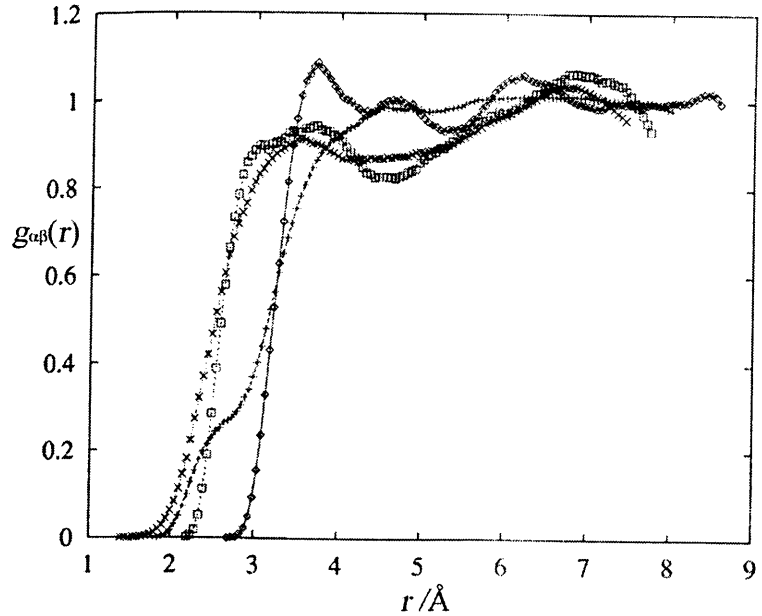

Figure 8.30. The pdfs between benzene (B) and water (W) molecules: CB-HW (+), HB-HW (×), CB-O (□), HB-O (◊) obtained by Laaksonen (1998) from MD simulations.

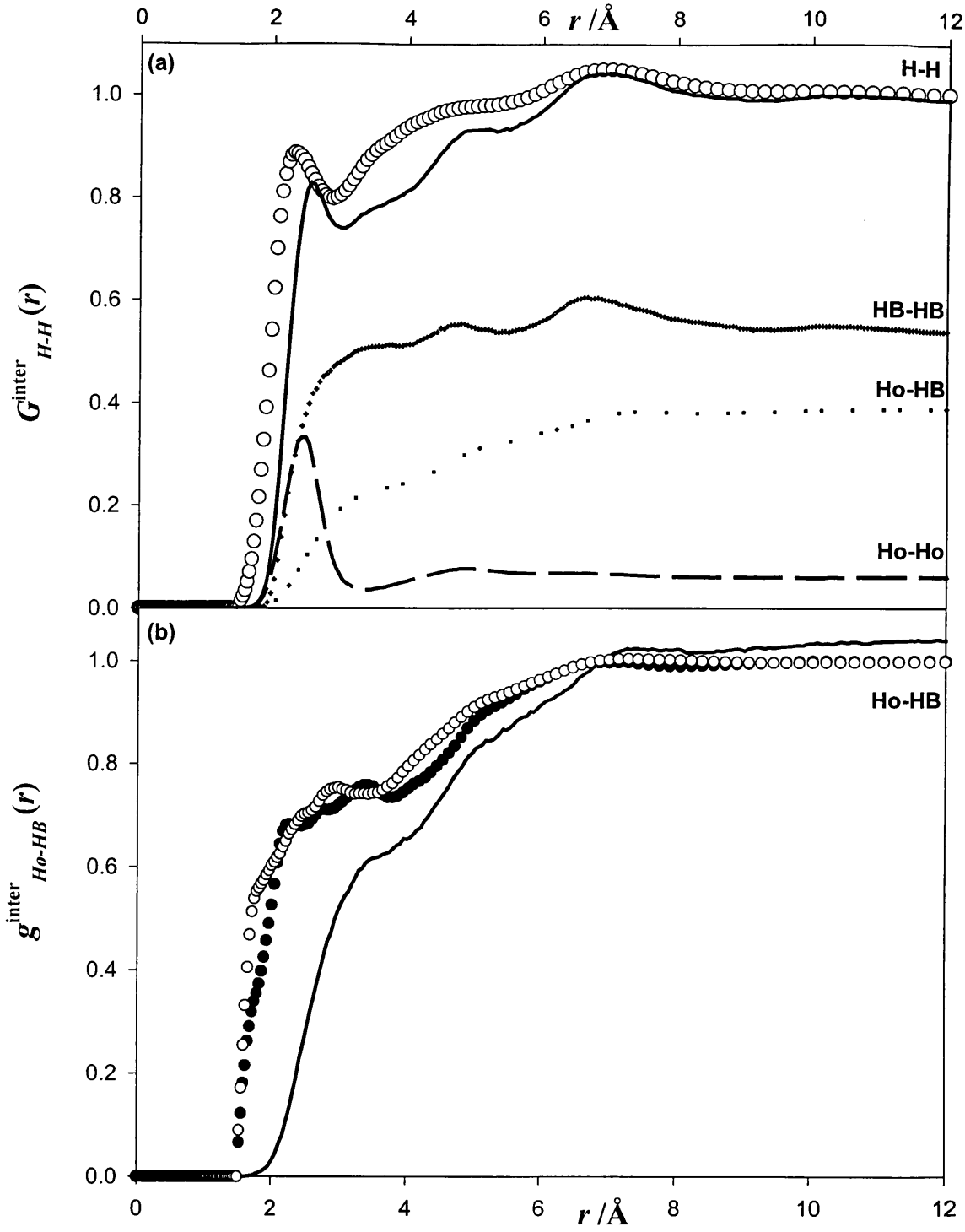

Figure 8.31. (a) The simulated (line) intermolecular H-H partial along with its neutron counterpart (symbols). Also presented, the simulated Ho-Ho (line), HB-HB (dotted line) pairs weighted in the ratio of the H-H partial distribution function. (b) The simulated Ho-HB pdf (line) compared to the one extracted from ND experiment (method1: black circles, method 2:white circles).

Chapter 9

Conclusions

9.1 Summary of the main findings

Pure methanol: Neutron diffraction (ND) measurements on three methanol (CD_3OD, $CD_3O(H/D)$ and CD_3OH) samples have been used to determine intra- + inter-(distinct) and inter-molecular differential cross section (DCS) functions. These functions were then used to extract the X-Ho (X=C, O, and H) and X-X partial distribution functions by employing the difference techniques of ND. The O-Ho and C-H overlapping distances in the distinct $G(r)$ have been isolated in the X-Ho and X-X partials. These distances are 0.98 ± 0.01 Å and 1.08 ± 0.01 Å, respectively, in comparison to 0.961 ± 0.001 Å and 1.096 ± 0.001 Å, obtained from an intra-molecular fitting to the DCS data. The extent to which the inter-molecular structure is affected by a difference in the model chosen for the molecular structure has been investigated. Although the total inter-molecular and partial X-X distribution functions are found to be identical with the two molecular models chosen, quantitative differences in the peak height and shape can be seen in the X-Ho partial distribution function, especially at low r. The average position of the O···Ho hydrogen bond observed at 1.75 ± 0.03 Å in the X-Ho partial lies in the range (1.75-1.95 Å) of values predicted by various computer simulations.

Two different 3-site and one 6-site potential models for methanol were used to perform seven different molecular dynamics (MD) simulation runs that differed in the techniques employed for integrating the equations of motion and for treatment of the long range interactions. While the first five runs considered the methyl group to be a

united carbon atom, only the last two treated the methyl hydrogens explicitly as specific interaction sites (APR6) or as dead load (H1+CH_3). Since the last two were able to reproduce the measured diffusion coefficient, the total inter-molecular radial distribution functions computed from them are compared with those obtained from ND experiments. Within the same potential model, although a three site geometrical model is an oversimplification for the methanol molecule, the computed pdfs for the simulation runs using this model are found to be in very good agreement with those obtained by using a six sites geometrical model. This suggests that the effect on the inter-molecular structure resulting from a difference in the model chosen for the molecular structure is intrinsic only to neutron scattering experiments where intra- and inter- molecular distances are convoluted in Q-space. In contrast, the equations of motions in computer simulations are calculated in ($\boldsymbol{r}$, $\boldsymbol{p}$) space. Since both the APR6 and H1+CH_3 models reproduce equally well the ND results at the total inter-molecular radial distribution function level, it is not possible to say that one model is better than the other. However, a comparison of the simulated inter-molecular $G_{XX}(r)$, $G_{XHo}(r)$ and $g_{HoHo}(r)$ partials with the corresponding ND functions reveals that although the APR6 model treats the methyl hydrogens as specific interaction sites, the H1+CH_3 model treating these hydrogens as dead load does a better job, though only qualitatively, in reproducing the experimental structural features. The results also revealed that the methyl hydrogens do not participate in any inter-molecular bonding.

Pure benzene: The neutron diffraction (ND) data on three benzene (C_6D_6, C_6H_6 and $C_6(H/D)_6$) samples have been used for the first time in the present work to extract the three inter-molecular C-C, C-H and H-H partial distributions functions. The ND structural results are compared with those obtained by MD simulations performed using three different model potentials. All the simulated C-C partials are found to be in better agreement with the corresponding experimental function obtained from ND rather than X-rays. It should be noted that since the C-C partial obtained from this earlier X-ray work was the only experimental function available, most of the potential models used so far in simulating the structural behaviour of benzene were tested and validated against this. All the models used in the current simulations reproduce very well the experimental inter-molecular radial distribution functions of C_6D_6 and $C_6(H/D)_6$ samples. However, significant discrepancies between the MD and ND results exist for the C-H and H-H partial pdfs. Such marked differences in the C-H

and H-H pdfs contribute towards the poor agreement between the ND and MD results for the inter-molecular rdf of C_6H_6 since these partials are heavily wheighted in this sample.

Benzene-methanol mixture: The neutron diffraction (ND) data on seven benzene-methanol samples in the molar ratio 1:2 have been used to determine the intra- + inter-(distinct) molecular DCS functions. In these measurements, the Hydrogen / Deuterium (H/D) substitutions were made on the hydroxyl hydrogen (Ho) and benzene hydrogens (HB). The results show that the intra-molecular structures of benzene and methanol did not change in passing from the pure components to the mixture. Thus, the intra-molecular structure factors of the pure components were used to separate the inter- and intra-molecular DCSs in the mixture samples. Since the inter-molecular rdfs comprise of twenty-one pair distribution functions (pdfs) they cannot provide any useful structural information. The difference techniques of H/D substitution were used to separate some of these pdfs. The larger HB-HB distances found in the HB-HB pdf in the mixture reflect that methanol molecules come in-between the benzene molecules. This should result in weaker benzene-benzene interactions, associated with a loss in orientational correlations between these molecules in the mixture relative to those in pure benzene. The HB-HB partial in the mixture is however very much similar to that in pure benzene, suggesting that such orientational correlations, if they exit in pure benzene, should be dominated largely by a simple packing of the molecules.

With regard to the structure of the methanol molecules in the mixture, the inter-molecular O···Ho and Ho-Ho bond distances in the mixture are found to be the same as those in pure methanol. Moreover, the Ho-Ho and O···Ho running co-ordination numbers in the mixture are similar to those in pure methanol. It appears therefore, that at the investigated composition, the hydrogen bonding characteristics of pure methanol are retained in the mixture, and that the methanol molecules are still strongly self-associated. Although the solute-solvent (HB-Ho) correlations were hard to extract from the experimental data, these confirm that association of benzene with methanol is very weak, suggesting that benzene plays the role of an inert solute in the mixture.

The ND structural results are compared with those obtained through MD simulations. The inter-molecular potential model used in simulating the mixture behaviour was built from the model potentials used in the computer simulation studies of pure components and tested against the ND experimental results on pure benzene and methanol. The simulated structure of the mixture was interpreted with the help of the results obtained from the simulation of the pure components. Similar to the experimental findings, the simulated results show that the hydrogen bonding in pure methanol is not disrupted by the addition of benzene. An investigation of the solute-solvent and solute-solute correlations does not support the view that a π-hydrogen bond is formed between benzene and methanol. This seems plausible since only a weak association is found between the solute and the solvent molecules. The three pdfs pertaining to benzene in the mixture are very similar to those in pure benzene, further supporting the assertion already made that benzene plays the role of an inert solute in the mixture. Although the two potential models chosen in simulating the mixture behaviour give a reasonably good account of the extent to which addition of benzene affects the structure of methanol, the agreement between the simulated and experimental structure at the pdf level is only qualitative, and warrants further refinement of the used potentials.

9.2 Further work

The experimental structural studies of mixture of polar and apolar compounds can be usefully extended to cover a variety of other systems such as water-cyclohexane, water-benzene... For instance, ND experiments were performed recently on cyclohexane-methanol (CM) liquid mixtures in a molar ratio 1:2. However, in these experiments, H/D substitution technique could be successfully applied only on the hydroxyl hydrogen of methanol. Additional ND measurements are required in order to extract all the solute-solute and solute-solvent correlations. The results of these studies will be valuable in view of the results already obtained for the benzene-methanol (BM) mixture because the two mixtures are complementary. It may be recalled that the indication of the absence of a π-hydrogen bond between benzene and methanol was obtained by studying how the self-association of methanol molecules changed in going from pure liquid to the mixture. Because such a π-hydrogen bond is

impossible in the case of CM system, a comparison between BM and CM systems should provide further evidence that association between benzene and methanol is very weak. However, because cyclohexane and methanol in the molar ratio 1:2 are miscible only above 50°C, the ND measurements on this system were performed at 60°C. Thus, a quantitative comparison between the results of the BM and CM systems can be made only if additional ND measurements using H/D substitution are performed for the BM system and pure methanol at 60°C. It would also be interesting to study how the hydrogen bonding of methanol in the BM system is broken by increasing the benzene content. However, in the benzene-rich region the Ho-Ho signal may be even more difficult to extract than in the 1:2 BM system investigated here. An alternative to the BM system for studying the π-hydrogen bond formation in the liquid state is chloroform-benzene. This mixture may be more appropriate since in this system the chloroform does not form hydrogen bonds.

9.3 Open questions

The high quality of the experimental results presented in this thesis is partly due to the use of a unique instrument (SANDALS) currently exploiting the most powerful pulsed neutron source in the world. Since this instrument is specially optimised for the H/D substitution technique, it was ideally suited for the measurements reported in this thesis. Up until mid 1980's, the isotopic substitution on hydrogen nuclei could not be exploited due to unavailability of proper instrument, severe experimental difficulties, and huge inelasticity corrections required in data treatment of samples containing lighter nuclei such as H or D. Since inelasticity effects often introduce significant systematic errors in the ND data, results obtained by exploiting the H/D substitution technique were not able to critically examine the suitability of different inter-molecular potential models used in computer simulations, as has been achieved in this work. It is evident that although the force field models considered in this study gave a qualitative account of the investigated structure of liquids and liquid mixture, these models need to be further refined to achieve a better agreement with the experimental results. This is necessary if one wishes to further interpret the simulation results, for example in predicting the preferred orientation correlations that may exist in the liquid. From this respect, it is difficult to comprehend why two

different potential models, exp-6 and LJ-12-6 used in the simulations predict two different dimer conformations (T-shaped vs. parallel displaced), yet produce similar pdfs in benzene.

Although, more powerful neutron facilities (such as ESS) and more sophisticated diffractometers are being developed, it would be useful to search for new methods for the ND data analyses. For instance, a rigorous estimation of the inelasticity effects has yet to be achieved, and the only approximate methods to do this are based on theoretical developments made in the fifties. Also, the growing sophistication of computer hardware will enable computer simulations to be used more effectively in devising accurate force field models from *ab-initio* and/or semi empirical methods. While dealing with molecular liquids where intra- and inter- molecular distances overlap, separating the two contributions from the ND data presents serious problems. The artefacts of using an inappropriate molecular model may not become obvious in the inter-molecular rdfs, but they become significant in the extracted partial distribution functions. Although experimental methods exist in the gas or solid phase to investigate the molecular geometry quite accurately, such methods are lacking in the liquid state. While it is possible to assess the intra-molecular changes in going from a gas to a liquid phase from spectroscopic measurements, the information gained is of little use for a diffractionist. Thus, the removal of the intra-molecular structure from the distinct DCS, almost invariably involves fitting a Debye type of function to the ND data. Since this function involves many parameters, the uniqueness of the fitted parameters cannot be guaranteed.

Ab-initio MD simulation methods will un-doubtfully play an important role in the future. An attractive development in these simulation methods has been the introduction of the Car-Parrinello (1985) technique, in which the motion of the nuclei is handled classically, but the energy and forces for each configuration of the system are found by solving the electronic problem "on the fly". Currently, the method is principally used for systems with loosely bound valence electrons, i.e., those in which the electronic structure is insensitive to the nuclear geometry. The time may come when computer power will be sufficiently great for the method to be applied more generally. Laasonen *et al.* (1993), Fois et al. (1994) and Sprik et al. (1996) have already shown that it can be used in simulating liquid water, with only a small number

of molecules, though. If such methods become widespread, the development of a potential energy surface as an intermediate step between the electronic wave-function calculation and the molecular dynamics simulation will no longer be required. In particular, for the structural investigation of mixtures such as benzene-water, benzene-methanol, cyclohexane-methanol or methanol-water by conventional computer simulations, it is difficult to assess the relevance of using the force fields designed for the pure components. Such issues may well be taken care of by the *ab-initio* MD simulations.

Appendix A

The structure of benzene-water mixture

A.1 The structural study of the pure components

A.1.1 Introduction

For a detailed interpretation of the structural results of the benzene-water mixture, it was desirable to study the structures of both the pure components under the same thermodynamic conditions (310° C and 164 bar) as that of the mixture. The H/D substitution technique of ND was employed on the hydrogens of water and benzene. For benzene, the critical temperature, T_C = 289° C, and the critical pressure p_C = 48.9 bar. Thus, under the experimental conditions, benzene is a supercritical fluid. However, since the saturation pressure of water at 310° C is 100 bar, at 164 bar it is a liquid just below the critical point. The structure of water has been the subject of considerable research. It has been studied previously by ND with H/D substitution over various thermodynamic state points (Soper et al., 1997), including the one at 300° C and 100 bar (Tromp et al., 1994; Soper et al., 1997), which is not very far from our own measurements. In contrast to water, the structure of benzene has mainly been investigated under ambient conditions. The only ND structural study of liquid benzene (C_6D_6) reported so far, presented results at the distinct and inter-molecular rdf level. These measurements were made as a function of temperature (Cabaço et al., 1997) from 9 to 75° C under ambient pressure. Within the investigated temperature range only very small changes of the intra- as well as inter-molecular structure of C_6D_6 were found. From this respect, comparison of the structural results of the room temperature benzene (RTB) (see chapter 7) with those of supercritical benzene (SCB) obtained here at the partial pair distribution function (pdf) level should

provide a better insight of the change in the intra- and inter-molecular structure in going from the liquid at room temperature to the supercritical fluid at 310° C.

A.1.2 Experimental and data reduction

For this experiment we used a high pressure Ti/Zr cell capable to sustain pressures up to ~ 3 kbar and specially designed for use on the SANDALS diffractometer at ISIS. This container (see figure A.1) consists of six cylindrical holes (1.5 mm diameter) drilled into a (4.1×4.05×0.66 cm) solid parallelepiped. Two heaters were mounted onto the cell. These heated both the top and the bottom of the cell without obstructing the neutron beam. Temperature was measured with two thermocouples attached at the bottom and the top of the cell. During the counting time, the two temperatures differed by less than ±1 K. A pressure transducer and a digital indicator were used to monitor the pressure inside the cell within ±1 bar of the selected value. The deuterated benzene and water samples used were respectively, 99.6% and 99.8% pure, purchased from Cambridge Isotope Laboratories, Inc. The measurements were performed on six samples in which the isotopic composition was varied as follows:

C_6D_6	(I)
C_6H_6	(II)
$C_6(H/D)_6$	(III)
D_2O	(IV)
H_2O	(V)
$(H/D)_2O$	(VI)

The multiple scattering and absorption contributions in such thick-walled container are quite significant. Since correction routines for making these corrections treat a sample holder being either flat or cylindrical, the cell was assumed to be flat with an effective thickness of the sample as 0.045 cm. For correctly accounting these effects, we chose a value of the wall thickness to give the correct high-Q limit for the DCS of the empty container. The effective thickness of the sample was then varied until we got the correct high Q limit for the cell filled with deuterated benzene. Once this was done, the raw data for all the samples were corrected for background,

container scattering, absorption, multiple scattering and normalised to the scattering from a vanadium slab using the suite of programs described in sections 5.5.1-5. The various total TOF DCSs for each detector group corresponding to these six samples were extracted. The observed values at the high-Q limit (in barns molecule^{-1}, see table A.1) of these functions for C_6D_6, C_6H_6 and $C_6(H/D)_6$ are respectively, 7±0.5, 33±1 and 20.6±0.8 as compared to the theoretical values of 6.44, 41.81 and 24.12 calculated from equation (4.36). For heavy, light and the mixture (heavy + light) water, the observed values are respectively, 1.71±0.1, 10.3±0.4 and 6.3±0.1 as compared to the theoretical values of 1.57, 13.4 and 7.5. Although the inelasticity corrections have so far not been applied to any of the above data, the agreement is fair. Figure A.2 shows, as expected that the diffraction pattern of any light sample (H_2O and C_6H_6) has effectively a higher value at the high-Q limit than the corresponding heavier sample, and the high Q limit of the light + heavy mixture sample lies in-between the two values. After applying the inelasticity corrections using the method described in sections 5.5.6.d and 5.8.2.a, data from different detector groups were combined (see section 5.5.7) and normalised to a molecular unit to give the single normalised distinct DCS for each sample (see figure A.3).

A.1.3 Structural results of water

a. The distinct rdfs

Each of the three experimentally extracted distinct differential cross section (DCS) (see figure A.3a) was Fourier transformed using the minimum noise reconstruction (MIN) technique described in section 5.6. The low-r cut-off (0.75 Å) was chosen to be lower than any known intra-molecular distance in water. The Q_{max} (30 Å^{-1}) used for Fourier transformation was a compromise between minimising the statistical noise effects at high-Q and, accounting for all the structural features at low-r. Interestingly, the intra- and inter-molecular contributions to the $G^{dist}(r)$s (see figure A.4) for this system overlap over a very narrow range of ~0.4 Å. While the region beyond ~1.9 Å contains purely inter-molecular correlations, only the intra-molecular structure contribute to the rdfs at r values less than 1.5 Å. In this respect, the first peak at ~0.97 Å arises from the O-H intra-molecular distances. The size and sign of this peak

varies according to the isotopic composition of the sample (see table A.2). For instance, for protonated H_2O, the resulting peak is negative. Since, the neutron weight of the O-H pair is roughly the same for both D_2O and $(H/D)_2O$, the size of this peak is similar for both the distribution functions. However, when the integration of $4\pi\rho\, c_H\, r^2 g(r)$ is carried out over the range of these peaks, it gives values for the O-H co-ordination numbers, $\bar{n}_O^H$ ~25% lower than the expected value 2. For $(H/D)_2O$, the peak at 1.55 Å observed in the rdf of D_2O, is merged into the second peak of $(H/D)_2O$ due to its small contribution (~11% as compared to ~48% for D_2O), but it becomes broad and prominent in H_2O since this is the only positive intra-molecular contribution (see table A.2) in this case.

b. The distinct pdfs

The three different isotopic contrasts on the hydrogen give rise to different weights for the three DCS. Since each one of them comprises of O-H, H-H and O-O correlations, setting X=O, S=H and i =1, 2, 3, respectively for D_2O, H_2O and $(H/D)_2O$ in the expressions (4.44-54), the distinct O-H, H-H and O-O partial structure factors (PSFs) (see figure A.5) were separated using HDSUB_B suite of programs (described in section 5.8). The distinct O-H, H-H and O-O pdfs obtained by Fourier transformation using the MIN technique are shown in figure A.6, and their back Fourier transforms (see figure A.5) are in reasonable agreement with their corresponding original functions from which they were obtained. These PSFs seem to be relatively noisy probably due to the errors such as the existence of temperature gradients, which might have averaged out during long data collection times and inadequate absorption and multiple scattering corrections due to the thick container. Nevertheless, the three extracted functions are in good agreement with the previous results (Postorino et al., 1993; Tromp et al., 1994; Soper et al., 1997). In the O-H and H-H pdfs (see figure A.6), the intra-molecular O-H and H-H contributions at 0.97 Å and 1.55 Å are now relatively well separated from the inter-molecular correlations. In the inter-molecular region of the O-H pdf, two peaks occur at 2.1 Å and 3.4 Å. The previous ND studies showed that the first inter-molecular peak at ~1.9 Å in the O-H pdf of room temperature (RT) water shifts to ~2.1 Å at 300° C and 100 bar. Moreover, its height reduces to ⅓ rd of that at RT. As the water was taken to a region above its critical

point the peak completely disappeared. From this respect, our results showing the O-H peak also at 2.1 Å corroborate the earlier findings. However, on a quantitative level the present results should be treated with caution since the intra-molecular O-H co-ordination number is found to be only 75% of the expected value 2. Nevertheless, they present nice structural trends in agreement with the previous findings.

A.1.4 Structural results of supercritical benzene

a. Distinct radial distribution functions (rdfs)

The experimentally extracted distinct differential cross sections (DCS) for the three H/D substituted SCB samples (see figure A.3b) are compared with their RT counterparts in figure A.7. Some differences can clearly be seen. In comparison to RTB, apart from the higher low-Q limits of the three SCB DCSs arising due to relatively high isothermal compressibility (9.7 10^{-10} Pa^{-1} and ~106.9 10^{-10} Pa^{-1} for RTB and SCB, respectively), the first peak at 1.36 $Å^{-1}$ in C_6D_6 has shifted to 1.13 $Å^{-1}$ in SCB. Also, the peak at 1.96 $Å^{-1}$ has become a shoulder in the SCB. For C_6H_6 and $C_6(H/D)_6$, the two first peaks at 1.36 and 3.2 $Å^{-1}$ have also shifted slightly towards lower-Q values. Such shifts in peak positions to low-Q values and reduction in the peak heights are the expected trends in going from a room temperature to a supercritical system. These functions were Fourier transformed using the minimum noise reconstruction (MIN) technique described in section (5.6). As for the room temperature benzene (RTB), the low r cut-off (0.80 Å) was chosen to be lower than any known intra-molecular distance in benzene. The Q_{max} (30 $Å^{-1}$) used for the Fourier transformation was a compromise between minimising the statistical noise effects at high-Q and, accounting for all the structural features at low-r. The $G^{dist}(r)$ for the three samples plotted in figure A.8 with their RT counterparts can be split into three regions. The region beyond ~5 Å contains purely inter-molecular correlations, but it appears featureless. In the region between 0.8 Å and 1.5 Å where only intra-molecular correlations contribute, the positions of the first and second peaks at 1.09 and 1.395 Å, respectively arising from the C-H and C-C intra-molecular distances, are in good agreement with their RT counterparts. The third region from 1.5 Å to 5 Å, contains both inter- and intra-molecular correlations. The features observed in this

region in the rdfs of SCB resemble those in their RT equivalents. The results suggest that the intra-molecular structure of benzene has not changed much in passing from RTB to SCB. Again, as expected the peaks in the three RTB rdfs are slightly narrower and sharper than those in SCB. Both SCB and RTB rdfs presented in figure A.8 have been normalised to the same density value. A temperature effect on the vibrational states of the C-H and C-C intra-molecular distances could make these peaks broader and smaller in the SCB relative to those in the RTB.

b. Separation of intra- and inter- molecular correlations

The intra-molecular contribution of SCB was extracted from the distinct DCS by fitting equation 4.40 to the distinct DCS of deuterated benzene in the high-Q range (6- 30 $Å^{-1}$). This was done in a manner similar to that for the RTB (see section 7.2.2). As we already saw from the survey of the intra-molecular structure of benzene investigated experimentally (see table 7.1), the geometry of benzene molecule hardly changes throughout its three phases. In this respect, the C-H and C-C bond lengths obtained from the SCB rdfs are in close agreement with those found from the RTB rdfs. Since the peaks in the region 1.5 Å to 5 Å of the distinct C_6D_6 rdf arise from non-bonded intra-molecular correlations, and their positions are in good agreement with those in the RTB for which a planar hexagonal geometry was adopted, the same model was chosen in the present study. In contrast to the RTB, the C-C and C-H bond lengths were not kept fixed. Both the bond lengths and the Debye-Waller factors, γ_{ij} were varied to fit the distinct DCS of the deuterated benzene by using equation 4.40. The intra-molecular distances obtained from the fit for the SCB and RTB are close to each other (see table A.3). The calculated intra-molecular structure factors along with their corresponding distinct DCSs are shown in figure A.3b. The larger values for almost all the Debye-Waller factors of SCB as compared to RTB are reasonable because of a temperature difference of 285 K between RTB and SCB. A damped intra-molecular structure factor for the SCB as compared to the RTB (see figure A.9) is the consequence of such the temperature effect. This aspect will be discussed in the next section where the C-C and C-H distinct pdfs are separated. from the distinct rdfs. The inter-molecular DCSs obtained after subtracting the intra-molecular structure factors from the distinct DCSs for the three samples were normalised to the molecular

unit, and these are shown in figure A.10. The corresponding inter-molecular rdfs, obtained by Fourier transformation of the inter-molecular DCSs by using the minimum noise reconstruction (MIN) technique (see section 5.6) are plotted in figure A.11. The back Fourier transformations also shown in figure A.10 are in poor agreement with the inter-molecular DCS functions from which the rdfs were obtained. This again highlights the fact that on a quantitative level these data should be treated with caution. Qualitatively, however the inter-molecular rdfs for SCB are shifted towards higher distances relative to those for the RTB. The results for C_6H_6 are still seem to contain some residual inelasticity effects.

c. H/D substitution analyses

I. Distinct pdfs

Similarly to the RTB (see table 7.2), the three different isotopic contrasts on the hydrogen in SCB give rise to different weights for the three DCSs. Since each one of them comprises of C-C, C-H and H-H correlations, setting X=C, S=H and i =1, 2, 3, respectively for C_6D_6, C_6H_6 and $C_6(H/D)_6$ in the expressions (4.44-54), the distinct C-H and C-C partial structure factors (PSFs) (see figure A.12) were separated using HDSUB_B (described in section 5.8). The distinct C-C and C-H pdfs obtained by Fourier transformation, using the MIN technique, are compared with those obtained for the RTB in figure A.13. It is worth noting that if residual inelasticity effects are still present in the data, firstly they should cause a systematic offset in the data, and secondly they should manifest themselves in the real space as high frequency ripples at low r. However, these effects cannot be seen in the data. Moreover, the back Fourier transforms of these functions shown (see figure A.12) superimposed on the functions from which they are obtained, are in good agreement with each other. Because the intra-molecular features of the C-H and the C-C pdfs dominate these functions, it provides a check on the geometry of the benzene molecule used for the separation of the intra-molecular distances from the distinct DCSs. For instance, the C-C pdf exhibits two well-defined peaks at 1.395 Å (1.396 Å for RTB) and ~2.44 Å (~2.42 Å for RTB) corresponding respectively to the C_1-C_2, C_1-C_3 (see figure 7.1) distances. Also, a shoulder on the right side of the C_1-C_3 peak at ~2.80 Å associated to the C_1-C_4 distance is similar to that observed in RTB (at ~2.80 Å). The distinct

C-H pdf shows three peaks at 1.092 Å, 2.156 Å and 3.40 Å (in comparison with 1.082 Å, 2.156 Å, and 3.40 Å for RTB) corresponding respectively, to the C_1-H_1, C_1-H_2 and C_1-H_3 types of intra-molecular distances. A small hump centred at ~3.89 Å in this function is associated with the C_1-H_4 types of distances. These observed values are consistent with the intra-molecular distances calculated by assuming a planar and hexagonal geometry for the benzene molecule. Because the C-H (see figure A.13a) and C-C (see figure A.13b) pdfs for SCB and RTB were normalised to the same density, the size of the well-separated C_1-H_1 and C_1-C_2 peaks of SCB should match those of RTB unless the widths of the SCB peaks are larger than those of RTB due to a temperature effect on the intra-molecular structure. From this respect, figure A.13 insets (I and II) show a small broadening of the experimental and computed C_1-C_2 peaks in SCB compared to those in the RTB. However, the C-H co-ordination number, $\bar{n}_C^H$, and the C-C co-ordination number, $\bar{n}_C^C$, obtained by integrating $4\pi\rho\ c_H\ r^2\ g_{CH}(r)$ and $4\pi\rho\ c_C\ r^2\ g_{CC}(r)$, respectively over the range of these peaks, are found to be 75% and 79% of the expected values 1 and 2, respectively. These errors are larger than those observed (~6%) in RTB. while those for pure benzene are within 6% of the expected values. To some extent, larger errors in going from a near-triple-point to a supercritical state of a system can be expected and understood. Nevertheless, the errors arising from the possible temperature gradients in the cell and inappropriate absorption and multiple scattering corrections of the thick container cannot be ruled out.

II. inter-molecular pdfs

From the inter-molecular DCSs, following the same procedure as for the distinct DCSs, we attempted to extract the inter-molecular H-H, C-H and C-C PSFs (see figure A.14). Their Fourier transforms are shown in figure A.15. The back Fourier transform of the H-H pdf compares reasonably with the data from which it was obtained. Similar comparison for the C-H and C-C functions is rather poor. The three SCB pdfs are compared with their RT counterparts in figure A.15. It can be seen that the first inter-molecular peak at ~2.4 Å in the H-H pdf of RTB has shifted to ~2.6 Å in the SCB. In addition, the peak at ~3.5 Å in RTB has become broader and slightly shifted by ~0.2 Å towards higher *r*. For the C-H and C-C pairs significant changes

can be seen in going from RTB to SCB. Although, it is difficult to ascertain the detailed structural features of these pdfs at a quantitative level, these functions, as expected, are more damped and shifted to higher distances in the SCB relative to those in the RTB.

A.2 Benzene-water system: a failed experiment

A.2.1 Introduction

Benzene is a classical example of a molecule that exhibits hydrophobic behaviour in water. Whereas hydrophobic hydration deals with the structure of water in the vicinity of an apolar molecule, the hydrophobic interaction refers to the solvent induced interactions between the apolar molecules. In order to characterise the hydrophobic properties, which is a subject of relevance in many biochemical and chemical processes such as in petroleum industries where hydrocarbon-water mixtures are encountered, we performed Neutron diffraction (ND) structural measurements on benzene-water (BW) mixture. This system, like other hydrocarbon-water systems forms two partially miscible liquid phases of low mutual solubility. At 25°C the solubility of benzene in water is 0.42×10^{-3} mole fraction. As the temperature and pressure are raised, the mutual solubility increases (Rebert and Kay, 1959; Connolly, 1966). A particularly interesting part of the phase diagram is located at pressures in the region 150-170 bar and temperatures in the range 300 to 320°C. An upper critical solution temperature for this system is reported as 306.4°C and 156 bar (Rebert and Kay, 1959). Above 315°C there is a liquid-vapour two-phase region. In the phase diagram window between 306.4°C and 315°C and pressure close to 164 bar, where the mixture is homogeneous, it is possible to make measurements on the mixture over the whole composition range. There is no similar window of total miscibility in the phase diagram of water + alkanes, and the BW system is unique in this respect. Measurements were made in a benzene to water molar ratio 1:1 at 310°C and 165 bar. Apart from the thermodynamics considerations, this system is complementary to the benzene-methanol (BM) system investigated earlier (see chapter 8). Water is a strong hydrogen bonded liquid, and at 310°C the kinetic energy opposes the forces striving to produce local ordering. As for the BM liquid mixture, the suitability of isotopic

H/D substitutions on both benzene and water allows to extract the benzene-benzene, benzene-water and water-water correlations. From these measurements on the mixture along with similar measurements on its pure components under the same thermodynamic conditions (see section A.1), it is possible to investigate how addition of benzene disrupts the hydrogen bonding in water, and results in a possible association between water and the π-electron system of benzene.

A.2.2 Experimental and data reduction

At the time of the experiment SANDALS instrument was mounted with 14 groups of detectors covering scattering angles (2θ) from 3.8 to 31.2°. In order to make the measurements under the required thermodynamic conditions, a rig was designed and fabricated to mix the two components at the required composition, temperature and pressure. Benzene and water were pumped through two pumping meters into a preheated T-shaped chamber. Once the mixtures were equilibrated at the required temperature and pressure, they were pumped into a cell through an inlet tube. For this experiment we used the same high pressure Ti/Zr cell used for the pure components and specially designed for use on the SANDALS. The temperature and pressure were measured and controlled in the same way as for the pure components. During the counting time, the temperature differed by less than ±1 K and the pressure inside the cell was within ±1 bar of the selected value. The measurements were performed on eight samples in which the isotopic composition was varied as follows:

$C_6D_6 + D_2O$	(I)
$C_6D_6 + H_2O$	(II)
$C_6D_6 + (H/D)_2O$	(III)
$C_6H_6 + D_2O$	(IV)
$C_6(H/D)_6 + D_2O$	(V)
$C_6(H/D)_6 + (H/D)_2O$	(VI)
$C_6H_6 + H_2O$	(VII)
$C_6H_6 + (H/D)_2O$	(VIII)

Where, $(H/D)_2O = 0.5\ H_2O + 0.5\ D_2O$ and $C_6(H/D)_6 = 0.5\ C_6H_6 + 0.5\ C_6D_6$. The

container was treated in the same way as for the pure components. The effective thickness of the sample was varied until we got the correct vanadium high-Q limit for the cell filled with six cylindrical vanadium rods of same diameter as the cylindrical holes. Once this was done, the raw data for the mixtures were corrected for background, container scattering, absorption, multiple scattering and normalised to scattering from a vanadium slab using the suite of programs described in sections 5.5.1-5. Under the assumption that the dynamic corrections are negligible (see section 5.5.6), the total TOF DCS (see equation 5.36) for each detector group and each sample is given by

$$\Sigma_S(\theta,Q) = \sum_{i=1}^{2} x_i \sum_{\alpha i} c_{\alpha i} \overline{b_{\alpha i}^2} \Sigma_{\alpha i}^{\text{self}}(Q,\theta) + \sum_{i,j=1}^{2} x_i x_j \sum_{\alpha i}^{Nmi} \sum_{\beta j}^{Nmj} \overline{b_{\alpha i}}\,\overline{b_{\beta j}} c_{\alpha i} c_{\beta j} (S_{\alpha i \beta j}(Q) - 1), \qquad \text{(A.1)}$$

where b_{α_i} is the scattering length of the nucleus α in the molecule i, and the sum runs over all different (Nmi) types of α nuclei appearing c_α times in the molecule i whose molar composition is x_i. The total DCSs for various mixture samples for the first group of detectors are shown in figure A.16. At this stage, only a qualitative comparison between the experimental high-Q limit and the calculated values from

$$\left(\frac{\partial\sigma}{\partial\Omega}\right)_{\text{self}} = \sum_{i=1}^{2} x_i \left(\sum_{\alpha_i}^{\text{Nm}_i} c_{\alpha_i} \bar{b}_{\alpha_i}{}^2 + c_{\alpha_i} b_{\alpha_i}^{\text{incoh}\ 2} \right) \qquad \text{(A.2)}$$

can be made because the inelasticity corrections have not yet been applied to any of the data (see section 5.8.2). While observed and theoretically calculated values for the pure liquids and liquid mixture studied in chapters 6-8 for a fully deuterated sample, protonated sample and a mixture of light + heavy sample lie within ~3-5%, 6-12% and 4-9%, respectively the values observed here do not fall within these ranges of the theoretical values (see table A.4). In addition, no matter how fair is this agreement, the high-Q limit of a light sample should be at a higher value than that for a heavy sample, and the high-Q limit of the light + heavy mixture sample must lie in between these two values (see e.g., figure 5.12). Figure A.16a however shows that out of the three mixtures IV, VII and VIII, the "light" mixture VII has a lower high-Q limit than the other two samples. This is contrary to our expectation and gives a hint that something must have gone wrong. A possible reason could be that the

composition of the various mixtures might have varied from one sample to another. Additionally, the total TOF DCSs of mixtures I, II and III displayed in figure A.16b show that the three diffraction patterns are very similar. This means that benzene and water did not form a homogeneous mixture inside the container. This could have happened if large temperature gradients existed inside the cell, even though the temperature at the top and the bottom of the container were kept and controlled at 310° C. Since the temperature range of miscibility of this system is very narrow, small temperature gradients would result in the formation of two immiscible layers: water-in-benzene at the top and benzene-in-water at the bottom (at 310°C and 165 bar ρ_{H_2O} = 0.6989g/cm^3 (Deul and Franck (1991)) and $\rho_{C_6H_6}$ = 0.5655g/cm^3, (Deul et al. (1991)). For the same number of benzene and water molecules, since the volume occupied by the water in the cell is smaller than that of benzene, the neutron beam must have been predominantly scattered by the benzene molecules. This may explain why the diffraction patterns (I, II and III) look very much like that of C_6D_6 (see figure A.16b).

A.3 Recommendations for a future successful attempt on BW mixture and to improve the results on pure components

The can used in the experiment was not an ideal choice. Although this cell is able to sustain up to 3 kbar and is accordingly quite thick, the pressure required for studying our BW system (165 bar) is smaller enough to be handled by a thinner container. Two points are important: thickness of the cell, which firstly does not guarantee proper corrections for the multiple scattering and absorption corrections. Secondly, it leads to large temperature gradients within the cell, which were not calibrated. To design a new cell, it is possible to use finite element analysis to simulate in the vacuum a hypothetical container mounted with heaters and filled with the benzene-water sample under the required thermodynamic conditions. Such analysis will indeed be helpful provided it is complemented with some experimental temperature measurements on the real system for validating the analysis. Since the method allows to incorporate the dynamics of the heat transfer, the equilibration time needed for the mixture to become homogeneous can also be studied. From this respect, starting from the two BW phases and by varying the temperature of the two heaters placed at the

top and bottom of the cell, it would be interesting to study the possible formation of a thermal instability such as the Rayleigh-Bénard convection (known also as Bénard's cells) (Rosenhead, 1963; Batchelor, 1954). This would enable the two components to get mixed on their own.

Table A.1. The thermodynamic conditions and the sample parameters used in the data analyses of the pure components.

Parameters \ Samples	C_6D_6	C_6H_6	$C_6(H/D)_6$	D_2O	$(H/D)_2O$	H_2O
Temperature / (°C)	310±1	310±1	310±1	310±1	310±1	310±1
Pressure / (bar)	164.5±0.4	164.5±0.4	164.5±0.4	164.5±0.4	164.5±0.4	164.5±0.4
[d] number density / (molecule Å^{-3})	0.00435	0.00435	0.00435	0.02336	0.02336	0.02336
σ_a at 1.8 Å / (b molecule^{-1})	0.0321	2.0166	1.0243	2.556×10^{-3}	0.334	0.665
[a] b_c C / (fm)	6.646	6.646	6.646	--	--	--
[a,b] b_c H / (fm)	6.629	-3.739	1.445	6.650	1.456	-3.739
[a] b_c O / (fm)	--	--	--	5.803	5.803	5.803
$\left(\sum_\alpha c_\alpha \bar{b}_\alpha\right)^2$ / (b molecule^{-1})	63.445	3.042	23.568	3.649	0.759	0.028
[c] $lim_{Q\to\infty}\left(\frac{\partial\sigma}{\partial\Omega}\right)_{dist}$ /(b molecule^{-1})	6.440 (7±0.5)	41.812 (33 ±1)	24.126(20.6±0.8)	1.577(1.71±0.1)	7.484(6.3±0.1)	13.391(10.3±0.4)

[a] from Sears (1992); [b] calculated according to the isotopic composition and purity of the sample; [c] theoretical values are compared with the experimental values given in parenthesis; [d] the density was taken from Deul and Franck (1991).

Table A.2. The neutron weights of the radial distribution functions in liquid water.

pair α-β	D_2O	$(H/D)_2O$	H_2O
O H	0.423	0.445	-30.99
O O	0.092	0.443	12.03
H H	0.485	0.112	19.97

Table A.3. Average benzene structure in terms of intra-molecular distances ($r_{\alpha\beta}$ / Å) and associated Debye-Waller factors ($\gamma_{\alpha\beta}$ / Å) obtained by least squares refinement as compared to other available experimental data.

parameters	*SCB*	*RTB*	*Benzene (l)*	*Benzene(g)*	*benzene(s)*
r C-C	1.409	1.397[r]	1.390[g], 1.416[j], 1.38[k],1.395[m] 1.41[n], 1.378[o], 1.389[p]	1.397[d], 1.397[e], 1.396[f]	1.392[a], 1.398[b], 1.398[c], 1.3978[h], 1.3972[i], 1.41[l]
r C-H	1.079	1.084[r]	1.082[g], 1.09[j], 1.09[k], 1.081[m] 1.072[o], 1.083[p]	1.084[d], 1.083[f],	1.077[b], 1.090[c], 1.0825[h], 1.0864[i], 1.085[l]
γ C_1-C_2	0.0825	0.0605	0.064764[g], 0.0849[n], 0.038[o], 0.0104[p]	0.0459[q]	
γ C_1-C_3	0.1132	0.0776	0.076902[g], 0.101[n], 0.035[o], 0.0017[p]	0.0547[q]	
γ C_1-C_4	0.086	0.0873	0.082208[g], 0.06[n], 0.037[o], 0.0034[p]	0.0597[q]	
γ C_1-H_1	0.096	0.0776	0.092246[g], 0.037[o], 0.0715[p]	0.0771[q]	
γ C_1-H_2	0.143	0.1089	0.1218[g], 0.07[o], 0.0713[p]	0.1004[q]	
γ C_1-H_3	0.141	0.1326	0.119784[g], 0.08[o], 0.0989[p]	0.0960[q]	
γ C_1-H_4	0.111	0.0873	0.116396[g], 0.08[o], 0.1370[p]	0.0942[q]	
γ H_1-H_2	0.219	0.1931	0.18914[g], 0.08[o], 0.1283[p]	0.1561[q]	
γ H_1-H_3	0.162	0.1640	0.160258[g], 0.08[o], 0.1674[p]	0.1321[q]	
γ H_1-H_4	0.163	0.1059	0.142646[g], 0.08[o], 0.095[p]	0.1191[q]	
R_{factor}	0.058	0.053			

a: crystal structure of benzene at -3°C by X-rays diffraction from Cox et al. (1958); b: ND of solid benzene at -55°C, from Bacon et al. (1964); c: ND of solid benzene at -135°C, from Bacon et al. (1964); d: raman spectroscopic measurements, from Langseth and Stoicheff (1956); e: electron diffraction measurements, from Bastiansen (1957); f: infrared measurements of C_6H_6 and C_6D_6 , from Cabana et al. (1974); g: ND measurements of C_6D_6 in the temperature range 282-348K, from Cabaço et al. (1997); h: neutron powder diffraction data collected at 4K on C_6D_6 , from David et al. (1992); i: single crystal neutron structure refinement of C_6D_6 at 15K, from Jeffrey et al. (1987); j: ND measurements of C_6D_6 at room temperature, from Misawa and Fukunaga (1990). k: ND measurements on C_6D_6 at room temperature, from Felici et al. (1990); l: NMR investigation of solid benzene, from Andrew and Eades (1953); m: ND measurements on C_6D_6 at room temperature, from Matsumoto (1982); n: X-rays diffraction of C_6H_6 at 298K, from Narten (1967); o: ND measurements of room temperature C_6D_6 at a reactor source using λ=0.5 Å, p: using λ=0.7 Å, from Bartsch et al. (1985); q: calculated from spectroscopic data, from Bastiansen and Cyvin (1957); r: fixed to the value given by Langseth and Stoicheff (1956), and Cyvin (1968).

Table A.4. The thermodynamic conditions and the sample parameters used in the data analyses of the benzene-water mixtures.

Samples / Parameters	C_6D_6 + D_2O	C_6D_6 + $(H/D)_2O$	C_6D_6 + H_2O	C_6H_6 + D_2O	C_6H_6 + $(H/D)_2O$	C_6H_6 + H_2O	$C_6(H/D)_6$ + $(H/D)_2O$	$C_6(H/D)_6$ + D_2O
Temperature / °C	310±1	310±1	310±1	310±1	310±1	310±1	310±1	310±1
Pressure / bar	165	165	165	165	165	165	165	165
[d]number density /molecule $Å^{-3}$	0.00548	0.00548	0.00548	0.00548	0.00548	0.00548	0.00548	0.00548
σ_a at 1.8 Å / b molecule^{-1}	1.732×10^{-2}	0.183	0.349	1.009	1.1753	1.341	0.679	0.513
[a]b_c C / fm	6.646	6.646	6.646	6.646	6.646	6.646	6.646	6.646
[b]b_c HB (benzene)/fm	6.629	6.629	6.629	-3.739	-3.739	-3.739	1.445	1.445
[b]b_c HW (water) /fm	6.650	1.456	-3.739	6.650	1.456	-3.739	1.456	6.650
[a]b_c O / fm	5.803	5.803	5.803	5.803	5.803	5.803	5.803	5.803
$\left(\sum_{i=1}^{2} x_i \sum_{\alpha_i}^{Nm_i} c_{\alpha_i} \bar{b}_{\alpha_i}\right)^2$ / b molecule^{-1}	24.382	22.965	21.591	16.570	15.406	14.285	18.998	20.288
[c] $lim_{Q\to\infty}\left(\frac{\partial\sigma}{\partial\Omega}\right)_{dist}$ / b molecule^{-1}	~5.62 (4.01)	~5.56 (6.96)	~5.59 (9.92)	~23.79 (21.69)	~23.74 (24.65)	~22.03 (27.60)	~14.93 (15.80)	~14.69 (12.85)

[a] from Sears (1992); [b] calculated according to the isotopic composition and purity of the sample; [c] theoretical values given in parenthesis are compared with the experimental values; [d] density was taken from Deul and Franck (1991).

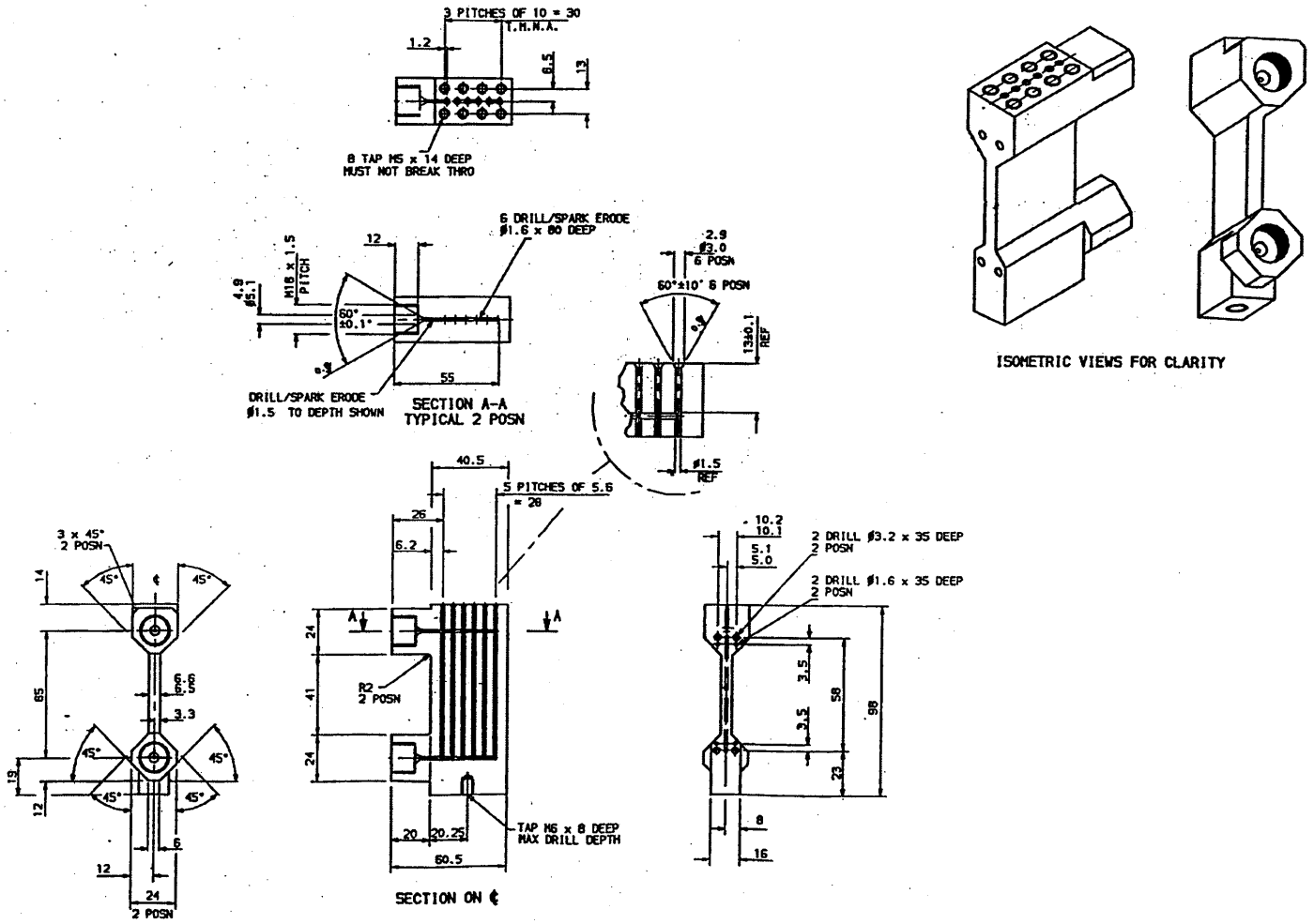

Figure A.1. Diagrams of SANDALS Ti/Zr 3Kbar cell used for holding the various benzene-water mixture samples and its pure components.

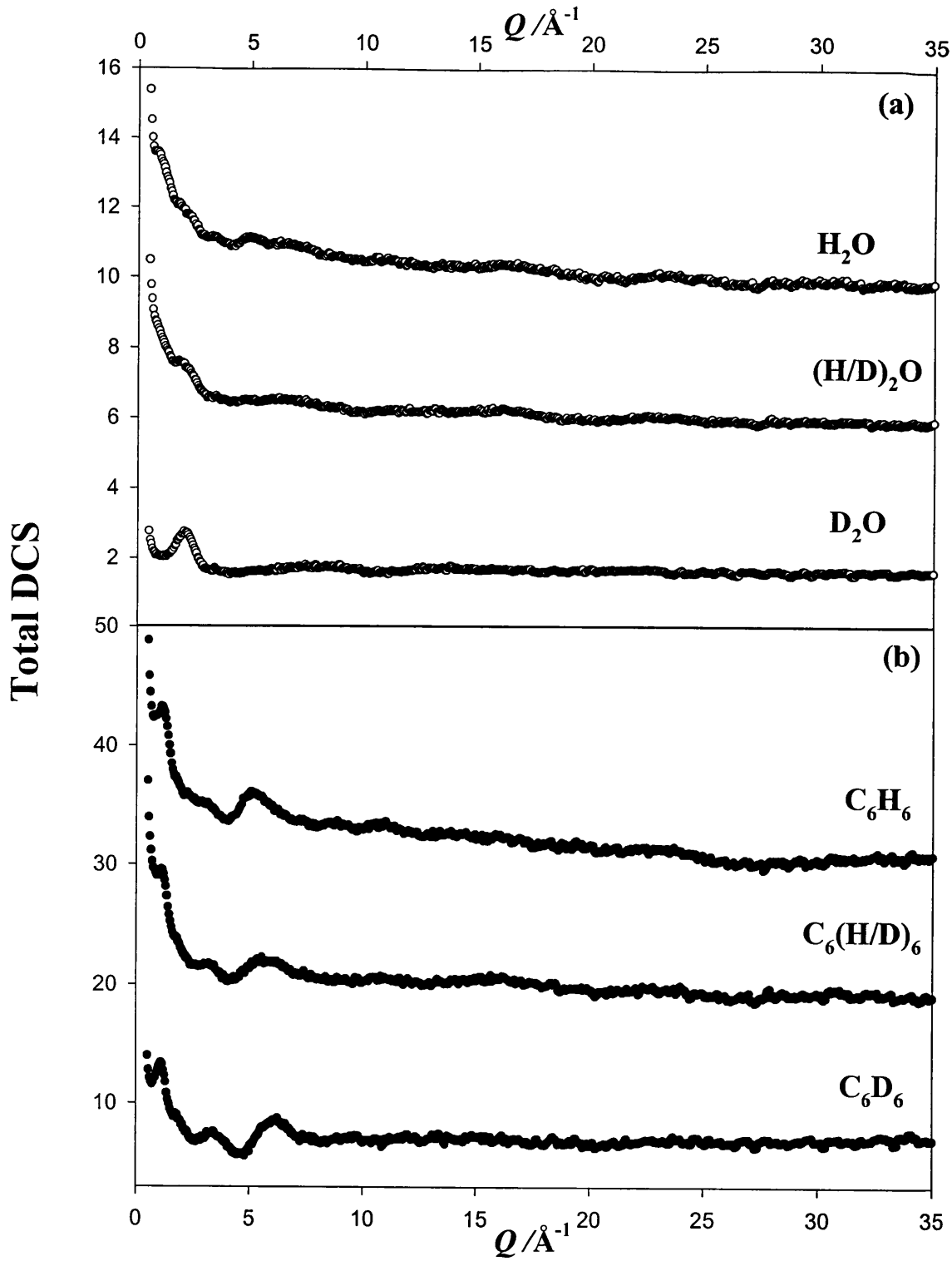

Figure A.2. (a) The total DCSs obtained for H_2O, D_2O and $(H/D)_2O$ corresponding to the first group of detectors. (b) The total DCSs obtained for C_6H_6, $C_6(H/D)_6$ and C_6D_6 corresponding to the first group of detectors.

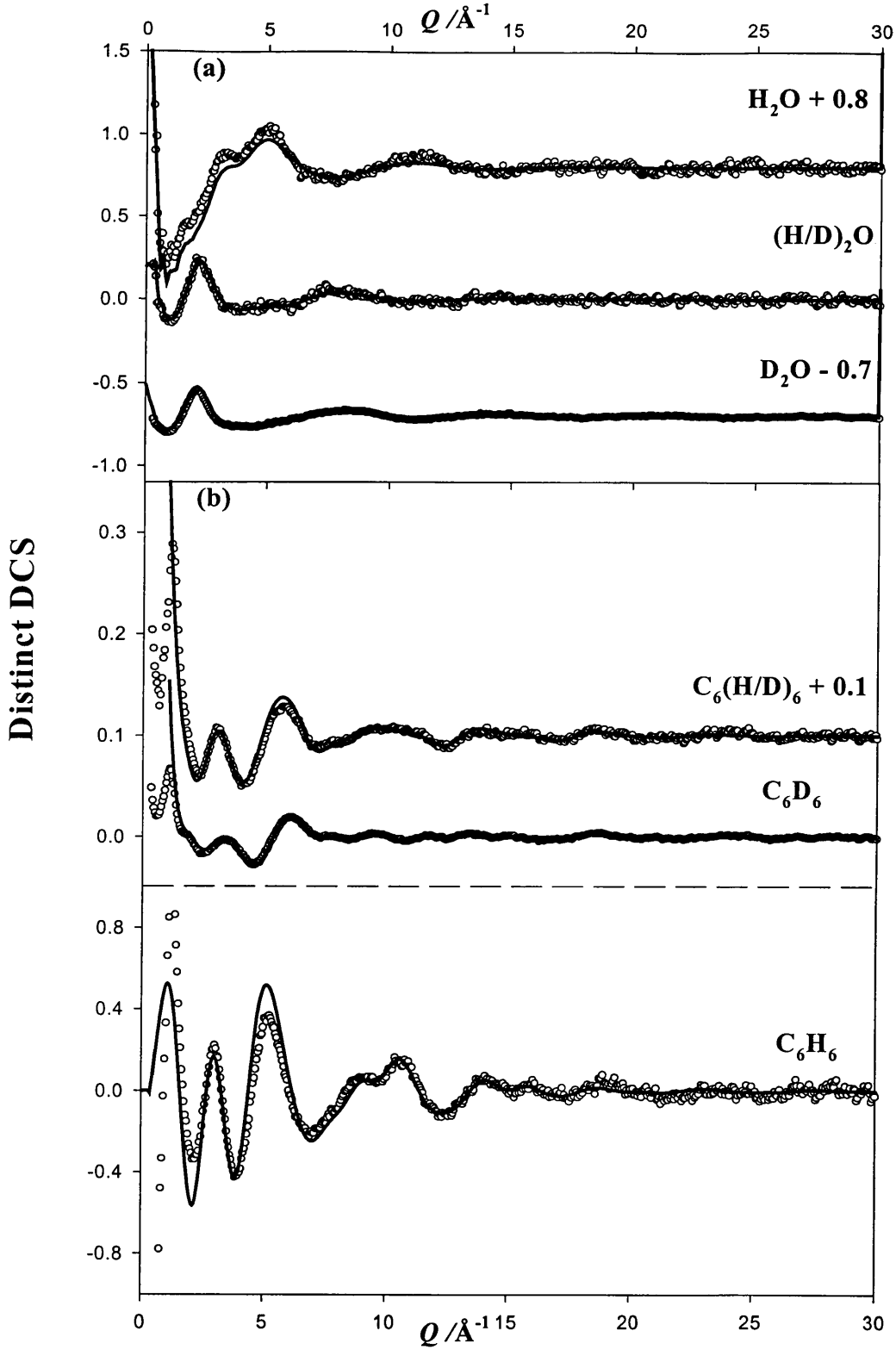

Figure A.3. (a) The distinct DCSs normalised to the scattering unit for H_2O, D_2O and $(H/D)_2O$ (circles) along with the corresponding back Fourier transforms of the radial distribution functions shown in figure A.4 (lines). (b) The distinct DCSs normalised to the scattering unit for C_6H_6, $C_6(H/D)_6$ and C_6D_6 (circles) presented along with their intra-molecular DCS (lines).

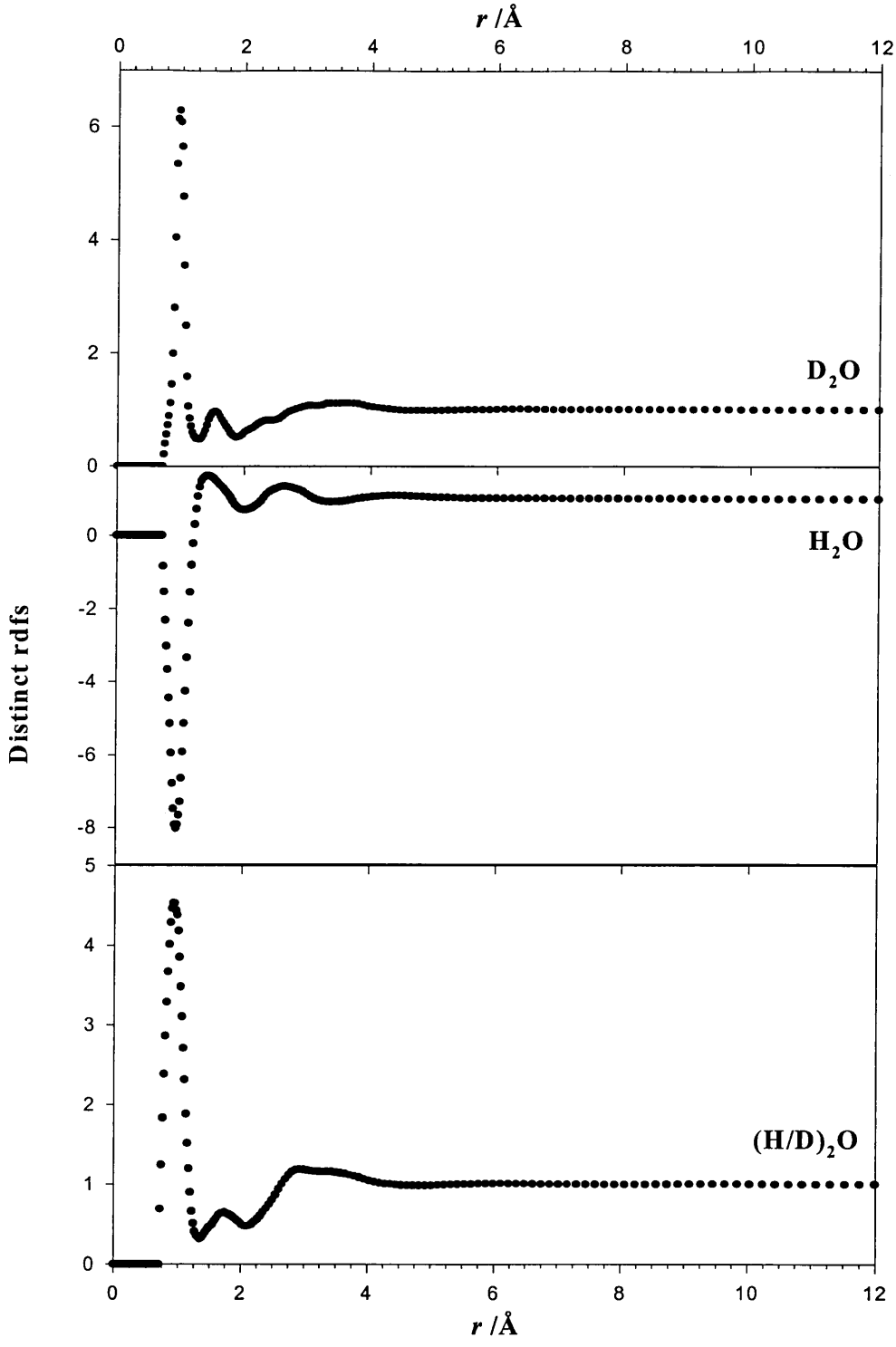

Figure A.4. The three distinct radial distribution functions of D_2O, H_2O and $(H/D)_2O$.

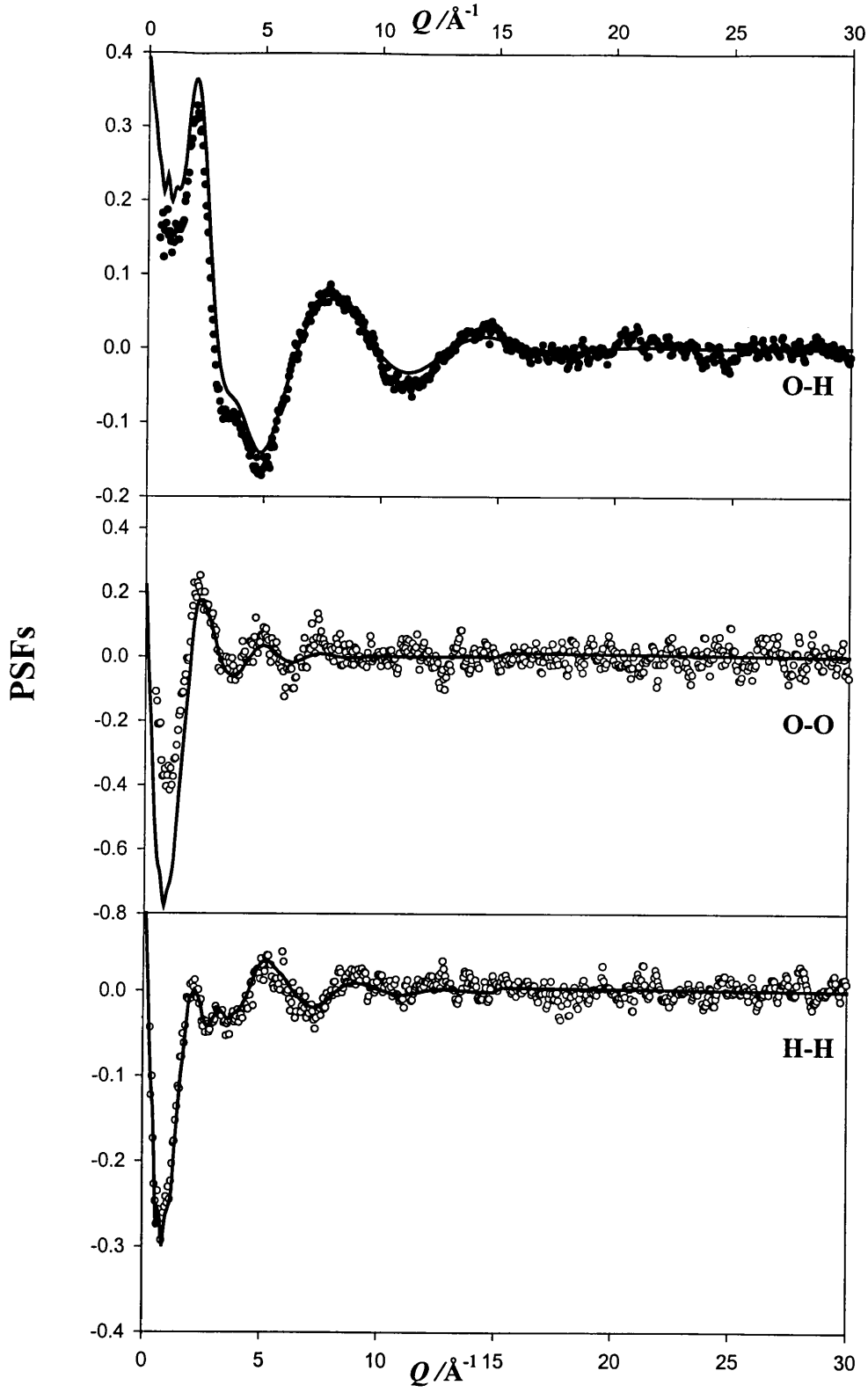

Figure A.5. The O-H, and H-H distinct partial structure factors (PSFs), and the intermolecular O-O PSF obtained from second- and higher- order difference method (symbols). The back Fourier transforms (lines) of the pdfs of figure A.6 are superimposed on the original data from which they were obtained.

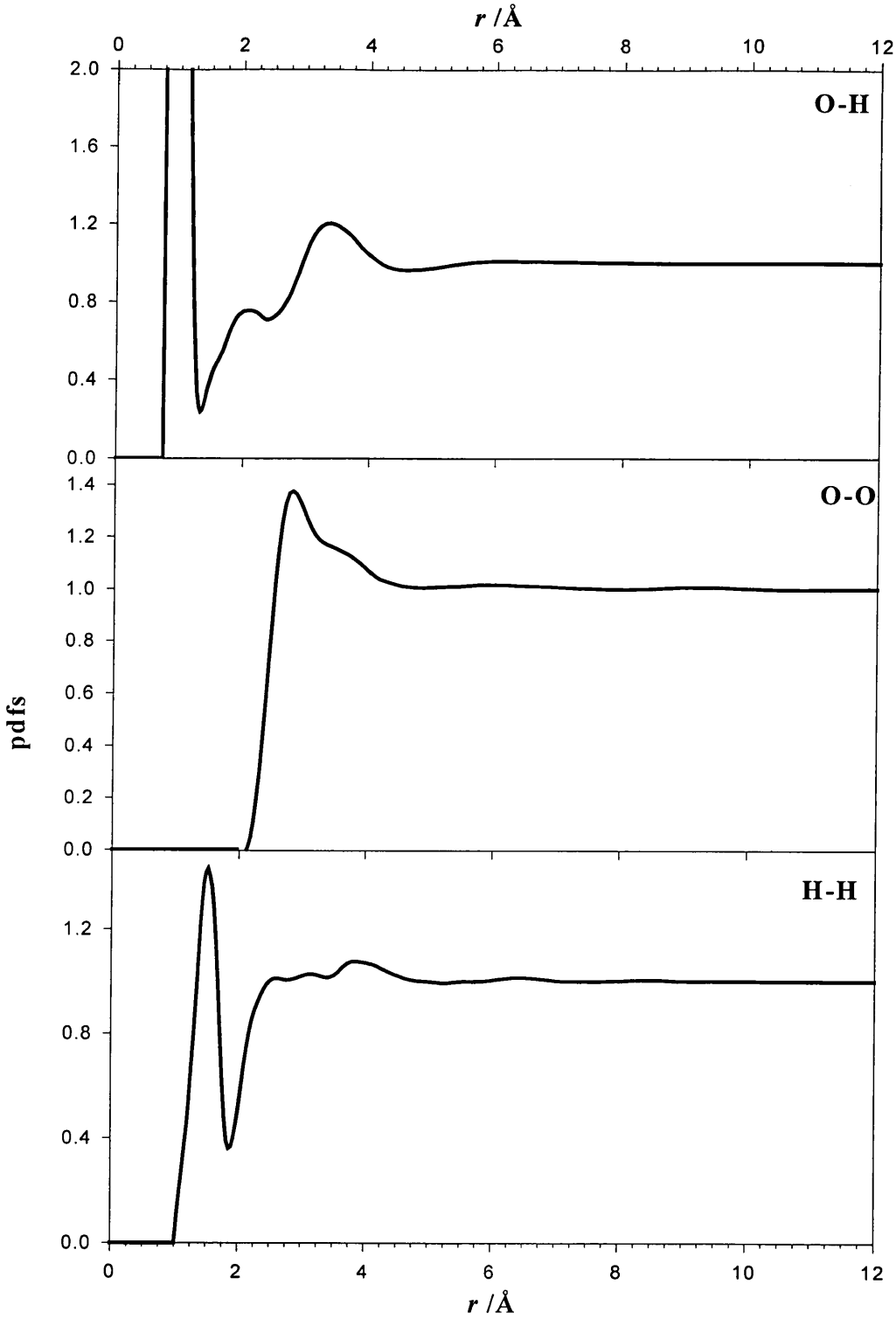

Figure A.6. The O-H and H-H inter- + intra-, and O-O inter-molecular pdfs obtained after Fourier transformation of the corresponding PSFs of figure A.5.

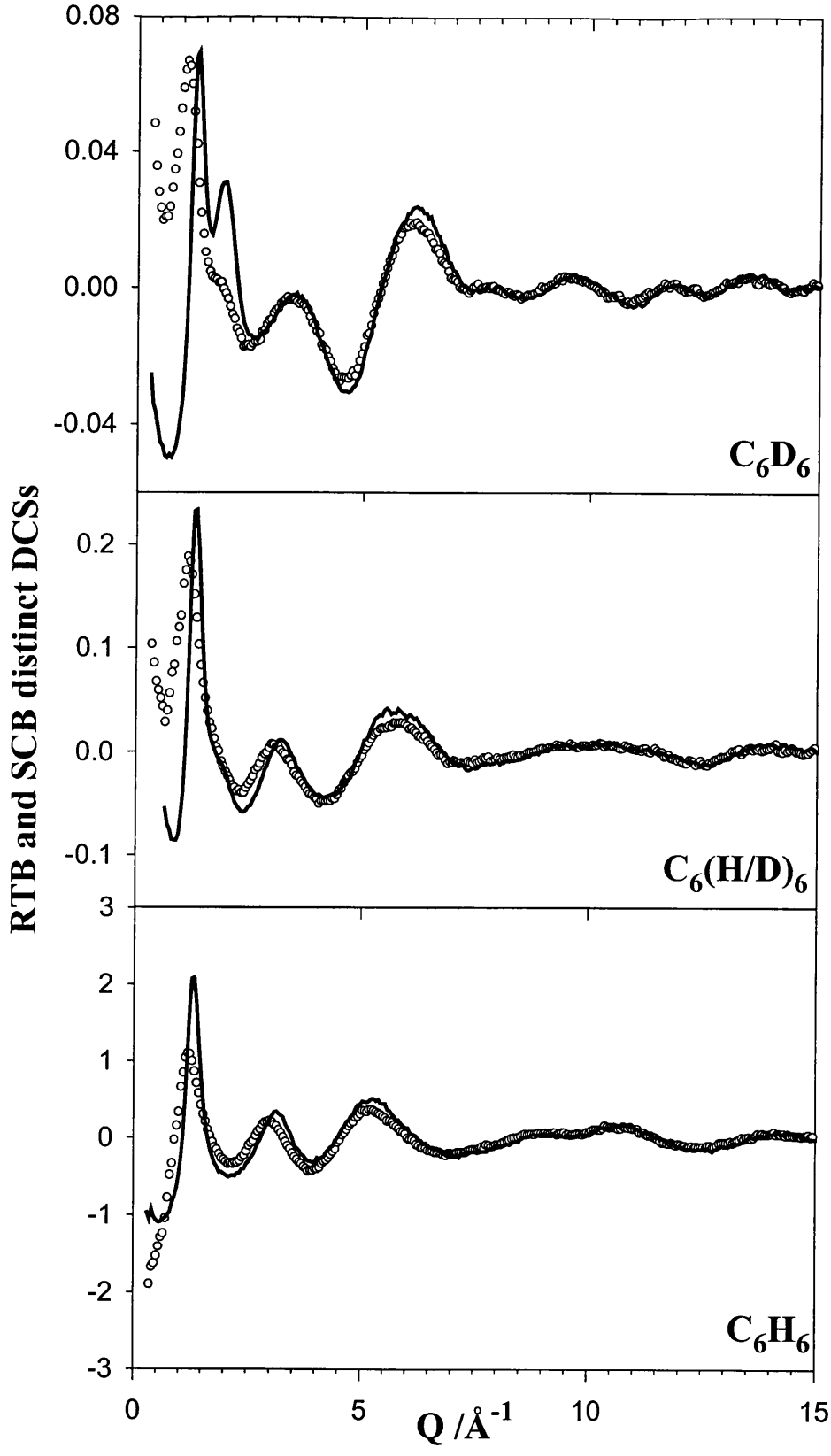

Figure A.7. The distinct DCSs for the three super critical benzene samples (symbols) presented along with their room temperature counterparts (lines) discussed in chapter 7.

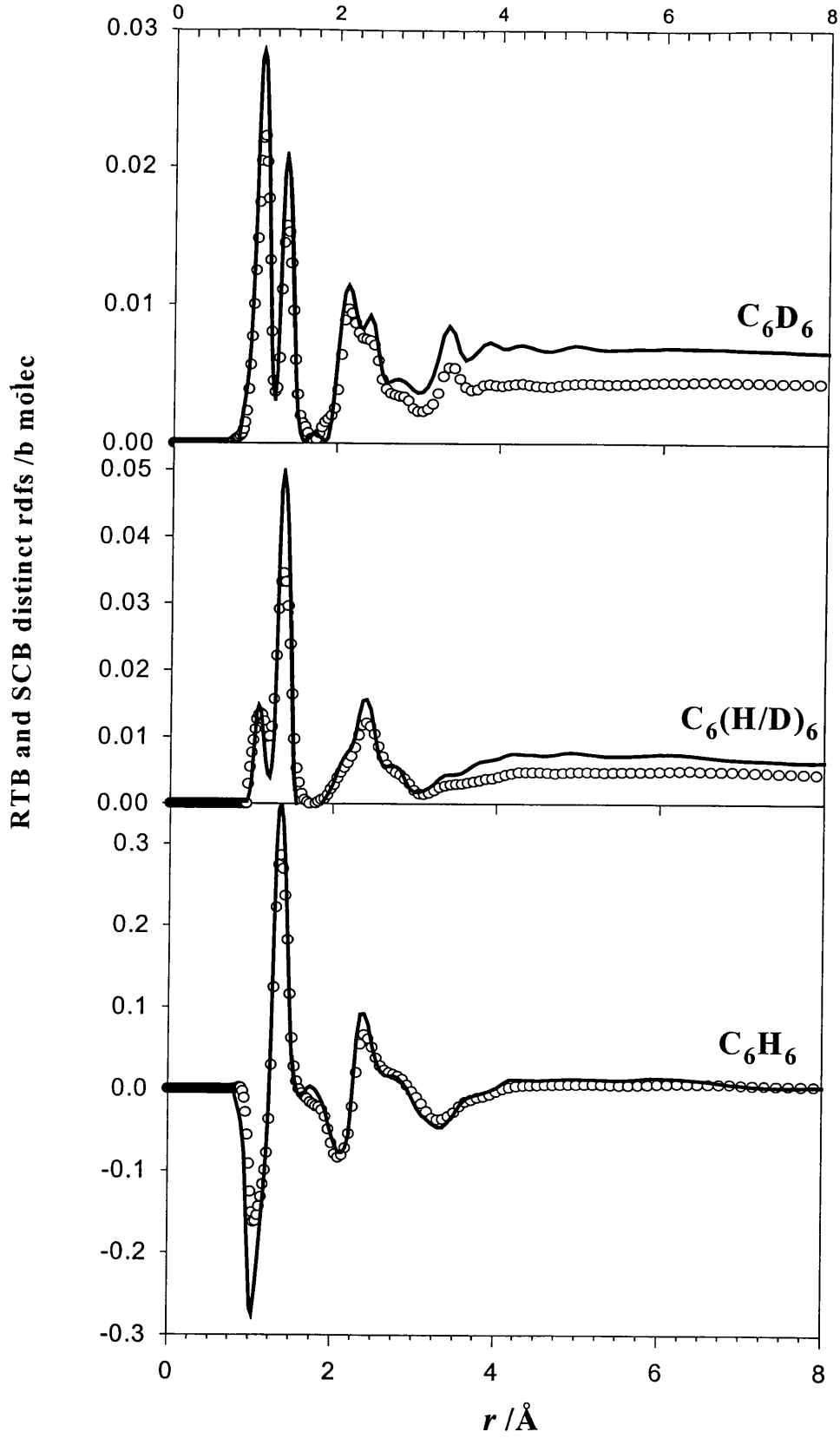

Figure A.8. The distinct rdfs for the three SCB samples (symbols) compared to those for the RTB samples (lines). These functions are all presented on an absolute scale (each rdf was multiplied by its corresponding molecular number density).

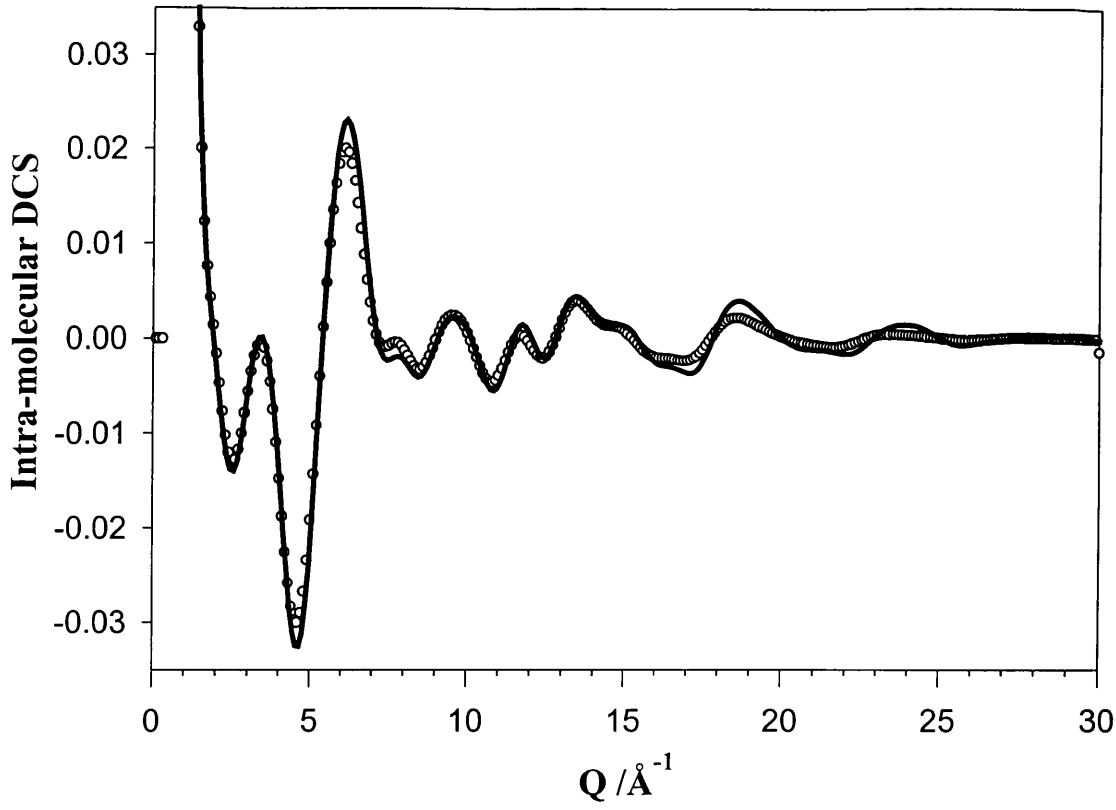

Figure A.9. The intra-molecular DCS of SCB obtained by fitting equation 4.40 to the distinct DCS of super critical C_6D_6 in the high-Q range (6-30 Å^{-1}) compared with its room temperature equivalent.

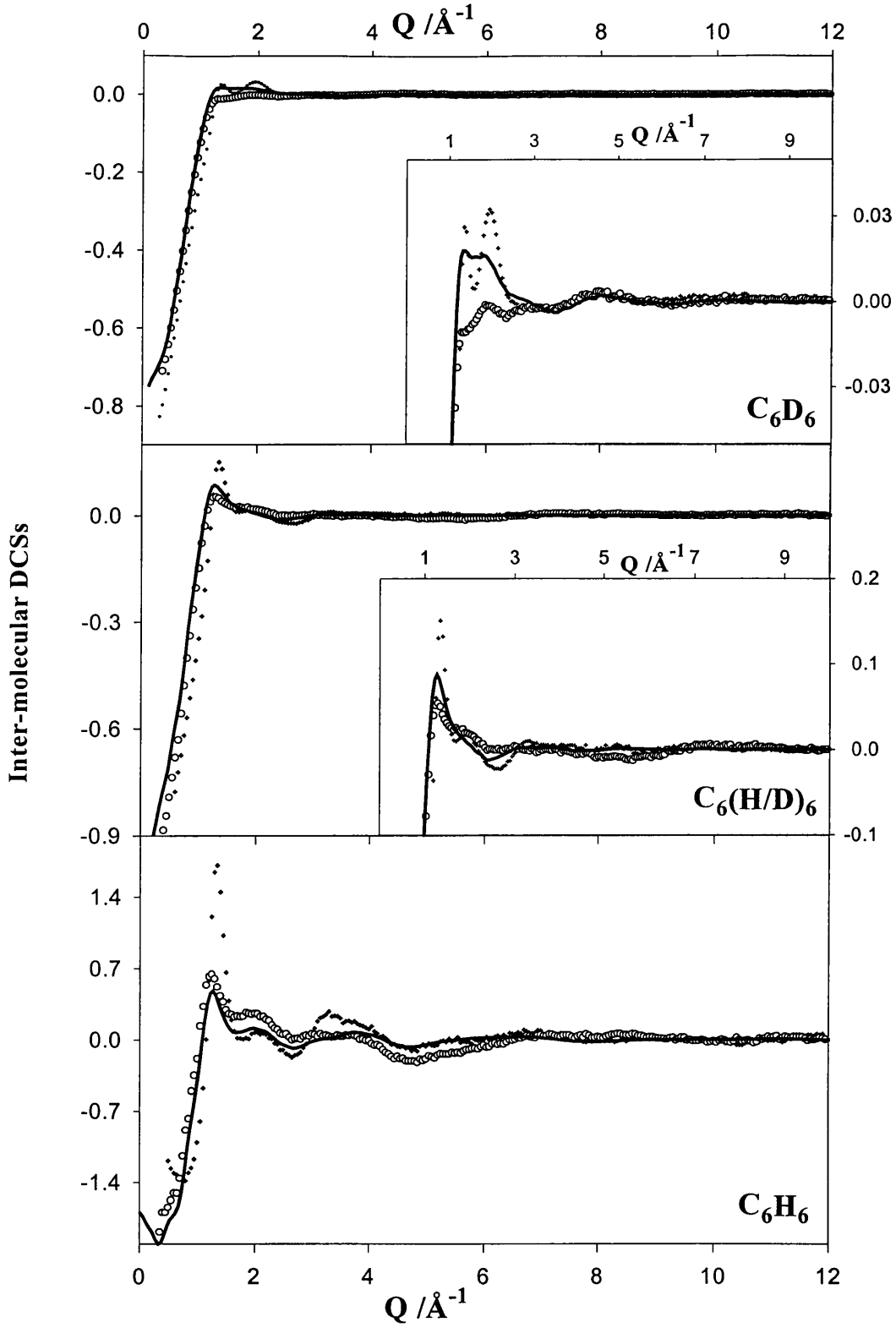

Figure A.10. The three inter-molecular DCSs of SCB (circles) along with the back Fourier transforms (lines) of the corresponding rdfs shown in figure A.11. These experimental functions are also compared with their RT equivalents (+). Insets show the same functions on an enlarged scale

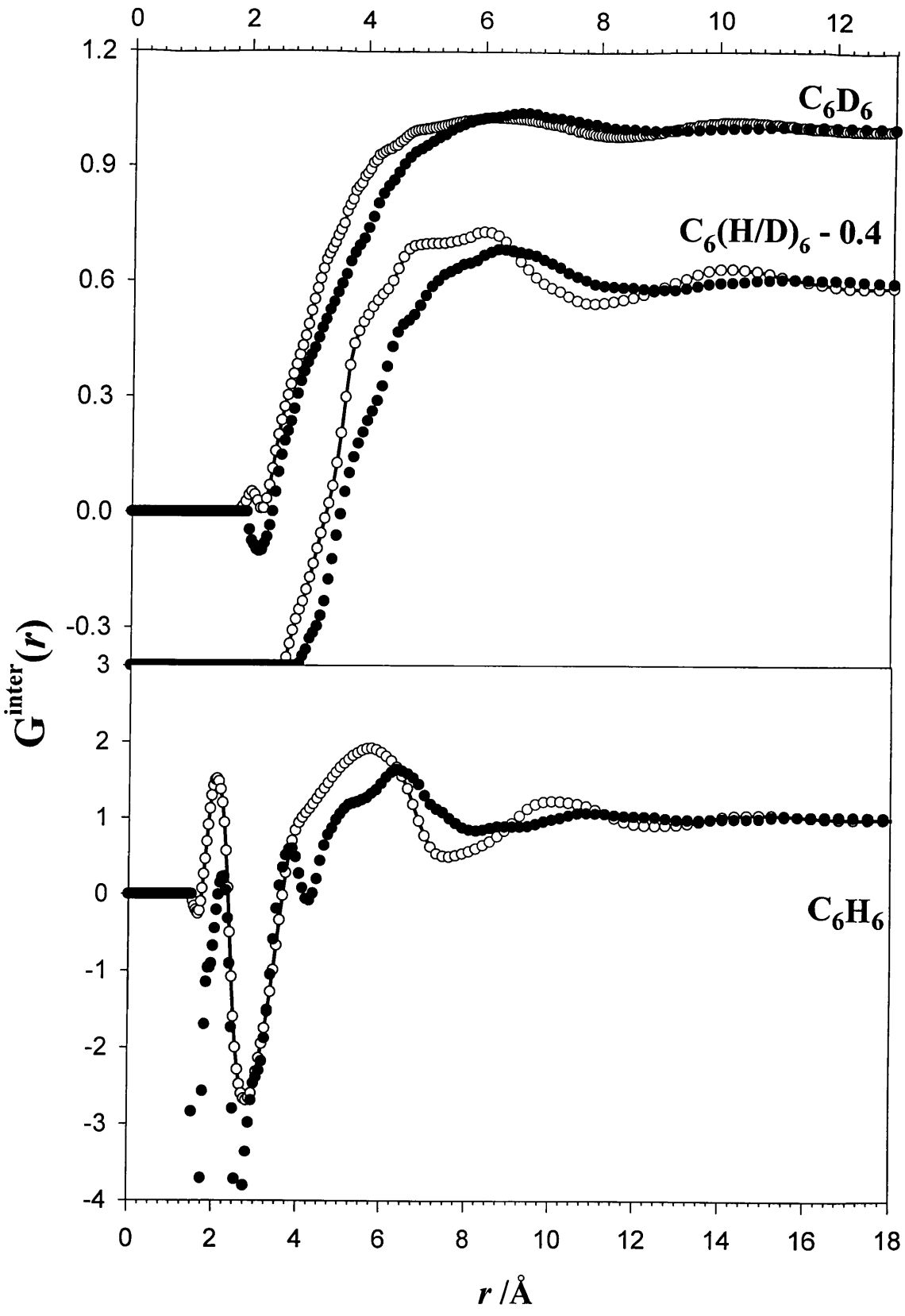

Figure A.11. The C_6H_6, $C_6(H/D)_6$ and C_6D_6 inter-molecular rdfs obtained for SCB by Fourier transformation of the SCB DCS functions shown in figure A.10 (black circles). These functions are compared with their RTB counterparts (white circles).

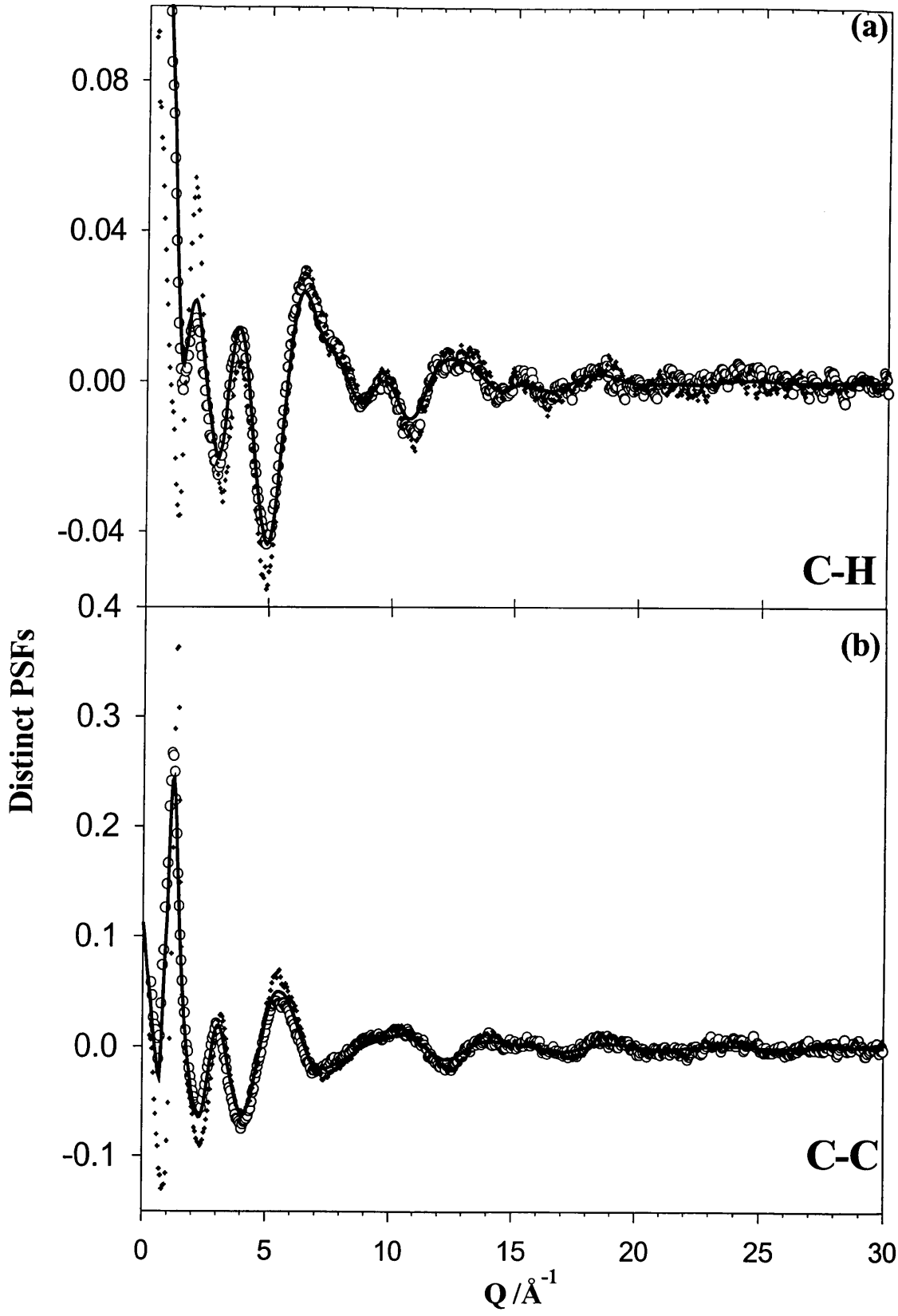

Figure A.12. The C-H and C-C distinct partial structure factors for SCB (white circles) along with the back Fourier transforms of the corresponding distinct pdfs (lines) presented in figure A.13. The similar experimental RTB functions (+) are also presented for comparison.

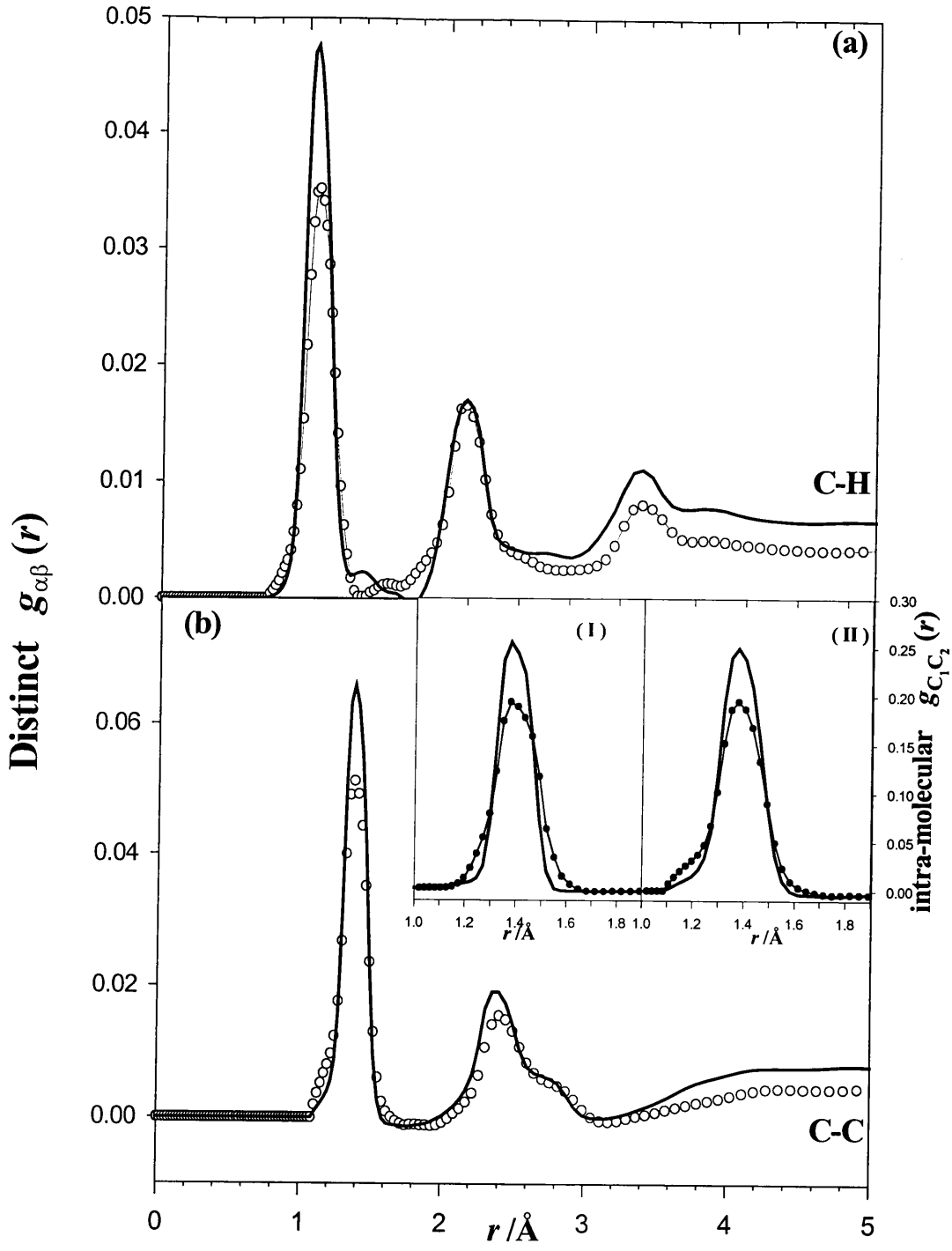

Figure A.13. (a) The C-H distinct pdfs for SCB (white circles) and RTB (lines). (b) The C-C distinct pdfs for SCB (white circles) and RTB (lines). These functions are all presented on an absolute scale (each rdf was multiplied by its corresponding molecular number density). Insets show the C_1-C_2 intra-molecular contributions in SCB (circles) and RTB (lines) calculated from equation 4.40 using the bond lengths and Debye-waller factors given in table A.4 (I), as compared to the experimental ones (II).

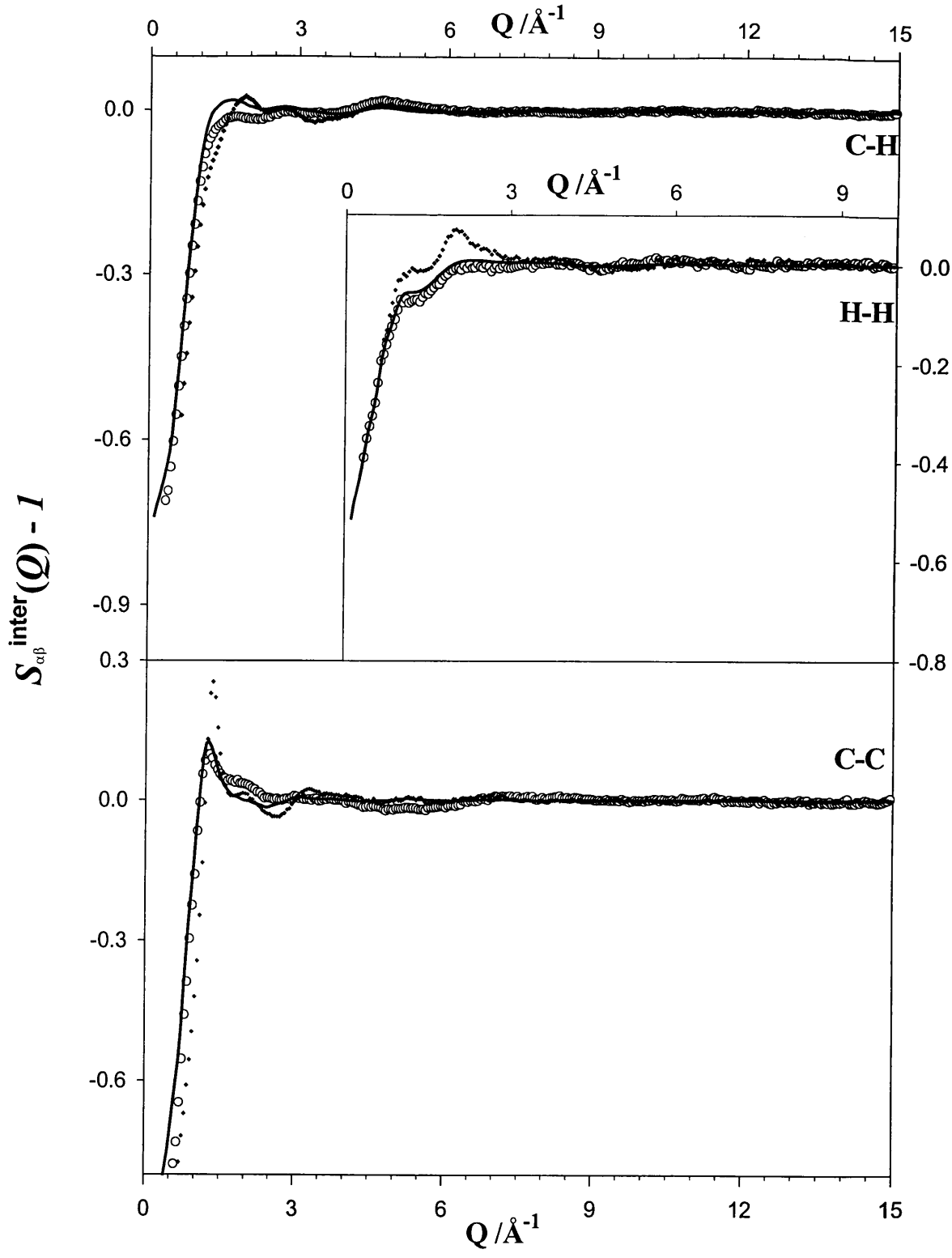

Figure A.14. The C-C, C-H and H-H inter-molecular PSFs for SCB (circles) obtained from the second- and higher- order differences, after removing the intra-molecular structure from the three distinct DCSs presented in figure A.7. The back Fourier transforms (lines) of the pdfs presented in figure A.15 are superimposed on the original data from which they were obtained. These SCB functions obtained are compared with their room temperature counterparts (+).

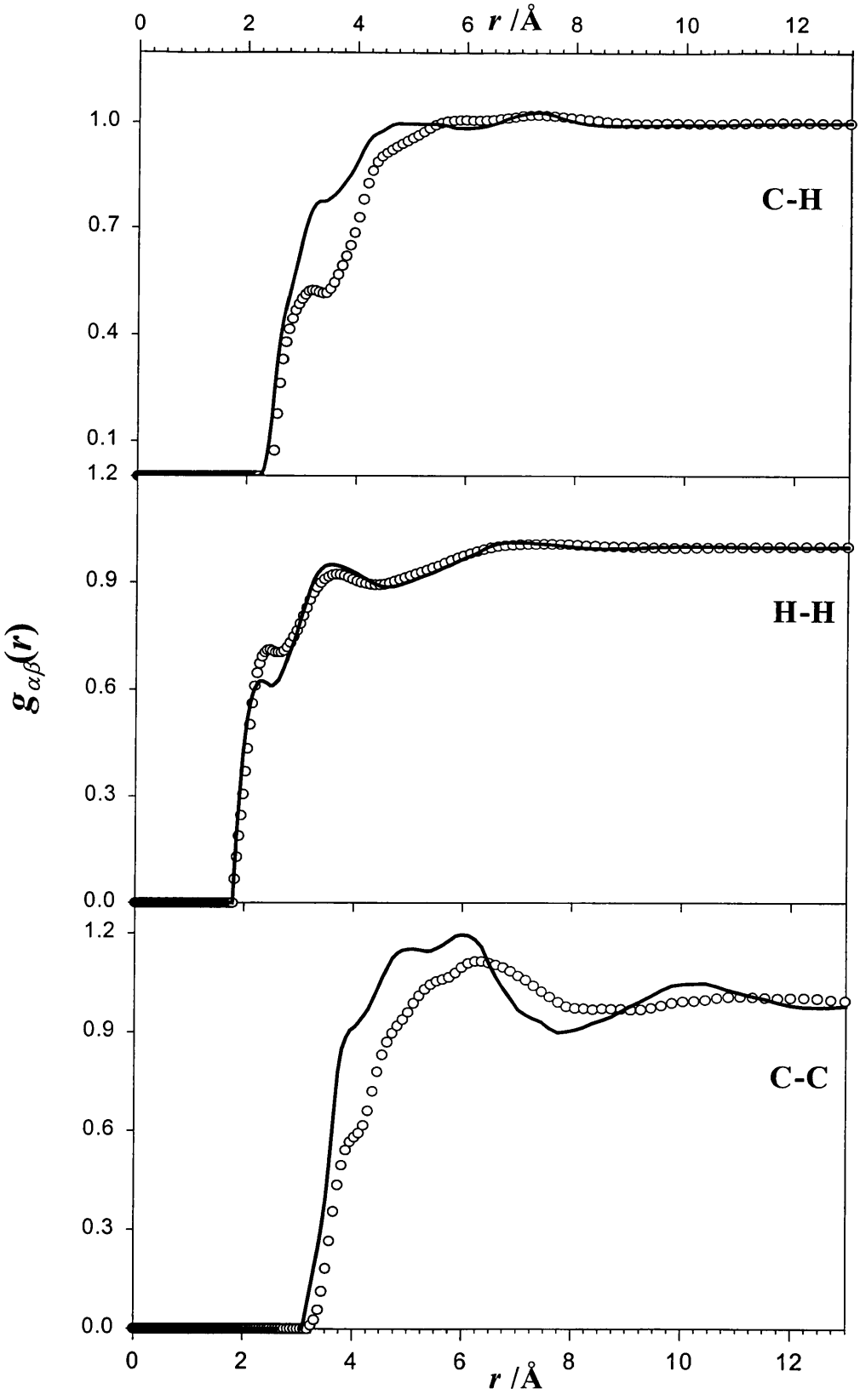

Figure A.15. The C-C, C-H and H-H inter-molecular pdfs of SCB (circles) obtained after Fourier transformation of the corresponding PSFs shown in figure A.14 compared to their room temperature equivalent functions (lines).

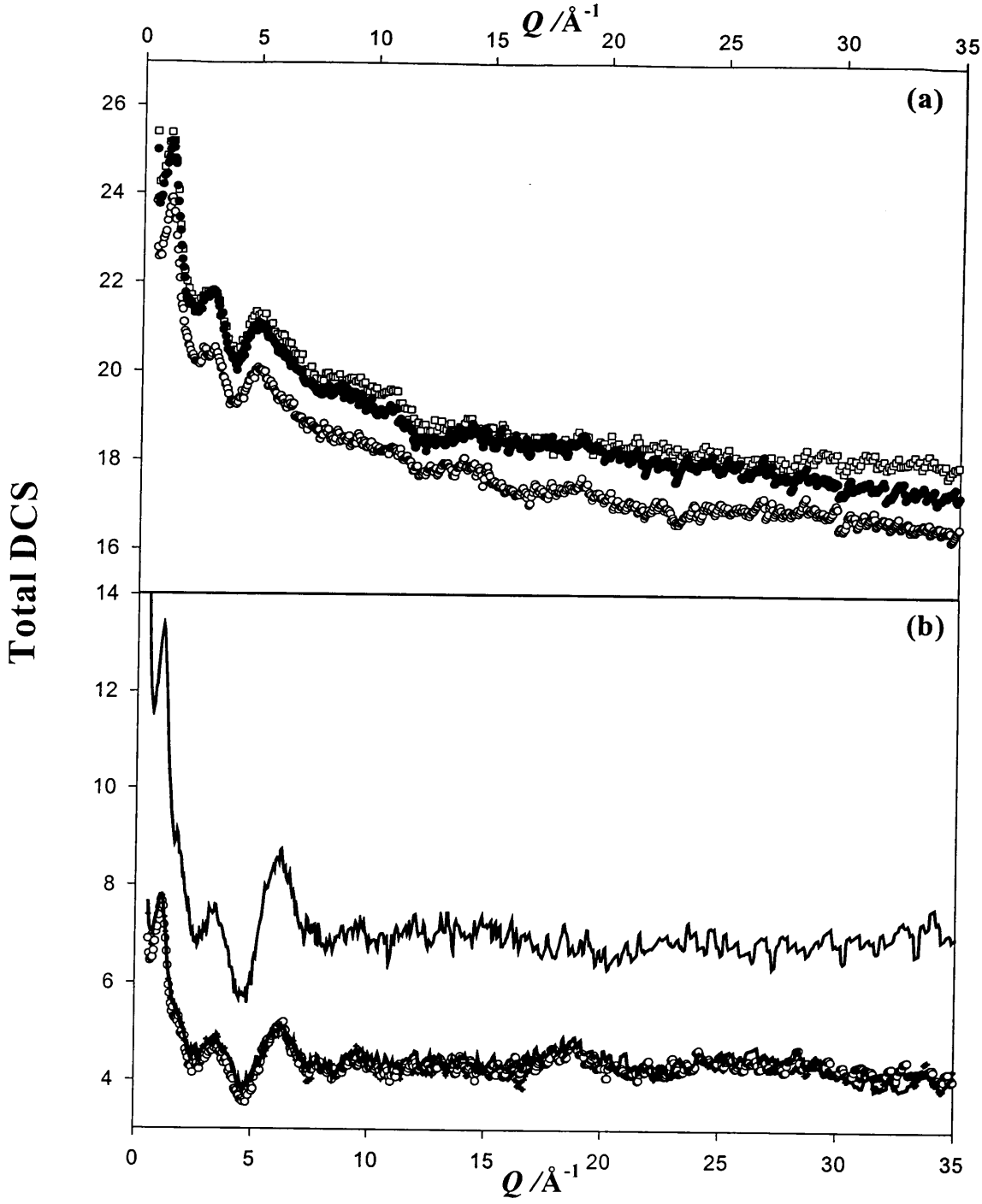

Figure A.16. (a) The total DCSs obtained for C_6H_6 +D_2O (squares), C_6H_6 +H_2O (white circles) and C_6H_6 + $(H/D)_2O$ (black circles) corresponding to the first group of detectors. (b) The total DCSs obtained for C_6D_6 +D_2O (line), C_6D_6 +H_2O (+) and C_6D_6 + $(H/D)_2O$ (white circles) corresponding to the first group of detectors.

References

Adachi, Y. and Nakanishi, K. (1991). *Mol. Simul.* **6**, 299

Adachi, Y. and Nakanishi, K. (1993). *Fluid Phase Equil.* **83**, 69

Adam, F. S., Banon, A. and Santamaria, (1984). *J. Chem. Phys.* **86**, 433

Adya, A. K. and Wormald, C. J. (1992). *Mol. Phys.* **77**, 1217

Adya, A. K. and Wormald, C. J. (1993). *Mol. Phys.* **78**, 1075

Adya, A. K., Takagi, R. and Gaune-Escard, M. (1998). *Z. Naturforsh.* **53a**, 1037

Adya, A.K., Bianchi, L. and Wormald, C.J. (2000). *J. Chem. Phys.* **112**, 4231

Alder, B. J. and Wainwright, T. E. (1959). *J. Chem. Phys.* **39**, 459

Allen, M. P. and Tildesley, D. J. (1987). *Computer simulation of liquids*. Clarendon Press, Oxford,

Alonso, J., Bermejo, F. J., Garcia-Hernandez, M., Martinez, J. L. and Howells, W.S. (1991). *J. Molec. Struc.* **218**, 147

American Petroleum Institute, Research Project 44 (1953). *Selected values of physical and thermodynamic properties of hydrocarbons and related compounds*. Carnegie Press: Pittsburgh, PA,

Anderson, J., Ullo, J.J. and Yip, S. (1987). *J. Chem. Phys.* **86**, 4078

Andrew, E. R. and Eades, R. G. (1953). *Proc. Roy. Soc.* **A218**, 537

Anwander, E. H. S., Probst, M. M. and Rode, B. M. (1992). *Chem. Phys.* **166**, 341

Arunan, E. and Gutowsky, H. S. (1993). *J. Chem. Phys.* **98**, 4294

Augspurger, J. D., Dykstra, C. E. and Zweir, T. S. (1992). *J. Phys. Chem.* **96**, 7252

Augspurger, J. D., Dykstra, C. E. and Zweir, T. S. (1993). *J. Phys. Chem.* **97**, 980

Bacon, G. E., Curry, N. A. and Wilson, S. A. (1964). *Proc. Roy. Soc.* **A279**, 98

Barker, J. A. and Henderson, D. (1976). *Rev. Mod. Phys.* **48**, 587

Bartsch, E., Bertagnolli, H., Schulz, G. and Chieux, P. (1985). *Ber. Bunsenges. Phys. Chem.* **89**, 147

Bartsch, E., Bertagnolli, H. and Chieux, P. (1986). *Ber. Bunsenges. Phys. Chem.* **90**, 34

Bartsch, E. and Bertagnolli, H. (1987). *Ber. Bunsenges. Chem.* **91**, 745

Bastiansen, O. (1957). *Acta Cryst.* **10**, 861

Bastiansen, O. and Cyvin, S. J. (1957). *Nature* **180**, 980

Batchelor, G. K. (1954). *Quart. J. R. met. Soc.* **80**, 339

Benmore, C. J. and Soper, A. K. (1998). *Tech. Rep. R.A.L.-Tr-98-006*, Jan. 98, p16

Berendsen, H. J. C. and Van Gunsteren, W. F. (1986). *Molecular dynamics simulations of statistical mechanical systems,* Proceedings of the Enrico Fermi Summer school. Varenna, 1985, Soc. Italiana di Fisica, Bologna, p 43-65

Berkovitch-Yellin, Z. and Leiserowitz, L. (1984). *Acta Crystallogr.* **B40**, 159

Bianchi, L., Adya, A. K., Kalugin, O. N. and Wormald, C. J. (1999). *J. Phys.: Condens. Matter* **11**, 9151

Bianchi, L., Kalugin, O.N., Adya, A. K. and Wormald, C. J. (2000). *Molec. Simul.* **25** (in press)

Binder, K. editor, (1984). *Monte-Carlo methods in statistical physics*, 2nd ed., Springer-Verlag, Berlin

Blum L. and Narten, A. H. (1976a). *J. Chem. Phys.* **64**, 2804

Blum, L. and Narten, A. H. (1976b). *Adv. Chem. Phys.* **34**, 203

Born, M. and Von Karman, Th. (1912). *Z. Phys.* **13**, 297

Bredas, J. L. and Street, G. B. (1989). *J. Phys. Chem.* **90**, 7291

Buck, U., Siebers, J. and Wheatley, R. J. (1998). *J. Chem. Phys.* **108**, 20

Cabaço, M. I., Danten, Y., Besnard, M., Guissani, Y. and Guillot, B. (1996). *Chem. Phys. Let.* **262**, 120

Cabaço, M.I., Danten, Y., Besnard, M., Guissani, Y. and Guillot, B. (1997). *J. Phys Chem. B* **101**, 6977

Cabaço, M.I., Danten, Y., Besnard, M., Guissani, Y. and Guillot, B. (1998). *J. Phys Chem. B* **102**, 10712

Cabana, A., Bachand, J. and Giguere, J. (1974). *Can. J. Phys.* **52**, 1949

Caldwell, J. W. and Kollman, P. A. (1995). *J. Phys. Chem.* **99**, 6208

Car, R. and Parrinello, M. (1985). *Phys. Rev. Lett.* **55**, 2471

Chamberlain, O. (1950). *Phys. Rev.* **77**, 305

Chandler, D. and Andersen, H. C. (1972). *J. Chem. Phys.* **57**, 1930

Chao, I. and Chen, J-C. (1996). *Angew. Chem.* **108**, 200

Cheney, B. V. and Schultz, M. W. (1990). *J. Phys. Chem.* **94**, 6268

Cheng, B-M., Grover, J. R. and Walters, E. A. (1995). *Chem. Phys. Lett.* **232**, 364

Ciccotti, G., Ferrario, M. and Ryckaert, J. P. (1982). *Mol. Phys.* **47**, 1253

Ciccotti, G., Frenkel, D. and McDonald, I. R. editors, (1987). *Simulation of liquids and solids*, North Holland, Amsterdam.

Claessens, M., Ferrario, M. and Ryckaert, J-P. (1983). *Mol. Phys.* **50**, 217

Clarke, J. H. R. (1997). *molecular dynamics simulation for molecules*, CCP5 Spring School "methods in molecular simulation", Bristol, 7-11 April 97

Cohen-Tannoudji, C., Diu, B. and Laloë, F. (1977). *Mecanique quantique*, vol. 2, Hermann, Paris,

Connolly, J. F. (1966). *J. Chem. Engg. Data* **11**, 13

Cox, E. G., Cruickshank, D. W. J. and Smith, J. A. S. (1958). *Proc. Roy. Soc.* **A247**, 1

Cyvin, S. J. (1968). *Molecular vibrational and mean square amplitudes*. Amterdam: Elsevier, p 245

David, W. I. F., Ibberson, R. M., Jeffrey, G. A. and Ruble, J. R. (1992). *Physica B* **180 & 181**, 597

Debye, P. and Scherrer, P. (1916). *Z. Phys.* **17**, 277

DeGennes, P.G. (1959). *Physica*, **25**, 825

De Leeuw, S. W., Perram, J. W. and Smith, E. R. (1980). *Proc. R. Soc. Lond.* **A373**, 27

Deul, R. and Franck, E. U. (1991). *Ber. Bunsenges. Phys. Chem.* **95**, 847

Deul, R., Rosenzweig, S. and Franck, E. U. (1991). *Ber. Bunsenges. Phys. Chem.* **95**, 515

Dougherty, D. A. and Stauffer, D. A. (1990). Science **250**, 1558

Edwards, F. G., Enderby, J. E., Howe, R. A. and Page, D. I. (1975). *J. Phys. C: Solid state phys.* **8**, 3483

Egelstaff, P. A. and Soper, A. K. (1980a). *Mol. Phys.* **40**, 553

Egelstaff, P. A. and Soper, A. K. (1980b). *Mol. Phys.* **40**, 569

Enderby, J. E. and Barnes, A. C. (1990). *Rep. Prog. Phys.* **53**, 85

Enderby, J. E. and Neilson, G. W. (1981). *Rep. Prog. Phys.* **44**, 593

Engdahl, A. and Nelander, B. (1985). *J. Chem. Phys.* **89**, 2860

Engdahl, A. and Nelander, B. (1987). *J. Chem. Phys.* **91**, 2253

Evans, D. J. and Watts, R. O. (1975). *Mol. Phys.* **29**, 777

Evans, D.J. (1977). *Mol. Phys.* **34**, 317

Evans, D. J. and Watts, R. O. (1976a). *Mol. Phys.* **31**, 83

Evans, D. J. and Watts, R. O. (1976b). *Mol. Phys.* **32**, 93

Falcone, D. R., Douglass, D. C. and McCall, D. W. (1967). *J. Phys. Chem.* **71**, 2754

Falk, M. and Whalley, E. (1961). *J. Chem. Phys.* **34**, 1554

Felici, R., Cilloco, F. and Bosi, P. (1990). *Mol. Phys.* **70**, 455

Fermi, E. and Zinn, W. H. (1946). *Phys. Rev.* **70**, 103

Fincham, D. (1992). *Molec. Simul.* **8**, 165

Fois, E. S., Sprik, M. and Parrinello, M. (1994). *Chem. Phys. Lett.* **223**, 411

Fredericks, S. Y., Jordan, K. D. and Zweir, T. S. (1996). *J. Phys. Chem.* **100**, 7810

Frenkel, D. and Smit, B. (1996). *Understanding molecular simulation: from algorithms to applications*, Academic Press, San Diego

Furic, K., Mohacek, V. and Mamic, M. (1993). *Spectrochim. Acta* **A49**, 2081

Gao, J., Habibollazadeh, D. and Shao, L. (1995). *J. Phys. Chem.* **99**, 10400

Garrett, A. W. and Zwier, T. Z. (1992). *J. Chem. Phys.* **96**, 7259

Gear, C. W. (1966). *The numerical integration of ordinary differential equations of various orders*. Report ANL 7126, Argonne National laboratory,

Gear, C. W. (1971) *Numerical initial value problems in ordinary differential equations*. Prentice-Hall, Englewood Cliffs, NJ.

Goates, J. R., Snow, R. L. and James, M. R. (1961). *J. Chem. Phys.* **65**, 335

Goldstein, H. (1980). *Classical mechanics*, 2nd edn. Addison-Wesley, Reading, MA.

Gotch, A. J. and Zwier, T. S. (1992). *J. Chem. Phys.* **96**, 3388

Gregory, J. K. and Clary, D. C. (1996). *Mol. Phys.* **88**, 33

Gupta, S., Sediawan, W. B. and Mc Laughlin, E. (1988). *Mol. Phys.* **65**, 961

Gutowsky, H. S., Emilsson, T. and Arunan, E. (1993). *J. Chem. Phys.* **99**, 4883

Hagemeister, F. C., Gruenloh, C. J. and Zwier, T. S. (1998). *J. Phys. Chem. A* **102**, 82

Haile, J. M. (1992). *molecular dynamics simulation: elementary methods*. Wiley & Sons, Inc.,

Hannon, A. C. (1999). *Encyclopedia of Spectroscopy and Spectrometry*. Lindon, J., Tranter, G. and Holmes, J. editors. Academic Press, London,

Hansen, J-P. and McDonald, I. R. (1986) *Theory of simple liquids*, Academic Press, London

Harvey, G. C. (1938). *J. Chem. Phys.* **6,** 158

Haughney, M., Ferrario, M. and Mc Donald, I. R. (1986). *Mol. Phys.* **86**, 849

Haughney, M., Ferrario, M. and Mc Donald, I. R. (1987). *J. Phys. Chem.* **91**, 4934

Hawlicka, E., Palinkas, G. and Heinzinger, K. (1989). *Chem. Phys. Lett.* **144**, 255

Hockney, R. W. (1970). *Methods Comput. Phys.* **9**, 136

Hockney, R. W. and Eastwood, J. W. (1981). *Computer simulations using particles*, McGraw-Hill, New York,

Hurle, R.L. and Woolf, L.A. (1980). *Aust. J. Chem.* **33**, 1947

Ivash, E. V. and Dennison, D. M. (1953). *J. Chem. Phys.* **21**, 1804

Jaffe, R. L. and Smith, G. D. (1996). *J. Chem. Phys.* **105**, 2781

Jeffrey, G. A., Ruble, J. R., McMullan, R. K. and Pople, J. A. (1987). *Proc. Roy. Soc. Lond.* **A414**, 47

Jeffrey, G. A. and Saenger, W. (1991). *Hydrogen Bonding in Biological Structures*, Springer, Berlin,

Johnson, E. and Hazoume, R. P. (1979). *J. Chem. Phys.* **70**, 1599

Jorgensen, W. L. (1979). *J. Chem. Phys.* **71**, 5034

Jorgensen, W. L. (1980). *J. Am. Chem. Soc.* **102**, 543

Jorgensen, W. L. (1981). *J. Am. Chem. Soc.* **103**, 341

Jorgensen, W. L. (1986). *J. Phys. Chem.* **90**, 1273

Jorgensen, W. L., Madura, J. D. and Swenson, C. J. (1984). *J. Am. Chem. Soc.* **106**, 6638

Jorgensen, W. L. and Tirado-Rives, J. (1988). *J. Am. Chem. Soc.* **110**, 1657

Jorgensen, W. L. and Briggs, J. M. (1989). *J. Am. Chem. Soc.* **111**, 4190

Jorgensen, W. L., Briggs, J. M. and Contreras, M. L. (1990). *J. Phys. Chem.* **94**, 1683

Jorgensen, W. L. and Severance, D. L. (1990). *J. Am. Chem. Soc.* **112**, 4768

Jorgensen, W. L., Maxwell, D. S. and Tirado-Rives, J. (1996). *J. Am. Chem. Soc.***118**, 11225

Kalos, M. H. and Whitlock, P. A. (1986). *Monte-Carlo method*, Vol. 1: Basic, Wiley, New York

Karlstrom, G., Linse, P., Wallqvist, A. and Jonsson, B. (1983). *J. Am. Chem. Soc.* **105**, 3777

Katzoff, S. (1934). *J. Chem. Phys.* **2**, 841

Kim, K. S., Lee, J. Y., Lee, S. J., Ha, T-K. and Kim, D. H. (1994). *J. Am. Chem. Soc.* **116**, 7399

Kimura, K. and Kubo, M. (1959). *J. Chem. Phys.* **30**, 151

Klemperer, W. (1993). *Nature* **362**, 698

Kohn, W. and Sham, L. J. (1965). *Phys Rev.* **A140**, 1133

Laaksonen, A., Wang, J. and Boyd, R. J. (1995). *Chem. Phys. Let.* **241**, 380

Laaksonen, A., Stilbs, P. and Wasylishen, R. E. (1998). *J. Chem. Phys.* **108**, 455

Laasonen, K., Sprik, M., Parrinello, M. and Car, R. (1993). *J. Chem. Phys.* **99**, 9080

Langseth, A. and Stoicheff, B. P. (1956). *Can. J. Phys.* **34**, 350

Lee, J. Y., Lee, S. J., Choi, H. S., Cho, S. J., Kim, K. S. and Ha, T-K. (1995). *Chem. Phys. Lett.* **232**, 67

Lees, R. M. and Baker, J. G. (1968). *J. Chem. Phys.* **48**, 5299

Le Fevre, R. J. W. (1953). *Dipole moments: their measurement and application in chemistry*. John Wiley: N.Y.

Letcher, T. M., Koteswari Prasad, A. and Mercer-Chalmers, J. (1991). *S. Afr. J. Chem.* **44**, 17

Lide, D. R. editor (1995). *Handbook of Chemistry & Physics*. CRC Press: Boca Raton, Fl

Linse, P. (1984). *J. Am. Chem. Soc.* **106**, 5425

Linse, P. (1989). *J. Comput. Chem.* **9**, 505

Lovesey, S. W. (1986). *Theory of neutron scattering from condensed matter*. Vol.1, International series of monographs on physics 72, Oxford science publications

Lowden, L. and Chandler, D. (1974). *J. Chem. Phys.* **61**, 5228

Magini, M., Paschina, G. and Paccaluga, G. (1982). *J. Chem. Phys.* **77**, 2051

Maitland, G. C., Rigby, M., Smith, E. B. and Wakeham, W. A. (1981). *Intermolecular forces*. Clarendon Press, Oxford,

Marchi, M. and Klein, M. (1989). *Z. Naturforsh.* **44a**, 585

Matsumoto, T. (1982). *A.I.P. Conf. Proc.* **82**, 90

McClellan, A. L. (1989). *Tables of experimental dipole moments*. Rahara Enterprise: El Cerrito, CA,

McCool, M. A., Collings, A. F. and Woolf, L. A. (1972). *J. Chem. Soc. Far. Trans.* **68**, 1489

Meeron, E. (1960). *J. Math. Phys.* **1**, 192

Mildner, D. F. R. and Carpenter J. M. (1977). *Acta Crytallogr.* **A33**, 962

Misawa, M. and Fukunaga, F. (1990). *J. Chem. Phys.* **93**, 3495

Muller, G., Lutz, M. and Harder, S. (1996). *Acta Crystallogr.* **B52**, 1014

Montague, D. G., Gibson, I. P. and Dore, J. C. (1981). *Mol. Phys.* **44**, 1355

Montague, D. G., Dore, J. C. and Cummings, S. (1984). *Mol. Phys.* **53**, 1049

Montague, D. G. and Dore, J. C. (1986). *Mol. Phys.* **57**, 1035

Munk, P., Qin, A. and Hoffman, D. E. (1993). *Collect. Czech. Chem. Commun.* **58**, 2612

Narten, A. H. (1967). *J. Chem. Phys.* **48**, 1630

Narten, A. H. (1977). *J. Chem. Phys.* **67**, 2102

Narten, A. H. and Habenschuss, A. (1984). *J. Chem. Phys.* **80**, 3387

Neumann, M. (1985). *J. Chem. Phys.* **82**, 5663

Neilson, G.W. and Adya A.K. (1997). *Annual Reports Roy. Soc. Chem. Section C*, **93**, 101

Nishikawa, T. (1956). *J. Phys. Soc. Japan* **11**, 781

Numerical Algorithm Group (1995a). *NAG Fortran Library manual: Work 17*, Vol. 4: E04JAF, NAG Ltd.

Numerical Algorithm Group (1995b). *NAG Fortran Library manual: Work 17*, Vol. 4: E04CCF, NAG Ltd.

Paalman, H. H. and Pings, C. J. (1962). *J. Appl. Phys.* **33**, 2635

Palinkas, G., Hawlicka, E. and Heinzinger, K. (1987). *J. Phys. Chem.* **91**, 4334

Palinkas, G., Baco, I. and Heinzinger, K. (1991). *Mol. Phys.* **73**, 897

Percus, J. K. and Yevick, G. J. (1958). *Phys. Rev.* **110**, 1

Pettit, B. M. and Rossky, P. J. (1983). *J. Chem. Phys.* **78**, 1599

Pierce, W.C. (1937). *J. Chem. Phys.* **5**, 717

Placzek, G. (1952). *Phys. Rev.* **86**, 377

Postorino, P., Tromp, R. H., Ricci, M. A., Soper, A. K. and Nielson, G. W. (1993). *Nature* **366**, 668

Postorino, P., Ricci, M. A. and Soper, A. K. (1994). *J. Chem. Phys.* **101**, 4123

Powles, J. G. (1973a). *Adv. Phys.* **22**, 1

Powles, J. G. (1973b). *Mol. Phys.* **26**, 1325

Powles, J. G. and Rickayzen, G. (1976). *Mol. Phys.* **32**, 323

Powles, J. G. (1978a). *Mol. Phys.* **36**, 1161

Powles, J. G. (1978b). *Mol. Phys.* **36**, 1181

Powles, J. G. (1979). *Mol. Phys.* **37**, 623

Pribble, R. N. and Zwier, T. S. (1994). *Science* **265**, 75

Pribble, R. N., Garrett, A. W., Haber, K. and Zwier, T. S. (1995). *J. Chem. Phys.* **103**, 531

Pribble, R. N., Hagemeister, F.C. and Zwier, T. S. (1997). *J. Chem. Phys.* **106**, 2145

Pusztai, L. and McGreevy, R. L. (1998). *J. Phys. : Condens. Matter* **10**, 525

Rahman, A., Singwi, K. S. and Sjölander, A. (1962) *Phys. Rev.* **126**, 986

Rebert, C. J. and Kay, W. B. (1959). *AIChE. J.* **11**, 285

Rickayzen, G. and Powles, J. G. (1976). *Mol. Phys.* **32**, 301

Riddick, J. A., Bunger W. B. and Sakano T. K. (1986). *Organic solvents, physical properties and methods of purification*. 4th edition, Wiley, N.Y.

Robyr, P., Meier, B. H., Fischer, P. and Ernst, R. R. (1994). *J. Am. Chem. Soc.* **116**, 5315

Rosenhead L., editor (1963). *Laminar Boundary layers*. Fluid motion memoirs, Clarendon press, Oxford

Rodham, D. A., Suzuki, S., Suenram, R. D., Lovas, F. J., Dasgupta, S., Goddard III, W. A. and Blake, G. A. (1993). *Nature* **362**, 735

Ryckaert, J. P., Ciccotti, G. and Berendsen, H. J. C. (1977). *J. Comput. Phys.* **23**, 237

Ryckaert, J. P. (1985). *Mol. Phys.* **55**, 549

Satanoka, H., Abe, K. and Hirota, M. (1988). *Bull. Chem. Soc. Jpn.* **61**, 2031

Schmidt, M. W., Baldridge, K. K., Boatz, J. A., Elbert, S. T., Gordon, M. S., Jensen, J. H., Koseki, S., Matsunaga, N., Nguyen, K. A., Su, S. J., Windus, T. L., Dupuis, M. and Montgomery, J. A. (1993). *J. Comput. Chem.* **14**, 1347

Sears, V. (1975). *Adv. Phys.* **24**, 1

Sears, V. (1989). *Neutron optics, an introduction to the theory of neutron optical phenomena and their applications*, Oxford University Press

Sears, V. (1992). *Neutron news* **3**, 29

Seiler, P. and Dunitz, J. D. (1989). *Helv. Chim. Acta* **72**, 1125

Serrallach, A., Meyer, R. and Gunthard, H. H. (1974). *J. Molec. Spectros.* **52**, 94

Shilov, I. Y., Rode, B. M. and Durov, V. A. (1999). *Chem. Phys.*, **241**, 75

Shimanouchi, T. (1972). *Tables of molecular vibrational frequencies*, NSRDS-NBS 39 (U.S. Dpt. of Commerce, Washington D. C.), Vol. 1

Smith, W. and Forester, T. R. (1996). *J. Mol. Graphics* **14**, 137

Smith, G. D. and Jaffe, R. L. (1996). *J. Chem. Phys.* **100**, 9624

Soper, A. K. and Egelstaff, P. A. (1980). *Nucl. Inst. Meth.* **178**, 415

Soper, A. K. (1986). *Chem. Phys.* **107**, 61

Soper, A. K., Howells, W. S. and Hannon, A. C. (1989). ATLAS-*Analysis of Time-of-Flight Diffraction Data from Liquid and Amorphous Samples*, R.A.L report No -89-046,

Soper, A. K. (1990). *Neutron Scattering Data Analyses* (Instr. phys. conf. ser. 107), Johnson M. W. editor (Bristol IOP), p. 57

Soper, A. K. and Luzar, A. (1992). *J. Chem. Phys.* **97**, 1320

Soper, A. K., Andreani, C. and Nardone, M. (1993). *Phys. Rev.* **E47**, 2598

Soper, A. K., Bruni, F. and Ricci, M. A. (1997). *J. Chem. Phys.* **106**, 247

Spirko, V., Engkvist, O., Soldan, P., Selzle, H. L., Schlag, W. and Hobza, P. (1999). *J. Chem. Phys.* **111**, 572

Sprik, M., Hutter, J. and Parrinello, M. (1996). *J. Chem. Phys.* **105**, 1142

Squires, G.L. (1978). *Introduction to the theory of thermal neutron scattering*, Cambridge University Press

Steinhauser, O. (1982). *Chem. Phys.* **73**, 155

Steytler, D. C., Dore, J. C. and Montague, D. C. (1985). *J. Non-Cryst. Solids* **74**, 303

Stuart, A. V. and Sutherland, G. B. B. M. (1956). *J. Chem. Phys.* **24**, 559

Sun, H. (1998). *J. Phys. Chem. B* **102**, 7338

Suzuki, S., Green, P. G., Bumgarner, R. E., Dasgupta, S., Goddard III, W. A. and Blake, G. A. (1992). *Science* **257**, 942

Svishchev, I. M. and Kusalik, P. G. (1994). *J. Chem. Phys.* **100**, 5165

Swallen, J. D. (1955). *J. Chem. Phys.* **23**, 1739

Tanaka, Y., Ohtomo, N. and Arakawa, K. (1985). *Bull. Chem. Soc. Jpn.* **58**, 270

Tauer, K. J. and Lipscomb, W. (1952). *Acta Crystall.* **5**, 606

Tromp, R.H., Postorino, P., Nielson, G. W., Ricci, M.A. and Soper, A.K. (1994). *J. Chem. Phys.* **101**, 6210

Van Gunsteren, W. F. and Berendsen, H. J. C. (1977). *Mol. Phys.* **34**, 1311

Van Gunsteren, W. F. and Mark, A. E. (1998). *J. Chem. Phys.* **108**, 6110

Van Hove, L. (1954). *Phys. Rev.* **95**, 249

Venkateswarlu, P. and Gordy, W. (1955). *J. Chem. Phys.* **23**, 1200

Verlet, L. (1967). *Phys. Rev.* **159**, 98

Waldman, M. and Hagler, A. T. (1993). *J. Comput. Chem.* **14**, 1077

Wang, J., Boyd, R. J. and Laaksonen, A. (1996). *J. Chem. Phys.* **104**, 7261

Wanna, J., Menapace, J. A. and Bernstein, E. R. (1986). *J. Chem. Phys.* **85**, 1795

Weitkamp, T., Neuefeind, J., Fischer, H. E. and Zeidler, M. D. (2000). *Mol. Phys.* **98**, 125

Wertz, D. L. and Kruh, R. K. (1967). *J. Chem. Phys.* **47**, 388

Wick, G. C. (1954). *Phys. Rev.* **94**, 1228

Williams, D. E. and Starr, T. L. (1977). *Comput. Chem.* **1**, 173

Williams, D. E. and Cox, S. R. (1984). *Acta Crystallogr.* **B40**, 404

Williams, D. E. and Houpt, D. J. (1986). *Acta Crystallogr.* **B42**, 286

Williams, D. E. (1992). *Rev. Comput. Chem.* **2**, 219

Windsor C. G. (1981). *Pulsed neutron scattering*. Taylor &Francis, London

Wood D. W. (1979). *Computer simulation of water and aqueous solutions in water*. A comprehensive treatise, Vol. 6: Recent Advances; edited by Franks, F. (Plenum)

Wormald, C. J. (1997). *Fluid Phase equilibria* **133**, 1

Wormald, C. J. and Sowden, C. J. (1997). *Int. J. Thermo.* **18**, 1465

Wright, D. and El-Shall, M. S. (1996). *J. Chem. Phys.* **105**, 11199

Yamaguchi, T., Hikada, K. and Soper, A. K. (1999). *Mol. Phys.* **96**, 1159

Yaws, C. L. (1977). *Physical properties, a guide*; McGraw-Hill: New York

Zachariasen, W. H. (1935). *J. Chem. Phys.* **1**, 158

Zinn, W. H. (1947). *Phys. Rev.* **71**, 752

Presentations and publications

Presentations at Conferences and Symposia

1. "Neutron diffraction studies of molecular liquids and liquid mixtures"
   Presented at the CCP5 spring school on methods in molecular simulation, University of Bristol, 1997 (6-11 April)

2. "Structural studies of molecular liquids and liquid mixtures by neutron diffraction"
   Talk given at the fifteenth international statistical mechanics & thermodynamics conference, Surrey university,1997 (16-18 April)

3. "Results of recent structural studies on liquid mixtures by neutron diffraction"
   Talk given at the ISIS liquid and amorphous user group meeting in abingdon (Oxfordshire) 24th June 1997

4. "Neutron diffraction studies of Benzene-Water liquid mixture"
   Talk given at the fifth Oxford summer school on neutron scattering 1997 (8-18 September)

5. "Structure of Molten Halides as revealed by Neutron, X-ray diffraction experiments and computer simulations".
   Presented at the European Research Conference on Molten Salts, June 27 - July 3 1998 (Porquerolles, France)

6. "Structural Studies of Benzene-Water and Benzene-Methanol Mixtures "
   Presented at the U.K. Neutron & Muon User Meeting 1998 (16-17 Sept.).

7. "Neutron diffraction and computer modelling: how the two techniques can reveal microscopic details of molecular liquids "
   Presented at the U.K. Liquid network workshop (5-7 Jan1999).

8. "The Structure of liquid methanol: A molecular dynamics study using a six-site model"
   Presented at the Lad celebration meeting, 29-30 March 1999.

9. "Structure of Benzene-Methanol Mixture and its pure components: neutron diffraction and computer modelling"
   Presented at the U.K. Neutron & Muon User Meeting 1999 (9-10 Sept.).

The published papers cited below have been removed from the e-thesis due to copyright restrictions

Publications:

1. "The structure of liquid methanol: a molecular dynamics study using a six-site model"
   Bianchi, L., Adya, A. K., Kalugin O. N. and Wormald, C. J.
   J. Phys: Condensed Matter (1999) **11**, 9151. (enclosed)

2. "Neutron Diffraction investigations of liquid methanol by H/D substitution technique"
   Adya, A. K., Bianchi L. and wormald, C. J.
   J. Chem. Phys. (2000) **112**, 4231. (enclosed)

3. "The structure of liquid methanol : a molecular dynamics simulation using three-site models"
   Bianchi, L., Kalugin, O.N., Adya, A. K. and Wormald, C. J.
   Molec. Simul. (2000), **25**. (enclosed)

4. "Structure of liquid benzene by neutron diffraction: a molecular dynamics study"
   Bianchi, L., Adya, A. K., Soper A. K. and Wormald, C. J.
   Mol. Phys. (to be submitted).

Two more papers reporting the experimental and simulated results of the benzene-methanol liquid mixture will be submitted this current year.